



**HAL**  
open science

# Coordination Chemistry Inspires Molecular Catalysis

Rinaldo Poli, Anne-Marie Caminade

► **To cite this version:**

Rinaldo Poli, Anne-Marie Caminade. Coordination Chemistry Inspires Molecular Catalysis. Zenodo, 2024, 10.5281/zenodo.10966127 . hal-04548441

**HAL Id: hal-04548441**

**<https://hal.science/hal-04548441v1>**

Submitted on 16 Apr 2024

**HAL** is a multi-disciplinary open access archive for the deposit and dissemination of scientific research documents, whether they are published or not. The documents may come from teaching and research institutions in France or abroad, or from public or private research centers.

L'archive ouverte pluridisciplinaire **HAL**, est destinée au dépôt et à la diffusion de documents scientifiques de niveau recherche, publiés ou non, émanant des établissements d'enseignement et de recherche français ou étrangers, des laboratoires publics ou privés.



Distributed under a Creative Commons Attribution 4.0 International License

Rinaldo POLI  
Anne-Marie CAMINADE

# Coordination Chemistry Inspires Molecular Catalysis

A book about the journey of 15 early stage researchers

ITN EJD  
2020 - 2024





# Coordination Chemistry Inspires Molecular Catalysis (CCIMC)

**Anne-Marie Caminade**, EDITOR

*Laboratoire de Chimie de Coordination, Toulouse*

**Rinaldo Poli**, EDITOR

*Laboratoire de Chimie de Coordination, Toulouse*

Developed from the Ph.D. Theses of 15 Early-Stage Researchers (ESRs), co-supervised within the framework of an Innovative Training Network (ITN) of the European Joint Doctorate (EJD) type, funded by the European Commission's Horizon 2020 Research and Innovation Programme (Marie Skłodowska-Curie grant agreement No 860322)





# The CCIMC Network

## Beneficiary Institutions

1. Centre National de la Recherche Scientifique – Laboratoire de Chimie de Coordination, Toulouse, France (Coordinator)
2. University of York, York, United Kingdom
3. Universitat Autònoma Barcelona, Bellaterra, Spain
4. Universitatea din Bucuresti, Bucharest, Romania
5. Universitat Rovira i Virgili, Tarragona, Spain
6. Uniwersytet Warszawski, Warsaw, Poland
7. Friedrich-Schiller-Universität, Jena, Germany
8. Universität Leipzig, Leipzig, Germany
9. Danmarks Tekniske Universitet, Lyngby, Denmark

## Partner Institutions

1. Université Paul Sabatier, Toulouse, France
2. Institut National Polytechnique, Toulouse, France
3. IFP Energies Nouvelles, Solaize, France
4. Fundacion Tecnalia Research & Innovation, San Sebastián, Spain
5. Henkel KGaA, Düsseldorf, Germany
6. Johnson Matthey PLC, Reading, United Kingdom
7. Elkem Silicones France SAS, Solaize, France
8. Rhodia Operations, Saint Fons, France
9. BASF SE, Ludwigshafen, Germany
10. Italmatch Chemicals S.p.A., Arese, Italy

## Early Stage Researchers

ESR1	Pawel KRZESINSKI	ESR9	Chantal J. ABOU-FAYSSAL
ESR2	Joris LANGLOIS	ESR10	Joel CEJAS SÁNCHEZ
ESR3	Irina BOZHINOVSKA	ESR11	Deepthy KRISHNAN
ESR4	Zinnia ARORA	ESR12	Max MILEWSKI
ESR5	Sara BONFANTE	ESR13	Massimo PETRICCONE
ESR6	Wimonsiri HUADSAI	ESR14	Aswin CHANDRAN
ESR7	Anastasiia SHERSTIUK	ESR15	Agustin MORALES
ESR8	Paven KISTEN		



UNIVERSITÄT  
LEIPZIG



UNIVERSITAT  
ROVIRA I VIRGILI



Danmarks  
Tekniske  
Universitet



# Table of Contents

ESR1. N-Heterocyclic Carbene Ligands Designed for Improved Stability and Efficiency of Ruthenium-Based Olefin Metathesis Catalysts <i>Pawel Krzesinski</i> .....	3
ESR2. Towards The Direct Synthesis Of Chiral Amines Via Asymmetric Rhodium Catalyzed Hydroaminomethylation Reactions <i>Joris Langlois</i> .....	21
ESR3. s-Block Metal-Mediated Hydroelementation <i>Irina Bozhinovska</i> .....	41
ESR4. Carbon Nanomaterial Supported Metal Complexes and Nanoparticles for Asymmetric Catalysis <i>Zinnia Arora</i> .....	59
ESR5. Zirconium- and Phosphine-assisted C–F Bond Activation and Functionalisation <i>Sara Bonfante</i> .....	79
ESR6. Activation of Carbon Dioxide with Highly Lewis Acidic Compounds <i>Wimonsiri Huadsai</i> .....	101
ESR7. Photoswitchable phosphines for light-modulated metal catalysts <i>Anastasiia Sherstiuk</i> .....	119
ESR8. Ir <sup>I</sup> ( $\eta^4$ -diene) Precatalyst Activation: Role of the Base <i>Paven Kisten</i> .....	137
ESR9. Metal Nanoparticles Embedded in Ligand- functionalized Water-soluble Core-shell Polymers for Application in Aqueous Biphasic Hydrogenation <i>Chantal J. Abou-Fayssal</i> .....	155
ESR10. Immobilization of Ruthenium Complexes on Supports. Applications in Catalysis <i>Joel Cejas Sánchez</i> .....	181
ESR11. Mono- and Bimetallic Nanoparticles Stabilized by Functionalized Ionic Liquids: Synthesis and Catalytic Applications <i>Deepthy Krishnan</i> .....	201
ESR12. Carboranylphosphines Meet Dendrimers: Electron-deficient Scaffolds for Ligand Design and Application in Catalysis <i>Max Milewski</i> .....	221
ESR13. Specifically Functionalized Dendrimers for Catalysis in Special Media <i>Massimo Petriccone</i> .....	235
ESR14. Coordination of Si–H and Ge–H Bonds to Ruthenium Metal Centres: Structure, Reactivity and Catalytic Applications <i>Aswin Chandran</i> .....	255
ESR15. Single Electron Reduction of NHC-CO <sub>2</sub> and NHC-CO <sub>2</sub> -BR <sub>3</sub> Adducts <i>Agustin Morales</i> .....	273





# Preface

This book collates, in fifteen chapters, the extended abstracts of the Ph.D. theses defended by the Early Stage Researchers (ESRs) who participated in the Innovative Training Network (ITN) entitled “Coordination Chemistry Inspires Molecular Catalysis” (CCIMC), which was a Network of the “European Joint Doctorate” (EJD) type. This project was funded by the the European Commission’s Horizon 2020 Research and Innovation Programme (Marie Skłodowska-Curie grant agreement No 860322) and was active between March 1<sup>st</sup>, 2020 and February 29<sup>th</sup>, 2024.

The main aim of the CCIMC project was the ESRs’ training on the basis of collaborative research projects and of an intense programme of training, comprising theoretical courses, tutorials, workshops, graded research reports, and the active participation of the ESRs in outreach and dissemination activities, as well as organizational efforts. Each ESR carried out his/her research jointly between two groups in two different research institutes (the Beneficiary Institutions) located in two different European countries. In addition, each ESR also received secondment research training in an industrial environment in one of the Partner Institutions (three months in most cases). At the end of their theses, the ESRs received a double or joint Doctorate Diploma on the basis of a bilateral agreement from the two academic institutions.

The research focus of the project was based on the development of catalytic processes, inspired by fundamental work in coordination chemistry. The various activities were classified in four work packages, covering the design and synthesis of innovative ligands, pre-catalyst development, new catalytic reactions and their mechanism, and the implementation of catalytic processes. The innovative ligand work package was particularly focused on N-heterocyclic carbenes (ESRs 1, 10, 15), on chirality (ESRs 2, 4, 8), on photoswitchable (ESR 7) and carborane-functionalized (ESR 12) phosphines, and on the immobilization of existing ligands on innovative supports such as nanostructured carbon materials (ESR 4), precision polymers (ESR 9), ionic liquids (ESR 11) and dendrimers (ESRs 10, 12, 13). Work on the pre-catalyst development comprised the implementation of the new ligands on known platforms for application in hydroaminomethylation (ESR 2), alkene metathesis (ESRs 1, 10), asymmetric (transfer) hydrogenation (ESR 8), and CO<sub>2</sub> reduction (ESR 15), the development of new catalytic systems including s-block metal complexes (ESRs 3, 6), metal complexes stabilized by Ge-based ligands (ESR 14) and new or better size- and morphology-controlled metal nanoparticles (ESRs 4, 9, 11), and the implementation of new confinement strategies on supports such as carbon nanotubes and graphene (ESR 4), precision polymers (ESR 9), dendrimers (ESRs 10, 12, 13) and ionic liquids (ESR 11). The work package on new catalytic reactions and mechanisms comprised new bond activation strategies, with the transformation of substrates with C-F bonds (ESR 5), reactions with organocalcium reagents (ESR 6), the organogermanation reaction (ESR 14), and the reductive C-C bond formation from CO<sub>2</sub> (ESR 15), as well as experimental and computational studies aimed at improving the Z-selectivity in olefin metathesis (ESR 1), the efficiency of tandem hydroaminomethylation (ESR 2), the stereocontrol in alkene hydroelementation (ESR 3), and at rationalizing the role of strong bases in the hydrogenation of polar substrates (ESR 8). Finally, work on the implementation of catalytic processes comprised the efforts towards achieving higher activities and/or new selectivities in known processes and to extend these to new substrates of industrial interest, all ESRs being involved in this project

objective. The fifteen chapters collected in this book give a brief overview of the main objectives and results obtained by each student.

We had the privilege and pleasure to coordinate this ITN-EJD, even though our task was not simple at the beginning: soon after the kickoff meeting, which took place at the beginning of March 2020, the Covid-19 pandemic broke out in Europe, significantly complicating not only the experimental work in the laboratories but also and especially the planned networking program. All interviews leading to the recruitment of the 15 ESRs and all networking activities for the first two years (1-week long events had been planned every 6 months), including the mid-term evaluation by the Project Office of the European Commission, had to be carried out online. Therefore, the ESRs did not have any opportunity to spend time together as a group until the pandemic faded away in the Spring of 2022. In spite of that, and thanks to the good will of the students and their supervisors, the project could be implemented more or less as initially planned. The fifteen ESRs finally managed to meet and spend exciting moments together, developing lifelong friendships.

The success of this ITN project would not have been possible without the devoted implication of our full-time project managers, first Candice George during the first 9 months and then Alida Lefter for the remainder of the project time, and beyond. We express our most heartfelt gratitude to these two outstanding coworkers for having made our Network coordination so smooth, taking off our shoulder such painful tasks as building and maintaining the web site, establishing the consortium agreement, leading the negotiations to establish the bilateral agreements and the amendments thereof, writing and uploading the project deliverables, organizing the Network events, and so forth. Our thanks also go to our academic colleagues and friends, who have supervised the research projects of the ESRs and have efficiently helped us manage the work packages and scientific tasks of the ITN. In addition, we wish to acknowledge and thank all the constructive input received from Jan Bäckvall, Matthias Beller and Giuliano Giambastiani, the three members of our Advisory Board, during our annual meetings with them.

Our most heartfelt feelings are for the fifteen ESRs. We are proud of what each one of them has become. We look forward to witnessing their future development and wish them success in their personal and professional endeavours.

We hope that reading this book will be enjoyable and perhaps inspirational for your own research efforts.

Anne-Marie CAMINADE  
CCIMC Deputy Coordinator

Rinaldo POLI  
CCIMC Coordinator

**Pawel KRZESINSKI**

**ESR1**

**Thesis co-directors**

Dr. Vincent César                      Laboratoire de Chimie de Coordination, Toulouse, France

Prof. Karol Grela                      Uniwersytet Warszawski, Warsaw, Poland

**Thesis defense**

Laboratoire de Chimie de Coordination, Toulouse, France, 12 February 2024



## N-Heterocyclic Carbene Ligands Designed for Improved Stability and Efficiency of Ruthenium-Based Olefin Metathesis Catalysts

### Introduction

No doubt catalysis is one of the most relevant tools used in the chemical industry, allowing to obtain a myriad of sometimes otherwise inaccessible molecules. Homogeneous catalysis has the advantage of more precise characterization of catalysts and intermediates which makes it more suitable for rational design. Catalyst's auxiliary ligands play a significant role in defining the activity, selectivity and stability of the resulting catalysts [1].

Almost all chemical reactions consist of a series of elementary steps, defined as a direct transformation of reactant molecules into products through a single transition state. Such a sequence of elementary steps is called a reaction mechanism and when it describes forms of catalyst, it is referred to as a catalytic cycle. A precatalyst is a stable compound that is used to generate the active catalyst *in situ* by a sort of activation process. An off-loop species is defined as a complex in equilibrium with a catalytic intermediate but itself not involved in the catalytic cycle. Finally, when the formation of an off-loop species is irreversible, catalyst deactivation takes place and the formed compound is called a dead or deactivated catalyst [2].

N-heterocyclic carbenes (NHCs) are neutral divalent carbon species having six valence electrons and at least one adjacent nitrogen atom. Nitrogen atoms are at the same time  $\sigma$ -electron-withdrawing and  $\pi$ -electron-donating. As a result, NHCs are singlet carbenes. One of the most significant advantages of NHCs is their relatively facile synthetic modularity which allows tuning of the ligand steric and electronic properties [3]. The overall electron-donating ability of the NHC ligands can be quantified by recording the average stretching frequency of the carbonyl ligands in complexes of nickel, rhodium and iridium [4]. The  $\sigma$ -donating properties can be assessed by measuring the  $^1\text{J}(\text{C}-\text{H})$  coupling constant between the carbon and the hydrogen atoms on the pre-carbenic position in the azolium precursors [5]. Furthermore,  $\pi$ -accepting abilities of the NHCs can be independently determined by recording the chemical shift of  $^{77}\text{Se}$  nuclei in corresponding seleno adducts [6].

Olefin metathesis (OM) is a carbon skeleton redistribution around an unsaturated carbon-carbon double bond by its scission and regeneration. The reaction is catalyzed by a transition metal complex. Considering ruthenium-based OM catalyst, the impact made by NHC ligands on this domain was arguably the greatest of all when compared with other transition metal catalysis. In 2005 Chauvin, Grubbs and Schrock were honored with The Nobel Prize in Chemistry for the development of the metathesis method in organic synthesis. Despite the incredible progress made in the discipline, there are still many hurdles to overcome, such as reaction stereoselectivity or the formation of tetrasubstituted carbon-carbon double bonds.

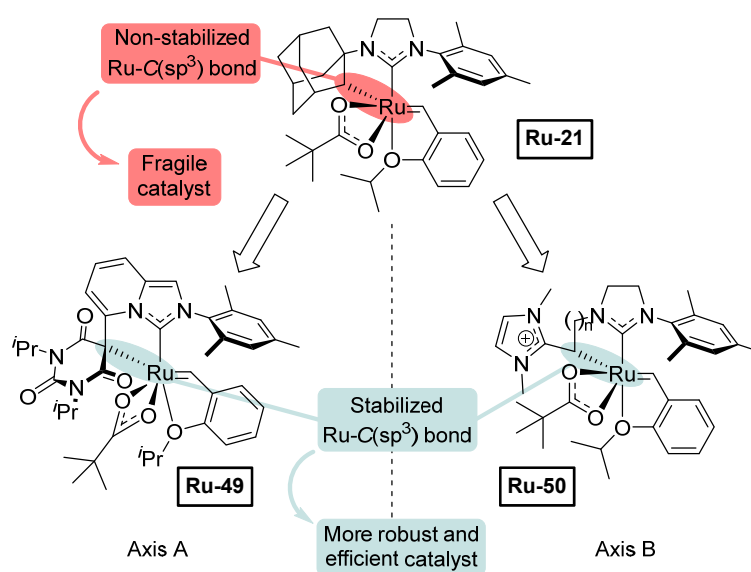
### Objectives of the thesis

The work described here aimed at NHC ligand design to give more stable, durable and thus more efficient OM catalysts. Two strategies were investigated to enhance the stability of corresponding NHC OM catalysts.

The first strategy builds on the solution presented by Grubbs and coworkers for a Z-selective OM catalyst bearing a chelating LX-type NHC ligand (**Ru21**, Scheme 1) [7]. The biggest weakness of those complexes derives from the presence of a ruthenium-alkyl bond which makes them prone to

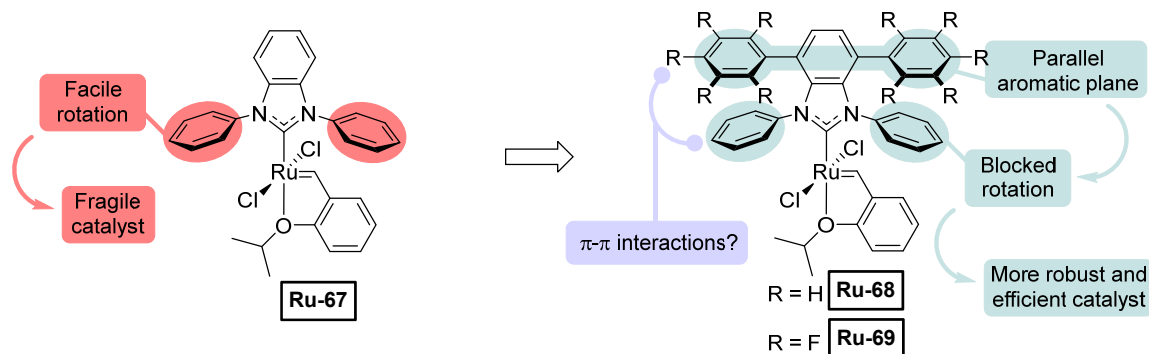
undergo decomposition pathways involving alkylidene ligand insertion into ruthenium-alkyl bond [8,9]. This work aimed at obtaining an OM catalyst bearing chelating NHC with a more stable ruthenium-carbon(sp<sup>3</sup>) bond. We envisaged that changing the adamantyl group to a more stabilized carbon ligand would result in a more durable catalyst. With those objectives in mind, we investigated the synthesis of bidentate NHC ligands comprising either a barbituric heterocycle (axis A) or *N*-heterocyclic olefin (NHO) moiety (axis B).

The imidazopyridinylidene NHC containing a barbituric heterocycle was chosen since it has proven a versatile platform for d<sup>6</sup> [Ru(II), Mn(I)] or d<sup>8</sup> [Pd(II), Rh(I), Ir(I), Au(III)] transition-metal centers, giving access to stable metal complexes [10]. However, the NHC-NHO ligand architecture is a completely novel approach and thus also interesting from the basic science perspective than application. Furthermore, the domain of NHO ligands is much less explored than the NHC field and examples of well-defined metal NHO complexes remain rather rare in literature [11].



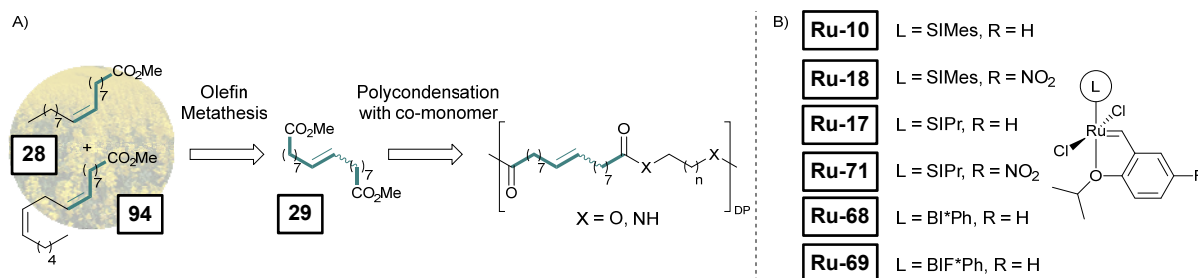
**Scheme 1.** The concept for a robust *Z*-selective OM catalyst.

The second strategy aimed at robust and efficient catalysts for the formation of tetrasubstituted carbon-carbon double bonds (Scheme 2). The commonly utilized approach is based on specialized ruthenium catalysts with sterically reduced NHC ligands, able to accommodate more crowded olefinic substrates during the catalytic steps (*e.g.* **Ru-67**) [12]. Yet, although highly active, these complexes are rather unstable, mainly due to intramolecular C-H activation at the ortho position of an *N*-aryl group of the NHC ligand, leading to catalyst deactivation [13]. Considering that the deleterious C-H activation process requires the rotation of the *N*-aryl arm of the NHC ligand, we reasoned that the introduction of a second decker of aromatic groups in benzimidazolyliedene-based *N*-phenyl NHC ligands would improve the stability and efficiency of the corresponding catalyst, while their activity in the challenging metathesis of sterically crowded bonds would be maintained. We also wanted to explore whether  $\pi$ - $\pi$  stacking interactions would contribute to blocking the rotation. For those purposes, attempted was the installation of phenyl groups into the backbone since the synthesis should be relatively feasible (**Ru-68**), but also pentafluorophenyl groups since it should result in stronger  $\pi$ - $\pi$  interactions (**Ru-69**).



**Scheme 2.** The concept for robust OM catalyst for the formation of tetrasubstituted carbon-carbon double bonds.

The last part of the work describes a potential application of the obtained catalytic systems in the synthesis of bio-based polyesters and polyamides (Scheme 3). To demonstrate the applicability of this study, a technical grade methyl oleate (**28**) was used as the starting material for the self-cross metathesis step. Such material derives from broadly available sunflower or rapeseed oil and contains a substantial amount (20 wt%) of methyl linoleate (**94**), which is the most abundant polyunsaturated fatty acid methyl ester (FAME). The resulting dimethyl octadec-9-enedioate (**29**) was used in a subsequent polycondensation reaction to obtain polymeric materials. In this research, we used commercially available catalysts and catalysts developed in the latter part.



**Scheme 3.** A) Proposed process of the synthesis of biobased polyesters and polyamides by self-CM of technical grade methyl oleate (**28**) and subsequent polycondensation reaction. B) Catalysts used in the study.

### Ruthenium complexes supported by a chelating NHC ligand comprising a barbituric heterocycle

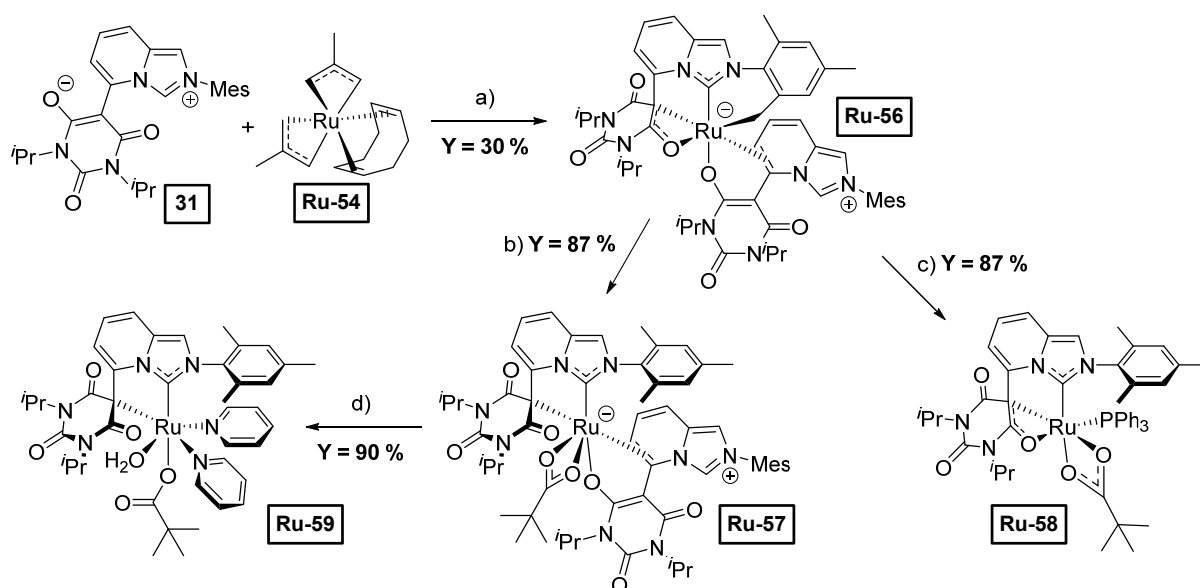
In this project complex **Ru-54** was studied as a metal precursor since its methallyl ligands could serve as an internal base to deprotonate the imidazopyridinium precursor **31** to form a ruthenium-NHC complex. The reaction of complex **Ru-54** with two equivalents of precursor **31** led to the formation of the stable complex **Ru-56** in 30 % isolated yield (Scheme 4). Indeed, the methallyl moiety of **Ru-54** served as an internal base to deprotonate the imidazopyridinium position of **31** and form a desired ruthenium-NHC complex. However, the reaction did not stop after the first protonolysis step and the second methallyl group was spent on the cyclometallation of the *ortho*-methyl group of the mesityl *N*-substituent. Surprisingly, rather than retain the cyclooctadiene (COD) ligand the metal center was stabilized by the coordination of a second molecule of imidazopyridinium precursor **31**. Interestingly, the coordination sphere was stabilized by the  $\eta^3$  coordination mode of the carbon-carbon-oxygen part of the malonate giving the 18e<sup>-</sup> complex **Ru-56**.

In the next step, we attempted to cleave the ruthenium-mesityl bond with the use of pivalic acid. Indeed, the reaction gave the complex **Ru-57** with free *N*-mesityl group, however, the coordination mode of barbituric heterocycle changed to  $\eta^1$ . Interestingly, when PPh<sub>3</sub> was added along



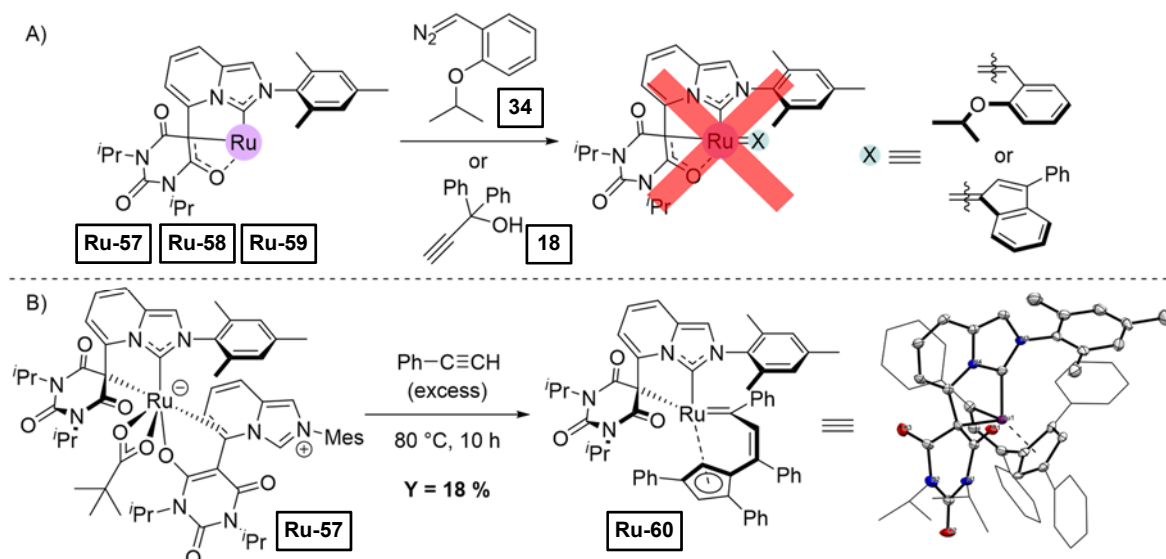
with pivalic acid, this resulted in complex **Ru-58** with  $\eta^3$  coordinated barbituric heterocycle. Furthermore, the steric bulk imposed by the barbituric heterocycle resulted in a *cis*-coordinated  $\text{PPh}_3$  ligand with respect to the NHC.

At last, we attempted the installation of the pyridine ligand in the hope of having a labile functionality suitable for the introduction of an alkylidene ligand. Indeed, the reaction of **Ru-57** with dry pyridine gave the complex **Ru-59** with two pyridine ligands coordinated, however, the crystal structure of **Ru-59** revealed a molecule of water coordinated as well. Since a dry substrate was used for this reaction, most probably the water was introduced during the working up of the reaction. All four new complexes were characterized using nuclear magnetic resonance (NMR) spectroscopy and X-ray diffractometry (XRD).



**Scheme 4.** Synthesis of ruthenium complexes **Ru-56**–**Ru-59** bearing the chelating NHC ligand. Reaction conditions: a) 2 equiv. of **31**, 1 equiv. of **Ru-54**, THF, 90 °C, 2 h; b) 2.2 equiv.  ${}^t\text{BuCO}_2\text{H}$ , THF, 80 °C, 15 h; c) 1.2 equiv.  $\text{PPh}_3$ , 1.2 equiv.  ${}^t\text{BuCO}_2\text{H}$ , DCE, 80 °C, 6 h; d) dry pyridine (excess), 80 °C, 2 h.

With the small library of ruthenium complexes bearing the targeted NHC ligand, the installation of an alkylidene ligand was attempted. First, the reaction of complexes **Ru-57**–**Ru-59** with diazomethane derivative **34** was tried, however, no reactivity was observed with the starting complexes remaining unchanged (Scheme 5A). Even the very promising pyridine derivative **Ru-59** exhibited no reactivity with **34**. Next, we attempted a reaction with propargyl alcohol **18** at 80 °C. This time a reactivity of the starting complexes was observed, however, no product could be isolated and characterized because a complex mixture of unidentified species was formed. At last, we turned our attention to phenylacetylene (Scheme 5B) as an alkylidene precursor. Quite similar reactivity pattern was observed to the reaction with **18** in the sense that a mixture of products was formed. However, this time it was possible to isolate the major product **Ru-60** from the reaction of **Ru-57** with phenylacetylene. Indeed, **Ru-60** contained an alkylidene functionality in its structure, however, an unexpected tetramerization of phenylacetylene occurred to form a cyclopentadienyl unit whose  $\eta^5$  coordination replaced the pivalic anion giving the piano stool complex **Ru-60** whose structure was confirmed by XRD.



**Scheme 5.** A) Attempts of reaction of complexes **Ru-57-Ru-59** with either diazomethane derivative **34** or propargyl alcohol derivative **18**. B) Reaction of complex **Ru-57** with phenylacetylene.

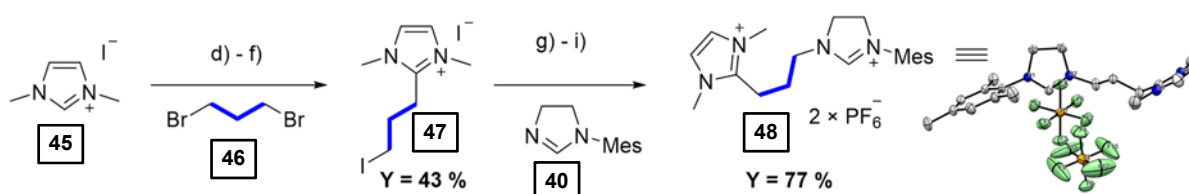
In summary, several ruthenium complexes bearing the targeted chelating NHC-barbiturate ligand were successfully synthesized. Depending on the nature of the other ligands present in the structure it was found that the barbiturate-derived NHC can flexibly accommodate between  $\eta^1$  coordination mode *via* malonate carbon and  $\eta^3$  *via* carbon-carbon-oxygen part of the malonate in order to stabilize the coordination sphere. Furthermore, the NHC-barbiturate ligand can even adopt a tetradentate coordination mode when the benzylic position of the *N*-mesityl NHC's substituent is cyclometalated (structure **Ru-56**).

It was possible to install an alkylidene ligand to a ruthenium complex bearing the chelating NHC-barbiturate ligand, however, an unexpected tetramerization of phenylacetylene occurred leading to the formation of a cyclopentadienyl co-ligand (complex **Ru-60**). Possibly isolation of complex **Ru-60** results from a preferred formation of ruthenium dicarbene species rather than the expected vinylidene complex.

### NHC-NHO ligand architecture

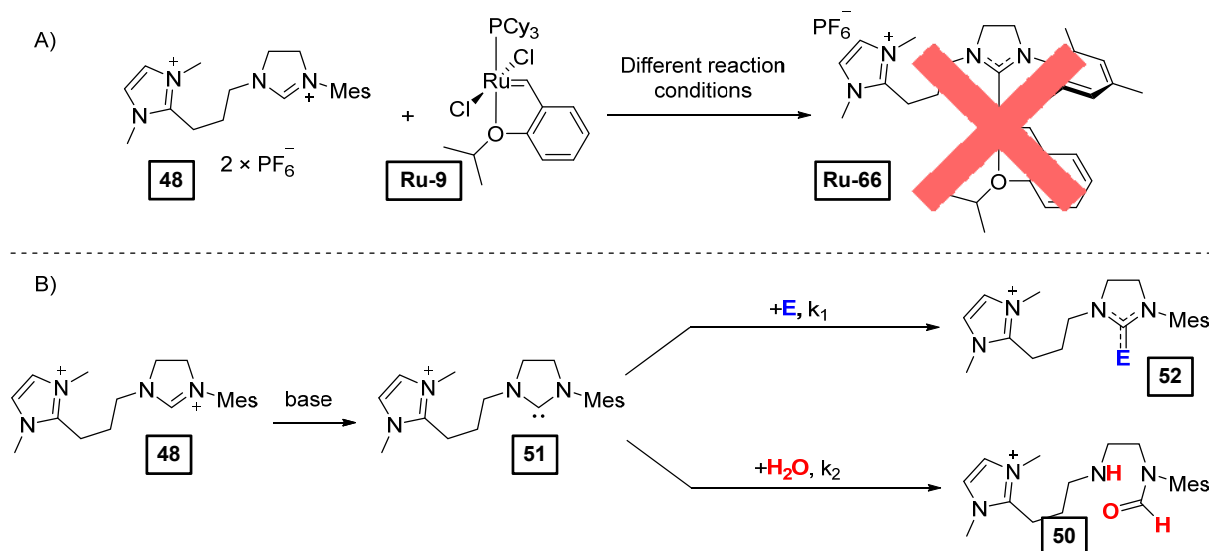
This project was started by the synthesis of the NHC-NHO ligand precursor **48** bearing an NHC and NHO pre-functionalities connected *via* two  $\text{CH}_2$  units (Scheme 6). From dimethylimidazolium iodide (**45**) the corresponding dimethylimidazolylidene NHC was formed by the deprotonation with lithium hexamethyldisilazide (LiHMDS) which next in a nucleophilic substitution reaction with 1,3-dibromopropane (**46**) and subsequent Finkelstein reaction gave the expected compound **47**. At last, ligand precursor **48** was obtained in the nucleophilic substitution reaction of **47** and *N*-mesitylimidazoline. The structure of **48** was confirmed by XRD.

With the NHC-NHO ligand precursor **48** in hand, the synthesis of the corresponding NHC-ruthenium OM catalyst (**Ru-66**, Scheme 7A) was attempted. However, no displacement of the  $\text{PCy}_3$  ligand from complex **Ru-9** by the postulated *in situ* generated NHC ligand derived from **48** was observed. We decided to shift at this point from the attempts to synthesize the corresponding ruthenium NHC catalysts and focus on a general study of the novel NHC-NHO ligand architecture.



**Scheme 6.** The synthesis of the second NHC-NHO ligand precursor **48** and its XRD structure (ellipsoids are drawn at 50 % probability, hydrogens were omitted for clarity); reaction conditions: d) 1.05 equiv. of LiHMDS, THF, rt, 80 min.; e) 20 equiv. of **46**,  $-80\text{ }^{\circ}\text{C}$  to rt, overnight. f) 5 equiv. of NaI, acetone, rt, overnight; g) 1.3 equiv. of **40**, MeCN,  $90\text{ }^{\circ}\text{C}$ , overnight; h) 3.4 equiv. of AgCl, water, rt, 30 min.; i) 5.6 equiv. of  $\text{KPF}_6$ , DCM,  $40\text{ }^{\circ}\text{C}$ , 7 days.

To better understand why the complex **Ru-66** was not formed, reactivity studies of the NHC-NHO were performed. We found that once the imidazolium position of **48** is deprotonated the formed NHC **51** can undergo two competing reactions (Scheme 7B). **51** can either form the desired complex with the electrophile (**52**), however, the imidazolynylidene ring can open due to the presence of traces of water, which gives *N*-formylated product **50**. It became clear at this point why the synthesis of the ruthenium-NHC complex **Ru-66** failed. The energy barrier of  $\text{PCy}_3$  replacement with an NHC in the structure of **Ru-9** is usually relatively high as heating is required. Consequently, the formation of the side product **50** is preferred instead.

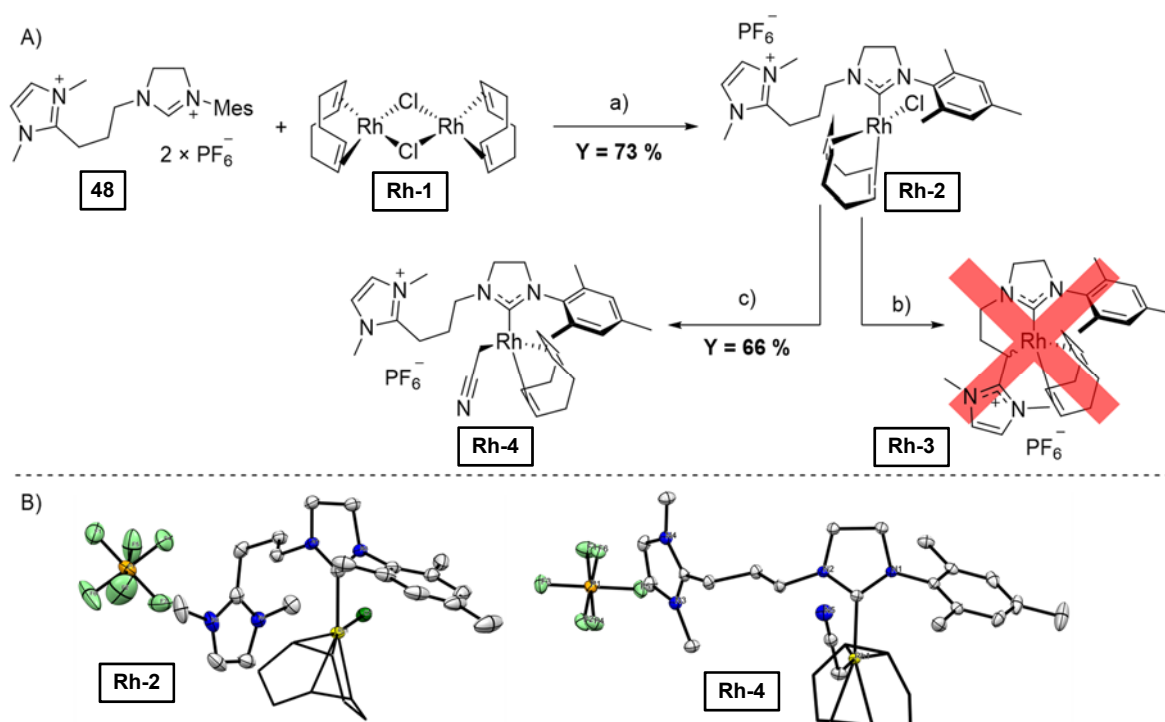


**Scheme 7.** A) The attempted synthesis of **Ru-66**. B) Proposed explanation for the observed reactivity of carbene **51**.

Learning the general reactivity pattern of our ligand, we set off to synthesize a metal complex bearing the targeted ligand coordinated in a monodentate mode through NHC and next attempt the coordination of the NHO moiety. We hypothesized that a dimeric structure of metal precursor might be reactive enough to give a metal-NHC complex in a good yield. Rhodium(I) metal center was chosen as the corresponding NHC complex should be air-stable, isolatable by column chromatography (CC) and after installation of CO ligands allow for measuring the ligand's electronic properties. Indeed, utilizing dimeric rhodium precursor **Rh-1** proved to be a good strategy and gave the rhodium-NHC complex **Rh-2** isolated by CC in 73 % yield (Scheme 8A). The structure of **Rh-2** was confirmed by XRD (Scheme 8B).

In the next step, deprotonation of the  $\alpha$ -imidazolium position was attempted in the hope of forming the corresponding NHO complex. When the reaction was performed in THF, although complex

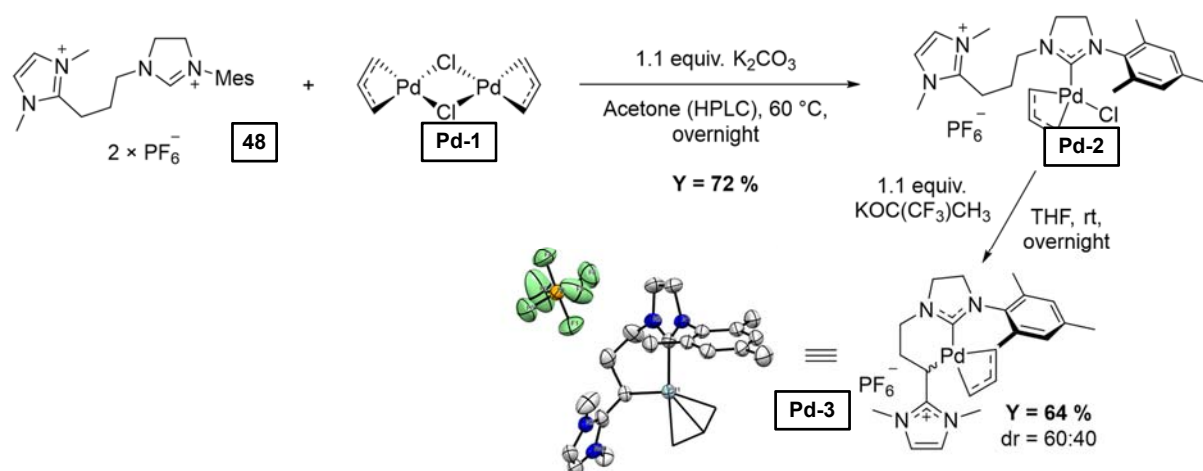
**Rh-2** reactivity was observed, no rhodium-NHC-NHO complex **Rh-3** could be isolated. Most probably an alkoxy ligand replaced chloride, although for unclear reasons the desired product **Rh-3** was not formed. Interestingly, when the same reaction was attempted in acetonitrile isolated was complex **Rh-4** bearing acetonitrile deprotonated ligand which replaced the chloride. Although rather unstable in air or in solution, complex **Rh-4** was characterized by NMR and XRD. To the best of our knowledge, no cyanomethyl rhodium complex has been reported so far.



**Scheme 8.** A) Synthesis of rhodium-NHC complex **Rh-2**, rhodium-NHC-cyanomethyl complex **Rh-4** and attempts to synthesize the rhodium-NHC-NHO complex **Rh-3**; reaction conditions: a) 0.5 equiv. of **48**, 1.1 equiv.  $K_2CO_3$ , acetone (HPLC), 60 °C, overnight; b) 1.1 equiv.  $KOtBu$ , THF, rt; c) 1.1 equiv.  $KOtBu$ , acetonitrile, rt, 4 h. B) XRD crystal structures of **Rh-2** and **Rh-4**, ellipsoids are drawn at 50 % probability, hydrogens were omitted for clarity.

With the met obstacles in the cyclometallation of a rhodium complex, we next turn our attention to palladium metal in the hope that it will be possible to obtain a palladium-NHC-NHO complex. Similarly to the case of **Rh-1**, utilizing a dimeric palladium precursor **Pd-1** gave the desired palladium-NHC complex **Pd-2** in a good yield of 71 % (Scheme 9). Furthermore, deprotonation of  $\alpha$ -imidazolium position in **Pd-2** gave the expected cyclometalated palladium-NHC-NHO complex **Pd-3** in 64 % yield. Diastereomers of **Pd-3** were formed in dr of 60:40. The structure of **Pd-3** was confirmed with XRD.

In summary, an NHC-NHO ligand precursor **48** was successfully obtained, however, the formation of the corresponding ruthenium-NHC complex was precluded due to an unexpected ring opening of the formed imidazolinyldene heterocycle. The reactivity of the novel class NHC-NHO ligand was explored in the coordination chemistry of rhodium(I) and palladium(II) metal centers, ultimately leading to the synthesis of the first NHC-NHO complex based on palladium. Furthermore, the first rhodium-cyanomethyl complex supported with the NHC ligand was obtained.



**Scheme 9.** Synthesis of the palladium-NHC-NHO complex **Pd-3** and its XRD crystal structure (ellipsoids are drawn at 30 % probability, hydrogens were omitted for clarity).

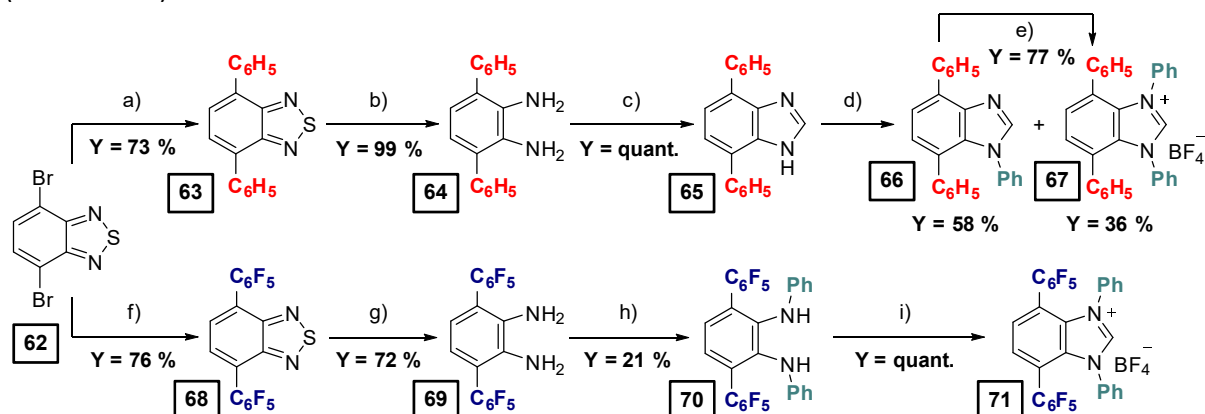
### NHC ligands bearing parallelly-stacked aromatics for efficient OM catalysts in tetrasubstituted C-C double bond formation

Commercially available 4,7-dibromo-2,1,3-benzothiadiazole (**62**) was chosen as a precursor for both phenyl and pentafluorophenyl substituted benzimidazolium salts **67** and **71** (Scheme 10). Suzuki coupling allowed for the installation of phenyl groups in the backbone motif giving functionalized benzothiadiazole **63** in 73 % yield and subsequent reductive sulfur extrusion gave access to the *o*-phenylenediamine derivative **64** in 99 % yield. Next, the bicyclic benzimidazole skeleton was obtained using standard cyclization protocol with triethyl orthoformate, affording **65** in quantitative yield. Products **63**, **64** and **65** were obtained on a gram scale without any purification steps by CC. In the final step, the desired benzimidazolium salt **67** was obtained using copper-catalyzed arylation with diphenyliodonium tetrafluoroborate. Although examples of *N*-R substituted imidazoles arylations to corresponding imidazolium salts can be found in the literature, as well as arylations from NH imidazoles to corresponding *N*-aryl imidazoles, worth highlighting is that such direct arylation of NH imidazole to imidazolium salt has never been reported in the literature. This protocol gave a mixture of the desired *N,N'*-diphenylbenzimidazolium salt **67** (36 % isolated yield) and neutral *N*-phenylbenzimidazole **66** (58 % isolated yield) which were separated using CC. The succeeding arylation of isolated **66** gave salt **67** in 77 % yield, therefore the two subsequent arylation reactions led to an overall yield of 81 % in compound **67**.

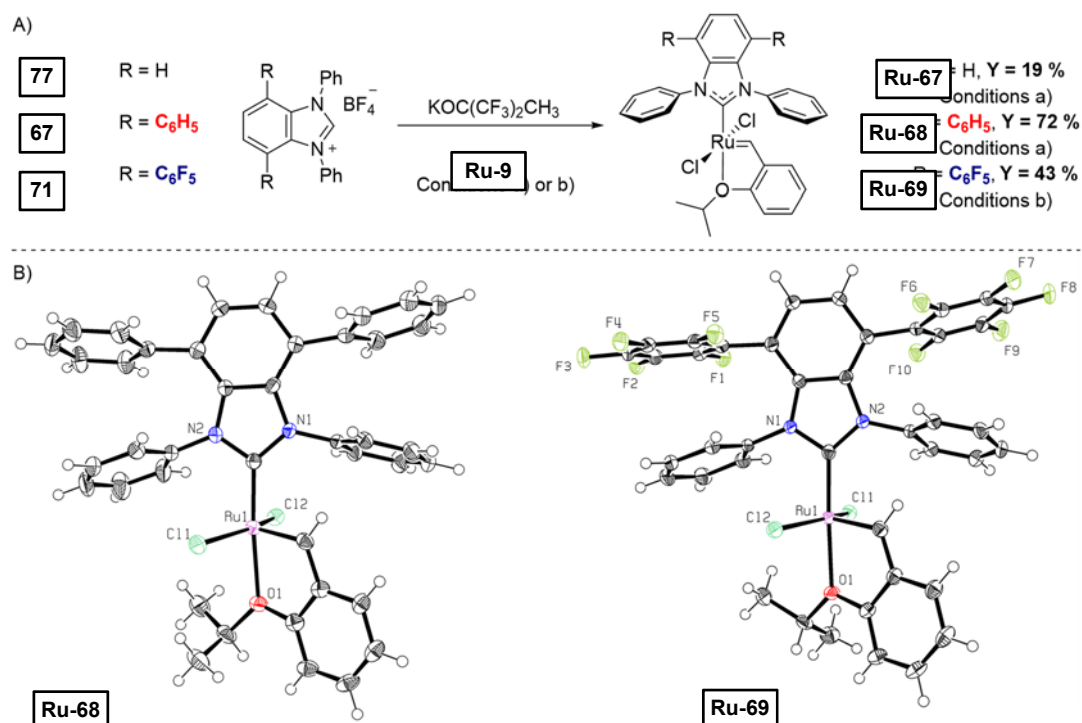
Synthesis of pentafluorophenyl substituted derivative **71** presented more synthetic challenges. A Kumada-Corriu coupling was successfully employed to graft pentafluorophenyl groups into the benzothiadiazole motif giving **68** in 76 % yield. The subsequent reductive sulfur extrusion step gave the *o*-phenylenediamine derivative **69** in 72 % yield. Unlike the synthesis of salt **67**, the *N*-phenyl groups were first installed through a Buchwald-Hartwig amination, giving compound **70** in 21% isolated yield. In a final step, the benzimidazolium salt **71** was obtained with quantitative yield using a modified cyclization protocol using triethyl orthoformate in the presence of  $\text{HBF}_4 \cdot \text{Et}_2\text{O}$ .

The corresponding Hoveyda-Grubbs complexes were obtained by displacement of the  $\text{PCy}_3$  ligand in **Ru-9** ruthenium precursor by the free NHCs generated using  $\text{KOC}(\text{CF}_3)\text{CH}_3$  as a base (Scheme 11A). Complex **Ru-69** was isolated using column chromatography, whereas complex **Ru-68** was purified by simple crystallization from a tetrahydrofuran-pentane mixture. Both complexes (brown-orange solids) are stable for months when stored in a protective atmosphere. It is noteworthy that upon

synthesis of known **Ru-67** we noticed its fragility when column chromatography was performed with regular solvents. Even with carefully degassed dry solvents, complex **Ru-67** was obtained in 19 % yield only, which is considerably lower than in the case of **Ru-68** and **Ru-69**, 72 % and 43 % respectively. The molecular structures of complexes **Ru-68** and **Ru-69** were confirmed by XRD experiments on single crystals grown by layering DCM complex solutions of **Ru-68** and **Ru-69** with pentane, respectively (Scheme 11B).



**Scheme 10.** Synthesis of benzimidazolium salts **67** and **71**; reaction conditions: a) 2.1 equiv. of  $\text{PhB(OH)}_2$ , 4 equiv. of  $\text{K}_2\text{CO}_3$ , 0.8 mol%  $\text{Pd(PPh}_3)_4$ , toluene/water 2.5 : 1 v/v, reflux, overnight; b) 9 equiv. of  $\text{NaBH}_4$ , 6 mol%  $\text{CoCl}_2 \times 6\text{H}_2\text{O}$ ,  $\text{EtOH/THF}$  3:1 v/v, reflux, 3 h; c)  $(\text{EtO})_3\text{CH}$  (excess), 6 equiv. of  $\text{HCl}_{\text{aq}}$ , reflux, overnight; d) 2 x 2 equiv. of  $\text{Ph}_2\text{IBF}_4$ , 2 x 5 mol%  $\text{Cu(OAc)}_2 \times \text{H}_2\text{O}$ ,  $\text{DMF}$ , 100 °C, 24 h, then 48 h; e) 2 equiv. of  $\text{Ph}_2\text{IBF}_4$ , 7.5 mol%  $\text{Cu(OAc)}_2 \times \text{H}_2\text{O}$ ,  $\text{DMF}$ , 100 °C, overnight; f) 3 equiv. of  $\text{BrMgC}_6\text{F}_5$ , 10 mol%  $\text{Pd(PPh}_3)_3$ ,  $\text{THF}$ , 70 °C, overnight; g) 3 equiv. of  $\text{NaBH}_4$ , 7 mol%  $\text{CoCl}_2 \times 6\text{H}_2\text{O}$ ,  $\text{EtOH/THF}$  3:1 v/v, 50 °C, 1 min. 30 sec.; h)  $\text{PhBr}$  (excess), 2.5 mol%  $\text{Pd}_2(\text{dba})_3$ , 7.5 mol%  $\text{P}^t\text{Bu}_3$ , 1.5 equiv. of  $\text{KHMDS}$ , 160 °C, 30 min.; i)  $(\text{EtO})_3\text{CH}$  (excess), 1 equiv. of  $\text{HBF}_4 \cdot \text{Et}_2\text{O}$ , 60 °C, 30 min.



**Scheme 11.** A) Synthesis of **Ru-67**, **Ru-68** and **Ru-69**; reaction conditions: a) 1.75 equiv. of **77** or **67**, 1.75 equiv.  $\text{KOC(CF}_3)_2\text{CH}_3$ , benzene, rt, 30 min. then 1 equiv. **Ru-9**, 60 °C, 1 h; b) 1.75 equiv. of **71**, 2 equiv. of  $\text{KOC(CF}_3)_2\text{CH}_3$ , benzene, rt, 15 min. then 1 equiv. of **Ru-9**, 60 °C, 30 min. B) XRD structure of **Ru-68** and **Ru-69**, ellipsoids are drawn at 50% probability.

The stability of the two newly obtained biplane-type NHC ruthenium complexes **Ru-68** and **Ru-69** was then quantitatively monitored and compared with the benchmark **Ru-67**. Since NHC ligand remains coordinated to the metal center throughout the entire catalytic cycle, the differences in complexes' stability should directly translate to the stability of actual propagating species, thus conveying their effectiveness in catalysis. Gratifyingly, **Ru-68** and **Ru-69** remained perfectly unchanged for approximately three weeks in solution at ambient temperature, while **Ru-67** slowly degraded to around 50% of the initial amount (Figure 1A, left). This fact confirmed our previous observation that upon isolation the top-covered complexes **Ru-68** and **Ru-69** are considerably more stable than **Ru-67**. Furthermore, the differences in stability were even more pronounced at higher temperature (Figure 1A, right), where **Ru-67** disappeared completely after about 27 hours while **Ru-68** and **Ru-69** were still detectable even after more than 100 hours in solution at 80 °C. Furthermore, the elevated temperature allowed to distinguish **Ru-68** from **Ru-69** in terms of stability and **Ru-69** proved to be the more stable pre-catalyst, which we assign to the beneficial impact of the  $\pi$ - $\pi$  interactions between *N*-phenyl groups and pentafluorophenyl backbone motifs.

To unambiguously confirm the nature of the catalyst deactivation pathway, we attempted to isolate the degradation product of **Ru-67**. The previous report featuring isolation and characterization of the decomposition product from BIPh ruthenium OM catalyst describes only its PCy<sub>3</sub> derivative. After steering **Ru-68** in dichloromethane at 40 °C for one week, the expected, tethered  $\eta^6$ -arene-NHC ruthenium complex **Ru-70** was isolated (Figure 1B), whose formation should proceed through the activation of an ortho C-H bond of one *N*-phenyl group followed by insertion into the alkylidene. The molecular structure of complex **Ru-70** was confirmed by XRD experiments on single crystals grown by layering dichloromethane complex solution with pentane.

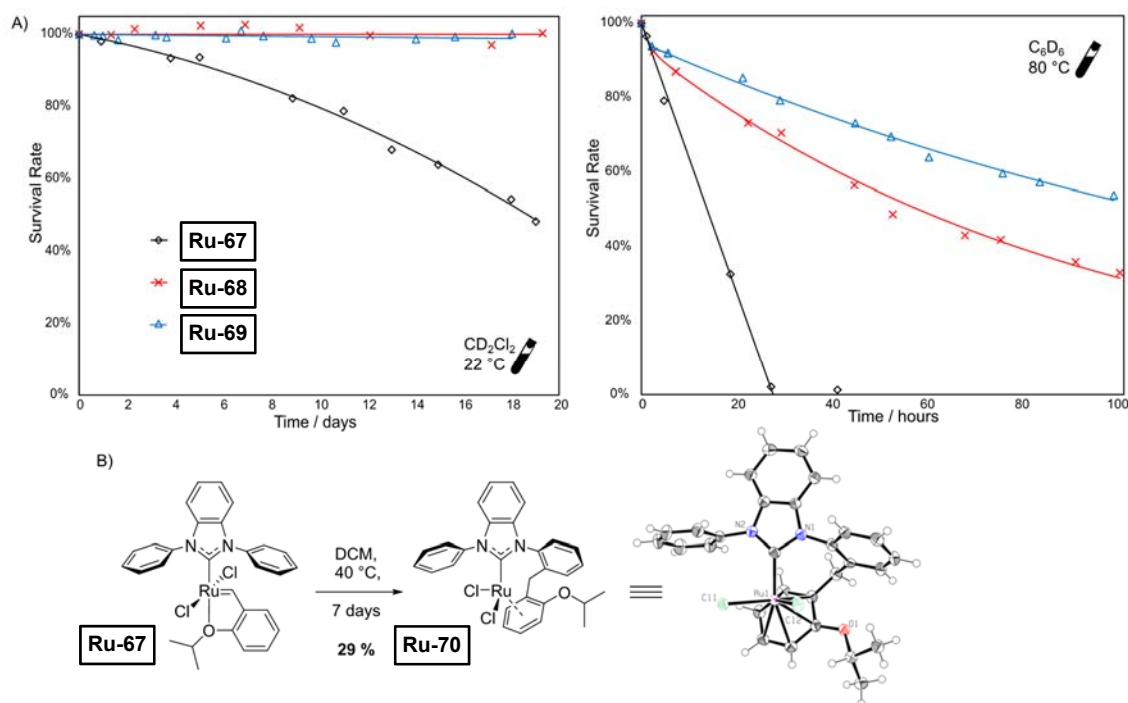


**Figure 1.** A) Stability tests in solution at ambient and elevated temperature. Measured by NMR (1,3,5-trimethoxybenzene added as reference). Lines are visual aid only. Conditions: (left) CD<sub>2</sub>Cl<sub>2</sub> at 22 °C, under argon; (right) C<sub>6</sub>D<sub>6</sub> at 80 °C, under argon. B) study of the decomposition of the complex **Ru-67** into the complex **Ru-70** and XRD structure of complex **Ru-70** (ellipsoids are drawn at 50% probability).

The catalytic performance of the new, “stacked” complexes was compared with the known benchmark **Ru-67** using a set of model reactions. Firstly, we checked their activity in RCM with tetrasubstituted carbon-carbon double bond formation. For that purpose diethyl 2,2-di(2-methylallyl)malonate (**78a**) was chosen as the model substrate and the time-conversion plots of its RCM reaction were constructed with 0.2 mol% of each catalyst, in toluene, at 80 °C (Figure 2). All complexes exhibited high activity, affording considerable conversions within the first 30 minutes, however, the reaction catalyzed by **Ru-67** reached its limits at a significantly lower conversion than the one recorded with **Ru-68** and **Ru-69**. This can be attributed to a more stable 14 e<sup>-</sup> catalytic species formed from the latter pre-catalysts versus those generated from **Ru-67**. Interestingly, although **Ru-68** gave higher conversions than **Ru-69** within the first hour of the reaction, after this point the trend reversed leading to 96 % conversion with **Ru-69** versus 91 % with **Ru-68** after 5 hours (and 72 % for the benchmark **Ru-67**).

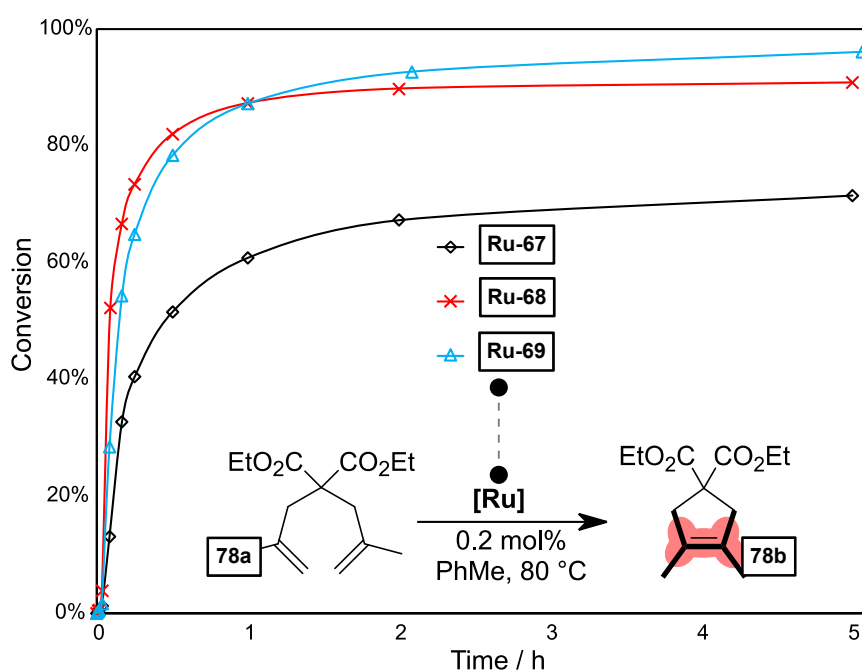
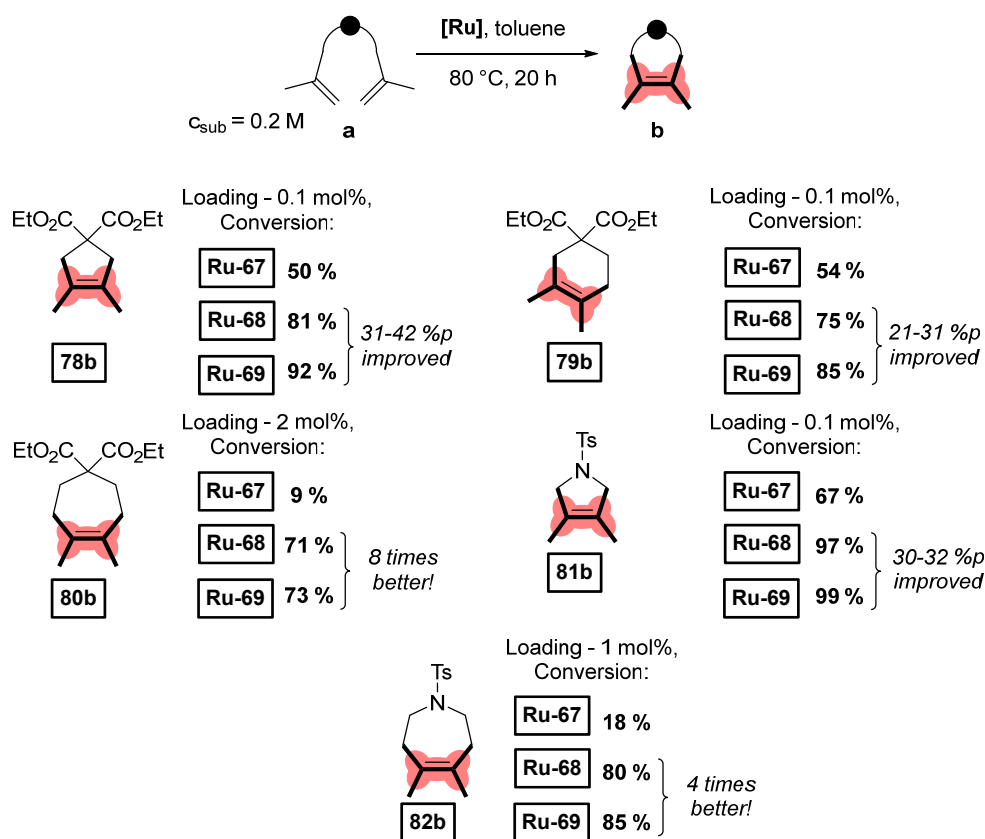


**Figure 2.** Time-conversion curves in RCM of diene **78a**. Conditions: catalyst 0.2 mol%, toluene, 80 °C under argon. Measured by GC with 1,3,5-trimethoxybenzene added as internal standard. Lines are visual aid only.

To further examine the differences in catalyst productivity, the previously described reaction of **78a** was reattempted at two times lower catalyst loading of 0.1 mol% (Scheme 12). The trend observed earlier was maintained and **Ru-67** gave a rather poor conversion for such reaction (50 %), whereas **Ru-68** and **Ru-69** gave much higher conversions of 81 % and 92 % respectively. The three BIPh-type catalysts were further tested in five more challenging RCM reactions featuring tetrasubstituted double carbon-carbon bond formation. Similar was the case of the formation of the six-membered ring (malonate **79b**) and five-membered tosylamide **81b**, where **Ru-68** and **Ru-69** gave up to 32 percentage points (%p) higher substrate conversions compared to **Ru-67**. The fluorinated complex **Ru-69** slightly but noticeably outperformed **Ru-68** in those two latter reactions. The superiority of the new catalysts **Ru-68** and **Ru-68** was even more pronounced in the more challenging formation of a less thermodynamically favored seven-membered ring (compounds **80b** and **82b**). In these latter cases, a higher catalyst loading of 2 mol% with malonate **80a** and 1 mol% with tosylamide **82b** was required to



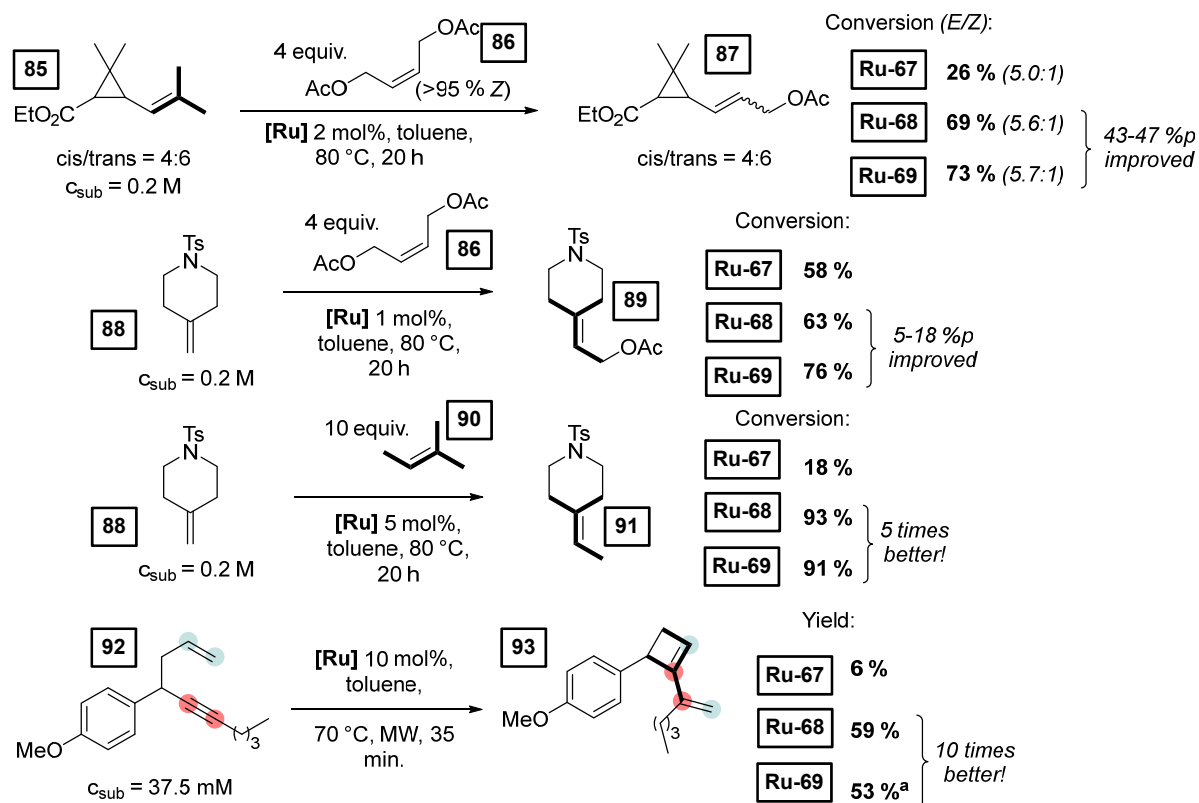
reach suitable conversions, however, such loading is still considered low in the context of the challenging formation of carbon–carbon tetrasubstituted bonds. Noteworthy, **Ru-68** and **Ru-69** gave conversions 4 to 8 times higher than **Ru-67** and again **Ru-69** was slightly better than **Ru-68** which overall correlates with the observed trend in stability tests.



**Scheme 12.** Scope and limitation study of catalysts **Ru-67**, **Ru-68** and **Ru-69** in RCM of challenging substrates. %p – percentage point difference from **Ru-67**.

To further evaluate the scope and limitations of catalysts **Ru-68** and **Ru-69**, several challenging CM reactions were investigated (Scheme 13). First, we studied the reaction between ethyl chrysanthemate (**85**) and Z-1,4-diacetoxy-2-butene (**86**). Catalysts **Ru-68** and **Ru-69** gave similar conversions of **85**, 69 % and 73 % respectively, giving product **87** selectively, whereas known **Ru-67** provided only 26 % of conversion. Next, the functionalization of the geminal carbon-carbon double bond of 4-methylene-1-tosylpiperidine (**88**) with either **86** or amylen (**90**) was probed. In the case of reaction with **86**, the use of **Ru-68** and **Ru-69** allowed for conversions up to 18 %p higher compared to benchmark **Ru-67**, leading to 76 % conversion for **Ru-69**.

Noteworthy, in the example of CM of **88** with amylen, the double-decker NHC catalysts **Ru-68** and **Ru-69** gave almost quantitative conversions of **88**, 93 % and 91 % respectively, which was 5 times higher than in the case of **Ru-67** reaching only 18 %. Last but not least, the highly challenging 1,5-enyne metathesis of substrate **92** to obtain crowded and strained cyclobutene derivative **93** was attempted. An additional difficulty arising in this reaction is that its selectivity can be compromised by a competing self-CM side reaction and by degradation of the resulting highly strained product. We were pleased to find that catalysts **Ru-68** and **Ru-69** gave good yields of 59 % and 53 % respectively, which was around 10 times higher than with **Ru-67** forming only traces of product which amounted to a 6 % yield.



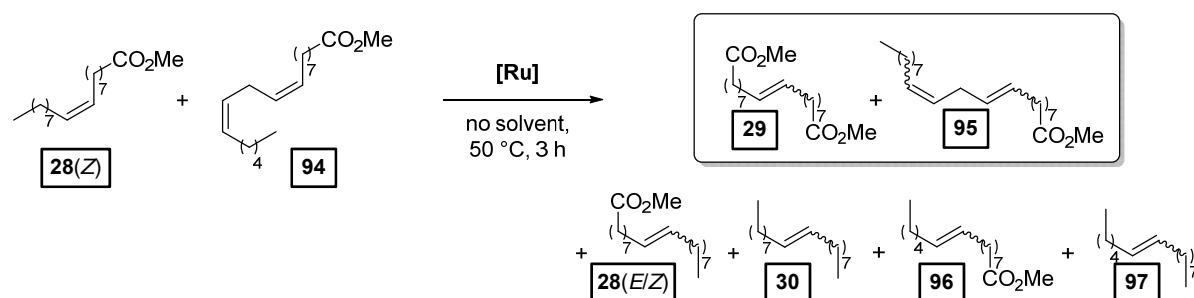
**Scheme 13.** Scope and limitation study of catalysts **Ru-67**, **Ru-68** and **Ru-69** in CM and cycloisomerization of challenging substrates. <sup>a</sup> Reaction conducted in perfluorotoluene. %p – percentage point difference from **Ru-67**.

In summary, we developed the two new biplane-type NHC ligands based on a benzimidazolylidene core, whose lower wings are set as *N*-phenyl rings to reduce their steric hindrance on the first coordination sphere and whose upper wings are phenyl or pentafluorophenyl rings, respectively. The corresponding second-generation Grubbs-Hoveyda complexes **Ru-68** and **Ru-69** were generated. Importantly, both complexes **Ru-68** and **Ru-69** were shown to be significantly more stable than the known BIPh-supported complex **Ru-67**. Moreover, the observed increased stability of the ruthenium precursors **Ru-68** and **Ru-69** was also translated to the active species and enabled their implementation as highly efficient, stable pre-catalysts in challenging olefin metathesis reactions for the formation of tri- and tetra-substituted carbon-carbon double bonds.

### CM of technical grade methyl oleate for the synthesis of bio-based polyesters and polyamides

We started off with the self-CM of **28(Z)** after its prior simple distillation from activated alumina to decrease the content of catalyst poisons. 100 ppm of **Ru-10** allowed to reach equilibrium in 3 h (50 °C, no solvent, Table 1, entry 1). Even though the reaction mixture contained a variety of products including several internal alkenes and monoesters (**28(E/Z)**, **30**, **95**, **96**, **97**), we were pleased to find that the equilibrium mixture contained predominantly **29** as a diester species. Upon decreasing the catalyst loading, we noticed that monoester **95** was also present in the reaction mixture and that the relation was inversely proportional (Table 1, entries 1-3). This suggests that at loadings lower than 100 ppm of **Ru-10** the reaction equilibrium is not reached. We wanted to avoid any monofunctional species such as **28**, **95**, or **96** in the isolated product since they would lead to a lower molecular mass of the resulting polyester, as monoesters would terminate a polymer chain. From gas chromatography, we

deduced that boiling temperatures of **95** and **29** would be very similar, which would make the purification of **29** challenging. Hence, we decided to focus on minimizing the formation of **95** as the primary objective of catalyst screening, rather than maximizing catalyst efficiency.



**Scheme 14.** Self-CM of methyl oleate (**28**) with 20 wt% of methyl linoleate (**94**) and the observed products.

All of the complexes gave reasonably similar conversions of substrates **28(Z)** and **94** around 95 %, except for **Ru-69** giving a lower 91 %. Catalysts **Ru-10**, **Ru-18**, **Ru-17** and **Ru-71** gave a ratio of **29** to **95** above 90:10, with **Ru-10** and **Ru-71** exceeding 95:5. **Ru-68** and **Ru-69** yielded much higher amounts of **95**, which can be attributed to their higher fragility due to lower steric protection of the NHCs. **Ru-10** gave a slightly higher yield of **29** than catalyst **Ru-71** (54 % versus 49 % respectively, the maximal yield being approximately 50 % resulting from the reaction equilibrium) and therefore it was chosen to continue with the development.

**Table 1.** Results of catalyst screening.

Entry	Catalyst	Loading [ppm]	Conversion of <b>28(Z)</b> + <b>94</b> [%]	Yield of <b>29</b> [%]	<b>29</b> to <b>95</b> wt. ratio	<i>E</i> to <i>Z</i> ratio of <b>29</b>
1		100	95	54	96:4	84:16
2	<b>Ru-10</b>	50	94	51	89:11	82:18
3		25	80	26	63:37	78:22
4	<b>Ru-18</b>		94	45	90:10	82:18
5	<b>Ru-17</b>		94	54	92:8	82:18
6	<b>Ru-71</b>	100	95	49	96:4	82:18
7	<b>Ru-68</b>		94	50	82:18	82:18
8	<b>Ru-69</b>		91	42	70:30	80:20

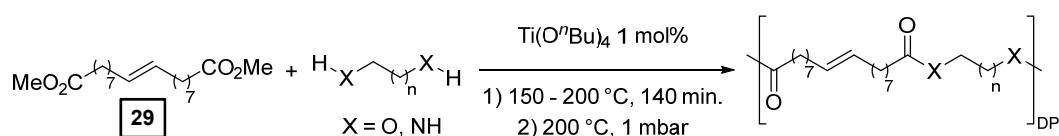
Reaction conditions: no solvent, 50 °C, 3 h.

With the selected catalyst, self-CM of methyl oleate was conducted with 300 g of substrate. After the reaction, product **29** was isolated by fractional distillation and subsequently purified by crystallization from methanol at -30 °C. Interestingly, this protocol gave pure **29** containing almost only *E* isomer (*E/Z* ratio of 97:3) in 36 % yield.

Having monomer **29** in hand, we attempted the melt polycondensation reaction with different co-monomers (Scheme 15). Titanium *n*-butoxide was used as the catalyst for this reaction. This

resulted in a red-brown solid insoluble in all the most common solvents including trifluoroacetic acid. This stood in contradiction to the findings reported by Warwel et al, where authors claimed to characterize the same polyesters using gel permeation chromatography (GPC), although no experimental data was provided thereof [14]. To confirm the formation of macromolecules, the reaction was stopped at an earlier stage and the formed oligomers (soluble in conventional organic solvents) were characterized by NMR spectroscopy.

The obtained oligomers and polymers were characterized by differential scanning calorimetry (DSC) and thermogravimetric analysis (TGA). The obtained polyesters have relatively low melting temperatures between 9 and 42 °C (Table 2, entries 1 – 7), which is characteristic of linear aliphatic polyesters. Significantly higher was the melting temperature for polyamide (152 °C, Table 2, entry 8), which is due to the formation of hydrogen bonds in comparison to polyesters. Heats of fusion varied from 25 to 73 J/g. Aliphatic polyesters exhibited degradation temperatures around 400 °C, however, the polyester containing 1,4-cyclohexanediol block unit showed an increased degradation temperature of 446 °C due to the higher rigidity of the polymer that such a monomer provides.



**Scheme 15.** Polycondensation reaction to obtain polyesters and polyamides from diester **29**.

**Table 2.** Polymerization of monomer **29** and characterization of obtained polyesters and polyamides.

Entry	Polyester	Vacuum time	Yield	DP <sup>a</sup>	M <sub>n</sub> (g/mol) <sup>a</sup>	T <sub>m</sub> (°C) <sup>b</sup>	ΔH (J/g) <sup>b</sup>	T <sub>d</sub> (°C) <sup>c</sup>	mass loss <sup>c</sup>
1		30 min.	51 %	1.7	592	42	64	403	97 %
2		19 h	52 %	n.d.	n.d.	14	25	413	96 %
3		225 min.	76 %	6.6	2238	34	72	395	98 %
4		21 h	81 %	n.d.	n.d.	11	55	398	97 %
5		180 min.	74 %	7.5	2539	38	73	397	98 %
6		21 h	88 %	n.d.	n.d.	10	60	398	96 %
7		19 h	24 %	n.d.	n.d.	9	35	446 <sup>d</sup>	78 % <sup>d</sup>
9		19 h	51 %	n.d.	n.d.	152	55	443	82 %

Reaction conditions: Ti(O<sup>t</sup>Bu)<sub>4</sub> 1 mol%, no solvent, 140 min. melt time with temperature increase from 150 to 200 °C. <sup>a</sup> – degree of polymerization (DP) and number average molecular weight (M<sub>n</sub>) were calculated from <sup>1</sup>H NMR by end group analysis. <sup>b</sup> – determined by DSC. <sup>c</sup> – T<sub>d</sub> (decomposition temperature) and mass loss of the samples were determined by TGA. <sup>d</sup> – evident mass loss of 50 % was observed at temperature 353 °C. n.d. – not determined due to polymer insolubility.

In summary, a novel process of obtaining functional polymer materials from technical grade methyl oleate was developed. Self-CM of methyl oleate (**28**) in the presence of substantial amounts of methyl linoleate (**94**) was investigated and the reaction was optimized to obtain dimethyl octadec-9-enedioate (**29**) with high selectivity and yield. Subsequent polycondensation with a co-monomer (diol or diamine) resulted in the formation of polymeric materials which were characterized using TGA and DSC.

## References

- [1] B. Cornils, W. Herrmann A., M. Beller, R. Paciello (Editors), *Applied Homogeneous Catalysis with Organometallic Compounds*, Wiley-VCH: Weinheim, Germany, **2017**. ISBN: 9783527651733. DOI: [10.1002/9783527651733](https://doi.org/10.1002/9783527651733).
- [2] R. Poli, *Comm. Inorg. Chem.* **2009**, *30*, 177–228. DOI: [10.1080/02603590903423942](https://doi.org/10.1080/02603590903423942).
- [3] L. Benhamou, E. Chardon, G. Lavigne, S. Bellemin-Lapponnaz, V. César, *Chem. Rev.* **2011**, *111*, 2705–2733. DOI: [10.1021/cr100328e](https://doi.org/10.1021/cr100328e).
- [4] T. Dröge, F. Glorius, *Angew. Chem. Int. Ed.* **2010**, *49*, 6940–6952. DOI: [10.1002/anie.201001865](https://doi.org/10.1002/anie.201001865).
- [5] K. Verlinden, H. Buhl, W. Frank, C. Ganter, *Eur. J. Inorg. Chem.* **2015**, *2015*, 2416–2425. DOI: [10.1002/ejic.201500174](https://doi.org/10.1002/ejic.201500174).
- [6] A. Liske, K. Verlinden, H. Buhl, K. Schaper, C. Ganter, *Organometallics* **2013**, *32*, 5269–5272. DOI: [10.1021/om400858y](https://doi.org/10.1021/om400858y).
- [7] K. Endo, R. H. Grubbs, *J. Am. Chem. Soc.* **2011**, *133*, 8525–8527. DOI: [10.1021/ja202818v](https://doi.org/10.1021/ja202818v).
- [8] M. B. Herbert, Y. Lan, B. K. Keitz, P. Liu, K. Endo, M. W. Day, K. N. Houk, R. H. Grubbs, *J. Am. Chem. Soc.* **2012**, *134*, 7861–7866. DOI: [10.1021/ja301108m](https://doi.org/10.1021/ja301108m).
- [9] K. Gajda, A. Sytniczuk, L. Vendier, B. Trzaskowski, N. Lugan, A. Kajetanowicz, S. Bastin, K. Grela, V. César, *Eur. J. Inorg. Chem.* **2023**, *26*, e202300169. DOI: [10.1002/ejic.202300169](https://doi.org/10.1002/ejic.202300169).
- [10] I. Benaissa, K. Gajda, L. Vendier, N. Lugan, A. Kajetanowicz, K. Grela, V. Michelet, V. César, S. Bastin, *Organometallics* **2021**, *40*, 3223–3234. DOI: [10.1021/acs.organomet.1c00458](https://doi.org/10.1021/acs.organomet.1c00458).
- [11] M. M. D. Roy, E. Rivard, *Acc. Chem. Res.* **2017**, *50*, 2017–2025. DOI: [10.1021/acs.accounts.7b00264](https://doi.org/10.1021/acs.accounts.7b00264).
- [12] N. Mukherjee, S. Planer, K. Grela, *Org. Chem. Front.* **2018**, *5*, 494–516. DOI: [10.1039/C7QO00800G](https://doi.org/10.1039/C7QO00800G).
- [13] S. H. Hong, A. Chlenov, M. W. Day, R. H. Grubbs, *Angew. Chem. Int. Ed.* **2007**, *46*, 5148–5151. DOI: [10.1002/anie.200701234](https://doi.org/10.1002/anie.200701234).
- [14] S. Warwel, F. Brüse, C. Demes, M. Kunz, M. R. gen Klaas, *Chemosphere* **2001**, *43*, 39–48. DOI: [10.1016/s0045-6535\(00\)00322-2](https://doi.org/10.1016/s0045-6535(00)00322-2).

**Joris LANGLOIS**

**ESR2**

**Thesis co-directors**

Prof. Cyril Godard                      Universitata Rovira i Virgili, Tarragona, Spain

Prof. Martine Urrutigoity      Laboratoire de Chimie de Coordination, Toulouse, France

**Thesis defense**

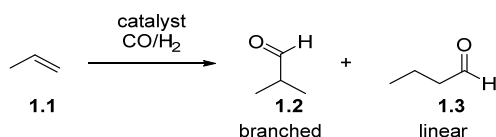
Department of Chemistry, University Rovira i Virgili, 15 December 2023



## Towards The Direct Synthesis Of Chiral Amines Via Asymmetric Rhodium Catalyzed Hydroaminomethylation Reactions

### Introduction

The use of carbon monoxide as C1 building block via metal-catalyzed carbonylation processes has revealed an efficient tool for the functionalization of organic molecules; moreover, the atom-economic nature of this type of reaction has increased the interest of both academia and industry [1]. Among the metals that catalyze carbonylation reactions, rhodium was largely studied due to its intrinsic properties that provide high activity and selectivity for this type of reaction [2]. Rhodium catalyzed hydroformylation constitutes an attractive strategy for the synthesis of aldehydes from readily available starting materials such as alkenes in a high atom economy process [3]. The reaction consists in the addition of “synthesis gas” (syngas), a mixture of CO and H<sub>2</sub>, to olefins in the presence of a catalyst. A formyl group and hydrogen are added through the π system of the alkene for the formation of aldehydes. Currently, several million tons of oxo-products are manufactured per year, mainly through the hydroformylation of propene **1.1**. The products *iso*-butyraldehyde **1.2** and *n*-butanal **1.3** are important intermediates to synthesize esters, acrylates, and 2-ethylhexanol (Scheme 1) [4].

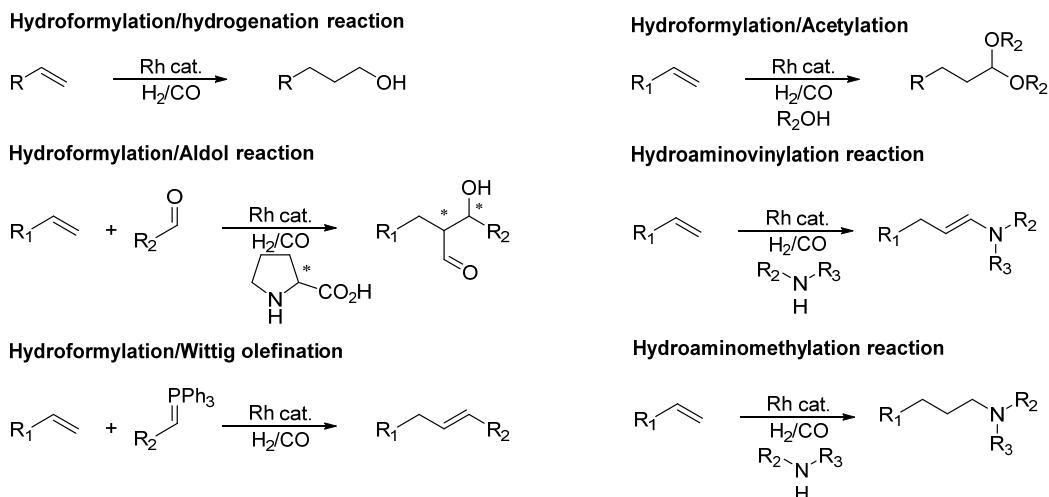


**Scheme 1.** Hydroformylation of propene.

From an organic point of view, aldehydes are products of interest due to their potential in terms of subsequent functionalization, that can lead to the formation of new carbon-carbon and carbon-heteroatom bonds [5]. However, despite the clear potential of asymmetric hydroformylation for the synthesis of chiral aldehydes, the application of this process at a large scale has not yet been completed. Aldehydes are generally not isolated as final products since the products of interest are usually derivatives. In this context, tandem processes with hydroformylation as the initial step constitute an interesting strategy. Indeed, the possibility to carry out several catalytic transformations in “one-pot” is even more attractive from an environmental and efficiency point of view. In this context, tandem catalytic processes are described as sequential catalytic transformations of the substrate through two, or even more, mechanistic pathways (Scheme 2) [6].

When hydroformylation is the first step of such processes, alcohols can be prepared by *in situ* reduction of the aldehyde using the hydrogen pressure present in the medium [7]. In the presence of a carbonyl compound such as an aldehyde and an organocatalyst, aldol reactions take place to expand the structure of the molecule [8]. It is also possible to create new C-C bonds if the aldehyde reacts with a phosphorus ylide via a Wittig reaction [9]. On the other hand, aldehydes can act as electrophiles and react with a nucleophile present in the media. If the nucleophile is an alcohol, hemiacetals or acetals can be created [10]. In the presence of a primary or secondary amine, imines and enamines can be easily prepared [11]. When these imines or enamines are hydrogenated to produce the corresponding amine, the reaction is called hydroaminomethylation (HAM).

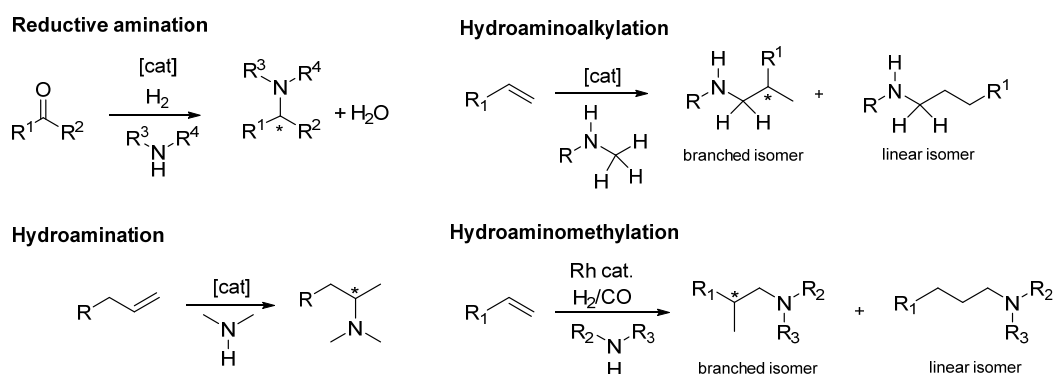




**Scheme 2.** Examples of hydroformylation tandem processes.

In this chapter, advances in the field of asymmetric hydroaminomethylation of alkenes is described. A part will also be devoted to the hydroformylation which is the first step of this tandem reaction. After a brief introduction of these reactions, the mechanisms of the processes will be detailed, and the most relevant catalytic results will be described according to the alkenes substrates. The efficient and selective synthesis of amines using readily available and abundant precursors is a long-standing goal of chemical research since they are powerful building blocks for the synthesis of pharmaceuticals, peptides, alkaloids and agrochemical, dyes, and monomers for polymerization [12].

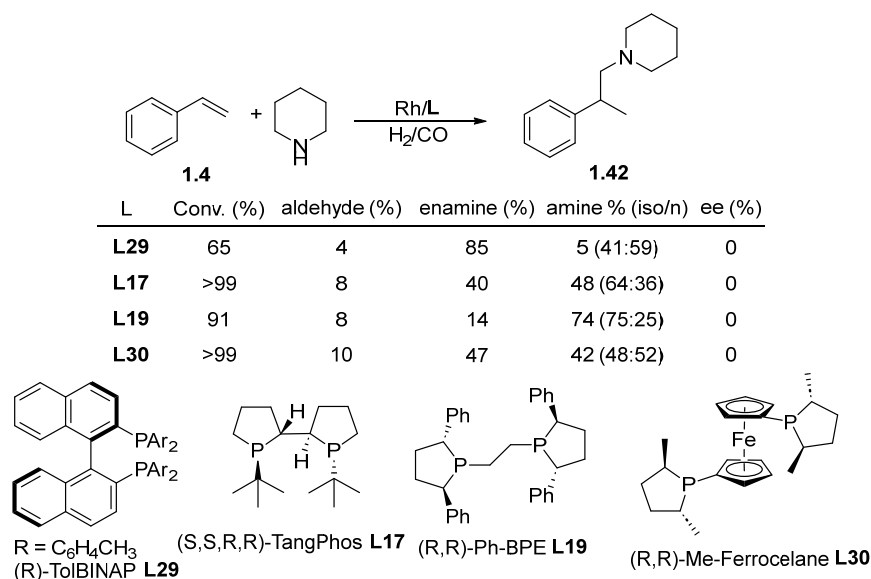
Chiral amine moieties are present in ca. 40% of pharmaceutical products. The introduction of these chiral units is therefore of high importance and usually performed through multistep processes [13,14]. As enantiomerically pure amines are required in large quantities in the pharmaceutical and agrochemical industry, the development of efficient methodologies for their preparation is of great significance and highly desirable. In the context of green chemistry, research on organometallic catalysis is still progressing to access and produce optically pure chiral amines. The main enantioselective metal-catalyzed reactions for the synthesis of chiral amines are reductive amination, hydroamination, hydroaminoalkylation and hydroaminomethylation (Scheme 3) [15].



**Scheme 3.** Transition metal catalyzed processes to access chiral amines.

A thorough study was performed by Kalck and co-workers on the asymmetric hydroaminomethylation of styrene with piperidine, using a variety of chiral diphosphine ligands which

had been previously reported as very efficient in both asymmetric hydroformylation and hydrogenation reactions (Scheme 4) [16]. The study also included  $^1\text{H}$  and  $^{31}\text{P}$  NMR investigations as well as DFT calculations.



**Scheme 4.** Rh-catalyzed hydroaminomethylation of styrene using chiral diphosphine ligands.

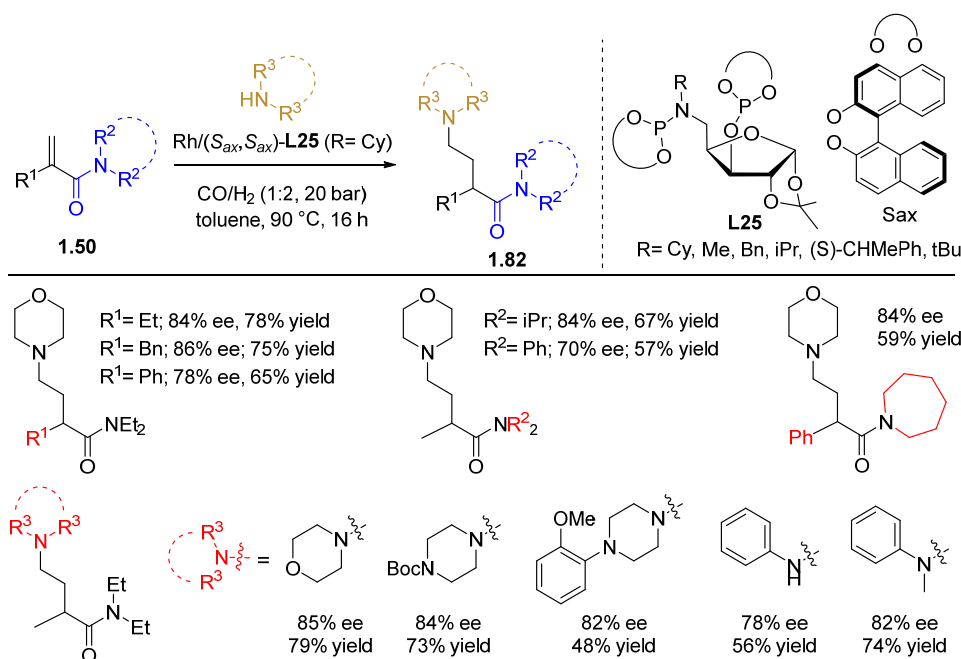
It was observed that the hydroformylation and the condensation proceeded rapidly, whilst the hydrogenation step was rate determining. In this reaction, the enantioselectivity should be induced in the hydrogenation step, since the chiral information obtained in the hydroformylation step is lost after condensation of the amine with the chiral aldehyde to form the corresponding enamine.

High to full conversions were obtained, and good chemo- and regioselectivity towards the branched intermediates were also attained, even if only diphospholane ligand **L17** provided the amine with high selectivity (Scheme 4). However, in all cases, no enantiomeric excess was obtained.

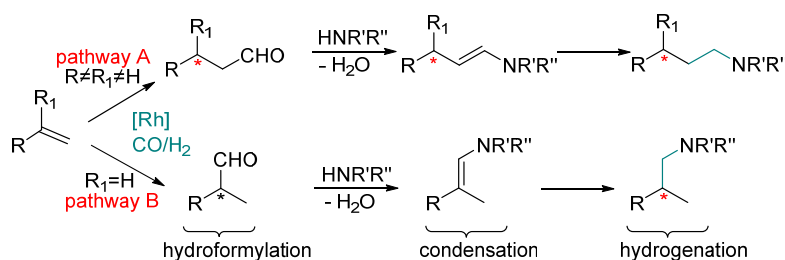
As detected by NMR spectroscopy, upon condensation of the amine, both (*E*)- and (*Z*)-enamines are produced. This is a crucial fact as the asymmetric hydrogenation of these enamines will lead to the opposite enantiomers, namely the (*S*) or (*R*)-products, respectively. DFT calculations established that the hydrogenation of both enamines is very close in energy (-12,2 vs -12,8 kcal/mol), therefore supporting why no enantiomeric excess could be obtained.

Godard and his group studied the asymmetric HAM of different  $\alpha$ -substituted acrylamides using a series of amines with the  $[\text{Rh}(\text{acac})(\text{CO})_2]/(S_{ax},S_{ax})\text{-L25}$  (R= Cy) catalytic system. The latter turned out to be active to directly yield chiral  $\gamma$ -aminobutyric acid (GABA) derivatives, with good to high yields (59-70%) and high enantioselectivities (70-86%) (Scheme 5).

In this thesis, we focused on the asymmetric HAM of 1,1-disubstituted alkenes with a chiral center obtained via asymmetric hydroformylation, as well as on the intramolecular version of 2-propenyl aniline derivatives whose chiral center is obtained by hydrogenation.



**Scheme 5.** Rh-catalyzed asymmetric hydroaminomethylation of  $\alpha$ -substituted acrylamides with various amines.



**Scheme 6.** Asymmetric induction in HAM.

## Objectives

**Objective 1:** Study the asymmetric hydroaminomethylation of 1,1-disubstituted alkenes.

**Objective 2:** Synthesis of 2-cyclopropylmethacrylamide derivatives and their reactivity in hydroformylation and hydroaminomethylation.

**Objective 3:** Development of heterogenized catalysts for the asymmetric hydroformylation and hydroaminomethylation of 1,1-disubstituted alkenes.

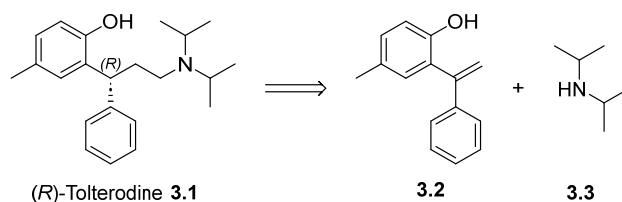
**Objective 4:** Intramolecular asymmetric hydroaminomethylation of monosubstituted alkenes.

**Objective 5:** Scale-up of a sugar-based phosphite phosphoramidite ligand.

## Rhodium catalyzed asymmetric hydroaminomethylation of 1,1-diarylethenes towards Tolterodine and its derivatives

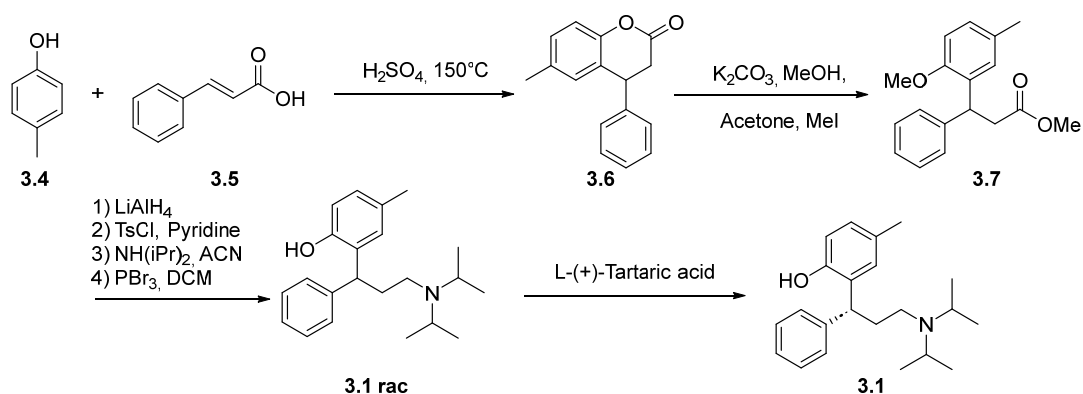
Following the strategy developed by our group for the production of chiral amines via the asymmetric hydroaminomethylation of 1,1-disubstituted alkenes forming chiral 1,1-disubstituted propylamines, the work presented in this chapter aimed at the synthesis of molecules of biological interest such as chiral 3,3'-diarylpropylamines. More precisely, the study presented here deals with

the asymmetric hydroaminomethylation of 1,1-diarylethene for the production of Tolterodine derivatives (Scheme 7).



**Scheme 7.** Retrosynthetic analysis of Tolterodine **3.1** via hydroaminomethylation.

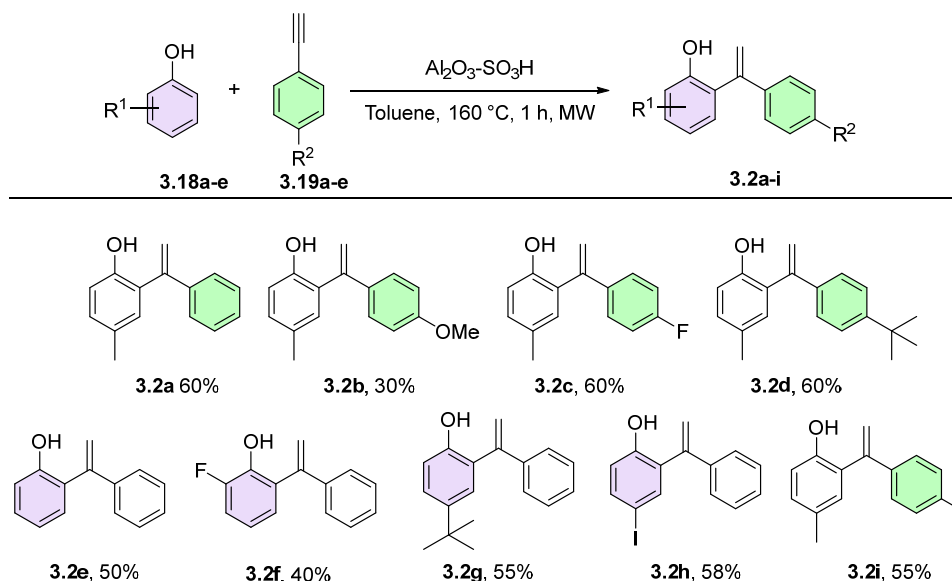
Tolterodine stands as a notable pharmaceutical compound within the realm of medicinal chemistry, categorized as an antimuscarinic drug that has garnered considerable attention for its remarkable efficacy in treating overactive bladder (OAB) and its associated urinary symptoms [17]. The annual bulk production of this active pharmaceutical ingredient (API) reaches approximately 0.5 tons in industrialized countries worldwide. In 2020, it ranked as the 271st most frequently prescribed medication in the United States, with over 1 million prescriptions dispensed [18]. The initial approach for synthesizing Tolterodine was detailed in a patent by Kabi Pharmacia AB in 1998 (Scheme 2) [19]. This route includes 8 consecutive synthetic steps and an overall yield <13%. The synthesis also employed non-environmentally friendly chemicals including pyridine, phosphorus tribromide, and dichloromethane.



**Scheme 8.** Synthesis of Tolterodine **3.1** patented by Kabi Pharmacia AB.

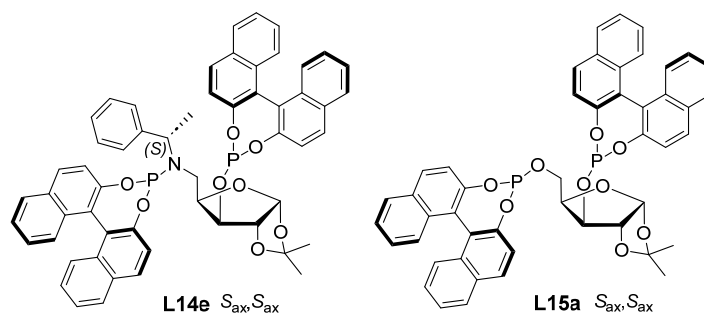
The work described in the following section represents the first Rh-catalyzed asymmetric hydroformylation and hydroaminomethylation of 1,1-diarylethene, leading to Tolterodine and derivatives.

1,1-diarylethenes were synthesized using a modified reported procedure [20]. Regioselective hydroarylation was performed using phenols **3.18** (1.5 equiv.) and phenylacetylenes **3.19** (1 equiv.) in the presence of an alumina-sulfuric acid heterogeneous catalyst at 160°C using microwave heating. The microwave assisted synthesis described constitutes a fast and effective manner of accessing these substrates using readily available products, in 30 to 60% yield after purification by column chromatography (Scheme 9).



**Scheme 9.** Synthesis of 1,1-diarylethenes via microwave assisted catalysis.

At this stage, the scope of 1,1-diarylethene substrates that can be used in the Rh-catalyzed asymmetric hydroaminomethylation reactions was evaluated using ligand **L14e** (Figure 1). In all cases, high conversions were obtained (Table 1) with ca. 50% chemoselectivity and ee's ranging from 14 to 36%. No clear conclusions could be drawn from the influence of the substrate substituents.

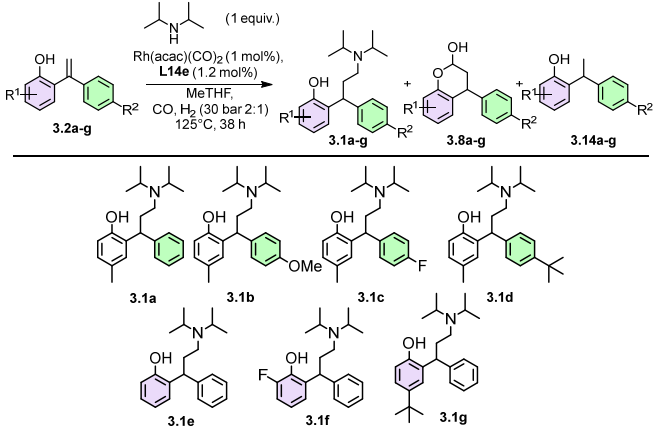


**Figure 1.** Best ligands used for HF and HAM of substrates **3.2a-3.2g**.

Next, we were interested in studying the asymmetric hydroformylation of substrates **3.2a-g** leading to the chromanols **3.8a-g** using the ligand **L14e**.

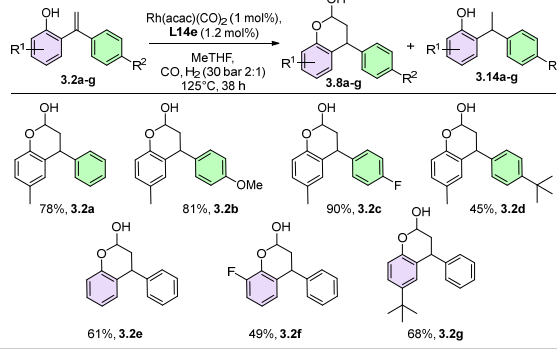
After the catalytic tests, the products **3.8** were isolated and oxidized into the chromanones **3.6** for determination of the enantiomeric excesses. The results are described in Table 2.

High conversions were obtained for all substrates (87-99%) with excellent chemoselectivity to the chromanol products (ca. 90%). In this reaction, the highest ee's (44 and 37%, entries 4 and 7 respectively) were obtained when a *tert*-butyl group was present in *para* position of one of the aryl substituents of the substrates. It is noteworthy that slightly higher chemo- and enantioselectivities were obtained in this hydroformylation reaction when compared to the results obtained in hydroaminomethylation. This again indicated that the presence of amine in the medium negatively affected the catalytic process.

**Table 1.** Asymmetric Rh-catalyzed hydroaminomethylation of **3.2a-g** to the chiral amines **3.1a-g** using **L14e**.


Entry	Substrate	Conv (%)	% <b>3.1</b> [yield]*	% ee ( <b>3.1</b> )	% <b>3.8</b>	% <b>3.14</b>
1	<b>3.2a</b>	90	48 [42]	36	42	10
2	<b>3.2b</b>	85	46 [32]	32	41	13
3	<b>3.2c</b>	93	46 [39]	33	45	9
4	<b>3.2d</b>	84	44 [30]	17	38	18
5	<b>3.2e</b>	90	44 [36]	14	46	10
6	<b>3.2f</b>	97	51 [47]	27	40	9
7	<b>3.2g</b>	86	43 [34]	25	43	15

<sup>a</sup> Reaction conditions: **1a** (0.12 mmol), Rh = [Rh(acac)(CO)<sub>2</sub>] (1 mol%), **L14e** (1.2 mol %), P = 30 bar (H<sub>2</sub>/CO, 1:2), MeTHF (0.2 mL), T = 125 °C, t = 38 h, 400 r.p.m. % ee of **3.1a** determined by chiral HPLC. \* isolated yield.

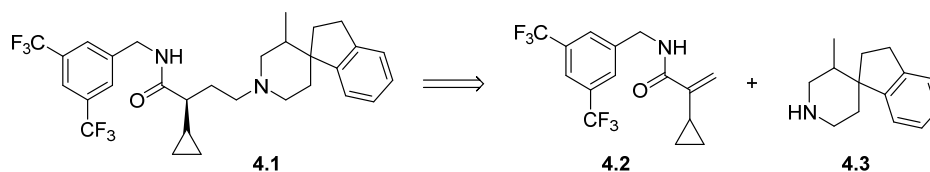
**Table 2.** Asymmetric Rh-catalyzed hydroformylation of **3.2a-g** to the chiral chromanols **3.8a-g** using **L14e**.


Entry	Substrate	Conv. (%)	% <b>3.8</b> [yield]*	ee <b>3.6</b> (%)	% <b>3.14</b>
1	<b>3.2a</b>	97	90 [78]	21	10
2	<b>3.2b</b>	87	88 [81]	22	12
3	<b>3.2c</b>	96	95 [90]	35	5
4	<b>3.2d</b>	96	88 [45]	44	12
5	<b>3.2e</b>	99	91 [61]	14	9
6	<b>3.2f</b>	99	94 [49]	28	6
7	<b>3.2g</b>	98	94 [68]	37	6

<sup>a</sup> Reaction conditions: **1a** (0.12 mmol), Rh = [Rh(acac)(CO)<sub>2</sub>] (1 mol%), **L14e** (1.2 mol %), P = 30 bar (H<sub>2</sub>/CO, 1:2), MeTHF (0.2 ml), T = 125 °C, t = 38 h, 400 r.p.m. % ee of **3.1a** determined by chiral HPLC. \*isolated yield.

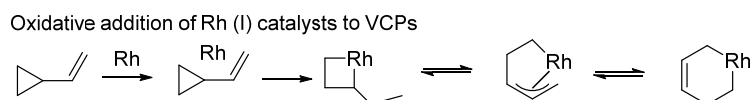
### Rh-catalyzed hydroaminomethylation of 1,1-cyclopropylmethacrylamides.

The possibility to access chiral GABA and derivatives through a direct approach is of major interest. As such, the asymmetric HAM of the cyclopropyl acrylamide **4.2** with the spirocyclic amine **4.3** could yield **4.1** based on the retrosynthetic route described in Scheme 10.



**Scheme 10.** Retrosynthetic analysis for the production of CCR2 antagonist **4.1** via HAM.

A drawback of this strategy involved the presence of a vinylcyclopropyl moiety in the starting material, which could undergo undesired side reactions. Vinylcyclopropanes (VCPs) have found extensive applications in transition-metal-catalyzed cycloaddition reactions due to the presence of an olefin group that guides the transition-metal towards the selective cleavage of C–C bonds [21]. VCPs were reported in reactions with Ru, Ni, Pd, Ir, Co, Fe and Rh based metal catalysts. Among them, Rh was one of the most studied as it was active in both C–C bond cleavage of activated and non-activated VCPs in either inter- or intramolecular processes. In the next section, only Rh-based C–C bond cleavage is described.



**Scheme 11.** Reactivity of VCPs with Rh.

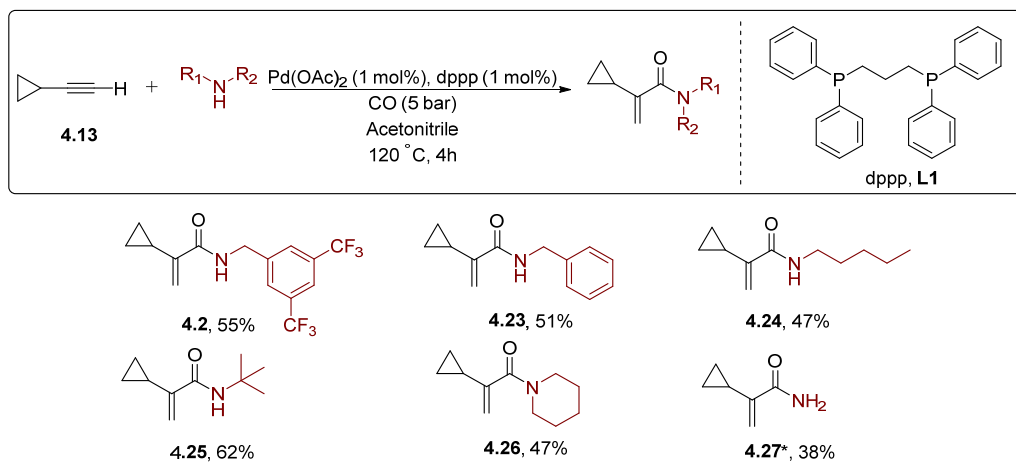
Cyclopropyl acetylene **4.13** and different amines were tested as substrates in the Pd-catalyzed hydroaminocarbonylation reaction based on previous reports involving different alkynes [22]. The substrates were reacted with carbon monoxide gas in the presence of Pd(OAc)<sub>2</sub> as the metal precursor and 1,3-bis(diphenylphosphino)propane (dppp) **L1** as ligand. For the synthesis of  $\alpha$ -cyclopropyl acrylamide **4.27**, ammonium carbonate was used as the amine source and the reaction was run for 6h (Scheme 12) [23].

Various new 1,1-disubstituted alkenes containing either primary, secondary or tertiary amide moieties were synthesized using this protocol. The primary amide **4.27** was synthesized in 38% yield and the four secondary amides **4.2**, **4.23**, **4.24** and **4.25** were synthesized in moderate to good yields (47 to 62%). The tertiary amide **4.26** was obtained in 47% yield.

Hydroformylation of secondary 2-cyclopropylacrylamides with **L3** provided new dihydropyridinone products which were isolated and fully characterized. Moreover, reduction of the catalytic crude revealed that the hydroformylation product **4.45** was also formed as the main linear aldehyde.

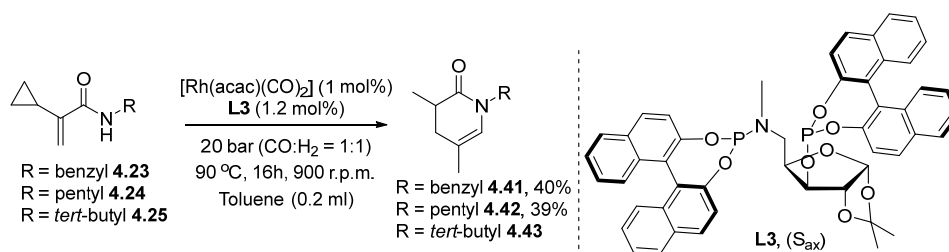
Notably, dppf provided a linear aldehyde, **4.45**, in 69% as observed by the triplet pattern of the aldehyde signal in <sup>1</sup>H NMR. The formation of products **4.41** and **4.45** could be explained through the mechanism displayed in Scheme 14. The formation of the cyclic dihydropyridinone **4.41** and the aldehyde **4.45** product indicated that C–C bond activation of cyclopropanes had taken place, as previously observed in the presence of Rh(I) catalysts. The possible mechanism described in Scheme

14 relies on the oxidative addition of Rh(I) into VCPs described in Scheme 11 [24]. As the catalysis is performed under syngas pressure, a rhodium hydride species is present in the system.

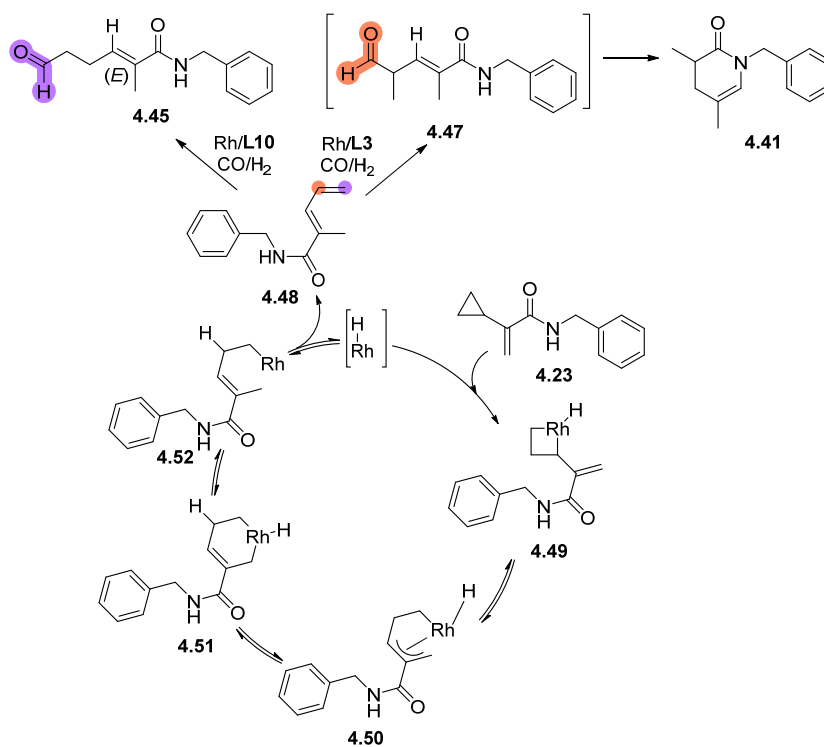


\*Prepared from ammonium carbonate for 6 h at 120°C

**Scheme 12.** Synthesis of 1,1-disubstituted alkenes via hydroaminocarbonylation.



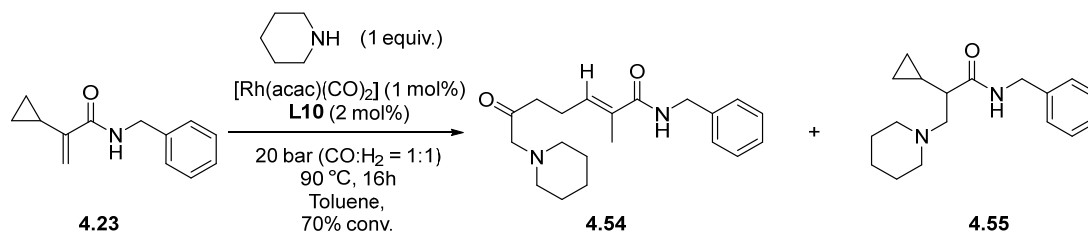
**Scheme 13.** Hydroformylation of **4.42** and **4.43** using ligand **L3**.



**Scheme 14.** Possible mechanism for the formation of dihydropyridinone **4.41** and aldehyde **4.45**.



The reactivity of N-benzyl-2-cyclopropylacrylamide **4.23** was tested in hydroaminomethylation using Rh(acac)(CO)<sub>2</sub> as rhodium precursor, **L10** as ligand, and with 1 equivalent of piperidine. The reaction was carried out at 1 mmol scale under 20 bar of syngas for 16 h at 90 °C.



**Scheme 15.** Reactivity of **4.23** under hydroaminomethylation conditions with piperidine.

The substrate was converted in 70% in mainly two products, **4.54** (44%) and **4.55** (48%). Surprisingly, the expected condensation of the amine on the resulting aldehyde **4.45** obtained previously in the hydroformylation of **4.23** with Rh/**L10** catalytic system was not detected. However, opening of the VCP occurred yielding the new product **4.54**. The second surprise was the formation of the cyclopropyl containing hydroamination product **4.55**. This unexpected result would suggest that a fast hydroamination would occur before the opening of the VCP.

### Rhodium catalyzed asymmetric hydroaminomethylation towards continuous flow.

Currently, over 90% of all industrial chemicals are produced through catalytic processes [25]. Hence, an important challenge in modern chemistry is the discovery of catalytic systems that combine the merits of both homogeneous (selectivity) and heterogeneous (recycling) catalysis. Numerous techniques were devised to retrieve and reuse homogeneous catalysts, as well as to efficiently separate the catalyst from the products. Among these methods, one of the prevailing approaches involves anchoring homogeneous catalysts onto solid supports, resulting in the so-called "heterogenized catalysts". These heterogenized systems can be produced through various approaches (Figure 2) [26].

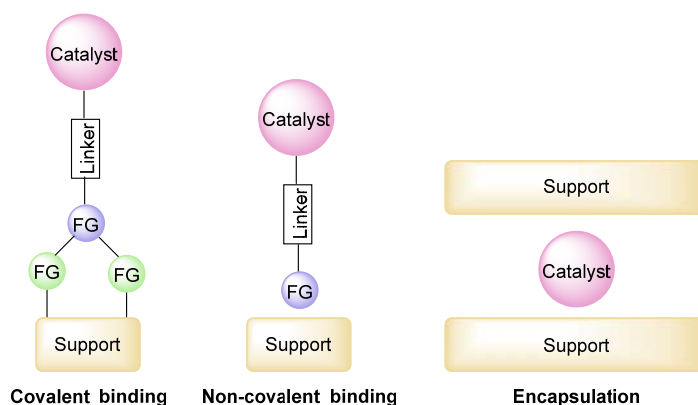


**Figure 2.** Main approaches for the immobilization of homogeneous catalysts onto solid supports.

In this work, we focused on the non-covalent immobilization of homogeneous catalysts for their application in hydroformylation and hydroaminomethylation reactions. Graphitic materials have attracted significant interest as potential supports for anchoring homogeneous catalysts through  $\pi$ - $\pi$

interactions. These interactions provide a stable foundation for the anchoring metal complexes and refer to non-covalent connections that arise between the electron densities of stacked aromatic systems. While benzene traditionally serves as the archetype for aromatic interactions, recent investigations have unveiled that larger aromatic systems, such as pyrene and coronene, provide even more resilient  $\pi$ - $\pi$  stacking bonds with CNTs [27]. Good results were reported in the Rh-catalyzed hydroaminomethylation reaction under flow conditions. However, the asymmetric version of this process was not reported to date.

Hence, here, our objective was the preparation of heterogenized chiral Rh catalysts for their application in the asymmetric hydroaminomethylation of acrylamides under batch and flow conditions. The design of the catalysts was based on a previous report from our group that described the efficient hydroaminomethylation of these substrates into chiral amines under homogeneous conditions [28]. These catalysts would be supported onto carbon support via  $\pi$ - $\pi$  interaction by introduction of a pyrene moiety in the backbone of the phosphite-phosphoramidite ligands (Figure 3). In the following sections, the results obtained to reach this objective will be described.

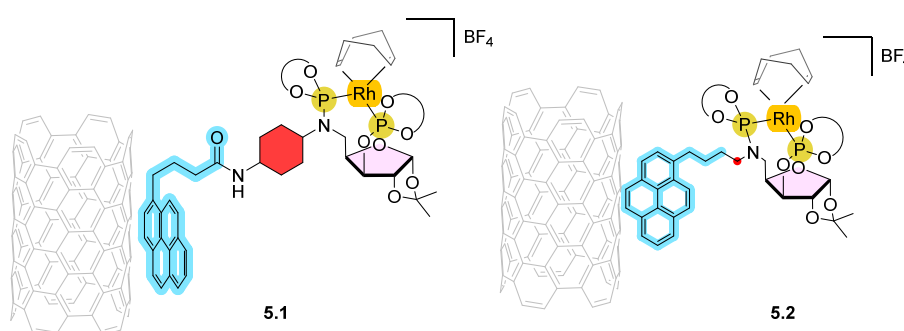
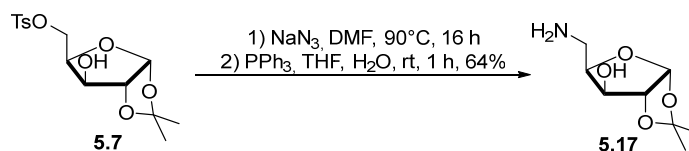


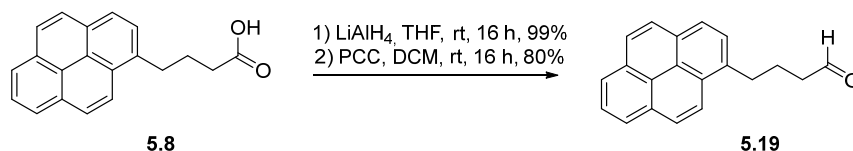
**Figure 3.** Aimed catalysts for the asymmetric HAM of acrylamides in continuous flow.

Using the same strategy as described for the synthesis of **5.5**, the amine moiety was introduced first in the xylose backbone followed by the incorporation of the pyrene. For this purpose, the tosyl **5.7** was reacted with sodium azide in dimethylformamide at 90 °C. The azide intermediate **5.16** was reduced with triphenylphosphine in a mixture of water and tetrahydrofuran at room temperature, yielding the water-soluble amino alcohol **5.17** in 64% yield over the two steps, after recrystallization in diethyl ether (Scheme 16).



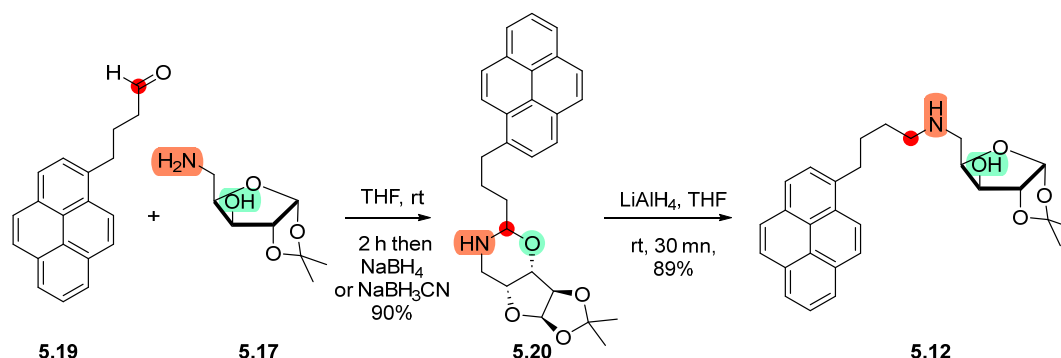
**Scheme 16.** Synthesis of the amino-alcohol **5.17** from the tosyl **5.7**.

In parallel, 1-pyrenebutyric acid **5.8** was reduced by  $\text{LiAlH}_4$  in THF at room temperature for 16 h to 1-pyrenebutanol **5.18** in quantitative yield. The 1-pyrenebutanol **5.18** was further oxidized using pyridinium chlorochromate (PCC) in dichloromethane to the 1-pyrenebutanal **5.19** in 80% yield (Scheme 17).



**Scheme 17.** Reduction and oxidation sequence of 1-pyrenebutyric acid **5.8** to 1-pyrenebutanal **5.19**.

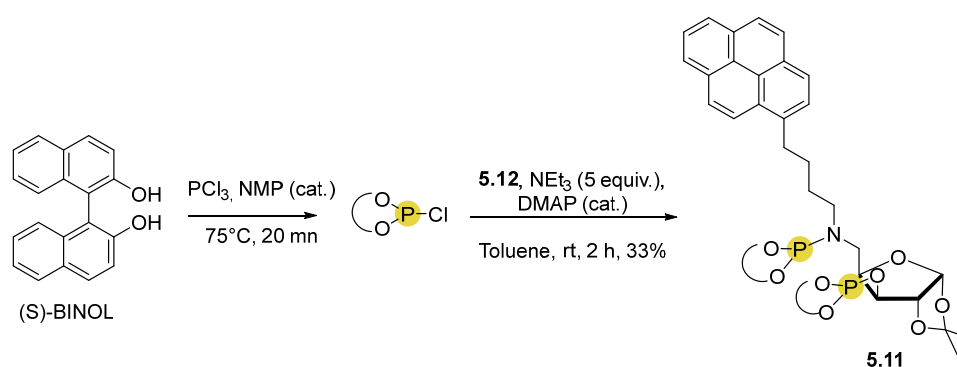
The amino-alcohol **5.17** and the aldehyde **5.19** partners were reacted in reductive amination to form the hemiaminal intermediate **5.20** in 90% yield. Surprisingly, neither sodium borohydride or sodium cyanoborohydride could open the 6 members ring intermediate **5.20**.



**Scheme 18.** Synthesis of pyrene-tagged amino alcohol linear backbone **5.12**.

However, when  $\text{LiAlH}_4$  was used in THF, the chiral pyrene-tagged amino alcohol linear backbone **5.12** was obtained in 89% yield (Scheme 18). Overall, this product was obtained in 41% yield from the tosyl intermediate **5.7** and the commercially available pyrene carboxylic acid **5.8**.

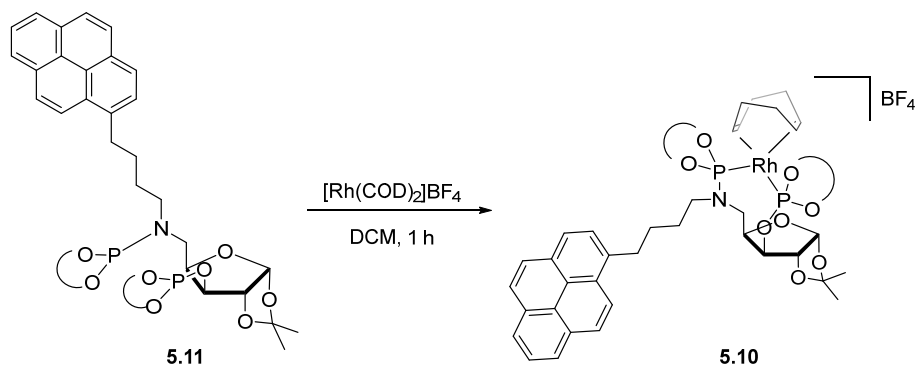
The amino-alcohol backbone **5.12** was reacted at rt for 2 h with the (*S*)-binolchlorophosphite formed *in situ* from phosphorus trichloride and (*S*)-BINOL (Scheme 19). The reaction time was critical since impurities that couldn't be separated by chromatography were detected by  $^{31}\text{P}$  NMR when the reaction time was increased. The new phosphite phosphoramidite pyrene tagged ligand **5.11** was obtained in a 33% yield after column chromatography.



**Scheme 19.** Synthesis of phosphite phosphoramidite ligand **5.11**.

The phosphite phosphoramidite ligand **5.11** was reacted in stoichiometric amount with  $[\text{Rh}(\text{COD})_2]\text{BF}_4$  in dichloromethane at 0°C and stirred at room temperature for 1 h (Scheme 20). The cationic complex **5.10** was immobilized on multiwall carbon nanotubes (MWCNT), reduced graphene oxide (rGO) and carbon beads (CB) and the corresponding Rh loadings are described in Table 3. The

highest rhodium loading was on **5.10@MWCNT** with 1.61 wt% followed by **5.10@CB** with 1.44 wt% and finally **5.10@rGO** with 1.10 wt%.

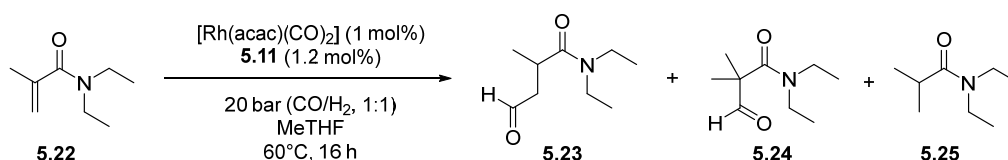


**Scheme 20.** Expected structure of the product **5.10** from the complexation of **5.11** with  $[\text{Rh}(\text{COD})_2]\text{BF}_4$ .

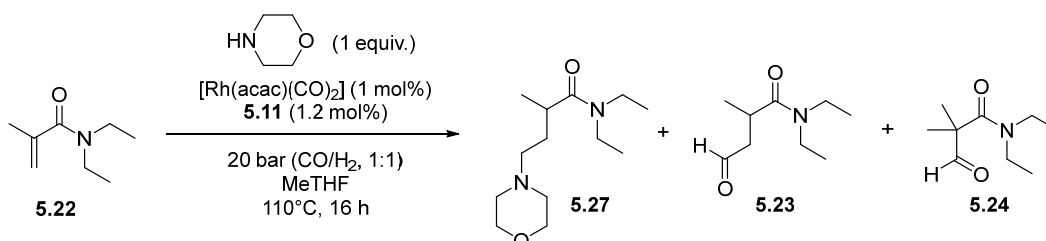
**Table 3.** Immobilization of **5.10** on carbon materials.

Catalyst	Rh loading wt%
<b>5.10@MWCNT</b>	1.61
<b>5.10@rGO</b>	1.10
<b>5.10@CB</b>	1.44

The successfully immobilized catalysts were then tested in asymmetric hydroformylation of acrylamide derivatives. The activity of the  $[\text{Rh}/\mathbf{5.11}]$  catalytic system was tested in homogeneous hydroformylation and hydroaminomethylation of **5.22**. The asymmetric hydroformylation of **5.22** (Scheme 21) resulted in an excellent 80% ee of **5.23**. The asymmetric hydroaminomethylation (Scheme 22) resulted in a good 67% ee of **5.27**. These results indicated that the introduction of the pyrene moiety in the ligand did not significantly affect the catalytic outcome of the reaction.



**Scheme 21.** Homogeneous asymmetric hydroformylation of **5.22** with the catalytic system  $[\text{Rh}/\mathbf{5.11}]$ .

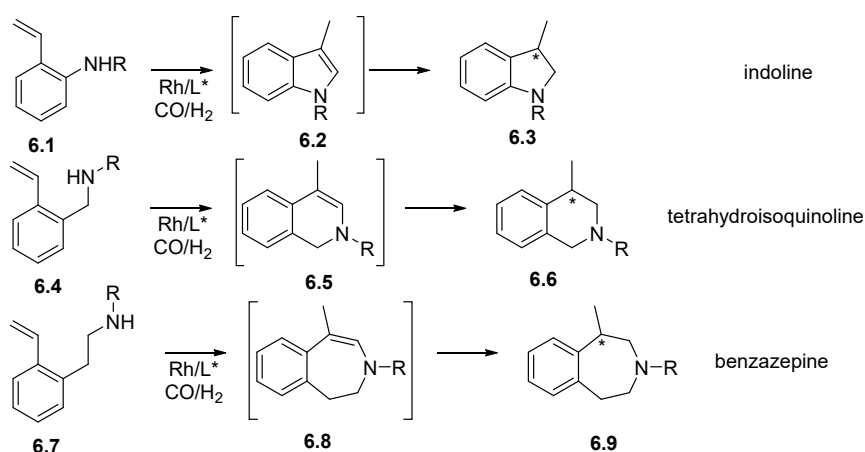


**Scheme 22.** Homogeneous asymmetric hydroaminomethylation of **5.22** with the catalytic system  $[\text{Rh}/\mathbf{5.11}]$ .

The immobilized catalysts were tested in batch hydroformylation in view of a continuous flow application. The catalysts presented a low activity, but the catalyst **5.10@MWCNT** provided a conversion of 30% at 110°C with a selectivity towards the linear aldehyde of 31% and a good enantioselectivity of 61%.

### Rhodium catalyzed intramolecular asymmetric hydroaminomethylation of alkenes.

Through intramolecular HAM, compounds such as indoline, tetrahydroisoquinoline or benzazepine derivatives, privileged scaffolds which exhibit interesting and important pharmacological activities, can be accessed in a one step process [29]. As presented in scheme 6, pathway B, the hydroaminomethylation of monosubstituted alkenes undergoes racemization during the condensation step between the aldehyde formed during the HF step and the amine reagent, and as such, the enantioselectivity must be induced during the hydrogenation of the imine/enamine to produce a chiral amine. In contrast with the intermolecular HAM [30], only one enamine isomer can be formed, making more efficient the asymmetric hydrogenation (Scheme 23).



**Scheme 23.** Intramolecular HAM of different substrates.

Substrates **6.33**, **6.34**, **6.39**, **6.42** were successfully synthesized according to reported procedure and tested in intramolecular hydroaminomethylation. As a general trend, the hydrogenation of the enamine intermediate is the limiting factor for the reaction to proceed and might require high pressure and temperature.

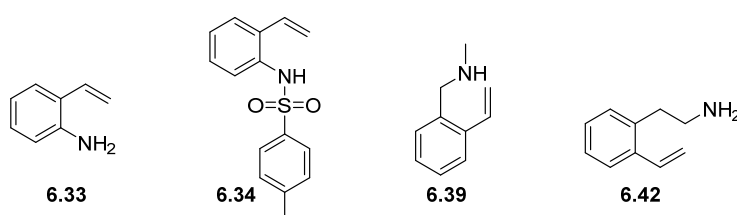


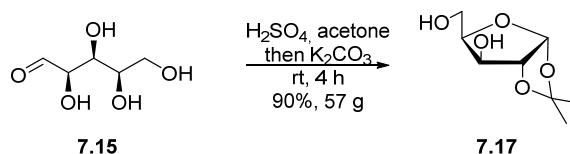
**Figure 4.** Substrates **6.33**, **6.34**, **6.39**, **6.42** used in intramolecular HAM.

Increasing the size of the enamine ring formed from 5 to 7-membered ring resulted in a more efficient hydrogenation under HAM conditions. However, no asymmetric hydroaminomethylation could be tested due to the lack of time.

### Secondment at Italmatch Chemicals: scale-up of a ligand synthesis based on D-xylose

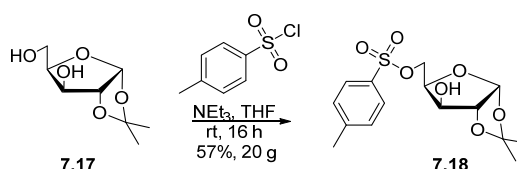
The lab scale-up was realized in three steps with an overall yield of 26%. The first step was the synthesis of the selective monoprotected ketal **7.17** (Scheme 24). *D*-xylose **7.15** was reacted with concentrated sulfuric acid in acetone for 1 h at room temperature. Then, the selective

monodeprotection of the ketal was realized *in situ* by adding potassium carbonate and stirred for 3 h. Then,  $K_2CO_3$  was added until neutral pH was reached, yielding **7.17** in 90% after work-up and evaporation of the aqueous phase.



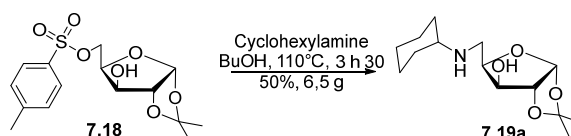
**Scheme 24.** Synthesis of the diol **7.17** in one step.

Activation of the primary alcohol was achieved with a slightly modified procedure. The diol **7.17** was reacted with 4-toluenesulfonyl chloride in triethylamine and tetrahydrofuran at room temperature for 16 h (Scheme 25). The product **7.18** was obtained in a similar 57% yield after precipitation in cold diethyl ether. The system  $NEt_3/THF$  was preferred to the pyridine/DCM system due to safety hazard and waste management.



**Scheme 25.** Synthesis of tosylated product **7.18**.

Finally, the amino alcohol **7.19a** was synthesized by reacting **7.18** with an excess of cyclohexylamine (4 equiv.) in 1-butanol at  $110^\circ\text{C}$  for 3 h 30 (Scheme 26). The product was obtained in 50% yield after acid base work up. Changing isopropanol to 1-butanol drastically reduced the reaction time as further heating was possible. The final aqueous treatment avoided the purification by column chromatography.



**Scheme 26.** Synthesis of the amino alcohol **7.19a**.

Then, an optimization of the continuous flow synthesis of chlorophosphite **7.30** was performed using syringe pumps. It was carried out with acetonitrile and a base. Samples were rapidly analyzed by  $^{31}\text{P}$  NMR to evaluate the conversion and selectivity. The optimal conditions included the use of diol solution with NMI (0.2 equiv.) in acetonitrile (1 M) and  $PCl_3$  in acetonitrile (1 M) for 1 min at room temperature.

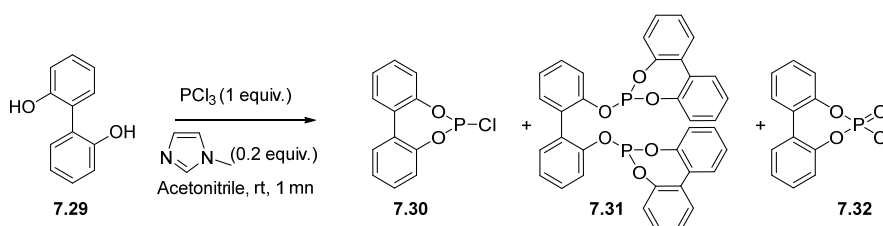


**Figure 5.** Flow synthesis of chlorophosphite **7.30**.

## General conclusions.

This manuscript details research work on various chemical reactions, including the homogeneous asymmetric hydroaminomethylation of specific compounds, the synthesis of chiral catalysts for this reaction, and the evaluation of reactivity of various compounds in hydroformylation and hydroaminomethylation reactions.

The first part described the results of asymmetric hydroformylation and hydroaminomethylation of 1,1-diarylethenes. It outlines the direct synthesis of Tolterodine and its derivatives via asymmetric hydroaminomethylation of these compounds, along with experimental conditions and yields obtained.

The second part focused on the synthesis of different compounds and their reactivity in rhodium-catalyzed reactions. The hydroformylation and hydroaminomethylation reactions of these compounds are studied, with observations on the reactivity of cyclopropylmethacrylamide and the formation of derivative products.

The third part addressed the development of heterogeneous catalysts for hydroformylation and hydroaminomethylation reactions. Pyrene-tagged ligands were synthesized and tested as immobilized catalysts, showing promising results despite relatively low activity.

The fourth part explored into the reactivity of ortho-substituted styrene derivatives in rhodium-catalyzed intramolecular hydroaminomethylation. The results indicate that the reaction is limited by the hydrogenation of the enamine intermediate.

Finally, the last part presented the results obtained during a stay at Italmatch Chemicals, highlighting the synthesis of different compounds and the scaling up of the synthesis of certain intermediates.

## References

- [1] M. Beller (Editor), *Catalytic Carbonylation Reactions, Top. Organomet. Chem.*, **2006**, *18*, 1-283. DOI: [10.1007/b105253](https://doi.org/10.1007/b105253).
- [2] C. Claver (Editor), *Rhodium Catalysis, Top. Organomet. Chem.*, **2018**, *61*, 1-288. DOI: [10.1007/978-3-319-66665-5](https://doi.org/10.1007/978-3-319-66665-5).
- [3] (a) B. Breit, *Aldehydes: synthesis by hydroformylation of alkenes*, in *Science of synthesis*, Thieme: Stuttgart, Germany, **2007**, Vol. 25, pp 277–282. DOI: 10.1055/sos-SD-025-00196. (b) R. Franke, D. Selent, A. Börner, *Chem. Rev.* **2012**, *112*, 5675–5732. DOI: [10.1021/cr3001803](https://doi.org/10.1021/cr3001803).
- [4] (a) B. Cornils, W. A. Herrmann (Editors), *Applied Homogeneous Catalysis with Organometallic Compounds, Vol. 1*, Wiley-VCH: Weinheim, Germany, **2002**. DOI: [10.1002/9783527618231](https://doi.org/10.1002/9783527618231). (b) K. Weissermel, H.-J. Arpe, *Industrial Organic Chemistry*, Wiley-VCH: Weinheim, Germany, **2008**. DOI: [10.1002/9783527619191](https://doi.org/10.1002/9783527619191).
- [5] (a) B. M. Trost, *Science* **1991**, *254*, 1471–1477. DOI: [10.1126/science.1962206](https://doi.org/10.1126/science.1962206). (b) B. Breit, *Acc. Chem. Res.* **2003**, *36*, 264–275. DOI: [10.1021/ar0200596](https://doi.org/10.1021/ar0200596).
- [6] (a) D. E. Fogg, E. N. dos Santos, *Coord. Chem. Rev.* **2004**, *248*, 2365–2379. DOI: [10.1016/j.ccr.2004.05.012](https://doi.org/10.1016/j.ccr.2004.05.012). (b) J. C. Wasilke, S. J. Obrey, R. T. Baker, G. C. Bazan, *Chem. Rev.* **2005**, *105*, 1001–1020. DOI: [10.1021/cr020018n](https://doi.org/10.1021/cr020018n).
- [7] P. Eilbracht, L. Bärfaker, C. Buss, C. Hollmann, B. E. Kitsos-Rzychon, C. L. Kranemann, T. Rische, R. Roggenbuck, A. Schmidt, *Chem. Rev.* **1999**, *99*, 3329–3366. DOI: [10.1021/cr970413r](https://doi.org/10.1021/cr970413r).

- [8] (a) S. Chercheja, S. K. Nadakudity, P. Eilbracht, *Adv. Synth. Catal.* **2010**, *352*, 637–643. DOI: [10.1002/adsc.200900780](https://doi.org/10.1002/adsc.200900780). (b) O. Abillard, B. Breit, *Adv. Synth. Catal.* **2007**, *349*, 1891–1895. DOI: [10.1002/adsc.200700216](https://doi.org/10.1002/adsc.200700216).
- [9] (a) B. Breit, S. K. Zahn, *Angew. Chem. Int. Ed.* **1999**, *38*, 969–971. DOI: [10.1002/\(SICI\)1521-3773\(19990401\)38:7<969::AID-ANIE969>3.0.CO;2-4](https://doi.org/10.1002/(SICI)1521-3773(19990401)38:7<969::AID-ANIE969>3.0.CO;2-4). (b) G. W. Wong, C. Landis, *Angew. Chem. Int. Ed.* **2013**, *52*, 1564–1567. DOI: [10.1002/anie.201208819](https://doi.org/10.1002/anie.201208819).
- [10] O. Diebolt, C. Cruzeuil, C. Müller, D. Vogt, *Adv. Synth. Catal.* **2012**, *354*, 670–677. DOI: [10.1002/adsc.201100707](https://doi.org/10.1002/adsc.201100707).
- [11] (a) M. Ahmed, R. P. J. Bronger, R. Jackstell, P. C. J. Kamer, P. W. N. M. van Leeuwen, M. Beller, *Chem. Eur. J.* **2006**, *12*, 8979–8988. DOI: [10.1002/chem.200600702](https://doi.org/10.1002/chem.200600702). (b) A. Mobaligh, S. A. Majeed, J. Ralf, B. Matthias, *Angew. Chem. Int. Ed.* **2003**, *42*, 5615–5619. DOI: [10.1002/anie.200352320](https://doi.org/10.1002/anie.200352320).
- [12] J. W. Blunt, B. R. Copp, R. A. Keyzers, M. H. G. Munro, M. R. Prinsep, *Nat. Prod. Rep.* **2012**, *29*, 144–222. DOI: [10.1039/C5NP00156K](https://doi.org/10.1039/C5NP00156K).
- [13] D. Ghislieri, N. J. Turner, *Top. Catal.* **2014**, *57*, 284–300. DOI: [10.1007/s11244-013-0184-1](https://doi.org/10.1007/s11244-013-0184-1).
- [14] T. C. Nugent (Editor), *Chiral amines synthesis: methods, developments and applications*. Wiley-VCH: Weinheim, **2010**. DOI: [10.1002/9783527629541](https://doi.org/10.1002/9783527629541).
- [15] A. Cunillera, C. Godard, C. Claver, M. Urrutigoity, P. Kalck, *Transition metal catalyzed chiral amines synthesis in Methodologies in amine synthesis: challenges and applications*, A. Ricci, L. Bernardi (Editors), Wiley-VCH: Weinheim, **2021**, p. 155–186. DOI: [10.1002/9783527826186.ch5](https://doi.org/10.1002/9783527826186.ch5).
- [16] D. Crozet, C. E. Kefalidis, M. Urrutigoity, L. Maron, P. Kalck, *ACS Catal.* **2014**, *4*, 435–447. DOI: [10.1021/cs400906b](https://doi.org/10.1021/cs400906b).
- [17] L. Nilvebrant, B. Hallen, G. Larsson, *Life Sci.* **1997**, *60*, 1129–1136. DOI: [10.1016/S0024-3205\(97\)00057-X](https://doi.org/10.1016/S0024-3205(97)00057-X).
- [18] Tolterodine - Drug Usage Statistics. [ClinCalc.com](https://www.clincalc.com), Retrieved 7 October 2022.
- [19] N. A. Joensson, B. A. Sparf, L. Mikiver, P. Moses, L. Nilvebrant, G. Glas, [EP 325571](https://doi.org/10.1016/j.tetlet.2019.03.006), **1998**.
- [20] A. Pramanik, A. Ghatak, S. Khan, S. Bhar, *Tetrahedron Lett.* **2019**, *60*, 1091–1095. DOI: [10.1016/j.tetlet.2019.03.006](https://doi.org/10.1016/j.tetlet.2019.03.006).
- [21] J. Wang, S. A. Blaszczyk, X. Li, W. Tang, *Chem. Rev.* **2021**, *121*, 110–139. DOI: [10.1021/acs.chemrev.0c00160](https://doi.org/10.1021/acs.chemrev.0c00160).
- [22] D. L. Wang, W. D. Guo, L. Liu, Q. Zhou, W. Y. Liang, Y. Lu, Y. Liu, *Catal. Sci. Technol.* **2019**, *9*, 1334–1337. DOI: [10.1039/C8CY02337A](https://doi.org/10.1039/C8CY02337A).
- [23] D. Wang, W. Guo, Q. Zhou, L. Liu, Y. Lu, Y. Liu, *ChemCatChem* **2018**, *10*, 4264–4268. DOI: [10.1002/cctc.201800791](https://doi.org/10.1002/cctc.201800791).
- [24] A. G. Dalling, T. Yamauchi, N. G. McCreanor, L. Cox, J. F. Bower, *Angew. Chem. Int. Ed.* **2019**, *58*, 221–225. DOI: [10.1002/anie.201811460](https://doi.org/10.1002/anie.201811460).
- [25] J. N. Armor, *Catal. Today* **2011**, *163*, 3–9. DOI: [10.1016/j.cattod.2009.11.019](https://doi.org/10.1016/j.cattod.2009.11.019).
- [26] (a) P. McMorn, G. J. Hutchings, *Chem. Soc. Rev.* **2004**, *33*, 108–122. DOI: [10.1039/B200387M](https://doi.org/10.1039/B200387M). (b) A. Corma, H. Garcia, *Top. Catal.* **2008**, *48*, 8–31. DOI: [10.1007/s11244-008-9056-5](https://doi.org/10.1007/s11244-008-9056-5).
- [27] F. Tournus, S. Latil, M. I. Heggie, J. C. Charlier, *Phys. Rev. B* **2005**, *72*, 1–5. DOI: [10.1103/PhysRevB.72.075431](https://doi.org/10.1103/PhysRevB.72.075431).
- [28] R. Miró, A. Cunillera, J. Margalef, D. Lutz, A. Börner, O. Pamies, M. Diéguez, C. Godard, *Org. Lett.* **2020**, *22*, 9036–9040. DOI: [10.1021/acs.orglett.0c03433](https://doi.org/10.1021/acs.orglett.0c03433).
- [29] (a) V. Kouznetsov, A. Palma, C. Ewert, *Curr. Org. Chem.* **2001**, *5*, 519–551. DOI: [10.2174/1385272013375391](https://doi.org/10.2174/1385272013375391). (b) A. Ansari, S. Satalkar, V. Patil, A. S. Shete, S. Kaur, A. Gupta, S.



Singh, M. Raja, *Bioorg. Med. Chem. Lett.* **2017**, 27, 217–222. DOI: [10.1016/j.bmcl.2016.11.080](https://doi.org/10.1016/j.bmcl.2016.11.080).  
(c) J. D. Philipson, M. F. Roberts, M. H. Zenk (Editors) *The chemistry and biology of isoquinoline alkaloids*, Springer Verlag: Berlin Heidelberg, **1985**. DOI: [10.1007/978-3-642-70128-3](https://doi.org/10.1007/978-3-642-70128-3).

[30] D. Crozet, C. E. Kefalidis, M. Urrutigoity, L. Maron, P. Kalck, *ACS Catal.* **2014**, 4, 435–447. DOI: [10.1021/cs400906b](https://doi.org/10.1021/cs400906b).

**Irina BOZHINOVSKA**

**ESR3**

**Thesis co-directors**

Prof. Agustí Lledós                      Universitat Autònoma de Barcelona, Bellaterra, Spain

Prof. Matthias Westerhausen      Friedrich-Schiller-Universität, Jena, Germany

**Thesis defense**

Universitat Autònoma de Barcelona, Bellaterra, June 2024 (scheduled)



## s-Block Metal-Mediated Hydroelementation

### Introduction

The addition of P(III) and P(V) compounds across alkynes or diynes is an example of formation of new P-C bonds in an atom-economic way [1-4]. However, this addition necessitates catalysts to overcome electrostatic and kinetic barriers [3,5-7]. As a method to this approach, we propose the use of alkali metal-based catalysts, which are ideal candidates for this task due to their non-toxicity, global abundance, and environmentally benign properties [8,9]. Nonetheless, the outcome of these reactions strongly depends on the nature of the alkali metal and the bulkiness of P-bound substituents [10,11]. It should be noted that there is no fundamental understanding of electronic and steric control for these reactions, particularly in terms of predictive experimental and theoretical capability, because these metals lack directing d-orbitals.

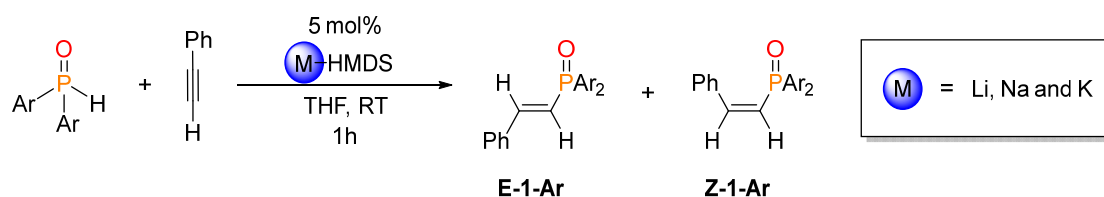
With the aim of forming stereo- and regioselectively P-C bonds via alkali-metal catalyzed reactions, this work focuses on a combined approach involving experimental and theoretical methods to determine the mechanistic steps by which these reactions ensue, to identify and underline the decisive factors which govern the stereo- and regio-selectivity and to ascertain which alkali metal is the most suited one. The combination of these two methods also enables us to understand why these reactions do not happen with several combinations of alkali cation and phosphine substituents. This project was initially divided into two parts: i) alkali metal mediated hydrophosphorylation (Pudovik reaction) of alkynes and diynes and ii) alkali metal catalyzed hydrophosphination of diynes. We set to achieve this goal by using M-HMDS (metal bis(trimethylsilyl)amides; M = Li, Na, and K) as precatalysts for the formation of new P-C bonds. For both projects we employed the same precatalyst and the same loading as to establish a homogenous protocol. We chose bis(trimethylsilyl)amide complexes as our precatalysts as they are commonly available, easy to synthesize from inexpensive starting materials, highly soluble in common organic solvents, and cheap. To elucidate the experimental outcome of the reactions, we have performed DFT calculations to achieve an understanding of the results from a theoretical standpoint.

Additionally, we also explored the oxidation of hetero cyclopentadienes with an incorporated phosphorus atom (product from the alkali metal-catalyzed hydrophosphination of diynes) and the subsequent dimerization of the oxidized product into a [2+2] adduct under visible light irradiation. In this part of the project, we aimed to evaluate the properties, which promoted the formation of oxide and the subsequent formation of the [2+2] adduct, in terms of HOMO-LUMO gap and the energy barriers facilitating the photoinduced cycloaddition. This additional project also combined DFT and experimental techniques.

### Alkali metal mediated Pudovik reaction

*Pudovik reaction Part I: alkali metal-mediated addition of di(organyl)phosphine oxides across phenylacetylene.*

In the initial stages of the project, we decided to elucidate the energy profile for the alkali metal mediated Pudovik reaction onto phenylacetylene (Scheme 1). For this section, we took the experimental data obtained by Westerhausen *et al.* [8].



**Scheme 1.** Alkali metal-mediated hydrophosphorylation of phenylacetylene with di(organyl)phosphine oxides via catalytic amounts of M-HMDS (M = Li, Na and K).

Interestingly the experimental results for the Pudovik reaction revealed a significant dependency on both the P-bound substituent and the nature of the s-block metal leading to different reaction times and product ratios. The following reactions were conducted in THF as a solvent. The summary of the experimental results is depicted in Tables 1 and 2.

**Table 1.** Dependency of the Pudovik reaction (addition of dimesitylphosphine oxide across phenylacetylene) on the alkali metal of the utilized bis(trimethylsilyl)amide precatalyst.

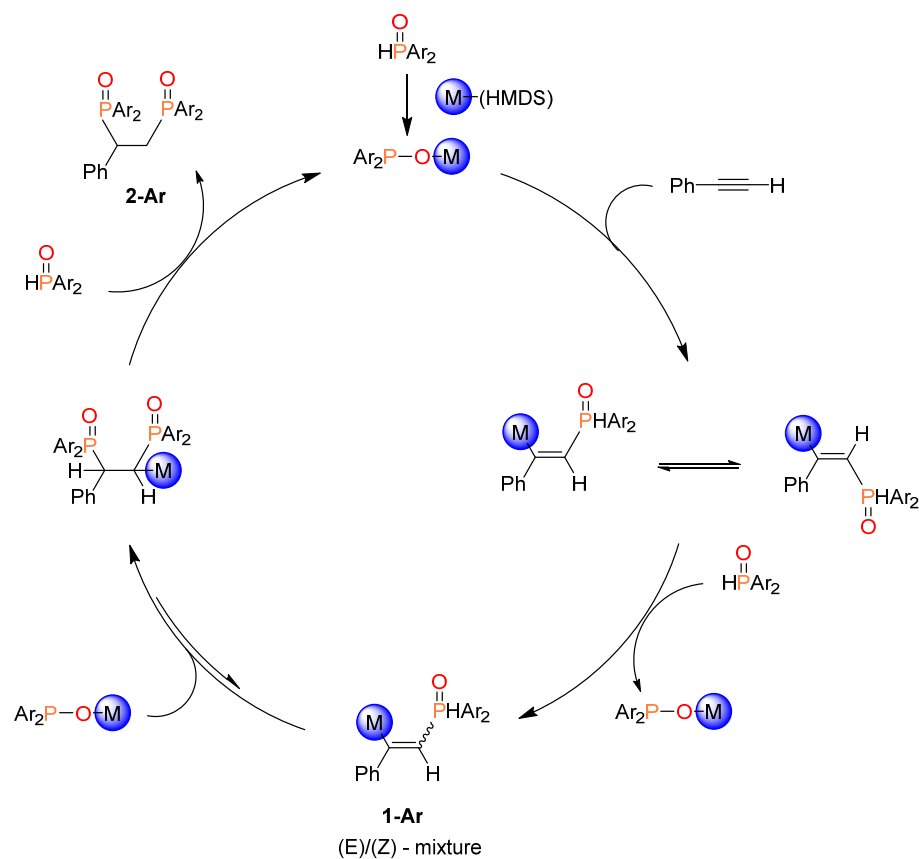
Entry	Metal	After 1h		After 27 h	
		Conv. [%]	E/Z	Conv. [%]	E/Z
1	Li	0	-	>8	5/1
2	Na	31	3/1	>99	31/1*
3	K	93	3/1	>99	5/1

\* The quantity of Z-1-Mes is reduced because of a preferred second Na-mediated hydrophosphorylation yielding 2-Mes.

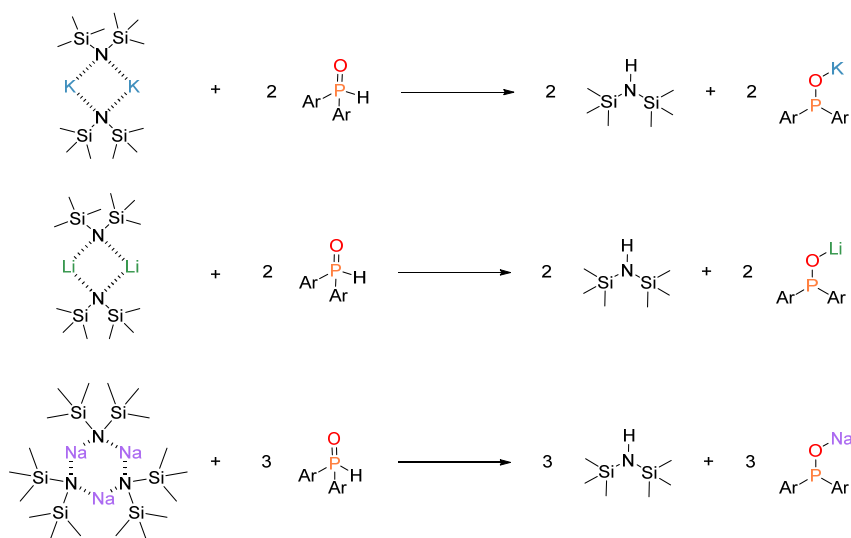
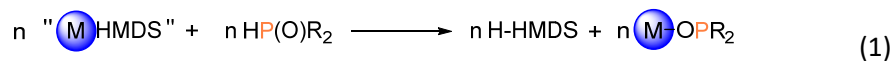
**Table 2.** Dependency of the hydrophosphination across phenylacetylene on the P-bound group of the di(organyl)phosphine oxide, using K-HMDS as precatalyst.

Entry	P-bound group	After 1h		
		Conv. [%]	1-Ar (E/Z)	2-Ar
1	Mes	93	3/1	/
2	Mes/Ph	76	36 (100/0)	64
3	Ph	14	<1	>99
4	Cy	0	/	/
5	OEt	0	/	/

To elucidate the experimental results, we considered the postulated mechanism presented in the original study as a basis for our present in silico study. The postulated reaction mechanism on which the computational study is based is depicted in Scheme 2. Before we started the exploration of the mechanism, we estimated the thermodynamic feasibility of the formation of the alkali metal phosphinites M-OPAr<sub>2</sub>, which are the active catalytic species, starting from the corresponding M-HMDS precatalyst and using stoichiometric amounts of HP(O)Ar<sub>2</sub> (reaction 1). For these calculations, we additionally considered the aggregation degree of M-HMDS in THF, a dimer for M = K, Li and a trimer for M = Na (Scheme 3) [12,13]. Furthermore, in the instance of M = K, we also examined the impact of different P-bound groups on the formation of the active catalytic species. We determined that in all cases the formation is feasible, regardless of the alkali cation and the P-bound substituent, according to the computed Gibbs energies for the reactions.



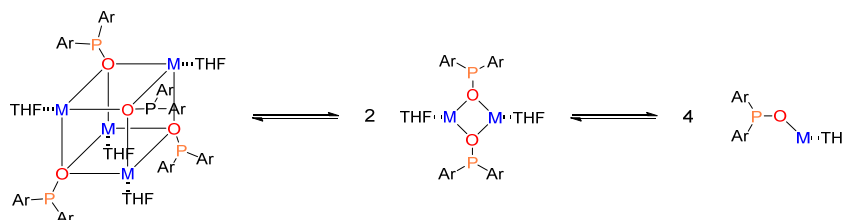
**Scheme 2.** Postulated mechanism for the formation of the **1-Ar** and the bis-phosphorylated compound **2-Ar** adapted from ref. [1].



**Scheme 3.** General scheme for generation of active catalyst species  $M\text{-OPAr}_2$  ( $M = \text{Li}, \text{Na}$  and  $\text{K}^*$ ;  $R = \text{Mes}$ ). \*For  $M = \text{K}$  also  $\text{Ar} = \text{Mes}, \text{Ph}, \text{OEt}$  and  $\text{Cy}$ .

However, it is known that the alkali metal phosphinites  $M\text{-OPAr}_2$  can form aggregates in solvents such as THF where tetrameric, dimeric, and monomeric species can (co)exist [2,13]. However, the only

active form is the monomeric complex. For this reason, we estimated the dissociation energies of the aggregates according to Scheme 4.



**Scheme 4.** General scheme of deaggregation for the clusters of active catalytic species ( $M = \text{Li}, \text{Na}, \text{K}$ ; P-bound groups 2 Mes, Mes/Ph and 2 Ph).

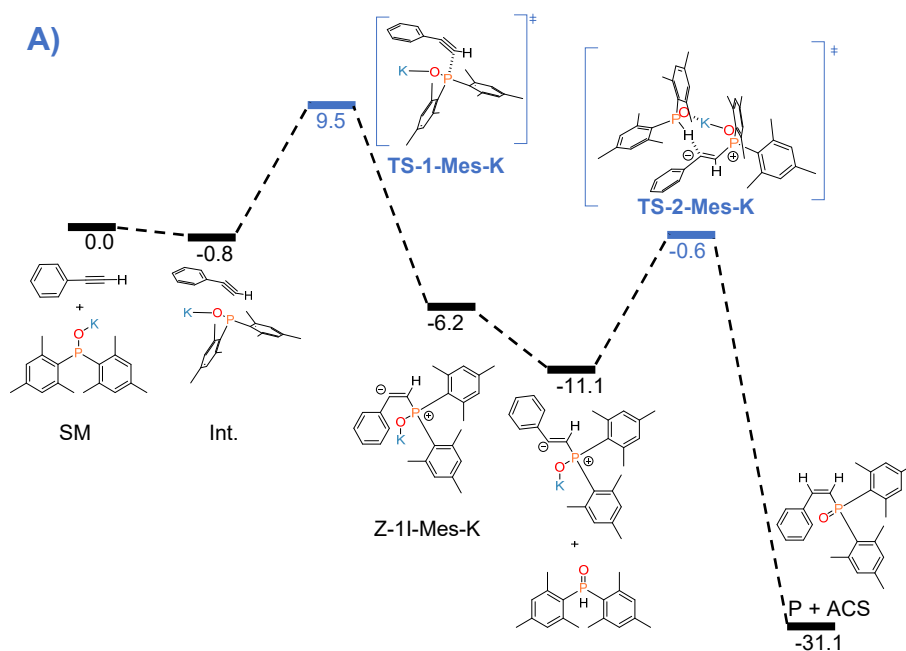
This part of the calculations provided some answers regarding the aspect why some of the reactions are hampered and do not ensue. The influence of the stepwise substitution of P-bound mesityl groups by phenyl groups on the dissociation/deaggregation energy is rather low with no significant trend. All the transformations are endergonic for the first transformation (tetramer into dimer), ranging from 27.9 to 29.4 kcal mol<sup>-1</sup>, and for the second transformation (dimer into monomer) from 17.5 to 22.1 kcal mol<sup>-1</sup>. Even though they are slightly elevated, all the conversions may be facilitated under the reaction conditions, which is in accordance with experimental data. However, we observed notable alkali metal-dependent variation for (Ar = Mes). The highest dissociation energy for the deaggregation for the tetrameric into the dimeric species for lithium metal mediated reaction is 42.3 kcal mol<sup>-1</sup>. Such a high dissociation energy could be one of the reasons suppressing this reaction. The rest of the dissociation energies were estimated to be lower than 30.0 kcal mol<sup>-1</sup>, and as such they could be surmounted under the reaction conditions. The estimated dissociation energies are in accordance with the analyzed experimental outcome.

Having estimated the Gibbs energy of the reaction of formation of the active catalytic species we then moved onto the calculation of energy profiles for the postulated mechanism (Figure 1). We were able to ascertain fully the reaction mechanisms for  $M = \text{Li}, \text{Na}$  and  $\text{K}$  with Ar = Mes and for  $M = \text{K}$  with Ar = Ph, Cy, OEt and a mixture of Ph and Mes as P-bound substituents. Addition of phosphorous nucleophile to the triple bond can give both *E*- and *Z*-isomers of the hydrophosphorylated products (Scheme 1). However, we were unable to locate a TS for the first nucleophilic attack that directly generates the intermediate which would be the precursor for the formation of the *E*-isomer. The calculated intermediate from the nucleophilic attack always formed as a precursor for the formation of the *Z*-isomer. The formation of the *E*-product takes place through an isomerization step of the initially formed pro-*Z*-intermediate (Figure 1B). All the computed barriers are lower than 30.0 kcal mol<sup>-1</sup>. The computed energy profiles suggest that the origin of the non-reaction observed in several cases was not in the barrier for the reaction, but rather in the steps beforehand (formation of the catalytically active species). Barriers are influenced by the nature of the alkali cation. The energy barriers were the highest with lithium and lowest with potassium which is in accordance with the experimental results of the best catalyst being the potassium complex and the worst being the lithium congener. The energy profile for the sodium-mediated reaction has barriers between potassium- and lithium-mediated reactions. Hence, it may be deduced that the identity of the alkali cation does play a significant role in the reaction mechanism, and it is inaccurate to look at alkali cations as spectators and as freely interchangeable. On the contrary, the energy barriers did not show significant difference amongst the different P-bound substituents, hence it was concluded that for P-bound Cy and OEt the prevailing factor which hinders this reaction is the lack of formation of the active mononuclear catalytic species.

Experimentally, the addition reaction is regioselective and yields the anti-Markovnikov product. The regioselectivity is decided at the nucleophilic addition stage. To figure out why there is no formation of the Markovnikov product, we computed the pathway leading to it for  $M = K$  and  $Ar = Mes$ . We were able to determine an energy barrier of  $19.8 \text{ kcal mol}^{-1}$  for the formation of the Markovnikov intermediate, whilst on the other hand the energy barrier for the formation of anti-Markovnikov was only  $7.3 \text{ kcal mol}^{-1}$ . Another noteworthy difference between these two steps is the different stability of the intermediates. According to the estimated calculations the anti-Markovnikov intermediate has a relative energy of  $-6.2 \text{ kcal mol}^{-1}$  below separated reactants, whilst the Markovnikov intermediate lies  $10.0 \text{ kcal mol}^{-1}$  above separated reactants. Hence, it may be concluded that the formation of the anti-Markovnikov intermediate is thermodynamically and kinetically preferred.

Calculations with a hydrogen atom (formally a proton) in the place of the metal ion were performed to assess the influence of the metal cation over the reaction barriers. This calculation was also conducted for P-bound mesityl substituents. Interestingly, the energy barrier almost doubles from  $10.2 \text{ kcal mol}^{-1}$  for the potassium mediated reaction ( $Ar = Mes$ ) to  $20.1 \text{ kcal mol}^{-1}$  for the metal free reaction. We were able to provide additional proof that the metal cation cooperates and lowers the energy barrier significantly, thus verifying one more evidence that alkali cations are not only spectators but that they rather play a significant role in the mechanism. Our findings regarding the role of the alkali cations in reaction mechanisms match with previous findings.

Overall, for this section we were able to calculate the Gibbs energy of the reaction of formation of the active catalytic species, the modes of interaction and to fully determine the postulated mechanism for the reactions depicted in Table 1 and 2. This allowed us to gain some in-depth knowledge on the steps which govern the regio- and stereoselectivity and allowed us to determine the influence of the nature of the cation and of the P-bound groups in the catalytic cycle. As an example, the Gibbs energy profiles calculated for the formation of *E*- and *Z*-isomers for the potassium-mediated Pudovik reaction ( $Ar = Mes$ ) are illustrated in Figure 1.





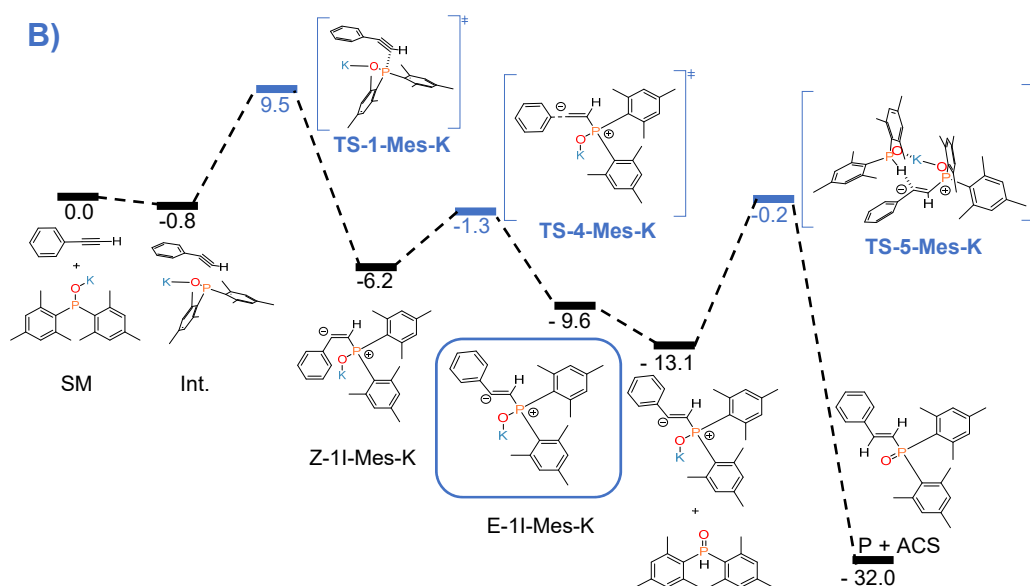
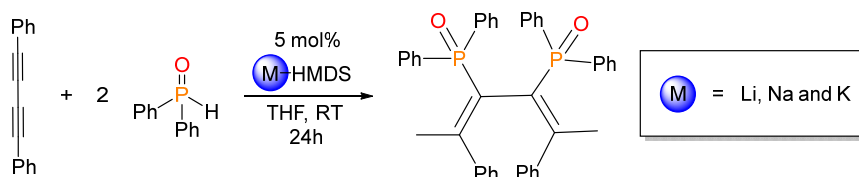


**Figure 1.** Computed Gibbs energy profiles in THF ( $\Delta G_{\text{THF}}$  in  $\text{kcal mol}^{-1}$ ) at 298 K for potassium-mediated hydrophosphorylation of phenylacetylene for the formation of Z-isomer (A) and E-isomer (B) with di(mesityl)phosphine oxide, using K-HMDS as precatalyst at a B3LYP-D3/Def2TZVP level of theory. (SM = starting materials, Int = initial intermediate. P=product, ACS = active catalytic species).

#### Pudovik reaction Part II: alkali metal-mediated addition of diphenylphosphine oxide across diphenylbutadiyne

The successful addition of di(aryl)phosphine oxides  $\text{Ar}_2\text{P}(\text{O})\text{H}$  across phenylacetylene using hexamethyldisilazanes (HMDS) of the alkali metals, we wanted to explore how the hydrophosphorylation of diphenylbutadiyne proceeds. Hence, we decided to test addition of diphenylphosphine oxide across 1,4-diphenylbutadiyne whilst using the same precatalysts (Scheme 5) as in the previous section. This part of the thesis was conducted at the industrial partner Italmatch.



**Scheme 5.** Alkali metal-mediated hydrophosphorylation of diphenylbutadiyne with diphenylphosphine oxide, using M-HMDS ( $M = \text{Li, Na, K}$ ) at room temperature yielding 1,4-diphenyl-2,3-bis(diphenylphosphoryl)buta-1,3-diene.

Experimentally, the same relationship than for phenylacetylene was found regarding the ability of the alkali metals ( $\text{K} > \text{Na} > \text{Li}$ ) to catalyze the Pudovik reaction and their chemical hardness  $M^+$  ( $M = \text{Li, Na, K}$ ). The reactions yielded a single product, namely 1,4-diphenyl-2,3-bis(diphenylphosphoryl)buta-1,3-diene. The reaction proceeded regio- and stereoselectively. The generated alkenylphosphine oxide is an already known compound and a comparison of the NMR parameters confirmed its identity. This compound was also obtained in the reaction catalyzed by  $[(\text{THF})_4\text{Ca}(\text{PPh}_2)_2]$  [14]. The change from alkaline earth- to alkali metal-based catalysts did not change the regio and stereoselectivity of this addition reaction.

Intriguingly for this section, the metal cations change their preferred mode of interaction with the  $\pi$ -system when switching from acetylene to diyne derivatives. In the latter instance, the metal cations will preferably interact with the diyne system instead of the aryl ring (Figure 2).

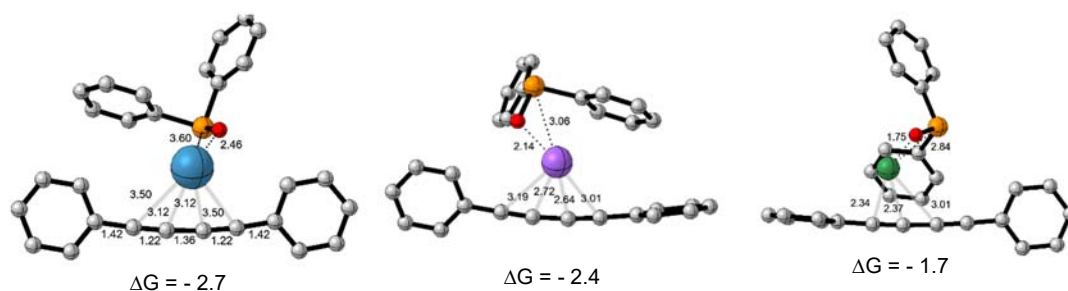


**Figure 2.** Most stable conformations computed for interactions of 1,4-diphenylbutadiyne with  $M\text{-OPPh}_2$  ( $M = \text{Li}$  (green),  $\text{Na}$  (purple),  $\text{K}$  (blue)). The binding energy  $\Delta G$  was calculated in  $\text{kcal mol}^{-1}$ .

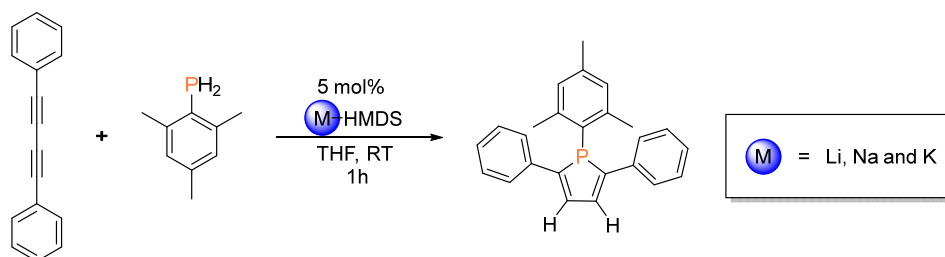
As a basis of our hypothetical mechanism for this section, we took the mechanism already computed for phenylacetylene and described in the previous section (Figure 1). We are currently still in the process of ascertaining the regioselective TS for this Section. However, from the estimated energy barrier for the TSs for 1<sup>st</sup> nucleophilic attack, 1<sup>st</sup> protonation, 2<sup>nd</sup> nucleophilic attack and 2<sup>nd</sup> protonation we can say that they follow the same trend as the empirical findings when varying the alkali metal cation, i.e., the highest energy barriers for all the steps were estimated for lithium and lowest for potassium, whilst sodium displays energy barriers between these two.

### Alkali metal mediated hydrophosphination

In this part of the thesis, we focused on the formation of new C-P bonds via hydrophosphination of alkynes, i.e., alkali metal-mediated addition of mesitylphosphine across diphenylbutadiyne via hexamethyldisilazanides. More precisely, we focused on conducting a combined computational and experimental analysis with the aim to shed more light on the reaction mechanism involved in the intramolecular hydrophosphination of butadiynes (Scheme 6).

#### *Influence of the metal on hydrophosphination*

To get accurate outcomes, we utilized freshly prepared alkali metal-mediated mesityl phosphinide and followed the methodology outlined below. The alkali metal phosphinide  $M\text{-P(H)Mes}$  was synthesized *in situ* by metalizing  $\text{H}_2\text{PMes}$  with 5 mol% of alkali metal hexamethyldisilazanides ( $M = \text{Li}, \text{Na}, \text{and K}$ ), resulting in the corresponding metal phosphinide (Scheme 6). The  $^{31}\text{P}$  NMR spectroscopy was used to confirm quantitative conversion. Mesityl phosphine and 5 mol%  $M\text{-HMDS}$  were combined in 5 mL of THF in a Schlenk flask at room temperature, followed by an addition of a stoichiometric quantity of 1,4-diphenylbutadiene, upon which the aliquot was protolyzed with methanol and the resulting product was identified by  $^{31}\text{P}$  NMR spectroscopy.



**Scheme 6.** Alkali metal-mediated hydrophosphination of diphenylbutadiyne with mesitylphosphine, using *M*-HMDS (*M* = Li, Na and K) at room temperature yielding 1-mesityl-2,5-diphenylphosphole.

The outcome of the reactivity study is summarized in Table 3. In less than an hour 1-mesityl-2,5-diphenyl-1*H*-phosphole formed quantitatively at room temperature. Thus, it was deduced that the alkali metal-mediated hydrophosphination proceeded regio- and stereo-selectively to generate the 1*H*-phosphole. This process could not be mediated by the pre-catalysts based on harder alkali metals, such as Li-HMDS (entry 1). However, fast conversion was detected for the complexes of the heavier metals such as sodium and potassium (entries 2 and 3). Surprisingly, in the case of lithium-mediated hydrophosphination neither addition of 18-crown-6 nor increasing the reaction temperature increased the rate of conversion. The conversion rate was determined via  $^{31}\text{P}$  NMR spectroscopically after one hour and it remained unchanged after 24 hours. No other products were formed, thus indicating that the generated phosphole is the single product from the reaction under these reaction conditions.

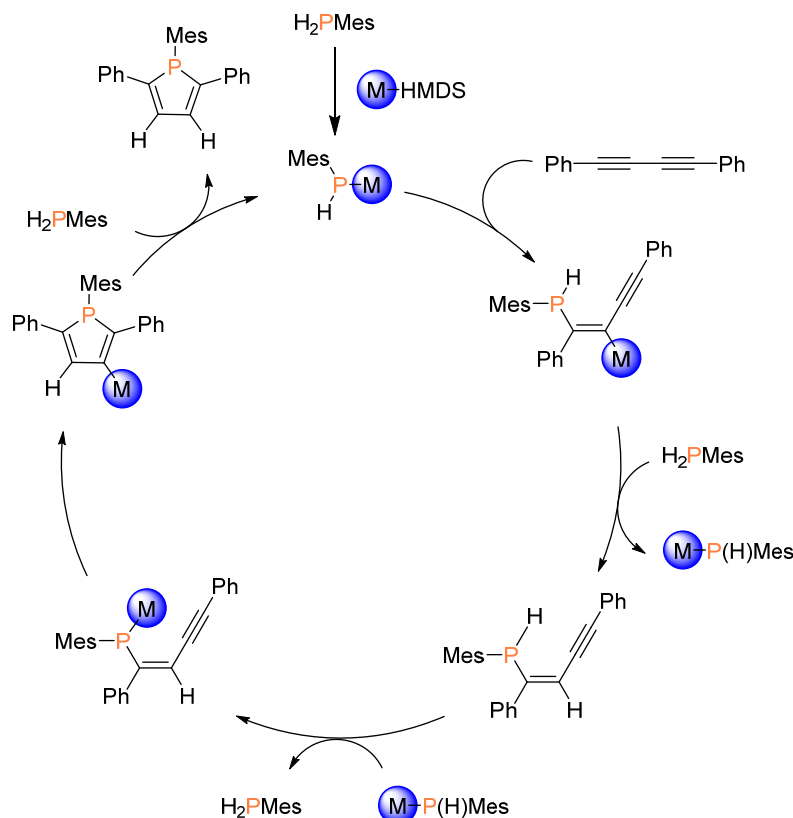
**Table 3.** Dependency of the hydrophosphination (addition of mesitylphosphine across 1,4-diphenylbutadiyne) on the alkali metal of the tested bis(trimethylsilyl)amides as pre-catalysts.

Entry	Metal	Conversion after 1h (%)
1	Li	/
2	Na	63
3	K	>99

Hence, the nature (hardness) of the alkali cation determines the conversion rate and, consequently, considering alkali cations as interchangeable and spectators in this hydrophosphination reaction is inherently wrong again.

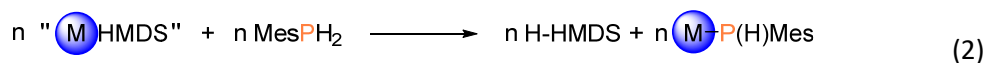
#### Postulated reaction mechanism

As we experimentally observed different conversion rates for the formation of the phosphole depending on the alkali metal atom, we investigated the mechanism of this reaction via theoretical methods to understand the influence and bonding pattern of the cation (cation hardness-reactivity relationship). Since the reaction strongly depends on the cation present in the system, the alkali cation cannot be neglected in our calculations. The postulated mechanism is depicted in Scheme 7. Before continuing onto discussing our postulated mechanism and the estimated energy barriers for those steps, it should be noted that Roesler *et al.* [15,16] have already proposed such a mechanism of formation of phosphole [17]. However, in their mechanism they suggested different reaction steps and the exclusion of the alkali cation i.e., they proposed a “naked” anionic mechanism. However, as experimentally verified in our case, we detected a dependence on the alkali cation and decided that incorporation of the cation in the postulated mechanism is imperative. Nonetheless, we also explored the reaction steps proposed by Roesler *et al.* in analogous manner for our model and we were able to exclude this proposal because it led to a higher energy barrier (above 25.0 kcal mol<sup>-1</sup>).



**Scheme 7.** Postulated mechanism for formation of the phosphole resulting from alkali metal-mediated hydrophosphination of diphenylbutadiyne ( $M = \text{alkali metal}$ ).

We propose that the initial step is the metalation of phosphine by  $M\text{-HMDS}$  ( $M = \text{Li, Na, and K}$ ) in order to generate the active catalytic species (i.e. metal phosphinides). Before continuing with the reaction mechanism we will discuss the thermodynamic feasibility of producing the alkali metal phosphinides that will act as the catalytic active species. The complexes  $M\text{-P(H)Mes}$  were synthesized *in situ* by metalating mesityl phosphines with alkali metal hexamethyldisilazides according to reaction 2. The aggregation modes considered for  $M\text{-HMDS}$  ( $M = \text{Li, Na, K}$ ) are identical to the ones used in the alkali metal-mediated Pudovik reaction.



We estimated a dissociation energy of  $34.6 \text{ kcal mol}^{-1}$  for  $\text{Li-P(H)Mes}$  formation, while the values for  $\text{Na-P(H)Mes}$  and  $\text{K-P(H)Mes}$  were  $30.1$  and  $10.2 \text{ kcal mol}^{-1}$ , respectively. This tendency of an increasing dissociation energy for the synthesis of active catalytic species in smaller congeners corresponded to the experimental trend of decreasing reactivity. As a result, this finding might be one of the factors prohibiting the lithium-mediated process giving rise to the active monometallic active species, compared to sodium- or potassium-mediated reactions. Having established the formation of the active catalytic species, we calculated the subsequent reaction steps. As an example, the Gibbs energy profile calculated for the most likely reaction pathway is illustrated in Figure 3 for potassium-mediated formation of phosphole, and the corresponding TS structures are depicted in Figure 4. The ensuing step was the addition of the metal-phosphorous bond onto the triple bond i.e., nucleophilic

attack from M-P(H)Ar onto the C<sub>internal</sub><sup>1</sup> from one of the C≡C triple bonds. This step showed a clear dependence on the metal cation. For this step we estimated energy barriers of 11.3 kcal mol<sup>-1</sup>, 11.9 kcal mol<sup>-1</sup>, and 16.9 kcal mol<sup>-1</sup> for potassium, sodium, and lithium, respectively. The intermediates for all three cations have *Z* configurations. This configuration is more suitable to proceed with ring closure through a nucleophilic attack onto the adjacent C<sub>internal</sub> triple bond unit yielding a 5-membered ring instead of *E*-intermediate. The latter intermediate would be more suitable to undergo double addition.

For the ensuing step to postulate a protonation step, instead of the isomerization as suggested by Roesler *et al.* [15], we were able to find two suitable routes: i) protonation by an additional molecule of mesitylphosphine or ii) protonation by an H-HMDS molecule. Regardless of the alkali cation present, the mesitylphosphine as a proton donor was favored with a slight preference of 2-3 kcal mol<sup>-1</sup> over H-HMDS. As the energy difference is so small it might be obvious that in the reaction mixture both molecules acted as proton donors. Regarding the cation, the energy barrier for the protonation varied from the lowest 4.9 kcal mol<sup>-1</sup> for potassium to the highest 16.8 kcal mol<sup>-1</sup> for the lithium case. It should be noted that during this step regeneration of M-P(H)Mes or M-HMDS ensued. We also checked the possibility of an intramolecular protonation via a phosphorous to carbon 1,4-proton migration. However, the lowest energy barrier we estimated for this process (24.1 kcal mol<sup>-1</sup>, potassium case) is much higher than that of the intermolecular mechanism commented above, and hence it was ruled out. Having fully formed *Z*-mono-phosphinated product, the ensuing step would be the deprotonation of the P-bound proton. We determined that the anions generated in the previous protonation step are able to do the deprotonation of the P-H proton. The estimated deprotonations were conducted with M-P(H)Mes and their barriers fell in the range between 7.6 (M = K) and 11.4 kcal mol<sup>-1</sup> (M = Li), whilst for M-Na we estimated a middle barrier of 9.2 kcal mol<sup>-1</sup>.

Having removed the proton, the ensuing step is the ring closure through a nucleophilic attack of phosphorous onto the adjacent C<sub>internal</sub> of the triple bond unit yielding a 5-membered ring (Figure 3). For this step we estimated energy barriers of 19.9 kcal mol<sup>-1</sup>, 22.0 kcal mol<sup>-1</sup>, and 16.5 kcal mol<sup>-1</sup> for potassium, sodium, and lithium, respectively. The final step yielding the phosphole was also estimated to proceed via the two routes as the previous protonation step. In this step, regeneration of M-P(H)Mes or M-HMDS, akin to the first protonation step, will proceed. The newly formed M-P(H)Mes or M-HMDS could be looped back into the catalytic cycle and as such they would be able to start the catalytic cycle again. It is noteworthy to mention that experimentally only formation of phosphole was observed.

---

<sup>1</sup> By C<sub>1</sub> or C<sub>internal</sub> we mean the C atom closest to the phenyl from the one of C≡C triple bonds present in the butadiyne.

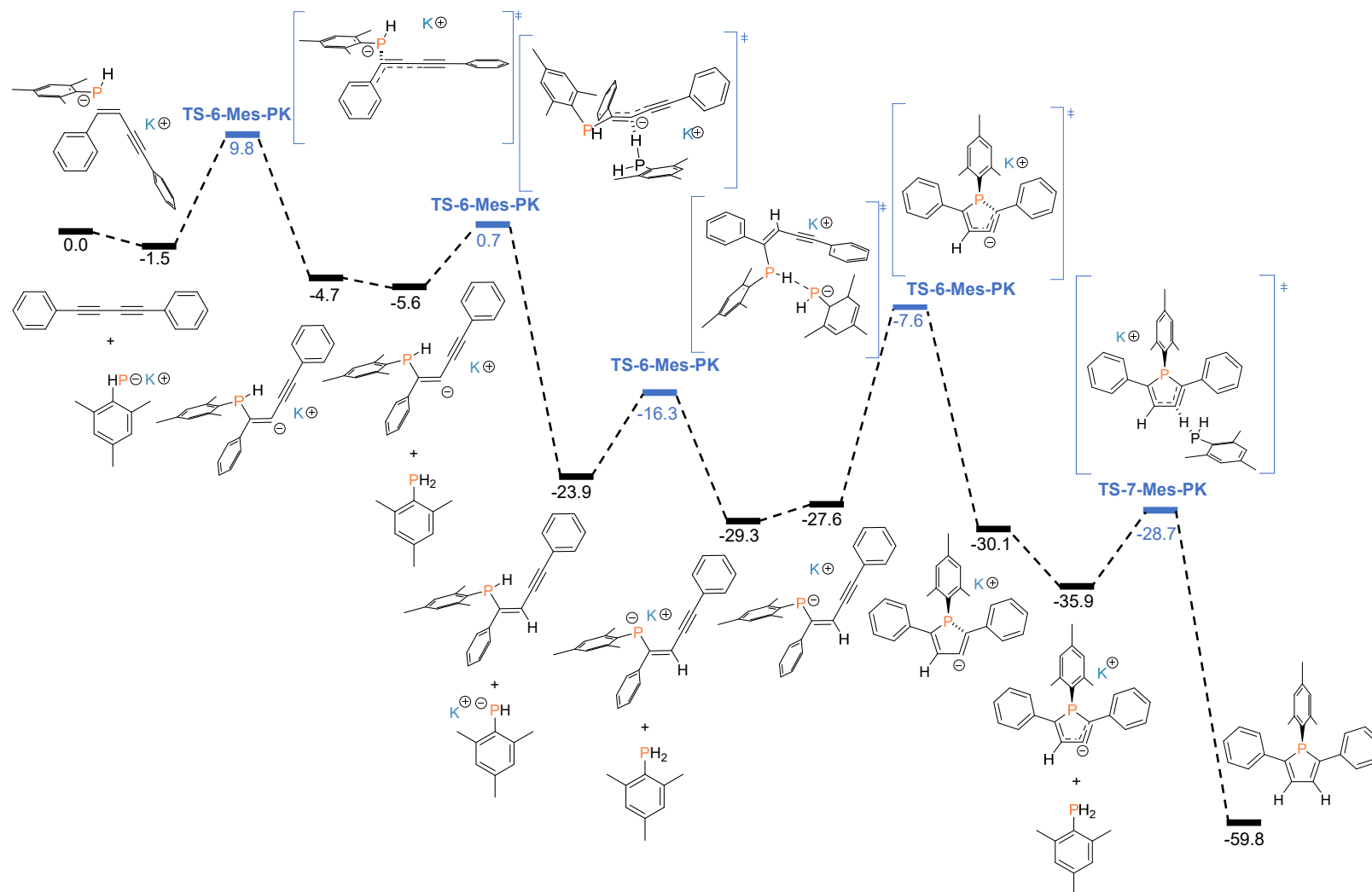


**Figure 3.** Computed Gibbs energy profile in THF ( $\Delta G_{\text{THF}}$  kcal mol<sup>-1</sup>) at 298 K for potassium-mediated formation of phosphole at a B3LYP-D3/Def2TZVP level of theory.

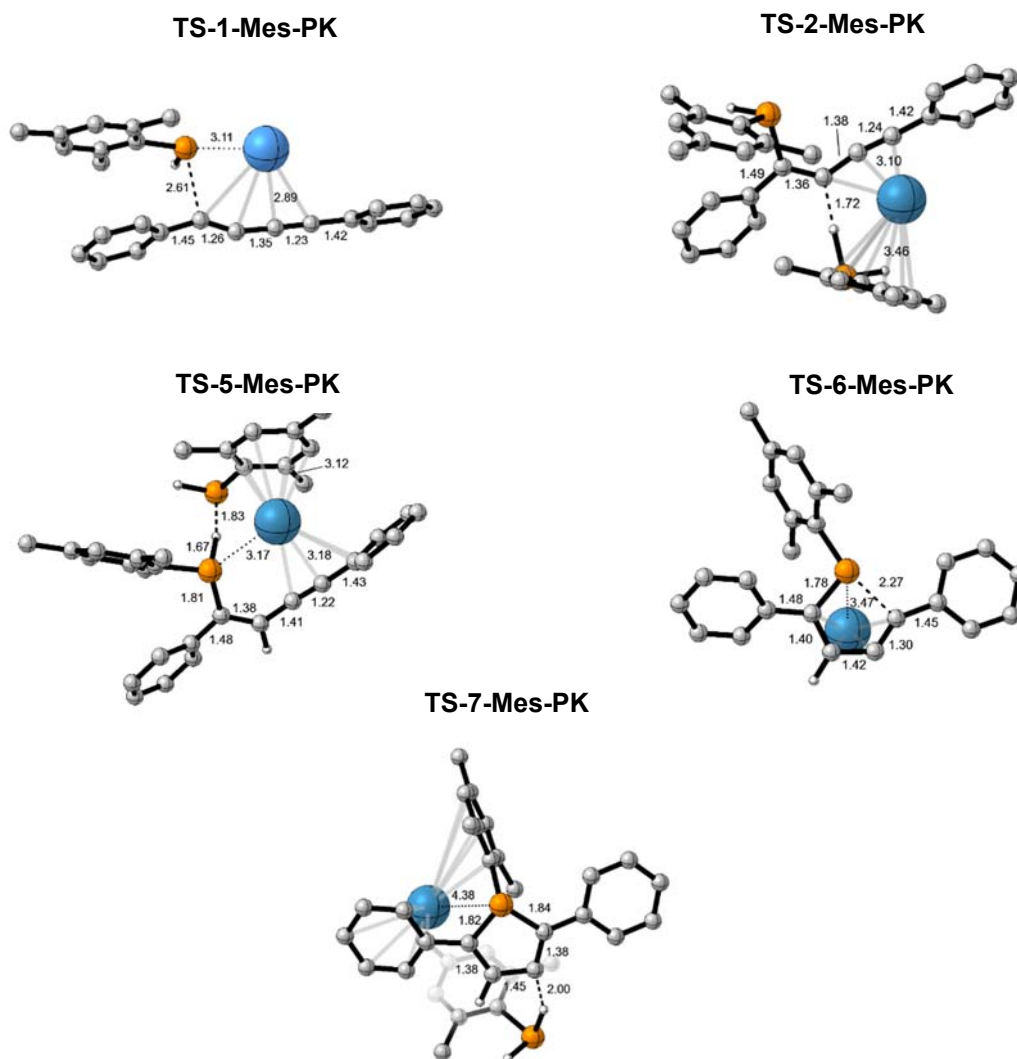
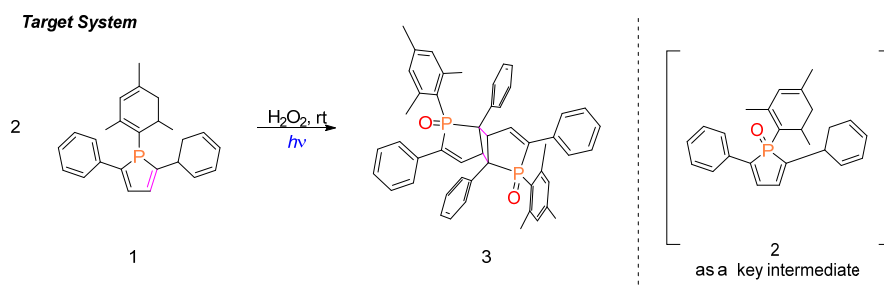


**Figure 4.** Optimized structures for transition states of the potassium-mediated formation of phosphole. Certain H atoms are omitted for clarity reasons. Distances are shown in Å.

### Oxidation of 2,5-disubstituted 1-*H*-phosphole and subsequent [2+2]-dimerization

Hitherto, chalcogen derivatives of phospholes are known adducts. The successful formation of the 1-mesityl-2,5-diphenyl-1*H*-phosphole convinced us to add an additional topic to this thesis: oxidation of 1-mesityl-2,5-diphenylphosphole [18-21]. We wanted to explore this topic to see how the addition of a chalcogen element would influence the properties of 2,5-disubstituted phospholes. Albeit we were trying to synthesize solely the phosphole oxide we serendipitously synthesized also the “head-to-tail” dimer of the phosphole oxide formed by a [2+2]-cycloaddition (Scheme 8). It should be noted that akin structures have been reported, more specifically, the [2+2]-cycloadduct of 1,2,5-triphenylphosphole has been obtained by irradiation [22]. Moreover, the [2+2]-cycloaddition product of the 1,2,5-triphenylphosphole oxide was obtained by oxidation of the parent phosphole by the water adduct of di(hydroperoxy)adamantane [23]. Looking through the literature and simultaneously conducting our own experiments we concluded that the newly formed dimer was generated by photo induction [24-26]. Hence, we decided to conduct combined experimental and theoretical studies on oxidation of 2,5-disubstituted 1*H*-phosphole and subsequent [2+2]-dimerization. To the best of our knowledge there is no such study conducted thus far.

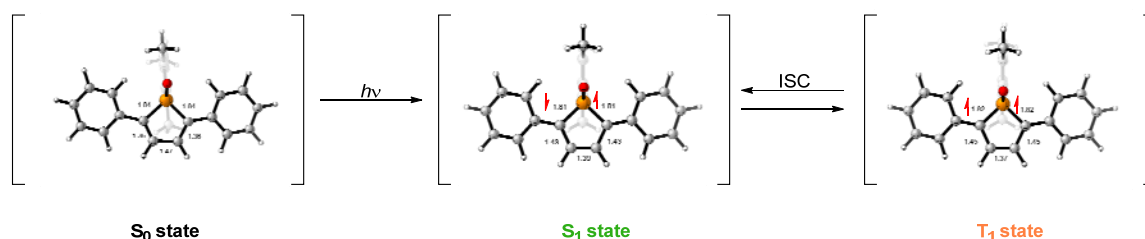


**Scheme 8.** Experimental conditions of the [2+2] cycloaddition reaction examined in this study.

*Computed reaction mechanism for oxidation and subsequent [2+2]-dimerization of 2,5-diphenylphosphole oxide*

Before postulating and determining the energy barrier for the dimerization of 1-mesityl-2,5-diphenylphosphole oxide we attempted to determine the energy barrier for the oxidation step, using  $\text{H}_2\text{O}_2$  as oxidant. We found that the oxidation proceeded by a single step, with an energy barrier of  $20.6 \text{ kcal mol}^{-1}$ . The obtained phosphole oxide may be found at  $-78.0 \text{ kcal mol}^{-1}$  below separated reactants, thus making this step very exergonic.

Having estimated the energy barrier with which the oxidation will proceed, we analyzed the mechanism by which the [2+2]-cycloaddition product formed. We first studied the photochemically induced excitation of the phosphole oxide, which happens upon absorption of light, by means of Time-Dependent DFT calculations (TD-DFT) (Scheme 9).



**Scheme 9.** Optimized structures for  $S_0$ ,  $T_1$  and  $S_1$  (from left to right) involved in the [2+2]-cycloaddition via light excitation leading to the [2+2]-cycloaddition product. The unpaired electrons are expressed with red arrows. Distances are shown in Å.

Phosphole oxide is excited from the ground singlet electronic state ( $S_0$ ) to the first singlet excited state ( $S_1$ ), that evolves to the more stable triplet species ( $T_1$ ).  $S_1$  can be reached with an excitation of 2.82 eV, feasible under visible light irradiation. The triplet state  $T_1$  lies below  $S_1$ , at 1.52 eV. The structures for the excited states which participate in the mechanism are depicted in Scheme 9. In this scheme we can see that the  $S_1$  species presents noticeable structural differences with respect to the ground state geometry: it has one double bond in the phosphole ring instead of two i.e., the distances  $C_1-C_2$  and  $C_3-C_4$  are elongated by  $0.07 \text{ Å}$ , whilst the  $C_2-C_3$  distance is shortened by  $0.08 \text{ Å}$  in comparison to the  $S_0$  state. Conversion from singlet excited species to triplet excited species will proceed via an intersystem crossing process (ISC).

The configuration of the  $T_1$  state is similar to the configuration of the  $S_1$  state, with elongation and shortening of  $0.02 \text{ Å}$  for  $C_1-C_2$  and  $C_3-C_4$  and  $C_2-C_3$  distance respectively. This change in bond lengths is induced by a change in the electron delocalization upon excitation. This species is a biradical, with two unpaired electrons at  $C_1$  and  $C_4$  carbon atoms of the ring. This phosphole oxide biradical



participates in the dimerization process, following the steps depicted in the Gibbs energy profile of the dimerization reaction (Figure 5). The optimized transition state structures associated with this reaction mechanism are depicted in Figure 6.

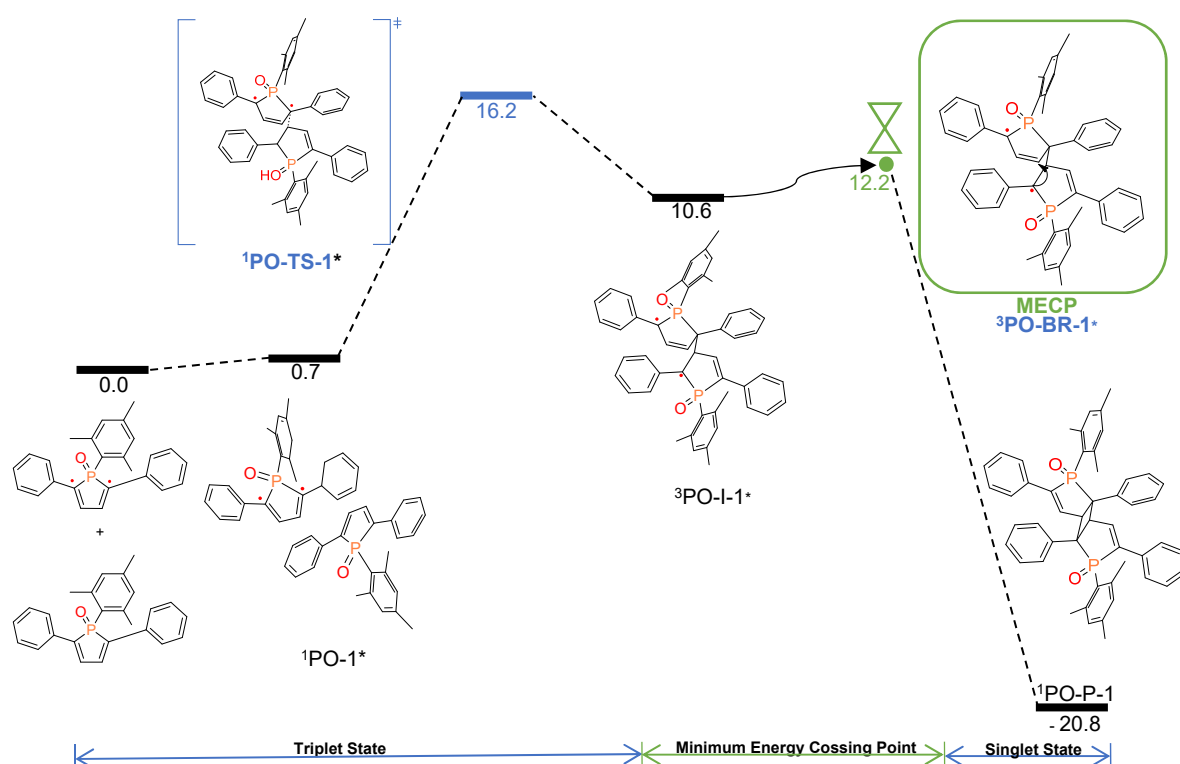


**Figure 5.** Computed Gibbs energy diagram in THF ( $\Delta G_{\text{THF}}^{\ddagger}$  kcal mol $^{-1}$ ) at 298 K for formation of the [2+2]cycloaddition product at a B3LYP-D3/Def2TZVP level of theory.

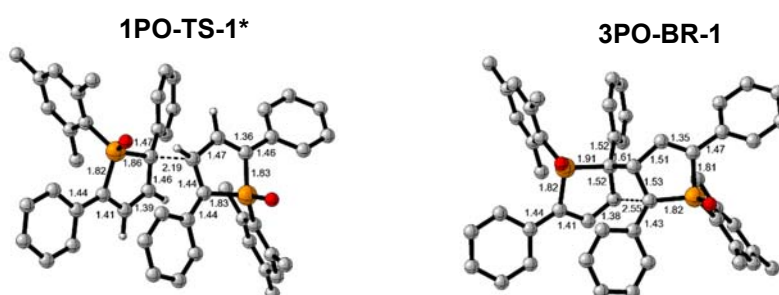


**Figure 6.** Selected optimized structures for the transition state and the MECP involved in the mechanism for formation of the [2+2]-cycloaddition product. Certain H atoms are omitted for clarity reasons. The distances presented are given in Å.

The excited triplet phosphole molecule will then react with an additional phosphole, leading to formation of a C-C bond. This reaction takes place in the triplet electronic state. Right after this step, the system reaches the intersystem crossing point (minimum energy crossing point, MECP), relaxes to the singlet state and forms the second C-C bond which closes the four-membered ring. The Gibbs energy diagram shows that the light-induced [2+2]-dimerization in the P(V) derivative is an exergonic process by 20.8 kcal mol $^{-1}$ . Hence, it may be deduced that the formation of the first C-C bond is the most energy-intensive step and involves an energy barrier of 16.2 kcal mol $^{-1}$ . We have also performed computational studies on the formation of the Diels-Alder [4+2]-cycloadducts from 1-mesityl-2,5-

diphenylphosphole oxide by thermal activation. The computed barrier is much higher than that for the formation of the [2+2] adduct.

However, the preference for the formation of a syn-anti and simultaneously a “head-to-tail” arrangement in the adduct over the anti-anti, syn-syn and “head-to-head” would need to be explored in more depth in the future. Nonetheless, this ordination does allow for the best interactions from steric point of view.

## Conclusions

The objectives of this project included the elucidation of the key points for influencing the stereo- and regio-selective outcome during catalytic P-C bond formation across unsaturated substrates and to clarify the mode of action for the alkali metal ions during the reaction by means of experimental and mechanistic studies. More concretely, in this work we focused on clarifying the reaction mechanism for the alkali metal-mediated Pudovik reaction, the addition of secondary phosphine oxides across phenylacetylene and 1,4-diphenylbutadiyne via alkali metal hexamethyldilazides (M-HMDS; M = Li, Na and K). Additionally, we investigated the addition of mesityl phosphine across 1,4-diphenylbutadiyne, promoted by the same pre-catalyst (M-HMDS; M = Li, Na, and K). This addition reaction yielded 1-mesityl-2,5-diphenylphosphole as the single product. Hence, we subsequently investigated the oxidation of the newly formed phosphole and its subsequent [2+2]-photo cycloaddition as additional objective both experimentally and theoretically.

In summary, we were able to achieve most of our objectives, however, we are still in the process of completion of the reaction mechanism for the addition of the alkali metal-mediated Pudovik reaction promoted by M-HMDS. Theoretical investigations on already published reactions and newly obtained experimental results for the alkali metal-catalyzed Pudovik reaction revealed the intricacy of these processes and offered a detailed description of the reaction mechanisms. To the best of our knowledge, these are the first reported mechanistic investigations on alkali metal-mediated Pudovik reactions. These calculations detailed the bonding mode of the alkali cations with the alkyne groups and the aryl substituents and how these modes influence the outcome of the reaction (i.e., the stereoselectivity, the conversion rate, *etc.*).

From the experimental results it can be deduced that the metal cations play a crucial role as the conversion showed dependence on the softness and the radius of the metal ions, regardless if we used P(III) or P(V) compounds for the addition. Overall, the lighter s-block metal congener Li-HMDS was not able to mediate any of the reactions, whilst the congeners of the heavier alkali metal bis(trimethylsilyl)amides M-HMDS (M = K and Na) effectively promoted both the hydrophosphination and the hydrophosphorylation. Therefore, we confirmed theoretically and experimentally that these cations are not only “spectator” species, but they rather play a significant role in the outcome of these conversions in each step of the reaction. Theoretical results also indicate that generation of the active monometallic species from the more stable aggregates is crucial for the activity shown by the metal. The new proposed method of phosphole synthesis in a single pot and at room temperature offers an alternative approach which may be implemented later for the synthesis of polyphospholes, which are highly promising material for use as organic light-emitting diodes (OLED) [18,20]. The serendipitous formation of the [2+2]-photo-cycloaddition product disclosed another property of phosphole oxides, which would need to be explored in the future.

These discoveries emphasize the potential that alkali metal-based catalysts hold for future catalytic applications, especially for formation of stereo- and regio-selective P-C bonds. Thus, it can be

deduced that the understanding of reaction mechanisms is highly advantageous for the development of non-toxic and easily available catalysts for future applications in homogeneous catalytic reactions. Expansion of this concept might lead to interesting applications also in hydrogenation, hydrosilylation, and hydroamination processes and beyond.

## References

- [1] T. M. A. Al-Shboul, V. K. Pálfi, L. A. Yu, R. Kretschmer, K. Wimmer, R. Fischer, H. Görls, M. Reiher, M. Westerhausen, *J. Organomet. Chem.* **2011**, *696*, 216–227. DOI: [10.1016/j.jorganchem.2010.08.058](https://doi.org/10.1016/j.jorganchem.2010.08.058).
- [2] S. Kriek, M. Westerhausen, *Inorganics* **2017**, *5*, 17. DOI: [10.3390/inorganics5010017](https://doi.org/10.3390/inorganics5010017).
- [3] C. A. Bange, R. Waterman, *Chem. Eur. J.* **2016**, *22*, 12598–12605. DOI: [10.1002/chem.201602749](https://doi.org/10.1002/chem.201602749).
- [4] S. Lau, T. M. Hood, R. L. Webster, *ACS Catal.* **2022**, *12*, 10939–10949. DOI: [10.1021/acscatal.2c03144](https://doi.org/10.1021/acscatal.2c03144).
- [5] B. T. Novas, R. Waterman, *ChemCatChem* **2022**, *14*, e202200988. DOI: [10.1002/cctc.202200988](https://doi.org/10.1002/cctc.202200988).
- [6] M. T. Whitelaw, S. Banerjee, A. R. Kennedy, A. Van Teijlingen, T. Tuttle, R. E. Mulvey, *Cell Rep.* **2022**, *3*, 100942. DOI: [10.1016/j.xcrp.2022.100942](https://doi.org/10.1016/j.xcrp.2022.100942).
- [7] A. W. J. Platten, A. M. Borys, E. Hevia, *ChemCatChem* **2022**, *14*, e202101853. DOI: [10.1002/cctc.202101853](https://doi.org/10.1002/cctc.202101853).
- [8] B. E. Fener, P. Schüller, N. Ueberschaar, P. Bellstedt, H. Görls, S. Kriek, M. Westerhausen, *Chem. Eur. J.* **2020**, *26*, 7235–7243. DOI: [10.1002/chem.201905565](https://doi.org/10.1002/chem.201905565).
- [9] S. M. Härling, B. E. Fener, S. Kriek, H. Görls, M. Westerhausen, *Organometallics* **2018**, *37*, 4380–4386. DOI: [10.1021/acs.organomet.8b00368](https://doi.org/10.1021/acs.organomet.8b00368).
- [10] V. Koshti, S. Gaikwad, S. H. Chikkali, *Coord. Chem. Rev.* **2014**, *265*, 52–73. DOI: [10.1016/j.ccr.2014.01.006](https://doi.org/10.1016/j.ccr.2014.01.006).
- [11] K. Hirano, M. Miura, *Tetrahedron Lett.* **2017**, *58*, 4317–4322. DOI: [10.1016/j.tetlet.2017.10.018](https://doi.org/10.1016/j.tetlet.2017.10.018).
- [12] R. A. Bartlett, M. M. Olmstead, P. P. Power, G. A. Sigel, *Inorg. Chem.* **1987**, *26*, 1941–1946. DOI: [10.1021/ic00259a026](https://doi.org/10.1021/ic00259a026).
- [13] S. M. Härling, B. E. Fener, S. Kriek, H. Görls, M. Westerhausen, *Organometallics* **2018**, *37*, 4380–4386. DOI: [10.1021/acs.organomet.8b00368](https://doi.org/10.1021/acs.organomet.8b00368).
- [14] T. M. A. Al-Shboul, H. Görls, S. Kriek, M. Westerhausen, *Eur. J. Inorg. Chem.* **2012**, 5451–5455. DOI: [10.1002/ejic.201201138](https://doi.org/10.1002/ejic.201201138).
- [15] F. Roesler, M. Kovács, C. Bruhn, Z. Kelemen, R. Pietschnig, *Organometallics* **2023**, *42*, 793–802. DOI: [10.1021/acs.organomet.3c00019](https://doi.org/10.1021/acs.organomet.3c00019).
- [16] F. Roesler, M. Kovács, C. Bruhn, Z. Kelemen, R. Pietschnig, *Chem. Eur. J.* **2021**, *27*, 9782–9790. DOI: [10.1002/chem.202101298](https://doi.org/10.1002/chem.202101298).
- [17] Y. Matano, M. Nakashima, H. Imahori, *Angew. Chem., Int. Ed.* **2009**, *121*, 4062–4065. DOI: [10.1002/ange.200900542](https://doi.org/10.1002/ange.200900542).
- [18] M. Hissler, C. Lescop, R. Réau, *Compt. Rend. Chim.* **2008**, *11*, 628–640. DOI: [10.1016/j.crci.2008.01.010](https://doi.org/10.1016/j.crci.2008.01.010).
- [19] L. D. Quin, X. P. Wu, *Heteroat. Chem.* **1991**, *2*, 359–367. DOI: [10.1002/hc.520020303](https://doi.org/10.1002/hc.520020303).
- [20] D. Joly, D. Tondelier, V. Deborde, B. Geffroy, M. Hissler, R. Réau, *New J. Chem.* **2010**, *34*, 1603. DOI: [10.1039/c0nj00122h](https://doi.org/10.1039/c0nj00122h).
- [21] E. Deschamps, L. Ricard, F. Mathey, *ChemInform* **1994**, *25*(44). DOI: [10.1002/chin.199444188](https://doi.org/10.1002/chin.199444188).
- [22] T. J. Barton, A. Nelson, *Tetrahedron Lett.* **1969**, *10*, 5037–5040. DOI: [10.1016/S0040-4039\(01\)88878-X](https://doi.org/10.1016/S0040-4039(01)88878-X).
- [23] F. F. Arp, R. Ashirov, N. Bhuvanesh, J. Blümel, *Dalton Trans.* **2021**, *50*, 15296–15309. DOI: [10.1039/d1dt03243g](https://doi.org/10.1039/d1dt03243g).
- [24] M. P. Duffy, Y. Lin, L. Y. Ting, F. Mathey, *New J. Chem.* **2011**, *35*, 2001–2003. DOI: [10.1039/c1nj20087a](https://doi.org/10.1039/c1nj20087a).
- [25] G. Bousrez, E. Nicolas, A. Martinez, S. Chevreux, F. Jaroschik, *Heteroatom Chem.* **2019**, 1–10. DOI: [10.1155/2019/2596405](https://doi.org/10.1155/2019/2596405).
- [26] Y. Matano, *Phospholes and Related Compounds: Syntheses, Redox Properties, and Applications to Organic Electronic Devices*, in *Organic Redox Systems* (T. Nishinaga, Editor), Wiley: **2016**, pp 477–501 (Wiley, 2016). DOI: [10.1002/9781118858981.ch16](https://doi.org/10.1002/9781118858981.ch16).

**Zinnia ARORA**

**ESR4**

**Thesis co-directors**

Prof. Vasile Pârvulescu    Universitatea din Bucuresti, Bucharest, Romania

Dr. Jérôme Durand,  
Dr. Maryse Gouygou    Laboratoire de Chimie de Coordination, Toulouse, France  
Dr. Karine Philippot

**Thesis defense**

Laboratoire de Chimie de Coordination, Toulouse, France, 15 March 2024



## Carbon Nanomaterial Supported Metal Complexes and Nanoparticles for Asymmetric Catalysis

### Introduction

Catalytic asymmetric synthesis is the "art" of providing exclusively one of the enantiomers of a target product in the presence of sub-stoichiometric amount of the suitable chiral catalyst. The synthesis of enantiomerically pure compounds requires to understand and follow the rules developed by nature in order to generate assimilable molecules by the living world [1]. Without the development of asymmetric catalysts, it would not have been possible to reach the actual level of advancement in pharmacy, or medicine domains [2–5].

The creativity developed in asymmetric catalysis offers not only the possibility to synthesize nature-like molecules but also to open new fields in chemistry. A perspective looks over organic synthesis would reveal that the need for enantiomerically enriched compounds is an ultimate challenge and that the search for efficient catalytic processes has pioneered this area of research. Despite the advantages of homogeneous catalytic systems, such as high enantioselectivities and activities for a wide range of chemical transformations, drawbacks like limited recovery and reuse of the expensive chiral catalysts and/or metal contamination of the products, particularly unacceptable for pharmaceutical production, significantly obstructed their practical applications [6,7]. The immobilization of the chiral catalytic phase has recently attracted a great deal of attention and appears as a promising solution to the above-mentioned problem. In addition, the demand for environmentally acceptable processes determined the minimization of waste whether from reagents or solvents and so the use of performant and recyclable catalysts. Immobilization of molecular catalysts is thus an attractive approach to combine the advantages of both homogeneous and heterogeneous catalysis [8].

Most reports describe the use of organic polymers and porous inorganic materials, such as zeolites, mesoporous silicas, and alumina as metal complex supports [9–12]. Carbon materials, especially nanostructured ones like carbon nanotubes (CNTs) or few-layer graphene, represent an interesting alternative to these conventional supports. However, despite the significant progress on nanocarbon-based catalysts, only a few applications in catalytic asymmetric transformations have been reported mainly for enantioselective hydrogenation reactions [13,14]. Not only metal complexes, metal nanoparticles (MNPs) are also currently largely studied for catalysis as they bring a bridge between the domains of homogeneous and heterogeneous catalysis [15].

Given these considerations, the main goal of this PhD project was to design new catalytic tools by immobilization of chiral species (complexes or nanoparticles) on the surface of nanostructured carbons (nanotubes or graphene) for enantioselective hydrogenations.

To achieve this, the primary goal was subdivided into sub-objectives. **a)** The synthesis of non-structured carbon materials CNTs, and their functionalization. **b)** The synthesis of phosphine-type chiral ligands to prepare metal complexes, immobilization of the obtained complexes on different functionalized CNTs, and catalytic application in asymmetric hydrogenation of C=C substrate. **c)** The development of synthesis tools to achieve small and well-defined chiral rhodium nanoparticles in the presence of phosphine-type chiral ligands as stabilizers, immobilization of the NPs on different functionalized CNTs, and catalytic application in asymmetric hydrogenation of C=C substrate.

## Synthesis of non-structured carbon materials CNTs, and their functionalization

CNTs were prepared by the catalytic-CVD method according to a procedure developed in LCC using  $\text{AlFeCoO}_4$  as a catalyst at a temperature of  $650\text{ }^\circ\text{C}$ . To introduce functionalities on the surface of CNTs, it is necessary to activate their surface. The prevalent method to introduce surface hydroxyl, carbonyl, and carboxylic acid groups is the oxidation of CNTs using nitric acid ( $\text{HNO}_3$ ) as an oxidative reagent.

To improve the affinity between the CNTs and chiral cationic rhodium complexes, the CNT surface was negatively charged. The CNT-O obtained through the oxidative treatment with  $\text{HNO}_3$  was further modified by two different routes to afford the functionalized supports i.e.,  $\text{CNT-COO}^-\text{Na}^+$ , and CNT-HPA.

### Synthesis of $\text{CNT-COO}^-\text{Na}^+$

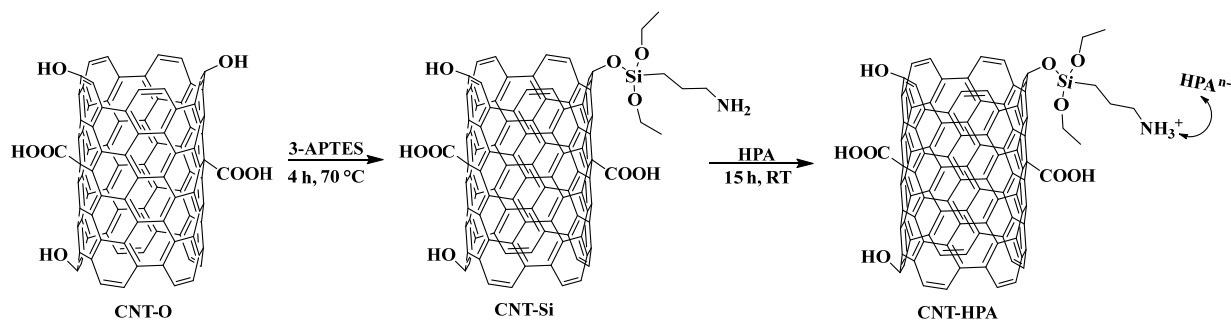
Purified CNT-O were neutralized with sodium hydroxide ( $\text{NaOH}$ ) under stirring for 24 h at room temperature (RT). The resulted sodium salt of CNT-O was then separated from the solution *via* filtration, washed with distilled water until reaching a neutral pH, and dried at  $120\text{ }^\circ\text{C}$  for 2 days (Scheme 1).



**Scheme 27.** Deprotonation of the oxidized carbon nanotubes (CNT-O) by  $\text{NaOH}$ .

### Synthesis of CNT-HPA

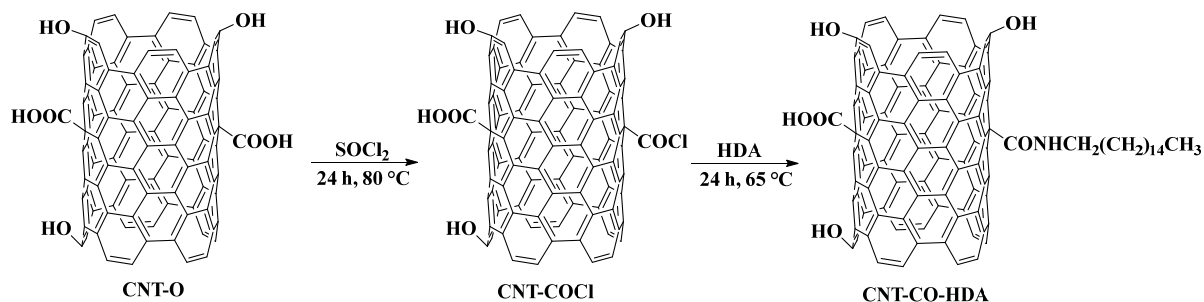
The synthesis of CNT-HPA (HPA= silicotungstic acid;  $\text{H}_4[\text{SiW}_{12}\text{O}_{40}]$ ) has been carried out in two steps. In the first step, the dried CNT-O was reacted with 3-aminopropyl triethoxysilane (3-APTES) in ethanol at  $70\text{ }^\circ\text{C}$  for 4 h resulting in silanized CNTs referred to as CNT-Si. The CNT-Si were then dried under a high vacuum at  $80\text{ }^\circ\text{C}$  for 24 h. In the second step, a 2-propanol solution of silicotungstic acid (HPA) was slowly added to the CNT-Si previously dispersed in 2-propanol (Scheme 2).



**Scheme 28.** Synthesis of CNT-HPA support using the silicotungstic acid.

### Synthesis of CNT-CO-HAD

In order to confine rhodium nanoparticles into the CNTs, long alkyl chains were introduced at the surface. The CNT-O was modified by acylation reactions to afford the CNT-CO-HDA support. The CNT-O was firstly treated with a solution of thionyl chloride ( $\text{SOCl}_2$ ) for 24 h at 80 °C. This treatment aimed to produce CNT-COCl as an intermediate for a subsequent amidation reaction. With this aim CNT-COCl was further reacted with hexadecyl amine (HDA;  $\text{CH}_3-(\text{CH}_2)_{15}-\text{NH}_2$ ) for 24 h at 65 °C, in order to attach long alkyl chains-bearing amido groups on the CNTs surface (Scheme 3).



**Scheme 29.** The formation of long alkyl chain-bearing amido groups on the surface of CNT.

All the functionalized CNTs were fully characterized by FT-IR, TGA, RAMAN, BET, TEM, and HR-TEM techniques. The different supports prepared were further used for the immobilization of Rh catalysts. CNT,  $\text{CNT-COO}^-\text{Na}^+$ , and CNT-HPA samples were used as support for the immobilization of rhodium complexes. CNT-O and CNT-CO-HDA were selected for the immobilization of the rhodium nanoparticles.

### Preparation of chiral rhodium complexes

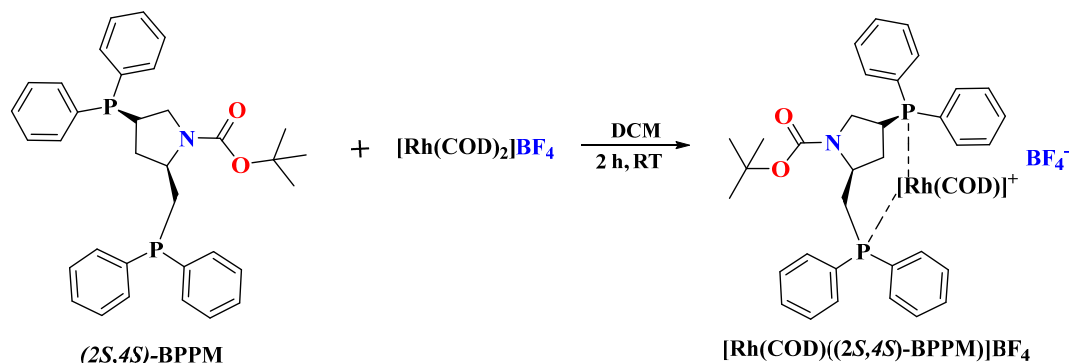
Asymmetric ligands from the group of C1-diphosphines with a chiral pyrrolidine backbone have been selected because the phosphinopyrrolidine-rhodium catalysts have been shown to be performant for the hydrogenation of many unsaturated substrates.

We chose the commercially available ligand (2*S*,4*S*)-BPPM to synthesize the cationic rhodium complex  $[\text{Rh}(\text{COD})(2*S*,4*S*)\text{-BPPM}]\text{BF}_4$ . Additionally, the (2*S*,4*S*)-PPM ligand was modified by pyrene group to produce the PPM-pyrene group to synthesize the  $[\text{Rh}(\text{COD})((2*S*,4*S*)\text{-PPM-pyrene})]\text{BF}_4$  complex. Both complexes were selected strategically to capitalize on electrostatic interaction or  $\pi$ - $\pi$  stacking, respectively, aiming to facilitate their immobilization on carbon nanotubes.

#### Synthesis of $[\text{Rh}(\text{COD})((2*S*,4*S*)\text{-BPPM})]\text{BF}_4$

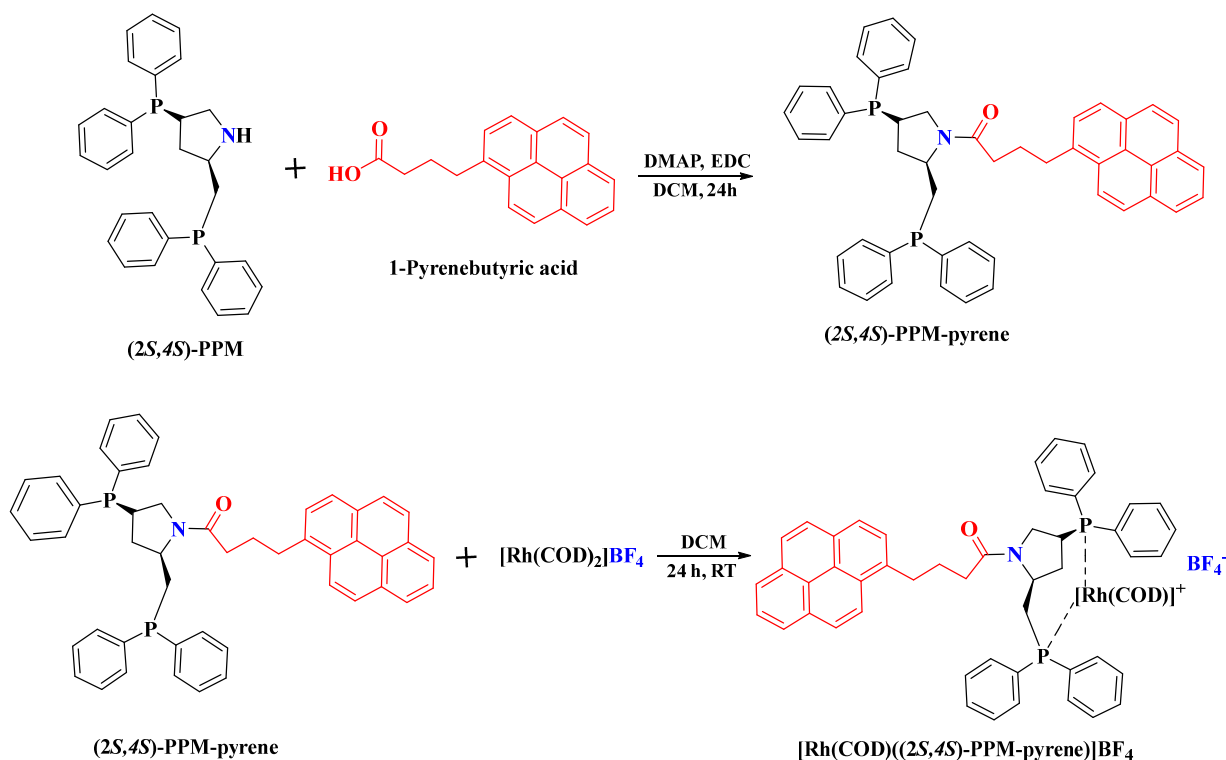
The chiral  $[\text{Rh}(\text{COD})(2*S*,4*S*)\text{-BPPM}]\text{BF}_4$  complex was prepared by mixing (2*S*,4*S*)-(-)-2-(diphenylphosphinomethyl)-4-(diphenylphosphino)-*N*-(*t*-butoxycarbonyl)pyrrolidine ((2*S*,4*S*)-BPPM) ligand with bis(1,5-cyclooctadiene)rhodium(I) tetrafluoroborate (1:1 ratio) in dry dichloromethane (DCM) for 2 h at room temperature (Scheme 4). The complex was isolated as a yellow solid and characterized by  $^{31}\text{P}$  NMR and mass spectrometry.





**Scheme 30.** Synthesis of [Rh(COD)((2*S*,4*S*)-PPM-pyrene)]BF<sub>4</sub>

The chiral pyrene ligand was prepared by condensation of (2*S*,4*S*)-4-(diphenylphosphino)-2-[(diphenyl-phosphino)methyl]pyrrolidine (2*S*,4*S*)-PPM with 1-pyrenebutyric acid in the presence of 4-dimethylaminopyridine (DMAP) and 1-ethyl-3-(3-dimethylaminopropyl)carbodiimide (EDC) in dry DCM as a solvent for 24 h under an argon inert atmosphere. Reaction of bis(1,5-cyclooctadiene) rhodium (I) tetrafluoroborate in dichloromethane with one equivalent of (2*S*,4*S*)-PPM-pyrene ligand quantitatively led to the cationic complex [Rh(COD)((2*S*,4*S*)-PPM-pyrene)]BF<sub>4</sub> (Scheme 5).



**Scheme 31:** Synthesis of (2*S*,4*S*)-PPM-pyrene ligand and [Rh(COD)((2*S*,4*S*)-PPM-pyrene)]BF<sub>4</sub> complex.

These complexes were immobilized using non-covalent interactions on three distinct carbon nanotube (CNT) supports, namely, CNT, CNT-COO<sup>-</sup>Na<sup>+</sup>, and CNT-HPA. Different systems of supported chiral rhodium complexes each distinguished by the different nature of chiral ligands, and different functionalized carbon supports were synthesized. A comprehensive overview of all the synthesized complexes and carbon supports that are used is given in Figure 1.

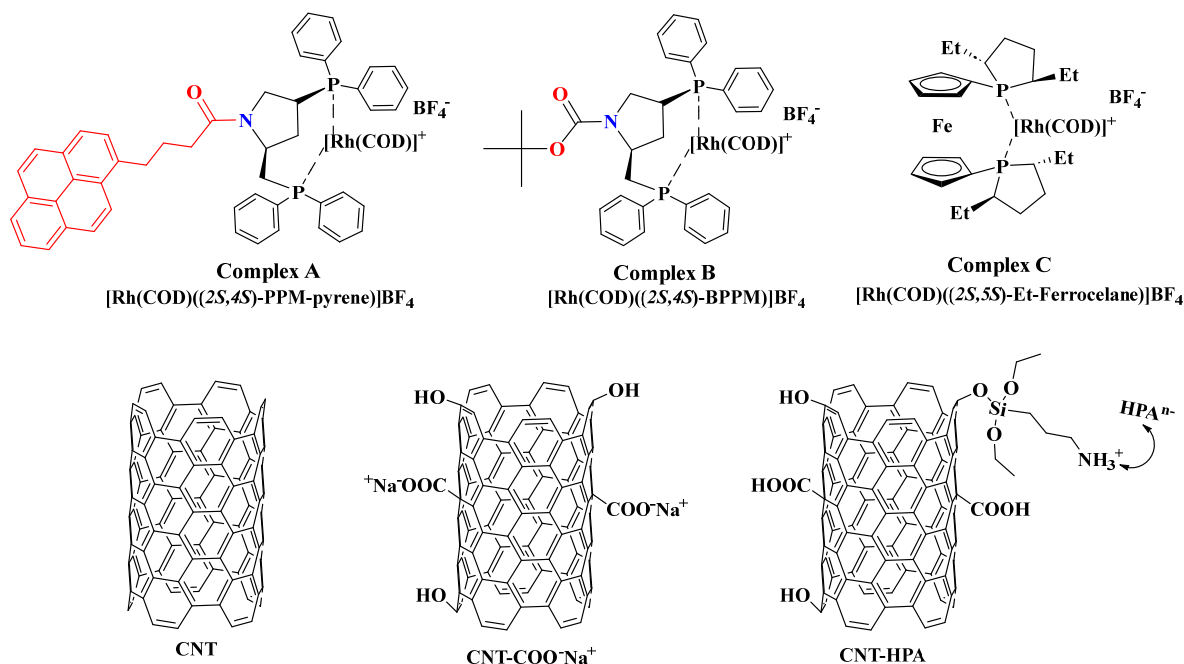
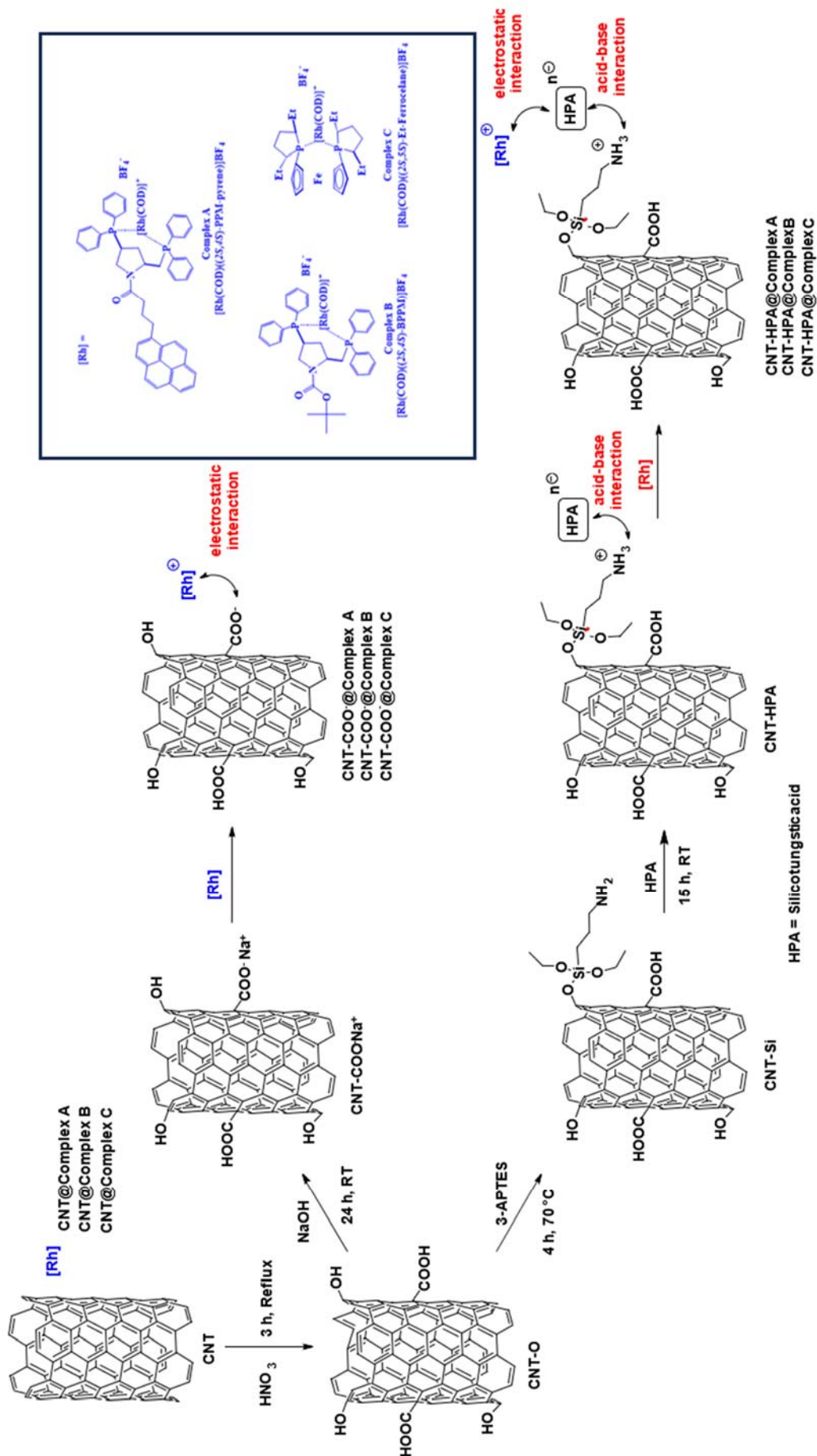


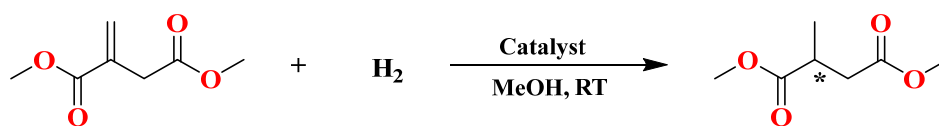
**Figure 6.** Rhodium complexes and functionalized carbon supports.

We have studied the non-covalent immobilization of all rhodium complexes,  $[\text{Rh}(\text{COD})((2S,4S)\text{-PPM-pyrene})]\text{BF}_4$  (**Complex A**) and  $[\text{Rh}(\text{COD})((2S,4S)\text{-BPPM})]\text{BF}_4$  (**Complex B**), and  $[\text{Rh}(\text{COD})((2S,5S)\text{-Et-Ferrocene})]\text{BF}_4$  (**Complex C**) onto carbon nanotubes as a support and their application in the enantioselective hydrogenation of dimethyl itaconate as a model substrate. The immobilization of the rhodium complexes on the CNT supports was first done by applying a  $\pi$ - $\pi$  interaction that relies on aromatic rings between the pristine CNT and all three complexes. The second strategy for immobilization of the rhodium complexes on the CNT supports was done by applying an ionic anchoring strategy that relies on the electrostatic interaction between the cationic Rh complex and the surface negatively charged of carboxylate-functionalized CNTs (CNT-COO<sup>-</sup>). The third strategy also implied an ionic anchoring but through a spacer-type anchoring agent, heteropoly acid HPA, that was previously grafted at the CNT surface thanks to an acid-base interaction. This approach induced an electrostatic interaction between the Rh complexes and the HPA-functionalized CNT far away from the CNT surface. The motivation of this HPA approach was to study the effect of distance from the CNT surface on the Rh complex performance. All three strategies are shown on the next page.

The obtained **CNT@Complex A**, **CNT@Complex B**, **CNT@Complex C**, **CNT-COO<sup>-</sup>@Complex A**, **CNT-COO<sup>-</sup>@Complex B**, **CNT-COO<sup>-</sup>@Complex C**, **CNT-HPA@Complex A**, **CNT-HPA@Complex B**, and **CNT-HPA@Complex C** materials were characterized by complementary techniques. The characterization results confirmed the anchoring of the Rh complexes in 7 cases out of 9 thus highlighting the all strategies were quite successful. Interestingly, XPS data evidenced that the Rh complexes interacted with both the ligand phosphorus atoms and CNT support with no electronic differences between the three complexes whatever the nature of the CNTs. This thus allowed to compare the effect of the support on the catalysis performance depending on the nature of CNTs.



The catalytic hydrogenation of dimethyl itaconate was studied with all the CNT-immobilized Rh-complexes in mild reaction conditions (RT, 5.5 bar H<sub>2</sub>) and the results were compared to those obtained with the non-immobilized complexes in the same reaction conditions (Table 1). Firstly, the three **A**, **B**, and **C** complexes in homogeneous conditions proved good activity and selectivity for the hydrogenation of DMI with 100% conversion in 0.5 h with 57%, 72%, and 71% of enantioselectivities respectively (Table 1, entries 1-3). The immobilized Rh complexes showed to be less rapid in hydrogenating DMI than their free counterparts, as usually observed in catalysis, but increasing the reaction time allowed to get full conversions. **CNT@Complex A** showed good activity with 34% of ee towards (*S*) methyl succinate (Table 1, entry 4) whereas **CNT@Complex B** produced low activity and enantioselectivity (10% towards (*S*) methyl succinate) (Table 1, entry 6). The recycling of the **CNT@Complex A** indicated good stability, namely, with a small change in the catalytic performances (Table 1, entry 4 vs 5). Such difference in enantioselectivity compared to the values collected with the free Rh complexes (*ca.* 56%) indicated that the support affected the hydrogenation reaction probably due to a modification of the ligand geometry that reduced the enantioselective hydrogenation of DMI. The immobilization of complexes on the CNT-COO<sup>-</sup>Na<sup>+</sup> support by electrostatic interactions occurs with partial (**complex B and C**) or total decoordination (**complex A**) of the chiral diphosphine ligand and probably partial or total direct coordination of Rh (I) to the carboxylate group on the surface. **CNT-COO<sup>-</sup>@Complex B** afforded a rather moderate activity compared to **CNT-COO<sup>-</sup>@Complex C**. Also, low enantioselectivity was observed with **CNT-COO<sup>-</sup>@Complex B** (8% ee towards (*S*) methyl succinate) while **CNT-COO<sup>-</sup>@Complex C** provided good ee to (*R*) methyl succinate (64-65%) (Table 1, entries 7-8). A recyclability study performed with recovered **CNT-COO<sup>-</sup>@Complex C** catalyst indicated the conversion remained total but with no ee was detected (Table 1, entry 9). Moreover, TEM analysis revealed the presence of Rh nanoparticles, thus indicating the decomposition of the catalyst in the recovering conditions applied. The presence of these Rh nanoparticles may explain the absence of enantioselectivity as the ligand may be not strongly attached to their surface. The catalytic tests with the **CNT-HPA@Complex A**, **CNT-HPA@Complex B**, and **CNT-HPA@Complex C** also showed high conversions in the hydrogenation of DMI into methyl succinate (83-100%) (Table 1, entries 10-16). In terms of enantioselectivity, **CNT-HPA@Complex A** showed moderate enantioselectivity (20% to (*S*) methyl succinate) (Table 1, entry 10). The **CNT-HPA@Complex B** generated a high ee of 57% to the (*S*) methyl succinate which was much higher than that generated by the **CNT-COO<sup>-</sup>@Complex B** (8%) (Table 1, entry 11 vs 7). The recyclability tests with the **CNT-HPA@Complex B** showed the catalysts remain active till 4 catalytic runs and showed a small decrease in the enantioselectivity after 3<sup>rd</sup> run (Table 1, entries 11-14). **CNT-HPA@Complex C** achieved a 58% ee to (*R*) methyl succinate (Table 1, entry 15). **CNT-HPA@Complex C** were less active but still enantioselective in the hydrogenation of DMI after recycling, showing a different behavior than their CNT-COO<sup>-</sup> counterparts. This emphasizes that in the presence of CNT-HPA support the chiral ligand of Rh complexes is less affected by the proximity of the support contrarily to catalysts based on CNT-COO<sup>-</sup>. It corroborates the interest in adding a spacer such as HPA between the Rh complex and the CNT support to limit the effect of the CNT surface environment on the catalytic behavior of the Rh immobilized complexes. Both catalysts **CNT-HPA@Complex B** and **CNT-HPA@Complex C** were tested in continuous flow conditions after showing good results in batch conditions. These both catalysts were active and selective in flow conditions. **CNT-HPA@Complex B** showed 47% of conversion with 43% of ee towards (*S*) methyl succinate in the first 20 minutes whereas **CNT-HPA@Complex C** showed 29% of conversion with 30% of ee towards (*R*) methyl succinate under the same conditions. This flow study was done only in the primary stage. More optimizations are required to obtain better results and understanding.

**Table 4.** Catalytic results for the hydrogenation of dimethyl itaconate onto the functionalized CNT immobilized Rh-complexes. <sup>a</sup>

Entry	Catalyst	S/C	Run	Time (h)	Conv. <sup>b</sup> (%)	Selectivity (%)	ee <sup>b</sup> (%)
1	<b>Complex A</b>	80		0.5	100	100	57 (S)
2	<b>Complex B</b>	80		0.5	100	100	72 (S)
3	<b>Complex C</b>	100		0.5	100	100	71 (R)
4	<b>CNT@Complex A</b>	95	1	4	29	100	34 (S)
5	<b>CNT@Complex A</b>	95	2	4	26	100	28 (S)
6	<b>CNT@Complex B</b>	128	1	24	40	100	10 (S)
7	<b>CNT-COO<sup>-</sup>@Complex B</b>	124	1	24	60	100	8 (S)
8	<b>CNT-COO<sup>-</sup>@Complex C</b>	303	1	24	100	100	64 (R)
9	<b>CNT-COO<sup>-</sup>@Complex C</b>	303	2	24	100	100	-
10	<b>CNT-HPA@Complex A</b>	217	1	24	100	100	20 (S)
11	<b>CNT-HPA@Complex B</b>	192	1	7	100	100	57 (S)
12	<b>CNT-HPA@Complex B</b>	192	2	7	100	100	54 (S)
13	<b>CNT-HPA@Complex B</b>	192	3	7	95	100	47 (S)
14	<b>CNT-HPA@Complex B</b>	192	4	7	88	100	43 (S)
15	<b>CNT-HPA@Complex C</b>	277	1	15	100	100	58 (R)
16	<b>CNT-HPA@Complex C</b>	277	2	15	25	100	27 (R)

<sup>a</sup> Reaction conditions for **CNT@Complex A**: 0.060 g of immobilized Rh-complex; for **CNT@Complex B**: 0.090 g of immobilized Rh-complex; **CNT-COO<sup>-</sup>@Complex B**: 0.09 g of immobilized Rh-complex; for **CNT-COO<sup>-</sup>@Complex C**: 0.050 g of immobilized Rh-complex; **CNT-HPA@Complex A**: 0.08 g of immobilized Rh-complex; for **CNT-HPA@Complex B**: 0.06 g of immobilized Rh-complex; and **CNT-HPA@Complex C**: 0.06 g of immobilized Rh-complex, 0.16 g of substrate, 5.5 bars of H<sub>2</sub>, 4 ml of MeOH. <sup>b</sup>Determined by chiral GC using a Beta DEX<sup>TM</sup> 225 column.

## Synthesis of chiral rhodium nanoparticles

Different systems of chiral rhodium nanoparticles were synthesized, each distinguished by the nature of the precursor or stabilizer, the carbon support, or also by the reaction conditions used for their synthesis. The organometallic approach for synthesizing metallic nanostructures capitalizes on the principles of organometallic and coordination chemistry. Based on previous results in the synthesis of small Rh NPs, the  $[\text{Rh}(\eta^3\text{-C}_3\text{H}_5)_3]$  [16–18], and  $[\text{Rh}(\mu\text{-Cl})(\text{C}_8\text{H}_{12})_2]$  [19] were chosen as Rh precursors. Two chiral ligands (2*S*,4*S*)-BPPM and (2*S*,4*S*)-PPM-pyrene, were selected as stabilizing ligands to synthesize chiral Rh NPs.

### Synthesis of chiral Rh nanoparticles from $[\text{Rh}(\eta^3\text{-C}_3\text{H}_5)_3]$ and the (2*S*,4*S*)-BPPM ligand

The synthesis of chiral Rh NPs using the  $[\text{Rh}(\eta^3\text{-C}_3\text{H}_5)_3]$  precursor and the (2*S*,4*S*)-BPPM ligand revealed that heating was required to decompose the Rh(III) precursor in the presence of the diphosphine ligand. Also, a molar ratio of  $[\text{P}]/[\text{Rh}] = 0.6$  was found necessary to produce small-sized and well-controlled chiral NPs. This combination of Rh precursor and ligand allowed forming **Rh-(2*S*,4*S*)-BPPM-NPs-1** constituted of  $ca. 1.7 \pm 0.3$  nm size well-dispersed RhNPs. EDX analysis coupled to HR-TEM performed on different areas of the grid showed the presence of both Rh and P elements, thus indicating the presence of the (2*S*,4*S*)-BPPM ligand close to the Rh NPs (Figure 2).

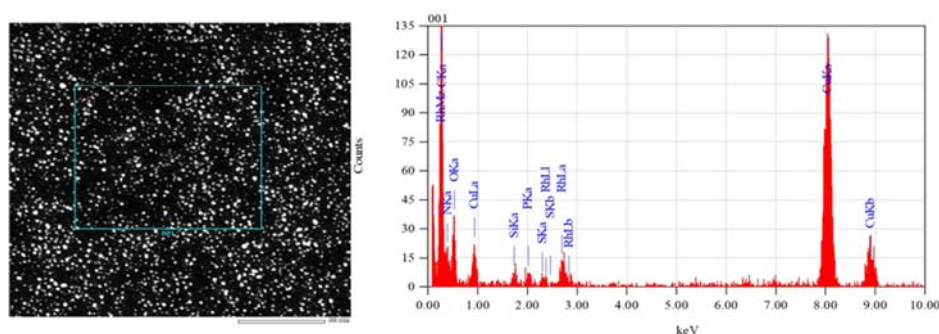


**Figure 7.** a) HR-TEM image of **Rh-(2*S*,4*S*)-BPPM-NPs-1** (0.3 eq) (scale bar = 50 nm) and b) the corresponding EDX spectrum.

Oxidized CNTs (CNT-O) were used as support to immobilize Rh NPs prepared from  $[\text{Rh}(\eta^3\text{-C}_3\text{H}_5)_3]$  precursor and (2*S*,4*S*)-BPPM ligand. The synthesis was done in one-pot conditions by adding the CNT-O to the reaction mixture composed of precursor and ligand in THF. The obtained **Rh-(2*S*,4*S*)-BPPM@CNT-O** NPs did not undergo agglomeration, yet they did not exhibit optimal dispersion in the CNT-O. Indeed, the confinement of NPs within the oxidized CNTs exhibited an alignment of close RhNPs, akin to a necklace formation (Figure 3).

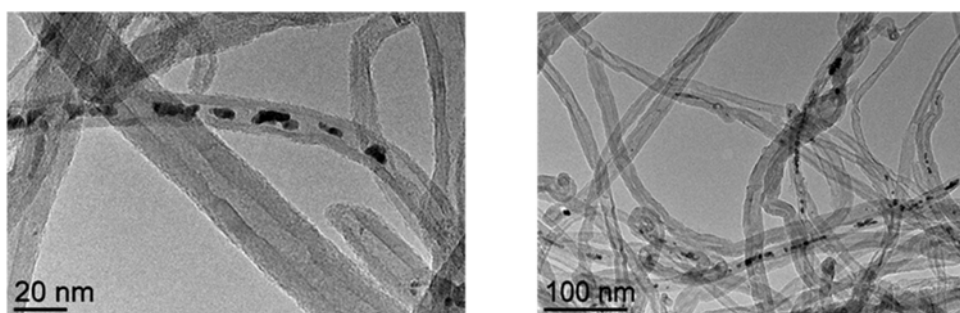
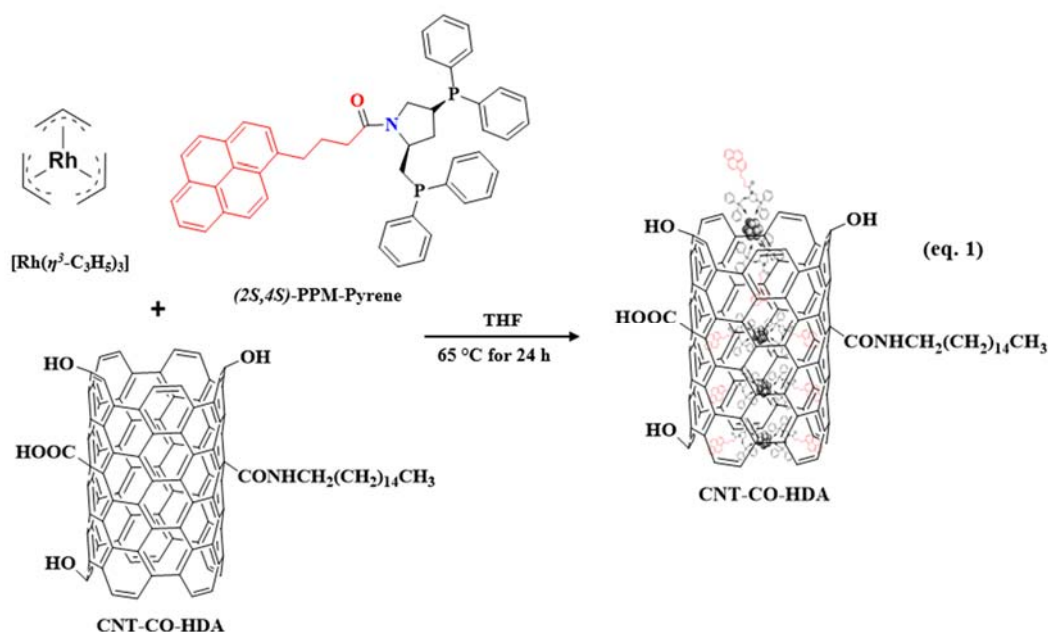


**Figure 8.** TEM images of **Rh-(2*S*,4*S*)-BPPM@CNT-O** at two different magnifications.

*Synthesis of chiral Rh nanoparticles from  $[Rh(\eta^3-C_3H_5)_3]$  and the (2S,4S)-PPM-pyrene ligand*

The (2S,4S)-PPM-pyrene ligand was also used as a stabilizer for the synthesis of chiral Rh NPs from  $[Rh(\eta^3-C_3H_5)_3]$  precursor, leading to **Rh-(2S,4S)-PPM-pyrene-NPs-2**. TEM analysis showed that the obtained Rh NPs were very close to each other and embedded within an organic matrix, probably due to the ligand, making a precise determination of their size was not possible. Compared to the first (2S,4S)-BPPM ligand, (2S,4S)-PPM-pyrene was found less effective for the formation of well-dispersed Rh NPs. This may be the effect of the presence of the pyrene groups that can interact each other by  $\pi$ - $\pi$  stacking and lead to the agglomeration of the NPs while remaining individual. To gain deeper insights into the embedding nature of the NPs, EDX-coupled HR-TEM results evidenced that the NPs were not well crystallized and that they all are in close proximity to the (2S,4S)-PPM-pyrene ligand, as phosphorous was clearly detected as surrounding the Rh metal. Inspired by previous results in the confinement of PtRu NPs, CNTs were modified by the grafting of amide groups with long alkyl chains at their surface (CNT-CO-HDA) in order to improve the confinement of Rh NPs synthesized from  $[Rh(\eta^3-C_3H_5)_3]$  precursor and (2S,4S)-PPM-pyrene ligand (eq 1).



These synthesis conditions led to a very efficient confinement of the chiral Rh NPs within the channels of CNT-CO-HDA, the surface amide groups repelling the deposition of Rh NPs at the external surface of the support (Figure 4).

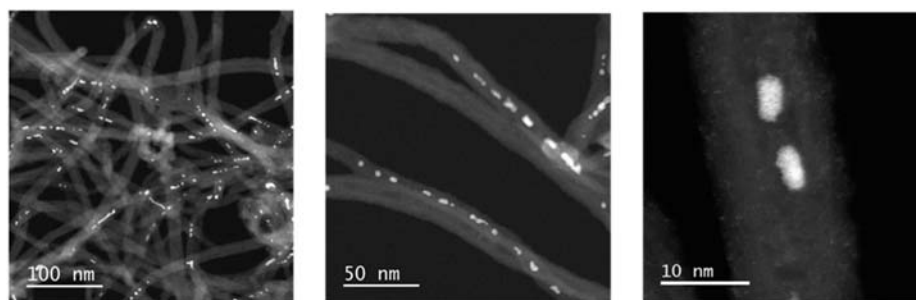


**Figure 9.** Bright field HR-TEM images of Rh-(2S,4S)-PPM-pyrene@CNT-CO-HDA at three different magnifications.

The asymmetric hydrogenation of dimethyl itaconate (DMI) was studied using these four systems of chiral NPs as catalysts: a) **Rh-(2S,4S)-BPPM-NPs-1**, b) **Rh-(2S,4S)-BPPM@CNT-O**, c) **Rh-(2S,4S)-PPM-pyrene-NPs-2**, and d) **Rh-(2S,4S)-PPM-pyrene-NPs-2@CNT-CO-HDA**. In all cases an excellent activity was obtained but with no enantioselectivity. The lack of enantioselectivity indicates that even in the case of the well-confined Rh NPs (**Rh-(2S,4S)-PPM-pyrene-NPs-2@CNT-CO-HDA**) the ligand is not blocked enough at the NP surface to allow the selective hydrogenation of the DMI in one preferential side.

*Synthesis of chiral Rh nanoparticles from  $[Rh(\mu-Cl)(C_8H_{12})]_2$  using the (2S,4S)-BPPM and (2S,4S)-PPM-pyrene ligands*

Following the protocol with the  $[Rh(\eta^3-C_3H_5)_3]$  precursor, Rh NPs, Rh-(2S,4S)-BPPM-NPs-3a stabilized by (2S,4S)-BPPM were synthesized from the  $[Rh(\mu-Cl)(C_8H_{12})]_2$  in THF solution under 3 bar of  $H_2$ , using a  $[P]/[Rh]$  ratio of 0.6 and 1eq. TEM images from the crude colloidal suspension at higher magnification allowed a better identification of the individual NPs indicating that they result from the agglomeration of NPs with the absence of coalescence. Similarly, Rh NPs, Rh-(2S,4S)-PPM-pyrene-NPs-4a stabilized by (2S,4S)-PPM-pyrene were synthesized from the  $[Rh(\mu-Cl)(C_8H_{12})]_2$  in THF solution resulting in the agglomerations of NPs (Figure 5). While the  $[Rh(\mu-Cl)(C_8H_{12})]_2$  complex decomposed easily at room temperature, that was different to the previous  $[Rh(\eta^3-C_3H_5)_3]$ , a less efficient Rh NP stabilization was observed in the presence of both ligand, even at a high  $[P]/[Rh]$  ratio as agglomerates were formed. This result prompted us to evaluate the synthesis of Rh NPs taking (2S,4S)-BPPM and (2S,4S)-PPM-pyrene as a stabilizer and  $[Rh(\mu-Cl)(C_8H_{12})]_2$  as a metal precursor in catalysis conditions, namely in the presence of DMI.

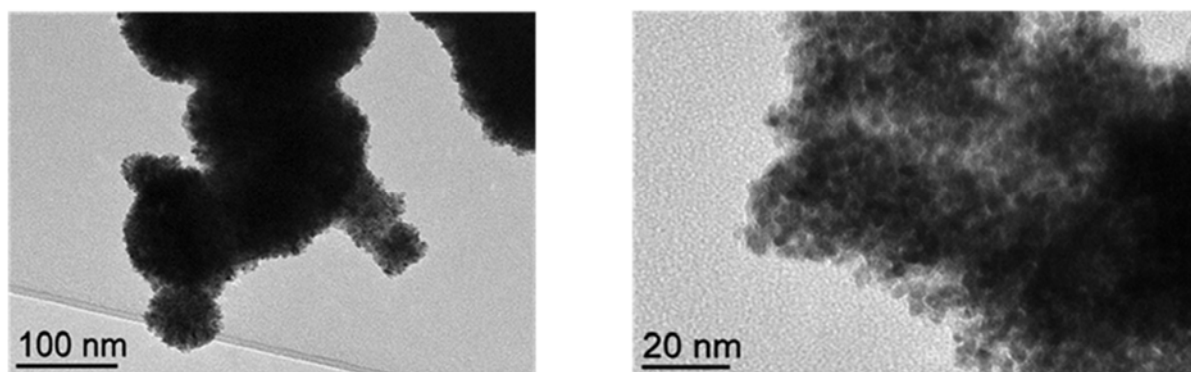


**Figure 10.** TEM images of **Rh-(2S,4S)-BPPM-NPs-3a** (left) and **Rh-(2S,4S)-PPM-pyrene-NPs-4a** (right) obtained with  $[P]/[Rh] = 1$ .

*Synthesis of chiral Rh nanoparticles from  $[Rh(\mu-Cl)(C_8H_{12})]_2$  using the (2S,4S)-BPPM and (2S,4S)-PPM-pyrene ligands under in-situ conditions*

Enantioselective hydrogenation of DMI could be achieved by forming the Rh NPs *in-situ* in catalysis conditions, namely in the presence of DMI. A series of experiments were done by modifying different parameters, such as the nature of Rh precursor ( $[Rh(\eta^3-C_3H_5)_3]$  or  $[Rh(\mu-Cl)(C_8H_{12})]_2$ ) or ligand ((2S,4S)-BPPM or (2S,4S)-PPM-pyrene), or changing the solvent (THF, toluene, isopropanol) or the temperature (RT, 40 °C, 60 °C). Different results in terms of Rh NP synthesis and catalytic performance were obtained, offering plenty of room to optimize the systems. Two systems that provided the best enantioselectivity results are highlighted. Using  $[Rh(\mu-Cl)(C_8H_{12})]_2$  precursor with (2S,4S)-BPPM with a ratio of  $[P]/[Rh] = 1$  led to *ca.* 2.5 nm size of sponge-like large Rh NPs (**Rh-(2S,4S)-BPPM-NPs-3b** sample)



(Figure 6). This sample led to an activity of 96 %, and more interestingly to a 16% of ee in asymmetric hydrogenation of DMI at 40 °C.

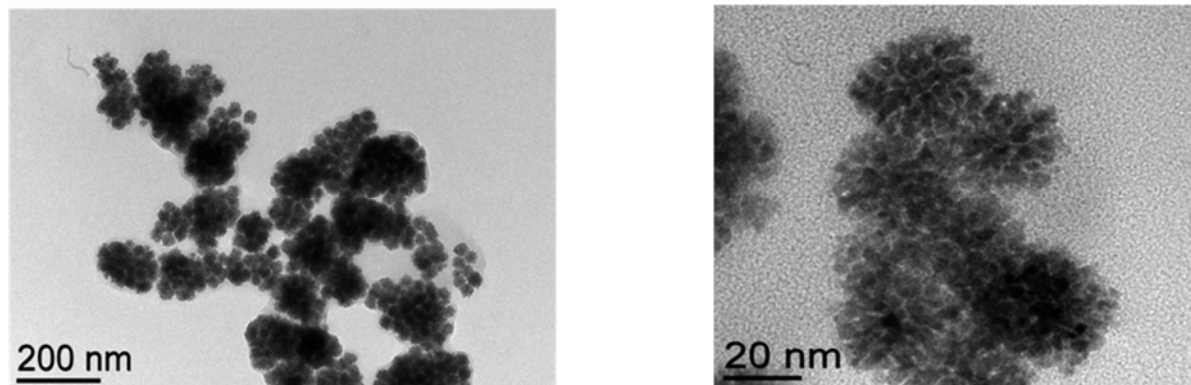


**Figure 11.** TEM images of **Rh-(2S,4S)-BPPM-NPs-3b** at two different magnifications.

Also, the synthesis of **Rh-(2S,4S)-PPM-pyrene-NPs-4b** performed with  $[\text{Rh}(\mu\text{-Cl})(\text{C}_8\text{H}_{12})]_2$  precursor and (2S,4S)-PPM-pyrene ligand showed well-controlled and well dispersed Rh NPs of *ca.* 2.6 nm (Figure 7). These NPs exhibited moderate catalytic activity (69%) and enantioselectivity (32%) for the DMI substrate at 40 °C. Effects of hydrogen pressure, temperature, and solvent were observed but complementary experiments are needed to enable a rationalization of their influence. Also, mercury tests have been done with **Rh-(2S,4S)-PPM-pyrene-NPs-4b**, which confirmed the role of the Rh NPs as catalytic species in the hydrogenation of DMI.

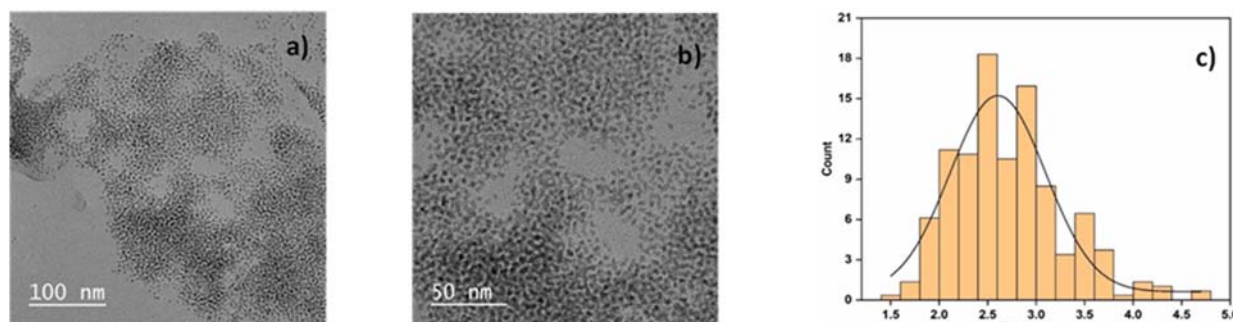


**Figure 12.** a) and b) TEM images of **Rh-(2S,4S)-PPM-pyrene-NPs-4b** at two different magnifications, and c) corresponding size distribution.

This work shows that the synthesis of chiral Rh NPs was possible starting from organometallic complexes and diphosphine-type ligands in mild conditions (low  $\text{H}_2$  pressure and temperature). The study performed in the hydrogenation of dimethyl itaconate with the different systems of Rh NPs prepared revealed either an excellent activity (100% conversion in 4 h at RT and 40 °C) but either no enantioselectivity or a moderate activity but with positive enantioselectivity (up to 36% ee). This work thus opened a new avenue for the preparation of chiral rhodium nanocatalysts but an optimization is required to develop more efficient nanocatalysts.

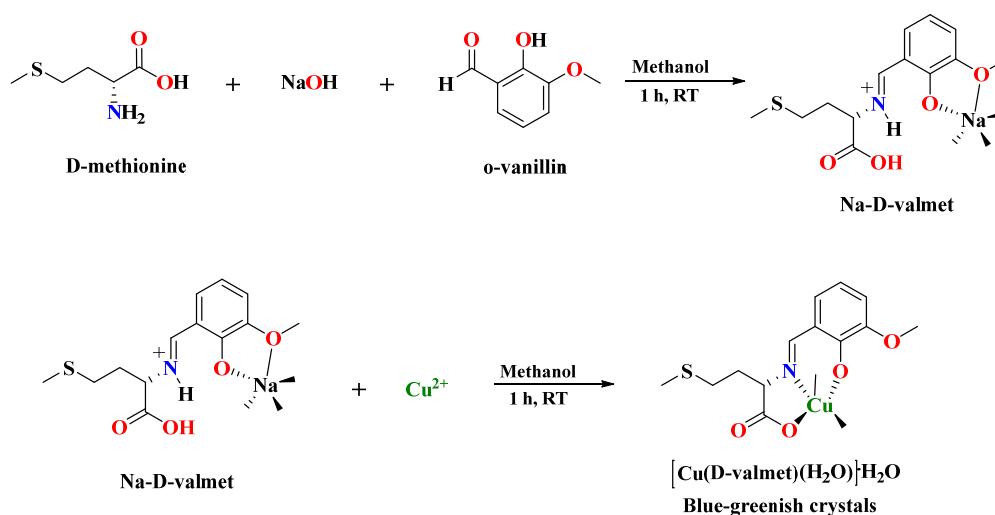
Given the observation of achieving ee when using Rh NPs of *ca.* 2.5 and 2.6 nm in size but not with smaller NPs, a perspective could be to develop the synthesis of larger Rh NPs. This could allow a more efficient anchoring of the chiral ligand at the Rh surface and favor a higher enantioselectivity.

## Chemistry of copper metal

The chemistry of the copper metal was also studied. The focus was on the synthesis of copper complexes employing chiral Schiff-base ligands. The subsequent step involves the immobilization of these complexes onto graphene oxide, and their effectiveness in catalyzing diverse reactions, namely the Henry reaction, cyanosilylation reaction, and aldol reaction, is thoroughly investigated and examined. The study aims to contribute to the understanding of the catalytic performance of these immobilized copper complexes and their significance in the context of asymmetric synthesis.

### Synthesis of $[Cu(D\text{-valmet})(H_2O)] \cdot H_2O$ or *Cu-D-valmet* complex

In the synthesis of the  $[Cu(D\text{-valmet})(H_2O)] \cdot H_2O$  or **Cu-D-valmet** complex, the initial step involved the preparation of the Na-D-valmet precursor. This precursor was synthesized through a condensation reaction between D-methionine and o-vanillin in the presence of NaOH, using MeOH as the solvent. Subsequently, a solution containing Na-D-valmet in a methanol-water mixture (5:1, v/v) was mixed with a solution of  $Cu(CH_3COO)_2 \cdot H_2O$  in MeOH (Scheme 6). After approximately one week, blue-greenish single crystals formed which were isolated *via* filtration and dried under ambient air. Likewise the synthesis of  $[Cu(L\text{-valmet})(H_2O)] \cdot H_2O$  or **Cu-L-valmet** complex was done.



**Scheme 32.** Synthesis of  $[Cu(D\text{-valmet})(H_2O)] \cdot H_2O$  or *Cu-D-valmet* complex.

Considering the favorable attributes associated with the metal-to-oxygen bond, the immobilization of copper complexes onto the GO-COOH support was accomplished. The methanolic solution containing copper complexes was added with the methanolic solution of the GO-COOH support. The resulting mixture was agitated for 24 h, allowing for sufficient interaction between the components. Subsequently, the desired product was obtained by subjecting the mixture to centrifugation and filtration, a process that was repeated 4-5 times to ensure proper purification. Finally, the obtained product was dried in an oven for 24 h to remove any residual solvent and moisture content. The carboxyl groups of the modified GO served as linkers for the immobilization of the chiral complexes (Scheme 7).

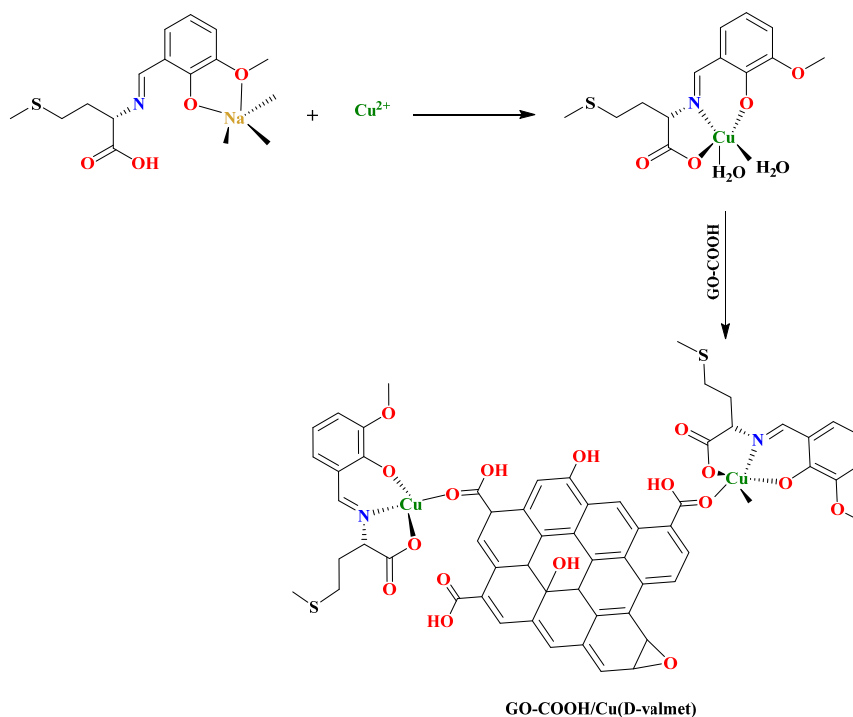
The catalytic potential of the synthesized complexes was examined through three constructed systems

i) A chiral ligand obtained *via* the condensation reaction of *o*-vanillin and D-, or L-methionine respectively, (i.e., **L-valmet**, **D-valmet**) in the enantiomeric sodium complexes, Na-D-valmet and Na-L-valmet.

ii) In the form of copper (II) complexes (i.e., **Cu-D-valmet** and **Cu-L-valmet**).

iii) Immobilized complexes (i.e., **GO-COOH/Cu(D-valmet)** and **GO-COOH/Cu(L-valmet)**).

Ligands **L-** and **D-valmet** in the Na form demonstrate base properties, making them potential homogeneous organocatalysts. When complexed with copper, these ligands act as homogeneous catalysts in all the three reactions, with the active species associated with basic nitrogen or free nitrogen complexed copper.



**Scheme 33:** Immobilization of Cu-D-valmet complex on GO-COOH support via coordinate covalent bond.

In the case of the Henry reaction, dominant role is played by the ligand's, resulting in an asymmetric Henry reaction in water. Supported copper complexes of L-valmet chiral Schiff-base ligand proved to be particularly active in asymmetric Henry reaction. It performed the coupling reaction of benzaldehyde and nitromethane in water with a spectacular increase of the conversion (92% vs 39%) and ee (96 vs 62%) compared to the free complex.

For the cyanosilylation reaction, the free nitrogen of copper complexes acts as the active species. The racemic formation in this case can be attributed to the involvement of an unsaturated Cu center (Lewis active sites), enabling the reaction but lacking stereoselectivity. The copper complexes exhibit high conversions even at RT. However, some of the coupling product undergoes hydrolysis to cyanohydrins due to the presence of coordinated water molecules after drying. The involvement of water in the hydrolysis of  $\alpha$ -(trimethylsilyl)-phenylacetonitrile becomes evident with increasing temperature, leading to an increased ratio between the two products as conversion increases. Immobilizing these complexes on GO-COOH results in either inhibited activity or minimal conversion, with complete hydrolysis of  $\alpha$ -(trimethylsilyl)-phenylacetonitrile to cyanohydrin.

Furthermore, the base properties of both ligands were also demonstrated in the aldol condensation reaction. Complexation of copper by these ligands decreases conversion but increases

selectivity towards the mono-condensated product. Immobilizing these complexes on GO-COOH slightly reduces conversion without significantly impacting selectivity. The GO-COOH support, with its mixed acid and base properties due to oxygenated functionalities, facilitates a catalytic aldol reaction with a balanced ratio between the two products. The results are shown in Figure 8.

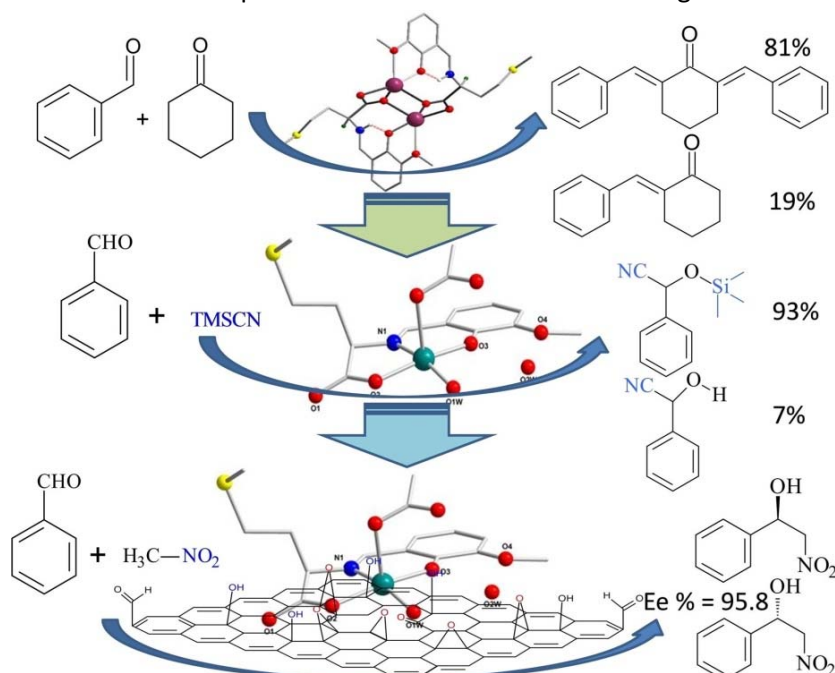


**Figure 13:** Catalytic potential of the synthesized complexes in Henry, cyanosilylation and aldol reaction.

In conclusion, valmet ligands serve as reliable catalysts for stereoselective reactions and, when complexed with copper, demonstrate effectiveness in cyanosilylation reaction. The immobilization of these complexes generates efficient heterogeneous catalysts for aldol condensation.

## Conclusions

This work first focused on the non-covalent immobilization of three chiral cationic rhodium complexes  $[\text{Rh}(\text{COD})((2S,4S)\text{-PPM-pyrene})]\text{BF}_4$  (**complex A**),  $[\text{Rh}(\text{COD})((2S,4S)\text{-BPPM})]\text{BF}_4$  (**complex B**) and  $[\text{Rh}(\text{COD})((2S,5S)\text{-Et-Ferrocene})]\text{BF}_4$  (**complex C**), onto functionalized or non-functionalized carbon nanotubes as a support and their application in the enantioselective hydrogenation of dimethyl itaconate as a model substrate. This involved the preparation and characterization of a series of carbon nanotubes, the initial CNTs, the oxidized carbon nanotubes CNT-O, and the functionalized carbon nanotubes CNT-COO $^-\text{Na}^+$ , CNT-HPA, CNT-CO-HDA from CNT-O. On the other hand, suitable chiral cationic rhodium complexes for immobilization,  $[\text{Rh}(\text{COD})((2S,4S)\text{-PPM-pyrene})]\text{BF}_4$  (**complex A**) and  $[\text{Rh}(\text{COD})((2S,4S)\text{-BPPM})]\text{BF}_4$  (**complex B**) were successfully prepared starting from (2S,4S)-BPPM and synthesized (2S,4S)-PPM-pyrene ligands.

Immobilization of the rhodium **complexes A, B, C** on CNT, CNT-COO $^-\text{Na}^+$ , and CNT-HPA carbon nanotube supports was studied according to three different strategies.

The first approach was based on  $\pi$ - $\pi$  interaction between the  $sp^2$  graphitic structure of CNTs and aromatic moieties present in the ligands of the Rh-complexes. Among these three complexes, **complex A** allowed efficient immobilization on CNTs through  $\pi$ - $\pi$  interaction. The immobilized complex demonstrated good stability during the recycling study which took place without any change in catalytic performances.

The second strategy implied electrostatic interaction between the cationic Rh complexes and the surface negatively charged of carboxylate-functionalized CNTs (CNT-COO<sup>-</sup>). The immobilization of the complexes occurs with partial (**complex B and C**) or total decoordination (**complex A**) of the chiral diphosphine ligand and probably partial or total direct coordination of Rh (I) to the carboxylate group on the surface. However, the immobilized [Rh(COD)((2*S*,5*S*)-Et-Ferrocene)]BF<sub>4</sub> **Complex C** displayed good enantioselectivity, reaching an enantiomeric excess of 65% toward (*R*)-methyl succinate almost comparable to that of the free complex. However it was found unstable under the catalytic conditions since the formation Rh(0) nanoparticles (NPs) were observed, which were found to be very active but not enantioselective in the hydrogenation of DMI.

The third approach implied an ionic anchoring based on the use of a spacer-type anchoring agent, heteropoly acid HPA, that was previously grafted at the CNTs surface thanks to an acid-base interaction. **Complexes A, B, and C** were successfully immobilized on CNT-HPA. They were found active in asymmetric hydrogenation providing different enantioselectivities, 20%, 63%, and 58% for **complexes A, B, and C**, respectively. In addition, the immobilized **complex B** was found stable and recyclable up to 4 times with a moderate loss of enantioselectivity. This result corroborates the interest in adding a spacer such as HPA between the Rh complex and the CNT support to limit the effect of the CNT surface environment on the catalytic behavior of the Rh immobilized complexes.

Immobilization of chiral rhodium complexes showed the best results with [Rh(COD)((2*S*,4*S*)-PPM-pyrene)]BF<sub>4</sub> **complex A** immobilized *via*  $\pi$ - $\pi$  stacking on CNTs and [Rh(COD)((2*S*,4*S*)-BPPM)]BF<sub>4</sub> **complex B** immobilized on CNT-HPA *via* an ionic anchoring through a spacer. Perspectives would be to improve the activity and enantioselectivity in asymmetric catalytic hydrogenation, which requires: i) optimization of the catalytic conditions, ii) variation of the chiral rhodium complexes immobilized on the support, iii) extension to other asymmetric hydrogenation and other asymmetric reactions. iv) transfer of batch-catalyzed hydrogenation into flow processes should also be considered in the future.

The synthesis of chiral rhodium nanoparticles (RhNPs) and their immobilization on functionalized carbon nanotubes were also studied. Well-dispersed chiral RhNPs could be prepared by decomposition of [Rh( $\eta^3$ -C<sub>3</sub>H<sub>5</sub>)<sub>3</sub>] precursor in the presence of (2*S*,4*S*)-BPPM ligand. A good confinement of these RhNPs was observed when using the CNT-O support. In addition, chiral RhNPs obtained from [Rh( $\eta^3$ -C<sub>3</sub>H<sub>5</sub>)<sub>3</sub>] and (2*S*,4*S*)-PPM-pyrene ligand were immobilized on CNT-CO-HDA with efficient confinement within the channels of these functionalized CNTs. In asymmetric hydrogenation of DMI, these immobilized RhNPs provided excellent activity but without enantioselectivity. The lack of enantioselectivity indicates that even in the case of the well-confined RhNPs the ligand is not blocked enough at the NP surface to allow the enantioselective hydrogenation of the DMI in one preferential side. However, we were able to demonstrate that it was possible to carry out the asymmetric hydrogenation with chiral Rh NPs formed *in-situ* in catalysis conditions that implied in the presence of DMI. Using [Rh( $\mu$ -Cl)(C<sub>8</sub>H<sub>12</sub>)<sub>2</sub>] precursors with (2*S*,4*S*)-BPPM ligand, the sponge-like large RhNPs led to an activity of 96 %, and more interestingly to an enantioselectivity of 16%. With [Rh( $\mu$ -Cl)(C<sub>8</sub>H<sub>12</sub>)<sub>2</sub>] precursor and (2*S*,4*S*)-PPM-pyrene ligand, the well-controlled and well-dispersed RhNPs exhibited moderate catalytic activity (69%) but with higher enantioselectivity (32%).

These results show the successful synthesis of chiral RhNPs and their use in asymmetric hydrogenation. This work has thus opened a new avenue for the preparation of chiral rhodium nanocatalysts but optimization is necessary to develop more efficient chiral nanocatalysts for asymmetric catalysis.

Finally, coordination immobilization of copper(II) complexes onto graphene oxide (GO) was performed by direct coordination of the metal center on -COOH surface group. Supported copper

complexes of L-valmet chiral Schiff-base ligand proved to be particularly active in asymmetric Henry reaction. It performed the coupling reaction of benzaldehyde and nitromethane in water with a spectacular increase of the conversion (92% vs 39%) and ee (95 vs 62%) compared to the free complex.

## References

- [1] R. E. Gawley, J. Aube, *Principal of Asymmetric Synthesis*, Elsevier, 2012. DOI: [10.1016/C2009-0-06104-2](https://doi.org/10.1016/C2009-0-06104-2).
- [2] J. Gal, *Chirality*, **2012**, *24*, 959–976. DOI: [10.1002/chir.22071](https://doi.org/10.1002/chir.22071).
- [3] T. J. Leitereg, D. G. Guadagni, J. Harris, T. R. Mon, R. Teranishi, *J. Agric. Food Chem.*, **1971**, *19*, 785–787. DOI: [10.1038/230455a0](https://doi.org/10.1038/230455a0).
- [4] U. Lepola, A. Wade, H. F. Andersen, *Int. Clin. Psychopharmacol.*, **2006**, *19*, 149. DOI: [10.1097/00004850-200405000-00005](https://doi.org/10.1097/00004850-200405000-00005).
- [5] J. Hyttel, K. P. Bøgesø, J. Perregaard, C. Sánchez, *J. Neural. Transm.*, **1992**, *88*, 157–160. DOI: [10.1007/BF01244820](https://doi.org/10.1007/BF01244820).
- [6] K. Motokura, S. Ding, K. Usui, Y. Kong, *ACS Catal.*, **2021**, *11*, 11985–12018. DOI: [10.1021/acscatal.1c03426](https://doi.org/10.1021/acscatal.1c03426).
- [7] T. Cheng, Q. Zhao, D. Zhang, G. Liu, *Green Chemistry*, **2015**, *17*, 2100–2122. DOI: [10.1039/C4GC02204A](https://doi.org/10.1039/C4GC02204A).
- [8] M. R. Axet, O. Dechy-Cabaret, J. Durand, M. Gouygou, P. Serp, *Coord. Chem. Rev.*, **2016**, *308*, 236–345. DOI: [10.1016/j.ccr.2015.06.005](https://doi.org/10.1016/j.ccr.2015.06.005).
- [9] B. Pugin, H. U. Blaser, *Top Catal.*, **2010**, *53*, 953–962. DOI: [10.1007/s11244-010-9514-8](https://doi.org/10.1007/s11244-010-9514-8).
- [10] R. Selke, M. Čapka, *J. Mol. Catal.*, **1990**, *63*, 319–334. DOI: [10.1016/0304-5102\(90\)85124-Z](https://doi.org/10.1016/0304-5102(90)85124-Z).
- [11] M. Mazzel, W. Marconi, M. Riocci, *J. Mol. Catal.*, **1980**, *9*, 381–387. DOI: [10.1016/0304-5102%2880%2980030-7](https://doi.org/10.1016/0304-5102%2880%2980030-7).
- [12] R. Augustine, S. Tanielyan, S. Anderson, H. Yang, *Chem. Commun.*, **1999**, 1257–1258. DOI: [10.1039/A903205C](https://doi.org/10.1039/A903205C).
- [13] L. J. Lemus-Yegres, M. C. Román-Martínez, C. S.-M. de Lecea, *J. Nanosci. Nanotechnol.*, **2009**, *9*, 6034–6041. DOI: [10.1016/j.micromeso.2007.05.005](https://doi.org/10.1016/j.micromeso.2007.05.005).
- [14] C. C. Gheorghiu, B. F. Machado, C. Salinas-Martínez de Lecea, M. Gouygou, M. C. Román-Martínez, P. Serp, *Dalton Trans.*, **2014**, *43*, 7455. DOI: [10.1039/C3DT53301H](https://doi.org/10.1039/C3DT53301H).
- [15] P. Serp, K. Philippot (Editors), *Nanomaterials in Catalysis*, Wiley-VCH: Weinheim, Germany, **2012**. ISBN: 9783527656875. DOI: [10.1002/9783527656875](https://doi.org/10.1002/9783527656875).
- [16] M. Ibrahim, M. A. S. Garcia, L. L. R. Vono, M. Guerrero, P. Lecante, L. M. Rossi, K. Philippot, *Dalton Trans.*, **2016**, *45*, 17782–17791. DOI: [10.1039/C6DT03104H](https://doi.org/10.1039/C6DT03104H).
- [17] M. Ibrahim, M. M. Wei, E. Deydier, E. Manoury, R. Poli, P. Lecante, K. Philippot, *Dalton Trans.*, **2019**, *48*, 6777–6786. DOI: [10.1039/c9dt01006h](https://doi.org/10.1039/c9dt01006h).
- [18] M. Ibrahim, R. Poreddy, K. Philippot, A. Riisager, E. J. Garcia-Suarez, *Dalton Trans.*, **2016**, *45*, 19368–19373. DOI: [10.1039/C6DT03668F](https://doi.org/10.1039/C6DT03668F).
- [19] C. J. Abou-Fayssal, C. Fliedel, R. Poli, A. Riisager, K. Philippot, E. Manoury, *Mater. Today Chem.*, **2023**, *34*, 101752. DOI: [10.1016/j.mtchem.2023.101752](https://doi.org/10.1016/j.mtchem.2023.101752).



**Sara BONFANTE**

**ESR5**

**Thesis co-directors**

Dr. Antoine Simonneau    Laboratoire de Chimie de Coordination, Toulouse, France

Prof. Jason Lynam,  
Dr. John Slattery            University of York, York, United Kingdom

**Thesis defense**

Laboratoire de Chimie de Coordination, Toulouse, France, 5 April 2024





## Zirconium- and Phosphine-assisted C–F Bond Activation and Functionalisation

### Introduction

Fluorine is the 9<sup>th</sup> element of the periodic table and it is the most electronegative, with a Pauling scale value ( $\chi$ ) of 4.0 [1]. It also exhibits a high first ionisation energy ( $IE_1 = 1679$  kJ/mol), making it challenging to abstract an electron from its 2p shell. Furthermore, fluorine exhibits a high electron affinity ( $EA = -328$  kJ/mol), meaning that the addition of an electron to atomic fluorine releases energy [2]. Many of these effects are a consequence of fluorine having the smallest van der Waals atomic radius ( $r_{vdW} = 1.47$  Å) among the period 2 elements. The C–F bond is the strongest C–X bond (bond dissociation energy = 513 kJ/mol;

Table 5, bottom) [2], deriving its strength mainly from the high ionic character (approximately 43%) resulting from the electronegativity difference between C and F ( $\Delta\chi = 1.5$ ) [3]. Due to the high strength of this bond, the cleavage of C–F bonds is generally challenging.

**Table 5.** Bond dissociation energy (BDE) of relevant C–X bonds (bottom).

Bond	BDE (kJ/mol)
C–F	513
C–H	413
C–O	351
C–C	348
C–Cl	328
C–N	292

The high biological activity of fluorinated organic compounds stems from the fact that fluorine can be used as isostere for hydrogen in organic molecules, causing dramatic changes in the properties of the molecule comparing to the corresponding hydrocarbon but usually preserving its geometry and shape due to the small radius [4]. The incorporation of fluorine often results in an increase in the acidity of adjacent functional groups and organic acids, along with an enhancement in the lipophilicity of the molecule [5]. Furthermore, the presence of fluorine in an organic molecule facilitates the formation of hydrogen bonding interactions. These phenomena strongly influence the biological activity of fluorinated organic compounds [4].

Fluorine is the 13<sup>th</sup> most abundant element in the Earth's crust, mainly occurring in the form of fluoride minerals such as fluorite ( $CaF_2$ ) [6]. However, naturally occurring fluorinated organic compounds are limited and their biosynthesis remains unclear [7]. The industrial synthesis of fluorine-containing organic molecules typically derives from the use of elemental  $F_2$  or HF, both obtained from the upgrading of  $CaF_2$  [8].

Fluorinated organic molecules can be found in a wide range of applications, including pharmaceuticals (where approximately 20% of commercial drugs contain at least one fluorine atom or a fluorinated functional group [9]), agrochemicals, medical imaging (such as Positron Emission Tomography [10]), materials (including fluoropolymers and liquid crystals), and more (Figure 14). Hence, there is a significant interest in developing efficient strategies for the synthesis of valuable fine chemicals that incorporate fluorine.

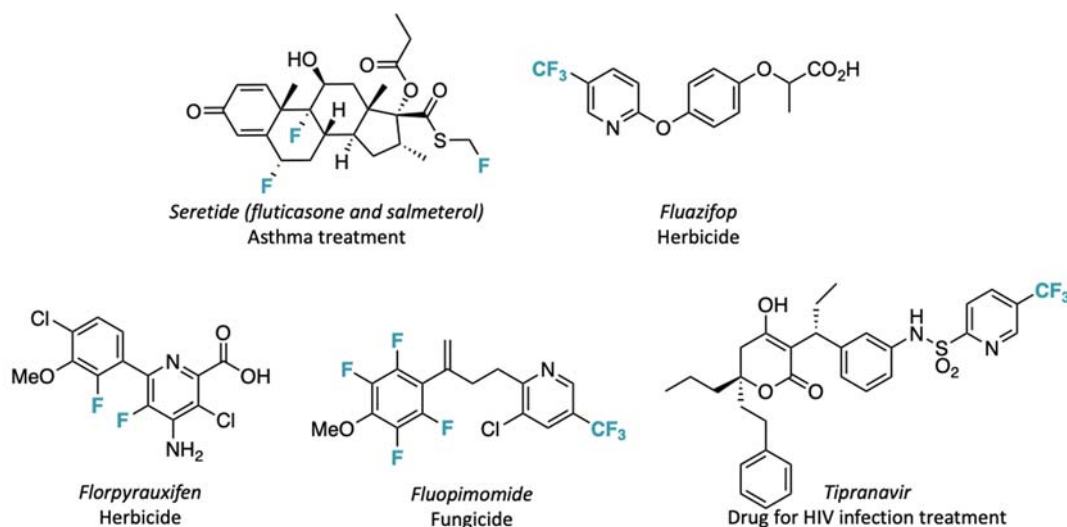


**Figure 14.** Selected examples of fluorine-containing organic molecules employed in pharmaceutical and agrochemical industries.

Moreover, due to their inert nature upon decomposition, fluorocarbons can be persistent in the environment. Hydrofluorocarbons (HFCs) and hydrofluoroolefins (HFOs) find applications in refrigeration, air-conditioning, foam-blowing, electronics and fire protection. Their high volatility leads to their release into the atmosphere as fluorinated gases, contributing to environmental pollution [11],[12]. Therefore, there is a need to explore alternative methods for the defluorination of fluorinated organic molecules. Two main pathways for the synthesis of partially fluorinated molecules have been developed:

- I. selective fluorination of non-fluorinated substrates;
- II. selective defluorination of perfluorinated and polyfluorinated molecules.

The first approach involves the use of fluorinating reagents, including nucleophilic, electrophilic and trifluoromethylating agents. The main challenge in this method arises from controlling the reactivity of fluorine sources. With strong nucleophilic fluoride sources (*e.g.* HF, KF or Me<sub>4</sub>NF), the fluoride anion exhibits weak nucleophilicity in the presence of hydrogen bond donors, leading to the formation of the stable anion HF<sub>2</sub><sup>-</sup> [5]. When hydrogen bond donors are rigorously excluded, fluoride's strong basicity and nucleophilicity often result in undesired side reactions. Among the electrophilic fluorinating reagents, the simplest is fluorine gas, which is highly reactive, very difficult and hazardous to handle. It is often unselective and can react with many common functional groups. Consequently, due to the harsh conditions usually required in these systems, the substrate scope and selectivity of these reactions are restricted to simple substrates, which can be employed as building blocks for subsequent functionalisations [5].

Researchers are overcoming this limitation by developing mild electrophilic fluorination reagents that enable the late-stage fluorination of complex organic molecules. These reagents allow milder reaction conditions to be used, they are easy to handle, less toxic and hazardous than traditional fluorinating reagents and exhibit enhanced selectivity. For instance, among the electrophilic fluorination reagents, the so-called "NF-reagents" stand out. These compounds feature a fluorine atom directly bonded to the electronegative nitrogen, which can be further activated by electron-withdrawing groups (*e.g.* carbonyl, sulfonyl) or a positive charge in the molecule. The advantage of all these reagents is that most are solid, non-volatile and non-explosive compounds, which may be handled with standard synthetic chemistry techniques [4]. For example, Selectfluor, an NF-reagent

developed thirty years ago, is industrially employed in the synthesis of fluticasone propionate, an active ingredient in Seretide, a drug used for asthma treatment [13]. Nevertheless, often directing groups (such as pyridyl, amino, N-perfluorotolylamide groups) are necessary to ensure regioselectivity in these reactions [14]. Alternatively, pre-activation of the substrate ( $\beta$ -ketocarbonyl compounds) can be necessary to promote the reaction [5].

The second strategy for the synthesis of complex fluorinated organic compounds is the selective activation of C–F bonds in polyfluorinated and perfluorinated organic molecules. This approach is interesting as it allows the transformation of highly fluorinated molecules, readily available through bulk industrial fluorination processes (*e.g.* employing HF, KF, F<sub>2</sub>), into more valuable fluorinated compounds. This is achieved through the selective activation of C–F bonds, converting them into C–H, C–C, C–O, C–S, C–N, C–P bonds. Transition metals (TMs) mainly promote these processes, either catalytically or stoichiometrically, although examples involving main-group elements are also present in the literature [15]. Considering the high strength of the C–F bond, the thermodynamic requirement to make this process feasible is the formation of other strong E–F bonds form, where E typically is H, Si, B, Al and TMs [16]. This method is a viable alternative to the C–F formation strategy, as it can lead to the synthesis of new compounds, new selectivity and synthetic routes that might not be accessible with the first approach [17]. The challenges associated with this method involve achieving precise control over the regio- and stereoselectivity and improving the functional group tolerance of the transformation [15].

### Aims and objectives

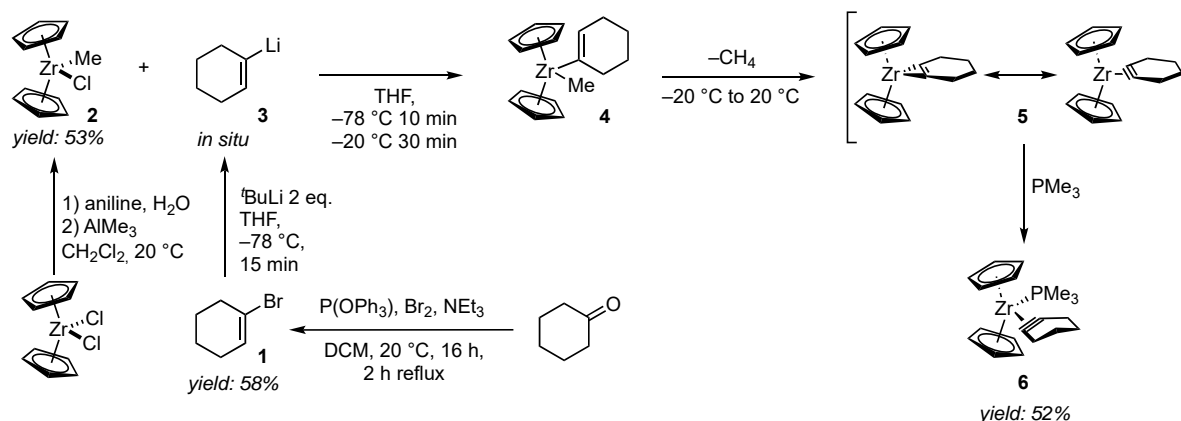
The aim of this Ph.D. project was to explore novel strategies for the regioselective activation and functionalisation of C–F bonds in readily available polyfluoroaromatic compounds promoted by early-transition metals and by *p*-block elements.

This project is structured into three sections. The aim of the first section was to establish a novel synthetic protocol for the controlled and regioselective functionalisation of fluorinated pyridines using a strained zirconocene-cycloalkyne complex. The objective was to obtain a fluorinated pyridine alkenylated in *ortho*-position, which could subsequently be further functionalised to yield a more complex, stereo-defined fluorinated organic compound. This investigation demonstrated that the zirconocene-cycloalkyne complex followed three different reactivity pathways, depending on the fluorination pattern of the polyfluoropyridine.

In the second section, the investigation of a side reaction observed in the first section is described. This reaction involved the C–F bond activation in *para*-position of pentafluoropyridine (**Py-F<sub>5</sub>**) promoted by simple trialkylphosphines. The outcome of this activation reaction depends on the reaction conditions, leading to either the hydrodefluorinated product or the reductive C–C homocoupling product. Additionally, the generation of differently substituted difluorophosphoranes was observed. This research highlighted the potential of metal-free systems, employing only simple phosphines to selectively and efficiently functionalise electron-poor perfluoroheteroaromatics.

The final objective was to demonstrate that simple trialkylphosphines are able to catalyse hydrodefluorination (HDF) and aminodefluorination reactions in the presence of silanes and silyl amides, without the need for complex constrained structures or the use of metals, as reported in the existing literature. The research showed that P<sup>*n*</sup>Bu<sub>3</sub> could exhibit reactivity akin to TMs during the catalytic cycle, characterised by reversible two-electron redox processes like oxidative addition and reductive elimination.

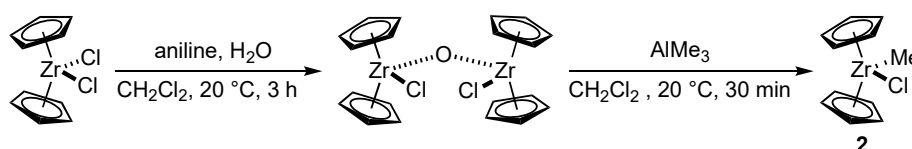
## C–F bond functionalisation promoted by a zirconium-cyclohexyne complex



**Scheme 34.** Synthetic protocol for the synthesis of the zirconocene- $\eta^2$ -cyclohexyne (5) and its corresponding  $\text{PMe}_3$  adduct (6).

The investigation started with the study of the synthesis of the zirconocene- $\eta^2$ -cyclohexyne complex (5) reported by Buchwald and co-workers (Scheme 34) [18]. The targeted Zr complex was prepared by degradation of an *in situ* generated 1-cyclohexenyl-methyl-zirconocene complex (4) via  $\beta$ -H abstraction, leading to methane evolution and the zirconocene-cyclohexyne complex 5. To facilitate its isolation, Buchwald *et al.* stabilised 5 with  $\text{PMe}_3$ , resulting in the phosphine adduct 6. Complex 6, or *in situ* prepared 5, were shown to react with various unsaturated organic molecules by insertion in the Zr–C bond [19].

To begin, 1-bromocyclohexene (1) was synthesised by reacting cyclohexanone with a slight excess of bromine, triphenylphosphite and  $\text{NEt}_3$  (Scheme 34) [20]. Subsequently, the formation of 2 *via*  $[(\text{Cp}_2\text{ZrCl})_2(\mu\text{-O})]$  was carried out (*ca.* 50%) (Scheme 35) [21].

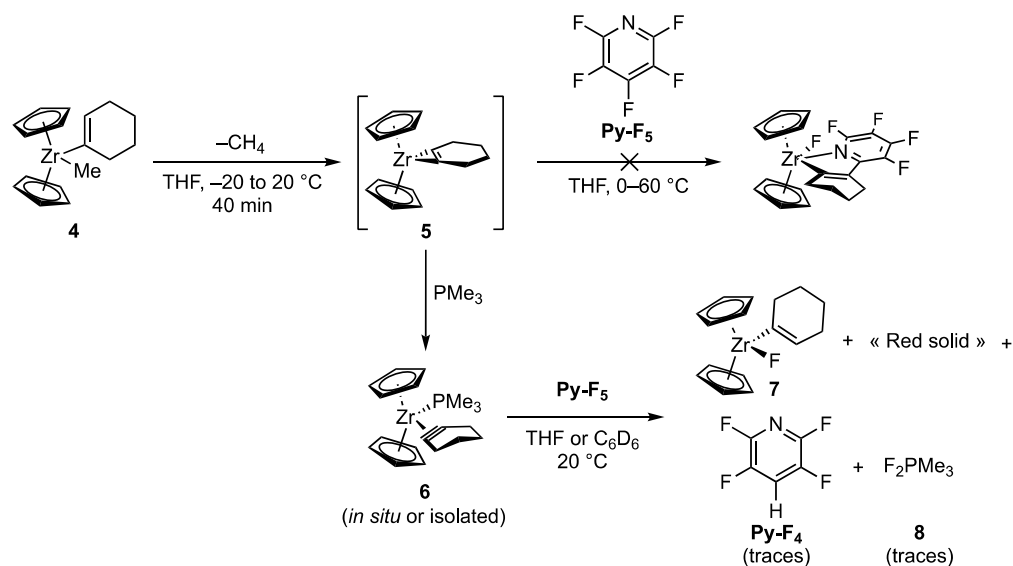


**Scheme 35.** Synthesis of the methylzirconocene chloride 2.

The formation of the desired oxo-bridged complex  $[(\text{Cp}_2\text{ZrCl})_2(\mu\text{-O})]$  was achieved in high isolated yields (78%) by reacting equimolar amounts of zirconocene dichloride, aniline and a slight excess of water (Scheme 35). The subsequent methylation with two equivalents of trimethylaluminum allowed the formation of 2 in moderate yields of 62% (relative to the oxo-bridged complex) and the reaction could be conducted on a relatively large scale (8 g).

The zirconocene- $\text{PMe}_3$  adduct 6 was successfully synthesised according to reaction Scheme 34 in 52% isolated yield. The formation of this complex was evidenced by the appearance of a singlet at  $\delta = -2.3$  ppm in the  $^{31}\text{P}\{^1\text{H}\}$  NMR spectrum, corresponding to the phosphorus nucleus of the coordinated phosphine, and the disappearance of the signal for free  $\text{PMe}_3$  ( $\delta(^{31}\text{P}) = -62.0$  ppm). The  $^1\text{H}$  and 2D-NMR analyses further confirmed the formation of the phosphine adduct 6.

The reactivity of complex **6** and the *in situ* generated **5** with differently fluorinated pyridines was investigated. **Py-F<sub>5</sub>** was chosen as the initial polyfluorinated pyridine for this study due to its reported high reactivity in the C–F bond addition reaction, as indicated in the study conducted by Etienne and coworkers [22]. As the 16-electron complex **5** is expected to be the active species for the C–F activation process, a solution of the *in situ* generated complex was treated with an excess of **Py-F<sub>5</sub>** but no reaction was observed according to <sup>1</sup>H and <sup>19</sup>F NMR spectroscopy, even upon heating up to 60 °C for several hours (Scheme 36, top reaction). Surprisingly, when PMe<sub>3</sub> was added to the reaction mixture, the complete consumption of the heteroaromatic compound occurred after 16 hours at 20 °C (Scheme 36, bottom reaction). Analysis of the mixture by <sup>19</sup>F NMR revealed a singlet at  $\delta = 51.0$  ppm in the spectrum, matching well with a Zr-bound fluoride, along with numerous signals in the region of the aromatic *ortho*, *meta* and *para* fluorine. From this observation, it was assumed that the presence of PMe<sub>3</sub> was crucial for the C–F bond activation and may act as an assisting ligand. As reported in the literature, phosphine assistance in metal-mediated C–F bond activation is a known phenomenon [23–26]. Typically, these examples involve the formation of a metallofluorophosphorane intermediate, which then undergoes either an alkyl or a fluoride transfer from the P<sup>V</sup> centre to the metal, leading to an alkylated or fluorinated metal complex, respectively [27].

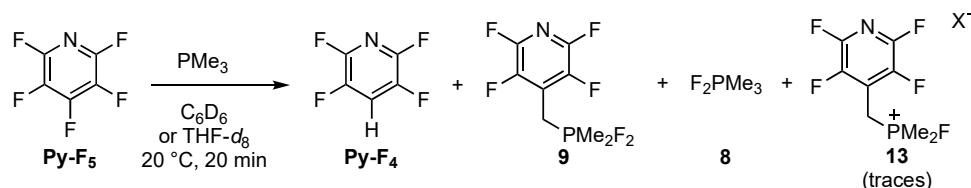


**Scheme 36.** Attempts of C–F functionalisation of pentafluoropyridine with zirconocene-cyclohexyne complexes **5** and **6**.

The reactivity of the isolated PMe<sub>3</sub> adduct **6** with an equimolar amount of **Py-F<sub>5</sub>** (Scheme 36, bottom reaction) was therefore investigated. After four hours at 20 °C in C<sub>6</sub>D<sub>6</sub>, the starting complex, **6**, was fully converted into 1-cyclohexenylzirconocene fluoride (**7**), accompanied by the formation of an unidentified dark red solid (17 mg out of 43 mg of starting complex **6** used) and unreacted **Py-F<sub>5</sub>**. Two more equivalents of **6** were needed to consume all the **Py-F<sub>5</sub>**. Complex **7** was characterised by a singlet resonance in the <sup>19</sup>F NMR spectrum at  $\delta = 51.0$  ppm corresponding to the Zr–F bond (the same chemical shift observed in the previous experiment). Traces of the hydrodefluorination product 2,3,5,6-tetrafluoropyridine (**Py-F<sub>4</sub>**), F<sub>2</sub>PMe<sub>3</sub> (**8**) and a fluorinated unidentified product were observed in the <sup>19</sup>F NMR spectrum. These species were analysed by multinuclear (<sup>1</sup>H, <sup>31</sup>P, <sup>19</sup>F, <sup>13</sup>C) and 2D-NMR spectroscopy. The formation of **7** was further confirmed by protonation or iodinolysis of the organic ligand. Different conditions for the C–F bond activation reaction of **6** with **Py-F<sub>5</sub>** were investigated

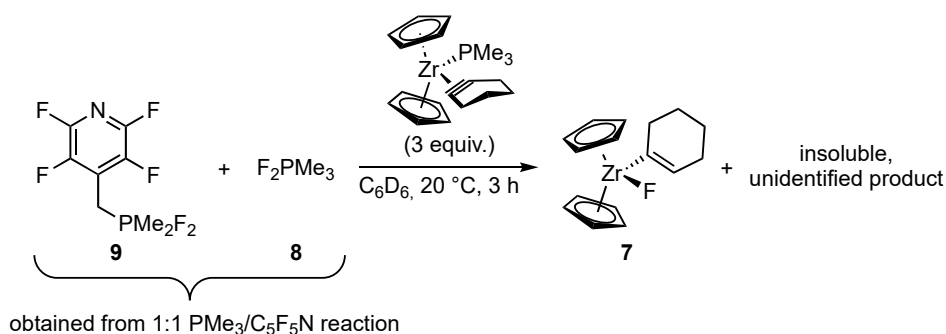
(Scheme 36, bottom reaction), but changing the solvent (benzene, toluene and cyclohexane), concentration of the zirconocene- $\text{PMe}_3$  adduct (0.1 M, 0.3 M), reagent ratio (complex **6** :  $\text{Py-F}_5$  = 1:1, 3:1, 5:1), lowering the temperature to 0 °C, and using pre-cooled solvent and reagents (−40 °C) had only little influence on the reaction outcome. At −40 °C the system was unreactive.

To shed more light on the mechanism of this reaction, a control experiment on the reactivity of trimethylphosphine towards pentafluoropyridine was carried out. Addition of an equimolar amount of  $\text{PMe}_3$  to a solution of  $\text{Py-F}_5$  in  $\text{C}_6\text{D}_6$  or  $\text{THF-d}_8$  at 20 °C triggered the formation of  $\text{Py-F}_4$ ,  $\text{F}_2\text{PMe}_3$ , the 4-methylenetetrafluoropyridine-substituted difluorophosphorane **9** and a phosphonium salt **13**, along with unreacted  $\text{PMe}_3$  (Scheme 37). The red solid was not observed.



**Scheme 37.** Reactivity test of  $\text{Py-F}_5$  (1 equiv.) with  $\text{PMe}_3$  (1–3 equiv.) in  $\text{C}_6\text{D}_6$  or  $\text{THF-d}_8$  at 20 °C.

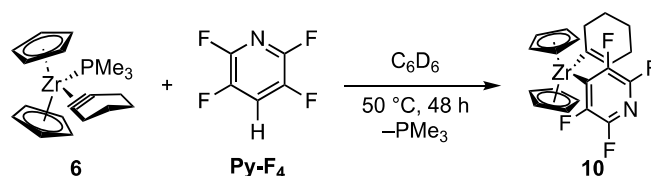
The spontaneous reaction of  $\text{PMe}_3$  with  $\text{Py-F}_5$  casts doubt on a Zr-mediated C–F bond activation for this substrate. The treatment of the mixture produced by the 1:1  $\text{PMe}_3/\text{Py-F}_5$  reaction in  $\text{C}_6\text{D}_6$  with the cyclohexyne complex **6**, according to Scheme 38, resulted in the consumption of **8** and **9** and the appearance of the zirconocene-fluoride **7** after 3 hours at 20 °C, as evidenced by the  $^{19}\text{F}$  NMR spectrum. Three equivalents of **6** (vs.  $\text{Py-F}_5$ ) were needed to consume all **8** and **9** to afford **7** rather selectively.



**Scheme 38.** Reaction of **6** (3 equiv.) with the compounds issued by the reaction of  $\text{PMe}_3$  (1 equiv.) and  $\text{Py-F}_5$  (1 equiv.) in  $\text{C}_6\text{D}_6$  at 20 °C.

This outcome strongly suggests that the C–F bond activation event observed in the reaction of **6** with  $\text{Py-F}_5$  was initiated by dissociated  $\text{PMe}_3$  reacting with the heteroaromatic to give **8** and **9**, which subsequently reacted with **6** to provide **7**. This is consistent with the dissociation energy values of the bonds involved: the Zr–F bond (BDE =  $623 \pm 63$  kJ/mol) is indeed stronger than the P–F (BDE  $\leq 405$  kJ/mol) and C–F bonds (BDE = 513 kJ/mol [28]). Considering the nucleophilic attack of the phosphine on the fluoroheteroaromatic as a crucial mechanistic step in the reaction outlined in Scheme 37, it was expected that the use of a less electron-poor pyridine (e.g. with a reduced degree of fluorination) could circumvent the undesired reactivity of  $\text{PMe}_3$  with the fluoroheteroarene. Therefore,  $\text{Py-F}_4$ , 2,4,6-trifluoropyridine ( $\text{Py-F}_3$ ) and 2,6-difluoropyridine ( $\text{Py-F}_2$ ) were identified as suitable candidates for this investigation.

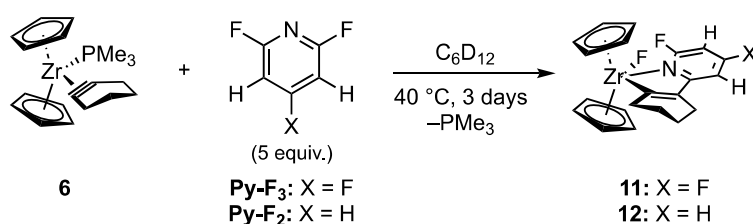
When **6** was reacted with an equimolar amount of **Py-F<sub>4</sub>**, complete consumption of the reagents was observed after 48 hours at 50 °C in C<sub>6</sub>D<sub>6</sub>. The main product was identified as the C–H activation product **10**. Multinuclear and 2D-NMR analyses further proved the formation of **7**.



**Scheme 39.** Synthesis of the C–H activation product **10** by reaction of **6** (1 equiv.) and **Py-F<sub>4</sub>** (1 equiv.) in C<sub>6</sub>D<sub>6</sub> at 50 °C for 48 hours.

Complex **10** is believed to result from 1,2-C–H addition over the Zr–( $\eta^2$ -C $\equiv$ C) bond in **6**, a hypothesis further supported by the absence of deuterium incorporation when the reaction was conducted in deuterated benzene. Further evidence for C–H activation was collected through NMR analyses of the reaction mixture after treatment with iodinolysis.

In the case of **Py-F<sub>3</sub>** and **Py-F<sub>2</sub>** the targeted 1,3-C–F bond addition over the Zr– $\eta^2$ -cycloalkyne motif took place, affording **11** and **12**, respectively (Scheme 40). Various solvents (THF, chlorobenzene, toluene, benzene, diethyl ether, cyclohexane) and temperatures were tested to find the optimal conditions for these reactions. The system exhibited the highest yield (71% isolated yield of **11**) and selectivity when cyclohexane was used as solvent at 40 °C.



**Scheme 40.** Synthesis of **11** and **12** by reaction of **6** (1 equiv.) with **Py-F<sub>3</sub>** or **Py-F<sub>2</sub>** (3–5 equiv.) in C<sub>6</sub>D<sub>12</sub> at 40 °C.

The addition product **11** is characterised by a singlet at  $\delta(^{19}\text{F}) = -35.4$  ppm, corresponding to the Zr–F bond, a doublet at  $\delta(^{19}\text{F}) = -60.7$  ppm ( $^4J_{\text{FF}} = 24.0$  Hz) and a doublet of doublets of doublets at  $\delta(^{19}\text{F}) = -94.8$  ppm ( $^4J_{\text{FF}} = 24.0$ ,  $^3J_{\text{FH}} = 9.5$  Hz,  $^3J_{\text{FH}} = 7.5$  Hz), associated with the *ortho*- and *para*-fluorine of the pyridine, respectively (Figure 15). Additionally, the formation of **11** was evidenced by the generation of 2-(2-iodocyclohexen-1-yl)-4,6-difluoropyridine, characterised by GC(EI)-MS and NMR analyses, after iodinolysis of the complex. Crystals suitable for a single crystal X-ray diffraction (sc-XRD) analysis were grown after vapour diffusion of tetramethylsilane, as an antisolvent, into a concentrated toluene solution of **11**. Its molecular structure is shown in Figure 16.

The Zr atom lies in a distorted trigonal bipyramid environment, with apical sites occupied by the nitrogen of the pyridine ligand and the fluoride. The former belongs to a 1-zircona-2-azacyclopentadiene motif that connects it to the alkenyl carbon found in the equatorial plane, forcing the F–Zr–N array to deviate significantly from linearity [F1–Zr1–N1 148.46(6)°] and imposing a tilt angle for the Cp–Zr–Cp moiety of 135.8°. Similar deviations from the ideal trigonal bipyramidal geometry are found in other crystallographically characterised five-coordinated, Cp-supported 1-zircona-2-azacyclopentadienes [29–34]. Compared to structurally related species [29–35], the angles measured



within the five-membered ring as well as the bond lengths of the conjugated part show no significant irregularity. However, the Zr–C bond is rather short and the Zr–N, rather long. In the considered family of compounds selected for comparison, the former varies slightly in length, while the Zr–N distance fluctuates depending on the L or X character of the nitrogen ligand and the N-substituent. In the present case, we explain the long Zr–N bond by the presence of the fluoride in *trans* relationship, coupled with the electron-poor properties of the difluoropyridine ring. The elongation of the Zr–N bond mechanically impacts the length of the Zr–C bond due to the rigidity of the 1-zircona-2-azacyclopentadiene core. An additional observation is that the N1–C11–F3 angle is quite acute [114.7(2)°], presumably as a result of a long-range interaction of the fluorine atom with the electropositive Zr atom.

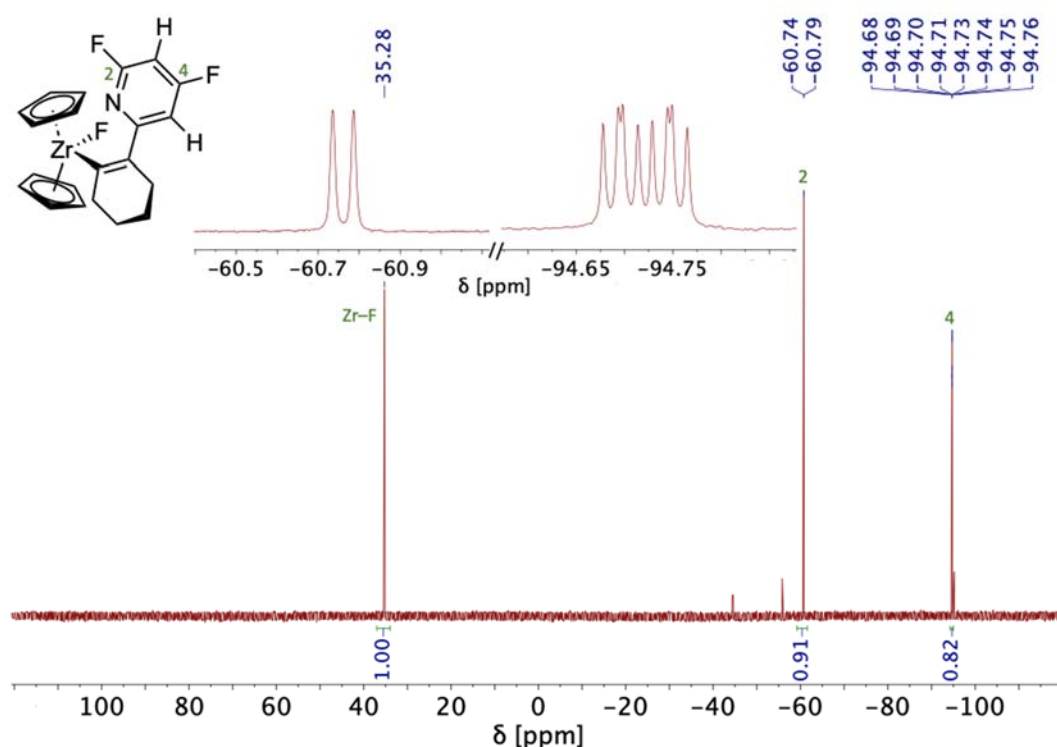


**Figure 15.**  $^{19}\text{F}$  NMR (377 MHz,  $\text{C}_6\text{D}_6$ ) spectrum of the crude reaction mixture of the reaction between the zirconocene- $\text{PMe}_3$  adduct **6** (1 equiv.) with  $\text{Py-F}_3$  (5 equiv.) in cyclohexane at 40 °C for 42 hours, dried and dissolved in  $\text{C}_6\text{D}_6$ . Magnifications of the signals of complex **11** are given.

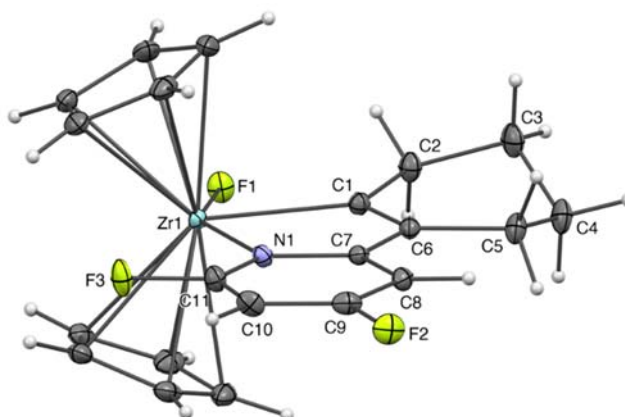


**Figure 16.** Molecular structure of **11** in the solid. Ellipsoids drawn at the 25% probability level.

Complex **12**, obtained from treating the zirconocene-PMe<sub>3</sub> adduct **6** with **Py-F<sub>2</sub>** (five equivalents) in cyclohexane at 40 °C for 3 days (Scheme 40), exhibits similar NMR features to **11**. The <sup>19</sup>F NMR spectrum displays a singlet at  $\delta = 34.7$  ppm, corresponding to the Zr–F bond, and a doublet at  $\delta = -64.3$  ppm (d,  $J = 7.6$  Hz). It is remarkable to note that the system was highly selective and, despite the presence of a proton in the *para*-position, the C–H bond activation product was not detected.

Several hypotheses may be given to explain the differences in reactivity of the four polyfluoropyridines towards **6**. The absence of a 1,3-C–F addition product after treatment with **Py-F<sub>5</sub>** can reasonably be attributed to the fast reaction of the latter with dissociated PMe<sub>3</sub>. The low Lewis basicity of **Py-F<sub>5</sub>** may also lead to a loosely bound adduct with the transient phosphine-free cyclohexyne complex **5**, hampering a C–F bond activation step to occur before the substrate reacts with the phosphine. Additionally, the structure of **11** (Figure 16) reveals a 1,3-allylic (<sup>1,3</sup>A) strain between the cycles' backbones (carbons C5 to C8), along the ring junction. This destabilising interaction would be exacerbated if the heteroaromatic ring was fully fluorinated and may exist before the C–C bond formation event, imparting a kinetic penalty for a C–F bond activation pathway.

The observation of the C–H activation product in the reaction with **Py-F<sub>4</sub>** may be the result of two factors: on the one hand, the high level of fluorination of the heterocycle makes it, akin to **Py-F<sub>5</sub>**, a poor Lewis base that is not likely to strongly bind the Zr centre. Besides, a potential C–F/CH<sub>2</sub> repulsion, resulting in the above-spotted <sup>1,3</sup>A strain in the cyclometalated product (Figure 16), is likely to arise from **Py-F<sub>4</sub>** coordination. Moreover, Perutz and co-workers conducted an extensive study on the competition between metal-assisted C–H and C–F bond activation processes and identified several factors, such as the nature of the metal and its ligands, as well as the fluorinated compound and its fluorine substitution pattern, both playing crucial roles in the selectivity of the system [25,36,37]. An important parameter is the presence of *ortho*-fluorine substituents in the generated metal-fluororaryl complex, which makes C–H bond activation more energetically favourable. The presence of fluorine atoms in *ortho* to the M–C bond increases the ionic character of this bond, resulting in a negative charge at the *ipso*-carbon of the M-aryl bond. This charge is stabilised by *ortho*-fluorine substituents through hyperconjugation to the C–F antibonding  $\sigma^*$  orbitals and due to the electron-withdrawing character of fluorine [36]. In our system, the metalation of the acidic C–H provides a metal-4-pyridyl compound with highly stabilising two-fold *ortho*-fluorine substitution.

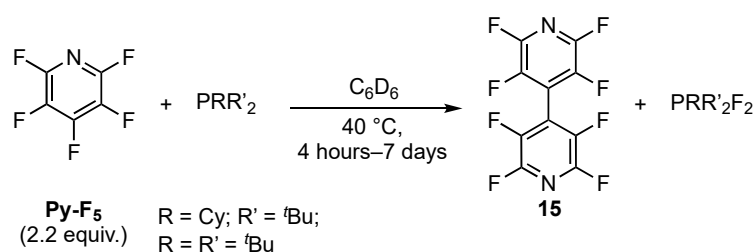
In the case of **Py-F<sub>3</sub>** and **Py-F<sub>2</sub>**, higher Lewis basicity may allow the heteroarene to better interact with the Zr atom after PMe<sub>3</sub> dissociation and thus bringing its *ortho* C–F bonds closer to the reactive cyclohexyne ligand. This sets the stage for a regioselective C–F bond activation to take place [22]. The formation of complex **7** was not observed in these systems as the fluorinated pyridines were not sufficiently electrophilic to react with the dissociated PMe<sub>3</sub>. Remarkably, in the case of **Py-F<sub>2</sub>** the 4-position is not fluorinated, yet complete chemoselectivity for C–F over C–H activation was observed. This is likely the result of a stronger Zr...N interaction favouring C–F activation as well as the absence of fluorine in the 3- and 5-positions that would stabilise the C–H activation product.

### Stoichiometric reactivity between trialkylphosphines and **Py-F<sub>5</sub>**

The stoichiometric reactivity between PMe<sub>3</sub> and **Py-F<sub>5</sub>** was further investigated to gain a better understanding of the system. The objective was to assess whether changing the system conditions, including the phosphine, solvent, temperature and reagent ratio, could limit or suppress this reactivity.

The preparation of an equimolar solution of PMe<sub>3</sub> and **Py-F<sub>5</sub>** in C<sub>6</sub>D<sub>6</sub> triggered the formation of **Py-F<sub>4</sub>**, **8** and **9**, along with a fourth minor species **13** not unambiguously identified and unreacted PMe<sub>3</sub>,

according to NMR and GC(EI)-MS analysis. Different parameters, including temperature, reagent ratio, phosphine and solvent were screened at an NMR scale. Using a 3:1 **Py-F<sub>5</sub>**/PMe<sub>3</sub> ratio, the phosphine was completely consumed, but some **Py-F<sub>5</sub>** remained. The phosphine scope study revealed that the reactivity observed between PMe<sub>3</sub> and **Py-F<sub>5</sub>** extends to other more sterically hindered phosphines (*e.g.* PEt<sub>3</sub>, PMe<sub>2</sub>Ph, P<sup>*t*</sup>Pr<sub>3</sub>, PCy<sub>3</sub>) while still maintaining high reactivity and that for most solvents (excluding CD<sub>3</sub>CN) there is no solvent effect on the reaction outcome. The conditions for the reaction require the phosphine to have a proton in the  $\alpha$ -carbon to the phosphorus and not excessively bulky R groups. The kinetic limit of the system was reached when P(<sup>*t*</sup>Bu)<sub>2</sub>Cy was employed. In this case an alternative reactivity pathway was favoured, resulting in the formation of the simple difluorophosphorane and 4,4'-octafluorobipyridine (**15**) (Scheme 41). The same outcome was observed in the absence of a proton in the  $\alpha$ -carbon in the phosphine, such as with P<sup>*t*</sup>Bu<sub>3</sub>. Furthermore, the investigation of the solvent effect suggested that this second reaction pathway was promoted, even with less sterically hindered phosphines, by the use of a more polar solvents such as acetonitrile.

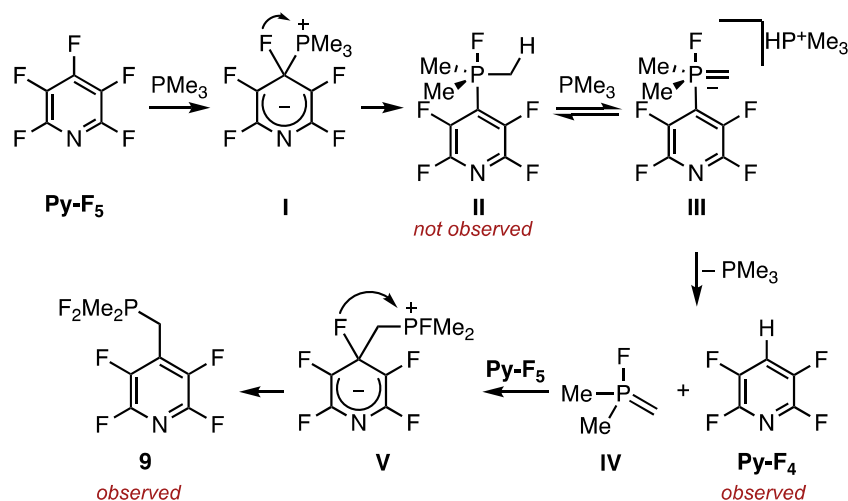


**Scheme 41.** Reactivity of P(<sup>*t*</sup>Bu)<sub>2</sub>Cy and P<sup>*t*</sup>Bu<sub>3</sub> with **Py-F<sub>5</sub>** in C<sub>6</sub>D<sub>6</sub> at 40 °C for 4 hours and 7 days, respectively.

In parallel to other strategies reported in the literature for the synthesis of these species, this approach offers a useful and versatile route for preparing F<sub>2</sub>PR<sub>3</sub> compounds under simple and mild reaction conditions. The potential advantage of this method lies in the generally low cost of phosphines and **Py-F<sub>5</sub>**. Moreover, it could also be used as a pathway for the synthesis of compound **15**.

The presence of the formal HDF product **Py-F<sub>4</sub>** in the reaction of Scheme 37 is reminiscent of the recent work from the group of García on the PEt<sub>3</sub>-promoted HDF of fluoroaromatics [38,39]. The methodology they reported differs from the above-mentioned experiments by the reaction conditions, in their case traces of water were critical to observe the desired outcome. Strict exclusion of moisture in our case rules out the involvement of García's mechanism to explain the formation of **Py-F<sub>4</sub>**, although the nucleophilic attack of the phosphine onto the 4-position of **Py-F<sub>5</sub>** must be a common initial elementary step in both reactions. Considering the reaction between PMe<sub>3</sub> and **Py-F<sub>5</sub>** and given that the formation of **9** cannot be explained by other means than the occurrence of a PMe<sub>3</sub>-derived ylide, it is proposed that the observed outcome of the reaction of **Py-F<sub>5</sub>** and PMe<sub>3</sub> stems from the mechanism depicted in Scheme 42. After the nucleophilic attack of PMe<sub>3</sub> onto **Py-F<sub>5</sub>**, the zwitterionic Meisenheimer complex **I** would evolve into the fluorophosphorane **II**. In the latter, the acidity of the Me groups may be high enough to be deprotonated by PMe<sub>3</sub> (pK<sub>a</sub> varying from ~9 in THF up to 15.5 in CH<sub>3</sub>CN), followed by proton transfer from [HPR<sub>3</sub>]<sup>+</sup> to the tetrafluoropyridyl carbon and formation of **Py-F<sub>4</sub>** [40-43]. Alternatively, a tetrafluoropyridyl anion, obtained by dissociation from fluorophosphorane **II**, may act as the base, deprotonating another molecule of intermediate **II**. This would result in ion pair **III**, with a hydro- or fluorophosphonium as counterion, that would undergo P–bond protolysis to release PMe<sub>3</sub>, **Py-F<sub>4</sub>** and the P-fluorinated ylide **IV** [44]. The latter could then attack another equivalent of **Py-F<sub>5</sub>** to lead to complex **9** *via* another Meisenheimer complex **V**, followed by C-to-P fluoride transfer sequence. Overall, this rationale explains well the observed ~1:1 **Py-F<sub>4</sub>**:**9** ratio. A

light-activated mechanism was excluded, as a test experiment conducted in the absence of light yielded the same outcome.



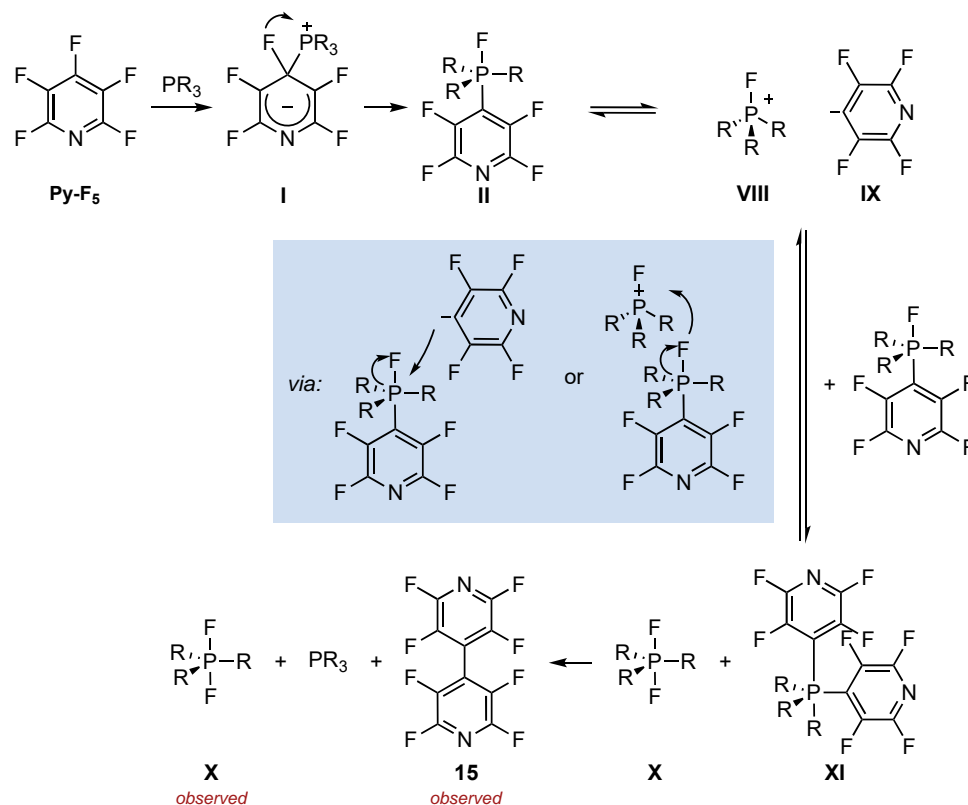
**Scheme 42.** Proposed reaction mechanism of **Scheme 37**.

When the reaction between trialkylphosphines and **Py-F<sub>5</sub>** was conducted in CD<sub>3</sub>CN, or when bulky phosphines (such as P(<sup>t</sup>Bu)<sub>2</sub>Cy) or phosphines lacking a proton in the C<sub>α</sub> were employed (e.g. P<sup>t</sup>Bu<sub>3</sub>), the formation of the simple difluorophosphorane and the reductive coupling product **15** took place instead. The proposed mechanism for this reaction is reported in Scheme 43. Similar to the previous mechanisms, the Meisenheimer complex **I** formation and its conversion into fluorophosphorane **II** take place. The 2,3,5,6-tetrafluoropyridyl group could be expected to be a better leaving group than other Ar- fragments owing to the delocalisation of the negative charge due to the high degree of fluorination of [Py-F<sub>4</sub>]<sup>-</sup>, the presence of polar solvents and the steric repulsion arising from bulky R groups on the phosphine. Furthermore, the absence of any evidence of compound **II** in both our systems and the existing literature [38,39] suggests that **II** is highly reactive. The generation of difluorophosphorane **X** and phosphorane **XI** could occur through two distinct pathways:

- *via* pyridyl attack on the phosphorus centre, leading to the release of fluoride, which then migrates to the P<sup>+</sup> of **VIII** (Scheme 43, blue box on the left);
- through the attack of **VIII** which acts as a Lewis acid by abstracting a fluoride from **II**, followed by the interaction of the resulting P<sup>+</sup> with the 2,3,5,6-tetrafluoropyridyl anion **IX** (Scheme 43, blue box on the right).

Finally, the ligand-ligand coupling in species **XI** would form **15**, as previously reported in similar systems [45-47], along with the liberation of free PR<sub>3</sub>.

A comparable solvent effect was observed in the context of the PCy<sub>3</sub>-catalysed intermolecular acylfluorination of alkynes in toluene [48].



**Scheme 43.** Proposed mechanism for the formation of **15**.

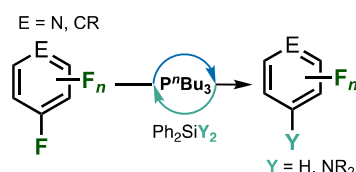
Tobisu *et al.* proposed the participation of a fluorophosphorane intermediate in the catalytic cycle which, after ligand coupling and release of the acylfluorination product, regenerates the  $\text{P}^{\text{III}}$  catalyst. In polar solvents such as acetonitrile, the reaction yields the simple difluorophosphorane  $\text{F}_2\text{PCy}_3$  and the hydroacylated product, with the acylfluorination product detected only in minimal amounts. The authors proposed that the fluorophosphorane is in equilibrium with the corresponding phosphonium salt, which is more stable in acetonitrile. The phosphonium species is expected to decompose more readily than the fluorophosphorane and the protonation of the system would lead to the formation of  $\text{F}_2\text{PCy}_3$  and the hydroacylated product. Traces of water (*via* nucleophilic attack onto phosphonium ion) or cyclohexyl groups (through  $\beta$ -hydrogen elimination) could act as proton sources in this system.

### $\text{P}^{\text{III}}\text{Bu}_3$ -catalysed hydro- and aminodefluorination of polyfluoroaromatics

In recent years, there has been a significant interest in the activation and functionalisation of small molecules and strong bonds by main-group element compounds that mimic the reactivity of TMs. An essential concept driving this research is metallomimetic behaviour, where main-group elements can be induced to exhibit reactivity similar to that of transition metals [49]. One of the peculiar reactivity of TMs is to undergo reversible two-electron redox processes, such as oxidative addition and reductive elimination. Nevertheless, redox cycles with main-group elements are relatively rare. Among these elements, the pnictogens stand out, as they often provide access to stable species in various oxidation states [50]. A crucial structural feature that seems to enable the observation of redox cycling in Pn-containing systems involves the introduction of geometric constraints around pnictogen atoms [51]. Recent studies in this field described how geometrically constrained pnictogens can effectively hydrodefluorinate perfluorinated aromatics, both stoichiometrically and catalytically

[52-54]. These works highlight the crucial role of this structural design in accessing the  $Pn^{III}/Pn^V$  redox cycle, enabling the specific reactivity desired for this transformation.

The new results reported in this study demonstrated that complex molecular architectures are not required for  $P^{III}$  systems to act as catalysts for HDF or aminodefluorination of highly fluorinated arenes and heterocycles. Simple trialkylphosphines were found to be fast and effective catalysts for these reactions with a range of substrates, but especially for highly electron-poor ones (Scheme 44). This is an important observation, as some trialkylphosphines, particularly the  $P^nBu_3$  used here, are cheap, readily available from commercial suppliers and easy to handle.



**Scheme 44.** Representative scheme of our system for the catalytic reaction of HDF and hydroamination.

The reaction optimisation showed that the combination of  $P^nBu_3$  and  $Ph_2SiH_2$  as hydride source in acetonitrile provided the best reaction conditions allowing selective HDF of **Py-F<sub>5</sub>** to give **Py-F<sub>4</sub>** in excellent yield (93%), after only 20 minutes at 20 °C. This performance stands among the best reported for catalytic aromatic HDF by a main-group-element catalyst [52-56]. Moreover, this phosphine-silane combination proved to be most economical and readily available among those tested.

The substrate scope for HDF was investigated, extending the studies to various fluoroarenes and heterocycles (Figure 17). In addition, it was possible to explore preliminary aminodefluorination reactions (products **24** to **27**) to allow C–F functionalisation by amines.

Exploration of the degree of fluorination of fluoropyridines and the regioselectivity of the HDF reaction gave insights into the reaction mechanism and synthetic possibilities. With **Py-F<sub>4</sub>** as a substrate, it was possible to observe the formation of **17**, but in low yield and requiring much more forcing conditions (13% after 5 days at 70 °C). This explains the selectivity of the HDF in Scheme 44, as a second HDF at the less activated *ortho*-position of the pyridine is substantially slower than the initial reaction at the *para*-position of **Py-F<sub>5</sub>**. The presence of other tri- and difluoropyridines suggests that the rate of HDF at the *ortho*- and *meta*-positions is similar to each other and slower than the rate of HDF at the *para*-position. Reducing the degree of fluorination of the substrate, but maintaining a C–F bond at the most reactive *para*-position also allowed HDF and formation of **Py-F<sub>2</sub>** (79% yield), but the reaction was relatively slow and a small amount of unreacted **Py-F<sub>3</sub>** (5%) was present, along with some 2,4-difluoropyridine (14%), which results from *ortho*-HDF, after 6 days. It is clear that more electron-poor heteroaromatics lead to faster reactions, which is consistent with the mechanistic proposal. The catalytic HDF reaction is not limited to pyridines. Reaction of other electron-poor aromatics, such as pentafluorobenzonitrile, perfluorotoluene, hexafluorobenzene and perfluorobiphenyl led to the formation of the mono or diHDF product in good yields (84–93%). Extending the catalytic methodology to other C–F functionalisation reactions was also explored. Preliminary studies investigated C–F amination by silylamides in the presence of catalytic  $P^nBu_3$ . Thus, when **Py-F<sub>5</sub>** was reacted with  $Ph_2Si(Cl)(NEt_2)$  with 10 mol% of  $P^nBu_3$  at 60 °C for 18 h a good yield (75%) of the aminated product **24** was seen, alongside a small amount of unreacted **Py-F<sub>5</sub>** (10%).

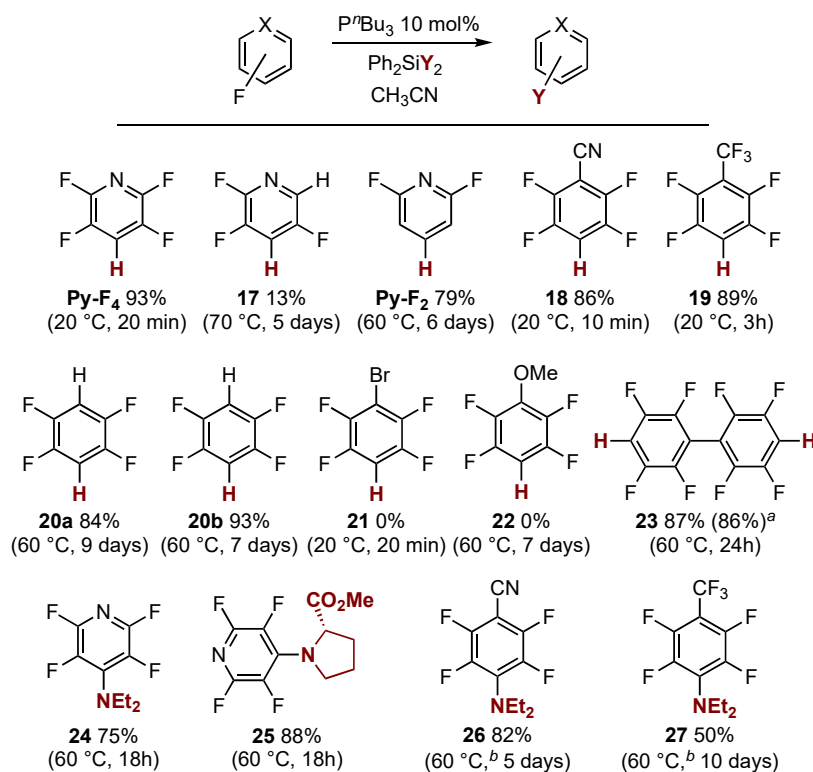
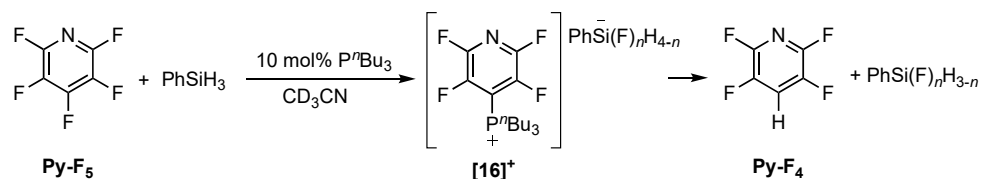


**Figure 17.** Results of substrate scope studies.  $Ph_2SiH_2$  was used for all HDF reactions and  $Ph_2Si(Cl)(NR_2)$  were used for aminodefluorination reactions. <sup>a</sup> Isolated yield after flash column chromatography shown in parentheses. <sup>b</sup> Reactions were stirred at 60 °C for 4 days, followed by the remaining period at 80 °C.

Extending this reaction to more complex amines also proved possible. Reaction of **Py-F<sub>5</sub>** with  $Ph_2Si(Cl)(pro)$  (where pro is *L*-proline methyl ester) gave a very good yield of **25** (88%) alongside a small amount of unreacted **Py-F<sub>5</sub>**. This demonstrated that potentially sensitive functional groups are tolerated by this catalytic aminodefluorination reaction and that it may find application in the preparation of highly functionalised, fluorinated amines, *e.g.* in pharmaceutical or agrochemical synthesis. Extending the fluoroarene substrates beyond **Py-F<sub>5</sub>** also proved possible, with both pentafluorobenzonitrile and perfluorotoluene also reacting with  $Ph_2Si(Cl)(NEt_2)$  in the presence of 10 mol%  $P^nBu_3$  to give **26** and **27** in 82% and 50% yield respectively. However, these substrates proved more sluggish under the reaction conditions optimised for HDF and further optimisation is desirable in future studies to extend the aminodefluorination reactions beyond these preliminary results.

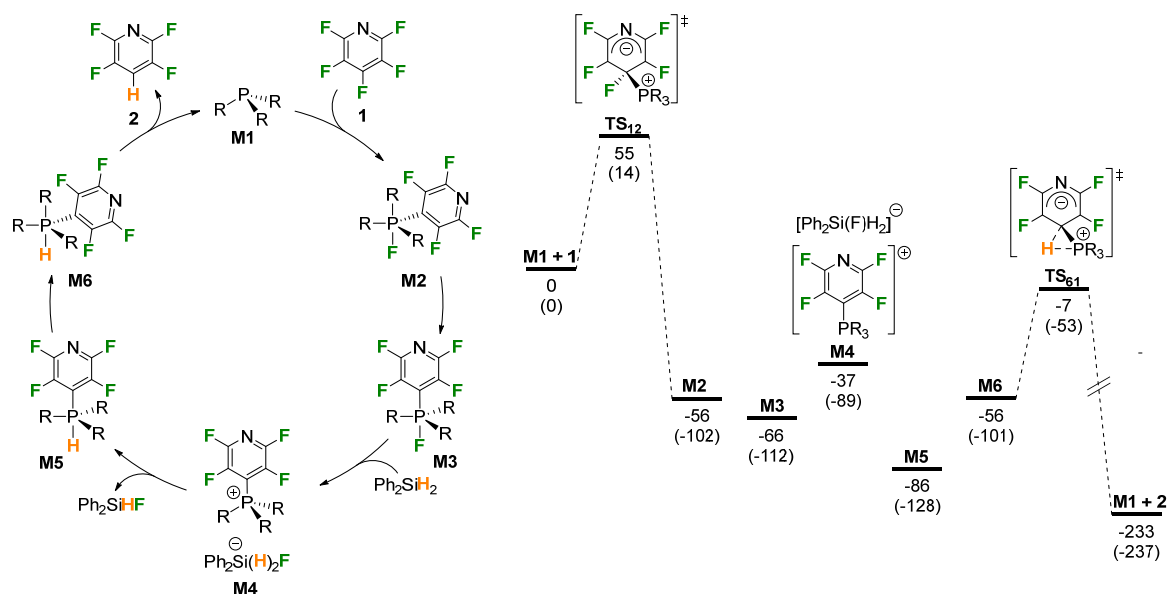
Experimental and computational mechanistic studies were undertaken to probe the pathways underpinning the HDF reaction. Under the optimised reaction conditions for the HDF of **Py-F<sub>5</sub>** the reaction occurred too quickly to observe any intermediates. However, for slower reactions it was possible to gain insights through the observation of intermediate phosphorus-containing species. When **Py-F<sub>5</sub>** was reacted with  $PhSiH_3$ , with 10 mol%  $P^nBu_3$  in MeCN at 20 °C, after 1 h the <sup>31</sup>P NMR spectrum showed very clean conversion of  $P^nBu_3$  into a new species with an apparent septet resonance at  $\delta = 38.1$  ppm ( $J = ca. 5$  Hz). This was accompanied by new complex multiplet signals in the <sup>19</sup>F NMR at  $\delta = -88.5$  and  $-130.3$  ppm. The only other resonances present in the <sup>19</sup>F NMR were from unreacted **Py-F<sub>5</sub>**, the HDF product **Py-F<sub>4</sub>** and the fluorosilane produced by H/F exchange. The resonance at  $\delta = 38.1$  ppm in the <sup>31</sup>P NMR spectrum is characteristic of a phosphonium cation and was therefore assigned to the  $[(C_5F_4N)P^nBu_3]^+$  ion, **[16]<sup>+</sup>**. This was confirmed by independent preparation of  $[(C_5F_4N)P^nBu_3]Br$  (**[16]Br**) by reaction of  $P^nBu_3$  with 4-bromo-2,3,5,6-tetrafluoropyridine (Scheme 45).

At the end of the catalytic reaction, when **Py-F<sub>5</sub>** was fully consumed, the signal for **[16]<sup>+</sup>** disappeared and free phosphine was observed in the reaction mixture (<sup>31</sup>P δ = -32.1 ppm), suggesting its role as a resting state.



**Scheme 45.** HDF reaction of **Py-F<sub>5</sub>** (1 equiv.) with **PhSiH<sub>3</sub>** (1 equiv.) and **P<sup>n</sup>Bu<sub>3</sub>** (10 mol%) in **CD<sub>3</sub>CN** at 20 °C.

To investigate whether **[16]<sup>+</sup>** was a relevant catalytic intermediate, **Ph<sub>2</sub>SiH<sub>2</sub>** was added to the independently prepared sample of **[16]Br** in **MeCN**. After 10 minutes at 20 °C there was no change in the <sup>31</sup>P or <sup>19</sup>F NMR spectra. The mixture was heated to 40 °C overnight and similarly showed no reaction between **[16]Br** and the silane. However, on addition of one equivalent of anhydrous **[Me<sub>4</sub>N]F** to the system at 20 °C, **Py-F<sub>4</sub>** was seen to form after only 10 minutes, alongside the formation of fluorosilane **Ph<sub>2</sub>Si(F)<sub>n</sub>H<sub>2-n</sub>** and some unreacted **[16]<sup>+</sup>**. Over time, the amount of **Py-F<sub>4</sub>** increased as **[16]<sup>+</sup>** decreased. This suggested that **[16]<sup>+</sup>** is an intermediate in the catalytic cycle, but that it does not react directly with the silane to form the HDF product. We propose that addition of fluoride to the silane to form a silicate anion, **[Ph<sub>2</sub>Si(F)H<sub>2</sub>]<sup>-</sup>**, is necessary to promote H<sup>-</sup> transfer and liberation of the hydrodefluorinated product. Looking at the catalytic reaction as a whole, the experimental mechanistic studies suggested that the phosphine catalyst adds to the fluoroarene/heteroarene to initially form a fluorophosphorane, e.g. **P(F)(<sup>n</sup>Bu)<sub>3</sub>(C<sub>5</sub>F<sub>4</sub>N)**, but that the silane then acts as a Lewis acid to abstract a fluoride ion from the phosphorane to form a phosphonium salt, e.g. **[(C<sub>5</sub>F<sub>4</sub>N)P<sup>n</sup>Bu<sub>3</sub>][Ph<sub>2</sub>Si(F)H<sub>2</sub>]**. The hydrosilicate anion then transfers a hydride to the phosphonium ion to form another phosphorane that eliminates the hydrodefluorinated product and re-generates the phosphine (Scheme 46).



**Scheme 46.** Proposed catalytic cycle and computed potential energy surface (PES) for **R = Me**. All energies at the **PBE0/def2-TZVP//BP86/SV(P)** level in **MeCN**. Relative Gibbs energies (in **kJ mol<sup>-1</sup>** at 298 K) shown outside brackets and relative enthalpies (in **kJ mol<sup>-1</sup>** at 298 K) shown in brackets.



This H/F exchange between P and Si is driven by differences in the fluoride ion and hydride ion affinities of the phosphorane and silane, which have been discussed and computed for related species [36]. The reactivity of non-fluorinated pyridylphosphonium salts with nucleophiles to form substituted pyridines has also been reported and, like the processes observed here, is proposed to occur *via* phosphorane intermediates [57]. Underpinning all of this reactivity is the facile redox cycling between P<sup>III</sup> and P<sup>V</sup> oxidation states that is remarkable to see in simple trialkylphosphines.

DFT calculations were performed to support the experimental mechanistic studies. These showed that initial reaction of the phosphine with pentafluoropyridine takes place through a Meisenheimer-like transition state (Scheme 46, **TS<sub>12</sub>**) to form a fluorophosphorane (**M2**) in a similar manner to that proposed by García and coworkers for reaction of **Py-F<sub>5</sub>** with PEt<sub>3</sub> [38]. This is associated with a low barrier of 55 kJ mol<sup>-1</sup>. The structure of **TS<sub>12</sub>** (Figure 18) shows the early nature of this transition state, where P-C bond formation and C-F bond elongation precedes fluorine transfer to phosphorus to form the phosphorane. This step is effectively initiated by a nucleophilic addition of PR<sub>3</sub> to the pentafluoropyridine and explains the preference for electron-poor arenes/heteroarenes in this reaction, where this will be promoted. No additional intermediates or transition states for fluorine transfer to phosphorus were identified. The addition of **Py-F<sub>5</sub>** to the phosphine leads to a formal oxidation state change from P<sup>III</sup> to P<sup>V</sup> and so can be characterised as an oxidative addition process, albeit one that is highly asynchronous in terms of C-F bond cleavage and reminiscent of concerted S<sub>N</sub>Ar mechanisms. The key structural parameters of **TS<sub>12</sub>** are almost identical to those calculated by Dobrovetsky and coworkers for addition of **Py-F<sub>5</sub>** to a geometrically constrained σ<sup>3</sup>-P compound, suggesting a similar activation process, despite the very different structural frameworks involved [54].

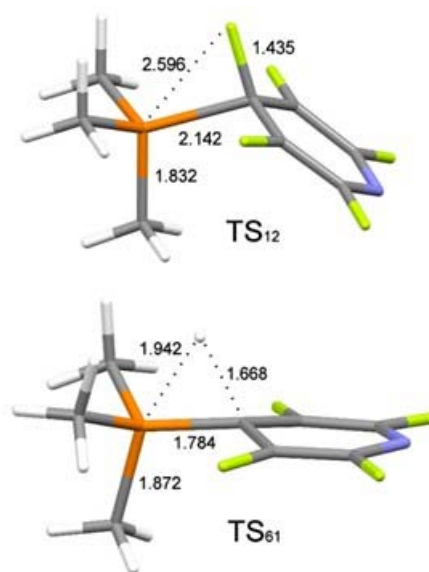


**Figure 18.** Transition states for addition of **PMe<sub>3</sub>** to **Py-F<sub>5</sub>** (**TS<sub>12</sub>**) and elimination of **Py-F<sub>4</sub>** from phosphorane **M6** (**TS<sub>61</sub>**). Hydrogen is shown in white, carbon in grey, phosphorus in orange, nitrogen in blue and fluorine in green. Selected distances (in Å) are shown.

The fluorophosphorane that is initially formed (**M2**) can undergo isomerisation to a lower energy isomer (**M3**) with fluorine *trans* to the tetrafluoropyridyl group, both in the apical positions. Fluoride transfer to Ph<sub>2</sub>SiH<sub>2</sub> results in the formation of the observed phosphonium ion [**16**]<sup>+</sup>, in this case as the salt **M4**. Moving between neutral and ionic manifolds in this way will be strongly influenced by solvation effects. This leads to a small mismatch between the computed energies and the experimental

observations, where **M4** is higher in energy than the phosphoranes, although phosphonium ions and not the phosphoranes are observed experimentally. This is likely due to limitations in using a dielectric continuum solvation model, which under-solvates the ions and raises their energies relative to neutral species. The neutral/ionic manifold switch may help to explain the solvent effect seen in this system, where moving from *o*-C<sub>6</sub>H<sub>4</sub>F<sub>2</sub> ( $\epsilon$  13.4 = at 25 °C) to the more polar MeCN ( $\epsilon$  = 35.9 at 25 °C) led to an increase in the catalytic rate. It is well known that more polar solvents like MeCN promote the formation of ionic species from phosphoranes and this would facilitate the formation of **M4**.

Hydride transfer from the silicate anion then leads to phosphorane **M5**, which can isomerise to form **M6**. This is very different from the mechanistic proposal of Dobrovetsky for HDF by geometrically constrained  $\sigma^3$ -P systems, where it was suggested that PhSiH<sub>3</sub> reacts directly with the fluorophosphorane through a transition state that involves concerted hydride transfer to P and fluoride transfer to Si. The experiments described above showed that for simple trialkylphosphines, phosphonium ions are intermediates and these do not react directly with the neutral silanes. It may be that the positive charge on Dobrovetsky's constrained  $\sigma^3$ -P systems disfavors this pathway and leads to this divergence in mechanistic behaviour.

The final step involves reductive elimination of **Py-F<sub>4</sub>** from **M6** via **TS<sub>61</sub>** (Figure 17). This transition state is more concerted than **TS<sub>12</sub>**, although still somewhat asynchronous, presumably because direct concerted reductive elimination from the axial and equatorial positions of a phosphorane is symmetry forbidden [58]. **TS<sub>61</sub>** is again Meisenheimer-like, although less so than in the constrained  $\sigma^3$ -P systems of Radosevich [53], where the C–H bond length of a related reductive elimination TS is 1.33 Å, and Dobrovetsky where it is 1.53 Å. It seems as though the substituents and geometric environment around phosphorus have a significant impact on the reductive elimination process. These final steps give rise to the energetic span for the reaction, which is defined by the turnover-determining intermediate (TDI) **M5** and transition state (TDTS) **TS<sub>61</sub>**, and give an overall barrier for the catalytic reaction of 79 kJ mol<sup>-1</sup>. This low barrier is consistent with the observed fast reaction between **Py-F<sub>5</sub>** and Ph<sub>2</sub>SiH<sub>2</sub> when a sterically relatively small phosphine like P<sup>*n*</sup>Bu<sub>3</sub> is used as the catalyst (full conversion in 20 minutes at 20 °C in MeCN). The calculated energetic span for HDF of **Py-F<sub>5</sub>** by a constrained  $\sigma^3$ -P system was significantly larger (140 kJ mol<sup>-1</sup>), which is consistent with the slower reactions observed in that study [54].

## Conclusions

Over the past two decades, the functionalisation of C–F bonds of perfluorinated compounds has attracted significant attention due to the numerous industrial applications of fluorinated organic compounds and the inherent challenges associated with these transformations, including the high strength of the C–F bond and the difficulty in the control of the reaction's selectivity. Furthermore, as fluorocarbons tend to be inert upon decomposition, they are persistent in the environment and the exploration of alternative methods for defluorination is of great interest.

This work presents novel protocols for the regioselective C–F bond functionalisation of polyfluorinated aromatics which are promoted by zirconium and catalysed by phosphines. Mechanistic investigations supported by experimental and, in selected examples, computational studies, complement the synthetic findings.

The reactivity of a zirconocene complex featuring a highly strained cyclohexyne ligand toward differently fluorinated pyridines was investigated. This complex, isolated by coordination of a PMe<sub>3</sub> ligand, exhibited different reactivity pathways depending on the fluorination pattern of the

heteroaromatic. Remarkably, the reactive metal-alkyne bond could insert into the *ortho*-C–F bonds of 2,4,6-trifluoropyridine and 2,6-difluoropyridine, resulting in the net alkenylation of the polyfluorinated heterocycle. The reaction of the complex with 2,3,5,6-tetrafluoropyridine led instead to the 1,2-C–H addition over the Zr-( $\eta^2$ -C $\equiv$ C). Conversely, the reaction with pentafluoropyridine mainly involved a parasitic S<sub>N</sub>Ar reaction of the dissociated PMe<sub>3</sub> ligand with the substrate, generating a series of difluorophosphoranes that triggered decomposition of the Zr complex.

These results led to the investigation into the stoichiometric reactivity between simple phosphines and pentafluoropyridine. Various trialkylphosphines exhibited the ability to activate the *para*-F of the heteroaromatic, leading to the formation of the products arising from hydrodefluorination or reductive homocoupling, along with methylenetetrafluoropyridyl-substituted or simple difluorophosphoranes, depending on the reaction conditions.

Because metal-free C–F bond activation is highly topical, these findings set the stage for the development of a metallomimetic catalytic system for the hydrodefluorination and aminodefluorination of polyfluorinated aromatics in the presence of silanes or silylamides. Remarkably, the catalyst employed for these transformations is the simple and readily available P<sup>n</sup>Bu<sub>3</sub>. It undergoes facile redox cycling between the P<sup>III</sup> and P<sup>V</sup> oxidation states, enabling oxidative addition of the substrate, pseudotransmetalation and reductive elimination of the product throughout the catalytic cycle – typical steps observed in classical transition-metal-catalysis. The key features of this catalytic system are simplicity and cost. As all reagents are commercially available and easy to handle, there is no barrier to entry to these catalytic reactions, broadening their potential applicability in a range of settings.

## References

- [1] L. Pauling, *J. Am. Chem. Soc.* **1932**, *54*, 3570–3582. DOI: [10.1021/JA01348A011](https://doi.org/10.1021/JA01348A011).
- [2] D. O'Hagan, *Chem. Soc. Rev.* **2008**, *37*, 308–319. DOI: [10.1039/B711844A](https://doi.org/10.1039/B711844A).
- [3] B. E. Smart, *Fluorocarbons*, Wiley: New York, **1983**. ISBN: 9780470771716. DOI: [10.1002/9780470771716.ch14](https://doi.org/10.1002/9780470771716.ch14).
- [4] P. Kirsch, *Modern Fluoroorganic Chemistry*, Wiley: New York, **2004**. ISBN: 9783527306916. DOI: [10.1002/352760393X](https://doi.org/10.1002/352760393X).
- [5] T. Liang, C. N. Neumann, T. Ritter, *Angew. Chem. Int. Ed.* **2013**, *52*, 8214–8264. DOI: [10.1002/anie.201206566](https://doi.org/10.1002/anie.201206566).
- [6] E. Lück, G. von R. Lipinski, *Ullmann's Encyclopedia of Industrial Chemistry*, Wiley-VCH: Weinheim, Germany, **2012**. ISBN: 3-527-32943-9. DOI: 10.1002/14356007.
- [7] D. O'Hagan, C. Schaffrath, S. L. Cobb, J. T. G. Hamilton, C. D. Murphy, *Nature* **2002**, *416*, 279. DOI: [10.1038/416279a](https://doi.org/10.1038/416279a).
- [8] G. Villalba, R. U. Ayres, H. Schroder, *J. Ind. Ecol.* **2007**, *11*, 85–101. DOI: [10.1162/JIEC.2007.1075](https://doi.org/10.1162/JIEC.2007.1075).
- [9] M. Inoue, Y. Sumii, N. Shibata, *ACS Omega* **2020**, *5*, 10633–10640. DOI: [10.1021/acsomega.0c00830](https://doi.org/10.1021/acsomega.0c00830).
- [10] K. Chen, X. Chen, *Semin. Oncol.* **2011**, *38*, 70–86. DOI: [10.1053/j.seminoncol.2010.11.005](https://doi.org/10.1053/j.seminoncol.2010.11.005).
- [11] W. T. Tsai, *Chemosphere* **2005**, *61*, 1539–1547. DOI: [10.1016/J.CHEMOSPHERE.2005.03.084](https://doi.org/10.1016/J.CHEMOSPHERE.2005.03.084).
- [12] D. Zaelke, N. Borgford-Parnell, *J. Environ. Stud. Sci.* **2015**, *5*, 169–175. DOI: [10.1007/S13412-014-0215-7](https://doi.org/10.1007/S13412-014-0215-7).
- [13] J. Zhou, C. Jin, W. Su, *Org. Process Res. Dev.* **2014**, *18*, 928–933. DOI: [10.1021/OP5001226](https://doi.org/10.1021/OP5001226).
- [14] L. M. Milner, N. E. Pridmore, A. C. Whitwood, J. M. Lynam, J. M. Slattery, *J. Am. Chem. Soc.* **2015**, *137*, 10753–10759. DOI: [10.1021/jacs.5b06547](https://doi.org/10.1021/jacs.5b06547).
- [15] L. V. Hooker, J. S. Bandar, *Angew. Chem. Int. Ed.* **2023**, *62*, e202308880. DOI: [10.1002/anie.202308880](https://doi.org/10.1002/anie.202308880).

- [16] R. N. Perutz, T. Braun, *Transition Metal-mediated C-F Bond Activation*, in *Comprehensive Organometallic Chemistry III*, Elsevier Ltd, **2007**, Vol. 1, pp 725–758. DOI: [10.1016/B0-08-045047-4/00028-5](https://doi.org/10.1016/B0-08-045047-4/00028-5).
- [17] T. Ahrens, J. Kohlmann, M. Ahrens, T. Braun, *Chem. Rev.* **2015**, *115*, 931–972. DOI: [10.1021/CR500257C](https://doi.org/10.1021/CR500257C).
- [18] S. L. Buchwald, *J. Am. Chem. Soc.* **1986**, *108*, 7441–7442. DOI: [10.12775/eo.2012.008](https://doi.org/10.12775/eo.2012.008).
- [19] S. L. Buchwald, R. B. Nielsen, *Chem. Rev.* **1988**, *88*, 1047–1058. DOI: [10.1021/CR00089A004](https://doi.org/10.1021/CR00089A004).
- [20] A. Spaggiari, D. Vaccari, P. Davoli, G. Torre, F. Prati, *J. Org. Chem.* **2007**, *72*, 2216–2219. DOI: [10.1021/jo061346g](https://doi.org/10.1021/jo061346g).
- [21] K. Garrec, S. P. Fletcher, *Org. Lett.* **2016**, *18*, 3814–3817. DOI: [10.1021/acs.orglett.6b01829](https://doi.org/10.1021/acs.orglett.6b01829).
- [22] N. Romero, Q. Dufrois, N. Crespo, A. Pujol, L. Vendier, M. Etienne, *Organometallics* **2020**, *39*, 2245–2256. DOI: [10.1021/acs.organomet.0c00218](https://doi.org/10.1021/acs.organomet.0c00218).
- [23] A. Nova, M. Reinhold, R. N. Perutz, S. A. MacGregor, J. E. McGrady, *Organometallics* **2010**, *29*, 1824–1831. DOI: [10.1021/om100064Z](https://doi.org/10.1021/om100064Z).
- [24] A. Nova, *J. Am. Chem. Soc.* **2008**, *130*, 15499–15511. DOI: [10.1021/ja8046238](https://doi.org/10.1021/ja8046238).
- [25] E. Clot, O. Eisenstein, N. Jasim, S. A. MacGregor, J. E. McGrady, R. N. Perutz, *Acc. Chem. Res.* **2011**, *44*, 333–348. DOI: [10.1021/ar100136X](https://doi.org/10.1021/ar100136X).
- [26] T. Braun, R. N. Perutz, *Chem. Commun.* **2002**, *2*, 2749–2757. DOI: [10.1039/B206154F](https://doi.org/10.1039/B206154F).
- [27] N. A. Jasim, *Organometallics* **2004**, *23*, 6140–6149. DOI: [10.1021/om049448P](https://doi.org/10.1021/om049448P).
- [28] Y. R. Luo, *Comprehensive Handbook of Chemical Bond Energies*, CRC Press: Boca Raton, **2007**. ISBN: 9780429128684. DOI: [10.1201/9781420007282](https://doi.org/10.1201/9781420007282).
- [29] J. Zhao, S. Zhang, W. X. Zhang, Z. Xi, *Organometallics* **2012**, *31*, 8370–8374. DOI: [10.1021/om300949A](https://doi.org/10.1021/om300949A).
- [30] J. Zhao, S. Zhang, W. X. Zhang, Z. Xi, *Organometallics* **2011**, *30*, 3464–3467. DOI: [10.1021/om200404P](https://doi.org/10.1021/om200404P).
- [31] P. Arndt, C. Lefebvre, R. Kempe, U. Rosenthal, *Chem. Ber.* **1996**, *129*, 207–211. DOI: [10.1002/cber.19961290214](https://doi.org/10.1002/cber.19961290214).
- [32] P. Binger, F. Sandmeyer, C. Krüger, *Organometallics* **1995**, *14*, 2969–2976. DOI: [10.1021/om00006A047](https://doi.org/10.1021/om00006A047).
- [33] V. V. Burlakov, *Eur. J. Inorg. Chem.* **2014**, *31*, 5304–5310. DOI: [10.1002/ejic.201402618](https://doi.org/10.1002/ejic.201402618).
- [34] G. Bender, G. Kehr, C. G. Daniliuc, B. Wibbeling, G. Erker, *Dalton Trans.* **2013**, *42*, 14673–14676. DOI: [10.1039/C3DT51497H](https://doi.org/10.1039/C3DT51497H).
- [35] L. Becker et al., *Chem. Eur. J.* **2014**, *20*, 3061–3068. DOI: [10.1002/chem.201304478](https://doi.org/10.1002/chem.201304478).
- [36] O. Eisenstein, J. Milani, R. N. Perutz, *Chem. Rev.* **2017**, *117*, 8710–8753. DOI: [10.1021/acs.chemrev.7B00163](https://doi.org/10.1021/acs.chemrev.7B00163).
- [37] E. Clot, C. Mégret, O. Eisenstein, R. N. Perutz, *J. Am. Chem. Soc.* **2009**, *131*, 7817–7827. DOI: [10.1021/ja901640M](https://doi.org/10.1021/ja901640M).
- [38] A. A. Facundo, *New J. Chem.* **2019**, *43*, 6897–6908. DOI: [10.1039/c9nj00721K](https://doi.org/10.1039/c9nj00721K).
- [39] A. Arévalo, A. Tlahuext-Aca, M. Flores-Alamo, J. J. García, *J. Am. Chem. Soc.* **2014**, *136*, 4634–4639. DOI: [10.1021/ja412268Y](https://doi.org/10.1021/ja412268Y).
- [40] W. A. Henderson, C. A. Streuli, *J. Am. Chem. Soc.* **2002**, *82*, 5791–5794. DOI: [10.1021/ja01507A008](https://doi.org/10.1021/ja01507A008).
- [41] K. Abdur-Rashid et al., *J. Am. Chem. Soc.* **2000**, *122*, 9155–9171. DOI: [10.1021/ja994428D](https://doi.org/10.1021/ja994428D).
- [42] A. Streitwieser, A. E. McKeown, F. Hasanayn, N. R. Davis, *Org. Lett.* **2005**, *7*, 1259–1262. DOI: [10.1021/ol047315U](https://doi.org/10.1021/ol047315U).
- [43] K. Haav, J. Saame, A. Kütt, I. Leito, *Eur. J. Org. Chem.* **2012**, *11*, 2167–2172. DOI: [10.1002/ejoc.201200009](https://doi.org/10.1002/ejoc.201200009).
- [44] E. Fluck, R. Braun, *Phosphorus, Sulfur Silicon Relat. Elem.* **1988**, *40*, 83–90. DOI: [10.1080/03086648808072897](https://doi.org/10.1080/03086648808072897).
- [45] X. Zhang et al., *Nature* **2021**, *594*, 217–222. DOI: [10.1038/s41586-021-03567-3](https://doi.org/10.1038/s41586-021-03567-3).
- [46] M. C. Hilton, X. Zhang, B. T. Boyle, J. V. Alegre-Requena, R. S. Paton, A. McNally, *Science* **2018**, *362*, 799–804. DOI: [10.1126/science.aas8961](https://doi.org/10.1126/science.aas8961).

- [47] B. T. Boyle, M. C. Hilton, A. McNally, *J. Am. Chem. Soc.* **2019**, *141*, 15441–15449. DOI: [10.1021/jacs.9b08504](https://doi.org/10.1021/jacs.9b08504).
- [48] H. Fujimoto, T. Kodama, M. Yamanaka, M. Tobisu, *J. Am. Chem. Soc.* **2020**, *142*, 17323–17328. DOI: [10.1021/jacs.0c08928](https://doi.org/10.1021/jacs.0c08928).
- [49] H. Braunschweig, *J. Am. Chem. Soc.* **2017**, *139*, 1802–1805. DOI: [10.1021/jacs.6b13047](https://doi.org/10.1021/jacs.6b13047).
- [50] J. M. Lipshultz, G. Li, A. T. Radosevich, *J. Am. Chem. Soc.* **2021**, *143*, 1699–1721. DOI: [10.1021/jacs.0c12816](https://doi.org/10.1021/jacs.0c12816).
- [51] J. Abbenseth, J. M. Goicoechea, *Chem. Sci.* **2020**, *11*, 9728–9740. DOI: [10.1039/d0sc03819a](https://doi.org/10.1039/d0sc03819a).
- [52] Y. Pang et al., *J. Am. Chem. Soc.* **2021**, *143*, 12487–12493. DOI: [10.1021/jacs.1c06735](https://doi.org/10.1021/jacs.1c06735).
- [53] S. Lim, A. T. Radosevich, *J. Am. Chem. Soc.* **2020**, *142*, 16188–16193. DOI: [10.1021/jacs.0c07580](https://doi.org/10.1021/jacs.0c07580).
- [54] K. Chulsky, I. Malahov, D. Bawari, R. Dobrovetsky, *J. Am. Chem. Soc.* **2023**, *145*, 3786–3794. DOI: [10.1021/jacs.2c13318](https://doi.org/10.1021/jacs.2c13318).
- [55] K. Kikushima et al., *Angew. Chem. Int. Ed.* **2017**, *56*, 16191–16196. DOI: [10.1002/anie.201708003](https://doi.org/10.1002/anie.201708003).
- [56] J. Zhang, X. Zhao, J. D. Yang, J. P. Cheng, *J. Org. Chem.* **2022**, *87*, 294–300. DOI: [10.1021/acs.joc.1c02360](https://doi.org/10.1021/acs.joc.1c02360).
- [57] M. C. Hilton, R. D. Dolewski, A. McNally, *J. Am. Chem. Soc.* **2016**, *138*, 13806–13809. DOI: [10.1021/jacs.6b08662](https://doi.org/10.1021/jacs.6b08662).
- [58] R. Hoffmann, J. M. Howell, E. L. Muetterties, *J. Am. Chem. Soc.* **1972**, *94*, 3047–3058. DOI: [10.1021/ja00764A028](https://doi.org/10.1021/ja00764A028).

**Wimonsiri HUADSAI**

**ESR6**

**Thesis co-directors**

Prof. Matthias Westerhausen    Friedrich-Schiller-Universität, Jena, Germany

Dr. Sébastien Bontemps        Laboratoire de Chimie de Coordination, Toulouse, France

**Thesis defense**

Department of Chemistry, Friedrich-Schiller-Universität, 19 March 2024



## Activation of Carbon Dioxide with Highly Lewis Acidic Compounds

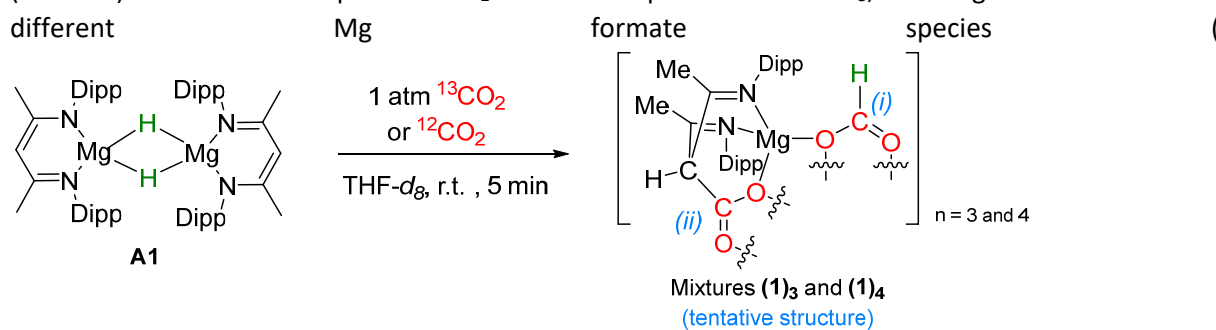
### Introduction

Carbon dioxide is easily available and an important C<sub>1</sub> building block in synthetic chemistry [1]. Therefore, its properties in coordination chemistry and its use in stoichiometric and catalytic reduction processes is of utmost importance. Global abundance and non-toxicity of the alkaline-earth metals Mg and Ca elicit a vivid development of their reagents for stoichiometric and catalytic applications [2]. To suppress redistribution reactions of the ligands (Schlenk-type equilibria) and precipitation of insoluble AeH<sub>2</sub>, the metal center can be shielded by very bulky ligands to stabilize heteroleptic molecules [3]. This strategy hinders far-reaching aggregation of hydrido alkaline-earth metal complexes despite the fact that Mg- and Ca-bound hydrido ligands avoid terminal binding modes and are commonly observed as bridging ligands. Therefore, bulky β-diketiminato and amidinato ligands were chosen to shield the reactive Ae-H moieties. For probing the reactivity of Ae-H functionalities towards CO<sub>2</sub>, we started our investigations with the well-known dinuclear β-diketiminato alkaline-earth metal hydrides of magnesium (**A1**) [4] and calcium (**A2**) [5].

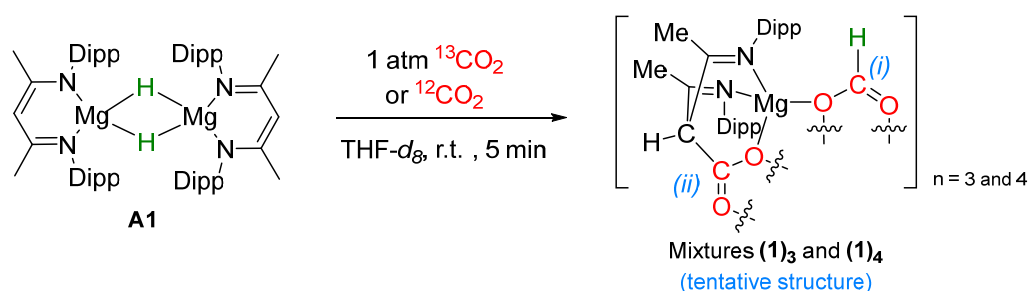
### Reactivity of [Ae]-based hydride complexes towards CO<sub>2</sub>

#### Reactivity of β-diketiminato Mg hydride with CO<sub>2</sub>

The first section discusses the reduction of CO<sub>2</sub> by employing [Ae]-based hydride complexes. Overall, even in the absence of the Lewis acid B(C<sub>6</sub>F<sub>5</sub>)<sub>3</sub>, the Mg hydride (**A1**) underwent a rapid reaction (<10 min) under one atmosphere of CO<sub>2</sub> at room temperature in THF-*d*<sub>8</sub>, resulting in the formation of different



Scheme 47). The <sup>1</sup>H DOSY NMR spectra indicated the presence of a mixture of compounds with different nuclearity in solution. These were assigned to the tetrameric and trimeric structures.



**Scheme 47.** The reaction of Mg hydride **A1** with CO<sub>2</sub> at room temperature.



In detail, the analysis of the resulting  $^1\text{H}$  and  $^{13}\text{C}\{^1\text{H}\}$  NMR spectra indicated a rapid reaction of **A1** with  $\text{CO}_2$ , as evidenced by the disappearance of the hydride signal of the Mg-H moieties within 10 minutes at room temperature and the appearance of mixtures of compounds with new formate resonances. Two different sets of signals were observed. The most prominent proton NMR signal of these formate groups appeared as a sharp doublet at  $\delta(^1\text{H}) = 8.13$  ppm ( $^1J_{\text{CH}} = 200$  Hz, coupling with carbon of  $^{13}\text{C}$ -labeled  $\text{CO}_2$ ), denoted as \* in Figure 19. This proton signal was correlated with the carbon peak at  $\delta(^{13}\text{C}) = 169.4$  ppm in the  $^1\text{H}$ - $^{13}\text{C}\{^1\text{H}\}$  HSQC NMR spectrum. In addition, other broadening signals presumably from different species, were observed near or underneath these sharp peaks (marked as # in Figure 19).

Moreover, another  $\text{CO}_2$  molecule was found to react at the central methine unit of the  $\beta$ -diketiminato ligand, leading to the formation of the newly formed C–C bonds (ii) (Scheme 47). This reactivity was characterized by the appearance of doublet signals in the  $^1\text{H}$  NMR spectrum, originating from the CH backbone of the ligand. These signals, coupled to the carbon atoms of the newly formed carboxylato groups ( $-\text{OCO}$ ) derived from  $^{13}\text{C}$ -labeled  $\text{CO}_2$ , were detected in the range of 4.69 to 4.85 ppm with a  $^2J_{\text{CH}}$  of about 8 Hz (\* in Figure 19). Adjacent to these sharp peaks, broader signals, assumed to be from other species, were also observed (marked as # in Figure 19).

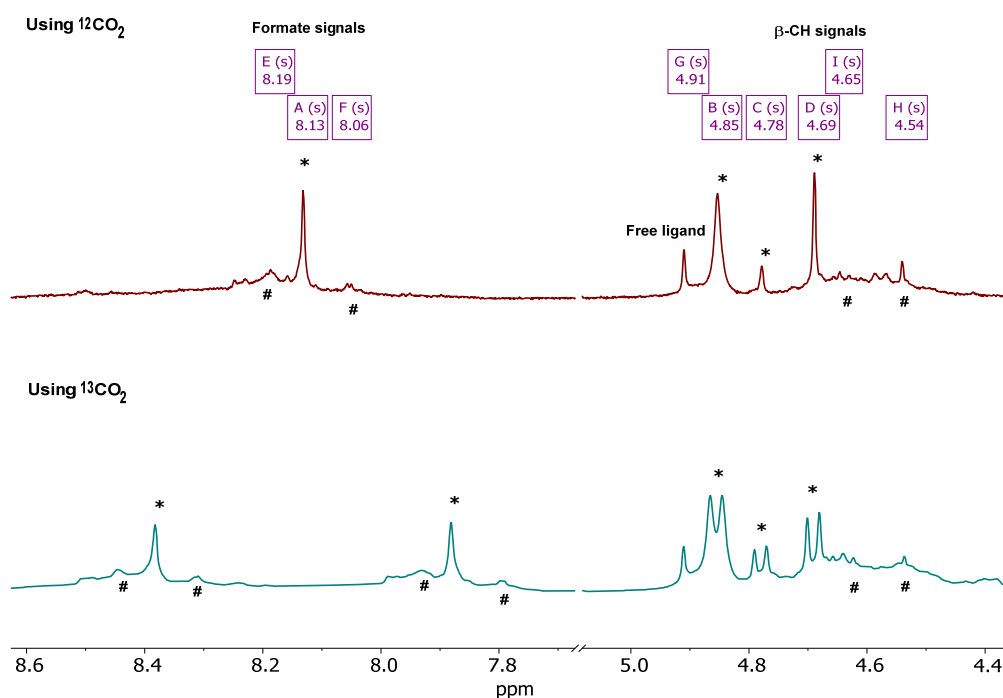


**Figure 19.** Mixture of compounds (**1**)<sub>3,4</sub> derived from  $^{13}\text{CO}_2$  and  $^{12}\text{CO}_2$ . Bottom: sections of the  $^1\text{H}$  NMR spectrum in the formate region and the central methine center of the ligand backbone derived from the reaction with  $^{12}\text{CO}_2$ . Top: compound mixture derived from  $^{13}\text{CO}_2$ . Signals with a \* label are assigned to the trimer and those with a # label are assigned to the tetramer.

Furthermore, the details of the composition and nuclearity of the species present in the solution mixture of (**1**)<sub>3,4</sub> were determined using diffusion-ordered NMR spectroscopy (DOSY) at 298 K. This DOSY analysis revealed two distinct diffusion coefficients ( $D$ ) and hydrodynamic radius ( $R_{\text{H}}$ ) for the system in  $\text{THF-}d_8$  (conc. 18 mM). These  $D$  values are  $3.6 \times 10^{-10} \text{ m}^2 \text{ s}^{-1}$  with a calculated  $R_{\text{H}}$  of 12.0 Å and  $D$  of  $4.2 \times 10^{-10} \text{ m}^2 \text{ s}^{-1}$  with a calculated  $R_{\text{H}} = 10.5$  Å along the self-diffusion dimension (Figure 20). The former diffusion constant, which is approximately twice the radius of the starting dimeric Mg (**A1**) ( $R_{\text{H}} = 6.8$  Å), suggests the presence of a tetrameric structure in the solution. On the other hand, the

latter diffusion coefficient, with a slightly smaller solution volume, indicates a more compact structure in solution, implying a trimeric character.

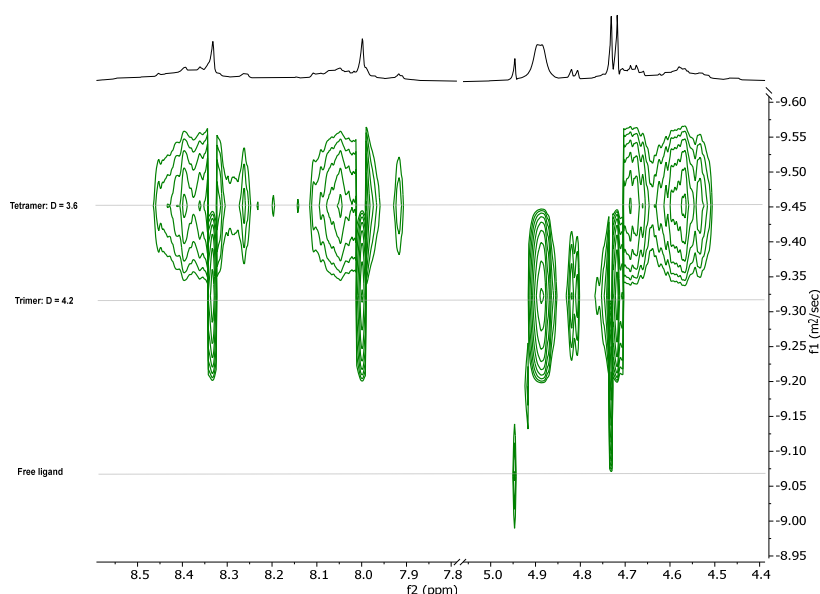
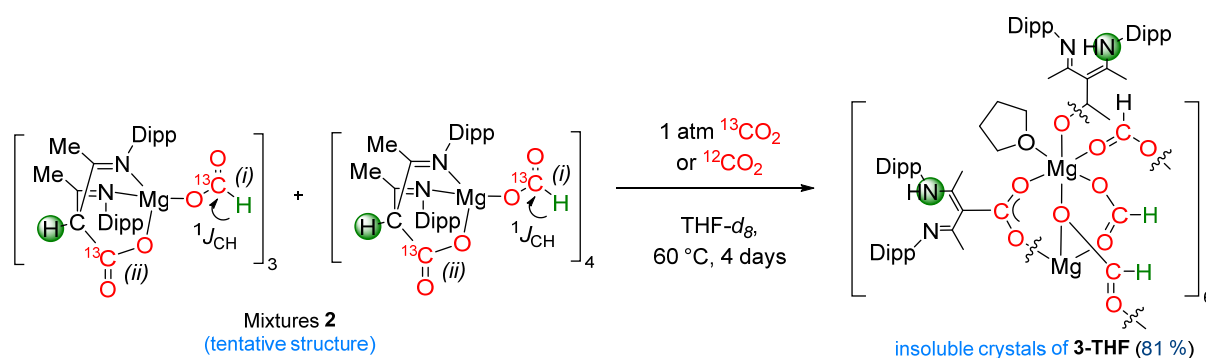


**Figure 20.**  $^1\text{H}$  DOSY NMR of the mixture  $(\mathbf{1})_{3,4}$  (600 MHz, 298 K,  $\text{THF-d}_8$ ). The horizontal scale shows the  $^1\text{H}$  chemical shifts (ppm), whereas the vertical dimension shows the diffusion scale ( $\times 10^{-10} \text{ m}^2\text{s}^{-1}$ ). The visualization of the spectrum was processed using the exponential processing method. The self-diffusion coefficients ( $D$ ) were obtained by fitting the peak areas at the formate signal (8.13 ppm) to the Stejskal-Tanner equation from the  $T1/T2$  analysis in TopSpin 4.1.4 software.

Subsequent heating of a mixture of compounds  $(\mathbf{1})_{3,4}$  (maintained under one atmosphere of  $\text{CO}_2$ ) at  $60^\circ\text{C}$  for 4 days resulted in the transformation of these compounds to the compound  $(\mathbf{2-THF})_6$  as a hexamer (as depicted in Scheme 48). This transformation involved the decoordination of the two nitrogen donors in the ligand of compounds  $(\mathbf{1})_{3,4}$  during the heating process. Simultaneously, the proton shifted from CH-backbone of the ligand, where the carbon atoms of the Nacnac ligands were modified through transannular bonding of  $\text{CO}_2$  (ii) in mixture  $(\mathbf{1})_{3,4}$ , to the nitrogen atom. This shift resulted in the generation of free amines ( $-\text{NH}$  moieties) within the Nacnac ligand. These processes facilitated the coordination of the carboxylate groups,  $[(\text{DippNacnac})-\text{OCO}]$ , to Mg metal centers. Ultimately, the reaction underwent hexamerization, resulting in the formation of  $(\mathbf{2-THF})_6$ .

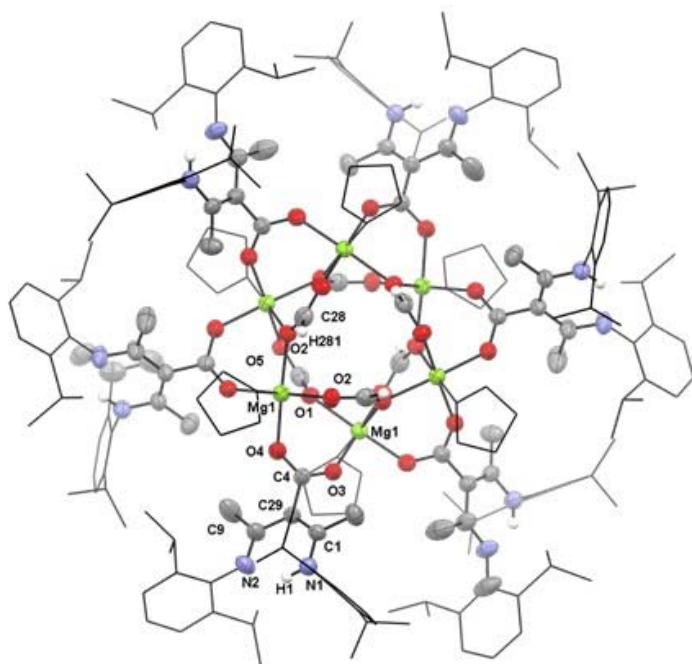


**Scheme 48.** The synthesis of compound  $(\mathbf{2-THF})_6$ .

Over the course of the 4-day reaction at 60 °C, block-shaped colorless crystals of compound (**2-THF**)<sub>6</sub> gradually grew and accumulated under one atmosphere of CO<sub>2</sub> in THF-d<sub>8</sub>. These crystals were obtained in a good yield (from 77% to 81%) and were analyzed by X-ray diffraction analysis.

The molecular structure of (**2-THF**)<sub>6</sub> is depicted in Figure 21 (a), while Figure 21 (b) represents its monomeric unit along with selected bond distances. Within its molecular structure, the hexamer has a crystallographic center of inversion, rendering the six hexagonal sides of the hexamer identical. Each Mg center adopts an octahedral geometry, with coordination by two carboxylate ligands and three formate groups, as well as an additionally coordinated THF molecule. The ligand derived from the  $\beta$ -diketiminato system exhibits a terminal  $\kappa^2O,O'$  carboxylato ligand, while those arising from the formate moieties ( $-OCHO$ ) bridge the two Mg centers *via* a symmetrical mode,  $\mu$ -formato- $\kappa O:\kappa O'$ . The first Mg center is bridged to the second Mg center by the Mg–O(1) bond distance of 2.067(5) Å, which is similar to the Mg–O(2) distance in the molecule. Interestingly, the oxygen atoms O(2) are also bridged toward the third Mg center, displaying a comparable distance of 2.095(5) Å to the other two in the molecule. Additionally, the decoordination of the two nitrogen donor ligands at the Mg center is also demonstrated. The C–N bonds within the ligand clearly consist of both single bonds and double bonds, with C(1)–N(1) and C(9)–N(2) bond distances of 1.335(8) and 1.293(9), respectively. This indicates the formation of a free bidentate Nacnac ligand with free NH moieties within the structure of complex (**2-THF**)<sub>6</sub>.

(a) Hexameric Mg formate (**2-THF**)<sub>6</sub>



(b) Monomeric unit of (**2-THF**)<sub>6</sub>

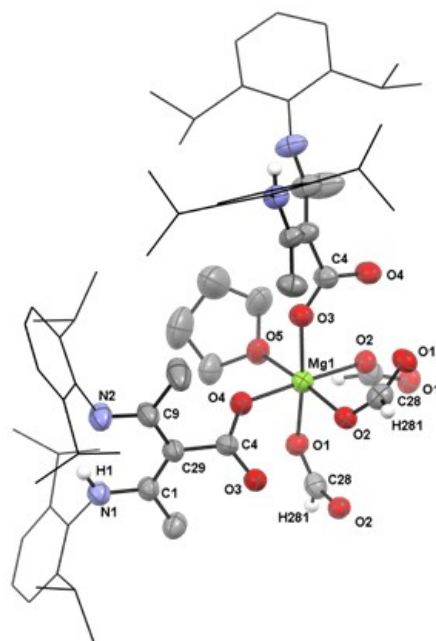
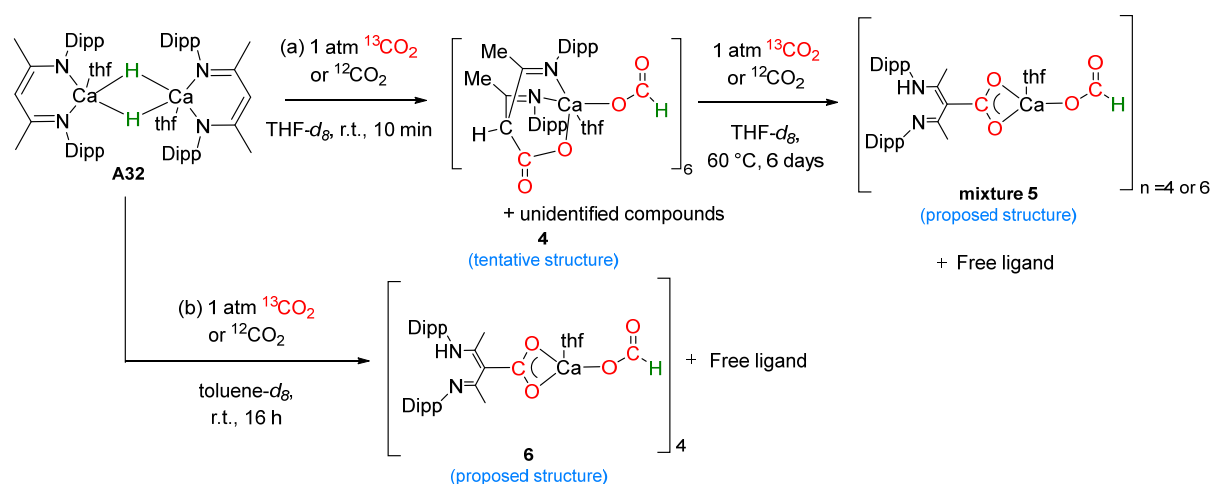


**Figure 21.** ORTEP representations of molecular structure of hexameric Mg-formate (b) and monomer unit (a) of (**2-THF**)<sub>6</sub> with selective atom labelling. Displacement ellipsoids are set at 30% probability; hydrogen atoms except H(1) and H(281) are omitted for clarity. The 2,6-*i*Pr<sub>2</sub>C<sub>6</sub>H<sub>3</sub> groups are shown as wireframes for simplicity. Selected bond distances (Å): Mg1–O(1), 2.087(5); Mg1–O(2), 2.103(6); Mg1–O(4), 2.005(5); Mg1–O(5), 2.160(6); O2–C(28), 1.262(8); O1–C(28), 1.231(8); O4–C(4), 1.242(8); O3–C(4), 1.270(8); N1–C(2), 1.442(8); N1–C(1), 1.336(8); N1–H(1), 0.863(19); N2–C(9), 1.293(9); C28–H(281), 0.983.

### Reactivity of $\beta$ -diketiminato Ca hydride with $\text{CO}_2$

Further studies involving the reactions of Ca hydride (**A2**) with  $\text{CO}_2$  (1 atm) showed a reactivity similar to that of Mg (**A1**), with the observed NMR spectra showing resonances corresponding to a different mixture of formate species with different nuclearity depending on the reaction conditions (as depicted in Scheme 49). Several attempts of crystallization under different conditions failed, often resulting in gel-like materials in concentrated solutions.



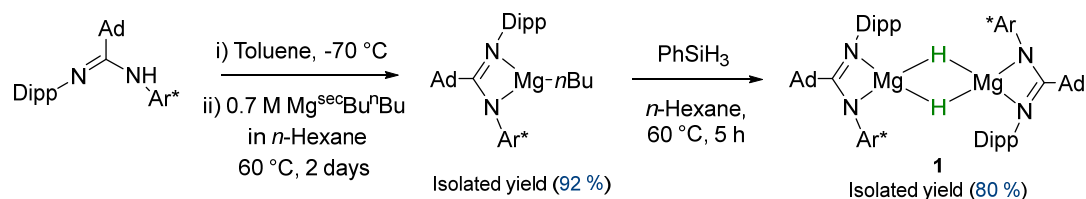
**Scheme 49.** The reaction of calcium hydride **A2** with  $\text{CO}_2$  in different reaction conditions and the proposed products.

### Synthesis and reactivity of amidinate Mg hydride (**6**)<sub>2</sub>

In contrast to  $\beta$ -diketiminato ligands, the two-coordinate amidinate ligand systems exhibit a distinct profile with larger coordination sites. These features could possibly modify the reactivity of the complex. Accordingly, the preparation of the amidinato Mg hydride complex (**6**)<sub>2</sub> was conducted. Through the hydrosilane metathesis reaction, Mg complex (**6**)<sub>2</sub> was obtained in 80% yield (Scheme 50). This Mg hydride was crystallographically characterized, and the molecular structure of (**6**)<sub>2</sub> is depicted in Figure 22.

In the molecular structure of (**6**)<sub>2</sub>, the complex forms a hydride-bridged dimer, with the metal centers  $N,N'$ -chelated by amidinate ligands. The coordination mode is similar to that of the closely related amidinato-Mg hydride complex with the  $\kappa^2$ - $N,N'$  coordination mode [6]. A comparison of the structures of (**6**)<sub>2</sub> and **A1** reveals that the  $N\text{--}Mg\text{--}N$  angles in (**6**)<sub>2</sub> are  $64.55(8)^\circ$  and  $63.34(8)^\circ$  for Mg(1) and Mg(2), respectively, which is smaller than the angle of the  $\beta$ -diketiminato Mg hydride **A1** of  $93.14(9)^\circ$  [7]. This observation suggests that the Mg center in (**6**)<sub>2</sub> is less shielded, and the accessibility of the substrates to the complex is more facilitated than in **A1**.

With the amidinate Mg hydride complex (**6**)<sub>2</sub> in hand, an investigation on its reactivity with  $\text{CO}_2$  was conducted. It was observed that Mg hydride (**6**)<sub>2</sub> cleanly reacted with 1 atm of  $\text{CO}_2$  at room temperature in  $\text{THF-d}_8$  to yield a single new species (**7**)<sub>2</sub> within 16 h (Scheme 51). Compound (**7**)<sub>2</sub> was isolated from concentrated THF at ambient temperature with a 72% yield. This observation was further confirmed through a single crystal X-ray diffraction analysis (Figure 23). Compound (**7**)<sub>2</sub> is a centrosymmetric amidinato magnesium formate dimer, where two Mg centers are bridged by formate units in a  $\mu_2$ -fashion, originating from the reduction of  $\text{CO}_2$  through hydride transfer.



**Scheme 50.** Synthetic procedure for the formation of magnesium compound (**6**)<sub>2</sub> via hydrosilane metathesis.

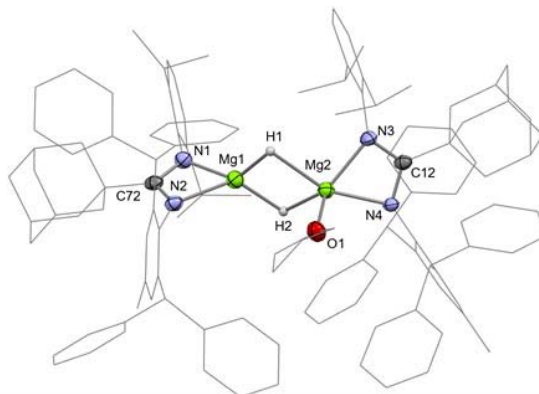
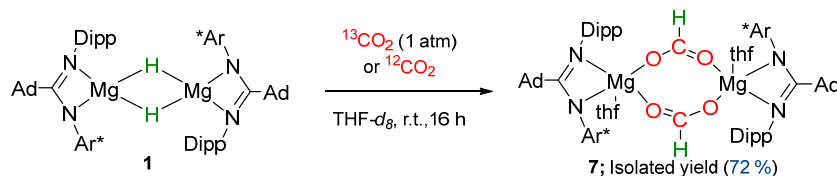


**Figure 22.** ORTEP representation of the molecular structure of (**6**)<sub>2</sub> with selective atom labeling. Displacement ellipsoids are set at 50% probability; hydrogen atoms except for the hydride protons H(1) and H(2) are omitted for clarity. The 2,6-*i*Pr<sub>2</sub>C<sub>6</sub>H<sub>3</sub> and 2,6-bis(diphenylmethyl)-4-methylphenyl moieties, adamantly and THF coordinated parts, have been set as wireframes for clarity reasons. Selected bond lengths (Å): Mg1–Mg2, 2.8533(12); Mg1–N(1), 2.046(2); Mg1–N(2), 2.087(2); Mg1–H(1), 1.8454(9); Mg1–H(2), 1.8842(8); Mg2–N(3), 2.049(2); Mg2–N(4), 2.142(2); Mg2–O(1), 2.0801(19); Mg2–H(1), 2.1816(8); Mg2–H(2), 1.9119(9). Selected bond angles (°): H(1)–Mg1–H(2), 91.38(4); H(1)–Mg2–H(2), 81.09(3); N(1)–Mg1–N(2), 64.55(8); N(3)–Mg2–N(4), 63.34(8).



**Scheme 51.** Reaction of magnesium hydride (**6**)<sub>2</sub> with CO<sub>2</sub> to give dimeric compound (**7**)<sub>2</sub>.

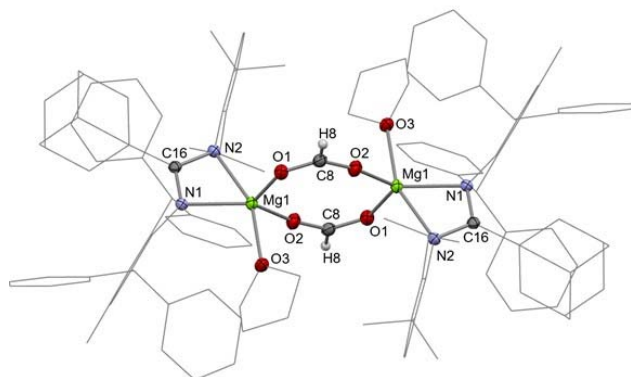
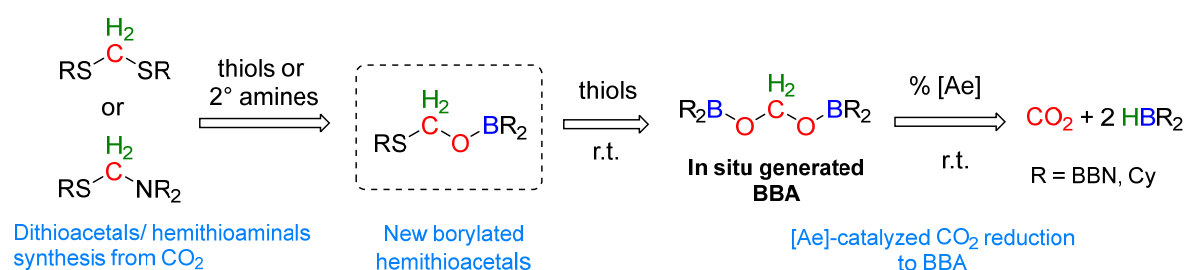


**Figure 23.** ORTEP representation of the molecular structure of (**7**)<sub>2</sub> with selective atomic labeling. Displacement ellipsoids are set at 50% probability; hydrogen atoms except for the formate protons are omitted for clarity. The 2,6-*i*Pr<sub>2</sub>C<sub>6</sub>H<sub>3</sub> and 2,6-bis(diphenylmethyl)-4-methylphenyl moieties, adamantly and THF-coordinated parts, have been set as wireframes for clarity. Selected bond lengths (Å): Mg1–N(1), 2.096(2); Mg1–N(2), 2.162(2); Mg1–O(1), 1.961(2); Mg1–O(2), 1.9404(19); Mg1–O(3), 2.1349(18); O1–C(8), 1.245(3); O2–C(8), 1.242(3). Selected bond angles (°): N(1)–Mg–N(2), 61.88(7); O(1)–Mg–O(2), 112.44(8); O(2)–Mg–N(2), 101.59(8); O(1)–Mg–N(2), 103.79(8); N(1)–Mg–O(3), 95.27(8); O(1)–Mg–O(3), 88.59(8); O(1)–Mg–N(1), 113.24(8). Symmetry operations: (i)  $-x+2, -y+1, -z+1$ .

### Hydroboration of CO<sub>2</sub> mediated by [Ae]-based catalysts and C-S bond formation [8].

In this following section, we have demonstrated the efficient activity of [Ae]-based hydride complexes in the selective hydroboration of CO<sub>2</sub> to produce a 4e<sup>-</sup> reduction of CO<sub>2</sub> yielding bis(boryl)acetal (BBA). In this process, two different hydroboranes, namely borabicyclo[3.3.1]nonane (9-BBN) and dicyclohexylborane (HBCy<sub>2</sub>), were employed as reducing agents. Subsequently, the *in situ* generated BBAs were used as a source of C<sub>1</sub> units to produce compounds containing C-S bonds. Interestingly, this approach allowed the synthesis of new borylated hemithioacetal compounds (R'S-CH<sub>2</sub>-OBR<sub>2</sub>) under mild and neutral reaction conditions. These hemithioacetals were then transformed into dithioacetals by the addition of a second thiol equivalent in the presence of acid H<sub>2</sub>SO<sub>4</sub> or to hemithioaminals through reactions with secondary amines (Scheme 52).

#### Our strategy



**Scheme 52.** Selective alkaline earth catalyzed 4e<sup>-</sup> Reduction of CO<sub>2</sub> to give BBA as an intermediate to generate compounds containing S-CH<sub>2</sub> bonds.

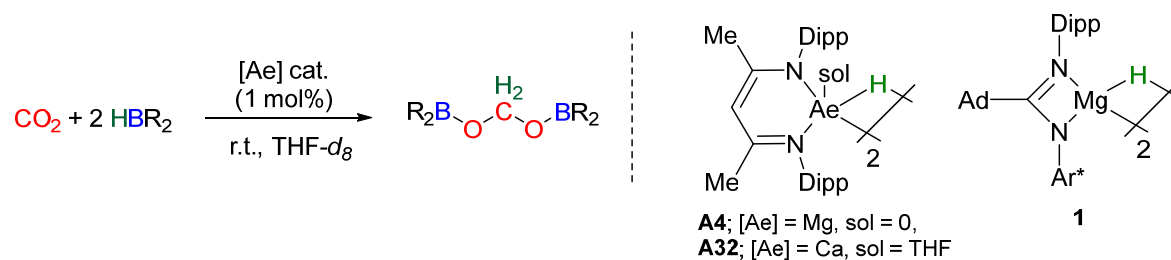
#### Catalytic hydroboration of CO<sub>2</sub>

Initially, the catalytic activity of Mg (**A1**) and Ca (**A2**) hydride complexes with 9-BBN was evaluated. In this regard, these experiments utilized 1 mol% catalytic loading of either complex Mg (**A1**) or Ca (**A2**) together with 0.13 mmol of 9-BBN in THF-*d*<sub>8</sub> in a pressurized NMR tube. For internal reference in the NMR conversion, hexamethylbenzene was introduced. After degassing the sample, it was exposed to isotopically <sup>13</sup>C-enriched CO<sub>2</sub> (1 atm), and the reaction was monitored by <sup>1</sup>H and <sup>13</sup>C{<sup>1</sup>H} NMR analyses at room temperature.

In terms of catalytic activity, the Mg (**A1**) and Ca (**A2**) complexes proved to be efficient catalysts with high selectivity in driving the 4e<sup>-</sup> reduction of CO<sub>2</sub> at room temperature. When used at 1 mol% catalytic loading, BBA<sup>BBN</sup> achieved remarkable *in situ* yields of 79% and 87% for Mg hydride (**A1**) and Ca hydride (**A2**), respectively, under 1 atm of CO<sub>2</sub> pressure (Table 6, entries 1 and 2). These reactions were completed within 7 h 25 min for Mg hydride (**A1**) and 1 h 40 min for Ca hydride (**A2**), resulting in TONs of 79 and 87 and TOFs of 11 and 52 h<sup>-1</sup> for Mg and Ca compounds, respectively. The speciation's kinetic plots were also constructed to illustrate the changes in product yield and 9-BBN conversion over time (in minutes) (Figure 24).

Furthermore, the catalytic reactivity of our newly developed amidinato-Mg hydride complex (**6**)<sub>2</sub> towards the reduction of CO<sub>2</sub> with 9-BBN was explored. An analogous CO<sub>2</sub> hydroboration with 9-BBN, using catalytic amounts of Mg complex (**6**)<sub>2</sub> (1 mol%) in THF-*d*<sub>8</sub>, was conducted. Surprisingly, the TOF decreased to 8 h<sup>-1</sup> (requiring 16 h for complete borane conversion), accompanied by the formation of a mixture consisting of BBA (76%) and methoxyborane (22%).

**Table 6.** Hydroborations of  $\text{CO}_2$  to  $\text{BBA}^{\text{BBN}}$  and  $\text{BBA}^{\text{Cy}}$  are catalyzed by  $\beta$ -diketiminate Mg (**A4**), Ca (**A32**), complexes, or amidine Mg (**6**)<sub>2</sub>.



HBR <sub>2</sub>	Catalyst	Time	Yield of BBA(%)	TON (TOF)/ h <sup>-1</sup>	Yield of R <sub>2</sub> BOCHO (%)	Yield of R <sub>2</sub> BOCH <sub>3</sub> (%)	Conversion of HBR <sub>2</sub> (%)
9-BBN	<b>A1</b>	7 h 25 min	79	79 (11)	3	12	94
	<b>A2</b>	1 h 40 min	87	87 (52)	2	5	95
	( <b>6</b> ) <sub>2</sub>	16 h	76	76 (8)	-	22	97
HBCy <sub>2</sub>	<b>A1</b>	18 min	95	95 (317)	-	-	95
	<b>A2</b>	19 min	90	90 (284)	9	-	98

<sup>[a]</sup> Reaction conditions: 1 atm  $\text{CO}_2$ , 0.13 mmol HBR<sub>2</sub>, 1 mol% catalyst, 650  $\mu\text{l}$  THF-*d*<sub>8</sub>, 25 °C. <sup>[b]</sup> Yields were calculated in situ using hexamethylbenzene as an internal standard. <sup>[c]</sup> The TON numbers were calculated from the BBA yields.

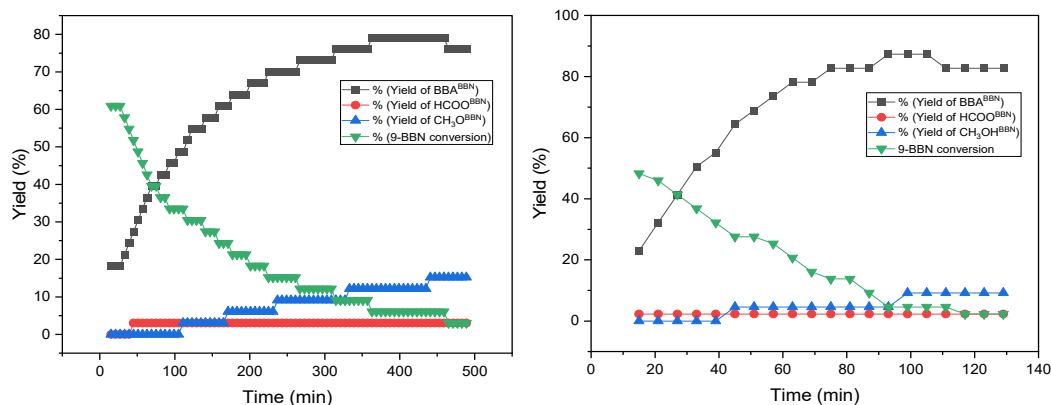


**Figure 24.** Plot of the evolution of reactant and products versus time in the hydroboration of  $\text{CO}_2$  with 9-BBN with 1 mol% of amidinato Mg hydride **A1** (left) and Ca hydride **A2** (right).

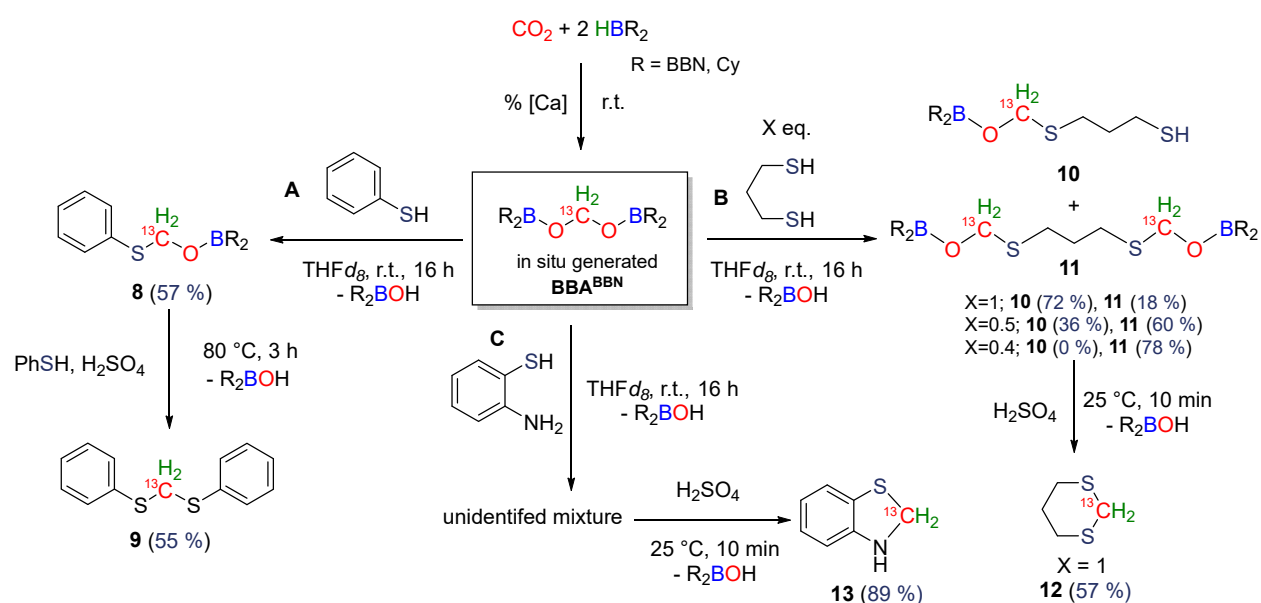
In addition, the catalytic reactions of  $\text{CO}_2$  (1 atm) with 1 mol% of catalyst Mg hydride (**A1**) or Ca hydride (**A2**) with HBCy<sub>2</sub> in THF-*d*<sub>8</sub> were performed. These reactions led to the selective generation of  $\text{BBA}^{\text{Cy}}$ , with yields of 95% and 90% within only 18 and 19 min, respectively, with the calculated TOF of 317 and 284 h<sup>-1</sup> measured for Mg hydride **A1** and Ca hydride **A2**, respectively (Table 6, entries 4-5). The observed TOF values are particularly high for  $\text{CO}_2$  hydroboration reactions catalyzed by [Ae]-based complexes and also for BBA synthesis from  $\text{CO}_2$ . Nevertheless, the use of the amidinate-Mg catalyst (**6**)<sub>2</sub> provided mixtures of  $\text{BBA}^{\text{Cy}}$  and methoxyborane, with only 56% of  $\text{BBA}^{\text{Cy}}$  conversion observed after 1 h 25 minutes.

Overall, among the [Ae]-based catalysts employed, Ca hydride (**A2**) demonstrated superior effectiveness and selectivity, resulting in high TOFs and BBA yields. Conversely, the Mg amidinate

catalyst exhibited lower efficiency and selectivity in CO<sub>2</sub> reduction with hydroboranes to BBA. The observed reactivity trend can be summarized as **A2**>**A1**>(6)<sub>2</sub>, which is consistent with the trend in hydricity of the metal center, suggesting that CO<sub>2</sub> insertion into the metal hydride bond is a rate-determining step. Nonetheless, the poor catalytic performance of the amidinato Mg complex **1** in comparison to β-diketiminato Mg and Ca complexes remains unclear. It is plausible that the amidinato Mg compound (6)<sub>2</sub> underwent deactivation during catalysis, and the actual active species responsible for catalyzing CO<sub>2</sub> hydroboration may differ from those initially present.

### C–S bond formation from BBA

After the successful preparation of BBA compounds by selective double CO<sub>2</sub> hydroboration, their reactivity with thiol compounds was investigated. Thereby, the Ca-based catalyst (**A2**) was selected to selectively generate the BBA compound. First, the reactivity of BBA<sup>BBN</sup> was investigated. In this study, <sup>13</sup>C-labeled CO<sub>2</sub> was employed for the *in-situ* generation of BBA<sup>BBN</sup>, which allows us to closely monitor the fate of the carbon atom arising from CO<sub>2</sub>, particularly the methylene moiety (<sup>13</sup>CH<sub>2</sub>).



**Scheme 53.** Reactivity of BBA<sup>BBN</sup> toward thiophenol, 1,3-propanedithiol, and 2-aminothiophenol.

As a result, the combination of the *in situ* generated <sup>13</sup>C-BBA<sup>BBN</sup> with one equivalent of thiophenol (pathway **A**) resulted in the formation of a novel borylated hemithioacetal, identified as compound **8**, with a 57% NMR yield at room temperature within 16 hours (Scheme 53). During the reaction, the formation of adduct **8** was clearly evident in the NMR spectra, as indicated by the disappearance of the methylene signal of <sup>13</sup>C-BBA<sup>BBN</sup> at δ(<sup>1</sup>H) 5.54 (d, <sup>1</sup>J<sub>CH</sub> = 165.1 Hz) and δ(<sup>13</sup>C{<sup>1</sup>H}) 87.0 ppm in THF-*d*<sub>8</sub>. Simultaneously, a new methylene signal corresponding to compound **8** appeared at δ(<sup>1</sup>H) 5.38 (d, <sup>1</sup>J<sub>CH</sub> = 159.5 Hz) and δ(<sup>13</sup>C{<sup>1</sup>H}) 70.6 ppm.

In addition, when two equivalents of thiophenol were introduced under similar reaction conditions, the expected compound **9** was not formed, even at elevated temperatures. Instead, the characteristic methylene resonance of intermediate **8** was detected in the NMR spectra. However, when sulfuric acid (H<sub>2</sub>SO<sub>4</sub>) was added to the reaction solution, it resulted in the formation of the preliminary protonated **8** species at room temperature. In the process, the OBR<sub>2</sub> fragment within **8**

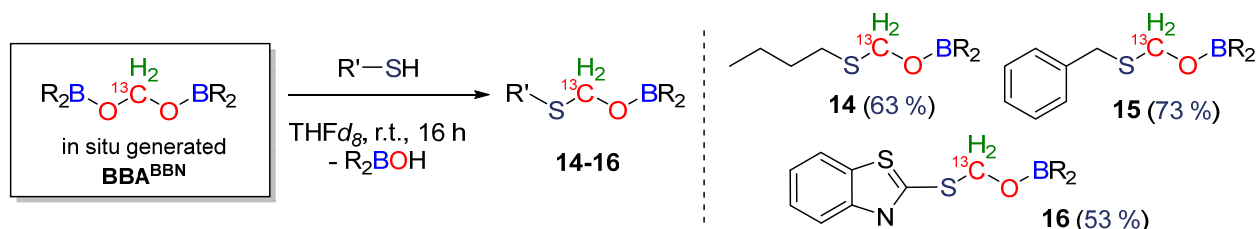


was protonated, facilitating the interaction with the added second equivalent of thiophenol. As a result, compound **9** was generated within 3 h at 80 °C with a yield of 55% on BBA basis (Scheme 53).

In addition to thiophenol, an acyclic dithiol was utilized to react with the BBA<sup>BBN</sup> compound, resulting in the formation of hemithioacetals under neutral conditions at room temperature (pathway **B**, Scheme 53). When one equivalent of 1,3-propanedithiol was used, a mixture of hemiacetal compounds was generated. A major species, identified as hemithioacetal compound **10**, was observed, yielding 72% *in situ* based on BBA. Its signals in the <sup>1</sup>H NMR and <sup>13</sup>C{<sup>1</sup>H} NMR spectra were assigned at 5.07 ppm and 68.7 ppm, respectively. Another species, identified as a minor product, was the diborylated hemithioacetal **11**, with a very similar NMR signature to that of adduct **10**, obtained with an 18% NMR yield. Notably, the introduction of sulfuric acid into the solution containing compounds **10** and **11** led to the rapid formation of dithiane **12** with a yield of 57% within 10 minutes. On the contrary, the addition of 0.4 equivalents of 1,3-propanedithiol to BBA<sup>BBN</sup> favored the formation of compound **11** with an increase of the NMR yield to 78% (Scheme 53).

In addition, the reaction of the *in situ* generated BBA<sup>BBN</sup> with 2-aminothiophenol led to the formation of an unidentified mixture at room temperature, which completely converted the BBA substrate (pathway **C**, Scheme 53). Under acidic conditions, the generation of the 2,3-dihydrobenzothiazole compound **13** was detected, which was obtained in 89% yield based on the BBA reactant (Scheme 53).

To broaden the range of thiol compounds and to explore the reactivity of BBA<sup>BBN</sup> with various thiols, experiments were conducted with 1-butanethiol, benzylmercaptan, and 2-mercaptobenzothiazole reacting with BBA<sup>BBN</sup> (Scheme 54). These reactions proceeded smoothly at room temperature, yielding hemithioacetal compounds (**14-16**) with favorable NMR yields of 63%, 73%, and 53%, respectively, within 16 hours. Analysis of the <sup>1</sup>H NMR spectra of compounds **8** and **14-16** revealed variations in the methylene moieties at  $\delta(\text{CH}_2)$  5.38, 5.06, 4.94, and 6.32 ppm, respectively. These signals fell within a narrow range ( $67.1 < \delta(\text{CH}_2) < 70.9$ ) in the <sup>13</sup>C{<sup>1</sup>H} spectra.



**Scheme 54.** Reactivity of BBA<sup>BBN</sup> toward various thiol reactants. Yield based on the quantity BBA<sup>BBN</sup>.

In addition to BBA<sup>BBN</sup>, the interaction of BBA<sup>CV</sup> with thiol was also investigated. The reaction between 0.5 equivalents of 1,3-dipropandithiol and *in situ* generated BBA<sup>CV</sup> resulted in the formation of the di-borylated compound **11**, albeit with a slightly lower yield of 60% based on BBA compared to the BBA<sup>BBN</sup> substrate under the same conditions. Interestingly, in this reaction unidentified by-products were detected in addition to the desired compound.

Previously, it was emphasized that the intermediates proposed in the mechanism involving the condensation reaction of BBA with E-H functionality have never been experimentally characterized or isolated. In our case, the hemithioacetal (R'S-CH<sub>2</sub>-OBR<sub>2</sub>) was identified as an intermediate like those reported in the existing literature (see Figure 25). Consequently, the identification of this hemithioacetal intermediate suggests a sequential mechanism, which led us to study the reactions of

hemithioacetal **8** with different nucleophilic reagents to gain insight into the possible mechanism (see Scheme 55).

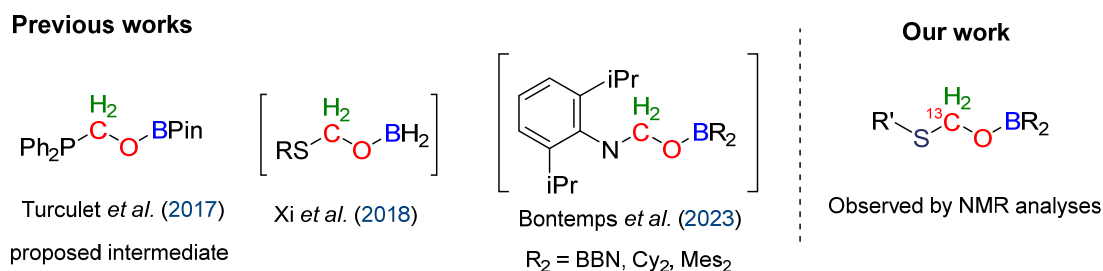
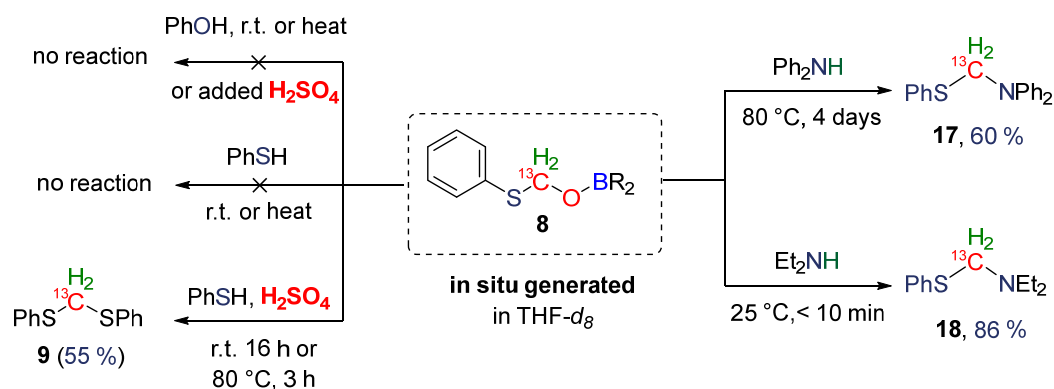


**Figure 25.** Proposed O-borylated hemiacetal intermediates.



**Scheme 55.** Reaction of compound **8** toward phenol, thiophenol and amine.

Accordingly, when hemithioacetal **8** was subjected to a reaction with phenol, the expected products were not formed (Scheme 55). Previously, similar results were observed with an excess of thiophenol (2 equivalents), where the reaction proceeded with only one equivalent of thiol substrate, producing hemithioacetal even at higher temperatures (Scheme 53). However, in the presence of sulfuric acid, hemithioacetal **8** reacted with a second equivalent of thiophenol to give dithioacetal **9**. Consequently, these reactants did not appear to be nucleophilic enough to undergo successive nucleophilic attacks on the electrophilic carbon of hemithioacetal **8**, preventing the release of the O-boryl moiety.

Using strong nucleophilic agents such as diphenylamine and diethylamine, we successfully synthesized hemithioaminals **17-18** through the reaction of hemithioacetal **8** under neutral conditions (Scheme 55). It is noteworthy that this reaction did not proceed at room temperature, even with an extended reaction time of up to 3 days. Interestingly, the reaction of compound **8** with linear diethylamine produced the related hemithioaminal compound **18** in 86% yield in less than 10 minutes at room temperature. Therefore, this observation emphasizes the importance of the nucleophilicity of the reactant.

### Tandem hydrosilylation of CO<sub>2</sub> mediated by [Ae]-based hydride complexes.

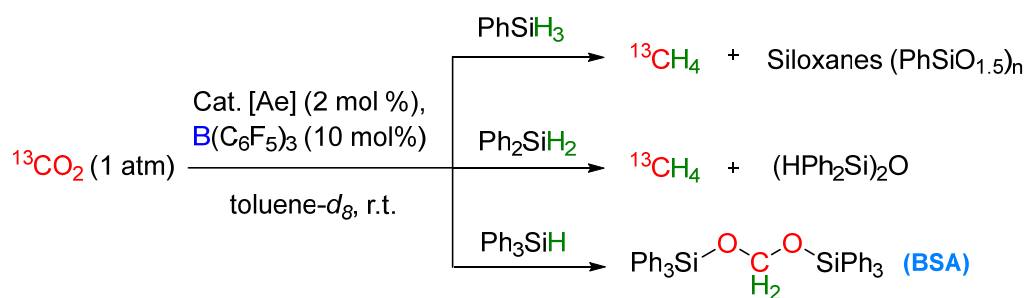
In this section, we present the tandem hydrosilylation of CO<sub>2</sub> by various hydrosilanes using [Ae]-based hydride catalysts in combination with Lewis-acid B(C<sub>6</sub>F<sub>5</sub>)<sub>3</sub> as a co-catalyst, which allowed us to extend previous studies on the first and only example of Mg-catalyzed hydrosilylation of CO<sub>2</sub>

reported by Parkin *et al.* in 2017 and 2019 [9,10]. In our study, we have notably provided the first example of [Ca]-catalyzed CO<sub>2</sub> hydrosilylation by hydrosilanes.

The reactivity and selectivity of Ae-H containing compounds for the hydrosilylation of CO<sub>2</sub> reduction processes are unique for each catalytic system and depend on the steric bulk surrounding the Si-H bonds [11]. Therefore, the use of different hydrosilanes, including mono-, di-, and tri-phenylsilanes (PhSiH<sub>3</sub>, Ph<sub>2</sub>SiH<sub>2</sub>, and Ph<sub>3</sub>SiH) has been investigated. The neutral hydride compounds of β-diketiminato [(<sup>Dipp</sup>Nacnac)Mg(μ-H)<sub>2</sub>] (**A1**), its Ca analog (**A2**), or amidinate-Mg hydride (**6**)<sub>2</sub> were employed as the precatalysts in combination with B(C<sub>6</sub>F<sub>5</sub>)<sub>3</sub> for CO<sub>2</sub> reduction with hydrosilanes. As a result, the reduction of CO<sub>2</sub> with PhSiH<sub>3</sub> and Ph<sub>2</sub>SiH<sub>2</sub> in the presence of excess B(C<sub>6</sub>F<sub>5</sub>)<sub>3</sub> were found to be effective in reducing CO<sub>2</sub> to the CH<sub>4</sub> level and Ph<sub>3</sub>SiH to the bis(silyl)acetal, BSA, level. The [Ae]/B(C<sub>6</sub>F<sub>5</sub>)<sub>3</sub> catalyst systems are sensitive to steric hindrance around the silane substrate that effect the rate of the reaction, for example, Ph<sub>2</sub>SiH<sub>2</sub> reacts slower than PhSiH<sub>3</sub> (

Table 7, entries 1-6), while the bulkier Ph<sub>3</sub>SiH requires a prolonged reaction time to yield BSA ( Table 7, Entries 7-9) [12].

**Table 7:** CO<sub>2</sub> hydrosilylation by [Ae]-based catalysts with different hydrosilanes.



Hydrosilanes	catalysts	t (h)	Si product (NMR% yield) <sup>c</sup>	TON <sup>d</sup> (TOF/h <sup>-1</sup> )
PhSiH <sub>3</sub>	<b>A1</b>	20 min	CH <sub>4</sub> (58) (PhSiO <sub>1.5</sub> ) <sub>n</sub> (25%)	117(353.9)
	<b>A2</b>	7 h	CH <sub>4</sub> (20) (PhSiO <sub>1.5</sub> ) <sub>n</sub> (23%)	131(18.7)
	( <b>6</b> ) <sub>2</sub>	2 h 40 min	CH <sub>4</sub> (26) (PhSiO <sub>1.5</sub> ) <sub>n</sub> (25%)	144(53.9)
Ph <sub>2</sub> SiH <sub>2</sub>	<b>A1</b>	4 h	CH <sub>4</sub> (13) (HPh <sub>2</sub> Si) <sub>2</sub> O (44%)	121(24.1)
	<b>A2</b>	1 h 45 min	CH <sub>4</sub> (28) (HPh <sub>2</sub> Si) <sub>2</sub> O (41%)	115(72.9)
	( <b>6</b> ) <sub>2</sub>	5 h 40 min	CH <sub>4</sub> (12) (HPh <sub>2</sub> Si) <sub>2</sub> O (44%)	105(18.6)
Ph <sub>3</sub> SiH	<b>A1</b>	74 h	BSA (97%)	46(0.6)
	<b>A2</b>	30 h	BSA (98%)	49(1.5)
	( <b>6</b> ) <sub>2</sub>	220 h	BSA (97%)	50(0.3)

<sup>a</sup>Reaction conditions: toluene-*d*<sub>8</sub> (0.1 ml, 298 K), [Si-H]<sub>0</sub> = 0.14 mmol, [cat]<sub>0</sub> = 0.0028 mmol (2 mol% per Si-H bond), [B(C<sub>6</sub>F<sub>5</sub>)<sub>3</sub>] = 0.014 mmol (10 mol% per Si-H), [M]/[B] = 1/5 ratio, n(CO<sub>2</sub>)<sub>0</sub> = 1.3 × 10<sup>-4</sup> mol (1 atm, 298 K), internal standard (mesitylene): 0.14 mmol. <sup>b</sup>The conversion of hydrosilane is determined by the integration of the <sup>1</sup>H NMR resonances vs. those of the standard, mesitylene. <sup>c</sup>Yield of the Si product is determined by the integration of the corresponding <sup>1</sup>H NMR peak vs. those of the standard, mesitylene. <sup>d</sup>TON Number is calculated on the basis of Si-H bonds consumed per mmol of catalyst. TOF is calculated as TON h<sup>-1</sup>. CH<sub>4</sub> yield is calculated as [mmol of reacted silane/4/(mmol of silane)] × 100. Si by product calculated in relation to the CH<sub>4</sub>.

In addition, the nature of the [Ae] catalysts play a significant role in dictating the overall rate of the reaction as measured in terms of the TOF values. Among them, the combination of [Mg-**A1**]/B(C<sub>6</sub>F<sub>5</sub>)<sub>3</sub> showed the best performance within the series by using PhSiH<sub>3</sub> as a reducing agent, providing a fast kinetic rate. On the other hand, in Ph<sub>2</sub>SiH<sub>2</sub> and Ph<sub>3</sub>SiH systems, the [Ca-**A2**]/B(C<sub>6</sub>F<sub>5</sub>)<sub>3</sub> catalyst exhibits high activity towards the reduction of CO<sub>2</sub> to the CH<sub>4</sub> and BSA, respectively.

The kinetics of each catalytic reaction have been studied. The differences in the overall reaction order were observed in varied [Ae]/B(C<sub>6</sub>F<sub>5</sub>)<sub>3</sub> catalyst systems, indicating different mechanisms and rate determining steps. Specifically, the zeroth-order reaction may involve a sophisticated reaction mechanism in which each reduction step may be catalyzed by a different active species. For instance, the [Ca]-catalyzed hydrosilylation of CO<sub>2</sub>, which has the zeroth-reaction order, was postulated to proceed through a hypervalent six-coordinate silicon intermediate, where the Ca catalyst (**A2**) does not react with CO<sub>2</sub> but with PhSiH<sub>3</sub> to give hypervalent species in the first step, instead of a common FLP-type hydrosilylation mechanism.

Further studies on Eyring and Arrhenius analyses provided an activation parameter for the reduction of CO<sub>2</sub> by Ph<sub>3</sub>SiH using the [Ca]/B(C<sub>6</sub>F<sub>5</sub>)<sub>3</sub> catalyst. The reactions were carried out at four temperatures between 298 K and 353 K under the standard condition of 2 mol% of Ca hydride (**A2**) catalyst with 10 mol% of B(C<sub>6</sub>F<sub>5</sub>)<sub>3</sub>. The resulting silane conversion vs. time at different temperatures is depicted in Figure 26. Extraction of the observed rate constants forms plots of [Ph<sub>3</sub>SiH] or [BSA] vs. time, which allows the construction of the Arrhenius and Eyring plots.

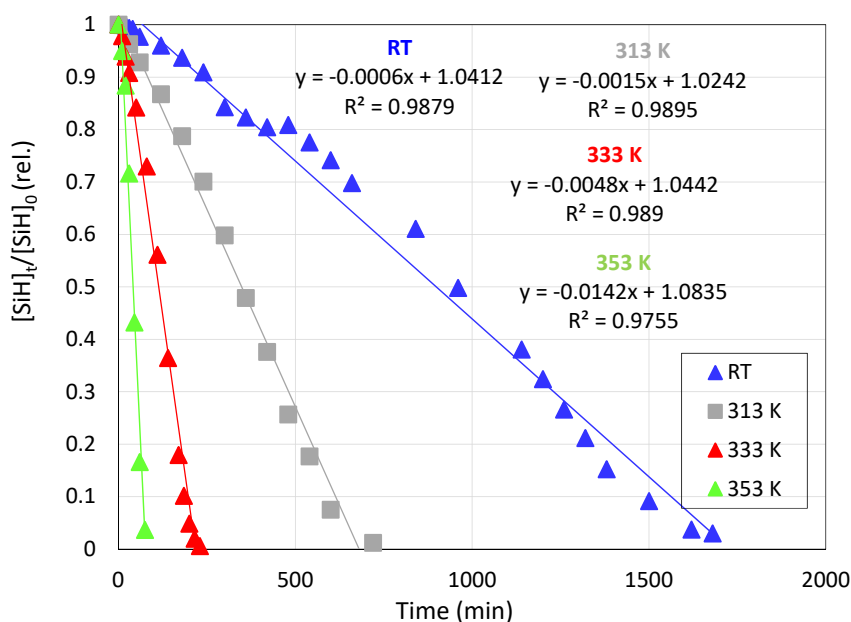


**Figure 26.** Plot of  $[Ph_3SiH]_t/[Ph_3SiH]_{t=0}$  vs. time for variable temperatures using 2 mol% of **A2** and 10 mol% [**B**] as a catalyst, toluene-*d*<sub>8</sub>, and 1 atm of <sup>13</sup>CO<sub>2</sub> pressure.

The activation energy value ( $E_a$ ) could be obtained from the slope of the best-fit line from the data plot of  $\ln(k_{obs})$  vs.  $1/T$ . The activation energy of the process was found to be 50.63 kJ mol<sup>-1</sup>. The enthalpy of activation ( $\Delta H^\ddagger$ ) can then be obtained from the slope of the linear regression from the data plot of  $\ln(k_{obs}/T)$  vs.  $1/T$ , which was found to be 44.21 kJ mol<sup>-1</sup> (Figure 27). The entropy of activation ( $\Delta S^\ddagger$ ) can be obtained from the intercept of the y-axis, giving a value for  $\Delta S^\ddagger$  of -169 J mol<sup>-1</sup>K<sup>-1</sup>. The corresponding Gibbs free energies ( $\Delta G^\ddagger$ ) at 298 K were found to be 94.6 kJ mol<sup>-1</sup> [13,14].

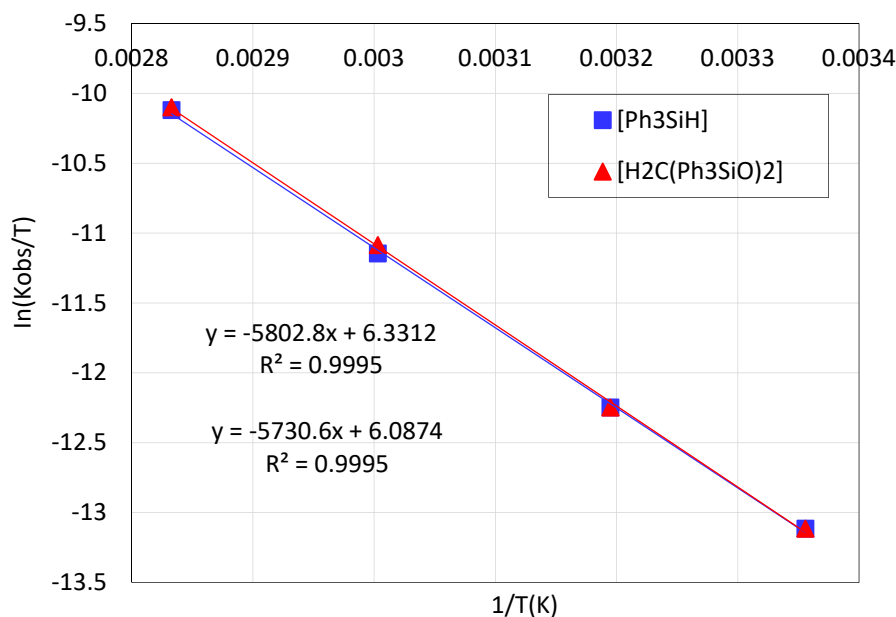


**Figure 27:** Eyring plot to determine the activation parameters for  $[Ca]/[B(C_6F_5)_3]$  catalyst in  $CO_2$  reduction by  $Ph_3SiH$ .

Comparing the  $\Delta H^\ddagger$  and  $\Delta S^\ddagger$  values for  $CO_2$  reduction by  $Ph_3SiH$  using  $[Ca]/[B(C_6F_5)_3]$  catalyst, the reaction appears to be governed by entropic rather than enthalpic contributions, resulting in a significantly negative activation entropy of ca.  $-170 \text{ J K}^{-1} \text{ mol}^{-1}$ . This is indicative of the associative formation of activated complexes through the assembly of two or more reaction components and must be accounted for in any mechanistic rationale. In other words, it suggests the assembly of a highly organized rate-determining transition state.

Collectively, by considering the observed data, the [Ae] metal plays a significant role in enabling a nucleophilic attack upon  $CO_2$  in the first step of the reaction, whereas  $B(C_6F_5)_3$  activates the silane to mediate the subsequent steps of catalytic turnover. The nature of the [Ae]-based hydride catalysts is important for the overall rate and order of the reaction.

## Conclusion

In conclusion, we have shown that the reactivity of Mg and Ca hydride complexes supported by  $\beta$ -diketiminato and amidinate ligands for  $CO_2$  reduction allows the investigation of the precedented [Ae]-catalyzed  $CO_2$  hydroboration to yield selective BBA and subsequent C–S bond formation. Furthermore, it has been demonstrated that these [Ae]-based complexes, in combination with  $B(C_6F_5)_3$  efficiently reduce  $CO_2$  with hydrosilanes to various silylated compounds, depending on the silane used. In our perspective, further mechanistic possibilities and kinetic differences of these Mg and Ca-based catalytic systems will be explored. Additionally, the scope of this research could be extended to investigate the reactivity of group 2 metal hydride complexes with CO *via* CO homologation.

## References

- [1] (a) M. Aresta, A. Dibenedetto, *Dalton Trans.* **2007**, 2975–2992. DOI: [10.1039/b700658f](https://doi.org/10.1039/b700658f); (b) M. Aresta, A. Dibenedetto, A. Angelini, *Chem. Rev.* **2014**, *114*, 1709–1742. DOI: [10.1021/cr4002758](https://doi.org/10.1021/cr4002758).

- [2] S. Harder, *Early Main Group Metal Catalysis Concepts and Reactions*, Wiley-VCH Verlag GmbH & Co. KGaA, Boschstr. 12, 69469, Weinheim, Germany, **2020**. DOI: [10.1002/9783527818020](https://doi.org/10.1002/9783527818020).
- [3] A. G. Avent, M. R. Crimmin, M. S. Hill, P. B. Hitchcock, *Dalton Trans.* **2005**, 278–284. DOI: [10.1039/b415468a](https://doi.org/10.1039/b415468a).
- [4] S. P. Green, C. Jones, A. Stasch, *Angew. Chem. Int. Ed.* **2008**, *47*, 9079–9083. DOI: [10.1002/anie.200803960](https://doi.org/10.1002/anie.200803960).
- [5] M. H. Chisholm, J. C. Gallucci, K. Phomphrai, *Inorg. Chem.* **2004**, *43*, 6717–6725. DOI: [10.1021/ic0490730](https://doi.org/10.1021/ic0490730).
- [6] C. N. de Bruin-Dickason, T. Sutcliffe, C. Alvarez Lamsfus, G. B. Deacon, L. Maron, C. Jones, *Chem. Commun.* **2018**, *54*, 786–789. DOI: [10.1039/C7CC09362D](https://doi.org/10.1039/C7CC09362D).
- [7] S. P. Green, C. Jones, A. Stasch, *Angew. Chem. Int. Ed.* **2008**, *47*, 9079–9083. DOI: [10.1002/anie.200803960](https://doi.org/10.1002/anie.200803960).
- [8] W. Huadsai, M. Westerhausen, S. Bontemps: “Alkaline Earth Catalyzed CO<sub>2</sub> Hydroboration into Acetal Derivatives Leading to C–S Bond Formation”, *Organometallics* **2023** *42*, 2921–2926, DOI: [10.1021/acs.organomet.3c00335](https://doi.org/10.1021/acs.organomet.3c00335).
- [9] M. Rauch, G. Parkin, *J. Am. Chem. Soc.* **2017**, *139*, 18162–18165. DOI: [10.1021/jacs.7b10776](https://doi.org/10.1021/jacs.7b10776).
- [10] M. Rauch, Z. Strater, G. Parkin, *J. Am. Chem. Soc.* **2019**, *141*, 17754–17762. DOI: [10.1021/jacs.9b08342](https://doi.org/10.1021/jacs.9b08342).
- [11] (a) F. J. Fernández-Alvarez, L. A. Oro, *ChemCatChem* **2018**, *10*, 4783–4796. DOI: [10.1002/cctc.201800699](https://doi.org/10.1002/cctc.201800699); (b) J. Chen, M. McGraw, E. Y. X. Chen, *ChemSusChem* **2019**, *12*, 4543–4569. DOI: [10.1002/cssc.201901764](https://doi.org/10.1002/cssc.201901764).
- [12] T. Matsuo, H. Kawaguchi, *J. Am. Chem. Soc.* **2006**, *128*, 12362–12363. DOI: [10.1021/ja0647250](https://doi.org/10.1021/ja0647250).
- [13] W. Huang, T. Roisnel, V. Dorcet, C. Orione, E. Kirillov, *Organometallics* **2020**, *39*, 698–710. DOI: [10.1021/acs.organomet.9b00853](https://doi.org/10.1021/acs.organomet.9b00853).
- [14] M. North, M. Omedes-Pujol, *Beilstein J. Org. Chem.* **2010**, *6*, 1043–1055. DOI: [10.3762/bjoc.6.119](https://doi.org/10.3762/bjoc.6.119).



**Anastasiia SHERSTIUK**

**ESR7**

**Thesis co-directors**

Prof. Evamarie Hey-Hawkins      Universität Leipzig, Leipzig, Germany

Prof. Rosa Maria Sebastián      Universitat Autònoma de Barcelona, Bellaterra, Spain

**Thesis defense**

Faculty of Chemistry and Mineralogy, University of Leipzig, 9 February 2024





## Photoswitchable phosphines for light-modulated metal catalysts

### Introduction and Objectives

The last century has witnessed enormous progress in the field of homogeneous catalysis, which has led to the development of a large variety of catalytic systems to enhance the reactivity and selectivity of chemical reactions. Switchable catalysis is a new emerging topic in this area that paves the way to reach even higher levels of control of catalytic reactions. Inspired by nature, where enzymatic processes in cells involve sophisticated feedback loops and trigger-induced effects for spatial and temporal control [1], switchable catalysis aims to provide a bio-like level of control over chemical transformations through the response to tunable external stimuli, such as light, pH, metal coordination, redox switching or mechanical forces [2-4].

Among all these external stimuli to accomplish switchable catalysis, light stands out because of a series of advantageous properties: it is non-invasive, cheap, ubiquitous, environmentally friendly, easily tunable in terms of wavelength, power and polarization, and even more importantly, provides precise temporal and spatial control – i.e., light doses can be administered locally (using lenses) and for very short lapses of time (using pulsed illumination sources) with high degree of precision. Photoswitchable catalysis (Figure 1) enables the reversible control of a catalytic system between distinct states through light irradiation. This approach is valuable for applications requiring high spatial or temporal precision in chemical reactions, such as bioconjugation or polymer synthesis. To ensure the modulation in catalytic properties photoswitchable moieties undergoing light-induced isomerization are introduced into the catalyst structure. Within homogeneous catalysis, transition metal complexes hold a unique position due to their versatility and extensive capacity to facilitate various chemical transformations. Consequently, the prospect of further developing them into photoswitchable systems is advantageous, resulting in a reversible modulation of catalytic activity and precise control over chemical reactions. The modulation of catalytic activity in metal catalysts is possible through alterations in geometrical and/or electronic effects of the catalytic center.

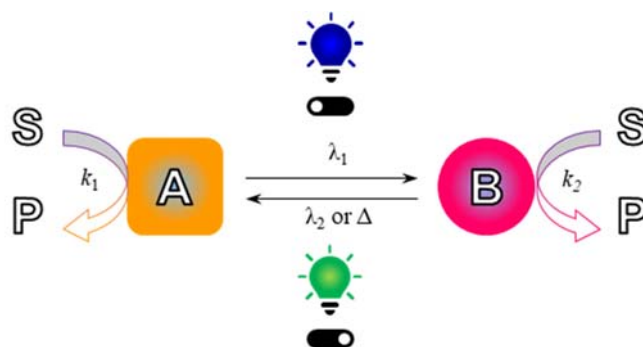


**Figure 1.** The general concept of photoswitchable catalysis, where a catalyst presents two different states with distinct catalytic properties (A and B) that can be mutually interconverted through light absorption.

The success of the molecular design of a photoswitchable metal catalyst depends on two main structural features: the photoisomerizable scaffold and the binding group chosen to complex the metal. The choice of the former is essentially determined by the change in the metal properties required to accomplish catalysis modulation – i.e., whether it will be achieved by altering the electron density on the metal center or the geometry around it. In many instances, both of these parameters are important, and the final preference should be based on taking into account all the electronic and

steric factors that can affect the catalytic properties of the metal center. As for the selection of the binding group, it is mainly dependent on the nature of the metal that would be active in the catalysis. Existing examples include not only NHCs and crown ethers but also pyridine [5,6], salen [7], oxazoline [8,9], cyano [10] and phosphine [11] groups.

Phosphines play a crucial role in the advancement of modern catalysis due to their particular electronic and steric properties, which makes them very versatile ligands for metal complexation (Figure 2a) [12]. Thus, phosphines are known for their capacity to bind a variety of metals in both high and low oxidation states thanks to their adjustable electronic features [13]. When acting as  $\sigma$ -donors, they bind metals through electronic density donation from the lone pair of electrons of their phosphorous atom to the empty orbitals of the metal. At the same time, these ligands can act as  $\pi$ -acceptors, receiving electron density from filled metal d orbitals into phosphorous antibonding  $\sigma^*$  orbitals [14]. The contribution of these two types of electronic interactions and, therefore, the nature of the metal-phosphine bond is influenced by the substituents incorporated at the phosphorus atom [15]. Phosphines containing electron-withdrawing groups exhibit reduced electron density on phosphorus, resulting in a diminished  $\sigma$ -donor capacity; this effect is accompanied by the lowering of phosphorous  $\sigma^*$  orbital energy, thus increasing their tendency to act as  $\pi$ -acceptors. In contrast, the introduction of electron-donating groups to phosphines enhances their  $\sigma$ -donor character at the expense of their  $\pi$ -acceptor properties. Therefore, the modulation of phosphine electronic features could significantly change the nature of its bonding to a metal center and, eventually, affect its catalytic activity.

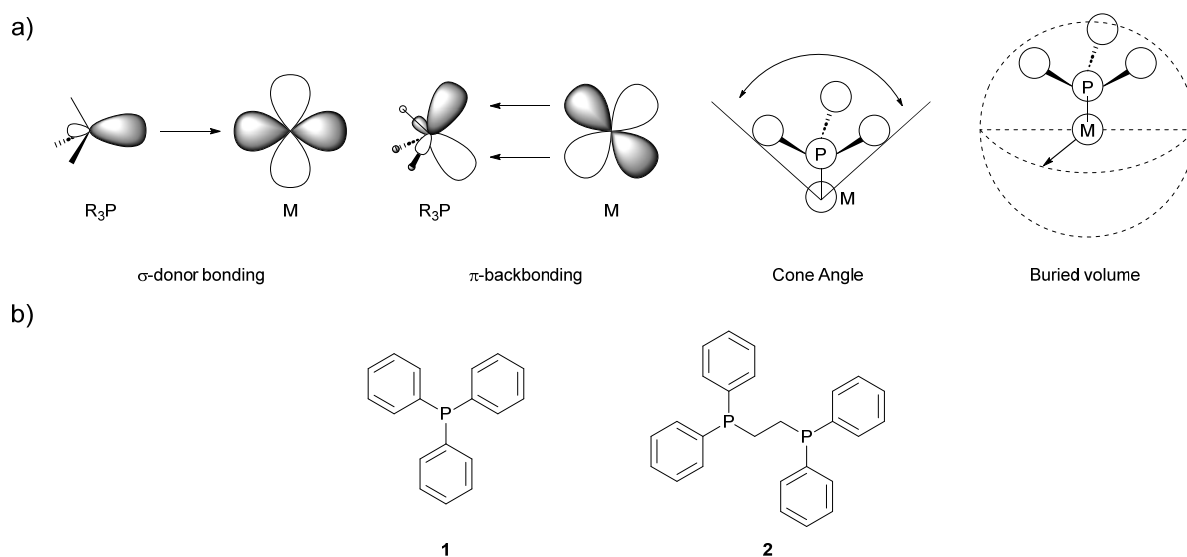
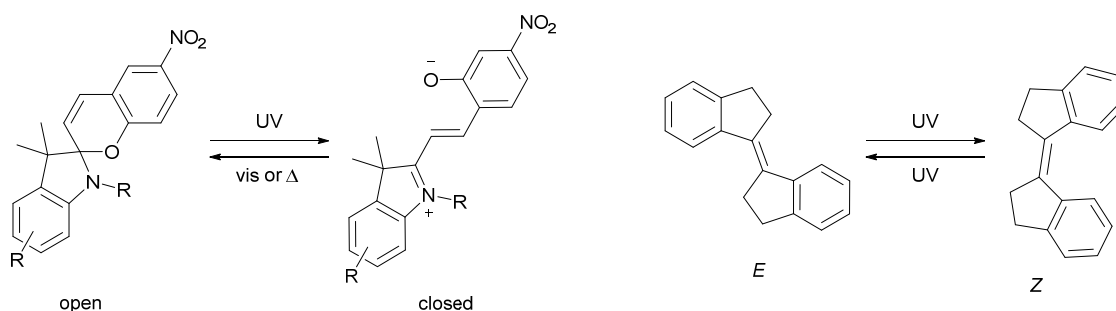


**Figure 2.** a) Electronic and structural properties of tertiary phosphine ligands in metal complexes. b) Example of monodentate triphenylphosphine ligand **1** and bidentate 1,2 bis(diphenylphosphino)ethane **2**.

Steric effects imparted by tertiary phosphines also play a very significant role in the catalytic activity of coordinated metals [12,16]. To rationalize this behavior, phosphine ligands can be described through Tolman cone angle and percent buried volume. Tolman defined the cone angle as the “apex angle of a cylindrical cone, centered at 2.28 Å from the center of the P atom, which touches the van der Waals radii of the outmost atoms of the model” [17,18]. As for the buried volume [19], it is defined as the percentage of a sphere ( $r = 3.5$  Å) around the metal center that is occupied by a given ligand. These steric descriptors of phosphines should be considered during the design of photoswitchable

catalysts, as the size of the ligand affects the reactivity of the attached metal center [20]. In addition, ligands containing more than one phosphine group in their structure can act as bidentate or even tridentate ligands (Figure 2b), thus opening a different way to alter their influence on catalytic metal centers by varying their coordination mode or the steric and electronic properties of the linker.

The light-responsive scaffolds used in photoswitchable catalysis also exhibit a variety of tunable characteristic features [21]. Generally, existing molecular photoswitches can be divided into two main groups depending on the type of isomerization process induced by light. The first group is formed by the photoswitches that undergo ring-cyclization and ring-opening reactions; for example, the spiropyran in Scheme 1. The second group of photoswitches are characterized by a light-triggered *E/Z* isomerization around a double bond. This is the case of the 1,1'-biindane in Scheme 1, an illustrative example of the stiff stilbene photoswitches used for the preparation of molecular rotors and for which Ben Feringa was awarded with the Nobel Prize in Chemistry in 2016 [22]. Additionally, photoswitches are also divided depending on the stimuli required for their back-isomerization. Those that are thermally unstable in their photoinduced state and isomerize back to their most stable configuration with time in the dark are called thermally reversible type or T-type (e.g. spiropyrans). On the other hand, photoswitches that only undergo back-isomerization under light irradiation are classified as photochemically reversible type or P-type (e.g. 1,1'-biindane).



**Scheme 1.** Examples of different types of photoswitches. Left: a spiropyran photoswitch undergoing ring-closing and ring-opening reactions upon light irradiation; in this case, reversed back-isomerization is also possible through thermal relaxation in the dark (T-type). Right: 1,1'-biindane photoswitch undergoing *E/Z* photoisomerization only upon light irradiation (P-type).

Various parameters are utilized to assess the light-induced efficacy of molecular photoswitches. Firstly, photoisomerization quantum yields ( $\Phi_i$ ) serve as a metric for the efficiency of the process in the excited state - i.e., they quantify the number of molecules undergoing the isomerization reaction per photon absorbed, excluding those that revert back to the initial ground state without isomerizing through alternative processes such as luminescence emission or internal conversion [23]. Secondly, the composition of the photostationary states (PSS) [24] defines the extent of the photoreaction - i.e., the composition of the final equilibrium mixtures of the two interconverting isomers that are achieved under continuous irradiation when the rates of the photoisomerization process and the back-reaction become equal. The composition of PSSs depends on factors such as the absorbance of the two isomers at the irradiation wavelength, their respective photoisomerization quantum yields, and, in the case of T-type photochromes, the thermal lifetime of the photoinduced isomer along with the irradiation intensity. Thirdly, fatigue resistance [25] characterizes the decline in performance of the molecular photoswitch over repetitive photoisomerization cycles, a phenomenon attributed to photo-degradation.

Typically, photoisomerization is accompanied by alteration in the geometrical and electronic properties of the photoswitch, which in turn leads to ample variation of their physicochemical properties (*e.g.* polarity, light absorbance and redox potentials). The extent of these changes depends on the specific scaffold, providing a high degree of flexibility in selecting desired outcomes.

Given the scarcity of examples utilizing photoswitchable phosphine ligands in transition metal catalysis [11], this doctoral project focused on development of the novel photoswitchable phosphine ligands for their incorporation into transition metal complexes, eventually aiming to enable light-induced modulation of their catalytic properties. Two different approaches were explored toward this goal, which involved the utilization of two distinct photoswitchable scaffolds: dithienylethenes (DTEs) and diazocines.

To ensure electron density modulation, dithienylethene (DTE)-based phosphine ligands were envisioned. DTEs are a well-known class of molecular photoswitches which, in their more thermodynamically stable open isomer, consist of two thiophene moieties connected through a Z-ethene bridge (Figure 3a) [26]. This is a particular case of the broader family of DAE photoswitches, wherein the thiophene rings may be substituted with other aryl groups. Due to the occurrence of free rotation between the ethene linker and the thiophene rings, the structure of the open-state DTE is non-planar. Consequently, electronic communication between the two aryl groups is absent, resulting in strong absorption primarily in the UV, and occasionally violet, regions (Figure 3b) [27].

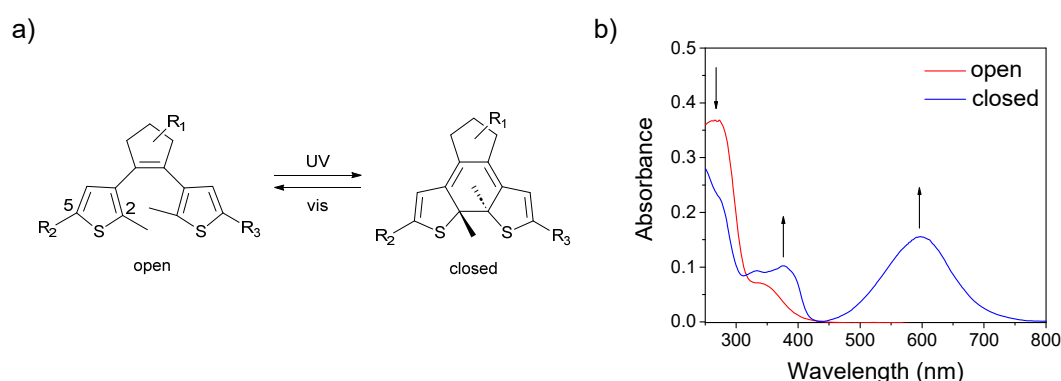


**Figure 3.** a) Ring-closing and ring-opening photochemical reactions of DTEs. b) Typical UV-vis absorption spectra of the open and closed forms of DTEs ( $R_1 = H$ ,  $R_2 = R_3 = COCF_3$ ).

Upon exposure to UV light, the open state of DTEs undergoes a  $6\pi$  electrocyclization reaction to produce the corresponding closed isomer, which displays an absorption band in the visible region due to its extended conjugation path (Figure 3b). The closed state of DTEs typically exhibits thermal stability, precluding spontaneous back-isomerization in the absence of external stimuli over time in the dark. The recovery of the open isomer therefore necessitates exposure to visible light, inducing an electrocyclic ring-opening reaction [27].

Thus, introduction of a diphenylphosphanyl group in one thiophene ring and an electron-withdrawing substituent in the other was expected to result in two distinct states of the phosphine. In the open state where the two thiophene rings are fully isolated, no electronic communication should occur between these two groups and, consequently, the phosphine ligand must have a strong  $\sigma$ -donor character. However, conjugation between the phosphanyl and EWG groups should occur upon photocyclization, thus decreasing the  $\sigma$ -donating ability of the phosphine. To further amplify this effect, two DTE moieties were devised to be introduced to the same phosphorus atom, whose

electronic properties could then be modulated by electronic communication to two EWGs simultaneously.

To explore the potential of the geometry alterations on catalytic activity, the goal of modulating the coordination mode of bisphosphine ligand upon the photoisomerization was set. Diazocine scaffold (Figure 4a) was sought of due to its specific properties. First, due to ring strain, the most stable configuration of diazocines is the *Z* isomer. Second, because of the non-planar structure of the *Z* and *E* diazocine isomers deriving from the short  $C_2$  bridge, they exhibit stronger  $n \rightarrow \pi^*$  absorption bands in the visible region of the spectrum that are fairly separated, which can therefore be used to promote all-visible reversible photoisomerization (Figure 4b). Thus, *Z*-to-*E* photoisomerization takes place by irradiation with violet-blue light (370-400 nm) with high efficiencies [28].

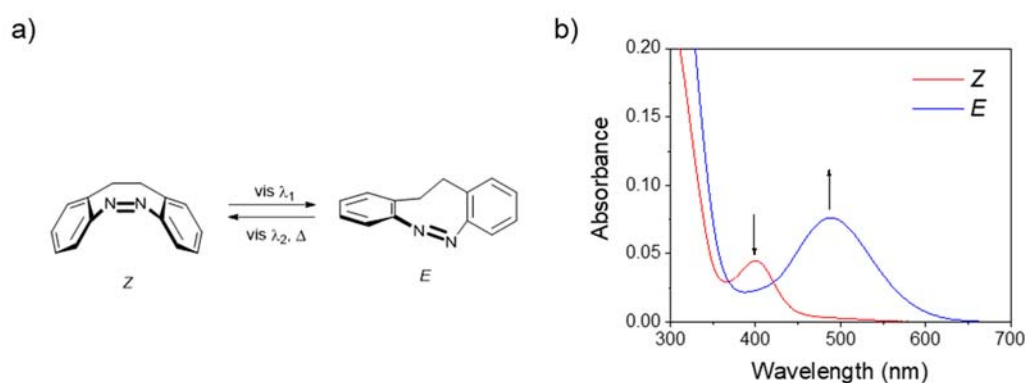


**Figure 4.** a) *Z/E* isomerization of diazocines. b) Typical UV-vis absorption spectra of the *Z* and *E* diazocine isomers.

While two phosphine groups can be in close proximity in the *Z* geometry, they should be rather far away in the *E* state, thus ensuring the switching of their coordination mode between mono- and bidentate. However, this scaffold is rather underrepresented in the literature and the challenge involves finding a suitable synthetic route for the preparation of diazocine-based phosphines. For instance, the electrophilicity of the  $N=N$  bond precludes the usage of many organometallic reagents [29], while the high ring-strain of diazocines can easily result in degradation at harsh reaction conditions. Consequently, despite reported synthesis of brominated diazocines, there are limited examples of their further functionalization [5,29,30,31].

### Dithienylethene-based photoswitchable phosphines

In a first step, the photomodulation of metal catalysts was pursued by exploring the electronic effects achieved on phosphine ligands through the photoisomerization of connected DTE photoswitches.

To validate this concept, the preparation of DTE-based phosphine ligands containing electron-withdrawing groups (EWGs): trifluoroacetyl – **DTE-COCF<sub>3</sub>** and perfluorophenyl – **DTE-C<sub>6</sub>F<sub>5</sub>**, and of an additional compound containing an electronically neutral substituent (phenyl group, **DTE-Ph**) was first undertaken (Figure 5). Ligands' synthesis involved the derivatization of a common dichlorinated DTE substrate promoted through sequential chlorine/lithium exchange reactions. Introduction of the phosphanyl and EWG groups was accomplished by quenching the resulting organolithiated compounds with the required electrophile. As for phenyl ring installation, it was accomplished through subsequent borylation and Suzuki coupling reactions.

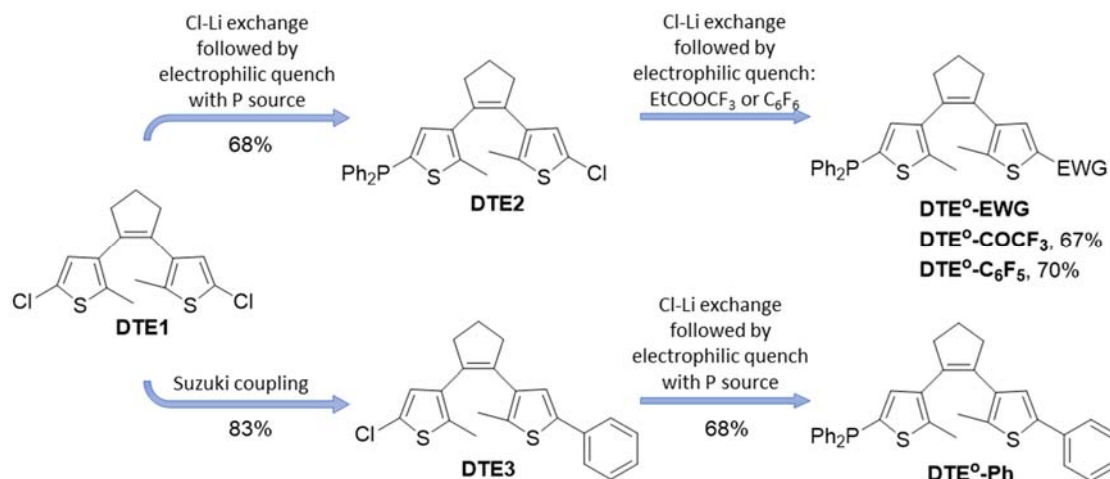


**Figure 5.** Synthesis of DTE-based photoswitchable phosphines.

Upon light irradiation in cyclohexane solution, the obtained DTE-based ligands underwent successful reversible photoisomerization under UV (for ring-closing) and visible light irradiation (for ring-opening). In addition, TD-DFT calculations at the CAM-B3LYP-D3/6,31G(d,p) level were performed to further investigate the electronic excitations of these compounds, for which ground state geometries were first computed. For ligands, only their photocyclizable antiparallel conformation was considered in the calculations. All open state phosphine ligands were characterized by a strong absorption in the UV region with maxima around  $\lambda_{\text{abs}} \approx 290$  nm (Figure 6), which was reproduced in computations and could be attributed to  $\pi\text{-}\pi^*$  transitions (HOMO - LUMO+1 or HOMO - LUMO) of their core. In the case of **DTE-COCF<sub>3</sub>**, a shallower absorption band ranging up to  $\lambda_{\text{abs}} \approx 400$  nm was detected due to the lowering of the energy of the LUMO caused by the introduction of a strong EWG. For open state ligands, a broad, red-shifted absorption band emerged in the visible part of the spectrum upon UV illumination of their cyclohexane solutions, which changed from colorless to deep blue ( $\lambda_{\text{abs}} = 598$  nm for **DTE<sup>c</sup>-COCF<sub>3</sub>**) or deep pink ( $\lambda_{\text{abs}} \approx 518$  nm for **DTE<sup>c</sup>-C<sub>6</sub>F<sub>5</sub>** and **DTE<sup>c</sup>-Ph**) (Figure 6).

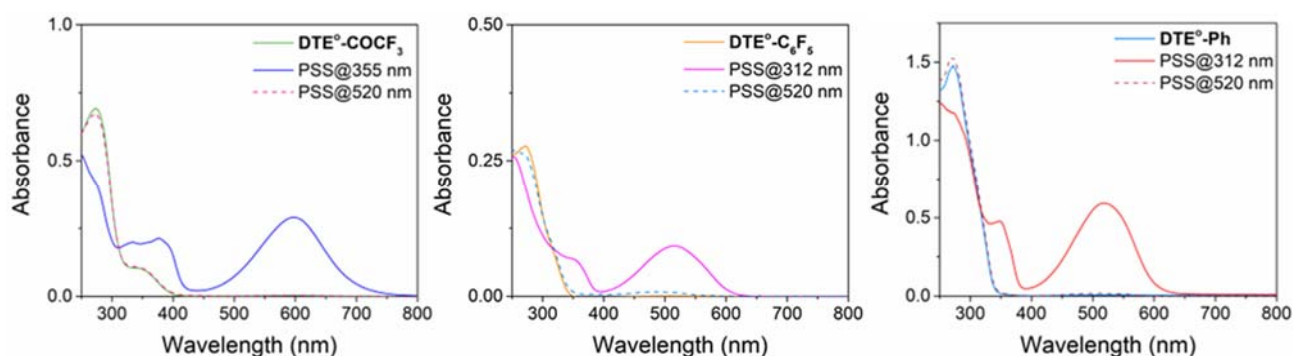


**Figure 6.** Variation of the absorption spectrum of free ligands **DTE<sup>o</sup>-COCF<sub>3</sub>** ( $c = 3.0 \cdot 10^{-5}$  M), **DTE<sup>o</sup>-C<sub>6</sub>F<sub>5</sub>** ( $c = 1.0 \cdot 10^{-5}$  M) and **DTE<sup>o</sup>-Ph** ( $c = 5.2 \cdot 10^{-5}$  M) in cyclohexane upon sequential irradiation with UV ( $\lambda_{\text{exc}} = 355$  or  $312$  nm) and green light ( $\lambda_{\text{exc}} = 520$  nm) until the corresponding ring-closing and ring-opening photostationary states (PSSs) are obtained, respectively.

The equilibrium between the open (o) and closed (c) isomers achieved upon ring-closure was defined as a photostationary state (PSS), while the cycloreversion proceeds quantitatively. The best photoswitching performance was observed for the ligand containing a trifluoroacetyl group (**DTE-COCF<sub>3</sub>**) (Table 1), exhibiting high ring-cyclization quantum yield and conversion (91% c at the PSS@365

nm) as well as good fatigue resistance. These favorable results were attributed to the effect of the strong EWG in its structure.

**Table 1.** Photochemical properties of DTE-based ligands and complexes.

	$\lambda_{\text{abs}}^{\text{o}}$ [nm] ( $\epsilon$ [ $\text{M}^{-1} \text{cm}^{-1}$ ]) <sup>a</sup>	$\lambda_{\text{abs}}^{\text{c}}$ [nm] ( $\epsilon$ [ $\text{M}^{-1} \text{cm}^{-1}$ ]) <sup>b</sup>	PSS <sub>o-c</sub> composition [%] <sup>c</sup>	$\Phi_{\text{o-c}}$ <sup>d</sup>	$\Phi_{\text{c-o}}$ <sup>e</sup>
<b>DTE-COCF<sub>3</sub></b>	268 (35 673), 339 (6 431)	598 (12 261)	9:91	0.480	0.012
[PdCl <sub>2</sub> ( <b>DTE-COCF<sub>3</sub></b> ) <sub>2</sub> ]	271 (34 149), 355 (19 065)	604 (18 870)	10:45:45	0.148/ 0.048	0.013/ 0.014
<b>DTE-C<sub>6</sub>F<sub>5</sub></b>	272 (28 303)	519 (11 379)	19:81	0.530	0.015
[PdCl <sub>2</sub> ( <b>DTE-C<sub>6</sub>F<sub>5</sub></b> ) <sub>2</sub> ]	268 (40 394), 357 (14 367)	532 (19 391)	30:45:25	0.047/ 0.019	0.015/ 0.018
<b>DTE-Ph</b>	273 (28 117)	518 (13 673)	61:39	0.485	0.011
[PdCl <sub>2</sub> ( <b>DTE-Ph</b> ) <sub>2</sub> ]	270 (42 700), 359 (15 400)	538 (16 310)	29:44:27	0.060/ 0.023	0.015/ 0.014

<sup>a</sup> Wavelength and molar absorptivity coefficient of the absorption band maxima of the open isomer (for complexes, **oo** state) in cyclohexane. <sup>b</sup> Wavelength and molar absorptivity coefficient of the maximum of the visible absorption band of the closed isomer (for complexes, **cc** state) in cyclohexane. <sup>c</sup> Composition of the PSS reached for the photocyclization process in toluene-*d*<sub>8</sub> upon irradiation at  $\lambda_{\text{exc}} = 365 \text{ nm}$  (**DTE-COCF<sub>3</sub>** and all the complexes) or  $312 \text{ nm}$  (**DTE-C<sub>6</sub>F<sub>5</sub>** and **DTE-Ph**). DTE<sup>o</sup>:DTE<sup>c</sup> and DTE<sup>oo</sup>:DTE<sup>oc</sup>:DTE<sup>cc</sup> concentration ratios are given for free ligands and complexes, respectively. <sup>d</sup> Photocyclization quantum yields measured in cyclohexane at  $\lambda_{\text{exc}} = 355 \text{ nm}$  (**DTE-COCF<sub>3</sub>** and all the complexes) or  $312 \text{ nm}$  (**DTE-C<sub>6</sub>F<sub>5</sub>** and **DTE-Ph**). For the complexes, separate  $\Phi_{\text{o-c}}$  values are given for the **oo** → **oc** and **oc** → **cc** ring-closing processes. <sup>e</sup> Photocycloreversion quantum yields measured in cyclohexane at  $\lambda_{\text{exc}} = 532 \text{ nm}$ . For the complexes, separate  $\Phi_{\text{c-o}}$  values are given for the **cc** → **oc** and **oc** → **oo** ring-opening processes.

To estimate the change in electron density on the phosphorus atom of the ligands upon photoisomerization (Figure 7), phosphine selenides were prepared. The nature of the phosphine-selenium bond allowed the estimation of each ligand's  $\sigma$ -donating ability through NMR measurements. Experimental results demonstrated that electron density modulation depended on the introduced substituent, with **DTE-COCF<sub>3</sub>** showing the highest modulation.

To further investigate the photomodulation of the electronic features for the prepared DTE-based phosphines, a set of properties derived from the DFT calculations of their ground state structures was analyzed. As a first step, the variation of the Mulliken charges on the phosphorus atom ( $\Delta^{c-o}(q_{\text{p}}^{\text{Mulliken}})$ ) and the percentage of s character of the lone pair of electrons at phosphorus ( $\Delta^{c-o}(\%s_{\text{p}})$ ) for open anti-parallel and closed conformations of **DTE-COCF<sub>3</sub>**, **DTE-C<sub>6</sub>F<sub>5</sub>** and **DTE-Ph** were considered (Table 2). According to the Mulliken charges, photocyclization decreases electron density on phosphorus, while through NBO analysis [32] an increase in s orbital participation in the phosphorus lone pair of electrons can be anticipated. More importantly, the variation of these parameters was found to increase with the electron-withdrawing power of the introduced electron-modulating group, thus again validating that **DTE-COCF<sub>3</sub>** and, to a lesser extent, **DTE C<sub>6</sub>F<sub>5</sub>** suffer the largest change in the phosphine's electronic properties upon photoisomerization.



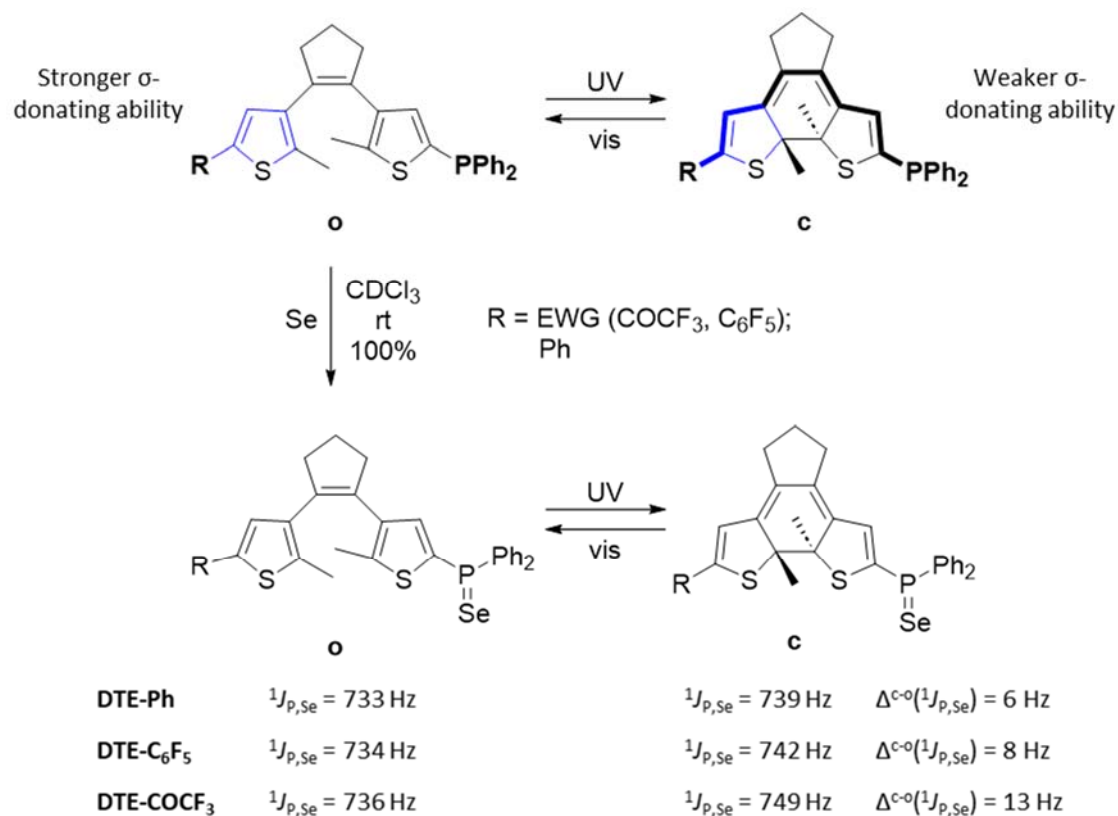


**Figure 7.** Structure of the DTE-based phosphines prepared, where photoswitching of the dithienylethene backbone caused a change in phosphine electronic properties that was dependent on the introduced EWG substituent.

As a second step, the effect of the light-induced modulation of the DTE-based phosphine ligands on the bond energy in their Pd<sup>II</sup> complexes was investigated. For this, the difference in phosphine-Pd<sup>II</sup> binding energy ( $\Delta^{c-o}(\text{BE}_{\text{P-Pd}})$ ) between the **oo** and **cc** isomers of their 2:1 trans phosphine palladium(II) complexes (Table 2) was calculated. As expected, due to the loss of the phosphine's  $\sigma$ -donating ability, a varying decrease in  $\text{BE}_{\text{P-Pd}}$  for the complexes bearing ring-closed DTE ligands is observed, depending on the nature of the introduced electron-modulating group. Thus, weakening of the phosphine-palladium(II) binding upon photocyclization was observed for the ligands bearing the EWG pentafluorophenyl and, especially, trifluoroacetyl substituents.

**Table 2.** Experimental and computed parameters to estimate the photomodulation of the properties of the phosphine ligands **DTE-COCF<sub>3</sub>**, **DTE-C<sub>6</sub>F<sub>5</sub>** and **DTE-Ph**.

	Free ligands			Pd <sup>II</sup> complexes <sup>a</sup>
	$\Delta^{c-o}({}^1J_{\text{p,se}})$ [Hz] <sup>b</sup>	$\Delta^{c-o}(q_{\text{P}}^{\text{Mulliken}})^c$	$\Delta^{c-o}(\%s_{\text{P}})^d$	$\Delta^{c-o}(\text{BE}_{\text{P-Pd}})$ [kcal·mol <sup>-1</sup> ] <sup>e</sup>
<b>DTE-COCF<sub>3</sub></b>	14	0.014	0.79	-1.98
<b>DTE-C<sub>6</sub>F<sub>5</sub></b>	7	0.004	0.42	-0.92
<b>DTE-Ph</b>	5	<0.001	0.34	-0.64

<sup>a</sup> *trans*-[PdCl<sub>2</sub>(**DTE-COCF<sub>3</sub>**)<sub>2</sub>], *trans*-[PdCl<sub>2</sub>(**DTE-C<sub>6</sub>F<sub>5</sub>**)<sub>2</sub>] and *trans*-[PdCl<sub>2</sub>(**DTE-Ph**)<sub>2</sub>]. <sup>b</sup> Difference in  ${}^1J_{\text{p,se}}$  for the corresponding selenides measured in CDCl<sub>3</sub>. <sup>c</sup> Difference in Mulliken charges in electronic units on the phosphorus atom. <sup>d</sup> Difference in percentage of s character of the phosphorus lone pair of electrons. <sup>e</sup> Difference in phosphine-Pd<sup>II</sup> bond energy (per one bond) between the **oo** and **cc** isomers.

When two equivalents of the phosphine ligands were used to react with trans-[PdCl<sub>2</sub>(PhCN)<sub>2</sub>], monometallic palladium(II) 1:2 type complexes were formed (Figure 8a). Single crystals suitable for X-ray structure determination were obtained for the three complexes, which revealed that formed Pd complexes have a square-planar geometry with trans orientation of the phosphine ligands (Figure 8b). The main difference observed between the crystal structures of these compounds was the conformation of their DTE ligands. In [PdCl<sub>2</sub>(DTE<sup>o</sup>-Ph)<sub>2</sub>] and [PdCl<sub>2</sub>(DTE<sup>o</sup>-COCF<sub>3</sub>)<sub>2</sub>], the ligands are locked in a distorted parallel open state conformation with a distance of 4.31 Å and 5.19 Å, respectively, between the carbon atoms that should react upon ring-closing photoisomerization (C16 – C26). As previously described in the literature [26], this type of conformation cannot undergo the light-induced conrotatory electrocyclization reaction to produce the corresponding closed isomer and, consequently, no photochromism was observed in the solid state for [PdCl<sub>2</sub>(DTE<sup>o</sup>-Ph)<sub>2</sub>] and [PdCl<sub>2</sub>(DTE<sup>o</sup>-COCF<sub>3</sub>)<sub>2</sub>]. Contrarily, in the case of [PdCl<sub>2</sub>(DTE<sup>o</sup>-C<sub>6</sub>F<sub>5</sub>)<sub>2</sub>], the DTE ligands are present in an antiparallel open state conformation with a shorter distance between the reactive carbons (C16 – C26, 3.69 Å), two structural features that are compatible with the photoinduced ring-closing reaction [33]. Indeed, irradiation at 312 nm yielded a color change from yellow to red and the process was reversed with irradiation at 520 nm, thus demonstrating solid state photoswitching for [PdCl<sub>2</sub>(DTE<sup>o</sup>-C<sub>6</sub>F<sub>5</sub>)<sub>2</sub>].

Irrespective of their behavior in the solid state, all DTE-based ligands and complexes prepared should photoisomerize in solution upon irradiation. However, while DTE-COCF<sub>3</sub>, DTE-C<sub>6</sub>F<sub>5</sub> and DTE Ph should just photoconvert between their ring-open and ring-closed isomers, a more complex situation is expected for their complexes. Because of their 2:1 phosphine:metal stoichiometry, these compounds must toggle between three different states where DTE-based ligands are both ring-open (**oo**), one of them ring-open and the other ring-closed (**oc**), or both ring-closed (**cc**). Complexation detrimentally affected ring-closing quantum yields due to ligand-to-metal charge transfer, resulting in less efficient photochemical reactions (Table 1). Despite this, photoswitching was not fully hindered by metal complexation, prompting further catalytic studies for the ring-open and ring-closed states of the Pd(II) compounds.

Catalytic tests were conducted for a model Stille coupling reaction between iodobenzene and tributylvinyltin in THF-*d*<sub>8</sub>, which revealed that higher conversions were achieved when using the ring-closed complexes bearing EWG substituents as pre-catalysts (Figure 3). Therefore, these results verified the initial hypothesis that the presence of these groups would selectively affect phosphine electron properties upon DTE photocyclization, thus ultimately modifying the catalytic performance of their metal complexes. In this case, reaction rate acceleration was expected to take place for the ring-closed state of the metal catalysts due to the lower binding strength of photocyclized DTE-based phosphines to palladium(0) species, a situation that was confirmed by DFT calculations of the catalytic cycle.

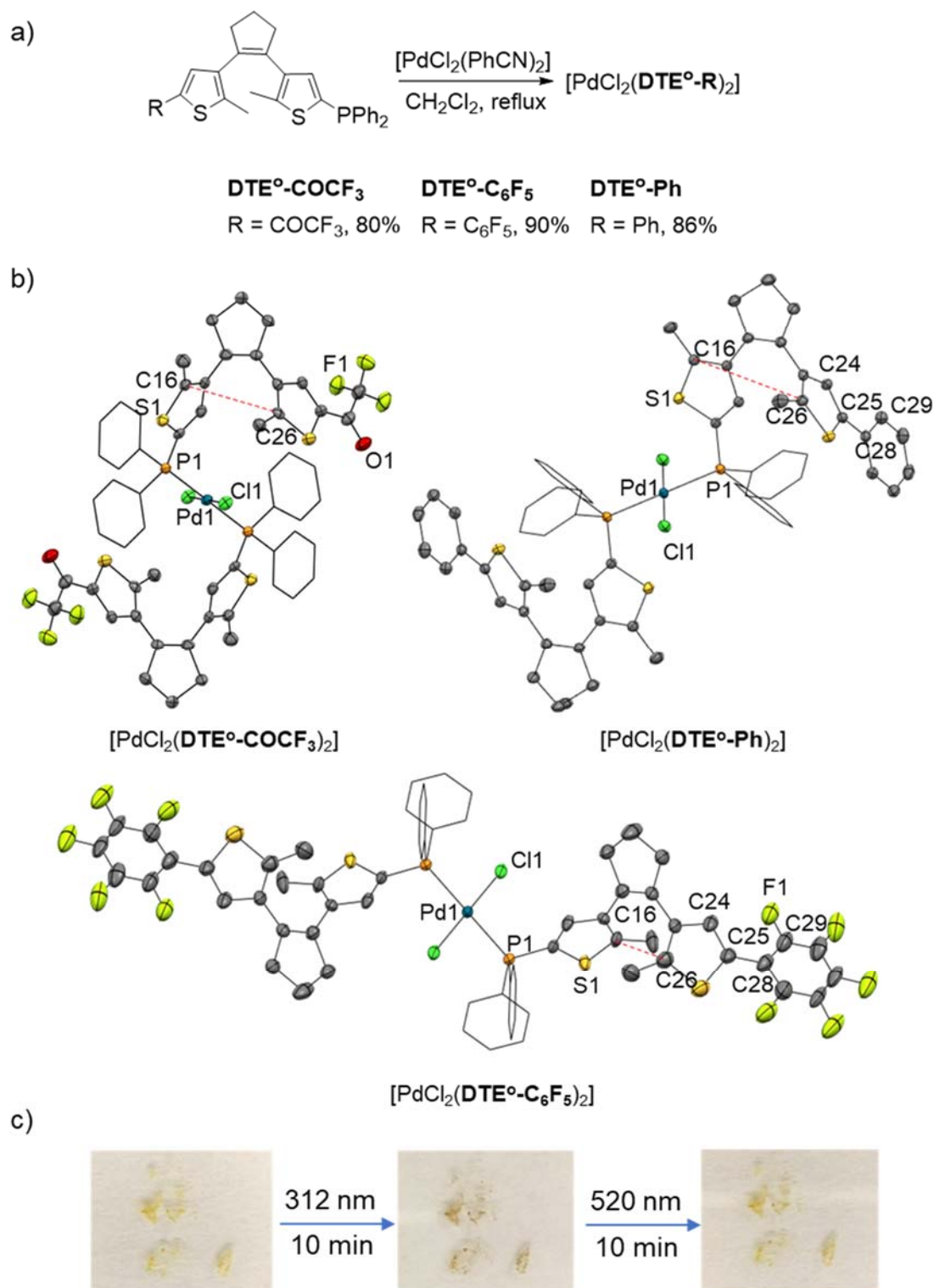


**Figure 8.** a) Synthesis of  $[\text{PdCl}_2(\text{DTE}^\circ\text{-COCF}_3)_2]$ ,  $[\text{PdCl}_2(\text{DTE}^\circ\text{-C}_6\text{F}_5)_2]$  and  $[\text{PdCl}_2(\text{DTE}^\circ\text{-Ph})_2]$ . b) Molecular structures of  $[\text{PdCl}_2(\text{DTE}^\circ\text{-Ph})_2]$ ,  $[\text{PdCl}_2(\text{DTE}^\circ\text{-COCF}_3)_2]$  and  $[\text{PdCl}_2(\text{DTE}^\circ\text{-C}_6\text{F}_5)_2]$ . Thermal ellipsoids set at 50% probability level. For clarity, P-bound phenyl rings are depicted in wireframe style, and co-crystallized solvent and hydrogen atoms are omitted. Distances between the reactive carbon atoms in DTE photoisomerization are marked with a dashed red line. c) Illustration of the solid-state photoisomerization of  $[\text{PdCl}_2(\text{DTE}^\circ\text{-C}_6\text{F}_5)_2]$ .

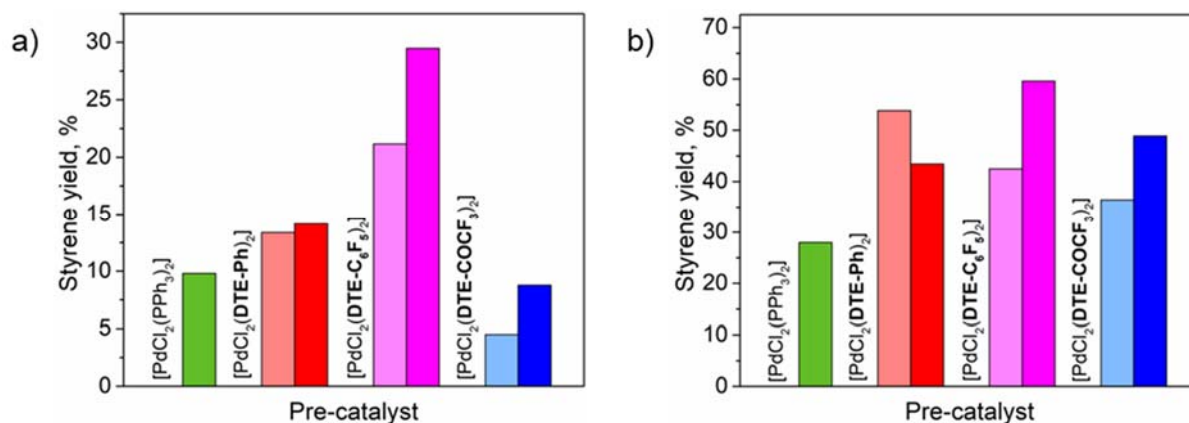
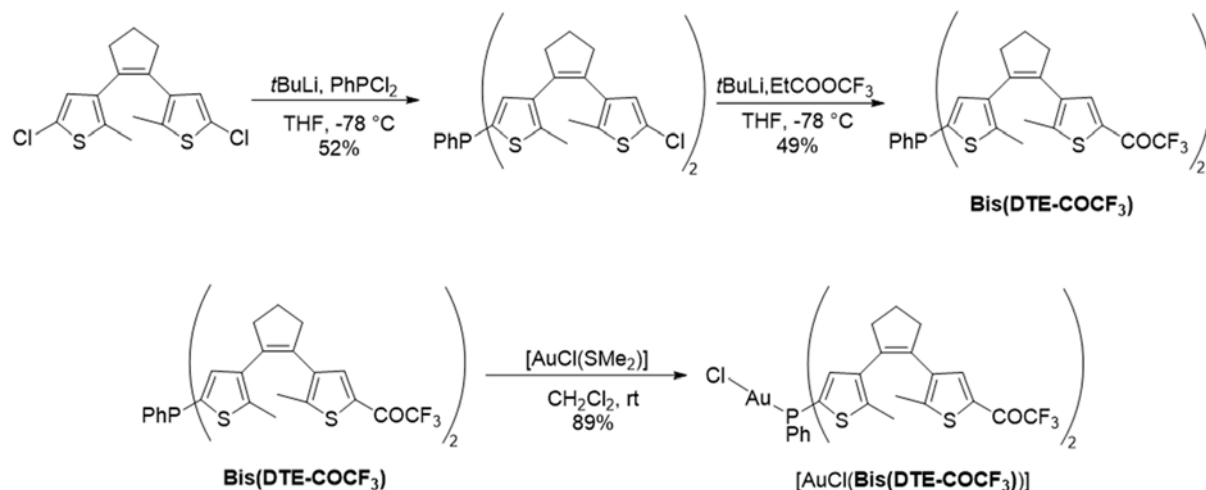


**Figure 8.** Comparison of the investigated complexes as pre-catalysts in the Stille coupling reaction between iodobenzene and tributylvinyltin (1.5 mol% [Pd], 0.30 mmol iodobenzene, 0.33 mmol tributylvinyltin, 1 mL THF). Data is shown for the open ( $[\text{PdCl}_2(\text{DTE}^{\text{O}}\text{-R})_2]$ , light red, light pink and light blue) and closed state-enriched mixture ( $[\text{PdCl}_2(\text{DTE}^{\text{C}}\text{-R})_2]$ , dark red, dark pink and dark blue) of the DTE-based complexes tested at rt (a) and 50 °C (b). The average yields of two repetitions were determined by  $^1\text{H}$  NMR using 1,3,5,-trimethoxybenzene as a standard.

As an extension of this strategy toward photoswitchable catalysis, a bisDTE ligand was designed that features two DTE moieties with trifluoroacetyl groups attached to phenylphosphine. To our knowledge, this would represent the first example reported of the introduction of more than one DTE unit to the phosphorus atom of phosphines. The synthesis of the bisDTE ligand **Bis(DTE-COCF<sub>3</sub>)** was conducted similarly as for **DTE-COCF<sub>3</sub>**, employing chlorine/lithium exchange reactions and quenching with an appropriate electrophile to install the desired phenylphosphine and trifluoromethyl ketone groups (Scheme 2). To study the complexation behavior of this ligand its gold(I) complex was also synthesized.



**Scheme 2.** Synthetic route to bisDTE-substituted phosphine **Bis(DTE-COCF<sub>3</sub>)** and its gold(I) complex.

Photochemical studies in solution revealed that fully open ligand **Bis(DTE<sup>oo</sup>-COCF<sub>3</sub>)** can successfully undergo isomerization into ring-closed **Bis(DTE<sup>oc</sup>-COCF<sub>3</sub>)** and **Bis(DTE<sup>cc</sup>-COCF<sub>3</sub>)** states, though with limited efficacy for the second photocyclization reaction (Table 3). To rationalize this behavior, the separate **oo**→**oc** and **oc**→**cc** photocyclization quantum yields were determined for **Bis(DTE-COCF<sub>3</sub>)** ( $\Phi_{\text{oo-oc}} = 0.435$  and  $\Phi_{\text{oc-cc}} = 0.020$ ). On the one hand,  $\Phi_{\text{oo-oc}}$  closely resembles the photocyclization quantum yield of reference **DTE-COCF<sub>3</sub>** ( $\Phi_{\text{o-c}} = 0.480$ ), which indicates that the first ring-closing step in **Bis(DTE-COCF<sub>3</sub>)** is not significantly affected by the presence of a nearby ring-open

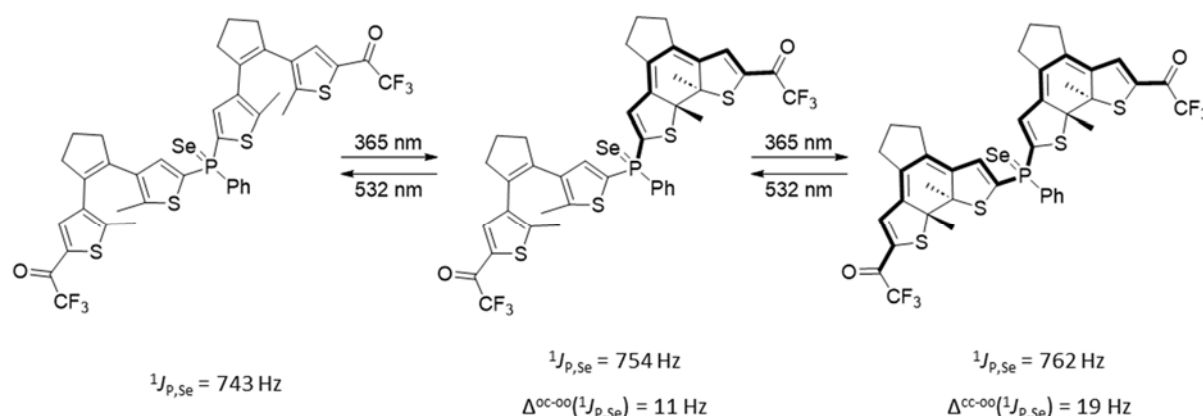
DTE unit. By contrast, a 20-fold reduction in  $\Phi$  was measured for the second ring-closing reaction of **Bis(DTE-COCF<sub>3</sub>)**, which proceeds notably less effectively when a close-by DTE unit is already in the closed state. As reported for many other multiphotochromic systems [34–36], energy transfer from the photoexcited open DTE group to the closed DTE unit in **Bis(DTE<sup>oc</sup>-COCF<sub>3</sub>)** must account for this situation, which eventually leads to photoconversion back to **Bis(DTE<sup>oo</sup>-COCF<sub>3</sub>)** instead of full photocyclization in **Bis(DTE<sup>cc</sup>-COCF<sub>3</sub>)**. Complexation with the metal did not preclude the photoswitching ability of the ligand, although, further lowering the quantum yield of the second ring-closing.

**Table 3.** Photochemical properties of DTE-based ligands **Bis(DTE-COCF<sub>3</sub>)** and of gold(I) complex **[AuCl(Bis(DTE-COCF<sub>3</sub>))]**.

	$\lambda_{\text{abs}}^{\text{o}}$ [nm] ( $\epsilon$ [M <sup>-1</sup> cm <sup>-1</sup> ]) <sup>a</sup>	$\lambda_{\text{abs}}^{\text{c}}$ [nm] ( $\epsilon$ [M <sup>-1</sup> cm <sup>-1</sup> ]) <sup>b</sup>	PSS <sub>o-c</sub> composition [%] <sup>c</sup>	$\Phi_{\text{oo-oc}}^{\text{d}}$	$\Phi_{\text{oc-cc}}^{\text{d}}$	$\Phi_{\text{cc-oc}}^{\text{e}}$	$\Phi_{\text{oc-oo}}^{\text{e}}$
<b>Bis(DTE-COCF<sub>3</sub>)</b>	273 (32 423), 336 (5 820)	599 (22 000)	7:84:9	0.435	0.020	0.032	0.022
<b>[AuCl(Bis(DTE-COCF<sub>3</sub>))]</b>	262 (47 527), 336 (7 727)	589 (26 542)	10:77:13	0.246	0.007	0.026	0.023

<sup>a</sup> Wavelength and molar absorptivity coefficient of the absorption band maxima of the open isomer (the **oo** state) in cyclohexane. <sup>b</sup> Wavelength and molar absorptivity coefficient of the maximum of the visible absorption band of the closed isomer (the **cc** state) in cyclohexane. <sup>c</sup> Composition of the PSS reached for the photocyclization process in toluene-*d*<sub>8</sub> upon irradiation at  $\lambda_{\text{exc}} = 365$  nm. DTE<sup>oo</sup>:DTE<sup>oc</sup>:DTE<sup>cc</sup> concentration ratios are given. <sup>d</sup> Photocyclization quantum yields measured in cyclohexane at  $\lambda_{\text{exc}} = 355$  nm. <sup>e</sup> Photocycloreversion quantum yields measured in cyclohexane at  $\lambda_{\text{exc}} = 532$  nm.

Importantly, the preparation of the corresponding phosphine selenides and their analysis by NMR demonstrated that the fully closed form of the ligand **1cc** experienced the largest modulation of electron density reported to date for photoswitchable phosphines ( $\Delta^{\text{cc-oo}}(^1J_{\text{P,Se}}) = 19$  Hz).



**Scheme 3.** Photoisomerization-induced variation of  $^1J_{\text{P,Se}}$  in the **oo**, **oc** and **cc** isomers of phosphine selenide.

To corroborate this experimental result, several descriptors commonly used to assess the electronic properties of ground state phosphines were computed using DFT calculations at the B3LYP-D3/6,31G(d,p) level. On the one hand, clear decrements in the Mulliken charge on the phosphorus atom of **Bis(DTE-COCF<sub>3</sub>)** were predicted upon DTE ring-closing ( $\Delta(q_{\text{P}}^{\text{Mulliken}})$ , Table 4). While the first DTE photocyclization process in **Bis(DTE-COCF<sub>3</sub>)** should result in a similar  $\Delta(q_{\text{P}}^{\text{Mulliken}})$ , value as for monoDTE-

based phosphine **DTE-COCF<sub>3</sub>**, the second ring-closing reaction should lead to further lowering of the electron density on phosphorus. This effect is typically accompanied by changes in composition of the lone pair at the phosphorus atom with an increased participation of the s orbital. Indeed, according to NBO analysis, the photoconversion from the **Bis(DTE<sup>oo</sup>-COCF<sub>3</sub>)** to the **Bis(DTE<sup>cc</sup>-COCF<sub>3</sub>)** state must lead to a progressive increment of the contribution of the s orbital to the lone pair of electrons at phosphorus, eventually reaching twice the variation computed for phosphine **DTE-COCF<sub>3</sub>**.

Finally, the ligand-metal bond energies of the respective gold(I) complexes formed with **Bis(DTE-COCF<sub>3</sub>)** and **DTE-COCF<sub>3</sub>** were evaluated. As expected, weaker phosphorus-gold(I) bonds were predicted after DTE ring-closing in both ligands. More importantly, double DTE photocyclization in [AuCl(**Bis(DTE-COCF<sub>3</sub>)**)] should result in almost a two-fold variation in ligand-metal binding energies compared to the complex with monoDTE-based phosphine **DTE-COCF<sub>3</sub>**. This result confirms the capacity to accomplish large photomodulation in the electronic properties of phosphines by tethering two photoswitchable DTE units to a central phosphorus atom.

**Table 4.** Experimental and computed parameters to estimate the photomodulation of properties for phosphines **Bis(DTE-COCF<sub>3</sub>)** and **DTE-COCF<sub>3</sub>**.

	$\Delta(^1J_{P,Se})$ [Hz] <sup>a</sup>		$\Delta(q_P^{\text{Mulliken}})^b$		$\Delta(\%s_P)^c$		$\Delta(\text{BE}_{P-Au})$ [kcal·mol <sup>-1</sup> ] <sup>d</sup>	
	oo → oc	oo → cc	oo → oc	oo → cc	oo → oc	oo → cc	oo → oc	oo → cc
<b>Bis(DTE-COCF<sub>3</sub>)</b>	11	19	0.011	0.036	0.52	1.58	1.52	2.13
	o → c		o → c		o → c		o → c	
<b>DTE-COCF<sub>3</sub></b>	14 <sup>26</sup>		0.014 <sup>26</sup>		0.79 <sup>26</sup>		1.23	

<sup>a</sup> Difference in <sup>1</sup>J<sub>P,Se</sub> for the corresponding selenides measured in CDCl<sub>3</sub>. <sup>b</sup> Difference in Mulliken charges in electronic units on the phosphorus atom. <sup>c</sup> Difference in percentage of s character of the lone pair of electrons at phosphorus. <sup>d</sup> Difference in phosphine-Au bond energy.

### Diazocine-based photoswitchable phosphine

In an attempt to achieve metal catalyst photomodulation based on geometric effects, the use of diazocine photoswitches was explored. By introducing two phosphanyl groups to this type of photoswitchable scaffold, it was envisioned to modify their coordination mode to metals under irradiation. Through DFT calculations, the preferred substitution pattern of the diazocine core to accomplish this goal was identified: it involved installing the two phosphanyl substituents at positions 1,10 of the diazocine (Figure 5). For this particular type of ligand structures, variation of the coordination mode was computationally revealed, as their *Z* isomer could act as a bidentate ligand while their *E* isomer could only monocoordinate metal centers due to the increased separation distance between the phosphanyl groups.

Encouraged by these results, several synthetic routes were explored to prepare the desired 1,10-disubstituted diazocine-based bisphosphines. However, functionalization of these positions of the diazocine core with diphenylphosphine groups could not be accomplished, in contrast to what was observed for other positions of the photoswitch scaffold. This indicates that the derivatization of diazocines at the target positions 1,10 is severely hampered by steric hindrance effects.

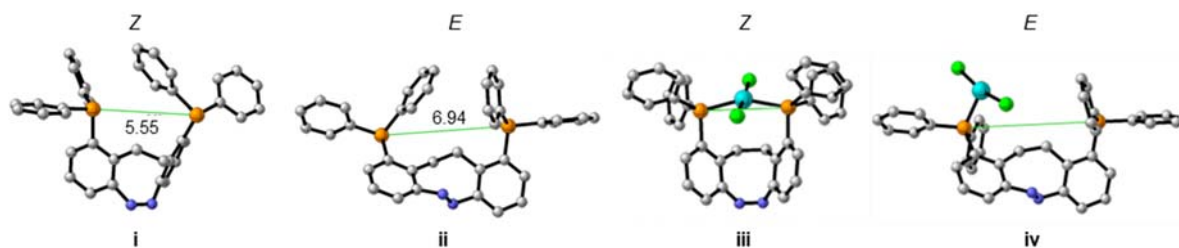


**Figure 5** – Computed structures of the Z and E states of the free ligands and palladium(II) complexes of a 1,10-disubstituted diazocine-based bisphosphine. A clear change in separation distance between the two phosphanyl groups occurs upon Z-E photoisomerization, which leads to a variation of the coordination mode to the metal center.

## Conclusions and outlook

A library of DTE-substituted ligands was developed in this thesis to validate two new concepts for the modulation of phosphine electron properties upon irradiation: (i) switching the communication between phosphanyl and electron-withdrawing groups installed at the 5 and 5' positions of the thiophene rings of the DTE core; and (ii) connecting two of these DTE photoswitches to the same phosphine. The resulting ligands showed ample variation of phosphine  $\sigma$ -donation ability upon DTE photoisomerization. Aiming to exploit this behavior in photoswitchable catalysis, they were complexed to metal centers and Pd<sup>II</sup> complexes were tested as pre-catalysts for a model Stille coupling reaction, where a change in catalytic activity was observed for the different isomerization states of the system. These results open new ways for the application of DTE-induced electronic changes on ligands in the field of photoswitchable catalysis.

As for the attempt to pioneer the use of diazocines to light-control metal-based catalysis, the synthesis of the target diazocine-based phosphines was not successful. Despite this, valuable knowledge was gained about how to use this type of scaffold for photoswitchable catalysis and what challenges must be faced during their derivatization. To ultimately bring this molecular design to life, further exploration of the synthetic approaches towards diazocine-based ligands is therefore required.

## References

- [1] T. Traut, *Enzyme Activity: Allosteric Regulation*, in *Encyclopedia of Life Sciences*, John Wiley & Sons, Ltd, **2014**. ISBN: 9780470015902. DOI: [10.1002/9780470015902.a0000865.pub3](https://doi.org/10.1002/9780470015902.a0000865.pub3).
- [2] J. Choudhury, *Tetrahedron Lett.*, **2018**, *59*, 487–495. DOI: [10.1016/j.tetlet.2017.12.070](https://doi.org/10.1016/j.tetlet.2017.12.070).
- [3] V. Blanco, D. A. Leigh, V. Marcos, *Chem. Soc. Rev.*, **2015**, *44*, 5341–5370. DOI: [10.1039/C5CS00096C](https://doi.org/10.1039/C5CS00096C).
- [4] G. C. Thaggard, J. Haimerl, R. A. Fischer, K. C. Park, N. B. Shustova, *Angew. Chem. Int. Ed.*, **2023**, e202302859. DOI: [10.1002/anie.202302859](https://doi.org/10.1002/anie.202302859).
- [5] D. Hugenbusch, M. Lehr, J.-S. von Glasenapp, A. J. McConnell, R. Herges, *Angew. Chem. Int. Ed.*, **2023**, *62*, e202212571. DOI: [10.1002/anie.202212571](https://doi.org/10.1002/anie.202212571).
- [6] H. Lee, J. Tessarolo, D. Langbehn, A. Baksi, R. Herges, G. H. Clever, *J. Am. Chem. Soc.*, **2022**, *144*, 3099–3105. DOI: [10.1021/jacs.1c12011](https://doi.org/10.1021/jacs.1c12011).
- [7] A. Kumar, R. Pandey, R. K. Gupta, V. Mishra, S. M. Mobin, D. S. Pandey, *Dalton Trans.*, **2014**, *43*, 6365–6376. DOI: [10.1039/c6dt00747c](https://doi.org/10.1039/c6dt00747c).
- [8] D. Sud, T. B. Norsten, N. R. Branda, *Angew. Chem. Int. Ed.*, **2005**, *44*, 2019–2021. DOI: [10.1002/anie.201105032](https://doi.org/10.1002/anie.201105032).
- [9] H. Z. Wei, Y. Wei, M. Shi, *Chem. Asian J.*, **2023**, *18*, e202300633. DOI: [10.1002/asia.202300633](https://doi.org/10.1002/asia.202300633).

- [10] B. Kaur, R. Raza, M. J. Stashick, N. R. Branda, *Org. Chem. Front.*, **2019**, *6*, 1253–1256. DOI: [10.1039/C9QO00221A](https://doi.org/10.1039/C9QO00221A).
- [11] F. Medici, N. Goual, V. Delattre, A. Voituriez, A. Marinetti, *ChemCatChem*, **2020**, *12*, 5573–5589. DOI: [10.1002/cctc.202000620](https://doi.org/10.1002/cctc.202000620).
- [12] P. C. J. Kamer, P. W. N. M. van Leeuwen. *Phosphorus(III) Ligands in Homogeneous Catalysis: Design and Synthesis*, John Wiley & Sons, Ltd, **2012**. ISBN: 9781118299715. DOI: [10.1002/9781118299715](https://doi.org/10.1002/9781118299715).
- [13] H. A. Mayer, W. C. Kaska, *Chem. Rev.*, **1994**, *94*, 1239–1272. DOI: [10.1021/cr00029a004](https://doi.org/10.1021/cr00029a004).
- [14] A. G. Orpen, N. G. Connelly, *Organometallics*, **1990**, *9*, 1206–1210. DOI: [10.1021/om00118a048](https://doi.org/10.1021/om00118a048).
- [15] C. H. Suresh, N. Koga, *Inorg. Chem.*, **2002**, *41*, 1573–1578. DOI: [10.1021/ic0109400](https://doi.org/10.1021/ic0109400).
- [16] C. A. Tolman, *Chem. Rev.*, **1977**, *77*, 313–348. DOI: [10.1021/cr60307a002](https://doi.org/10.1021/cr60307a002).
- [17] C. A. Tolman, W. C. Seidel, L. W. Gosser, *J. Am. Chem. Soc.*, **1974**, *96*, 53–60. DOI: [10.1021/ja00808a009](https://doi.org/10.1021/ja00808a009).
- [18] C. A. Tolman, *J. Am. Chem. Soc.*, **1970**, *92*, 2956–2965. DOI: [10.1021/ja00713a007](https://doi.org/10.1021/ja00713a007).
- [19] H. Clavier, S. P. Nolan, *Chem. Comm.*, **2010**, *46*, 841–861. DOI: [10.1039/B922984A](https://doi.org/10.1039/B922984A).
- [20] Z. Freixa, P. W. N. M. van Leeuwen. *Dalton Trans.*, **2003**, 1890–1901. DOI: [10.1039/B300322C](https://doi.org/10.1039/B300322C).
- [21] M. M. Russev, S. Hecht, *Adv. Mater.*, **2010**, *22*, 3348–3360. DOI: [10.1002/adma.200904102](https://doi.org/10.1002/adma.200904102).
- [22] B. L. Feringa, *Angew. Chem. Int. Ed.*, **2017**, *56*, 11060–11078. DOI: [10.1002/anie.201702979](https://doi.org/10.1002/anie.201702979).
- [23] E. Stadler, A. Eibel, D. Fast, H. Freißmuth, C. Holly, M. Wiech, N. Moszner, G. Gescheidt, *Photochem. Photobiol. Sci.*, **2018**, *17*, 660–669. DOI: [10.1039/C7PP00401J](https://doi.org/10.1039/C7PP00401J).
- [24] J. W. Verhoeven, *Pure Appl. Chem.*, **1996**, *68*, 2223–2286. DOI: [10.1351/pac199668122223](https://doi.org/10.1351/pac199668122223).
- [25] S. E. Braslavsky. *Pure Appl. Chem.*, **2007**, *79*, 293–465. DOI: [10.1351/pac200779030293](https://doi.org/10.1351/pac200779030293).
- [26] M. Irie, T. Fukaminato, K. Matsuda, S. Kobatake, *Chem. Rev.*, **2014**, *114*, 12174–12277. DOI: [10.1021/cr500249p](https://doi.org/10.1021/cr500249p).
- [27] M. Irie, *Chem. Rev.*, **2000**, *100*, 1685–1716. DOI: [10.1021/cr980069d](https://doi.org/10.1021/cr980069d).
- [28] R. Siewertsen, H. Neumann, B. Buchheim-Stehn, R. Herges, C. Näther, F. Renth, F. Temps, *J. Am. Chem. Soc.*, **2009**, *131*, 15594–15595. DOI: [10.1021/ja906547d](https://doi.org/10.1021/ja906547d).
- [29] H. Gilman, R. M. Pickens, *J. Am. Chem. Soc.*, **1925**, *47*, 2406–2416. DOI: [10.1021/ja01686a020](https://doi.org/10.1021/ja01686a020).
- [30] M. Reynders, A. Chaikuad, B. T. Berger, K. Bauer, P. Koch, S. Laufer, S. Knapp, D. Trauner, *Angew. Chem. Int. Ed.*, **2021**, *60*, 20178–20183. DOI: [10.1002/anie.202103767](https://doi.org/10.1002/anie.202103767).
- [31] O. Galangau, L. Norel, S. Rigaut, *Dalton Trans.*, **2021**, *50*, 17879–17891. DOI: [10.1039/D1DT03397B](https://doi.org/10.1039/D1DT03397B).
- [32] E. D. Glendening, C.R. Landis, F. Weinhold, *Wiley Interdiscip. Rev. Comput. Mol. Sci.*, **2012**, *2*, 1–42. DOI: [10.1002/wcms.51](https://doi.org/10.1002/wcms.51).
- [33] S. Kobatake, K. Uchida, E. Tsuchida, M. Irie, *Chem. Commun.*, **2002**, *23*, 2804–2805. DOI: [10.1039/B208419H](https://doi.org/10.1039/B208419H).
- [34] A. Perrier, F. Maurel, D. Jacquemin, *Acc. Chem. Res.*, **2012**, *45*, 1173–1182. DOI: [10.1021/ar200214k](https://doi.org/10.1021/ar200214k).
- [35] A. Fihey, A. Perrier, W. R. Browne, D. Jacquemin, *Chem. Soc. Rev.*, **2015**, *44*, 3719–3759. DOI: [10.1039/C5CS00137D](https://doi.org/10.1039/C5CS00137D).
- [36] N. M. W. Wu, M. Ng, V. W. W. Yam, *Nat. Commun.*, **2022**, *13*, 33–43. DOI: [10.1038/s41467-021-27711-9](https://doi.org/10.1038/s41467-021-27711-9).





**Paven KISTEN**

**ESR8**

**Thesis co-directors**

Prof. Simon Duckett,  
Prof. Jason Lynam, University of York, York, United Kingdom  
Dr. John Slattery

Prof. Rinaldo Poli      Laboratoire de Chimie de Coordination, Toulouse, France

**Thesis defense**

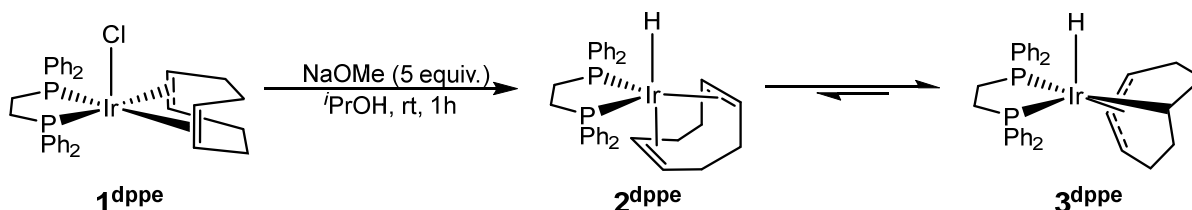
Department of Chemistry, University of York, 28 November 2023



## Ir<sup>I</sup>( $\eta^4$ -diene) Precatalyst Activation: Role of the Base

### Ir<sup>I</sup>( $\eta^4$ -diene) precatalyst activation by strong bases and formation of monohydrides

The reaction of **1**<sup>dpppe</sup> with NaOMe results in the formation of two iridium monohydride isomers, **2**<sup>dpppe</sup> and **3**<sup>dpppe</sup> (Scheme 1). These have been characterized by NMR spectroscopy and demonstrate the difference in the binding of the COD ligand. The hydride is proposed to form via beta hydrogen elimination from the alkoxide releasing acetone (formaldehyde in the case of methoxide).



**Scheme 1.** Reaction of **1**<sup>dpppe</sup> with a base containing a  $\beta$ -hydrogen to form **2**<sup>dpppe</sup> and **3**<sup>dpppe</sup>.

Following the successful synthesis and characterisation of **2**<sup>dpppe</sup> and **3**<sup>dpppe</sup>, the isomerization process was tracked via <sup>31</sup>P NMR monitoring (Figure 1), which led to observable kinetic metrics. These values were used to obtain the Gibbs energy difference of  $2.06 \pm 0.16$  kcal mol<sup>-1</sup>, and an energy barrier of  $22.19 \pm 0.04$  kcal mol<sup>-1</sup> for the isomerization of **2**<sup>dpppe</sup> to **3**<sup>dpppe</sup>. These values rationalise the preference for **3**<sup>dpppe</sup> rather than **2**<sup>dpppe</sup>.

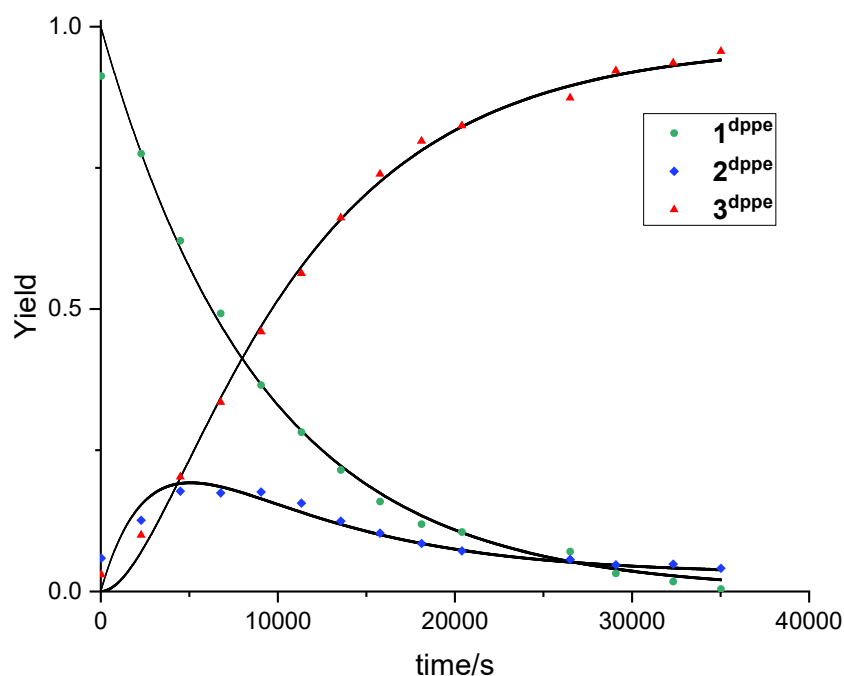
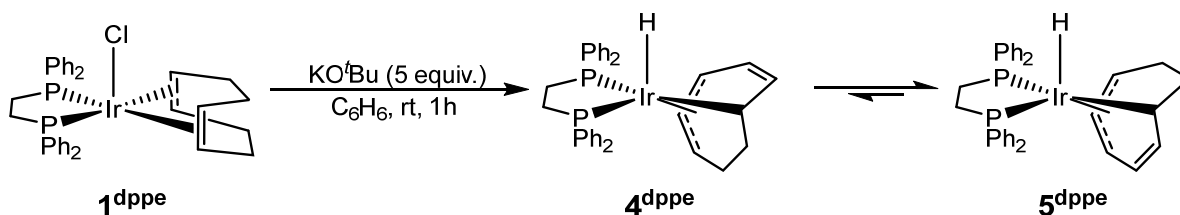


**Figure 1.** Time evolution of the <sup>31</sup>P{<sup>1</sup>H} data for the **1**<sup>dpppe</sup> decay and **2**<sup>dpppe</sup>-**3**<sup>dpppe</sup> isomerization. The continuous lines are the result of the non-linear least-squares fit.

While the kinetic study gives energy metrics, the exact nature of the isomerization process was unknown, as such a DFT study was performed to elucidate a potential isomerization mechanism. The results of this study indicate that the isomerization proceeds via a neutral intermediate

$[\text{Ir}(\text{C}_8\text{H}_{13})(\text{dppe})]$  ( $1^{\text{dppe}}$ ). Two transition states were proposed one that links  $2^{\text{dppe}}$  to  $1^{\text{dppe}}$  ( $\text{TS}_{(2-1)}^{\text{dppe}}$ ) and the other linking  $1^{\text{dppe}}$  to  $3^{\text{dppe}}$  ( $\text{TS}_{(1-3)}^{\text{dppe}}$ ) (Figure 2), the latter of which is observed experimentally.

To evaluate the effect of different bases, NaOMe was replaced by  $\text{KO}^t\text{Bu}$ . Consequently, when  $\text{KO}^t\text{Bu}$  was added to  $1^{\text{dppe}}$  in non-polar solvents such as benzene, toluene or THF two previously unreported complexes were seen ( $4^{\text{dppe}}$  and  $5^{\text{dppe}}$ ) (Scheme 2). These products correspond to structural isomers of an  $[\text{IrH}(\text{C}_8\text{H}_{10})(\text{dppe})]$  complex. Each product was extensively characterized using NMR spectroscopy, and the isomerization process between  $4^{\text{dppe}}$  and  $5^{\text{dppe}}$  was also studied using NMR spectroscopic methods (Figure 3).



**Scheme 2.** Reaction of  $1^{\text{dppe}}$  with  $\text{KO}^t\text{Bu}$  in benzene to form  $4^{\text{dppe}}$  and  $5^{\text{dppe}}$ .

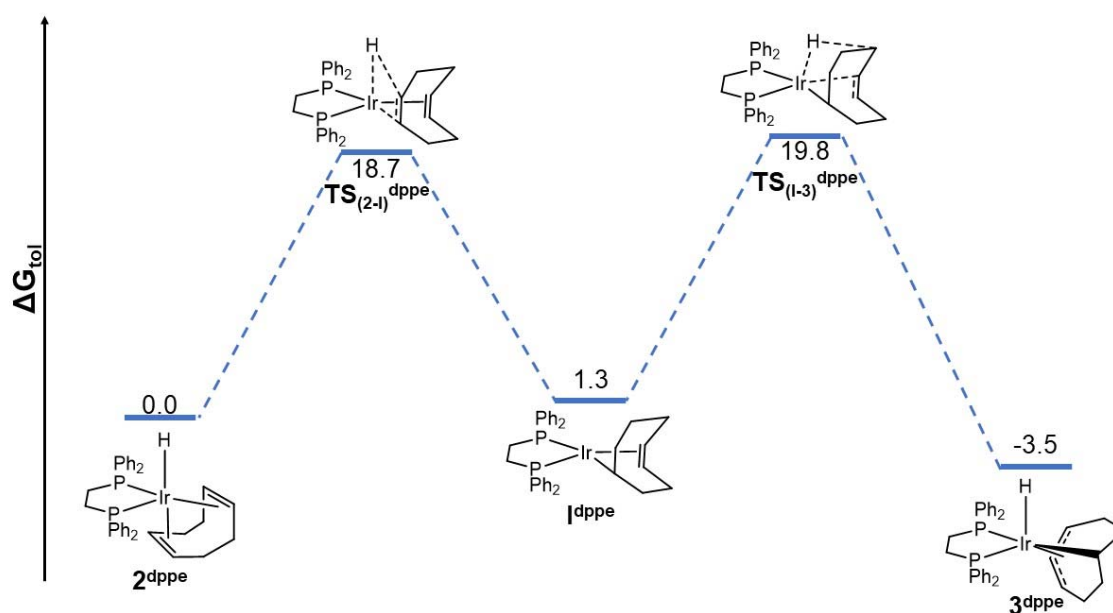


**Figure 2.** Gibbs energy profile (in  $\text{kcal mol}^{-1}$ ) for the isomerization of  $2^{\text{dppe}}$  to  $3^{\text{dppe}}$ . Relative energies shown with  $2^{\text{dppe}}$  as the reference point.

The immediate disappearance of  $1^{\text{dppe}}$  (within the time needed to record the first  $^{31}\text{P}\{^1\text{H}\}$  NMR spectrum after the addition of  $\text{KO}^t\text{Bu}$  to  $1^{\text{dppe}}$ ) reflects a rapid first step, allowing clean timescale separation from the second step, such that analysis of the latter by standard reversible first-order reaction kinetics was possible. By using the experimentally determined rate constants – the energy barrier associated with the isomerization could then be calculated by applying the Eyring relationship  $22.3 \pm 0.1 \text{ kcal mol}^{-1}$ , and the energy difference between  $4^{\text{dppe}}$  and  $5^{\text{dppe}}$  of  $0.51 \pm 0.04 \text{ kcal mol}^{-1}$  (in benzene- $d_6$ ).

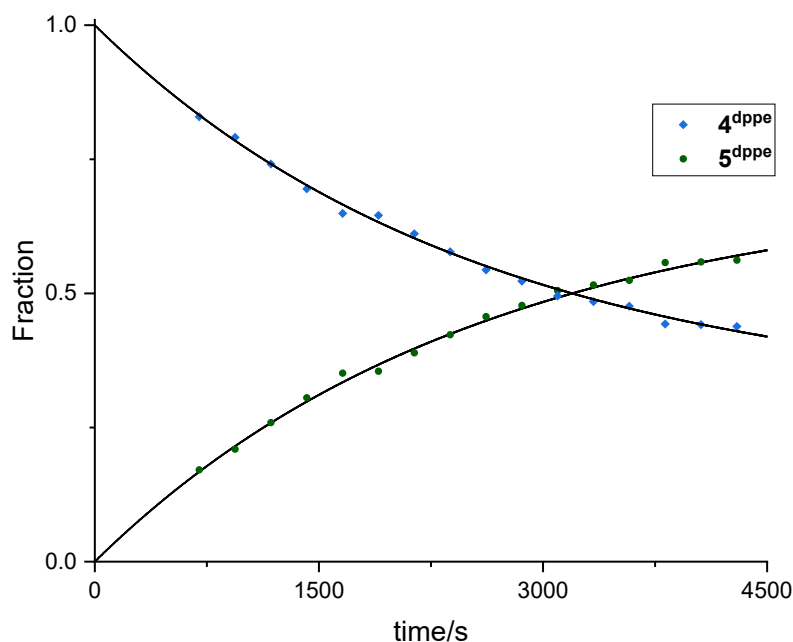
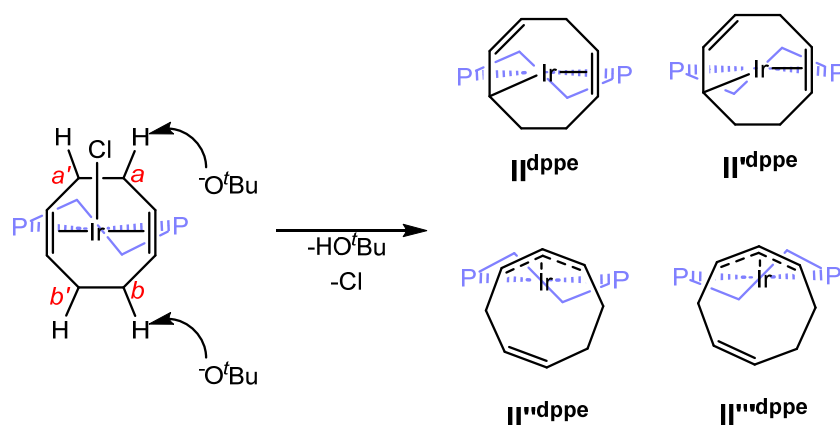


**Figure 3.** Time evolution of the  $^{31}\text{P}\{^1\text{H}\}$  NMR data for the first order kinetics of the  $4^{\text{dpp}}\text{e}$  to  $5^{\text{dpp}}\text{e}$  isomerization in benzene- $d_6$  at 298 K.

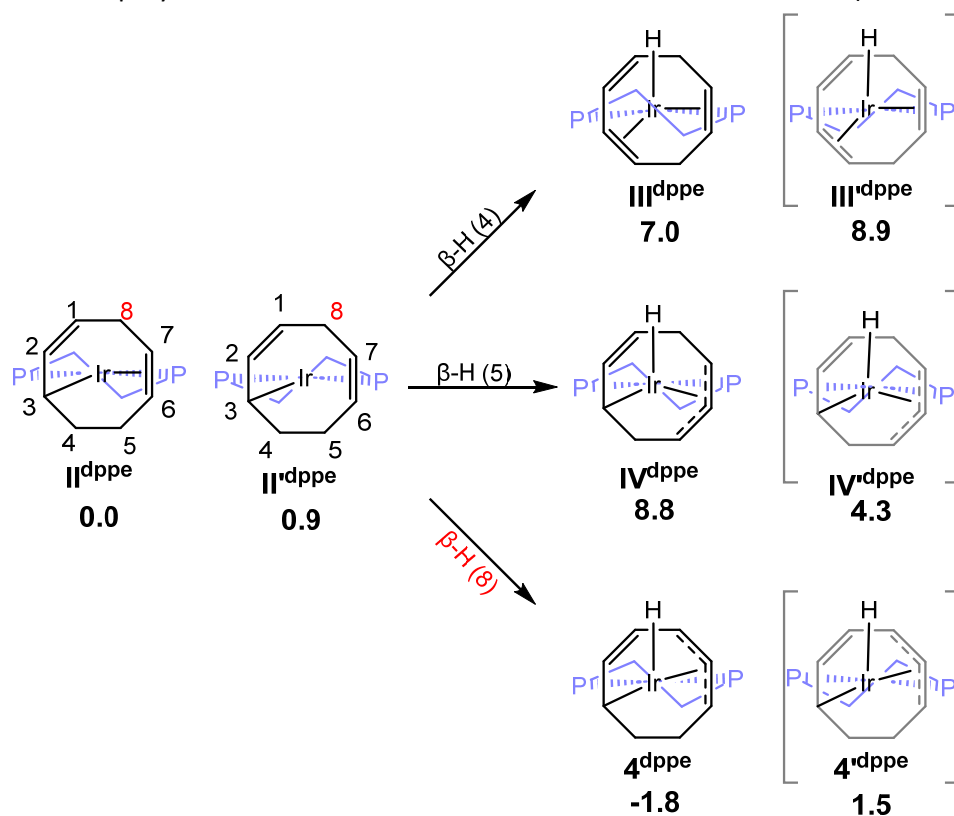
The exact nature of the formation of  $4^{\text{dpp}}\text{e}$  from  $1^{\text{dpp}}\text{e}$  without a  $\beta$ -hydrogen containing alkoxide initially caused much speculation about the exact nature of the reaction. Hence, a DFT study was conducted both on the formation of a monohydride from  $1^{\text{dpp}}\text{e}$  and on the isomerization of  $4^{\text{dpp}}\text{e}$  to  $5^{\text{dpp}}\text{e}$ . It was proposed that the reaction proceeds first via deprotonation of the COD ligand leading to a neutral 16-electron  $[\text{Ir}(\text{C}_8\text{H}_{11})(\text{dppe})]$



**Scheme 3.** Deprotonation of the COD ligand leading to two different  $[\text{Ir}(\text{C}_8\text{H}_{11})(\text{dppe})]$  ( $\text{II}^{\text{dpp}}\text{e}$  and  $\text{II}'^{\text{dpp}}\text{e}$ ) isomers and their respective conformers with a flipped  $\text{Ir}(\text{dppe})$  moiety ( $\text{II}''^{\text{dpp}}\text{e}$  and  $\text{II}'''^{\text{dpp}}\text{e}$ ) (phenyl rings removed for clarity).

The different pathways from  $[\text{Ir}(\text{C}_8\text{H}_{11})(\text{dppe})]$  to  $[\text{IrH}(\text{C}_8\text{H}_{10})(\text{dppe})]$  were all explored, however, the result that corresponded to the structural data for  $4^{\text{dpp}}\text{e}$  and indeed the lowest energy isomer was

when  $\beta$ -hydride elimination occurs at carbon C8 (Scheme 4, Figure 4).



**Scheme 4.** Generation of  $4^{dppe}$  from  $II^{dppe}$ . The phenyl groups on the dppe are omitted for clarity. (Relative energy profiles in kcal mol<sup>-1</sup>).

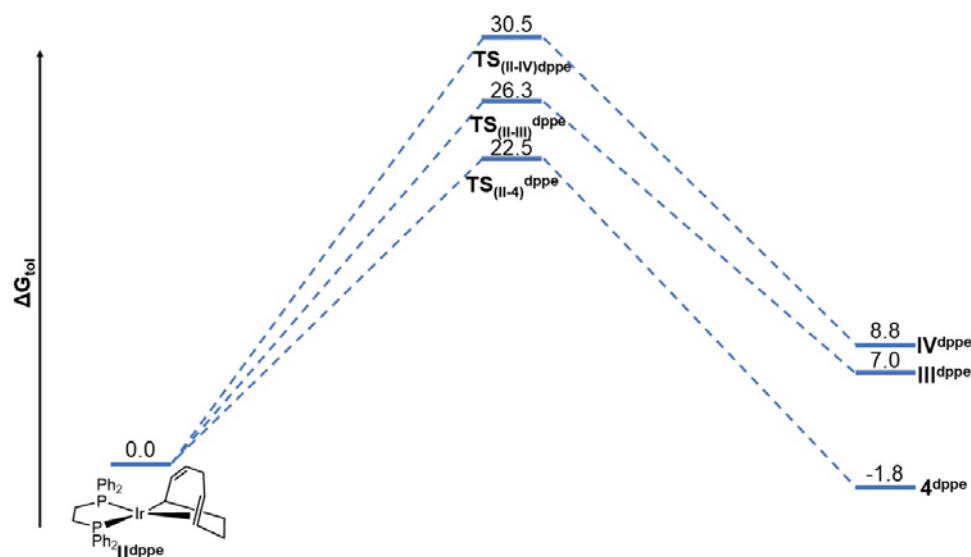


**Figure 4.** Gibbs-energy profile (in kcal mol<sup>-1</sup>) for all possible  $\beta$ -H elimination reactions from intermediate  $II^{dppe}$ .

It is notable that the lowest-energy product obtained from  $II^{dppe}$  ( $4^{dppe}$ ) features the uncoordinated alkene moiety *syn* relative to the hydride ligand. No direct pathway is available to transform intermediate  $II^{dppe}$  to isomer  $5^{dppe}$ , for which, on the other hand, the uncoordinated alkene moiety is located *anti* relative to the hydride ligand. Hence, the isomerization must occur through a different pathway. Exploration of the various possibilities to rotate the  $C_8H_{10}$  around the metal

coordination sphere revealed a low-energy pathway linking  $4^{dpppe}$  to a different structural isomer of  $5^{dpppe}$ ,  $5'^{dpppe}$ .  $5'^{dpppe}$  has an ethylene bridge in the equatorial plane, essentially a diastereomer of  $5^{dpppe}$ , 0.7 kcal mol<sup>-1</sup> higher than  $5^{dpppe}$  and 0.2 kcal mol<sup>-1</sup> higher than  $4^{dpppe}$ . The isomerization of  $4^{dpppe}$  to  $5^{dpppe}$  proceeds *via* the rearrangement schematically illustrated in Figure 5. This entails a rotation of the C<sub>8</sub>H<sub>10</sub> ligand relative to the Ir-H axis *via*  $TS_{(4-5)}^{dpppe}$  with simultaneous displacement toward the Ir atom of the two CH groups of the uncoordinated alkene, which become part of coordinated  $\eta^3$  moiety, and the inverse displacement of the two CH groups of the coordinated  $\eta^3$  moiety that end up forming the uncoordinated alkene moiety.

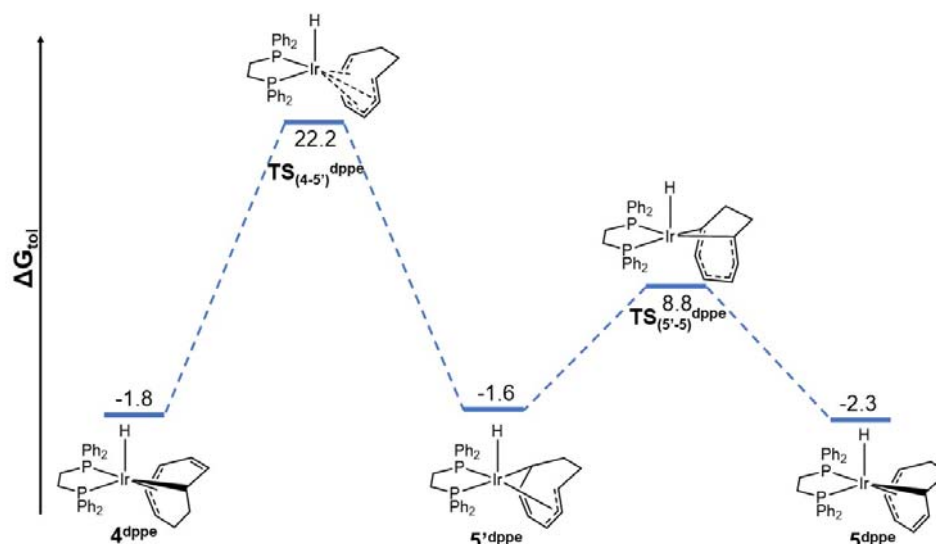


**Figure 5.** Gibbs energy profile (in kcal mol<sup>-1</sup>) for the isomerization of  $4^{dpppe}$  to  $5^{dpppe}$ .

The solid-state structure indicates that the cyclooctadienyl ligand is disordered with respect to C2 and C8. The atomic displacement parameters of the disordered pairs of carbons were constrained to be equal (C2 & C2A, C8 & C8A). This disorder is due to the two possible positions of the uncoordinated double bond (C2=C3 or C7=C8A). Separation of the two superimposed structures, leads to two different structural isomers, that represent  $4^{dpppe}$  (Figure 6) and  $5^{dpppe}$  (Figure 7). Both of which correspond remarkably well to the respective optimized DFT structures.

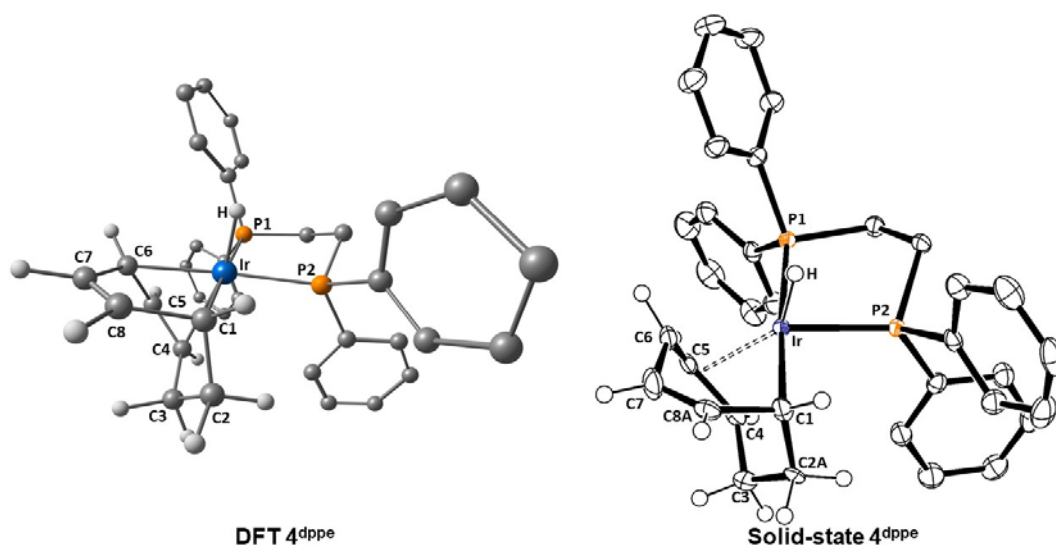




**Figure 6.** DFT and solid-state structure of  $4^{dpppe}$ . Anisotropic displacement ellipsoids are shown at 50% probability level. The hydrogen atoms on *dpppe* are omitted for clarity.

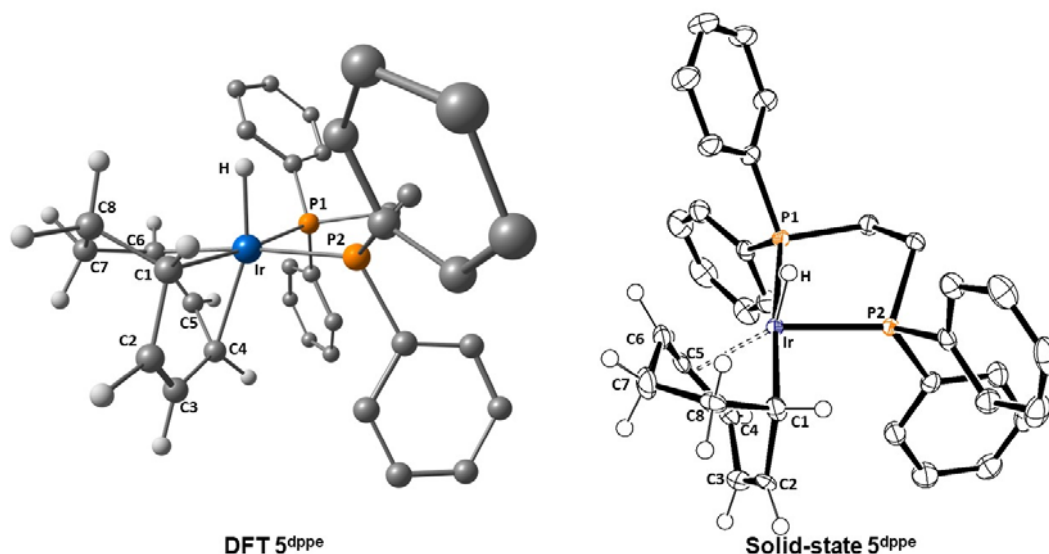
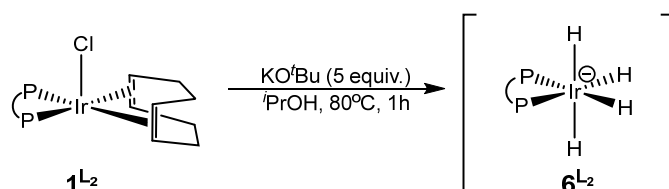


**Figure 7.** DFT and solid-state structure of  $5^{dpppe}$ . Anisotropic displacement ellipsoids are shown at 50% probability level. The hydrogen atoms on *dpppe* are omitted for clarity.

### Characterization of Anionic Ir<sup>III</sup> Tetrahydride Complexes and their role in Transfer Hydrogenation

A reproducible route to form three different anionic Ir<sup>III</sup> tetrahydride complexes from the chloride containing precursors ( $[\text{IrCl}(\text{COD})(\text{L}_2)]$  ( $\text{L}_2 = \text{dppe}, \text{dppf}, S\text{-BINAP}$ ) under hydrogenation and transfer hydrogenation conditions were demonstrated (Scheme 5).

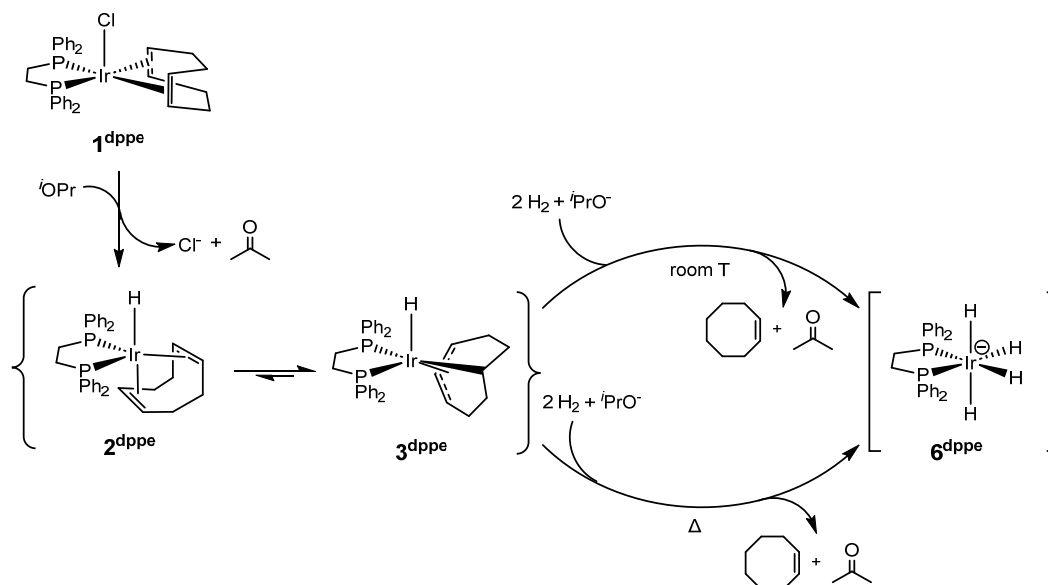


**Scheme 5.** Synthetic route towards forming an anionic tetrahydride  $6^{L_2}$  from the corresponding chloride precursor  $1^{L_2}$  under transfer hydrogenation conditions.  $\text{L}_2 = \text{dppe}, \text{dppf}, (S)\text{-BINAP}$ .

The clean formation of an anionic tetrahydrido product only occurred when a suitable counter cation is present in the solution (in this case from the base). In contrast, in the absence of a base, under hydrogenation conditions, a complicated mixture of iridium hydride derived products was observed. However, the subsequent addition of base to these mixtures results in a single tetrahydride product. In all cases the cyclooctadiene ligand was selectively removed as cyclooctene to yield what is deemed as the catalytically active species  $6^{L_2}$  (Scheme 6).

In the absence of a substrate, and when  $\text{H}_2$  pressure was released,  $6^{dpppe}$  dimerizes to form a neutral trihydride dimer (Figure 8). The crystal structure obtained is sufficient to support the dimerization process, however, this structure does not pinpoint the exact positions of the hydride ligands. Based on other dimeric iridium hydride complexes with diphosphine ligands reported in the literature such as  $[\text{Ir}(\text{H})_2(\text{dtbpe})]_2^+$  ( $\text{dtbpe} = 1,2\text{-bis}(\text{di-}t\text{-tert-butylphosphino})\text{ethane}$ ) [1] and

$[\text{Ir}(\text{H})_3(\text{dfepe})]_2$  [2] (dfepe =  $(\text{C}_2\text{F}_5)_2\text{-PCH}_2\text{CH}_2\text{P-(C}_2\text{F}_5)_2$ ) [3], a DFT investigation was conducted. Using the asymmetric unit cell structure of  $[\text{Ir}(\text{dppe})]_2$ , six hydride ligands were added to create three different isomers, with bridging hydride ligands as shown in Scheme 7. Each of these systems were then computed to find a local minimum. The isomer with two bridging hydride ligands was found to be the most stable of the three computed, and the only structure that reached a local minimum. However, in the case of both dppe and dppe, the presence of coordinating DMSO suppressed the formation of the tetrahydrido species and a neutral trihydride resulted from the reaction (Scheme 8).



**Scheme 6.** Idealized stoichiometry for the generation of  $6^{\text{dppe}}$  from  $1^{\text{dppe}}$  under both hydrogenation and transfer hydrogenation conditions in isopropanol.

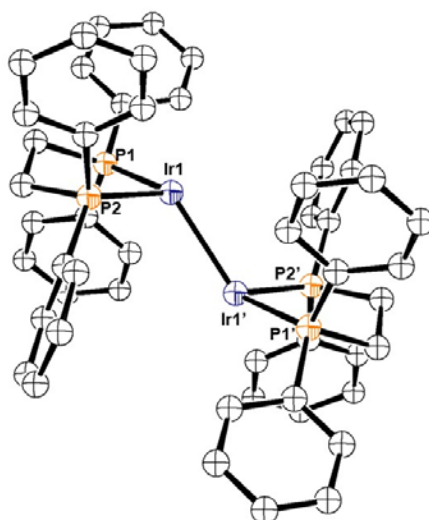
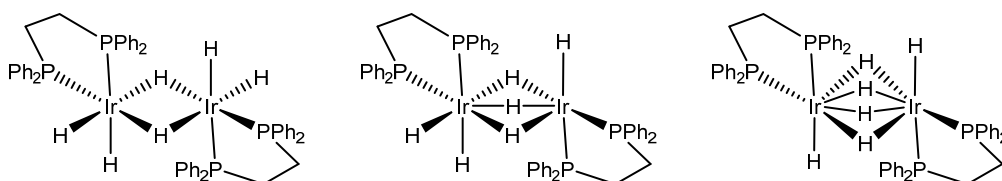
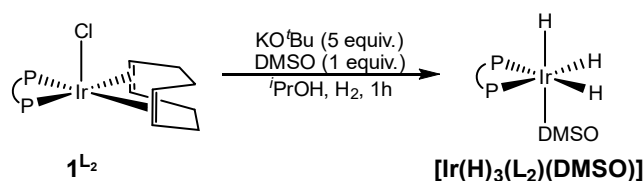


**Figure 8.** X-Ray structure of  $[\text{Ir}(\text{H})_3(\text{dppe})]_2$ . Anisotropic displacement ellipsoids are drawn at the 50% probability level. Hydrogen atoms on dppe are omitted for clarity.



**Scheme 7.** Geometries of the different isomers computed. The isomer on the left was found to be the lowest energy system.



**Scheme 8.** Formation of a neutral trihydride from **1**<sup>L<sub>2</sub></sup> via the addition of DMSO. L<sub>2</sub> = dppe, dppf.

The three different [IrCl(COD)(L<sub>2</sub>)] complexes were then evaluated for the hydrogenation of acetophenone, all of which showed negligible *ee*. The activity for each system increased drastically in the presence of KO<sup>t</sup>Bu and was accredited to the formation of the anionic tetrahydrido complexes (Figure 9).

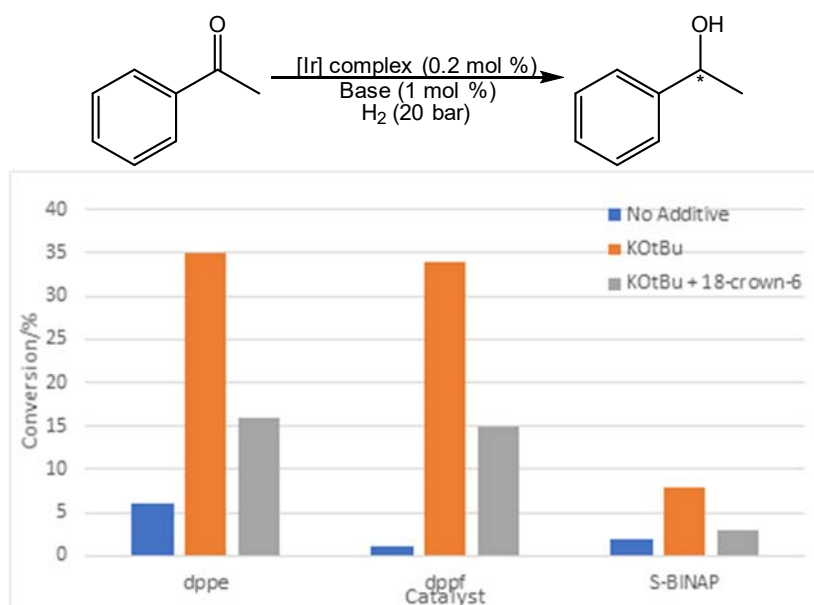
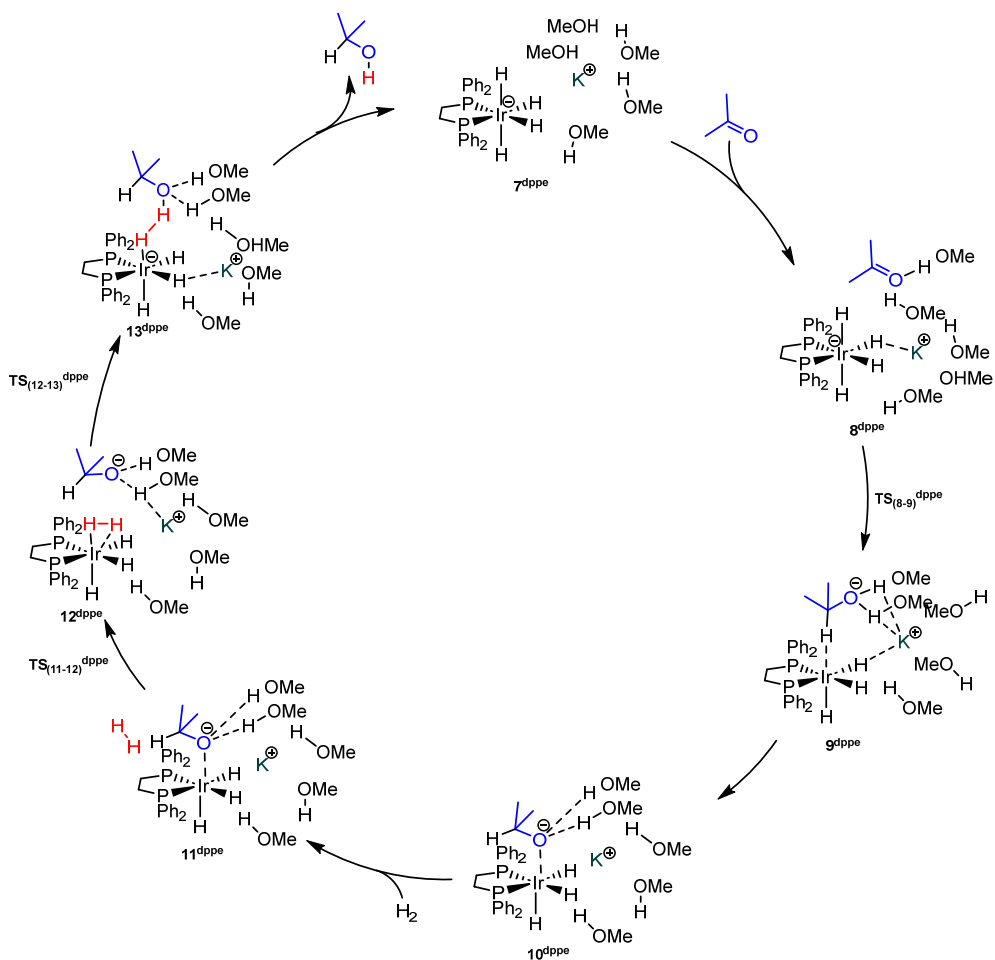


**Figure 9.** Results of the asymmetric hydrogenation of acetophenone with [IrCl(COD)(L<sub>2</sub>)] complexes.

A DFT study was conducted to provide a plausible hydrogenation mechanism (Scheme 9), two key transition states were not found (Figure 10), but the study did give an insight into the importance of a proper solvation model for the cation.

The input of the correct starting geometry for the model is of the utmost importance. The lowest energy structure for **7**<sup>dppe</sup>, is obtained when the cation is placed near the hydride side of the Ir anion rather than the ligand side, plus an acetone molecule infinitely far apart. When the acetone is closer to the catalyst, it can be observed that stabilization of the cation is provided by the MeOH molecules, and one of the hydrides (Figure 11). After the hydride transfer to the substrate, the K-H distance increases by 0.14 Å. At this point stabilization of the cation is provided by the substrate and is reflected in the close energy difference between **8**<sup>dppe</sup> and **9**<sup>dppe</sup>.



Scheme 9. Proposed cycle for acetone hydrogenation catalysed by  $7^{dppe}$ .

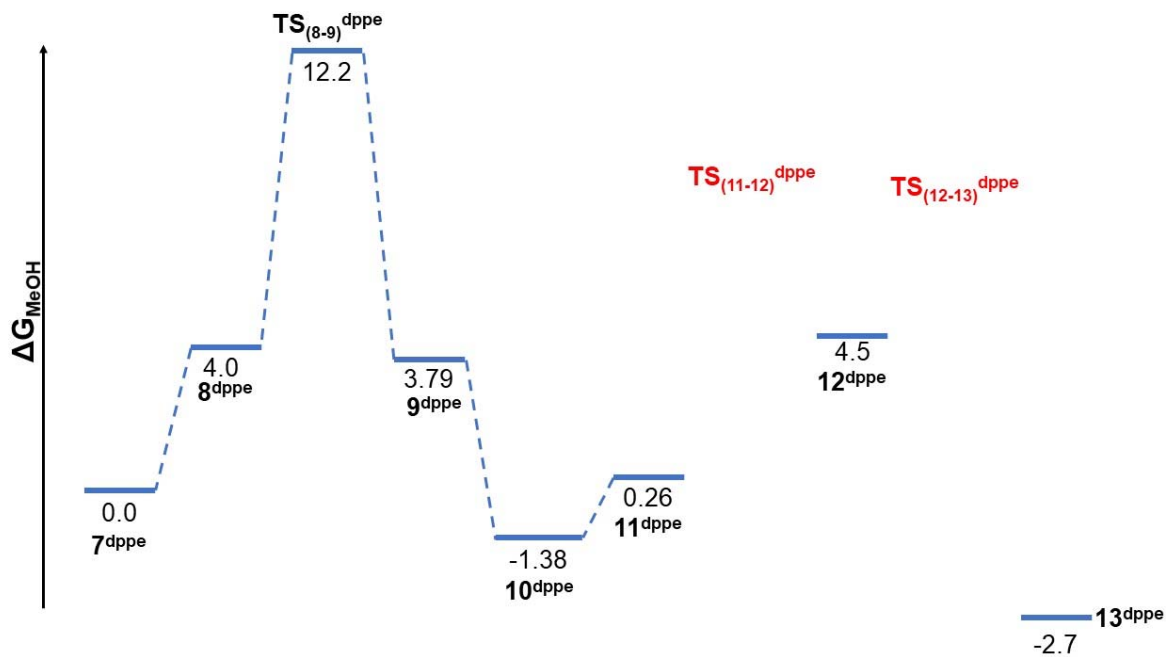
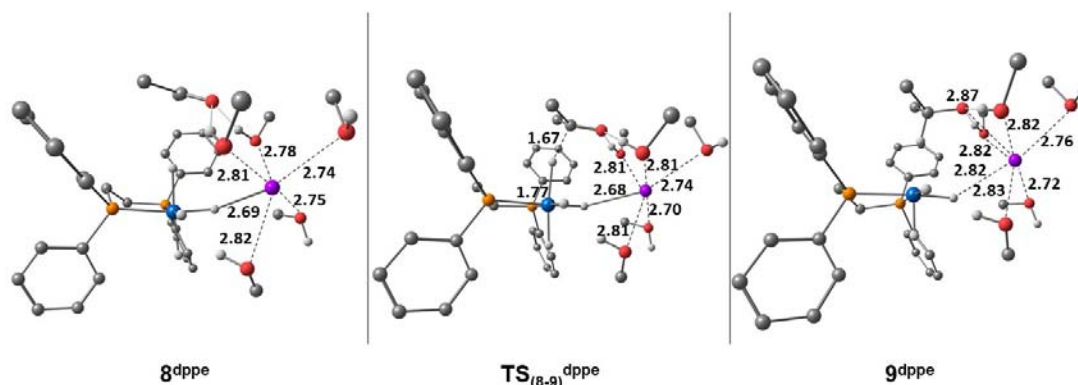


Figure 10. Computed Gibbs energy profiles for the hydrogenation of acetone with  $7^{dppe}$ . Energy profiles is in kcal mol<sup>-1</sup>. The labels shown reference the cycle in Scheme 9,  $TS_{(11-12)}^{dppe}$  and  $TS_{(12-13)}^{dppe}$  could not be located (shown in red).



**Figure 11.** Optimized structures for the hydride transfer step with  $6^{dppp}$ . Distances shown are in Å. C-H hydrogen (except on the alkoxide) atoms have been omitted for clarity.

### Ketone Hydrogenation Catalysed by Anionic Tetrahydrido Ir<sup>III</sup> Complexes and the Cation Effect

The role of anionic hydride complexes as active catalysts in hydrogenation and hydrogen transfer reactions has now become well-established. The present chapter has illustrated one such case for the active catalyst produced *in situ* by activation of  $[\text{IrCl}(\text{COD})(\text{P},\text{S}^{\text{R}})]$  ( $\text{P},\text{S}^{\text{R}} = \text{CpFe}[1,2\text{-C}_5\text{H}_3(\text{PPh}_2)(\text{CH}_2\text{S}^{\text{R}})]$ ;  $\text{R} = i\text{Pr}, \text{Ph}, \text{Bz}, \text{Cy}$ ) under  $\text{H}_2$  in the presence of a strong base. The stark dependence of the catalytic activity on the nature of the base alkali cation ( $\text{K}^+ > \text{Na}^+ > \text{Li}^+$ ) and the severe activity dampening observed when 18-crown-6 is added to the  $\text{K}^+$  system (Figure 12) confirm previous suggestions of an anionic active complex [4].

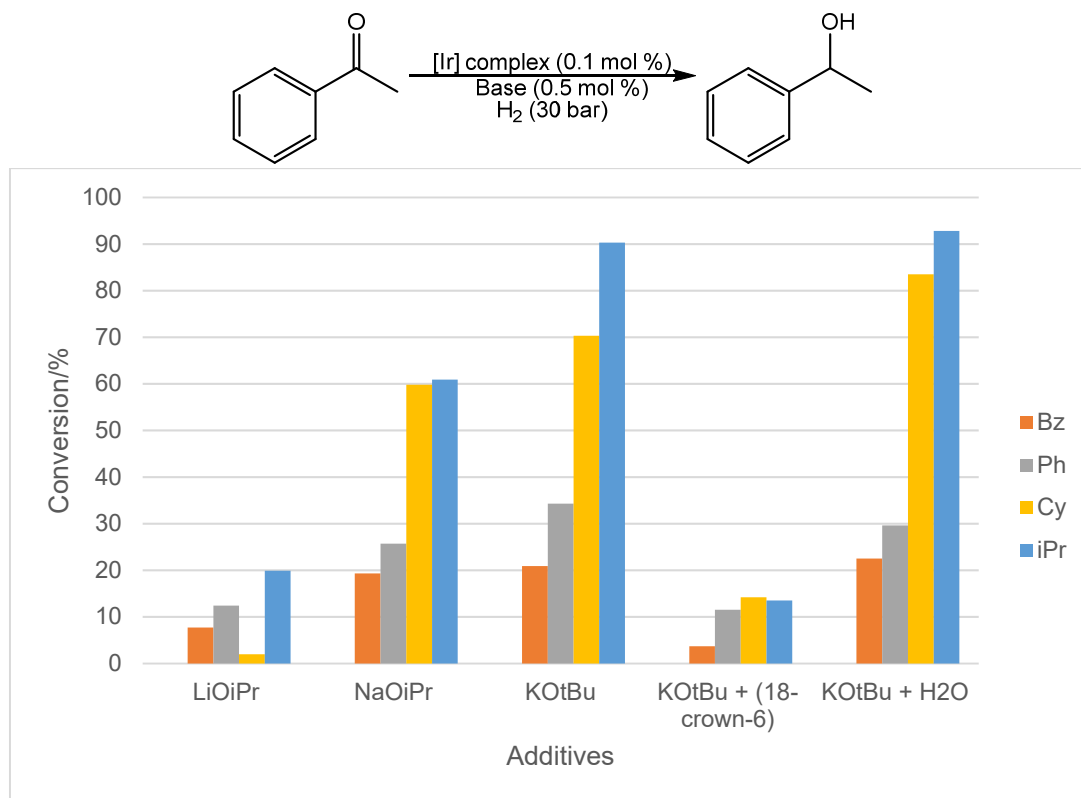
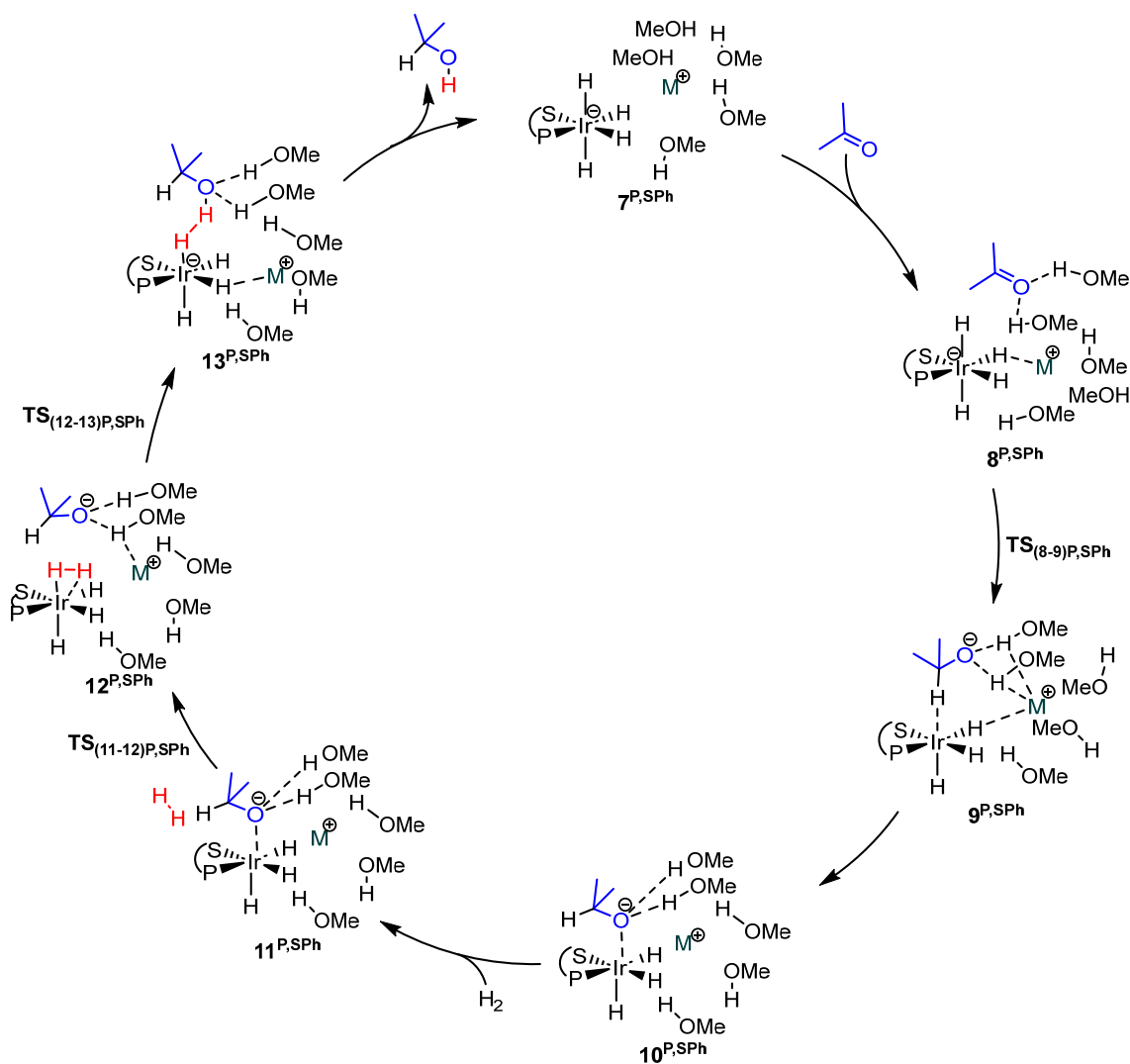


**Figure 12.** Results of the asymmetric hydrogenation of acetophenone with  $[\text{IrCl}(\text{COD})(\text{P},\text{S}^{\text{R}})]$  complexes. All catalysts show a preference for *S*-phenyl ethanol.

The proposition, made solely on the basis of DFT calculations in the same contribution,[4] that such a species is the Ir<sup>III</sup> tetrahydrido complex M<sup>+</sup>[IrH<sub>4</sub>(P,S<sup>R</sup>)], has found strong support by the observed formation of the related (and more stable) K<sup>+</sup>[IrH<sub>4</sub>(dppe)]<sup>-</sup> from [IrCl(COD)(dppe)] in isopropanol and KO<sup>t</sup>Bu under hydrogenation conditions (H<sub>2</sub> gas at 298 K) and even under transfer hydrogenation conditions (without H<sub>2</sub> at 353 K) [5]. This hypothesis is further supported by the DFT calculations carried out in this chapter, where the experimental trend of alkali metal cation-dependent activity has not only been reproduced but also rationalized, at the condition of using a fully explicit cation coordination sphere, M(MeOH)<sub>5</sub><sup>+</sup> (Scheme 10, Figure 13).



**Scheme 10.** Catalytic cycle of ketone hydrogenation catalysed by  $7^{S,Ph}$  proposed by DFT calculations ( $M = \text{Li}^+, \text{Na}^+, \text{K}^+$ ).

Intriguingly, the activity does not appear to depend on any activating effect by the cation on either the ketone substrate or the iridium hydride species, but rather on the coordination sphere rearrangement at the alkali metal cation when, in the turnover-determining transition state, the incipient alkoxide establishes a bond with the alkali metal cation, replacing one or more alcohol molecules (Figure 13).

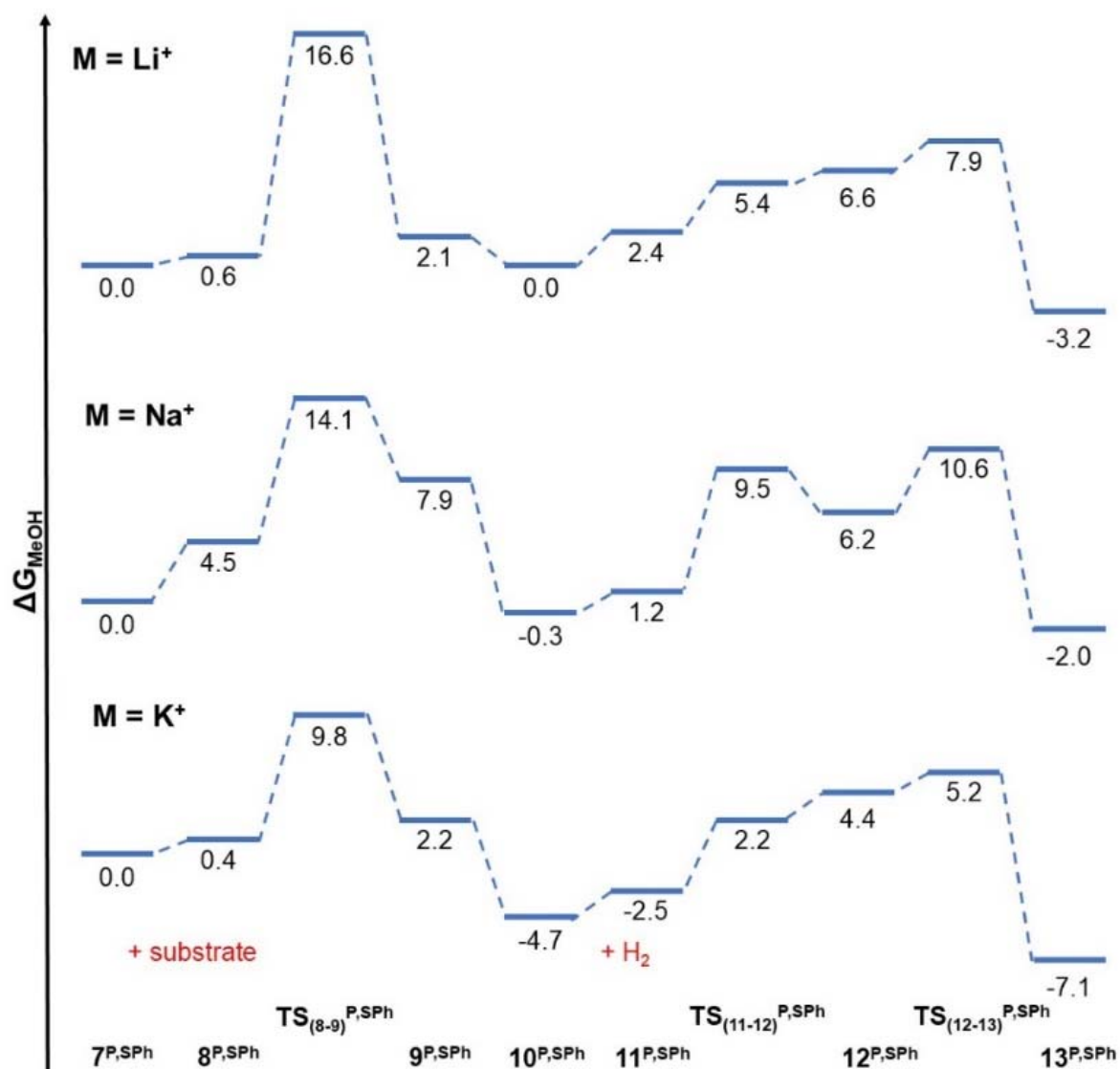


**Figure 13.** Computed Gibbs energy profiles for the hydrogenation of acetone with  $7^{P,SPH}$ . All energy profiles in  $\text{kcal mol}^{-1}$ . The labels shown reference the cycle in Scheme 10.

These results indicate that the inclusion of explicit solvent molecules (and enough of them) in the DFT calculations is of paramount importance to allow the appropriate interpretation of certain effects that may be observed in catalytic cycles that involve anionic active species. Contrarily to the strong alkali cation effect on the catalytic activity, its influence on enantioselectivity is small. To understand the origin of this behaviour, DFT calculations have been performed on the enantio-determining hydride transfer step using the real prochiral acetophenone substrate while employing the  $(P,S^{Ph})$  ligand.

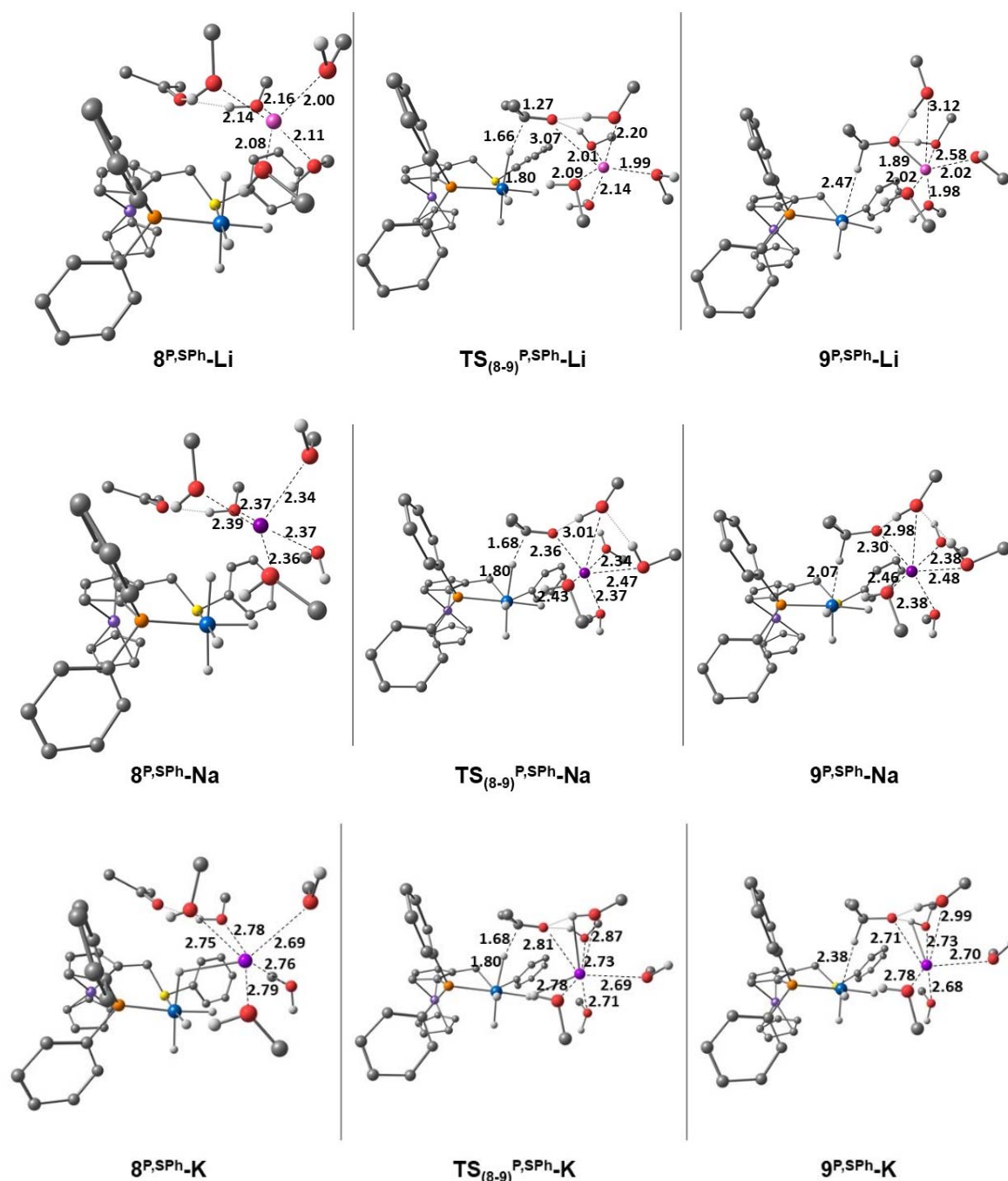


**Figure 14.** Optimized structures for the hydride transfer step for each of the three cations.  $\text{Li}^+$  (top),  $\text{Na}^+$  (middle),  $\text{K}^+$  (bottom). Distances shown are in Å. C-H hydrogen atoms have been omitted for clarity.

For this system, the *S* enantiomer of the ligand leads to a formation preference for the *S* enantiomer of the 1-phenylethanol product consistent with the experimental data, with all three alkali metal cations yielding essentially the same *ee*. The *pro-R* and *pro-S* transition states  $\text{TS}_{(7-8)}^{\text{dppe}}$  were computed for the three  $[\text{M}(\text{MeOH})_5]^+$  cations. Figure 15 shows the resulting transition state geometries, and important distances for each cation. The main interaction that discriminates between the two diastereomeric transition states involves a phenyl group of the phosphine ligand. This group interacts with the acetophenone methyl group (C-H- $\pi$ ) in the *pro-S* TS and with the acetophenone phenyl group ( $\pi$ - $\pi$ ) in the *pro-R* TS. The cation is in the less crowded space opposite to this key P-phenyl group. Consequently, the cation nature does not significantly alter the main interactions that govern



the *ee*. The calculated  $X_{\text{Ph}} \cdots \text{HC}_{\text{Me}}$  and  $X_{\text{Ph}} \cdots X_{\text{Ph}}$  distances for all computed systems, together with the Gibbs energy difference between both transition states ( $\Delta\Delta G_{\text{R-S}}$ ) has been found. The geometrical parameters describing the substrate-ligand interaction are very similar in all cases, in agreement with the limited influence of the cation on enantioselectivity.

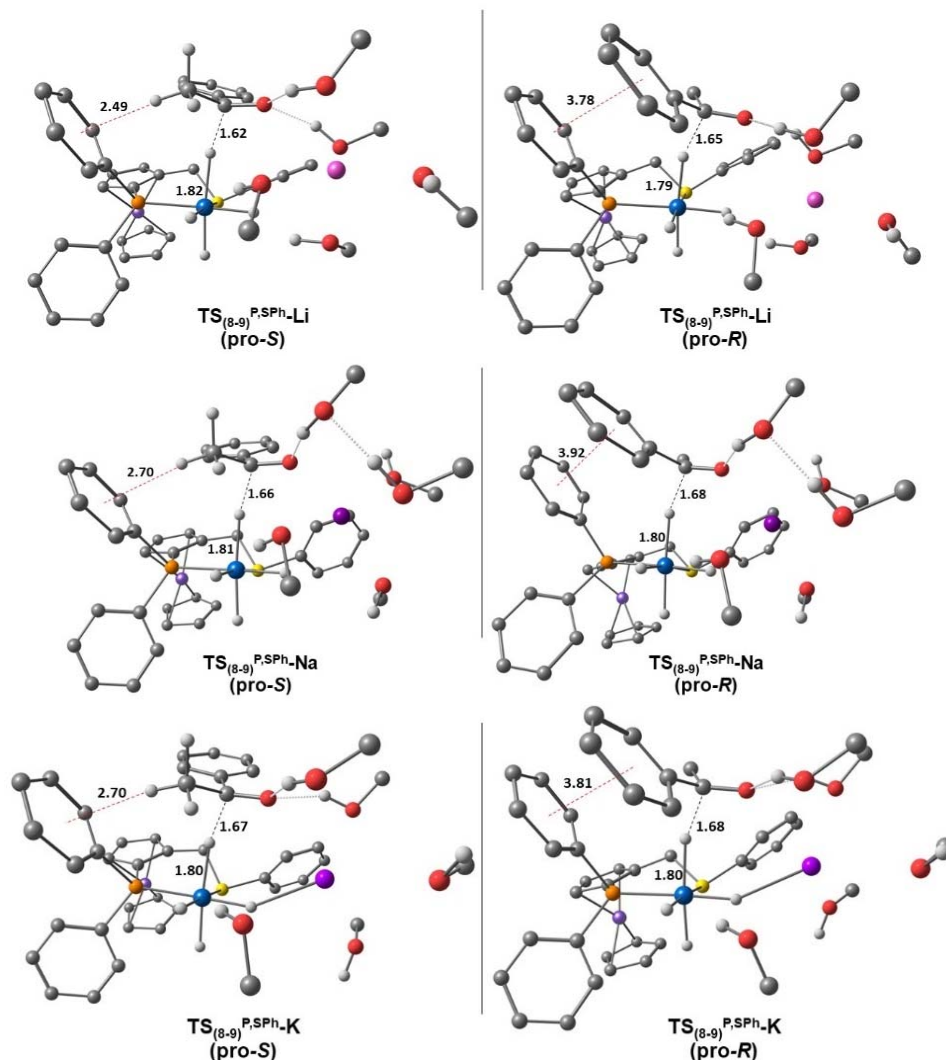


**Figure 15.** *pro-S* and *pro-R* transition states for hydride transfer to acetophenone, in presence of each cation. Distances in Å.

## Conclusion

Transfer hydrogenation catalysts are important in the synthesis of fine chemicals. Previous work has shown that a base is often necessary to achieve high activities for the asymmetric hydrogenation of polar substrates. New mechanistic views for such systems have emerged to account for the activity of such systems in which the ligand does not actively participate in proton donation which nevertheless need a strong base for activity. In this work, the role of the base in the associated chemistry of  $[\text{IrCl}(\text{COD})(\text{L}_2)]$  ( $\text{L}_2 = \text{dppe}, \text{dppf}, (S)\text{-BINAP}, \text{P}, \text{S}^{\text{IPr}}, \text{P}, \text{S}^{\text{Bz}}, \text{P}, \text{S}^{\text{Ph}}, \text{P}, \text{S}^{\text{Cy}}, (\text{P}, \text{S}^{\text{R}} = \text{CpFe}[1,2\text{-C}_5\text{H}_3(\text{PPh}_2)(\text{CH}_2\text{S}^{\text{R}})])$ ) systems was studied.

In the presence of an alkoxide with a  $\beta$ -hydrogen, two monohydride complexes of the form  $[\text{IrH}(\text{C}_8\text{H}_{12})(\text{dppe})]$  resulted from  $[\text{IrCl}(\text{COD})(\text{dppe})]$ , which interconvert and this was supported by complementary DFT studies which gave a similar result. When no  $\beta$ -hydrogen was present on the base,

two isomeric monohydride complexes were formed through COD deprotonation,  $[\text{IrH}(1-\kappa\text{-}4,5,6\text{-}\eta^3\text{-C}_8\text{H}_{10})(\text{dppe})]$ . DFT calculations were used to rationalize that the mechanism of interconversion proceeds *via* partial rotation of the cyclic  $\text{C}_8\text{H}_{10}$  ligand. These model complexes were transformed by heating in the presence of  $\text{KO}^t\text{Bu}$  (or  $\text{NaOMe}$ ) and isopropanol at  $80\text{ }^\circ\text{C}$ , to yield  $\text{M}[\text{IrH}_4(\text{dppe})]$  ( $\text{M} = \text{K}, \text{Na}$ ). Similar  $\text{Ir}^{\text{III}}$  products  $\text{M}[\text{Ir}(\text{H})_4(\text{L}_2)]$  ( $\text{L}_2 = \text{dppf}, (S)\text{-BINAP}$ ) were selectively generated from  $[\text{IrCl}(\text{COD})(\text{L}_2)]$  and demonstrated that anionic tetrahydrido iridium complexes can be formed under catalytically relevant conditions.

Finally, the alkali metal-dependent hydrogenation activity of these complexes towards benzophenone was examined. The active catalyst, generated *in situ* from  $[\text{IrCl}(\text{COD})]_2$  and  $(\text{P},\text{S}^{\text{R}})$  under  $\text{H}_2$  in the presence of a strong base was the solvated  $\text{M}[\text{Ir}(\text{H})_4(\text{P},\text{S}^{\text{R}})]$  salt. Their activity increased, for all R derivatives, in the order  $\text{Li} < \text{Na} < \text{K}$ . On the other hand, the nature of the cation did not affect the *ee*. DFT calculations revealed that the rate-determining barrier corresponds to outer-sphere hydride transfer and that the enantio-discriminating interactions are largely unaffected by the cation but rather through  $\pi\text{-}\pi$  interactions. It was found that the model used to describe the alkali-metal cation coordination sphere in the DFT studies is critical for reproducing the experimental results.

## References:

- [1] F. M. Chadwick, N. Olliff, A. S. Weller, *J. Organomet. Chem.* **2016**, *812*, 268–271. DOI: [10.1016/j.jorganchem.2015.12.001](https://doi.org/10.1016/j.jorganchem.2015.12.001).
- [2] R. C. Schnabel, P. S. Carroll, D. M. Roddick, *Organometallics* **1996**, *15*, 655–662. DOI: [10.1021/om950722c](https://doi.org/10.1021/om950722c)
- [3] R. C. Schnabel, D. M. Roddick, *Organometallics*, **1993**, *12*, 704–711. DOI: [10.1021/om00027a021](https://doi.org/10.1021/om00027a021).
- [4] J. M. Hayes, E. Deydier, G. Ujaque, A. Lledós, R. Malacea-Kabbara, E. Manoury, S. Vincendeau, R. Poli, *ACS Catal.* **2015**, *5*, 4368–4376. DOI: [10.1021/acscatal.5b00613](https://doi.org/10.1021/acscatal.5b00613).
- [5] P. Kisten, E. Manoury, A. Lledós, A. C. Whitwood, J. M. Lynam, J. M. Slattery, S. B. Duckett, R. Poli, *Dalton Trans.* **2023**, *52*, 2495–2505. DOI: [10.1039/D2DT04036K](https://doi.org/10.1039/D2DT04036K).



**Chantal J. ABOU-FAYSSAL**

**ESR9**

**Thesis co-directors**

Prof. Anders Riisager      Danmarks Tekniske Universtitet, Lyngby, Denmark

Dr. Eric Manoury,  
Dr. Karine Philippot      Laboratoire de Chimie de Coordination, Toulouse, France

**Thesis defense**

Department of Chemistry, Technical University of Denmark, 30 November 2023



## Metal Nanoparticles Embedded in Ligand- functionalized Water-soluble Core-shell Polymers for Application in Aqueous Biphasic Hydrogenation

### Introduction

The catalyzed transformation of organic compounds with metal nanoparticles (MNPs) [1] in micellar systems [2,3] combines the advantages of homogeneous and heterogeneous catalysis, including high activity, selectivity, and durability [4]. Nanocatalysis [5,6] with well-defined metal nanoparticle (MNPs) catalysts is a realm bridging homogeneous and heterogeneous catalysis. The nanoscale dimension of the catalysts provides distinctive properties not attainable with conventional, non-nanomaterials, thereby allowing for specific reactivity and advantageous properties, such as high efficiency, selectivity, stability, and ease of recovery/recycling [7–10]. In colloidal dispersions of ultrafine MNPs, surface energies and morphologies are influenced by the particle size leading to increased intrinsic surface reactivity [10]. For RhNPs multiple syntheses methods have been developed for size-control [11,12], including both methods based on the reduction of metal salts and the organometallic approach with the decomposition of Rh precursors. Typically, the size-control is achieved by employing various types of capping agents that prevent further growth of the RhNPs, whereas the following stabilization of the NPs in solution is ensured by the addition of stabilizing agents like *e.g.* surfactants (ammonium salts) [13–15], polymers [16–19], dendrimers [9] or ligands [12,20–26]. These stabilizers also facilitate good recyclability of the NPs when applied for catalysis. The MNPs provide a high surface-to-volume ratio resulting in a high number of potential catalytic sites [27], and the metal surface can be stabilized by appropriate ligands, similarly to molecular complexes. The confinement of MNPs inside a matrix (*e.g.* metal oxides, carbonaceous or polymeric materials) can further improve stability and catalytic performance. In particular, polymer-supported MNPs [26] have received significant attention in catalysis because of facile catalyst recovery and reuse. With such systems, using water as a solvent or dispersant phase yields aqueous biphasic systems [4,28,29] where simple phase separation facilitates catalyst recovery and recycling and allows reducing the use of volatile organic solvents and energy-intensive distillations, with a positive impact on the environment in the spirit of green chemistry. However, when the catalyst has low solubility in the organic reactant/product phase and the reactant has low solubility in water, the reaction may be limited to the organic/water interface and suffer from mass-transport restrictions. The use of surfactants or micellar systems can improve the mass-transport kinetics in biphasic aqueous/organic reactions by increasing the catalyst and substrate concentrations in the reaction zone [2,3,29,30]. Anchoring the catalyst in the hydrophobic cores of micelles permits to increase the local concentration of both catalyst and substrate and reduces the impact of mass transfer, provided the mass transport between the micellar cores and the bulk organic phase is facile. When the micelles are kinetically inert (slow exchange with the free surfactant in solution) or when they are rendered unimolecular by shell- or core-crosslinking, they operate as individual catalytic nanoreactors [31–33]. Some of us have developed synthetic protocols towards highly modular core-crosslinked micelles (CCMs) [34–41] as stable aqueous dispersions with a high polymer content (> 20 wt%), by reversible addition-fragmentation chain-transfer (RAFT) polymerization [42]. The first generation of CCMs displayed a neutral shell (CCM-N) made of random copolymer blocks of poly(ethylene oxide) (PEO) methacrylate and methacrylic acid [35]. Analogous CCMs with a polycationic shell (CCM-C) of homopolymer blocks

of 4-vinyl-*N*-methylpyridinium iodide (4VPMe<sup>+</sup>I<sup>-</sup>) were also prepared [36] (Figure 1).

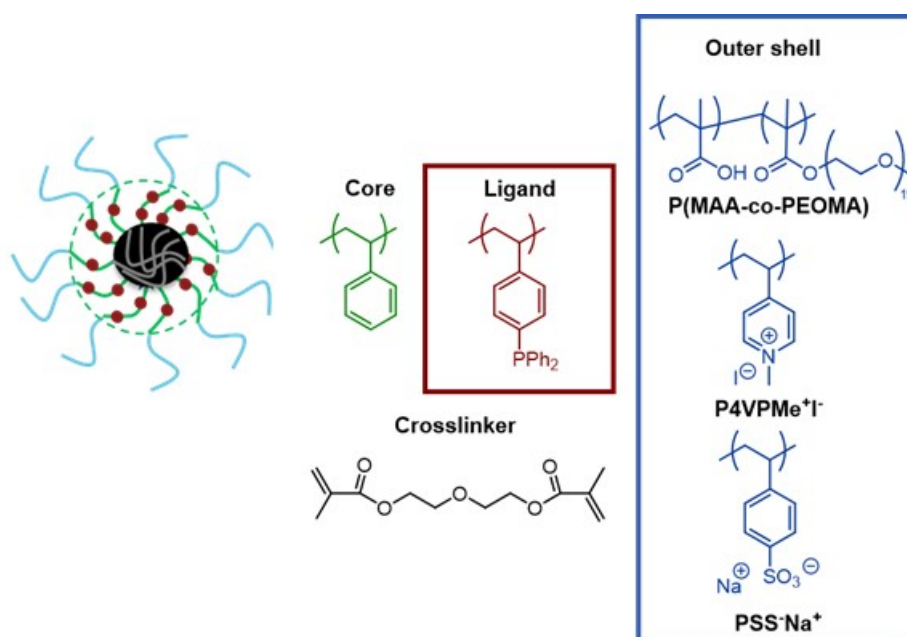


**Figure 1.** Cross-linked micelles functionalized with TPP (TPP@CCM) and various shells.

All the developed so far have a polystyrene-based core with diethylene glycol dimethacrylate (DEGDMA) as crosslinker, but have been functionalized with different core-linked ligands, providing L@CCM nanoreactors with L = triphenylphosphine (TPP) [34,37,40,43], bis(4-methoxyphenyl)phenylphosphine [33], nixantphos [35], and *N*-heterocyclic carbene [39]. Molecular pre-catalysts (*e.g.* [Rh(acac)(CO)<sub>2</sub>] or [Rh(COD)(μ-Cl)]<sub>2</sub>; acac = acetylacetonate, COD = 1,5-cyclooctadiene) were successfully fixated in the CCM cores by ligand coordination, generating catalytic nanoreactors for aqueous biphasic olefin hydroformylation [35,41,44,45] and hydrogenation [37,39,40].

### MNPs confined in CCM-C for application in aqueous biphasic hydrogenation catalysis

During investigations into substrate scope, where catalytic hydrogenation of acetophenone was attempted, the latex [RhCl(COD)(TPP@CCM-C)] turned black [40], suggesting the reduction of the molecular Rh<sup>I</sup> complex to Rh<sup>0</sup> metal. Retrospectively, this method proved highly effective in generating RhNPs within the cores of CCMs, prompting further investigations into biphasic hydrogenation involving RhNPs [35]. This objective was at the core of the current thesis project, specifically addressing significant challenges encountered in previous work. RhNP-TPP@CCM-C demonstrated excellent performance in the hydrogenation of 1-octene and styrene, with complete conversion and total selectivity towards the hydrogenation of the olefinic function. Notably, catalytic activity surpassed that of the Rh<sup>I</sup> molecular system. RhNP-TPP@CCM-C also proved recyclable for styrene hydrogenation over four cycles without loss of activity, with RhNPs remaining well dispersed when toluene was used for product recovery/catalyst recycling. However, when diethyl ether was used as the extraction solvent, a dramatic loss of activity was observed. This phenomenon was attributed to the extraction of RhNPs from the CCM-C core induced by diethyl ether, an oxygen-based solvent.

## Scope of the thesis work

The discovery described above of the formation of catalytically active RhNPs in the TPP@CCM-C system forms the basis of the research conducted in the context of this doctoral thesis. The overall objective of the research was to develop innovative solutions to enhance the confinement of MNPs, primarily RhNPs, in CCM-C, in order to achieve efficient, stable, and recyclable catalytic systems for biphasic aqueous liquid-liquid hydrogenation catalysis as the application domain. To achieve this goal, synthesis tools from CCM polymer chemistry and organometallic nanochemistry were combined, and several approaches to achieve the sub-objectives described below were explored. The main results of the research are presented in the following paragraphs. New syntheses of polymers incorporating TPPO ligands and polycationic shells were developed to improve the confinement of RhNPs with the aim of refining their activity, selectivity, and scope.

### Confinement of Rh nanoparticles in cross-linked micelles with functionalized triphenylphosphine oxide cores for aqueous biphasic hydrogenation catalysis

Based on the hypothesis presented in the previous section, new nanoreactors L@CCM with triphenylphosphine oxide (TPPO) ligands as central oxygen-based anchoring functions for RhNPs were developed. The following describes the synthesis and characterization of the new polymer latex TPPO@CCM-C, its loading with preformed RhNPs, and the application of the resulting nanoreactors RhNP-TPPO@CCM-C in the catalytic hydrogenation of styrene under aqueous biphasic conditions.

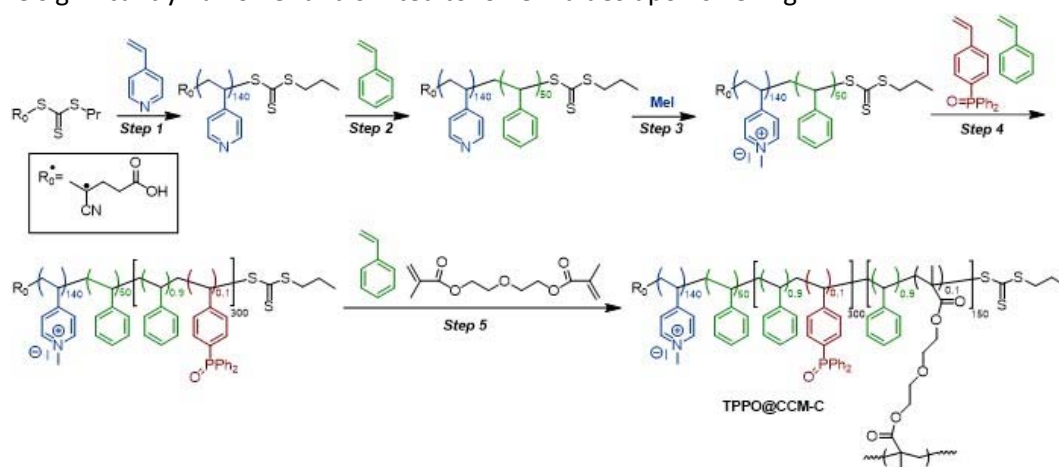
### Synthesis and characterization of the polymer

The synthesis of the new TPPO@CCM-C polymer was carried out following the same strategy used for the preparation of the closely related TPP@CCM-C polymer (Scheme 1). The target degrees of polymerization of each block were kept identical to those of TPP@CCM-C, as they were already optimized to provide stable latexes with a narrow particle size distribution [37,38]. Thus, the first three steps leading to the synthesis of the amphiphilic diblock macroRAFT agent,  $R_0-(VPMe^+I)_{140}-b-St_{50}-SC(S)SnPr$ , isolated as a stable solid and redispersed in water, were the same as in the TPP@CCM-C synthesis [38]. They involved the homogeneous RAFT polymerization of 4VP with CTPPA,  $R_0SC(S)SnPr$  where  $R_0 = CMe(CN)CH_2CH_2COOH$ , as transfer agent, forming  $R_0-4VP_{140}-SC(S)SnPr$  (step 1), then chain extension with a short polystyrene block (average degree of polymerization of 50) forming an  $R_0-VP_{140}-b-St_{50}-SC(S)SnPr$  diblock copolymer (step 2), and quaternization of the pyridine *N*-atoms with MeI (step 3).

The fourth step was a further chain extension of the  $R_0-(VPMe^+I)_{140}-b-St_{50}-SC(S)SnPr$  macroRAFT agent with a longer hydrophobic block (average degree of polymerization of 300) consisting of a statistical copolymer of styrene and a TPPO-functionalized styrene, namely SDPPO (4-styryldiphenylphosphine oxide) [33,46,47] (90/10 ratio), which was obtained by oxidation of SDPP with  $H_2O_2$ . This monomer has previously been homopolymerized [33,46,47] and copolymerized with styrene [48] and 9-(4-vinylphenyl)-9H-carbazole [49] by free radical polymerization, but not using the RAFT approach. All the polymerization steps were followed to completion (full consumption of monomers) by  $^1H$  NMR and the generated  $R_0-(VPMe^+I)_{140}-b-St_{50}-b-(St_{0.9}-CO-SDPPO_{0.1})_{300}-SC(S)SnPr$  amphiphilic macromolecules self-assembled in the form of micelles. The resulting latex remained well-dispersed over more than five months. The spherical micelles of the amphiphilic diblock copolymer



produced by step 4 had an average size of ca. 65 nm, as shown by DLS analysis (Figure 2a). These micelles were then crosslinked in a final step with DEGDMA (15 equiv. per chain), diluted with additional styrene (135 equiv. per chain), to yield the final product,  $R_0$ -(VPMe<sup>+</sup>I)<sup>-</sup><sub>140</sub>-*b*-St<sub>50</sub>-*b*-(St<sub>0.9</sub>-co-SDPPO<sub>0.1</sub>)<sub>300</sub>-*b*-(St<sub>0.9</sub>-co-DEGDMA<sub>0.1</sub>)<sub>150</sub>-SC(S)SnPr (TPPO@CCM-C), with a 10% crosslink density in the inner crosslinked core. The final TPPO@CCM-C polymer particles had spherical morphology and a slightly larger diameter (98.5 nm) than the intermediate micelles, as shown by DLS (Figure 2c) and TEM (Figure 2d) analyses. The size distribution became narrower and the  $D_z$  of the distribution was slightly reduced after swelling with CHCl<sub>3</sub>. This size reduction phenomenon upon swelling was also observed for related CCMs with an anionic shell (TPP@CCM-A) and was attributed to the dominant effect of micelles disaggregation rather than core swelling, which would cause an increase in average size [43]. Accordingly, the intensity profile in Figure 2b, which is more sensitive to the larger size micelles, became significantly narrower and shifted to lower values upon swelling.



**Scheme 1.** Synthesis route of the TPPO@CCM-C polymer.

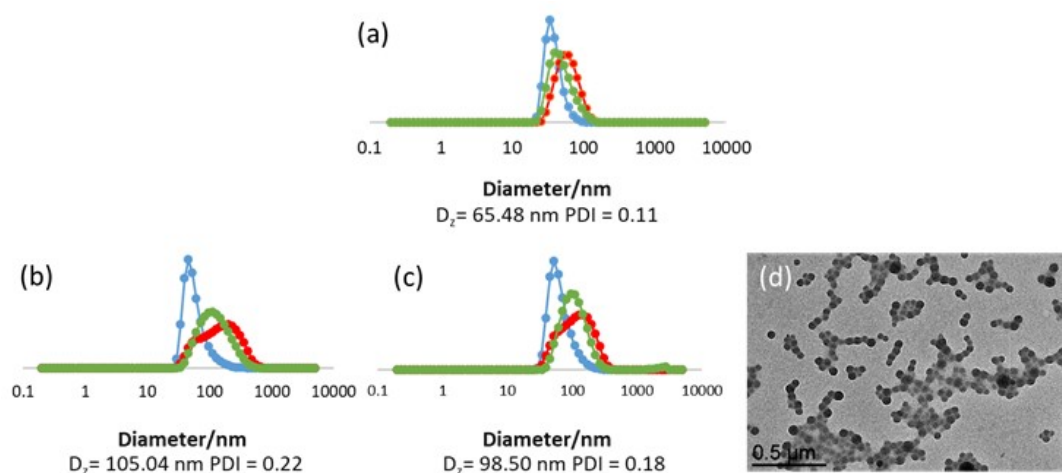


**Figure 2.** DLS size distributions of aqueous dispersions of (a) the diblock  $R_0$ -(VPMe<sup>+</sup>I)<sup>-</sup><sub>140</sub>-*b*-St<sub>50</sub>-*b*-(St<sub>0.9</sub>-co-SDPPO<sub>0.1</sub>)<sub>300</sub>-*b*-SC(S)SnPr micelles and of TPPO@CCM-C (b) before and (c) after swelling with CHCl<sub>3</sub>. Color coding: number (blue), volume (green) and intensity (red). d) TEM image of the TPPO@CCM-C.

### Synthesis of RhNP-TPPO@CCM-C

The first attempt to produce RhNP-TPPO@CCM-C consisted in loading the CCM-C with [Rh(COD)(μ-Cl)]<sub>2</sub>, in order to generate a core-anchored [RhCl(COD)(TPPO@CCM-C)] complex that could

be reduced to RhNPs by  $H_2$ , following the procedure previously developed to generate RhNPs embedded in TPP@CCM-C [40]. Mononuclear complexes with the  $[Rh(\eta^2:\eta^2\text{-diene})Cl(L)]$  stoichiometry (e.g. diene = COD, norbornadiene) where L is an O-atom donor ligand are rare [50–53], but the  $[RhCl(COD)(Ph_3PO)]$  complex has been described [54–56]. Nevertheless, this method proved unsuccessful as the organic phase was observed to remain yellow-colored, even after heating the reaction mixture at 60°C for 1 h or after stirring at room temperature for 24 h. This indicates that the formation of a Rh<sup>I</sup>-TPPO@CCM-C complex in the polymer core by cleavage of the di- $\mu$ -Cl-bridge moiety in  $[Rh(COD)(\mu\text{-Cl})_2]$  is not favorable under the applied conditions.

Therefore, an alternative strategy involving *ex-situ* synthesis of RhNPs and their subsequent transfer to the TPPO@CCM-C nanoreactors was considered. For this purpose, the RhNPs were produced by reduction of  $[Rh(COD)(\mu\text{-Cl})_2]$  with  $H_2$  in the presence of pyridine and TPP as stabilizing ligands. This ligand combination was inspired by previous reports, which showed TPP to be an effective stabilizer to produce ultrasmall RhNPs [12,20,26,57,58], while pyridine was used for the formation of RhNPs in ionic liquids [57]. The RhNPs synthesis was conducted in toluene, which has a high swelling power for the polystyrene-based CCM-C core [59]. The optimized conditions (TPP/Pyridine/Rh = 1/1/1, 60°C, 20 bar  $H_2$ , 20 h) led to a stable, black colloidal suspension of RhNPs, which displayed a mean diameter of  $1.2 \pm 0.4$  nm and a narrow size distribution (Figure 3).

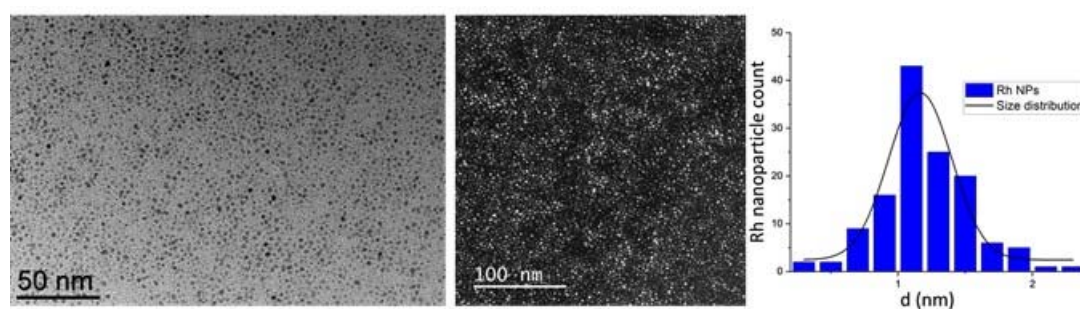


**Figure 3.** TEM images of RhNPs stabilized by TPP and pyridine (left) and the corresponding size distribution histogram ( $d_m = 1.2 \pm 0.4$  nm) (right).

The addition of the RhNPs colloidal suspension to the TPPO@CCM-C latex (P/Rh = 4/1) led to a fast and complete discoloration of the toluene phase while the latex became grey. This indicated the successful transfer of the RhNPs across the P(4VPM<sup>e+</sup>I) hydrophilic shell of the CCM-C and their anchoring to the TPPO functions in the polymer cores, which was corroborated by DLS and TEM characterization of the final RhNP-TPPO@CCM-C. The DLS analysis showed that the CCM-C polymer particles had very similar average size and size distribution before and after the loading with the RhNPs. The TEM analysis confirmed that the RhNPs were located inside the polymer particles and indicated an average size of ca.  $1.5 \pm 0.4$  nm. Despite the presence of the polymer that renders the measurement more difficult, it can be concluded that the RhNPs had quite similar sizes to the as-synthesized RhNPs. This result indicates that the RhNPs are not significantly altered by the ligand exchange in the CCM-C core.

### Hydrogenation of Styrene with colloidal suspension of RhNPs in toluene

The catalytic activity of the toluene colloidal suspension of TPP/pyridine-stabilized RhNPs was evaluated for the hydrogenation of styrene under mild reaction conditions (20 bar  $H_2$ , 25°C, 0.25 h)

with styrene/Rh = 10000/1. A styrene conversion of ~90% was observed, corresponding to a TOF of ~36900 h<sup>-1</sup> (cTOF of ~40700 h<sup>-1</sup>), with complete selectivity towards ethylbenzene (EB). This catalytic performance is superior to those previously described with RhNPs stabilized by TPP (TOF of ~6000 h<sup>-1</sup>) or diphosphate ligands (TOF of ~24000 h<sup>-1</sup>) under 40 bar H<sub>2</sub> in heptane at room temperature and 0.25 h [20]. The selectivity in favor of EB is not surprising, because previous investigations have underlined the tuneable properties of RhNPs [11,12,20–22] and the role of their size in controlling the selectivity of styrene hydrogenation. For instance, RhNPs with size in the 2-10 nm range exhibited a propensity for ring hydrogenation [60]. Conversely, selective hydrogenation to EB occurred under mild conditions using RhNPs with an average diameter of 1.5 nm [61], though benzene ring hydrogenation was observed under more forcing conditions. The dependence of reaction selectivities on the metal NP size has also been highlighted in other contributions [17,62–64].

### Hydrogenation with RhNP-TPPO@CCM-C latex under biphasic conditions

Next, the RhNP-TPPO@CCM-C latex was applied to the aqueous biphasic hydrogenation of styrene under the same temperature and pressure conditions as with the colloidal RhNPs suspension (20 bar H<sub>2</sub>, 25°C), with a styrene/Rh ratio of 2000/1, at different reaction times (Figure 4). Since styrene is a good solvent for polystyrene, no vectorizing solvent was needed and the hydrogenation was carried out with the neat substrate [37,40] using an agitation of 1200 rpm to ensure a good external mass transfer.

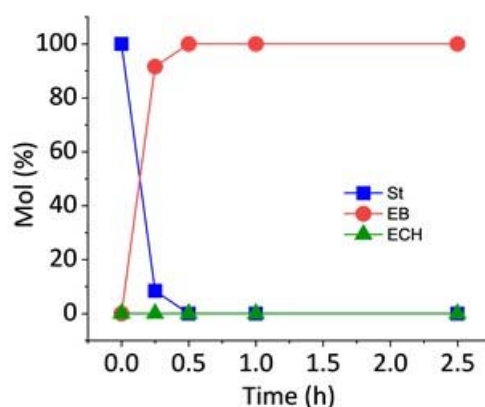


**Figure 4.** Time plot for the aqueous biphasic hydrogenation of styrene using RhNPs-TPPO@CCM-C. Reaction conditions: Styrene/Rh = 2000/1, 20 bar H<sub>2</sub>, 25°C.

A nearly complete styrene conversion (~94%) was obtained in only 0.25 h, corresponding to a TOF of 7733 h<sup>-1</sup> (cTOF of 9850 h<sup>-1</sup>), with an excellent selectivity (>99%) towards EB (Table 1, entry 1). This catalytic performance is superior to that previously achieved with RhNPs embedded in the TPP@CCM-C [20,21,40]. This difference may be related to the smaller size of the *ex-situ* synthesized TPP/pyridine-stabilized RhNPs used to get RhNP-TPPO@CCM-C compared to the *in-situ* synthesized TPP@CCM-C-stabilized RhNPs in RhNP-TPP@CCM-C (1.2 nm vs. < 5 nm). However, additional experiments indicated that the adsorbed TPP and pyridine stabilizers in the RhNP-TPPO@CCM-C catalyst also played a role (*vide infra*). An increase of the styrene/Rh ratio resulted in good and reproducible conversions within 0.25 h of 53% (styrene/Rh = 5000/1) and 24% (styrene/Rh = 10000/1), corresponding to TOFs of 10547 and 9062 h<sup>-1</sup> (cTOFs of 14300 and 12440 h<sup>-1</sup>), respectively, again with full selectivity towards EB (Table 1, entries 2 and 3). Upon stopping the stirring, a rapid phase

separation (< 3 min) was observed in all reactions, thus facilitating the product separation and catalyst recovery, as already reported for the RhNP-TPP@CCM-C nanoreactors featuring the same outer shell [40].

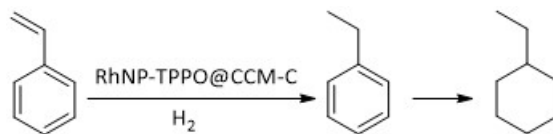


**Table 1.** Hydrogenation of styrene using RhNP-TPPO@CCM-C.<sup>a</sup>

Entry	Molar ratio of styrene/Rh	Conversion (%)	Product Yield (%)		TOF (h <sup>-1</sup> ) <sup>b</sup>
			Ethylbenzene	Ethylcyclohexane	
1	2000/1	94	94	<0.1	7733 (9850)
2	5000/1	53	52	<0.1	10547 (14300)
3	10000/1	24	23	<0.1	9062 (12440)

<sup>a</sup> Reaction conditions: 20 bar H<sub>2</sub>, 25 °C, 0.25 h. <sup>b</sup> Average values over the duration of the reaction, expressed as moles of substrate converted per moles of Rh in the catalyst per hour (TOF) or as moles of substrate converted per moles of surface Rh atoms per hour (cTOF, in parenthesis).

The recycling of the catalytic RhNP-TPPO@CCM-C latex was evaluated in two series of experiments at a fixed styrene/Rh ratio of 5000/1, by extracting the reaction products with diethyl ether or toluene, respectively, prior to the addition of a new batch of substrate for the next catalytic run. The extraction protocol was identical to that used in the previously reported recycling studies with the RhNP-TPP@CCM-C [40] and with the molecular Rh<sup>I</sup>-TPP@CCM [37] catalytic systems. The first catalytic runs yielded styrene conversion of 53% in 0.25 h. However, a gradual decrease in conversion, from 53% to *ca.* 9-15%, was witnessed after the fifth run for both series of recycles, using either toluene or diethyl ether for product extraction (Figure 5a). The ICP-MS analyses showed only a cumulative loss of ~2% of the catalyst inventory after the five catalytic runs when using diethyl ether as extraction solvent, indicating that the activity decrease was not caused by metal leaching and mechanical loss of latex. Moreover, after catalyst separation, whether toluene or diethyl ether was used as the extraction solvent, the organic phase was completely transparent and colorless while the aqueous phase remained grey, thus indicating the retention of the RhNPs in the CCM-C latex. In both cases, the TEM images obtained for the RhNP-TPPO@CCM-C catalyst after the fifth run evidenced a preserved confinement of the RhNPs in the CCM-C cores with well dispersed RhNPs. These results indicate that the interaction of the RhNPs with the core-linked TPPO ligands is sufficiently strong to retain them within the hydrophobic CCM-C cores, validating the initial hypothesis of the superior efficiency of oxygen-coordinating ligands. Though an artifact cannot be ruled out due to the less defined polymer-embedded RhNPs, a notable change was an increase of the particle size (from 1.5 ± 0.4 nm to 2.2 ± 0.9 nm after the fifth catalytic run). This may indicate a slight growth or aggregation of the NPs. However, given that the standard deviation value is larger than the size change (0.9 nm vs. 0.7 nm), the NPs can also be considered as to be in a similar size range, thus the interpretation of the activity drop as a result of a size change does not appear satisfactory.

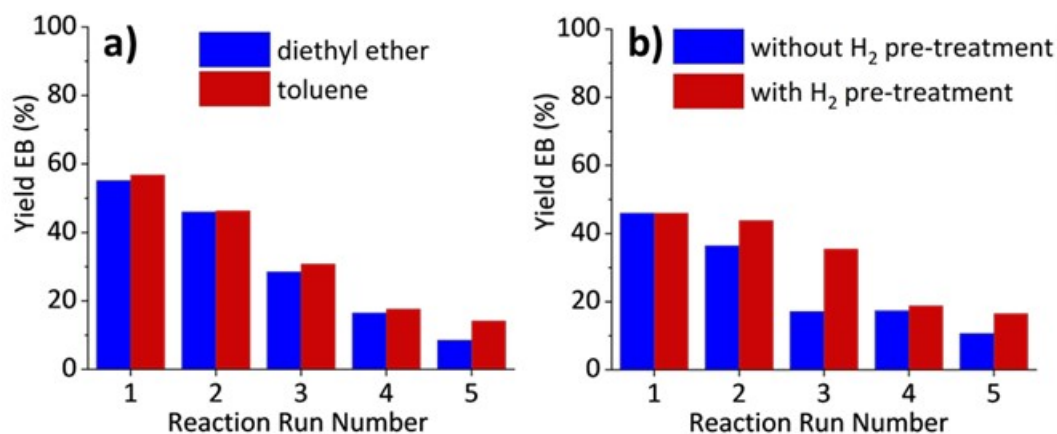


**Figure 5.** Reuse of RhNP-TPPO@CCM-C in five catalytic reactions of styrene hydrogenation (a) with intermediate product extraction by diethyl ether (blue) and toluene (red), (b) with product extraction by diethyl ether under argon with and without intermediate treatment with H<sub>2</sub> (20 bar H<sub>2</sub>, 25°C, 1 h). Reaction conditions: styrene/Rh = 5000/1, 20 bar H<sub>2</sub>, 25°C, 0.25 h.

Given that no significant metal leaching was detected and that no substantial NP agglomeration that may lead to loss of active surface was observed, progressive passivation of the RhNPs surface by rhodium oxide formation could be responsible for the decrease in catalytic performance over subsequent recycles. To verify this hypothesis, the catalyst recycling with product extraction by diethyl ether was completed under an inert argon atmosphere. In addition, the recovered RhNP-TPPO@CCM-C phase was treated with H<sub>2</sub> (20 bar H<sub>2</sub>, 25°C, 1 h) prior to each catalytic run, to remove any rhodium oxide layer. Despite these precautions in the recycling experiments, the styrene conversion still decreased to 10% along the five runs (Figure 5b). The similarity of these results to those achieved without inert atmosphere and reductive treatment (Figure 5a), suggests that passivation of the RhNPs was not the unique reason behind the decrease in the activity. A reduction of the anchoring TPPO ligands to TPP by H<sub>2</sub>, catalyzed by the RhNPs, is another possible hypothesis to explain the observed activity decrease, assuming a lower activity for RhNP-TPP relative to RhNP-TPPO. To assess this hypothesis, a toluene solution of TPPO- and TPP/pyridine-stabilized RhNPs (TPPO/Rh = 8/1) was exposed to H<sub>2</sub> (20 bar) at 60°C for 22 h. A <sup>31</sup>P NMR monitoring of the solution revealed no detectable TPPO reduction. This result seems to indicate that the TPPO ligands in the CCM-C core most likely remained unchanged under the conditions of the aqueous biphasic styrene reduction catalysis. The absence of TPPO reduction to TPP is also indirectly indicated by the demonstrated ability of diethyl ether to extract the RhNPs from the RhNP-TPP@CCM-C [40] whereas the TEM analysis shows that the RhNPs are well-retained in the micellar core. A final working hypothesis is that the stabilizers used for the *ex-situ* synthesis of RhNPs (TPP/pyridine) partially remained in the TPPO@CCM-C core after loading and promoted the catalytic activity of the RhNPs, and that the activity gradually decreased as these stabilizers/promoters were continuously washed out during the work-up for catalyst recovering and recycling. This hypothesis was tested by washing the fresh RhNP-TPPO@CCM-C latex, after RhNPs loading, three times with diethyl ether prior to use in catalysis. A GC-MS analysis of the diethyl ether extracts showed two peaks with MS spectra yielding molecular ions at *m/z* 112 and 83, respectively. These peaks match cyclooctane and tetrahydropyridine, respectively, resulting from the hydrogenation of the COD ligand from [Rh(COD)(μ-Cl)]<sub>2</sub> and of pyridine during the *ex-situ* synthesis of the RhNPs [11,22,61]. Subsequently, five subsequent catalytic runs (all reproduced three times) were carried out (20 bar H<sub>2</sub>, 25°C, 1 h) (Figure 6). The first catalytic run provided a low conversion of styrene

(~6%), whereas a constant styrene conversion of *ca.* 25% was achieved in the following four runs, corresponding to an average TOF of  $\sim 1025 \text{ h}^{-1}$  (cTOF  $\sim 1440 \text{ h}^{-1}$ ). The low conversion in the first run might indicate that an induction time would be necessary to deblock the active sites and/or the RhNPs experienced significant changes under catalytic conditions. Comparison of a series of TEM measurements performed with the diethyl ether-washed catalyst (prior to catalysis) before/after  $\text{H}_2$  treatment and after the first and fifth catalytic runs (Fig. S10), confirmed that the RhNPs mean size indeed changed from  $4.2 \pm 0.2 \text{ nm}$  to  $2.2 \pm 0.2 \text{ nm}$  before and after  $\text{H}_2$  treatment, respectively, and was further reduced to a static size of  $1.8 \pm 0.1\text{-}0.3 \text{ nm}$  after the first catalytic run. Thus, the removal of the stabilizers likely induced a slight size increase or agglomeration of the RhNPs, resulting in lower catalytic activity, as also previously reported for RhNPs in styrene hydrogenation [38,47], while the successive  $\text{H}_2$  treatment prompted reconstruction of the NPs possibly aided by the presence of TPPO@CCM-C. Notably, although a different reaction time was applied (1 h vs. 0.25 h), the styrene conversion value of *ca.* 25% obtained after the initial run is comparable to that obtained in the fourth and fifth recycles performed with intermediate product extraction by diethyl ether (Figure 6). This suggests that the diethyl ether washings performed between the consecutive catalytic runs (Figure 5) have a similar effect to those carried out on the fresh RhNP-TPPO@CCM-C prior to its implementation in catalysis. This indicates a possible role of the RhNP stabilizers (TPP, pyridine and tetrahydropyridine, see GC-MS results above) on the hydrogenation of styrene when they are not eliminated by solvent washings [66–69]. It is also to be noted that, as shown above, the RhNP-catalyzed styrene hydrogenation in toluene yields a much higher TOF for the RhNPs stabilized by TPP and pyridine ( $\sim 36000 \text{ h}^{-1}$ ) with respect to other RhNPs synthesized using other stabilizers, under similar experimental conditions [58]. This highlights that a careful choice of stabilizers to pre-synthesized RhNPs for their transfer in the CCM-C, or the integration of co-ligands in the cores of CCM-C could be a way to boost the catalytic performance, but this is out of the scope of the present work.

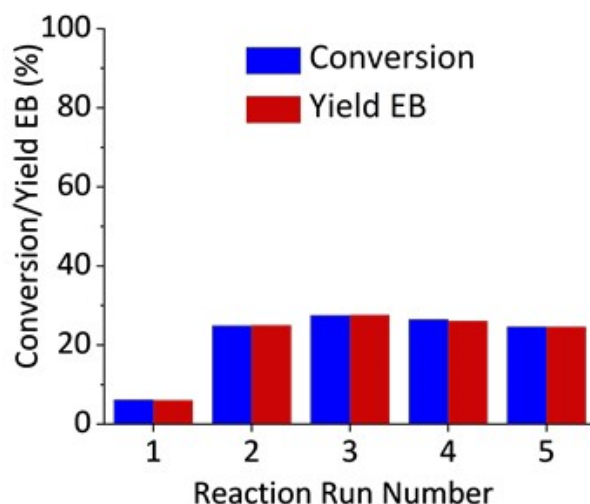


**Figure 6.** Hydrogenation of styrene with RhNP-TPPO@CCM-C after three washings with diethyl ether (run 1) and recycling of the catalyst in four additional reaction runs with product extraction by diethyl ether and intermediate  $\text{H}_2$  treatment (20 bar  $\text{H}_2$ , 25°C, 1 h). Reaction conditions: Styrene/Rh = 5000/1, 20 bar  $\text{H}_2$ , 25°C, 1 h.

### Aqueous biphasic hydrogenation with Rh nanoparticles synthesized in a single step within micelles with a polycationic shell and a cross-linked core functionalized with triphenylphosphine oxide

Given the previous results, a new one-step synthesis approach is described for the RhNP-TPPO@CCM-C catalyst, which does not require the use of additional stabilizers. The resulting catalyst has been carefully characterized and applied in the aqueous biphasic hydrogenation of styrene, as well as other selected substrates such as alkenes, alkynes, and carbonyl compounds.

#### One-pot synthesis and characterization of RhNP-TPPO@CCM-C

RhNPs embedded in the hydrophobic cores of a stable latex of TPPO@CCM-C were synthesized in a single step by heating a biphasic mixture containing the aqueous TPPO@CCM-C latex and a toluene solution of  $[\text{Rh}(\text{COD})(\mu\text{-Cl})_2]$  under  $\text{H}_2$  pressure. This could be performed without any additional stabilizer or base additive (Table 2, Entry 1) and without the need for a preliminary *ex-situ* synthesis of the RhNPs (as previously reported [70]). Comparative syntheses were also carried out in the presence of a base such as pyridine or  $\text{NEt}_3$  (Table 2, Entries 2 and 3, respectively), which can assist the reaction by trapping the HCl produced during the reduction of  $\text{Rh}^{\text{I}}$  to  $\text{Rh}^0$ , in addition to potentially contribute to the RhNP stabilization [40,70]. After the synthesis and phase separation, all three produced RhNP-TPPO@CCM-C latexes were black, signaling the successful formation and confinement of RhNPs in the core of the CCMs.

**Table 2.** Synthesis of RhNP-TPPO@CCM-C.<sup>a</sup>

Entry	Base	Molar TPPO/Rh/Base ratio	RhNPs average size (nm)	
			Before catalysis	After catalysis
1	-	4/1/0	$1.7 \pm 0.2$	$1.9 \pm 0.6$
2	Pyridine	4/1/4	$2.9 \pm 0.6$	$3.1 \pm 0.1$
3	$\text{NEt}_3$	4/1/4	$2.1 \pm 0.1$	$1.8 \pm 0.2$

<sup>a</sup>Reaction conditions: 20 bar  $\text{H}_2$ , 20 h, 60 °C, toluene, 1200 rpm.

TEM analyses confirmed the successful incorporation of the RhNPs in the TPPO@CCM-C in all cases (Figure 7). The RhNPs synthesized without base (Entry 1) showed a particularly narrow size distribution with a mean diameter ( $d_m$ ) of  $1.7 \pm 0.2$  nm. On the other hand, the RhNPs produced in the presence of pyridine or  $\text{NEt}_3$  (Table 2 Entries 2 and 3, respectively), were found agglomerated and with slightly larger average diameters ( $d_m = 2.9 \pm 0.6$  nm and  $d_m = 2.1 \pm 0.1$  nm, respectively, Figure 7).

When using only molecular TPPO (*i.e.* not linked to the CCM support) as a stabilizer under the same reaction conditions (toluene, TPPO/Rh = 4/1, 20 bar of  $\text{H}_2$ , 60 °C, 1200 rpm, for 20 h) and no base additive, a black colloidal suspension of RhNPs was also obtained. These RhNPs were also found to have a slightly larger average diameter ( $d_m = 2.4 \pm 0.2$  nm) than those embedded in the TPPO@CCM-C latex obtained without a base and were relatively well dispersed (Figure 8).

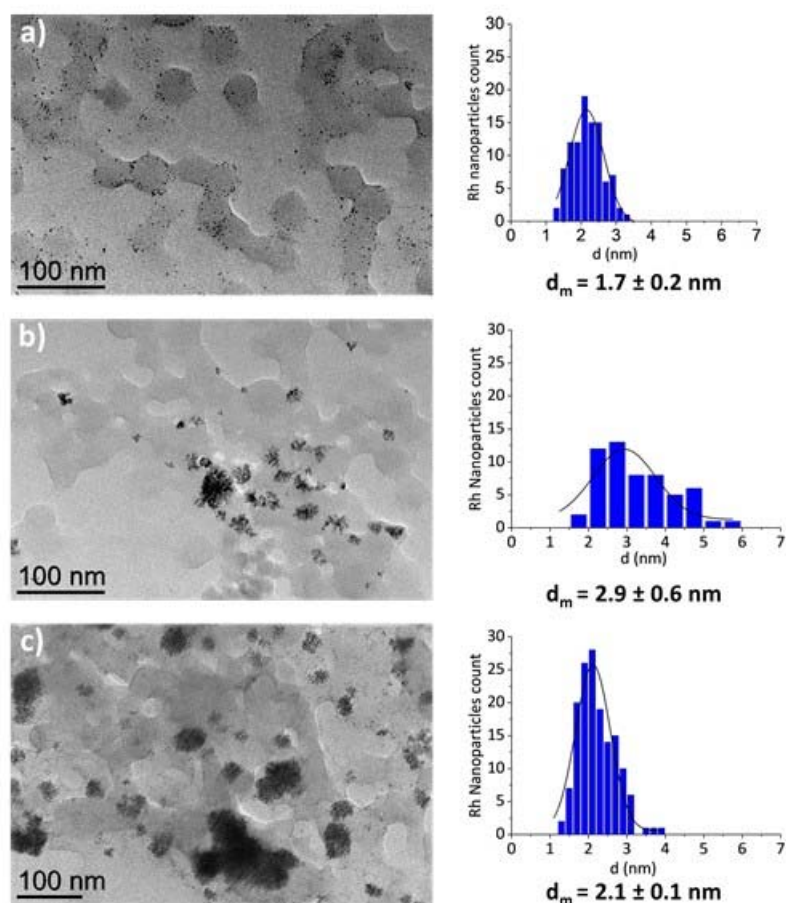


**Figure 7.** TEM images of the three one-pot-synthesized RhNP-TPPO@CCM-C latexes (left), and corresponding RhNP size distribution (right), obtained (a) without base, (b) with pyridine and (c) with  $NEt_3$ .

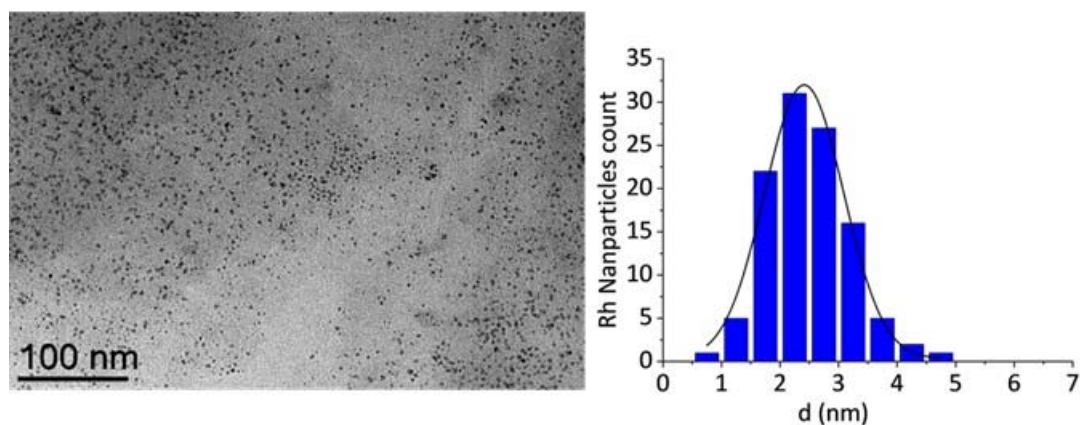


**Figure 8.** TEM image of RhNPs obtained using only molecular TPPO as a stabilizer (TPPO/Rh = 4/1) with the corresponding size distribution ( $d_m = 2.4 \pm 0.2$  nm). Reaction conditions: toluene solution, 20 bar  $H_2$ , 60 °C, 20 h.

Furthermore, when treating a  $[Rh(COD)(\mu-Cl)]_2$  solution in toluene under an  $H_2$  pressure in the absence of any polymer, stabilizer, and base, only large agglomerates were produced under the same reaction conditions (Figure 9).



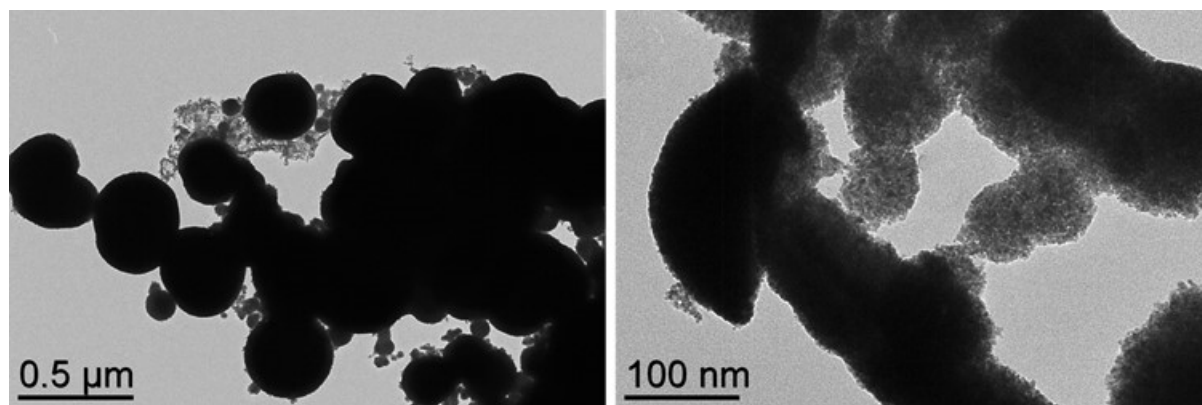


**Figure 9.** TEM image of Rh agglomerates generated in the absence of stabilizers. Reaction conditions: toluene solution, 20 bar  $H_2$ , 60 °C, 20 h.

The smaller size of the RhNPs in the TPPO@CCM-C obtained from the base-free one-pot procedure may result from a more efficient stabilization in the polymer, due to the combined interaction with the oxygen lone pairs of TPPO ligands in the CCM-C core and  $\pi$ -electrons of the phenyl groups in the styrene monomers. The confinement effect may also provide an improved rate of nucleation, resulting in a greater number of NPs and a consequent decrease in their average size [18,58,71–77]. In principle, the nucleation may predominantly occur either within the CCM cores or in the bulk toluene phase, followed by migration and anchoring within the CCM cores. Since small-sized NPs ( $d_m = 2.4 \pm 0.2$  nm) were generated in the presence of molecular TPPO in the toluene phase, even without base, whereas large agglomerates were generated in toluene without stabilizer, it seems likely that faster nucleation occurred within the CCM-C cores that contain TPPO ligands.

TG/DSC analyses of the TPPO@CCM-C and RhNP-TPPO@CCM-C polymers were further performed under  $N_2$  to examine their relative thermal stability (Figure 10). The TPPO@CCM-C sample showed an initial decomposition phase at 239 °C (ca. 20 wt.% loss), followed by a gradual weight loss at higher temperatures with a peak at 413 °C (total weight loss ca. 88 wt.%). The RhNP-TPPO@CCM-C sample, on the other hand, exhibited an initial degradation phase at a higher temperature (264 °C, ca. 50 wt.% loss) and a lower total weight loss (77 wt.%) with a second peak at 403 °C, suggesting an effect of the RhNPs on the decomposition of the Rh loaded polymer. The thermal stability of the RhNP-TPPO@CCM-C latex was insufficient to perform further investigations of the RhNPs active sites by conventional techniques such as carbon monoxide temperature-programmed desorption (CO-TPD), which requires high temperatures for the CO desorption [78,79] and may be affected by the polymer degradation.

To further corroborate the interaction between the polymer and the RhNPs, ATR-FTIR spectra of TPPO@CCM-C and RhNP-TPPO@CCM-C were compared to that of molecular TPPO (Figure 11). The strong P=O stretching band of TPPO ( $1182\text{ cm}^{-1}$ ) [80] was quite evident in TPPO@CCM-C, and a P=O signal was also visible in RhNP-TPPO@CCM-C, but this band was broad and redshifted ( $\sim 1180\text{--}1140\text{ cm}^{-1}$ ). This likely indicates that the P=O group is bound to the RhNP surface, as also previously observed for other metal-coordinated TPPO ligands [81,82].

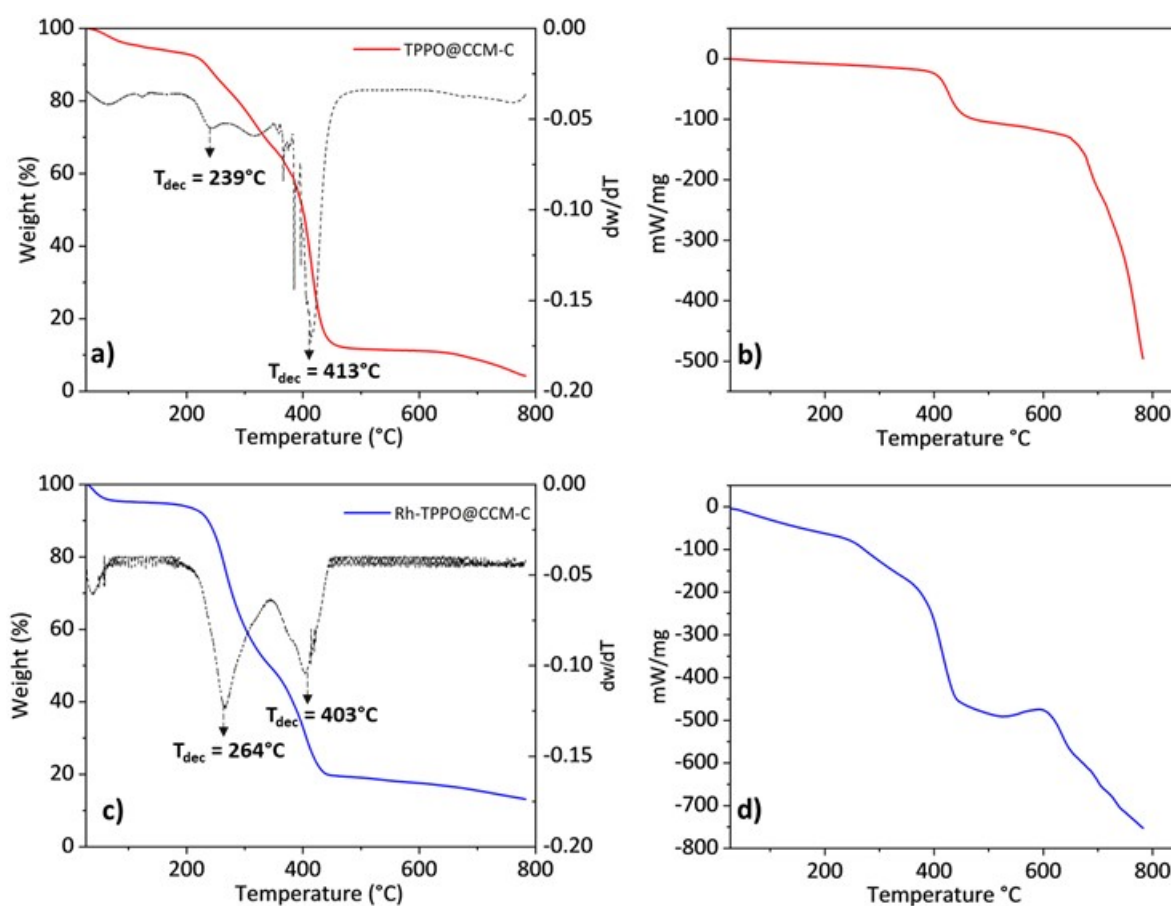


**Figure 10.** TGA (a,c) and DSC (b,d) profiles of TPPO@CCM-C (red, top) and RhNP-TPPO@CCM-C (blue, bottom).

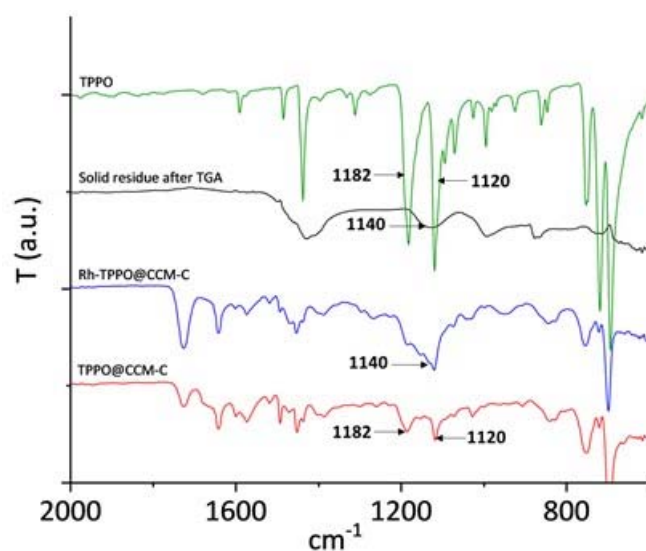


**Figure 11.** ATR-FTIR spectra of TPPO@CCM-C (red), RhNP-TPPO@CCM-C (blue), solid residue after TGA (black), and molecular TPPO (green), in the range of 700-2000  $\text{cm}^{-1}$ .

In line with this, XPS analyses performed on the TPPO@CCM-C and RhNP-TPPO@CCM-C systems indicated also a shift in binding energy in the presence of RhNPs in the core of the TPPO@CCM-C polymer, which is particularly notable for the O1s excitation ( $\Delta E = 0.58$  eV), further supporting the existence of RhNPs-polymer interactions in RhNP-TPPO@CCM-C.

### Aqueous biphasic hydrogenation with RhNP-TPPO@CCM-C

#### Hydrogenation of styrene without base additive

Using the RhNP-TPPO@CCM-C latex produced in the absence of base, an initial series of catalytic runs with different reaction times were carried out at 25 °C, 20 bar of H<sub>2</sub> pressure and stirring of 1200 rpm to limit external mass transfer, with a styrene/Rh ratio of 5000/1 (Figure 12). A complete conversion of styrene was reached after 2 h corresponding to an average TOF of 3000 h<sup>-1</sup> (cTOF 4300 h<sup>-1</sup>).

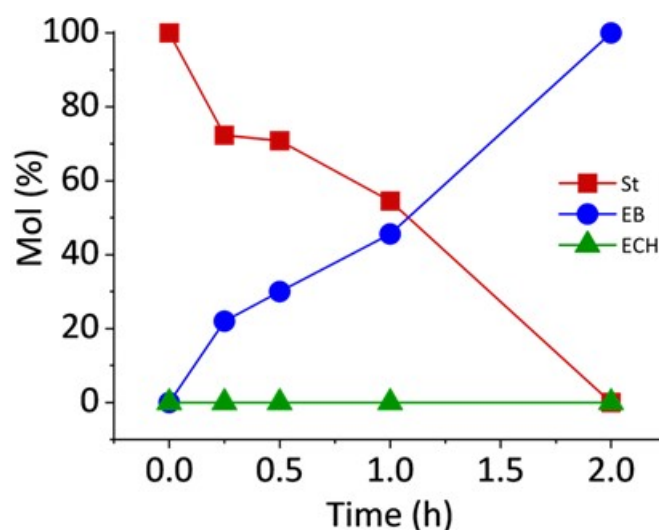


**Figure 12.** Time plot for the aqueous biphasic hydrogenation of styrene using RhNP-TPPO@CCM-C prepared without base. Reaction conditions: styrene/Rh = 5000/1, 20 bar H<sub>2</sub>, 25 °C, 1200 rpm.

Additional catalytic runs with a fixed reaction time of 0.25 h and different styrene/Rh ratios yielded the results reported in Table 3, Entries 1-3. The system showed excellent selectivity (>99%) towards the formation of ethylbenzene (EB) with formation of only trace amounts of the fully saturated product ethylcyclohexane (ECH), as also previously described for styrene hydrogenation using other RhNP-CCM catalysts [40,70]. Moreover, phase separation was fast in all reactions (< 3 min), facilitating product separation and catalyst recovery, as already observed for other aqueous biphasic applications of nanoreactors featuring the same outer shell (CCM-C) [37,40,70].

Hydrogenation of styrene was also performed with the same RhNP-TPPO@CCM-C latex at higher temperatures (30 °C-55 °C) with a styrene/Rh ratio of 5000/1 (Table 3, Entries 4-7). At 55 °C, a conversion of 83% could be obtained after 0.25 h, yielding a very high average TOF of 16100 h<sup>-1</sup> (cTOF 23600 h<sup>-1</sup>).

The more moderate conversions obtained in the 25-35 °C range allowed to estimate an apparent reaction activation energy ( $E_a$ ) of  $69 \pm 6$  kJ/mol from an Arrhenius plot (Figure 13) which is comparable to the  $E_a$  obtained for the gas-phase hydrogenation of styrene [83]. However, at higher reaction temperatures the apparent  $E_a$  decreased to  $4 \pm 1$  kJ/mol, indicating diffusion limitations (internal mass transfer).

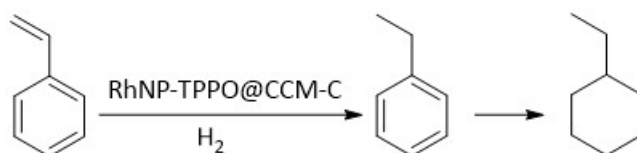


**Table 3.** Hydrogenation of styrene using RhNP-TPPO@CCM-C prepared without base.<sup>a</sup>

Entry	Molar styrene/Rh ratio	T (°C)	Conversion (%)	Selectivity (%)		TOF (cTOF) <sup>b</sup> (h <sup>-1</sup> )
				EB	ECH	
1	2000/1	25	82	>99	<0.1	7800 (11500)
2	5000/1	25	21	>99	<0.1	4500 (6500)
3	10000/1	25	8	>99	<0.1	3000 (4450)
4	5000/1	30	35	>99	>0.1	8000 (11600)
5	5000/1	35	58	>99	<0.1	11200 (16400)
6	5000/1	45	65	>99	<0.1	12900 (19000)
7	5000/1	55	83	>99	<0.1	16100 (23600)

<sup>a</sup> Reaction conditions: 20 bar H<sub>2</sub>, 25 °C, 0.25 h, 1200 rpm. <sup>b</sup> Corrected TOF (cTOF) calculated by considering only the surface Rh atoms (see Experimental Part). EB: ethylbenzene, ECH: ethylcyclohexane.

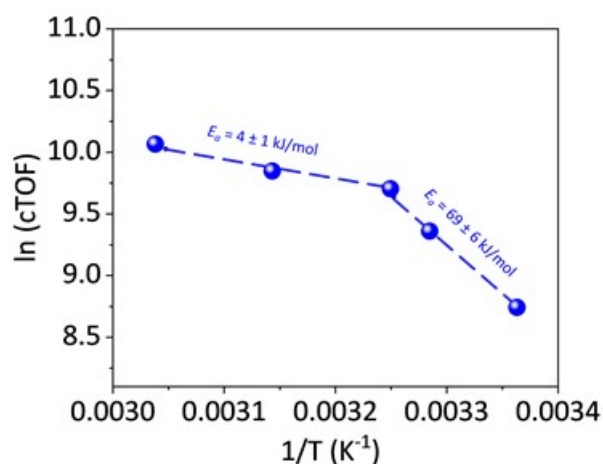


**Figure 13.** Arrhenius plot of the hydrogenation of styrene using RhNP-TPPO@CCM-C prepared without base. Reaction conditions: styrene/Rh = 5000/1, 20 bar H<sub>2</sub>, 0.25 h, 1200 rpm, accuracy of temperature measured with  $\pm 0.5$ -1 °C.

The RhNP-TPPO@CCM-C latex recycling was further evaluated for a series of runs with a styrene/Rh ratio of 5000/1 and 0.25 h of reaction time with intermediate product extraction by diethyl ether (Figure 14). The extraction procedure was similar to that previously applied to recycle the RhNP-TPPO@CCM-C and RhNP-TPPO@CCM-C latexes [37,40,70], as well as the latex of the molecular Rh<sup>I</sup>-TPPO@CCM [37,40]. A rather constant styrene conversion of ca. 21%, corresponding to an average TOF

of  $\sim 4500 \text{ h}^{-1}$  ( $c\text{TOF}$  of  $6500 \text{ h}^{-1}$ ), was obtained over the six consecutive reaction runs, but only when the recovered catalyst system was reactivated with  $\text{H}_2$  (20 bar, 1 h,  $25^\circ\text{C}$ ) prior to addition of new batch of substrate. A recycling experiment without this reactivation treatment gave erratic results, possibly because of passivation of the RhNPs by surface oxide layer formation during the work-up recycling procedures [58,65,70]. A TEM analysis (Figure 15) on the recovered latex after run six showed that the RhNPs remained well-dispersed, with a similar size distribution ( $1.9 \pm 0.6 \text{ nm}$ ) as prior to catalysis (see Table 2).

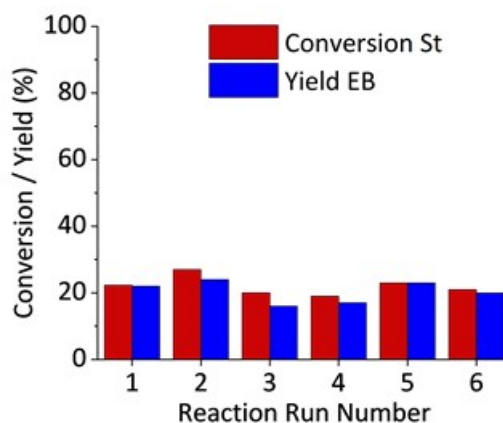


**Figure 14.** Reuse of RhNP-TPPO@CCM-C catalyst in six catalytic runs of styrene hydrogenation with product extraction by diethyl ether and intermediate  $\text{H}_2$  treatment (20 bar  $\text{H}_2$ ,  $25^\circ\text{C}$ , 1 h, 1200 rpm) and product extraction by diethyl ether. Reaction conditions: Styrene/Rh = 5000/1, 20 bar  $\text{H}_2$ ,  $25^\circ\text{C}$ , 0.25 h, 1200 rpm.

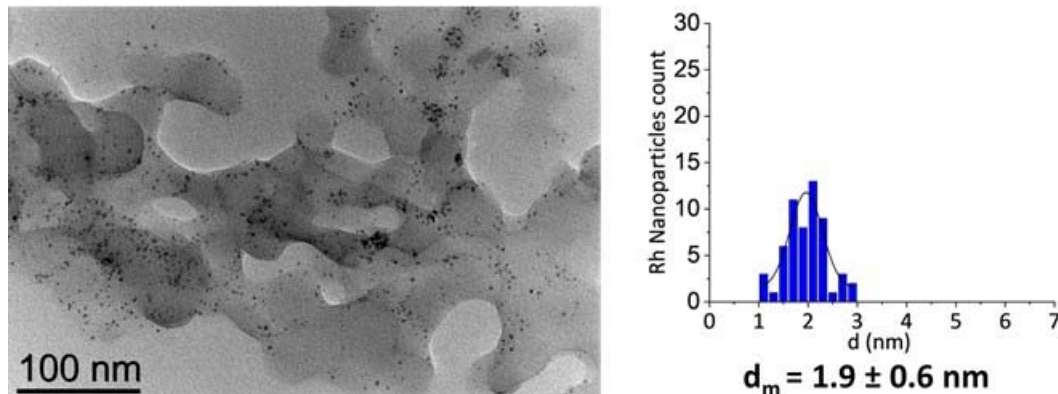


**Figure 15.** TEM image of RhNP-TPPO@CCM-C recording from an aliquot during recycling after run six (left) and corresponding size distribution ( $d_m = 1.9 \pm 0.6 \text{ nm}$ ) (right).

A reference hydrogenation experiment was carried out under the same conditions using a toluene phase of the TPPO-stabilized RhNPs as catalyst (20 bar of  $\text{H}_2$ ,  $25^\circ\text{C}$ , styrene/Rh = 10000/1, 0.25 h). This resulted in a styrene conversion of 53% (average TOF  $\sim 20000 \text{ h}^{-1}$ ,  $c\text{TOF}$   $21500 \text{ h}^{-1}$ ) with  $>99\%$  of EB selectivity. Using EB as substrate under the same reaction conditions yielded only 0.6% of ECH, confirming the high selectivity of the TPPO-stabilized RhNPs under these mild reaction conditions. The  $c\text{TOF}$  decreased from  $\sim 21500 \text{ h}^{-1}$  for the reaction carried out with the RhNP-TPPO/toluene catalytic system to  $\sim 6500 \text{ h}^{-1}$  for that conducted with the RhNP-TPPO@CCM-C/biphasic system, which indicate that the latter was influenced by internal mass transport restrictions of the styrene substrate and/or the EB product.

*Hydrogenation of styrene with base additive*

The RhNP-TPPO@CCM-C latexes obtained in the presence of pyridine (Table 2, Entry 2) or  $\text{NEt}_3$  (Table 2, Entry 3) were also evaluated for styrene hydrogenation, after extensive prewashing with diethylether prior to the first catalytic run (Figure 16).

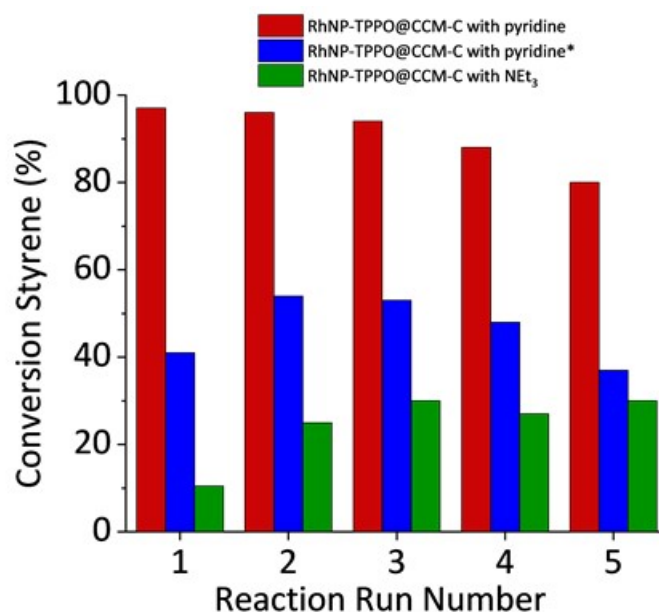


**Figure 16.** Reuse of the RhNP-TPPO@CCM-C latexes prepared with base additives in styrene hydrogenation with intermediate  $\text{H}_2$  treatment (20 bar  $\text{H}_2$ , 25 °C, 0.25 h, 1200 rpm) as well as product extraction by diethyl ether. Reaction conditions: Styrene/Rh = 5000/1 (\*6500/1), 20 bar  $\text{H}_2$ , 25 °C, 0.25 h, 1200 rpm.

When using the RhNP-TPPO@CCM-C latex prepared with  $\text{NEt}_3$ , the first catalytic run yielded a styrene conversion of ~10%, but the subsequent runs converged to a stable conversion of ca. 25-30%. Similar difference between the first and consecutive reaction runs were reported for the RhNP-TPPO@CCM-C latex obtained by transfer of *ex-situ* synthesized RhNPs [70] as well as other studies using  $\text{NEt}_3$  [58]. This can be explained by an induction time, possibly resulting from restructuring of the RhNPs surface under catalytic conditions which produced more catalytically active sites and consecutive higher conversion. On the other hand, the RhNP-TPPO@CCM-C latex prepared with pyridine showed much higher activity (conversion of ca. 97%), with an average TOF of  $\sim 18200 \text{ h}^{-1}$  (cTOF  $40000 \text{ h}^{-1}$ ) in the first run. However, the activity steadily decreased over the subsequent runs, most likely as a consequence of the continuous removal of adsorbed pyridine from the RhNPs surface during the successive recycling treatments that involve diethyl ether extractions. This result is analogous to that shown by the RhNP-TPPO@CCM-C latex obtained by incorporating the *ex-situ* synthesized RhNPs with stabilization by TPP and pyridine as stabilizers [70], and confirms that the presence of pyridine has a beneficial effect on the RhNPs catalytic activity, that might be due to a cleaner Rh surface as the result of less chlorides, present in the organometallic dimer, that may be better eliminated. The intimate reason for this promotion effect is currently unknown. Interestingly, when the catalyst recyclability was performed with a higher styrene/Rh ratio of 6500/1, the activity dropped in the first run (as expected) to an average TOF of  $\sim 10000 \text{ h}^{-1}$  (cTOF  $23000 \text{ h}^{-1}$ ), and the system proved less stable compared to the RhNP-TPPO@CCM-C synthesized in one-pot without base (Figure 17). A potential factor that influences the results may be alterations in internal mass transfer limitations, which are

likely to be more significant when the St/Rh ratio is higher (St/Rh = 5000/1 vs 6500/1). Additionally, TEM analyses of the recovered latexes synthesized in the presence of pyridine or  $\text{NEt}_3$  showed similar dispersion and RhNPs size distributions after the fifth catalytic runs ( $3.1 \pm 0.1$  nm and  $1.8 \pm 0.2$  nm, for pyridine and  $\text{NEt}_3$  respectively, Figure 17) as prior to the first catalytic runs ( $2.9 \pm 0.6$  nm and  $2.1 \pm 0.1$  nm for pyridine and  $\text{NEt}_3$  respectively) (see Figure 7).

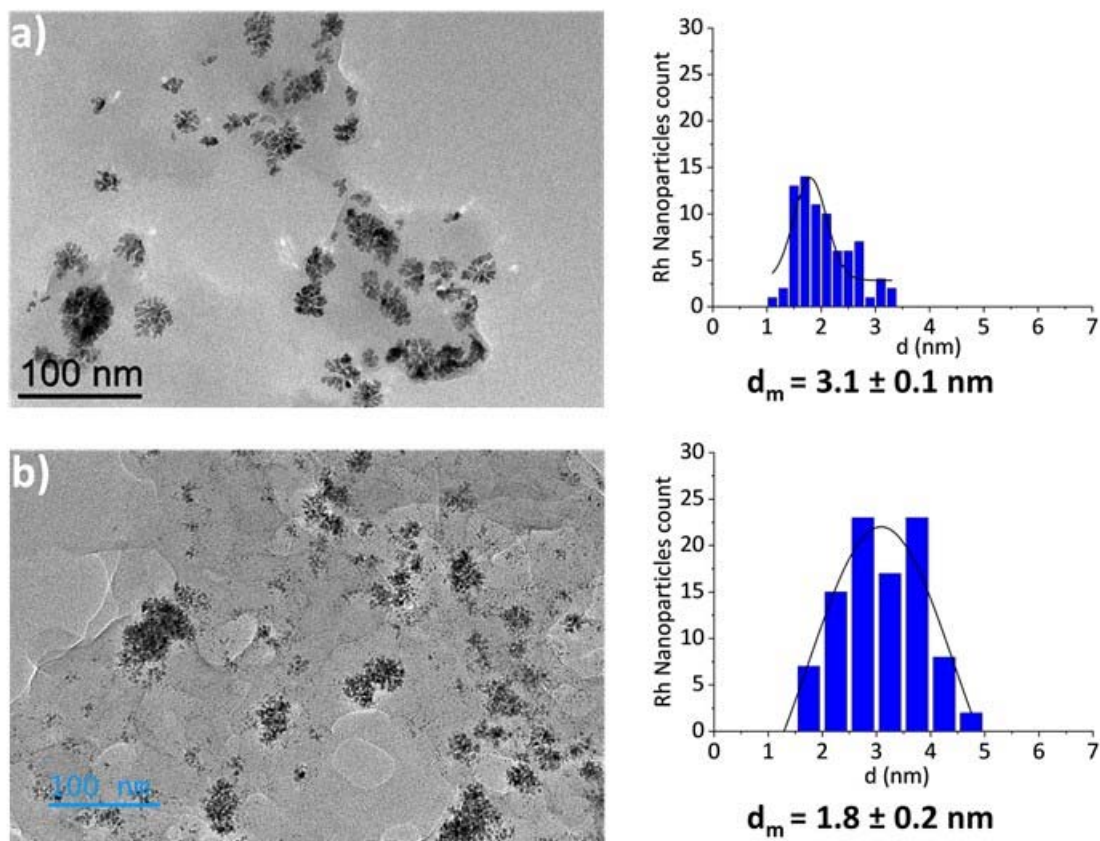


**Figure 17.** TEM images and (overlaid) the corresponding size distributions of spent RhNP-TPPO@CCM-C prepared with (a) pyridine (Table 2, Entry 2) and with (b)  $\text{NEt}_3$  (Table 2, Entry 3).

### Hydrogenation of styrene in the presence of Hg

To examine whether the RhNP-TPPO@CCM-C latex (synthesized without base) also contained catalytically active  $\text{Rh}^I$  species in addition to RhNPs, a styrene hydrogenation experiment (styrene/Rh = 5000/1) was also carried out in the presence of a large excess of Hg (Hg/Rh = 500/1), which is known to poison and deactivate the RhNPs[84]. No significant styrene conversion was observed (<0.1%) after 0.25 h of reaction, suggesting that no  $\text{Rh}^I$  is present in the TPPO@CCM-C core. A control TEM analysis of the recovered latex after the catalytic run with Hg (Figure 18) still showed the presence of small RhNPs in the polymer, but with a larger average diameter (ca.  $2.7 \pm 0.1$  nm vs.  $1.7 \pm 0.2$  nm) than prior to catalysis, along with much larger particles (average size  $16 \pm 5$  nm) that can be attributed to nanoscopic Hg droplets. The increase in the apparent size of the RhNPs could result from the formation of a Hg-Rh amalgam at the surface of the RhNPs [84,85]. This result indicates that Hg is able to cross the CCM hydrophilic shell.

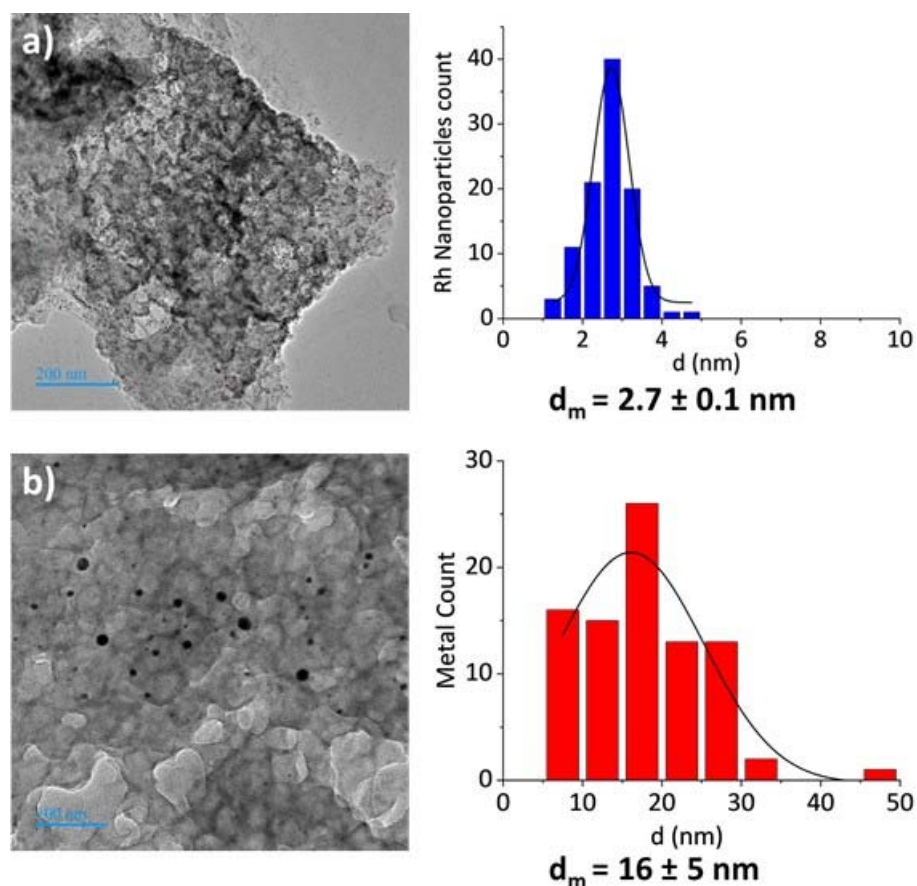


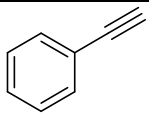
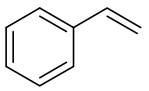
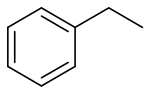
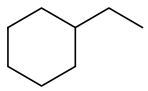
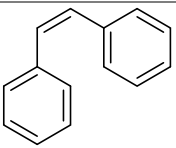
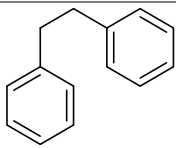
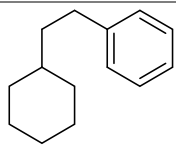
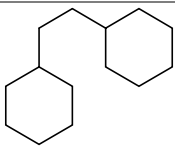
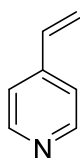
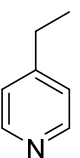
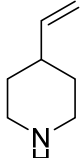
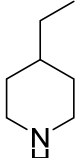
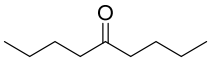
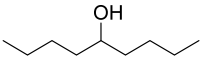
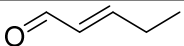
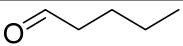
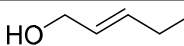
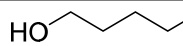
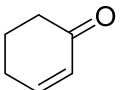
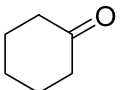
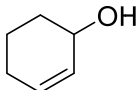
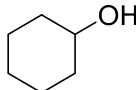
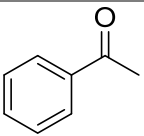
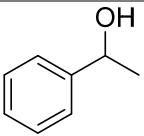
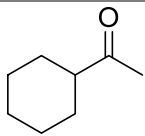
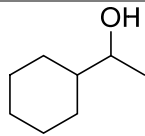
**Figure 18.** TEM images (left) of a) RhNPs and b) Hg particles and the corresponding size distributions (right) RhNPs ( $d_m = 2.7 \pm 0.1$  nm; left) and Hg particles ( $d_m = 16 \pm 5$  nm; right) in RhNP-TPPO@CCM-C.

### Hydrogenation of other substrates

Lastly, the applicability of the RhNP-TPPO@CCM-C latex synthesized without base was screened for the aqueous biphasic hydrogenation of other substrates, including selected aromatics, alkenes, alkynes and carbonyl compounds (substrate/Rh = 5000/1; performed with neat substrate and not optimized) (Table 4). The results confirmed a rather high hydrogenation activity (average TOFs of 1000-1100 h<sup>-1</sup>) and high selectivity towards the reduction of both double and triple carbon-carbon bonds in phenylacetylene (Entry 1) and 4-vinylpyridine (Entry 3). The catalytic activity was, however, significantly lower than for styrene under similar reaction conditions (cTOF 4500 h<sup>-1</sup>; see Table 4). Highly sterically hindered Z-stilbene (Entry 2) and the aliphatic  $\alpha,\beta$ -unsaturated substrate (*E*)-hex-2-enal (Entry 5) were only hydrogenated to a low extent under the applied conditions. Also, the carbonyl group of the aliphatic compound 5-nonanone (Entry 4) was hardly hydrogenated, whereas the cyclic (and activated)  $\alpha,\beta$ -unsaturated substrate 2-cyclohexen-1-one (Entry 6) yielded a good conversion (cTOF of 1000 h<sup>-1</sup>) with high selectivity (63.7%) to cyclohexanol, and acetophenone (Entry 7) showed an even higher conversion (cTOF of 3000 h<sup>-1</sup>), with a nearly quantitative selectivity toward phenylethanol (>99%). Notably, no significant hydrogenation of the aromatic ring was observed in any the reactions. Overall, the non-optimized results obtained during the screening clearly indicate the potential of the RhNP-TPPO@CCM-C catalyst synthesized without base for the hydrogenation of other types of unsaturated substrates than styrene.



**Table 4.** Aqueous biphasic hydrogenation using Rh-TPPO@CCM-C.<sup>a</sup>

Entry	Substrate / Conversion (%) <sup>b</sup>	Products / Selectivity (%) <sup>b</sup>			Average cTOF (h <sup>-1</sup> )
1	 30	 77.6	 22.4	 <0.1	1100
2	 <0.1	 nd	 nd	 nd	2.5
3	 79	 96.8	 nd	 nd	3200
4	 <0.1	 nd			2.5
5	 <0.1	 nd	 nd	 nd	2.5
6	 27	 1.4	 34.9	 63.7	1000
7	 86	 >99	 <0.1	 <0.1	3000

<sup>a</sup> Reaction conditions: Substrate/Rh = 5000/1, 20 bar H<sub>2</sub>, 25 °C, 0.25 h, 1200 rpm. <sup>b</sup> Conversions and selectivities determined by GC-FID. Product identification confirmed by <sup>1</sup>H NMR (Entries 4 and 5) and GC-MS (Entry 3). nd = not detected.

## Conclusion and perspectives

The aim of this PhD project was to develop new methods for efficient confinement of metal nanoparticles (MNPs) in polymeric core-crosslinked micelle (CCM) nanoreactors, with both cationic and anionic shells, for application of the resulting MNP@CCMs latexes in aqueous biphasic hydrogenation. To this end, novel core-crosslinked micelles functionalized with triphenylphosphine oxide and a polycationic shell were developed by extension of a previously optimized RAFT polymerization approach.

The first attempt to produce RhNP-TPPO@CCM-C consisted in loading the TPPO@CCM-C micelles with  $[\text{Rh}(\text{COD})(\mu\text{-Cl})_2]$ , in order to generate a core-anchored  $[\text{RhCl}(\text{COD})(\text{TPPO@CCM-C})]$  complex that could be reduced to RhNPs by  $\text{H}_2$ , following the same procedure as previously developed to get RhNPs embedded in TPP@CCM-C. This proved unsuccessful, indicating that the formation of a Rh<sup>I</sup>-TPPO@CCM-C complex by cleavage of the di- $\mu\text{-Cl}$ -bridge moiety in  $[\text{Rh}(\text{COD})(\mu\text{-Cl})_2]$  was not favorable in the polymer core under the applied conditions. Given that, an alternative strategy involving *ex-situ* synthesis of RhNPs using TPP and pyridine as stabilizers, affording ultrasmall RhNPs, and their subsequent transfer to the TPPO@CCM-C nanoreactors was envisaged. This strategy allowed the successful transfer of the RhNPs to the TPPO-functionalized cores. Although the resulting RhNP-TPPO@CCM-C latex proved effective in the aqueous biphasic hydrogenation of styrene, with only 2% of catalyst leaching, a gradual extraction of the TPP and pyridine ligands used for the *ex-situ* RhNPs synthesis during the work-up between recycles, induced a steady decrease of the catalytic activity. Nevertheless, a stable catalyst phase was obtained after preliminary extensive washing and an initial reaction run, yielding a TOF of  $\sim 1025 \text{ h}^{-1}$  (*c*TOF  $\sim 1440 \text{ h}^{-1}$ ), over several recycles.

To improve the system, a new approach has been developed consisting of a one-pot synthesis of RhNP-TPPO@CCM-C catalyst, which does not require the use of additional stabilizers. The produced RhNPs were smaller in size ( $1.7 \pm 0.2 \text{ nm}$ ) than their analogs synthesized under similar conditions in the presence of only TPPO as stabilizer ( $2.4 \pm 0.2 \text{ nm}$ ). This difference underlines the positive confinement effect on the RhNPs size, which leads to smaller NPs. The new catalyst demonstrated very good catalytic activity (*c*TOFs of  $4500\text{--}16000 \text{ h}^{-1}$ ) and full selectivity in the hydrogenation of neat styrene to ethylbenzene under mild conditions (20 bar  $\text{H}_2$ , 25–55 °C). The catalyst was also applicable for the hydrogenation of other unsaturated substrates under similar reaction conditions, including alkynes and carbonyl compounds, making the RhNP-TPPO@CCM-C latex highly attractive for aqueous biphasic catalysis including catalyst recycling. The overall obtained catalytic results with RhNP-TPPO@CCM-C showed that the nature of the core-functional ligands of the polymer micelles is a key parameter to improving the stability and the recycling of the catalytic latex.

## References

- [1] R. L. Johnston, *Metal nanoparticles and nanoalloys*, in *Frontiers of Nanoscience* (R. L. Johnston and J. P. Wilcoxon, Editors), Elsevier Ltd: Oxford, UK, **2012**, 3, 1–42. ISBN 978-0-08-096357-0. DOI: [10.1016/B978-0-08-096357-0.00006-6](https://doi.org/10.1016/B978-0-08-096357-0.00006-6).
- [2] T. Shen, S. Zhou, J. Ruan, X. Chen, X. Liu, X. Ge, C. Qian, *Adv. Colloid Interface Sci.* **2021**, 287, 102299. DOI: [10.1016/j.cis.2020.102299](https://doi.org/10.1016/j.cis.2020.102299).
- [3] T. Kotre, M. T. Zarka, J. O. Krause, M. R. Buchmeiser, R. Weberskirch, O. Nuyken, *Macromol Symp.* **2004**, 217, 203–21. DOI: [10.1002/masy.200451316](https://doi.org/10.1002/masy.200451316).
- [4] B. Cornils, W. A. Herrmann, C. H. Wong and H. W. Zanthoff (Editors), *Catalysis from A to Z: A Concise Encyclopedia*, 4<sup>th</sup> ed., Wiley-VCH: Weinheim, Germany, **2013**, ISBN 978-3-527-33307-3.
- [5] P. Serp, K. Philippot (Editors), *Nanomaterials in Catalysis*, Wiley-VCH: Weinheim, Germany, **2012**. ISBN: 9783527656875. DOI: [10.1002/9783527656875](https://doi.org/10.1002/9783527656875).
- [6] D. Astruc (Editor), *Nanoparticles and Catalysis*, Wiley-VCH: Weinheim, Germany, **2007**. ISBN: 9783527621323. DOI: [10.1002/9783527621323](https://doi.org/10.1002/9783527621323).
- [7] B. Chaudret, K. Philippot, *Oil & Gas Sci. Techn. - Rev. IFP*, **2007**, 62, 799–817. DOI: [10.2516/ogst:2007062](https://doi.org/10.2516/ogst:2007062).
- [8] A. Roucoux, J. Schulz, H. Patin, *Chem. Rev.* **2002**, 102, 3757–3778. DOI: [10.1021/cr010350j](https://doi.org/10.1021/cr010350j).
- [9] D. Astruc, F. Lu, J. R. Aranzaes, *Angew. Chem. Int. Ed.*, **2005**, 44, 7852–7872. DOI: [10.1002/anie.200500766](https://doi.org/10.1002/anie.200500766).

- [10] C. Burda, X. Chen, R. Narayanan, M. A. El-Sayed, *Chem. Rev.*, **2005**, 105, 1025–1102. DOI: [10.1021/cr030063a](https://doi.org/10.1021/cr030063a).
- [11] M. Guerrero, N. T. T. Chau, S. Noël, A. Denicourt-Nowicki, F. Hapiot, A. Roucoux, E. Monflier, K. Philippot, *Curr. Org. Chem.*, **2013**, 17, 364–399. DOI: [10.2174/1385272811317040006](https://doi.org/10.2174/1385272811317040006).
- [12] J. L. Castelbou, E. Bresó-Femenia, P. Blondeau, B. Chaudret, S. Castellón, C. Claver, C. Godard, *ChemCatChem*, **2014**, 6, 3160–3168. DOI: [10.1002/cctc.201402524](https://doi.org/10.1002/cctc.201402524).
- [13] E. Guyonnet Bilé, R. Sassine, A. Denicourt-Nowicki, F. Launay, A. Roucoux, *Dalton Trans.*, **2011**, 40, 6524–6531. DOI: [10.1039/c0dt01763a](https://doi.org/10.1039/c0dt01763a).
- [14] E. Guyonnet Bilé, E. Cortelazzo-Polisini, A. Denicourt-Nowicki, R. Sassine, F. Launay, A. Roucoux, *ChemSusChem*, **2012**, 5, 91–101. DOI: [10.1002/cssc.201100364](https://doi.org/10.1002/cssc.201100364).
- [15] E. Guyonnet-Bilé, A. Denicourt-Nowicki, R. Sassine, P. Beaunier, F. Launay, A. Roucoux, *ChemSusChem*, **2010**, 3, 1276–1279. DOI: [10.1002/cssc.201000206](https://doi.org/10.1002/cssc.201000206).
- [16] A. Borsla, A. M. Wilhelm, H. Delmas, *Cat. Today*, **2001**, 66, 389–395. DOI: [10.1016/S0920-5861\(00\)00635-0](https://doi.org/10.1016/S0920-5861(00)00635-0).
- [17] H. Mao, X. Liao, B. Shi, *Catal. Commun.*, **2011**, 16, 210–214. DOI: [10.1016/j.catcom.2011.09.038](https://doi.org/10.1016/j.catcom.2011.09.038).
- [18] C. Chaudhari, H. Imatome, Y. Nishida, K. Sato, K. Nagaoka, *Catal. Commun.*, **2019**, 126, 55–60. DOI: [10.1016/j.catcom.2019.02.019](https://doi.org/10.1016/j.catcom.2019.02.019).
- [19] H. Hirai, M. Ohtaki, M. Komiyama, *Chem. Lett.*, **1987**, 16, 149–152. DOI: [10.1246/CL.1987.149](https://doi.org/10.1246/CL.1987.149).
- [20] J. L. Castelbou, A. Gual, E. Mercadé, C. Claver, C. Godard, *Catal. Sci. Technol.*, **2013**, 3, 2828–2833. DOI: [10.1039/c3cy00388d](https://doi.org/10.1039/c3cy00388d).
- [21] C. Moreno-Marrodan, F. Liguori, E. Mercadé, C. Godard, C. Claver, P. Barbaro, *Catal. Sci. Technol.*, **2013**, 5, 3762–3772. DOI: [10.1039/c5cy00599j](https://doi.org/10.1039/c5cy00599j).
- [22] F. Martinez-Espinar, P. Blondeau, P. Nolis, B. Chaudret, C. Claver, S. Castellón, C. Godard, *J. Catal.*, **2017**, 354, 113–127. DOI: [10.1016/j.jcat.2017.08.010](https://doi.org/10.1016/j.jcat.2017.08.010).
- [23] C. Amiens, D. Ciuculescu-Pradines, K. Philippot, *Coord. Chem. Rev.*, **2016**, 308, 409–432. DOI: [10.1016/j.ccr.2015.07.013](https://doi.org/10.1016/j.ccr.2015.07.013).
- [24] M. R. Axet, S. Castellón, C. Claver, K. Philippot, P. Lecante, B. Chaudret, *Eur. J. Inorg. Chem.*, **2008**, 3460–3466. DOI: [10.1002/ejic.200800421](https://doi.org/10.1002/ejic.200800421).
- [25] J. L. Pellegatta, C. Blandy, V. Collière, R. Choukroun, B. Chaudret, P. Cheng, K. Philippot, *J. Mol. Cat. A* **2002**, 178, 55–61. DOI: [10.1016/s1381-1169\(01\)00298-9](https://doi.org/10.1016/s1381-1169(01)00298-9).
- [26] M. Ibrahim, M. Wei, É. Deydier, E. Manoury, R. Poli, P. Lecante, K. Philippot, *Dalton Trans.*, **2019**, 48, 6777–6786. DOI: [10.1039/C9DT01006H](https://doi.org/10.1039/C9DT01006H).
- [27] D. V. Talapin, E. V. Shevchenko, *Chem. Rev.*, **2016**, 116, 10343–10345. DOI: [10.1021/acs.chemrev.6b00566](https://doi.org/10.1021/acs.chemrev.6b00566).
- [28] P. P. R. W. Oskar Nuyken, *Macromol. Symp.*, **2002**, 177, 163–173. DOI: [10.1002/1521-3900\(200201\)177:1<163::AID-MASY163>3.0.CO;2-W](https://doi.org/10.1002/1521-3900(200201)177:1<163::AID-MASY163>3.0.CO;2-W).
- [29] M. Niyaz Khan, *Micellar Catalysis*; CRC Press: Boca Raton, **2006**, ISBN 9780429133749. DOI: [10.1201/9781420015843](https://doi.org/10.1201/9781420015843).
- [30] M. R. Buchmeiser (Editor), *Polymeric Materials in Organic Synthesis and Catalysis*, Wiley-VCH: Weinheim, Germany, **2003**, ISBN 3527305149. DOI: [10.1002/3527601856](https://doi.org/10.1002/3527601856).
- [31] M. Schrunner, F. Polzer, Y. Mei, Y. Lu, B. Haupt, M. Ballauff, A. Gödel, M. Drechsler, J. Preussner, U. Glatzel, *Macromol. Chem. Phys.*, **2007**, 208, 1542–1547. DOI: [10.1002/macp.200700161](https://doi.org/10.1002/macp.200700161).
- [32] Y. Lu, Y. Mei, M. Schrunner, M. Ballauff, M. W. Möller, J. Breu, *J. Phys. Chem.*, **2007**, 111, 7676–7681. DOI: [10.1021/jp070973m](https://doi.org/10.1021/jp070973m).
- [33] R. K. O'Reilly, C. J. Hawker, K. L. Wooley, *Chem. Soc. Rev.*, **2006**, 35, 1068–1083. DOI: [10.1039/b514858h](https://doi.org/10.1039/b514858h).
- [34] S. Chen, F. Gayet, E. Manoury, A. Joumaa, M. Lansalot, F. D'Agosto, R. Poli, *Chem. Eur. J.*, **2016**, 22, 6302–6313. DOI: [10.1002/chem.201504923](https://doi.org/10.1002/chem.201504923).
- [35] A. Joumaa, F. Gayet, E. J. Garcia-Suarez, J. Himmelstrup, A. Riisager, R. Poli, E. Manoury, *Polymers*, **2020**, 12, 1107. DOI: [10.3390/POLYM12051107](https://doi.org/10.3390/POLYM12051107).
- [36] H. Wang, C. Fliedel, E. Manoury, R. Poli, *Polymer*, **2022**, 243, 124640. DOI: [10.1016/j.polymer.2022.124640](https://doi.org/10.1016/j.polymer.2022.124640).

- [37] H. Wang, L. Vendrame, C. Fliedel, S. Chen, F. Gayet, F. D'Agosto, M. Lansalot, E. Manoury, R. Poli, *Chem. Eur. J.*, **2021**, *27*, 5205–5214. DOI: [10.1002/chem.202004689](https://doi.org/10.1002/chem.202004689).
- [38] H. Wang, L. Vendrame, C. Fliedel, S. Chen, F. Gayet, E. Manoury, X. Zhang, F. D'agosto, M. Lansalot, R. Poli, *Macromolecules*, **2020**, *53*, 2198–2208. DOI: [10.1021/acs.macromol.9b02582](https://doi.org/10.1021/acs.macromol.9b02582).
- [39] S. S. Sambou, R. Hromov, I. Ruzhylo, H. Wang, A. Allandrieu, C. Sabatier, Y. Coppel, J. C. Daran, F. Gayet, A. Labande, E. Manoury, R. Poli, *Catal. Sci. Technol.*, **2021**, *11*, 6811–6824. DOI: [10.1039/d1cy00554e](https://doi.org/10.1039/d1cy00554e).
- [40] H. Wang, A. M. Fiore, C. Fliedel, E. Manoury, K. Philippot, M. M. Dell'Anna, P. Mastroilli, R. Poli, *Nanoscale Adv.* **2021**, *3*, 2554–2566. DOI: [10.1039/d1na00028d](https://doi.org/10.1039/d1na00028d).
- [41] A. F. Cardozo, C. Julcour, L. Barthe, J. F. Blanco, S. Chen, F. Gayet, E. Manoury, X. Zhang, M. Lansalot, B. Charleux, F. D'Agosto, R. Poli, H. Delmas, *J. Catal.*, **2015**, *324*, 1–8. DOI: [10.1016/j.jcat.2015.01.009](https://doi.org/10.1016/j.jcat.2015.01.009).
- [42] F. D'Agosto, J. Rieger, M. Lansalot, *Angew. Chem. Int. Ed.*, **2020**, *59*, 8368–8392. DOI: [10.1002/anie.201911758](https://doi.org/10.1002/anie.201911758).
- [43] H. Wang, C. J. Abou-Fayssal, C. Fliedel, E. Manoury, R. Poli, *Polymers*, **2022**, *14*, 4937. DOI: [10.3390/polym14224937](https://doi.org/10.3390/polym14224937).
- [44] E. Lobry, A. F. Cardozo, L. Barthe, J. F. Blanco, H. Delmas, S. Chen, F. Gayet, X. Zhang, M. Lansalot, F. D'Agosto, R. Poli, E. Manoury, C. Julcour, *J. Catal.*, **2016**, *342*, 164–172. DOI: [10.1016/j.jcat.2016.07.023](https://doi.org/10.1016/j.jcat.2016.07.023).
- [45] S. Chen, A. F. Cardozo, C. Julcour, J. F. Blanco, L. Barthe, F. Gayet, M. Lansalot, F. D'Agosto, H. Delmas, E. Manoury, R. Poli, *Polymer*, **2015**, *72*, 327–335. DOI: [10.1016/j.polymer.2015.02.024](https://doi.org/10.1016/j.polymer.2015.02.024).
- [46] R. El Abed, F. Aloui, J. P. Genêt, B. Ben Hassine, A. Marinetti, *J. Organomet. Chem.*, **2007**, *692*, 1156–1160. DOI: [10.1016/j.jorganchem.2006.11.022](https://doi.org/10.1016/j.jorganchem.2006.11.022).
- [47] J. Sanmartín, M. R. Bermejo, C. A. McAuliffe, A. Sousa, M. Fondo, E. Gómez-Fórneas, *Inorg. Chim. Acta*, **1997**, *255*, 269–278. DOI: [10.1016/S0020-1693\(96\)05373-X](https://doi.org/10.1016/S0020-1693(96)05373-X).
- [48] N. Suzuki, T. Inoue, T. Asada, R. Akebi, G. Kobayashi, M. Rikukawa, Y. Masuyama, M. Ogasawara, T. Takahashi, *Chem. Lett.*, **2013**, *42*, 1493–1495. DOI: [10.1246/cl.130711](https://doi.org/10.1246/cl.130711).
- [49] C. Li, Y. Wang, D. Sun, H. Li, X. Sun, D. Ma, Z. Ren, S. Yan, *ACS Appl. Mater. Interfaces*, **2018**, *10*, 5731–5739. DOI: [10.1021/acsami.8b00136](https://doi.org/10.1021/acsami.8b00136).
- [50] S. Vanicek, M. Podewitz, J. Stubbe, D. Schulze, H. Kopacka, K. Wurst, T. Müller, P. Lippmann, S. Haslinger, H. Schottenberger, K. R. Liedl, I. Ott, B. Sarkar, B. Bildstein, *Chem. Eur. J.*, **2018**, *24*, 3742–3753. DOI: [10.1002/chem.201705051](https://doi.org/10.1002/chem.201705051).
- [51] M. Deimling, M. Kirchhof, B. Schwager, Y. Qawasmi, A. Savin, T. Mühlhäuser, W. Frey, B. Claasen, A. Baro, T. Sottmann, S. Laschat, *Chem. Eur. J.*, **2019**, *25*, 9464–9476. DOI: [10.1002/chem.201900947](https://doi.org/10.1002/chem.201900947).
- [52] J. Nowakowski, S. Nowakowska, G. Srivastava, M. Baljovic, J. Girovsky, N. Ballav, T. A. Jung, *ChemistrySelect*, **2016**, *1*, 891–895. DOI: [10.1002/slct.201600215](https://doi.org/10.1002/slct.201600215).
- [53] T. Nishimura, Y. Maeda, T. Hayashi, *Angew. Chem. Int. Ed.*, **2010**, *49*, 7324–7327. DOI: [10.1002/anie.201003775](https://doi.org/10.1002/anie.201003775).
- [54] F. H. Hu, L. S. Wang, S. F. Cai, *J. Chem. Eng. Data*, **2009**, *54*, 1382–1384. DOI: [10.1021/je800842z](https://doi.org/10.1021/je800842z).
- [55] P. Das, P. Chutia, D. Kumar Dutta, *Chem. Lett.*, **2002**, *7*, 766–767. DOI: [10.1246/cl.2002.766](https://doi.org/10.1246/cl.2002.766).
- [56] R. Bonnaire, D. Diavoust, N. Platzler, *Org. Mag. Reson.*, **1984**, *22*, 80–85. DOI: [10.1002/mrc.1270220205](https://doi.org/10.1002/mrc.1270220205).
- [57] A. Serrano-Maldonado, E. Martin, I. Guerrero-Ríos, *Eur. J. Inorg. Chem.*, **2019**, 2863–2870. DOI: [10.1002/ejic.201900223](https://doi.org/10.1002/ejic.201900223).
- [58] S. A. Stratton, K. L. Luska, A. Moores, *Catal Today.*, **2012**, *183*, 96–100. DOI: [10.1016/j.cattod.2011.09.016](https://doi.org/10.1016/j.cattod.2011.09.016).
- [59] X. Zhang, A. F. Cardozo, S. Chen, W. Zhang, C. Julcour, M. Lansalot, J. F. Blanco, F. Gayet, H. Delmas, B. Charleux, E. Manoury, F. D'Agosto, R. Poli, *Chem. Eur. J.*, **2014**, *20*, 15505–15517. DOI: [10.1002/chem.201403819](https://doi.org/10.1002/chem.201403819).
- [60] H. Ohde, M. Ohde, C. M. Wai, *Chem. Comm.*, **2004**, *4*, 930–931. DOI: [10.1039/b311522d](https://doi.org/10.1039/b311522d).
- [61] M. L. Buil, M. A. Esteruelas, S. Niembro, M. Oliván, L. Orzechowski, C. Pelayo, A. Vallribera, *Organometallics*, **2010**, *29*, 4375–4383. DOI: [10.1021/om1003072](https://doi.org/10.1021/om1003072).
- [62] J. Schulz, S. Levigne, A. Roucoux, H. Patin, *Adv. Synth. Catal.*, **2002**, *344*, 266–269. DOI: [10.1002/1615-4169\(200206\)344:3/4<266::AID-ADSC266>3.0.CO;2-O](https://doi.org/10.1002/1615-4169(200206)344:3/4<266::AID-ADSC266>3.0.CO;2-O).
- [63] N. Yan, Y. Yuan, P. J. Dyson, *Chem. Comm.*, **2011**, *47*, 2529–2531. DOI: [10.1039/c0cc04641h](https://doi.org/10.1039/c0cc04641h).

- [64] J. Schulz, A. Roucoux, H. Patin, *Chem. Eur. J.*, **2000**, *6*, 618–624. DOI: [10.1002/\(sici\)1521-3765\(20000218\)6:4<618::aid-chem618>3.0.co;2-a](https://doi.org/10.1002/(sici)1521-3765(20000218)6:4<618::aid-chem618>3.0.co;2-a).
- [65] C. Vollmer, E. Redel, K. Abu-Shandi, R. Thomann, H. Manyar, C. Hardacre, C. Janiak, *Chem. Eur. J.*, **2010**, *16*, 3849–3858. DOI: [10.1002/chem.200903214](https://doi.org/10.1002/chem.200903214).
- [66] E. Baralt, S. J. Smith, J. Hurwitz, I. T. Horváth, R. H. Fish, *J. Am. Chem. Soc.*, **1992**, *114*, 5187–5196. DOI: [10.1021/ja00039a033](https://doi.org/10.1021/ja00039a033).
- [67] H. Imai, T. Nishiguchi, K. Fukuzumi, *J. Org. Chem.*, **1977**, *42*, 431–434. DOI: [10.1021/jo00433a024](https://doi.org/10.1021/jo00433a024).
- [68] E. Baráth, *Catalysts*, **2018**, *8*, 671. DOI: [10.3390/catal8120671](https://doi.org/10.3390/catal8120671).
- [69] M. Studer, C. Wedemeyer-Exl, F. Spindler, H. U. Blaser, *Monatsh. Chem.*, **2000**, *131*, 1335–1343. DOI: [10.1016/S1381-1169\(98\)00200-3](https://doi.org/10.1016/S1381-1169(98)00200-3).
- [70] C. J. Abou-Fayssal, C. Fliedel, R. Poli, A. Riisager, K. Philippot, E. Manoury, *Mater. Today Chem.*, **2023**, *4*, 101752. DOI: [10.1016/j.mtchem.2023.101752](https://doi.org/10.1016/j.mtchem.2023.101752).
- [71] M. A. Gelesky, S. S. X. Chiaro, F. A. Pavan, J. H. Z. dos Santos, J. Dupont, *Dalton Trans.*, **2007**, 5546–5548. DOI: [10.1039/B708111A](https://doi.org/10.1039/B708111A).
- [72] L. M. Rossi, L. L. R. Vono, M. A. S. Garcia, T. L. T. Faria, J. A. Lopez-Sanchez, *Top. Catal.*, **2013**, *56*, 1228–1238. DOI: [10.1007/s11244-013-0089-z](https://doi.org/10.1007/s11244-013-0089-z).
- [73] F. Martinez-Espinar, P. Blondeau, P. Nolis, B. Chaudret, C. Claver, S. Castellón, C. Godard, *J. Catal.*, **2017**, *354*, 113–127. DOI: [10.1016/j.jcat.2017.08.010](https://doi.org/10.1016/j.jcat.2017.08.010).
- [74] M. Ibrahim, M. A. S. Garcia, L. L. R. Vono, M. Guerrero, P. Lecante, L. M. Rossi, K. Philippot, *Dalton Trans.*, **2016**, *45*, 17782–17791. DOI: [10.1039/c6dt03104h](https://doi.org/10.1039/c6dt03104h).
- [75] G. Vitulli, C. Evangelisti, P. Pertici, A. M. Caporusso, N. Panziera, P. Salvadori, M. G. Faga, C. Manfredotti, G. Martra, S. Coluccia, A. Balerna, S. Colonna, S. Mobilio, *J. Organomet. Chem.*, **2003**, *681*, 37–50. DOI: [10.1016/S0022-328X\(03\)00529-1](https://doi.org/10.1016/S0022-328X(03)00529-1).
- [76] H. Bin Pan, C.M. Wai, *J. Phys. Chem. C*, **2010**, *114*, 11364–11369. DOI: [10.1021/jp101368p](https://doi.org/10.1021/jp101368p).
- [77] T. T. Nguyen, P. Serp, *ChemCatChem*, **2013**, *5*, 3595–3603. DOI: [10.1002/cctc.201300527](https://doi.org/10.1002/cctc.201300527).
- [78] M. M. M. Jansen, J. Gracia, B. E. Nieuwenhuys, J. W. Niemantsverdriet, *Phys. Chem. Chem. Phys.*, **2009**, *11*, 10009–10016. DOI: [10.1039/b910497f](https://doi.org/10.1039/b910497f).
- [79] S. Murphy, C. Strebel, S. B. Vendelbo, C. Conradsen, Y. Tison, K. Nielsen, L. Bech, R. M. Nielsen, M. Johansson, I. Chorkendorff, J. H. Nielsen, *Phys. Chem. Chem. Phys.*, **2011**, *13*, 10333–10341. DOI: [10.1039/c1cp20371a](https://doi.org/10.1039/c1cp20371a).
- [80] G. B. Deacon, J. H. S. Green, *Spectrochim. Acta A*, **1968**, *24*, 845–852. DOI: [10.1016/0584-8539\(68\)80183-7](https://doi.org/10.1016/0584-8539(68)80183-7).
- [81] K. Senevirathne, A. W. Burns, M. E. Bussell, S. L. Brock, *Adv. Funct. Mater.*, **2007**, *17*, 3933–3939. DOI: [10.1002/adfm.200700758](https://doi.org/10.1002/adfm.200700758).
- [82] S. Carencio, C. Boissière, L. Nicole, C. Sanchez, P. Le Floch, N. Mézailles, *Chem. Mater.*, **2010**, *22*, 1340–1349. DOI: [10.1021/cm902007g](https://doi.org/10.1021/cm902007g).
- [83] C. Betti, J. Badano, C. Lederhos, M. Maccarrone, N. Carrara, F. Coloma-Pascual, M. Quiroga, C. Vera, *React. Kinet. Mech. Catal.*, **2016**, *117*, 283–306. DOI: [10.1007/s11144-015-0910-8](https://doi.org/10.1007/s11144-015-0910-8).
- [84] J. A. Widegren, R. G. Finke, *J. Mol. Catal. A*, **2003**, *198*, 317–341. DOI: [10.1016/S1381-1169\(02\)00728-8](https://doi.org/10.1016/S1381-1169(02)00728-8).
- [85] C. Guminski, *J. Phase Equil.*, **2002**, *23*, 537–540. DOI: [10.1361/105497102770331280](https://doi.org/10.1361/105497102770331280).

**Joel CEJAS SÁNCHEZ**

**ESR10**

**Thesis co-directors**

Prof. Karol Grela                      Uniwersytet Warszawski, Warsaw, Poland

Prof. Rosa Maria Sebastián    Universitat Autònoma de Barcelona, Bellaterra, Spain

**Thesis defense**

Department of Chemistry, University of Warsaw, 16 February 2024



## Immobilization of Ruthenium Complexes on Supports. Applications in Catalysis

### Introduction

Immobilized catalysts play a key role in advancing modern and sustainable chemistry, by means of anchoring a catalyst onto supports to facilitate its recovery, recycling, and reuse [1]. This approach offers several advantages, including the potential for enhanced catalyst activity, ease of handling and recovery through straightforward procedures, and the ability to reduce metal contamination in the final products [2,3]. With the ultimate goal of obtaining novel supported ruthenium complexes for their application in catalytic reactions, this Thesis has focused on the development of polyphosphorhydrazone-based (PPH) Janus dendrimers for grafting Ru-complexes and their applications in catalysis; and the preparation of novel Ru-NHC complexes and their immobilization on dendrimers and MOFs for olefin metathesis catalysis.

Bearing the previous approach in mind, one of the key objectives of this dissertation was the development of phosphorus Janus dendrimers as innovative catalyst supports. These novel dendrimers were expected to bridge the gap between homogeneous and heterogeneous catalysis, leading to the synthesis of a system that would behave as a homogeneous catalyst but possesses the recoverability and reusability possibilities of a heterogeneous approach [4]. Specifically, this project also aimed to immobilize ruthenium pre-catalysts onto the structure of phosphorus Janus dendrimers for applications in environmentally friendly solvents such as water. To achieve this, novel ruthenium complexes with unsymmetrical NHC ligands are synthesized, incorporating functionalities that enable their coupling to phosphorus Janus dendrimers. Simultaneously, these Janus dendrimers are designed to incorporate polyoxyethylenated chains to enhance water solubility, along with specific functional groups enabling the immobilization of the desired ligand/metal pre-catalyst. The synthesis of phosphorus Janus dendrimers is pursued through dendron synthesis and coupling procedures, to establish a comprehensive protocol for grafting dendrimeric halves. The prepared dendrimers will be assessed for their ability to immobilize ruthenium pre-catalysts, and the dendritic effect on the catalytic entity's activity and selectivity will be analyzed.

Furthermore, the versatility of both Ru-NHC complexes and phosphorus Janus dendrimers is set to be explored in parallel projects. In this context, the dendrimer capacity to graft alternative ruthenium complexes and their performance in environmentally friendly solvent catalysis will be evaluated. This evaluation also aimed to compare the catalytic performance –in terms of activity, efficiency, and recyclability of these systems– with single, non-immobilized versions of the same catalysts. Concurrently, the immobilization of Ru-NHC metathesis catalysts on heterogeneous supports (MOFs) was planned to assess their suitability for developing alternative approaches to catalytic system development.

### Synthesis of modified PPH Janus dendrimers for induced solubility in water

The initial part of this Thesis was dedicated to the synthesis of innovative PPH Janus dendrimers [5], designed to incorporate water-soluble PEG moieties on one side of the structure while featuring functional  $-P(S)Cl_2$  groups for ligand/metal pre-catalyst integration on the opposite side (Figure 1). In this context, the synthesis of dendrimeric structures imparting dual properties to the final structure



was envisioned to achieve the first-ever reported functional metal@dendrimer system for catalysis with documented applications. To achieve this, phosphorus dendrimers were crafted employing two distinct dendron structures. Each dendron bore either an acetylene or azide group at the core level to enable subsequent coupling. These dendrimers were grown up to the second generation, and the desired Janus dendrimer was then created through click chemistry, which facilitated the fusion of the two targeted dendrons by forming a 1,2,3-triazole.

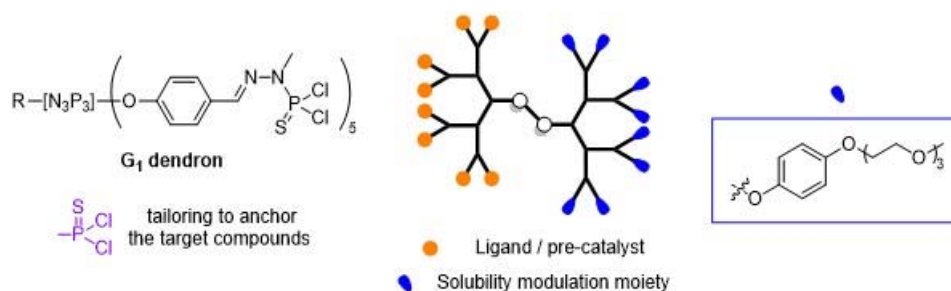
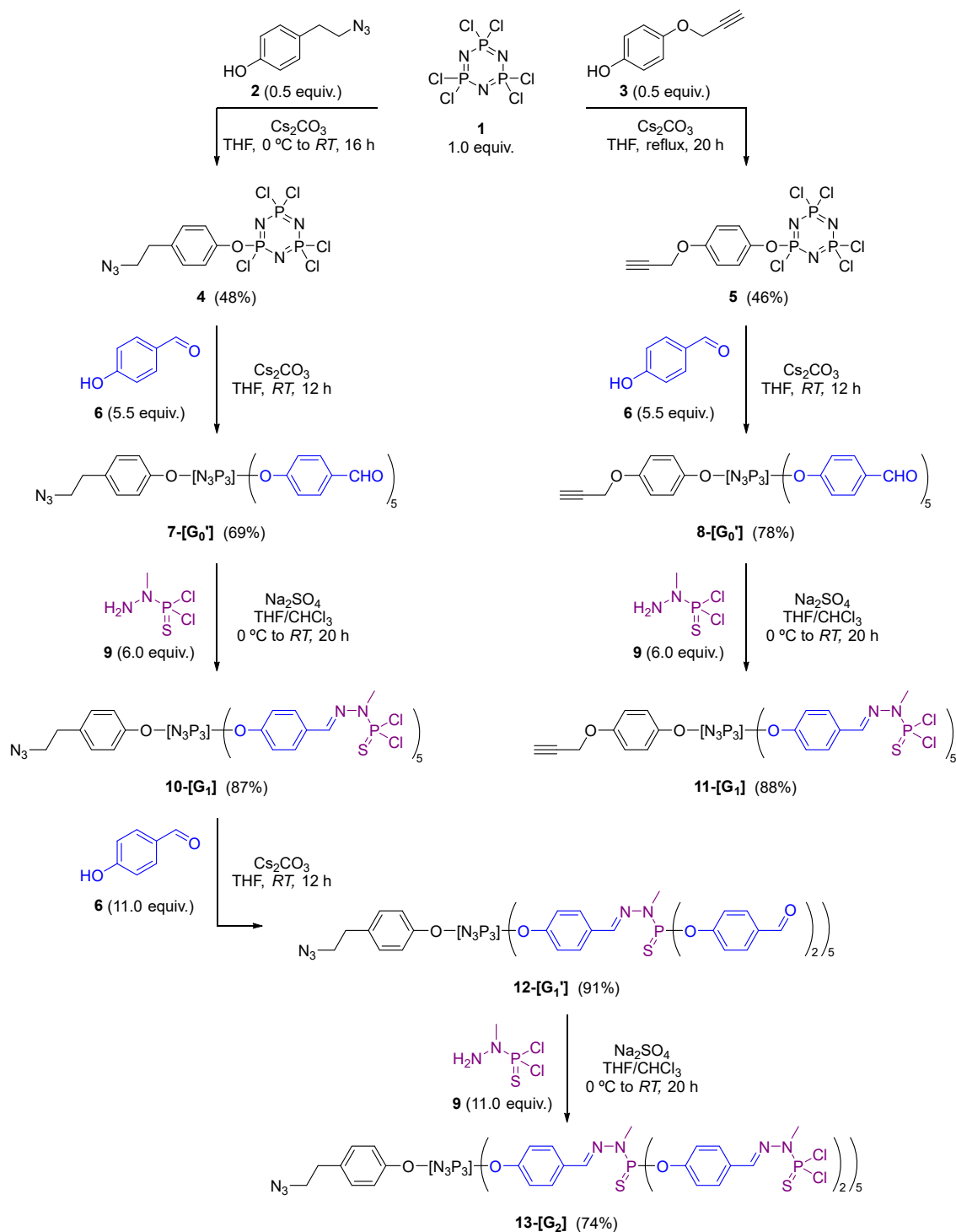


**Figure 28.** Schematic representation of the goal Janus dendrimer, bearing PEG chains to provide water solubility on one side (right, blue), and a grafting point for the incorporation of ligands/metal complexes (left, orange) for its use in supported aqueous catalytic reactions.

The synthesis of dendrons commenced with the preparation of the desired azide and acetylene derivatives, which were developed as phenol-based structures due to the well-documented reactivity of phenols with PPH dendrimers. In particular, the synthesis of 4-(2-azidoethyl)phenol (**2**) and 4-(prop-2-yn-1-yloxy)phenol (**3**) was performed following previously reported methodologies [6–8]. Having successfully obtained the two desired azido and acetylenic phenol derivatives, the next step in synthesizing the dendrons was to introduce **2** and **3** to the hexafunctionalized dendrimer core ( $N_3P_3Cl_6$ ) to create the monosubstituted cores (Scheme 1, top). Specifically, the methodology explored for dendron synthesis aimed at preparing  $AB_5$ -type dendrons, wherein one functionality at the core level would differ from the remaining five [9]. In the context of the dendritic systems of interest, this meant that the substitution of the core was carried out in such a way that five functionalities were employed for dendrimer growth, while the sixth functionality was the azide or acetylene derivative (compounds **2** and **3**). This method involved the introduction of the azide/acetylene derivative initially, followed by the subsequent penta-substitution with 4-hydroxybenzaldehyde in a second step.

In this regard, the synthesis of the azido and acetylenic dendrons was pursued as shown in Scheme 1. First, the monosubstituted core derivatives **4** and **5** were synthesized by a selective monosubstitution reaction of one P–Cl bond from the  $N_3P_3Cl_6$  core, and these structures were used as the starting building block for the creation of the dendron structures following the previously established methodologies by Caminade and Majoral [9,10]. The methodology consisted of the reaction of the remaining five P–Cl bonds with 4-hydroxybenzaldehyde to form the  $G_0'$  dendrons, followed by the reaction of the terminal aldehyde groups from the  $G_0'$  dendrons with *N*-methyl dichlorothiophosphorhydrazide (**9**), which would lead to the obtention of highly functionalizable  $-P(S)Cl_2$  groups. This way, first-generation dendrons were prepared for both azide (**10**-[ $G_1$ ]) and acetylene (**11**-[ $G_1$ ]) derivatives, which after stepwise synthesis also were crafted to the second generation (for the azide derivative **13**-[ $G_2$ ], Scheme 1, bottom), leading to the obtention of a compound with twenty P–Cl surface functionalities.

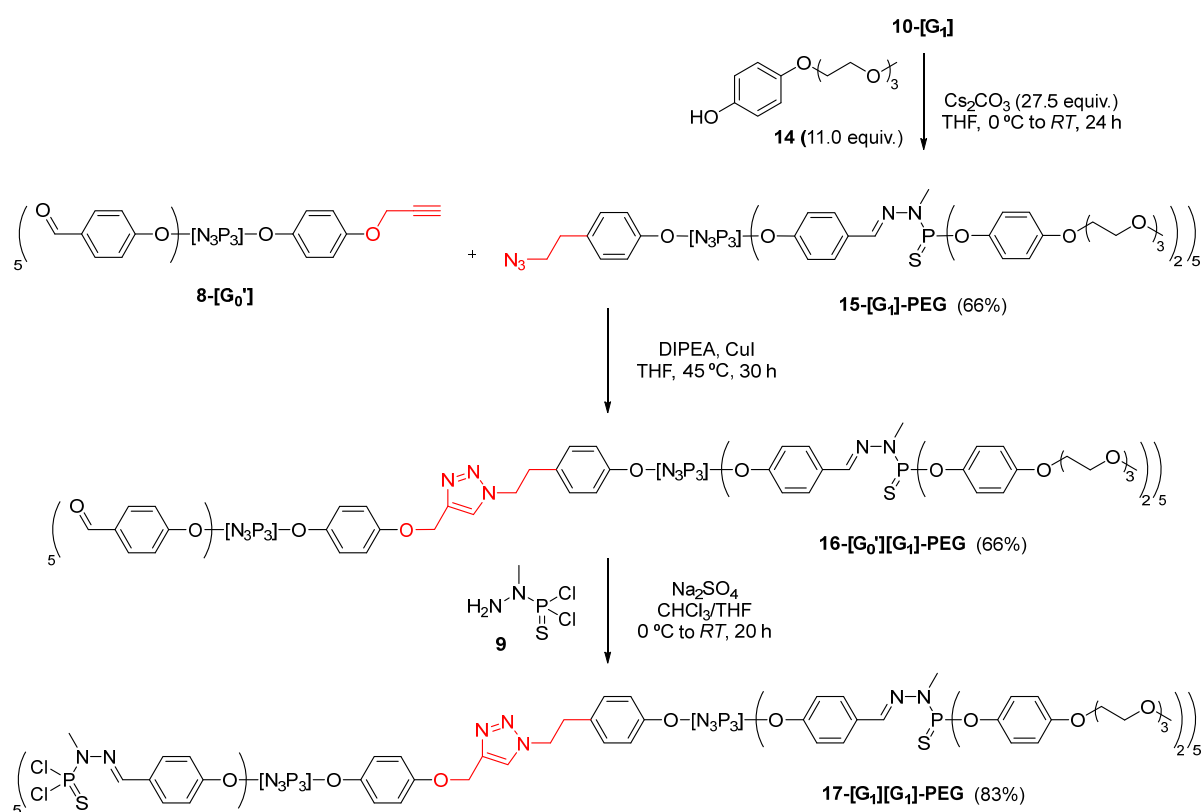


**Scheme 56.** Overview of the synthetic approach performed for the synthesis of PPH AB<sub>5</sub>-type dendrons bearing either azide or acetylene groups at the level of the core, up to the second-generation structures.

Upon synthesis of dendrons up to the second generation, the focus shifted towards developing a dendron that could induce solubility in water, by the introduction of PEG chains. To achieve this objective, the synthesis of **14** (4-(2-(2-(2-methoxyethoxy)ethoxy)-ethoxy)phenol) was undertaken for the later surface modification of **10-[G<sub>1</sub>]** azide dendron. PEG-modified phenol **14** was synthesized in two steps from hydroquinone and 2-(2-(2-methoxyethoxy)ethoxy)ethan-1-ol as previously reported [11], and later tested for the incorporation onto the dendron structure (Scheme 2). Of interest, phenol

**14** (in slight excess) was dissolved in THF and stirred at 0 °C in the presence of Cs<sub>2</sub>CO<sub>3</sub> for 2 h before the addition of **10-[G<sub>1</sub>]**, leading to the formation of the desired **15-[G<sub>1</sub>]-PEG** in moderate yields.

Upon synthesis of the desired functionalized dendrons, the preparation of Janus dendrimers was undertaken by the preparation of a hybrid **13-[G<sub>0'</sub>][G<sub>1</sub>]-PEG** dendrimer (Scheme 2) was performed by reacting the PEG-modified azide dendron **15-[G<sub>1</sub>]-PEG** and the acetylene dendron **8-[G<sub>0'</sub>]** in stoichiometric amounts by the formation of a 1,2,3-triazole through a “click” copper-catalyzed azide-alkyne cycloaddition at 45 °C in presence of *N,N*-diisopropylethylamine (DIPEA) and CuI as catalyst. Lastly, the final stage in obtaining the desired first-generation Janus dendrimer involved extending the aldehyde functionalities of **16-[G<sub>0'</sub>][G<sub>1</sub>]-PEG** to the full first generation **17-[G<sub>1</sub>][G<sub>1</sub>]-PEG** (Scheme 2). It entailed the reaction of **16-[G<sub>0'</sub>][G<sub>1</sub>]-PEG** with *N*-methyldichlorothiophosphorhydrazide **9** in the presence of anhydrous Na<sub>2</sub>SO<sub>4</sub>, as previously described for the growing of dendrons [12]. This led to the obtention of the targeted Janus dendrimer, bearing ten PEG chains on one side of the structure and ten P-Cl bonds on the other, ready to be coupled with the corresponding ligand or pre-catalyst of interest.



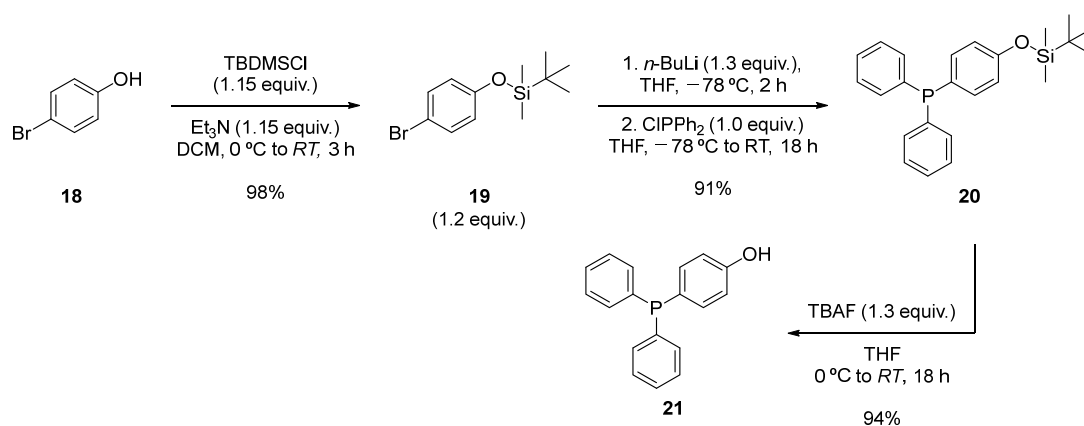
**Scheme 57.** Overview of the synthetic approach for the synthesis of a first-generation PPH Janus dendrimer **17-[G<sub>1</sub>][G<sub>1</sub>]-PEG** by the combination of two dendrons through “click” chemistry.

### Synthesis of a Ru(*p*-cymene)@Janus dendrimer catalytic system

To evaluate the applications of supported ruthenium complexes in catalysis, the next part of the Thesis was dedicated to preparing a metal@dendrimer system for catalytic applications in water-based systems. Based on the previous literature knowledge, the idea of preparing a novel Ru@dendrimer system was conceived. Therefore, the objective was to develop a novel catalytic system through the immobilization of metal pre-catalysts on the surface of the Janus dendrimer **17-[G<sub>1</sub>][G<sub>1</sub>]-PEG**.

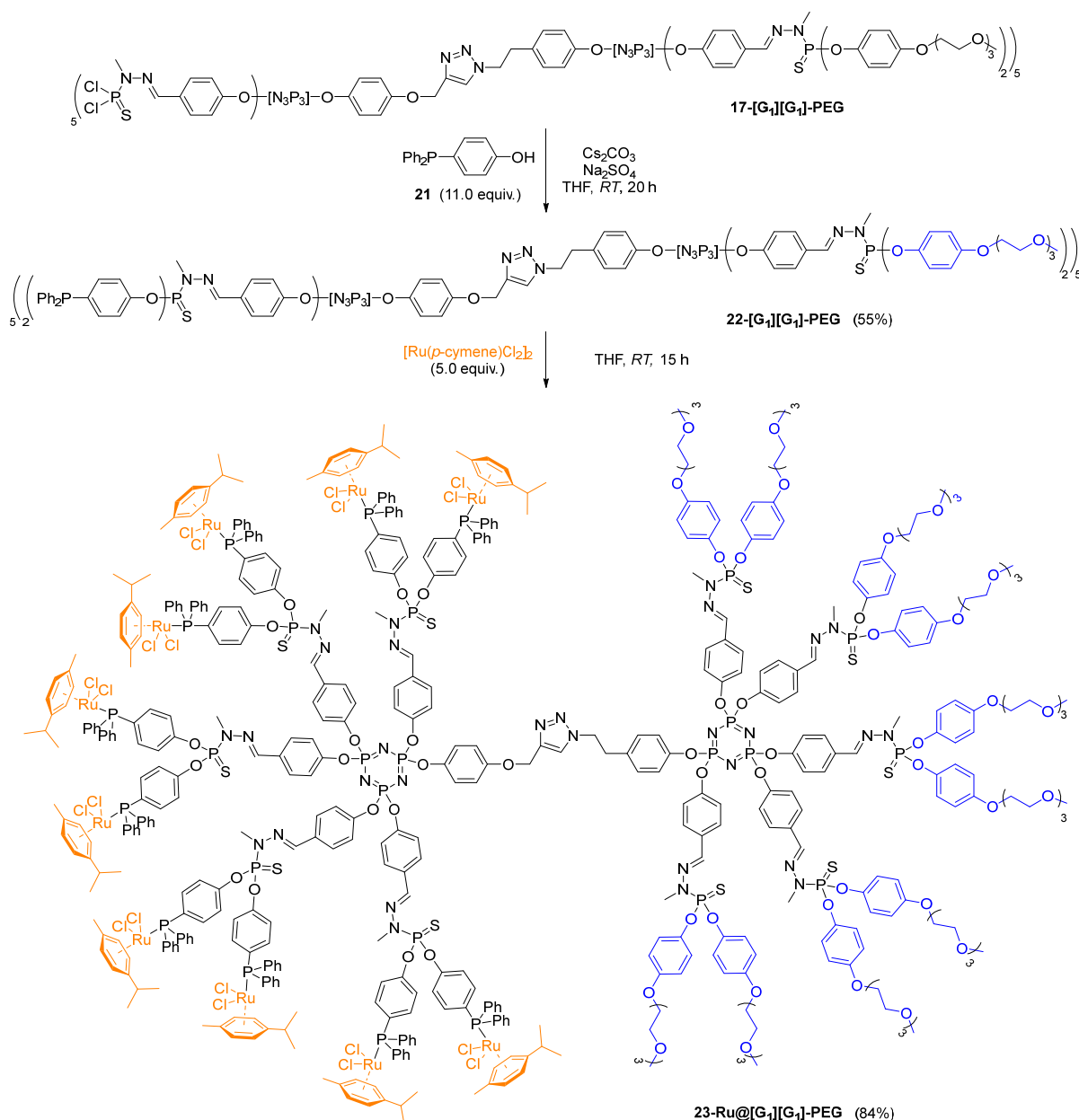
Specifically, it was aimed to immobilize  $[\text{Ru}(p\text{-cymene})\text{Cl}_2]_2$  complexes on the dendrimer surface, based on the ease of availability of such compound.

The synthesis of the Ru@Janus dendrimer system commenced with the preparation of a phosphine ligand (4-(diphenylphosphoryl)phenol **21**), which would be introduced onto the dendrimer structure before complexation of the pre-catalyst. This compound was chosen due to the presence of both a phenol group—which serves as a grafting point for the reaction with **17-[G<sub>1</sub>][G<sub>1</sub>]-PEG**—and the phosphine itself, which would be used for the complexation of the ruthenium catalyst. The desired phenol phosphine **21** was synthesized in three steps from 4-bromophenol (Scheme 3) [13]: first, 4-bromophenol was derivatized to introduce a silyl protecting group by reaction with TBDMSCl; later, the conversion into phosphine by a two-step lithiation and phosphination with chlorodiphenyl phosphine; and lastly, the phenolic OH group was regenerated by deprotection with tetrabutylammonium fluoride (TBAF) to reach the desired **21** in 84% yield over three steps.



**Scheme 58.** Synthesis of 4-(diphenylphosphoryl)phenol (**21**) from 4-bromophenol

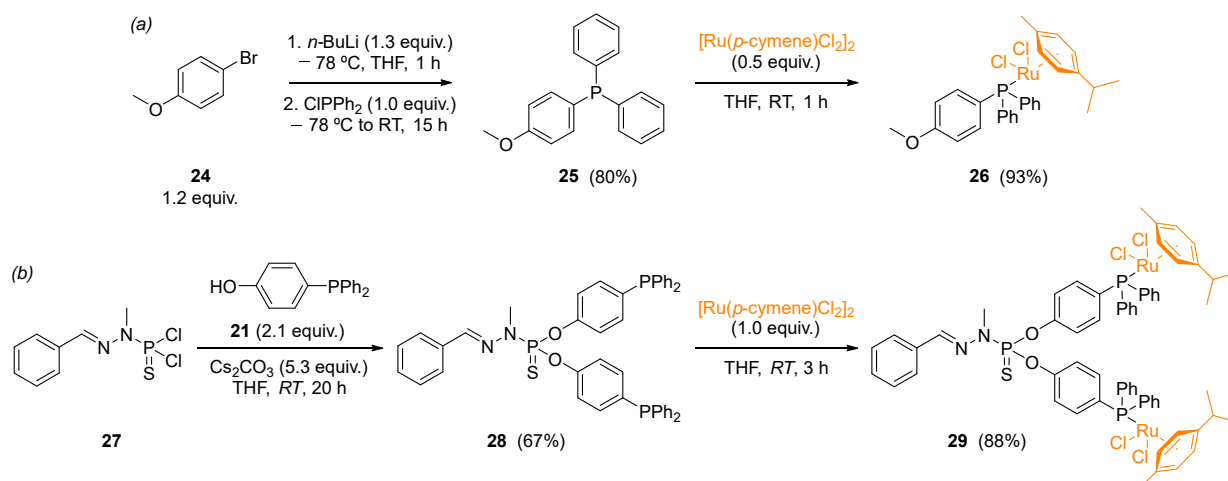
After the synthesis of **21**, the next step involved introducing it to the first-generation Janus dendrimer **17-[G<sub>1</sub>][G<sub>1</sub>]-PEG** (Scheme 4). To prepare the desired phosphine-terminated dendrimer, standard reaction conditions for the introduction of phenol derivatives to  $-\text{P}(\text{S})\text{Cl}_2$ -terminated dendrimers were employed, allowing the obtention of the desired phosphine-terminated **22-[G<sub>1</sub>][G<sub>1</sub>]-PEG** in a moderate 55% yield after work-up. Lastly, the targeted Ru@dendrimer system was obtained by anchoring to the phosphine-terminated dendron **22-[G<sub>1</sub>][G<sub>1</sub>]-PEG** a commercially available ruthenium complex. To accomplish this,  $[\text{Ru}(p\text{-cymene})\text{Cl}_2]_2$  was grafted to the dendrimer through the complexation ability of the terminal phosphines. As illustrated in Scheme 4, five equivalents of the ruthenium complex were reacted with one equivalent of dendrimer **22-[G<sub>1</sub>][G<sub>1</sub>]-PEG**—bearing ten phosphine groups—in THF at room temperature, following a similar procedure as previously reported in the literature [14]. The reaction proceeded smoothly, yielding the expected **23-Ru@[G<sub>1</sub>][G<sub>1</sub>]-PEG** dendrimer as an orange solid in good yield, which was easily purified by precipitation and further washings. The newly formed Ru@dendrimer species was fully characterized, with special mention to the  $^{31}\text{P}\{^1\text{H}\}$  NMR, revealing a significant deshielding effect of the terminal phosphine upon complexation. Furthermore, inductively coupled plasma (ICP) analysis was used for assessing the ruthenium content in the Janus dendrimer. The analysis demonstrated that the supported **23-Ru@[G<sub>1</sub>][G<sub>1</sub>]-PEG** contained a Ru content of 9.1%, aligning with the calculated theoretical value.



**Scheme 59.** Synthesis of a Ru@Janus dendrimer **23-Ru@[G<sub>1</sub>][G<sub>1</sub>]-PEG**, bearing ten PEG moieties on one side of the structure and ten Ru(*p*-cymene) units in the other.

### Catalytic tests for the isomerization of allyl alcohols

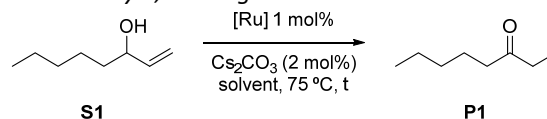
Dendrimers can have various effects when applied in catalysis, including modifications of catalytic activity due to the high local concentration of catalysts within dendrimers, effects arising from catalyst anchoring, potential electronic modifications, and the facilitation of catalyst recyclability and reusability within dendrimeric systems [15,16]. To properly assess the performance of the novel immobilized ruthenium complex **23-Ru@[G<sub>1</sub>][G<sub>1</sub>]-PEG**, it was essential to synthesize analogous ruthenium complexes for comparison purposes. These novel structures were prepared following the synthetic approach depicted in Scheme 5, yielding to the obtention of monometallic (**26**) and bimetallic (**29**) structures, designed to mimic the surface of the Ru@dendrimer **23**.



**Scheme 60.** Synthesis of Ru-complexes **26** and **29**, monometallic and bimetallic analogues of the Ru@dendrimer **23**, respectively.

Having successfully synthesized a PPH Janus dendrimer system containing Ru(*p*-cymene) complexes within its structure (**23**), along with analogous monometallic and bimetallic species (**26**, **29**), the next step was to evaluate the catalytic activity of the three prepared complexes. Ru(*p*-cymene)-type complexes have been well-documented in the literature for their applications as catalysts in various processes, including the isomerization of allyl alcohols and the hydration of acetylenes, among others [17,18]. For the evaluation, the isomerization of allyl alcohols was selected as the target reaction to assess the performance of the prepared complexes. This reaction typically involves the conversion of allyl alcohols into ketones or aldehydes through a two-step process that combines oxidation and reduction, but that is carried out in a one-pot manner using organometallic complexes. The initial catalytic tests for the novel Ru-complexes were conducted to evaluate their performance for the isomerization of 1-octen-3-ol to 3-octanone, firstly in conventional organic solvent conditions. In these experiments, a THF solution containing the substrate **S1** (1.0 equiv.), 1,3,5-trimethoxybenzene (used as an internal standard), and Cs<sub>2</sub>CO<sub>3</sub> (2 mol%) was prepared (Table 1). The reaction mixture was then heated to 75 °C, and 1 mol% of the ruthenium catalyst was added. It is worth noting that the same reaction conditions were applied for all three Ru-catalysts, and the conversion was assessed by gas chromatography (GC) comparing the crude mixtures with the original samples of substrates and products.

**Table 8.** Isomerization of 1-octen-3-ol to 3-octanone at 75 °C catalyzed by complexes **23**, **26** and **29** (1 mol% loading) with Cs<sub>2</sub>CO<sub>3</sub> (2 mol%) as co-catalyst, under given solvent conditions.



Entry	Catalyst	Solvent	Time to full conversion [h] <sup>a</sup>
1	<b>26</b> – monometallic	THF	3
2	<b>29</b> – bimetallic		1.5
3	<b>23</b> -Ru@[G <sub>1</sub> ][G <sub>1</sub> ]-PEG (10 [Ru])		1.5
4	<b>26</b> – monometallic	H <sub>2</sub> O/ <i>n</i> -heptane	–
5	<b>29</b> – bimetallic		–
6	<b>23</b> -Ru@[G <sub>1</sub> ][G <sub>1</sub> ]-PEG (10 [Ru])		24

<sup>a</sup> Conversion was determined through GC using 1,3,5-trimethoxybenzene as internal standard.

As anticipated, all three Ru-complexes achieved full conversion within the reported time frames in the literature (Table 1, entries 1-3) [17,18]. Monometallic complex **26** achieved full conversion after 3 hours of reaction. Remarkably, both the bimetallic complex **29** and the dendrimeric structure **23-Ru@[G<sub>1</sub>][G<sub>1</sub>]-PEG** yielded 3-octanone (**P1**) in short reaction times (1.5 h). These results were highly encouraging, as they indicated that the proximity of ruthenium centers could potentially lead to a cooperative effect, enhancing the efficiency of the reaction.

Following the promising results obtained in organic solvent conditions, the focus was shifted to utilizing water as the solvent for the catalytic process. Specifically, an *n*-heptane/water mixture (1:1) was chosen as the solvent system, considering it a valuable approach to reduce the usage of organic solvents by incorporation of a sustainable solvent such as water, and benefiting from the possibility of an easier recovery of the catalyst in biphasic media. Importantly, the presence of an *n*-heptane/water mixture resulted in the formation of a biphasic system where: (i) the substrate, product, and the internal standard resided in the organic *n*-heptane phase; and (ii) cesium carbonate and the Ru@dendrimer **23** remained in the water phase making easier its recovering and recycling. Catalytic tests were conducted following the previously established reaction conditions incorporating the use of a biphasic solvent system. Aliquots were sampled at specific intervals, and conversion was determined by GC (Table 1, entries 4-6). The catalytic results revealed that both the monometallic and bimetallic systems yielded no isomerization product after 24 hours of reaction. Intriguingly, when the **23-Ru@[G<sub>1</sub>][G<sub>1</sub>]-PEG** catalyst was employed, full conversion was achieved after 24 hours of reaction.

The obtained results were highly positive in terms of the activity of the Ru@dendrimer system. Notably, a positive dendritic effect was observed for the isomerization of 3-octen-1-ol in both organic solvent and biphasic mixtures. Particularly intriguing was the use of the biphasic system, where only **23-Ru@[G<sub>1</sub>][G<sub>1</sub>]-PEG** exhibited catalytic activity for the desired reaction, although activity was reduced, and long reaction times were required. Lastly, it was decided to investigate the recyclability of the dendrimeric system, to provide a greener approach to the use of a Ru@dendrimer catalyst. In this context, a catalytic test was conducted in the biphasic solvent conditions, and the reaction was allowed to proceed for 24 hours. After reaction time, the organic phase was separated from the aqueous phase and GC analyses confirmed the full conversion of **S1** to 3-octanone in the recovered phase. Subsequently, a mixture of **S1** and 1,3,5-trimethoxybenzene in fresh *n*-heptane was added to the water phase containing the Ru@dendrimer catalyst **23**. Repetition of this procedure resulted in the attainment of full conversion of 3-octanone for up to three consecutive runs (Figure 2). Moreover, the possibility of metal leaching was also investigated. Analysis of Ru content in the organic phase by ICP revealed no significant leaching, even after full conversion to 3-octenone. ICP results indicated the presence of less than 0.05% Ru contamination in the sample, confirming the excellent stability of the catalyst.

### Synthesis of unsymmetrical N-heterocyclic carbene (uNHC) ligands bearing a phenol handler

The significance and relevance of olefin metathesis catalysts are closely linked to the development of N-heterocyclic carbene (NHC) ligands. This connection primarily arises from the increased stability of Ru-NHC complexes compared to their phosphine counterparts [19]. Additionally, the ease of adjusting the electronic and steric properties of Ru-NHC complexes by modifying substituents within their structure further underscores their importance. Consequently, a wide range of NHC ligands have been developed in the literature, with most featuring symmetrical substituents in their structure. However, it is worth noting that, while unsymmetrical NHCs (uNHCs) generally exhibit

lower activity compared to their symmetrical counterparts, they hold promise as an attractive alternative for applications in non-conventional metathesis processes [20]. In this context, this thesis focuses on the development of novel uNHC ligands and their corresponding Hoveyda-II-type complexes.

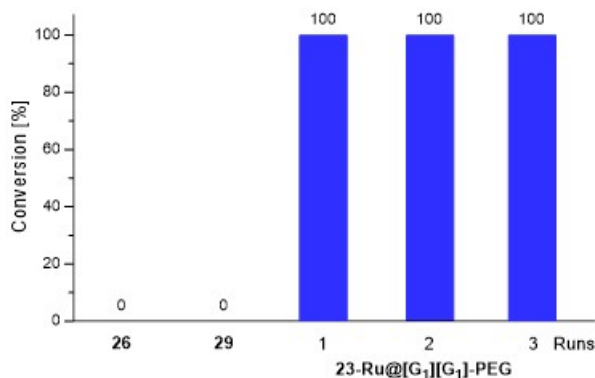


**Figure 29.** Isomerization of 1-octen-3-ol to 3-octanone in *n*-heptane/water mixture at 75 °C catalyzed by complexes **23**, **26** and **29** (1 mol%), showing a clear dendrimer effect; and recyclability experiments of dendrimer **23** up to three consecutive runs.

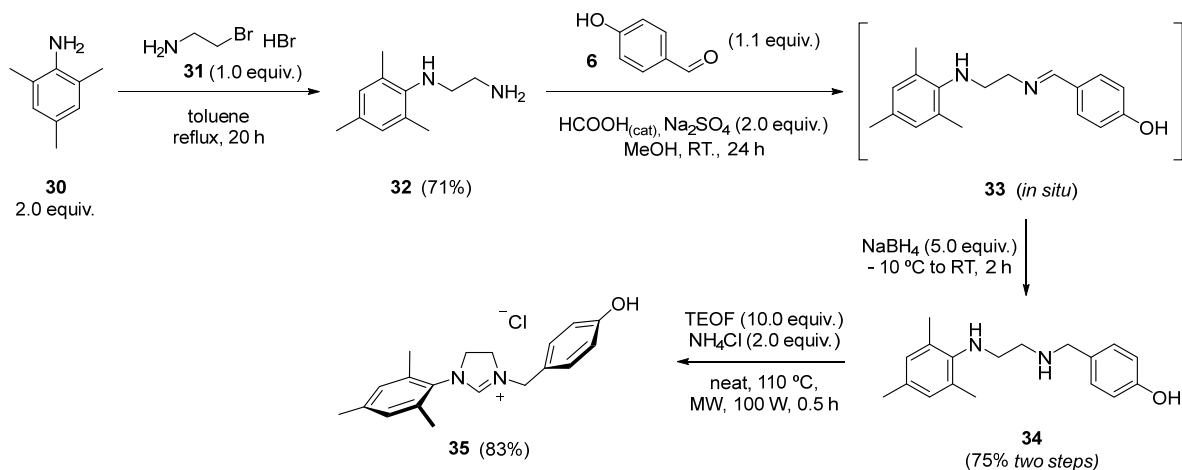
Of particular interest is the creation of Ru-NHC complexes featuring functional groups suitable for attachment to various supports. This includes investigating their incorporation onto dendritic supports or metal-organic frameworks (MOFs). The selection of appropriate functional groups for the uNHCs is a critical aspect of this endeavor. To achieve the desired objective, this section aimed to outline the synthesis of unsymmetrical N-heterocyclic carbenes (uNHCs). These uNHCs were designed to incorporate a mesityl group on one side and a phenolic group on the other. Furthermore, the research will explore how the presence of uNHCs influences the reactivity of Ru-NHC complexes, as well as the impact of temperature and solvent on olefin metathesis catalysis to assess the suitability of these novel complexes for metathesis catalysis.

The synthesis of the Ru-NHC complexes was started by the synthesis of NHC precursors bearing the previously mentioned phenolic arm [21]. The synthesis of unsymmetrical imidazolium ligand precursors **34** and **40** was accomplished using two pathways: through the condensation of *N*-(2,4,6-trimethylphenyl)-1,2-diaminoethane with 4-hydroxybenzaldehyde in the presence of a catalytic amount of formic acid (for **35**, Scheme 6), further reduction of the imine **33** to the corresponding diamine **34**, followed by cyclization with triethyl orthoformate to give the NHC precursor **35**; or through simple alkylation of Mes (Mes = 2,4,6-trimethylphenyl)-bearing imidazole with **38** (iodomethyl)phenol (for **40**, Scheme 7).

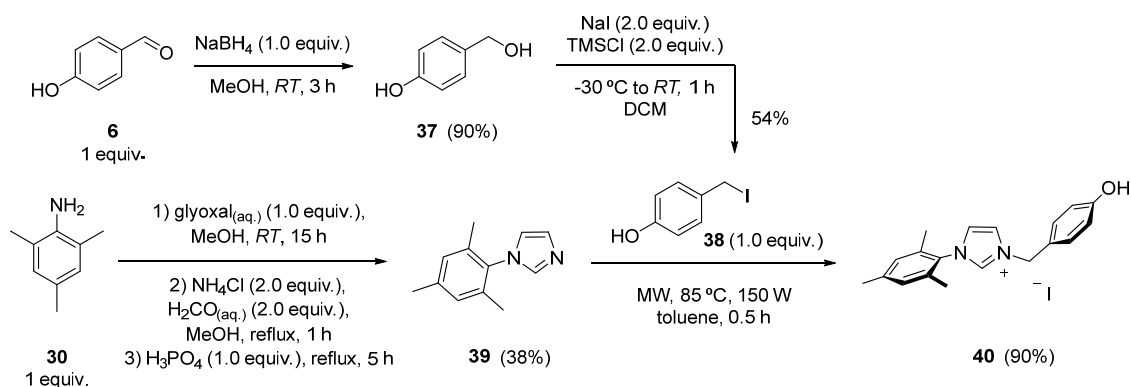
The synthesis of unsymmetrical N-heterocyclic carbene (uNHC) Hoveyda–Grubbs-type II-generation complexes involved the exchange of the phosphine ligand of the Hoveyda–Grubbs-type-I-generation catalyst with a uNHC ligand (Scheme 8). The process included treating the corresponding ligand precursor (**35** or **40**) with LiHMDS to generate a carbene *in situ*, followed by reaction with the Hoveyda–Grubbs-type-I-generation catalyst. Quenching with 5 equivalents of 4 N HCl in dioxane "liberated" the OH-group and provided the desired complexes **Ru1** and **Ru2** in moderate yields. Interestingly, in the case of the **Ru2** complex, the exchange of Cl<sup>-</sup> anions at the ruthenium coordination center to a labile iodide anion from the imidazolium ligand was observed. This phenomenon, known as "scrambling" [22], resulted in an undefined mixture of **Ru2** and **Ru3** complexes. To overcome this obstacle, it was decided to counter-exchange iodide anions to chlorides through treatment with silver



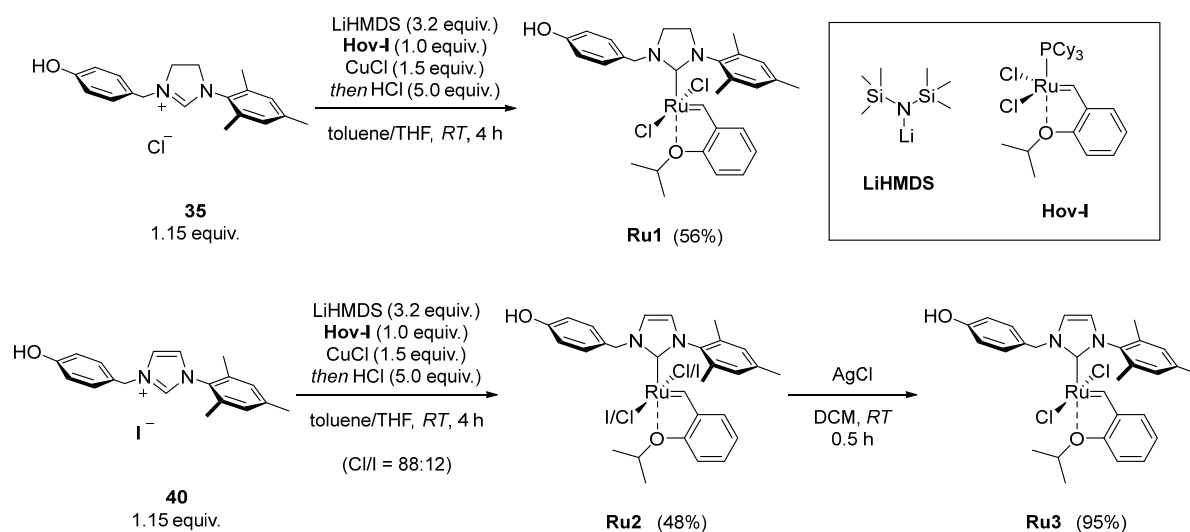
chloride (1.1 equiv. per **Ru2** in DCM at room temperature). This simple transformation yielded the pure **Ru3** complex in practically quantitative yield. The synthesized imidazolium ligand precursors (**35**, **40**) and catalysts (**Ru1**, **Ru3**) were fully characterized using a combination of NMR spectroscopy and HRMS (or elemental analysis), as well as IR spectroscopy. The chemical shifts of benzylidene protons of the obtained complexes ranged from 16.38 to 16.22 ppm, which is typical for this class of Hoveyda-type catalysts.



**Scheme 61.** Synthesis of the unsymmetrical NHC ligand precursor **35**, bearing a phenolic arm in the structure.



**Scheme 62.** Synthesis of 3-(4-hydroxybenzyl)-1-mesityl-1H-imidazol-3-ium iodide **40**.



**Scheme 63.** Synthesis of Ru-NHC complexes **Ru1** and **Ru3** bearing a phenolic arm in the structure.

Following the synthesis and characterization of the phenolic complexes **Ru1** and **Ru3**, the next step was to investigate the stability and activity of these complexes in solution. Concerning the stability studies, complexes **Ru1** and **Ru3** were dissolved in deuterated DCM ( $C_{[Ru]} = 0.02$  M) in an argon atmosphere at room temperature, followed by the addition of 1,3,5-trimethoxybenzene as an internal standard. The decomposition of the catalysts was quantified using  $^1\text{H}$  NMR spectroscopy with respect to 1,3,5-trimethoxybenzene, measuring the decrease in the intensity of benzylidene signals in  $^1\text{H}$  NMR spectra. Unfortunately, the analogous experiment performed in toluene failed due to precipitate formation. Both synthesized catalysts demonstrated high stability in deuterated DCM at room temperature, decomposing only 6% and 4% over 10 days (for **Ru1** and **Ru3**, respectively). Comparing these results to what was reported previously for structurally related uNHC catalysts shows a positive effect of the electron-donating OH-substituent in the *N*-benzyl "arm," visibly stabilizing the ruthenium center against decomposition [23].

After the synthesis and stability assessments of **Ru1** and **Ru3**, the activity and reaction profiles of these "phenolic" complexes were examined. To do so, the ring-closing metathesis (RCM) reaction of diethyl diallyl malonate (DEDAM, **S2**) was evaluated as a model reaction. For this purpose, malonate **S2** was dissolved in DCM or toluene ( $C_{[S2]} = 0.1$  M) and treated with 1 mol% catalyst (**Ru1** or **Ru3**). The reaction was monitored through GC to determine the time-dependent conversion of **S2**. As expected, similar to the other members of this uNHC catalysts family, both of the studied catalysts were found to be less active under ambient conditions but sufficiently activated at slightly elevated temperatures (Table 2). In the case of **Ru1**, the RCM experiment at room temperature in DCM showed a maximum conversion of 49%, demonstrating a rather moderate activity of the catalyst under ambient conditions. Similarly, the RCM reaction of malonate **S2** was conducted using the unsaturated complex (**Ru3**). The outcome of this catalytic run was more positive—the conversion after 24 h reached 79%. When toluene was used as a solvent at 50 °C, both catalysts showed satisfactory results, driving the reaction to full conversion. In this case, too, higher activity of **Ru3** was observed compared to its saturated congener **Ru1**.

**Table 2.** Outcome of the RCM of DEDAM (**S2**) under various conditions (solvent, temperature, and addition of a Lewis acid) for **Ru1** and **Ru3**.

Entry	[Ru]	Solvent	Additive	Temperature [°C]	Conversion [%] <sup>a</sup>
1	<b>Ru1</b>	DCM	–	RT	49
2		DCM	B(OEt) <sub>3</sub>	RT	56
3		Toluene	–	50	>99
4	<b>Ru3</b>	DCM	–	RT	79
5		Toluene	–	50	>99

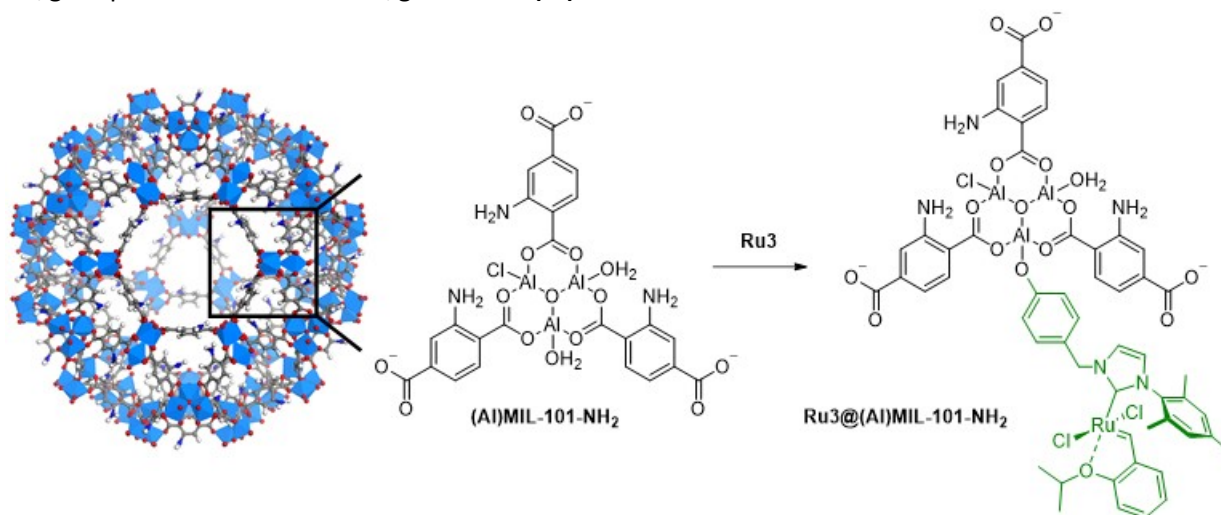
<sup>a</sup> Conversion assessed by GC using dodecane as an internal standard

### Immobilization of Ru-NHC complexes on Metal-Organic Frameworks

Subsequently, we undertook the task of immobilizing the newly synthesized Ru-NHC complexes onto metal-organic frameworks (MOFs) as heterogeneous supports. For the immobilization of Ru-NHC on MOFs, the more active **Ru3** complex was selected as the candidate for immobilization. Considering the relatively large size of the Hoveyda–Grubbs-type complexes and the stability of a potential solid support, (AI)MIL-101-NH<sub>2</sub> was chosen, which met the aforementioned criteria [24].

The catalyst **Ru3** (approximately 10 w/w%) was dissolved in DCM or toluene (1 mM), followed by the addition of an appropriate amount of **(Al)MIL-101-NH<sub>2</sub>**. After 1 hour of stirring, the mixture was centrifuged, and the supernatant was examined using spectrophotometric methods to determine the catalyst concentration in the supernatant. In both DCM and toluene, almost quantitative sorption was observed (99.2% and 99.4% of the catalyst was absorbed in **(Al)MIL-101-NH<sub>2</sub>**, respectively). Since the catalyst was held inside the MOF by reversible noncovalent interactions, the desorption was the next step to investigate. To assess the robustness of the catalyst's immobilization, it was washed the obtained **Ru3@ (Al)MIL-101-NH<sub>2</sub>** with toluene and DCM, starting with the less polar toluene. The material was placed on a G4 filtering funnel with a side argon inlet, and solvents were slowly filtered through the catalyst@MOF. The supernatants were monitored using UV-Vis. Interestingly, no significant leaching of the absorbed catalyst from **(Al)MIL-101-NH<sub>2</sub>** was observed under these challenging dynamic conditions—the total amount of **Ru3** washed out with toluene (20 mL) and DCM (20 mL) was less than 10%.

Powder X-ray diffraction (PXRD) studies revealed that the material remained crystalline after catalyst immobilization, but its porosity, expressed as BET surface area, dropped significantly from 1753 m<sup>2</sup>/g for pristine MOF to 564 m<sup>2</sup>/g for **Ru3@ (Al)MIL-101-NH<sub>2</sub>**.



**Scheme 64.** Approach for the immobilization of **Ru<sub>3</sub>** within the structure of **(Al)MIL-101-NH<sub>2</sub>**.

Having successfully immobilized **Ru<sub>3</sub>** within the structure of **(Al)MIL-101-NH<sub>2</sub>** and conducted sorption and leaching experiments, the next step was to test the activity of the newly obtained heterogeneous catalyst in metathesis, specifically in the model ring-closing metathesis of compound DEDAM in toluene at 80 °C with 1 mol% of the heterogenized catalyst (refer to Table 3). Based on the leaching experiment, the less polar medium resulted in negligible desorption from the solid support, making toluene a more favorable solvent in this case. In comparison to the homogeneous catalysis discussed earlier, where the conversion was quantitative, the heterogenized system **Ru<sub>3</sub>@ (Al)MIL-101-NH<sub>2</sub>** demonstrated poorer performance. After 24 hours of reaction, only 54% conversion was achieved under these conditions. Increasing the **Ru<sub>3</sub>@ (Al)MIL-101-NH<sub>2</sub>** loading up to 2 mol% did not lead to increased conversion.

Next, it was decided to test the new system on a set of olefin metathesis substrates with the standard loading (1 mol%) of **Ru<sub>3</sub>@MOF** (Table 4). Surprisingly, excellent results were obtained in the ring-closing metathesis (RCM) reaction of DATA (**S3**)—the conversion reached 65% in 3 hours and 91% in 24 hours. It should be mentioned here that attempts to improve the catalyst performance by treating

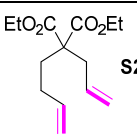
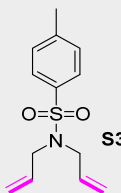
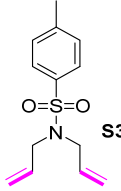
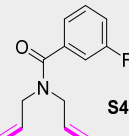
the MOF with dry HCl in Et<sub>2</sub>O after sorption of the catalyst were attempted. Interestingly, the conversion of DATA (**S3**) in the reaction catalyzed with **Ru3@AlMIL-101-NH<sub>2</sub>·HCl** reached 78% in just 15 minutes, but, unfortunately, did not increase after 24 hours. Disappointingly, the RCM reaction of the olefin metathesis substrates **S3** and **S4** conducted in a similar manner (1 mol% of **Ru3@AlMIL-101-NH<sub>2</sub>**) resulted in a poorer outcome, giving only 31% and 30% conversion, respectively.

**Table 3.** Results of the RCM of DEDAM (**S2**) with **Ru3** (homogeneous) and **Ru33@AlMIL-101-NH<sub>2</sub>** (heterogeneous) complexes in toluene.

Entry	[Ru]	Loading [mol%]	Time [h]	Conversion [%] <sup>a</sup>
1	Ru3	1.0	3	95
2			24	>99
3	Ru3@AlMIL-101-NH <sub>2</sub>	1.0	3	53
4			24	54
5		2.0	3	50
6			24	51

<sup>a</sup> Conversion was determined by GC using tetradecane as internal standard.

**Table 4.** Results of the RCM reaction of selected dienes **S2-S4** using **Ru38@AlMIL-101-NH<sub>2</sub>** complex (1 mol%) in toluene at 80 °C.

Entry	[Ru]@MOF	Substrate	Conversion [%] <sup>a</sup>		
			At split	In filtrate (24 h)	In suspension (24 h)
1	Ru3@AlMIL-101-NH <sub>2</sub>		26 (3 h)	26	31
2	Ru3@AlMIL-101-NH <sub>2</sub>		65 (3 h)	65	91 <sup>b</sup>
3	Ru3@AlMIL-101-NH <sub>2</sub> ·HCl		78 (0.25 h)	78	78
4	Ru3@AlMIL-101-NH <sub>2</sub>		13 (3 h)	14	30

<sup>a</sup> Conversion was determined by GC using tetradecane as internal standard.

<sup>b</sup> Isolated yield for the compound is 79 %.

In summary, two new unsymmetrical N-heterocyclic carbene (uNHC)-based ruthenium complexes featuring a phenolic OH function were successfully obtained and fully characterized. The more active complex was then effectively immobilized on the metal-organic framework (MOF) support. Desorption studies suggest that the highly porous structure of **AlMIL-101-NH<sub>2</sub>** provides a favorable

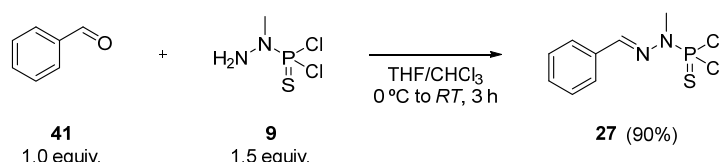
environment for the non-covalent immobilization of a phenol-tagged ruthenium catalyst. After immobilization, the Lewis acidic coordinatively unsaturated centers located inside the well-defined nanoscopic voids in a crystalline framework of the MOF strongly bind the ruthenium complex, resulting in negligible leaching even in polar solvents, such as DCM. The catalytic activity of this formed heterogeneous system was unfortunately lower than the activity of the corresponding homogeneous catalyst in solution; however, it demonstrated catalytic activity in selected olefin metathesis reactions. We believe that the results reported herein represent a valid proof-of-concept and are the very first example of catalyst immobilization through phenol–MOF interactions.

### Attempts on the immobilization of Ru-NHC complexes on dendrimers

Lastly, we embarked on the challenging task of immobilizing Ru-NHC complexes on PPH Janus dendrimers. In this regard, the goal was to obtain the first phosphorus Janus dendrimer applicable in olefin metathesis catalysis, specifically in aqueous media.

To analyze and optimize the reaction conditions for coupling the Ru-NHC complexes and dendrimers, the initial steps were carried out using a model dendrimer molecule, denoted as MDM **27**. MDM was chosen for its structure, which contains a  $-P(S)Cl_2$  group that mimics the surface of typical PPH dendrimers. This characteristic makes MDM an excellent candidate to fine-tune the reaction conditions for the desired coupling. The synthesis of MDM **27** followed the previously reported procedure [25], employing conventional conditions for dendrimer systems (Scheme 10). Specifically, benzaldehyde was subjected to a condensation reaction with *N*-methyldichlorothiophosphorhydrazide (**9**) involving the aldehyde and amino groups, resulting in the formation of **27** as a white solid in 90% yield.

In line with the extensive research conducted by the group of Caminade and Majoral, it has been established that MDM **27** can be tailored similarly to dendrimers. Notably, **27** can undergo reactions with phenols or amines for the substitution of the two chlorides in P–Cl bonds present on its surface.

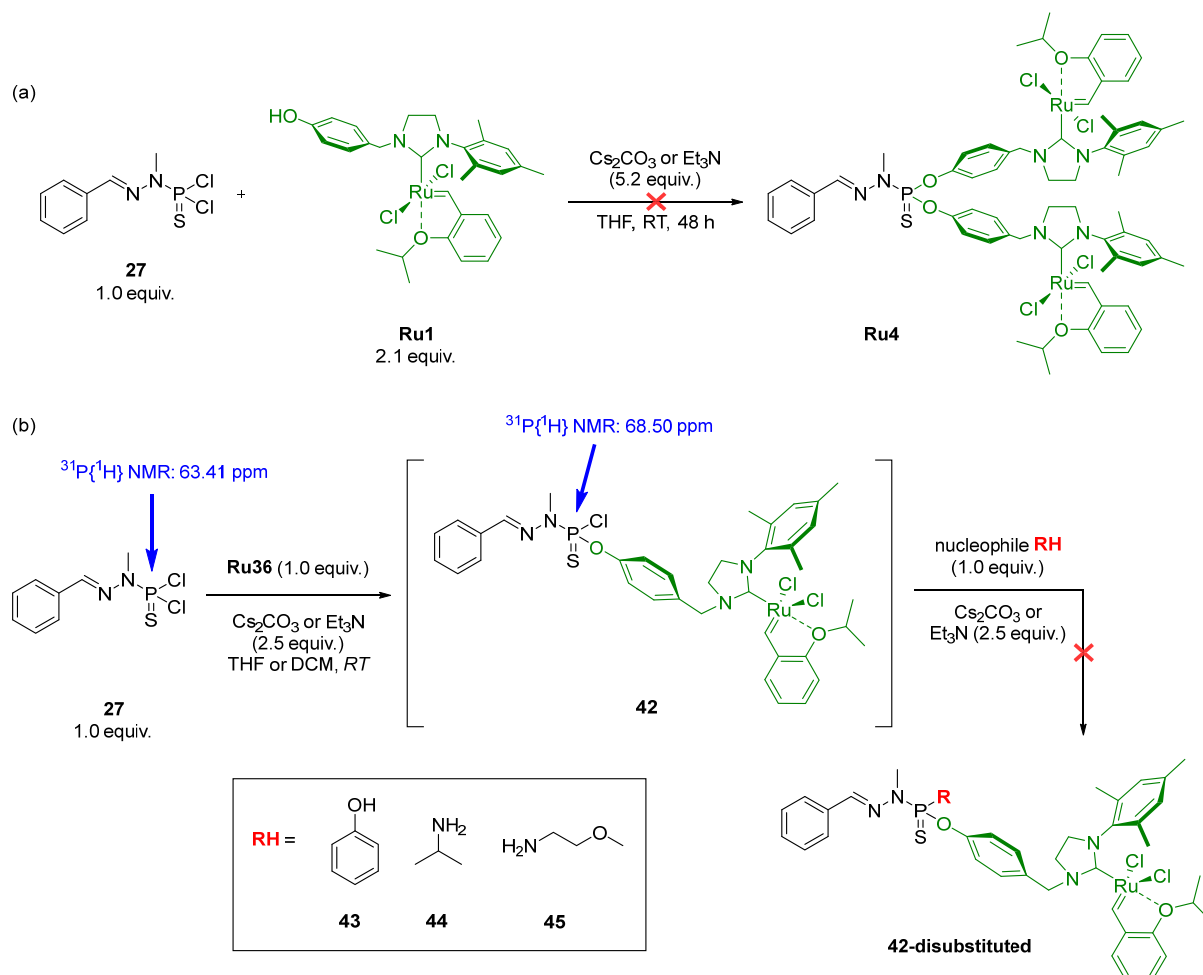


**Scheme 65.** Synthesis of model dendrimer molecule **27**.

The initial attempt to obtain a Ru-NHC@**27** complex involved employing the conventional substitution conditions commonly used for the synthesis of dendrons and dendrimers (illustrated in Scheme 11a). In this process, model **27** was dissolved in dry THF, and  $Cs_2CO_3$  and **Ru1** (in a slight excess) were added. The reaction mixture was stirred at room temperature, and the progression of the reaction was monitored using NMR spectroscopy. Unfortunately, attempts to obtain the desired product through this methodology were unsuccessful displaying decomposition products in the NMR mixtures. Given the preliminary results obtained and considering research conducted by Fogg's group regarding the bimolecular decomposition of olefin metathesis catalysts when they are in close proximity [26,27], it was hypothesized that the di-substitution of **27** to **Ru4** might have occurred, followed by rapid decomposition to form dimeric ruthenium species.

To try to address this issue, the second approach to obtain a Ru@dendrimer structure focused on the asymmetric substitution of **27** (Scheme 11b). The goal was to incorporate one Ru-complex unit into **27**, resulting in a mono-substituted species **42**, and then react it with a nucleophilic agent to complete the substitution. Model dendrimer **27** was reacted under basic conditions with 1.0 equivalent of **Ru1** to obtain the corresponding mono-substituted species **42**. Subsequently, several nucleophilic agents (**43–45**, known to react with dendrimeric structures) were tested for their ability to react with **42** and complete the substitution.

The formation of intermediate **42** was confirmed by NMR spectroscopy, specifically by the shift of the phosphorus peak in  $^{31}\text{P}\{^1\text{H}\}$  NMR to 68.5 ppm, typical for mono-substituted **27**-type species. Following the formation of **42**, attempts to introduce the previously mentioned nucleophilic species to produce the fully substituted model dendrimer were made. Unfortunately, despite using various compounds as potential nucleophilic agents (such as phenol, isopropylamine, or 2-methoxyethan-1-amine), none of the attempts resulted in successful formation of the desired Ru@model dendrimer molecules. Analysis of the reaction mixtures indicated that the introduction of such nucleophilic species to form disubstituted compounds was not achieved, and the attempts to isolate any Ru@model dendrimer molecules led to compound degradation.

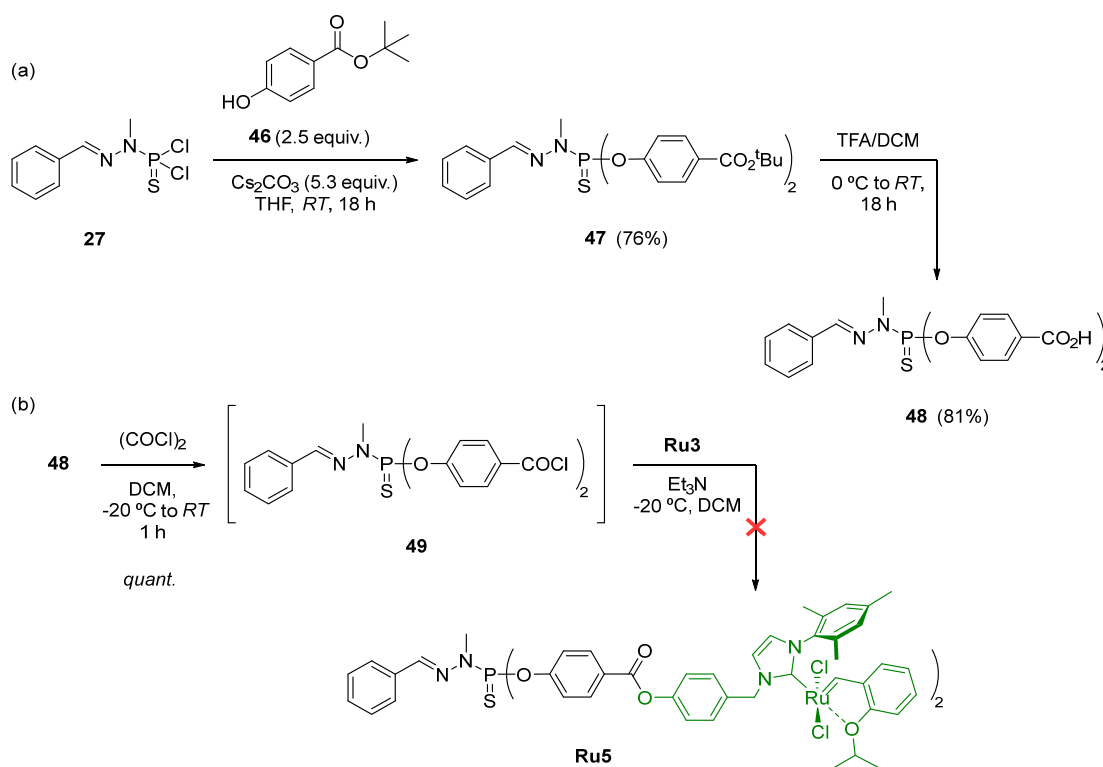


**Scheme 66.** (a) Reaction conditions for the attempt on the synthesis of **Ru39**; (b) Synthetic approaches attempted for the preparation of asymmetrically substituted model dendrimer **156** with one unit of **Ru36**.

The final attempt to prepare Ru@dendrimer structures was inspired by a recent development described by Grela's group [28]. In this approach, Ru-NHC complexes were synthesized through the derivatization a ruthenium complex which already contained a primary alcohol tag in the NHC backbone.

Therefore, and by applying a similar approach, the synthesis of a Ru-NHC@dendrimer system involved the reaction of the phenolic Ru-complexes with an acid-terminated model dendrimer. This acid-terminated model dendrimer, denoted as **48**, was synthesized in two steps from **27** (Scheme 12a) by substitution of **27** with *tert*-butyl 4-hydroxybenzoate and later hydrolysis of the ester.

The synthesis of Ru-NHC@model dendrimer **Ru5** was attempted by combining the approaches developed for the acid-terminated model dendrimer **48** and the acylation reaction of the "phenolic" ruthenium complexes. The process is outlined in Scheme 12b. First, acid-terminated model dendrimer **48** was subjected to oxalyl chloride in DCM at  $-20\text{ }^{\circ}\text{C}$  to generate the acyl chloride derivative **49**. Subsequently, the acyl chloride **49** solution generated *in situ* was slowly added to a DCM solution of **Ru3**, previously treated with an excess of triethylamine for 1 h. The reaction mixture was stirred for a period ranging from 1 to 16 hours, and its progress was monitored using NMR spectroscopy. The NMR results indicated the presence of two phosphorus species, as evidenced by two singlets at 60.88 ppm and 61.24 ppm, which was consistent with the formation of the desired product as well as a second phosphorus-containing species—either hydrolysis derivatives or decomposition products. However, no successful means of purification led to the isolation of the desired product. The synthesis of Ru-NHC@dendrimer **Ru5** represented a challenging endeavor, with complications arising during the purification process. Further optimization and investigation may be required to successfully obtain the desired product.



**Scheme 67.** (a) Synthesis of acid-terminated model dendrimer **162** in two steps from **155**; (b) Attempt on the synthesis of **Ru42** via acylation reaction from **162** and **Ru38**.

## Conclusions

The primary aim of this research has been to advance the field of catalysis by developing novel supported ruthenium complexes. This Thesis has centered on two key objectives: the preparation of PPH Janus dendrimers to facilitate the grafting of Ru-complexes on their surfaces for catalytic applications, and the synthesis of innovative Ru-NHC complexes for olefin metathesis, followed by the immobilization attempts onto dendrimers and MOFs.

In summary, although one of the targeted objectives of this Thesis—immobilization of Ru-NHC complexes on Janus dendrimers—was not achieved, the development of two unprecedented Ru-supported systems for catalysis has been unveiled. Specifically, the **Ru3@MOF** system has been developed, demonstrating that **(Al)MIL-101-NH<sub>2</sub>** offers a favorable environment for the non-covalent immobilization of a phenol-tagged ruthenium catalyst.

In parallel, the first-ever PPH Janus dendrimer with potential applications in catalysis has been reported. Specifically, **23-Ru@[G<sub>1</sub>][G<sub>1</sub>]-PEG** was synthesized, featuring PEG chains on one side of the structure and Ru(*p*-cymene) derivatives on the other side, making it a highly promising material for use in catalysis. The applicability of the Ru@dendrimer **23** in catalysis was tested for the isomerization of 1-octen-3-ol in both THF and biphasic *n*-heptane/water mixtures, demonstrating a positive dendritic effect in both scenarios. Notably, in the biphasic solvent system, only the dendrimeric complex **23-Ru@[G<sub>1</sub>][G<sub>1</sub>]-PEG** exhibited activity for the targeted reaction, while monometallic and bimetallic **26** and **29** showed no conversion of **S1** (after 24 h). Furthermore, the recyclability and reusability of the dendrimeric system were assessed, revealing full conversion of **S1** for up to three consecutive runs, with minimal metal contamination in the final product (<0.05%). These findings highlight the potential of dendrimeric catalysts in catalytic applications, particularly for reactions in aqueous or biphasic systems, and underscore the stability and effectiveness of the developed Ru@dendrimer complex.

## 1. References

- [1] A. M. Caminade, C. O. Turrin, R. Laurent, A. Ouali, B. Delavaux-Nicot, *Dendrimers: Towards Catalytic, Material and Biomedical Uses*, 1st ed.; John Wiley & Sons Ltd., **2011**. ISBN: 9780470748817.
- [2] A. M. Caminade, R. Laurent, *Coord. Chem. Rev.*, **2019**, *389*, 59–72. DOI: [10.1016/j.ccr.2019.03.007](https://doi.org/10.1016/j.ccr.2019.03.007).
- [3] E. Badetti, A. M. Caminade, J. P. Majoral, M. Moreno-Mañas, R. M. Sebastián, *Langmuir* **2008**, *24*, 2090–2101. DOI: [10.1021/la7013418](https://doi.org/10.1021/la7013418).
- [4] J. N. H. Reek, S. Arévalo, R. van Heerbeek, P. C. J. Kamer, P. W. N. M. van Leeuwen, *Adv. Catal.*, **2006**, *49*, 71–151. DOI: [10.1016/S0360-0564\(05\)49002-1](https://doi.org/10.1016/S0360-0564(05)49002-1).
- [5] J. Cejas-Sánchez, A. Kajetanowicz, K. Grela, A. M. Caminade, R. M. Sebastián, *Molecules* **2023**, *28*, 5570–5588. DOI: [10.3390/molecules28145570](https://doi.org/10.3390/molecules28145570).
- [6] C. D. Spicer, M. Pujari-Palmer, H. Autefage, G. Insley, P. Procter, H. Engqvist, M. M. Stevens. *ACS Cent. Sci.*, **2020**, *6*, 226–231. DOI: [10.1021/acscentsci.9b01149](https://doi.org/10.1021/acscentsci.9b01149).
- [7] A. Makarem, K. D. Klika, G. Litau, Y. Remde, K. Kopka, *J. Org. Chem.*, **2019**, *84*, 7501–7508. DOI: [10.1021/acs.joc.9b00832](https://doi.org/10.1021/acs.joc.9b00832).
- [8] Y. Q. Jiang, K. Wu, Q. Zhang, K. Q. Li, Y. Y. Li, P. Y. Xin, *Chem. Commun.*, **2018**, *54*, 13821–13824. DOI: [10.1039/C8CC08226J](https://doi.org/10.1039/C8CC08226J).
- [9] A. Zibarov, A. Oukhrib, J. Aujard Catot, C. O. Turrin, A. M. Caminade, *Molecules* **2021**, *26*, 1–24. DOI: [10.3390/molecules26134017](https://doi.org/10.3390/molecules26134017).
- [10] A. M. Caminade, J. P. Majoral, *Molecules* **2016**, *21*, 538–562. DOI: [10.3390/molecules21040538](https://doi.org/10.3390/molecules21040538).
- [11] A. Sourdon, M. Gary-Bobo, M. Maynadier, M. Garcia, J. P. Majoral, A. M. Caminade, O. Mongin, M. Blanchard-Desce, *Chem. Eur. J.*, **2019**, *25*, 3637–3649. DOI: [10.1002/chem.201805617](https://doi.org/10.1002/chem.201805617).



- [12] O. Alami, R. Laurent, M. Tassé, Y. Coppel, J. Bignon, S. El Kazzouli, J. P. Majoral, N. El Brahami, A. M. Caminade, *Chem. Eur. J.*, **2023**, *29*, e202302198. DOI: [10.1002/chem.202302198](https://doi.org/10.1002/chem.202302198).
- [13] L. Biancalana, L. K. Batchelor, A. De Palo, S. Zacchini, G. Pampaloni, P. J. Dyson, F. A. Marchetti, *Dalton Trans.*, **2017**, *46*, 12001–12004. DOI: [10.1039/C7DT02062G](https://doi.org/10.1039/C7DT02062G).
- [14] I. Angurell, C. O. Turrin, R. Laurent, V. Maraval, P. Servin, O. Rossell, M. Seco, A. M. Caminade, J. P. Majoral, *J. Organomet. Chem.*, **2007**, *692*, 1928–1939. DOI: [10.1016/j.jorganchem.2007.01.001](https://doi.org/10.1016/j.jorganchem.2007.01.001).
- [15] L. P. Wu, M. Ficker, J. B. Christensen, P. N. Trohopoulos, S. M. Moghimi, *Bioconjug. Chem.*, **2015**, *26*, 1198–1211. DOI: [10.1021/acs.bioconjchem.5b00031](https://doi.org/10.1021/acs.bioconjchem.5b00031).
- [16] C. O. Turrin, V. Maraval, J. Leclaire, E. Dantras, C. Lacabanne, A. M. Caminade, J. P. Majoral, *Tetrahedron* **2003**, *59*, 3965–3973. DOI: [10.1016/S0040-4020\(03\)00465-4](https://doi.org/10.1016/S0040-4020(03)00465-4).
- [17] P. Servin, R. Laurent, L. Gonsalvi, M. Tristany, M. Peruzzini, J. P. Majoral, A. M. Caminade, *Dalton Trans.*, **2009**, 4432–4434. DOI: [10.1039/B906393P](https://doi.org/10.1039/B906393P).
- [18] J. E. Bäckvall, U. Andreasson, *Tetrahedron Lett.*, **1993**, *34*, 5459–5462. DOI: [10.1016/S0040-4039\(00\)73934-7](https://doi.org/10.1016/S0040-4039(00)73934-7).
- [19] K. Grela, *Olefin Metathesis: Theory and Practice*; Grela, K., Ed.; Wiley: Hoboken, **2014**. ISBN: 9781118711613. DOI: [10.1002/9781118711613](https://doi.org/10.1002/9781118711613).
- [20] A. Fürstner, L. Ackermann, B. Gabor, R. Goddard, C. W. Lehmann, R. Mynott, F. Stelzer, O. R. Thiel, *Chem. Eur. J.*, **2001**, *7*, 3236–3253. DOI: [10.1002/1521-3765\(20010803\)7:15<3236::AID-CHEM3236>3.0.CO;2-S](https://doi.org/10.1002/1521-3765(20010803)7:15<3236::AID-CHEM3236>3.0.CO;2-S).
- [21] M. Nadirova, J. Cejas-Sánchez, R. M. Sebastián, M. Wiszniewski, M. J. Chmielewski, A. Kajetanowicz, K. Grela, *Catalysts* **2023**, *13*, 297–309. DOI: [10.3390/catal13020297](https://doi.org/10.3390/catal13020297).
- [22] M. Patrzalek, J. Piątkowski, A. Kajetanowicz, K. Grela, *Synlett* **2019**, *30*, 1981–1987. DOI: [10.1055/s-0037-1611834](https://doi.org/10.1055/s-0037-1611834).
- [23] P. Małecki, K. Gajda, R. Gajda, K. Woźniak, B. Trzaskowski, A. Kajetanowicz, K. Grela, *Organometallics* **2017**, *36*, 2153–2166. DOI: [10.1021/acs.organomet.7b00211](https://doi.org/10.1021/acs.organomet.7b00211).
- [24] P. Serra-Crespo, E. V. Ramos-Fernandez, J. Gascon, F. Kapteijn, *Chem. Mater.*, **2011**, *23*, 2565–2572. DOI: [10.1021/cm103644b](https://doi.org/10.1021/cm103644b).
- [25] G. Franc, E. Badetti, C. Duhayon, Y. Coppel, C. O. Turrin, J. P. Majoral, R. M. Sebastián, A. M. Caminade, *New J. Chem.*, **2010**, *34*, 547–555. DOI: [10.1039/B9NJ00568D](https://doi.org/10.1039/B9NJ00568D).
- [26] D. L. Nascimento, M. Foscatto, G. Occhipinti, V. R. Jensen, D. E. Fogg, *J. Am. Chem. Soc.*, **2021**, *143*, 11072–11079. DOI: [10.1021/jacs.1c04424](https://doi.org/10.1021/jacs.1c04424).
- [27] G. A. Bailey, M. Foscatto, C. S. Higman, C. S. Day, V. R. Jensen, D. E. Fogg, *J. Am. Chem. Soc.*, **2018**, *140*, 6931–6944. DOI: [10.1021/jacs.8b02709](https://doi.org/10.1021/jacs.8b02709).
- [28] L. Monsigny, S. J. Czarnocki, M. Sienkiewicz, W. Kopcha, R. Frankfurter, C. Vogt, W. Solodenko, A. Kajetanowicz, A. Kirschning, K. Grela, *Eur. J. Org. Chem.*, **2021**, *46*, 6424–6434. DOI: [10.1002/ejoc.202101092](https://doi.org/10.1002/ejoc.202101092).

**Deepthy KRISHNAN**

**ESR11**

**Thesis co-directors**

Prof. Anders Riisager      Danmarks Tekniske Universtitet, Lyngby, Denmark

Dr. Karine Philippot  
Dr. M. Rosa Axet      Laboratoire de Chimie de Coordination, Toulouse, France

**Thesis defense**

Department of Chemistry, Danmarks Tekniske Universtitet, 28 November 2023



## Mono- and Bimetallic Nanoparticles Stabilized by Functionalized Ionic Liquids: Synthesis and Catalytic Applications

### Ionic Liquids

The most practical definition of an ionic liquid (IL) is 'a liquid composed entirely of ions' [1]. There are diverse salts which are liquids at ambient temperature. ILs that are liquid at room temperature are called room temperature ionic liquids (RTILs). Most ILs are composed of a large organic cation of low symmetry, and a much smaller inorganic polyatomic anion with the charge highly delocalized. The liquid state is favored by small lattice enthalpy and large entropy changes, attributed to the large size and conformational flexibility of the two weakly coordinating ions [2]. While the structural arrangement of IL resembles that of a salt, the main difference is that the coulombic interactions between the ions in a salt is much stronger than in ILs as the result of the similarity between the size and nature of the ions, giving them a strong crystalline structure with relative high melting point, *e.g.* the melting point of NaCl is 801 °C [3]. ILs exhibit notably distinct physical characteristics which includes negligible vapor pressure, high charge density, high polarity, high dielectric constant, and capability to form supramolecular networks [4]. These properties can be designed through combination of various cations and anions as presented hereafter. The cationic center of an IL involves typically a positively charged nitrogen, phosphorus or sulfur atom. Those described thus far involve mainly ammonium, sulphonium, imidazolium, pyridinium, pyrrolidinium, phosphonium, oxazolium, *etc.* cations substituted with alkyl chains. Anions of ILs are usually organic or inorganic weakly basic compounds with a delocalized negative charge [5].

### Task-specific ionic liquids

Task-specific ionic liquids (TSIL) can be defined as ILs which incorporate a covalently linked reactive functionality [6]. The functional group (FG) like carboxylic acid (-COOH) [7], amine (-NR<sub>3</sub>) [8] or nitrile (-CN) [9] can be incorporated either into the anion or cationic part or both [10]. Such functionalities can impart additional properties to the ILs that can be thus employed for specific tasks, with several objectives. For instance, ILs with appended amines have been developed to favor the separation of CO<sub>2</sub> from gas stream *via* carbamate formation [11]. ILs modified with a hydroxyl group (-OH) have been used as a phase transfer catalyst for ethoxybenzene synthesis [12]. Metal-ligating groups incorporated into ILs can be used for metal-ion extraction from aqueous solution [13]. The physicochemical properties of these TSILs like solubility in molecular solvents, thermal stability and chemical properties like reactivity, depend on the nature of the functional groups incorporated [14]. A TSIL can be a RTIL with covalently attached FG that can act not only as a reaction medium but also as a reagent/catalyst. A TSIL can also be a binary system of functionalized salts, which may be solid at room temperature that can be dissolved in a conventional IL [15]. ILs have emerged as versatile components that can act both as solvent and stabilizers for the synthesis of metal nanoparticles (NPs), providing an efficient synthesis method. For instance, Guleria and coworkers used an imidazolium-based RTIL as a solvent, reducing and stabilizing agent to synthesize stable  $\alpha$ -Se NPs ( $d_m = 34$  nm) exhibiting antioxidant properties [16]. On a similar note, Garg *et al.* reported the synthesis of palladium NPs ( $d_m = 1.4$  and 1.7 nm) by employing a choline-based IL [17]. These IL-stabilized Pd NPs exhibited notable catalytic efficiency in hydrogenation reactions of substrates with various functional groups.

Thus, previous results show that ILs can be employed for the synthesis of metal NPs. ILs possess intriguing physical and chemical properties and presents the advantage to act both as stabilizer and solvent in the reaction, resulting in reduced utilization of chemicals and limited waste, which diminishes the environmental footprint. Careful tailoring of imidazolium based ILs with functional groups has proven a relevant way to improve catalytic performance of metal NPs.

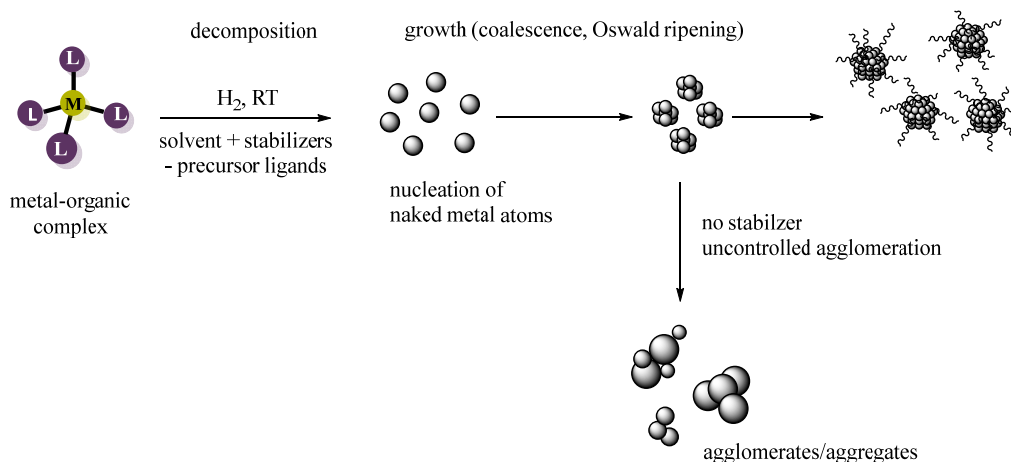
### Metal nanoparticles

Nanotechnology is a scientific discipline that deals with the preparation and use of nano-size particles within the size range of 1 to 100 nm. The term 'nanoparticle' originates from the Greek word 'nano,' meaning 'small' and, when used as a prefix, denotes a size of  $10^{-9}$  meter (= 1 nm) [18]. Metal nanoparticles (NPs) including transition metal NPs find versatile applications in various fields like molecular biology, medicine, physics, organic and inorganic chemistry, and material science [19,20]. Decreasing particle size to the nanoscale imparts unique and enhanced characteristics like morphology and particle size distribution, which are not exhibited by larger bulk materials [21]. Electronic properties of metal NPs are situated at the frontier between molecular species and bulk compounds [22]. Their surface-to-volume ratio is significantly higher than that of larger particles or atoms, leading to a high number of potential active sites on the surface [23]. This unique extrinsic property of the surface area of NPs contributes to them being highly attractive and influences also various intrinsic properties, including their strong surface reactivity which is size-dependent [24]. The properties observed at the nanoscale are mainly due to two key factors:

- 1) *Quantum size effect* [25]: In bulk metals, the electronic behavior is characterized by the presence of energy bands. The valence band contains the valence electrons, typically s- and d-electrons in the case of transition metals. The conduction band of metals partially overlaps with the valence band and hence is partially occupied by electrons responsible for the electrical conductivity of metals. In semiconductors the valence and conduction bands are separated by a specific energy gap, which is considerably larger in insulators. When a metal particle undergoes continuous size reduction the bands turn into discrete energy levels. At this stage, the bulk properties of the metal disappear and are substituted by "quantum dot," which are governed by the principles of quantum mechanics. Such confinement of charge carriers within a small space, resulting in discrete energy levels, is referred to as the "quantum size effect." It brings changes in the electronic properties of metals in NPs.
- 2) *Surface/interface effect* [26,27]: Metal NPs offer a higher number of potential active sites compared to bulk catalytic materials due to their high surface-to-volume ratio making them highly attractive as catalysts. Furthermore, the diverse shapes, crystallographic facets and different fractions of surface atoms located at their corners and edges can contribute to their versatility in catalytic applications.

An organometallic approach is generally employed for the synthesis of metal NPs. In this synthetic approach, metal-organic complexes (metal precursors) with zero or low oxidation state of the metal are decomposed at mild reaction conditions in the presence of carefully chosen ligands (Scheme 1). Olefinic complexes are preferred as hydrogenation of such complexes results in the reduction of the unsaturated ligands within their coordination sphere into their corresponding alkanes, which are inert towards the metallic surface [28]. For example, (1,5-cyclooctadiene)(1,3,5,7-cyclooctatetraene)ruthenium, [Ru(COD)(COT)], is easily decomposed under hydrogen (1-3 bar) at

room temperature [29], bis(1,5-cyclooctadiene)nickel,  $[\text{Ni}(\text{COD})_2]$  can be employed for the preparation of Ni NPs [30] and tetraallyldirhenium(II),  $[\text{Re}_2(\text{C}_3\text{H}_5)_4]$ , allowed to get pure Re NPs [31]. All these precursors generate byproducts like propane and cyclooctane which are inert to the metal surface and can be removed under vacuum. The stabilizing agent introduced at the beginning of the reaction plays a crucial role, as it governs the characteristics of the resulting nanostructures [28]. Some of the stabilizers include simple ligands such as alcohols [32], thiols [33], silanes [34], aminoalcohols [35], 3-aminopropyltriethoxysilane [36], amines [33], diphosphines [37] and ILs [38] as well as polymers [39] can also be used. Through this method, a wide variety of metal nanostructures can be obtained by adjusting the choice of metals, reaction conditions, and stabilizing agents.



**Scheme 1.** Schematic representation for the synthesis of metal nanoparticles (NPs) by the organometallic approach adapted from [28].

The organometallic approach for the synthesis of metal NPs provides numerous advantages, which are primarily centered around the precise control of the reaction conditions (which in-turn affect the surface of the particles) and the control over particle characteristics (size, size distribution and shape). Such control allows to obtain monodispersed NPs with desired properties. One potential challenge lies in the synthesis and handling of organometallic complexes that require inert conditions. Nevertheless, the advantages gained in terms of controlling the characteristics of NPs make the efforts involved justifiable. Indeed, having well-controlled metal NPs allow to finely investigate their properties for applications in different domains, including catalysis among others.

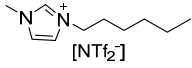
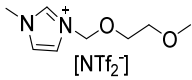
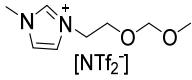
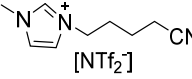
## Objectives and outlook

The main objectives of the thesis include:

- 1) The synthesis and characterization of ILs and functionalized ILs (FILs).
- 2) Utilization of the synthesized ILs for synthesis of transition metal NPs mainly employing ruthenium, nickel and rhenium. Complete characterization of these metal NPs/ILs systems through state of art techniques including TEM, TGA, XPS, NMR, ATR-IR etc.
- 3) Employment of the series of metal NPs/ILs systems in catalytic hydrogenation of substrates like styrene, cinnamyl alcohol, 2,3-benzofuran, trans-2-hexen-1-al, hexanal, benzonitrile, benzylamine, phenylacetylene and (*R*)-(+)-limonene to study the activity and reactivity of such systems.

The first part focuses on synthesizing task-specific (TS) ILs, namely MEM (1-methoxyethoxymethyl-3-methyl imidazolium bis(trifluoromethanesulfonyl)imide) and MME (1-methoxymethoxyethyl-3-methyl imidazolium bis(trifluoromethanesulfonyl)imide) (Table 1). This choice is inspired by the literature data evidence that methoxy functionality can lead to well dispersed and highly active metal NPs for catalysis. Numerous examples can be found in the literature of metal NPs that have been synthesized using polyethylene glycol (PEG) as stabilizer and that have shown high catalytic activity in several reactions. For instance, Pd NPs stabilized by PEG demonstrated remarkable catalytic activity and recyclability towards styrene and nitrobenzene hydrogenation under mild reaction conditions. The formed Pd NPs were well dispersed and had an average diameter of 4 nm [40]. As another non-exhaustive example, Sun and coworkers synthesized homogeneously distributed PEG-stabilized Rh NPs of 1.7 nm in size by simple reduction of  $\text{RhCl}_3 \cdot 3\text{H}_2\text{O}$  under hydrogen. The formed Rh NPs were found as a highly efficient and recyclable catalyst for the hydroformylation of olefins [41].

**Table 1.** Structure of synthesized imidazolium based ILs.

Ionic liquid	Structure
H	
MEM	
MME	
CN	

Various characterizations of the ILs have been performed, this includes ATR-IR Infrared (IR) spectroscopy analysis, Thermal gravimetry (TG) and differential scanning calorimetry (DSC) analyses, Elemental analysis (EA), X-ray photoelectron spectroscopy (XPS) analysis, NMR and Small angle X-ray scattering (SAXS) analysis. Two of the analysis have been provided in detail below:

**a) ATR-IR analysis**

Infrared (IR) spectroscopy is one of the most established and standard technique to characterize ILs [42–44]. This technique allows to identify the functional groups present. Vibrational studies of ILs with imidazolium as cation have been widely discussed in literature [45,46]. The region of high frequencies ranging from 2800 to 3200  $\text{cm}^{-1}$  displays a composite arrangement of overlapping bands that are specific to various stretching modes of C-H bonds. Within the range of 800 to 1600  $\text{cm}^{-1}$ , distinct bands that correspond to the vibrations of the imidazolium ring can be observed. The range of 400 to 800  $\text{cm}^{-1}$  also encompasses ring vibrations [47]. The stretching frequency of  $[\text{NTf}_2]^-$  anion ranges between 400 – 2000  $\text{cm}^{-1}$  [48]. Figure 1 depicts the IR analyses of the ILs H, MEM, MME, and CN. The bands at 1050, 1180, 1346  $\text{cm}^{-1}$  can be assigned to the stretching frequencies of SN,  $\text{CF}_3$ ,  $\text{SO}_2$ , respectively, in  $[\text{NTf}_2]^-$ . The bands at 1099 and 1098  $\text{cm}^{-1}$  correspond to the C-O stretching of MEM and MME, respectively. The CN stretching can be seen at 2248  $\text{cm}^{-1}$ . The bands at the high frequency region 2800 to 3200  $\text{cm}^{-1}$  correspond to the C-H bonds of the imidazolium cation. The absence of O-H stretching mode of water in the range 3400–3800  $\text{cm}^{-1}$  confirmed the high purity of all the ILs.

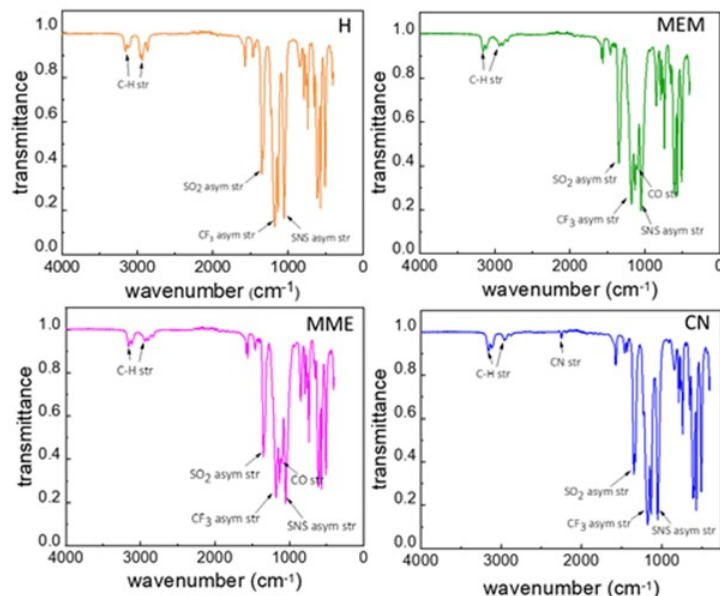


**Figure 1.** ATR-IR spectra of ILs.

### b) SAXS analysis

Small angle X-ray scattering (SAXS) analysis was performed on all the ILs in collaboration with Prof. John Slattery and Dr. Naomi Elstone at University of York, UK to study the nature of cation-cation, anion-anion, and cation-anion ordering (Figure 2). Two primary diffraction peaks can be observed in the ranges  $q \approx 8\text{--}9\text{ nm}^{-1}$  (peak II) and  $q \approx 12.9$  (peak III). The  $q$ -value is called the scattering vector and is a function of the scattering angle:

$$q = \frac{4\pi \sin\theta}{\lambda}, \quad 2\theta \text{ is the angle of deflection}$$

For H, one additional peak at  $q \approx 2\text{--}4\text{ nm}^{-1}$  can also be seen. Previous studies of imidazolium ILs with different anions have observed similar diffraction features [49–51]. Peak I depends strongly on the alkyl chain length and reflects on the structural heterogeneity on the nanometer scale of the ILs. Peak II at  $\sim 8.8\text{ nm}^{-1}$ , which is commonly called the "charge-ordering peak" (COP) is interpreted as relating to correlations between like charges (anion-anion and cation-cation separations) [52]. Comparing the ILs, the order of intensity of the peak is as follows  $\text{MME} > \text{MEM} \sim \text{CN} > \text{H}$  which can be seen by plotting the intensity of the peaks against the different. Peak III at  $\sim 13.5\text{ nm}^{-1}$  is commonly referred to as the "contact peak" (CP). The CP is interpreted as relating to correlations between ions of opposite charges i.e., the typical separation of the anions and cations [53]. The ILs follow the same intensity order as peak II.

A series of four imidazolium based ILs, one non-functionalized and three functionalized, namely H, MEM, MME, and CN, were synthesized in good yields by using the standard quaternization and anion exchange reaction synthesis procedure. A complete characterization including IR, TG, DSC, NMR, XPS and SAXS analyses was performed for all synthesized ILs. IR analysis allowed to establish the stretching frequency and the different functional groups of both the anion and the cation (CN, CO, SO<sub>2</sub>, CF<sub>3</sub>, etc.) thus confirming the identity of each IL. TG and DSC analyses gave information on the thermal behavior of the ILs. They were found to be thermally stable above 200°C for MEM and MME and 450°C in the case of H and CN. The binding energies ( $E_b$ ) of the elements present in each IL were obtained through XPS analysis. The purity of the ILs was evaluated from the NMR analysis. The presence of the



characteristic  $^1\text{H}$  and  $^{13}\text{C}$  NMR peaks also contributed confirming the structure of the ILs. The interactions and ordering of the cations and anions of the ILs were studied using SAXS technique. These synthesized and fully characterized ILs have been then used for the stabilization of transition metal NPs of Ru and Ni. The IL was also tested for the synthesis of Ru-Re bimetallic NPs.

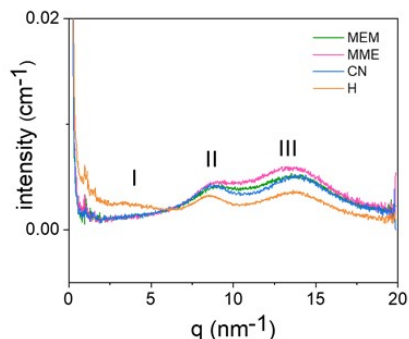
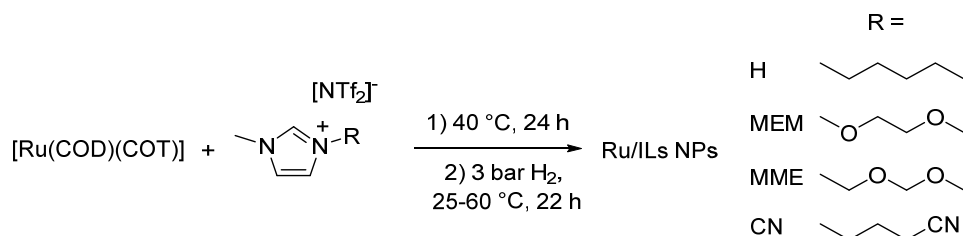


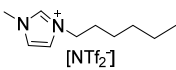
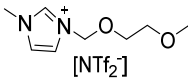
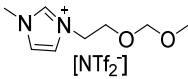
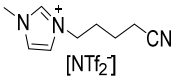
**Figure 2.** X-ray diffraction patterns for the series of ILs.

The synthesis and characterization of Ru NPs stabilized by two ether-FILs, 1-methoxyethoxymethyl-3-methylimidazolium bis(trifluoromethanesulfonyl)imide, [MEMIm][NTf<sub>2</sub>] or MEM, and 1-methoxymethoxyethyl-3-methylimidazolium bis(trifluoromethanesulfonyl) imide, [MMEIm][NTf<sub>2</sub>] or MME are reported following the organometallic approach. The novel Ru/FILs NPs systems (Ru/MEM and Ru/MME) were applied for hydrogenation of styrene and phenylacetylene to probe the surface reactivity of the Ru NPs. In particular, the influence of the ether functions on the catalytic performance was studied and compared to two counterpart catalytic systems based on Ru NPs stabilized by the non-functionalized IL 1-hexyl-3-methylimidazolium bis(trifluoromethanesulfonyl)imide (Ru/H) and the cyano-FIL [(CH<sub>3</sub>CH<sub>2</sub>CH<sub>2</sub>CH<sub>2</sub>CN)MIm][NTf<sub>2</sub>] (Ru/CN), respectively. The obtained results evidenced a clear influence of the FIL on the hydrogenation selectivity of the Ru NPs between vinyl and aromatic hydrogenation of styrene, thus demonstrating the key role of the FIL in the catalytic systems of [Ru(COD)(COT)] in the ILs was achieved in 24 h. Ru/ILs NPs systems were then synthesized by introducing 3 bar H<sub>2</sub> to the Fischer-Porter reactor containing the homogeneous mixture at room temperature except for the nitrile-FIL (CN), where complete decomposition of the Ru complex required a higher temperature of 60 °C (Scheme 2). During a period of 22 h, the color of the reaction turbid mixture was observed to change from yellow to black which indicated the decomposition of the Ru complex. The metal content of each batch of Ru/ILs NPs was established by ICP analysis and found to be close to the expected value of 0.2 wt.% Ru (Table 2).



**Scheme 2.** Synthesis of Ru/FILs NPs.

**Table 2.** Metal content of the Ru/FILs NPs and mean size of the formed Ru NPs.

Ru/FILs NPs	Ionic liquid	Ru content (wt.%) <sup>a</sup>	Ru NP mean size with standard deviation (nm) <sup>b</sup>
Ru/H		0.16	1.5 ± 0.8
Ru/MEM		0.20	2.2 ± 0.3
Ru/MME		0.17	1.3 ± 0.1
Ru/CN		0.20	1.3 ± 0.2

<sup>a</sup> Determined by ICP analyses. <sup>b</sup> Determined from analyses of TEM images.

XPS, TGA, NMR and TEM analyses were performed on the catalytic systems to fully characterize them. The TEM images of the Ru/FILs systems are provided in Figure 4.

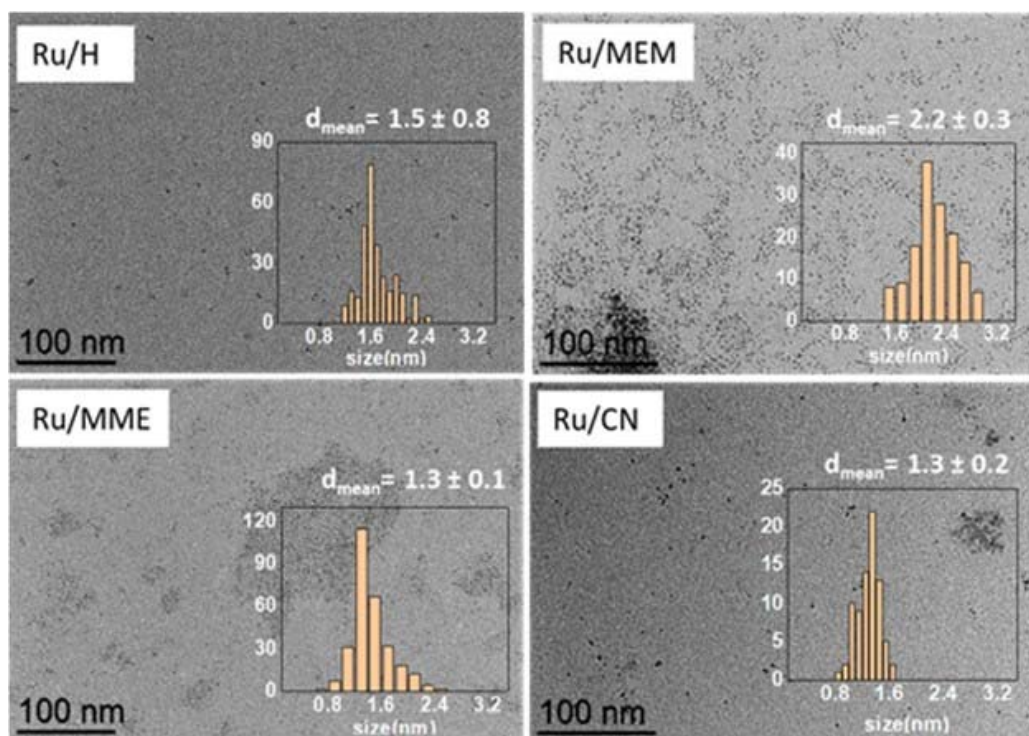
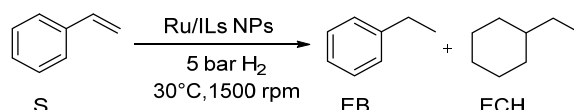


**Figure 4.** TEM images of Ru/FILs NPs with their corresponding size distribution (scale bar = 100 nm).

### Catalysis with Ru/ILs

The catalytic performances of the Ru/ILs NP systems were investigated for the hydrogenation of styrene (S) to form ethylbenzene (EB) and ethylcyclohexane (ECH) using mild reaction conditions (30 °C, 5 bar H<sub>2</sub>, S:Ru ratio 200:1) and vigorous stirring (1500 rpm) to avoid mass transfer issues during reaction with the moderately viscous IL phases (Scheme 3). Table 3 summarizes the catalytic results obtained. Note that the IL alone did not show any conversion of S when submitted to the same reaction conditions.



**Scheme 3.** Hydrogenation of styrene (S) to ethyl benzene (EB) and ethyl cyclohexane (ECH).

**Table 3.** Hydrogenation of (S) with Ru/FILs NPs catalysts. <sup>a</sup>

Catalyst system	Time (h)	Conversion (%) <sup>b</sup>	Selectivity (%) <sup>b</sup>	
			EB	ECH
Ru/H	0.5	>99	>99	0
Ru/H	24	>99	93	7
Ru/MEM	1	>99	>99	0
Ru/MEM	24	>99	78	22
Ru/MME	1.5	98	>99	0
Ru/MME	24	98	>99	0
Ru/CN	6	>99	>99	0
Ru/CN	24	>99	>99	0

<sup>a</sup> Reaction conditions: 0.02 mmol of Ru, 4 mmol of styrene, 0.3 mmol of octane (internal standard), 5 bar H<sub>2</sub>, 30 °C, 1500 rpm. <sup>b</sup> Determined by GC using internal standard technique.

As shown in Table 3, all the Ru/FILs NPs systems were active for the catalytic hydrogenation of S providing full substrate conversion in short reaction times (0.5–6 h). Importantly, the IL alone did not show any conversion of S when submitted to the same reaction conditions (results not shown). The highest TOF value (1,332 h<sup>-1</sup>) was reached with the Ru NPs embedded in the non-functionalized IL, namely Ru/H catalyst. The two methoxy-functionalized IL systems (Ru/MEM and Ru/MME) yielded high rates (TOFs of 629 h<sup>-1</sup> and 212 h<sup>-1</sup>, respectively), while the Ru/CN had the lowest activity (TOF of 10 h<sup>-1</sup>). The differences observed in terms of reaction rates may be correlated to the variation in polarity of the IL that can influence the solubility of the substrate, as styrene is expected being more soluble in non-polar domains than in polar ones. In line with this, the H IL that contains only alkyl chains in its structure presents the larger non-polar domains of the IL series [54] and interestingly, the Ru NPs stabilized in this IL led to the highest TOF. Oppositely, the more polar IL is expected to be the CN FIL and the CN-stabilized Ru NPs displayed the lower activity. The recyclability of each Ru/IL NP catalyst was tested in five successive catalytic runs at partial conversion. The obtained results are shown in Figure 5. Notably, the styrene conversion with the Ru/H catalytic system decreased gradually during the five catalytic runs, whereas the catalytic systems with the three FILs maintained similar styrene conversions upon reuse. ICP

analysis of the Ru/H phase from the first run to the fifth one showed a decrease in the Ru content from 0.2 to ~0.1 wt.%, thus confirming that Ru leaching from the IL phase during catalyst recycling was responsible for the lower conversion. In contrast, the Ru content remained essentially unchanged during the five catalytic runs with the Ru/MEM, Ru/MME and Ru/CN systems, which could indicate that Ru-FIL interactions improved the confinement of the Ru NPs in these systems compared to the Ru/H system and that the functionalization of IL had a positive influence on the stability of the catalysts [55]. Interestingly, TEM images of the spent Ru/IL catalysts showed no noticeable change in the mean size nor size distribution of the Ru NPs compared to the pristine systems, pointing out that the Ru NPs remained stable under the reaction conditions for all the systems and leaching was not related to Ru NPs instability. Hence, more likely, the larger non-polar domains in the unfunctionalized IL compared to the FILs enhanced the catalyst solubility in the non-polar washing solvent (pentane), thus leading to a gradual catalyst loss during the intermediate washings between the catalytic runs.

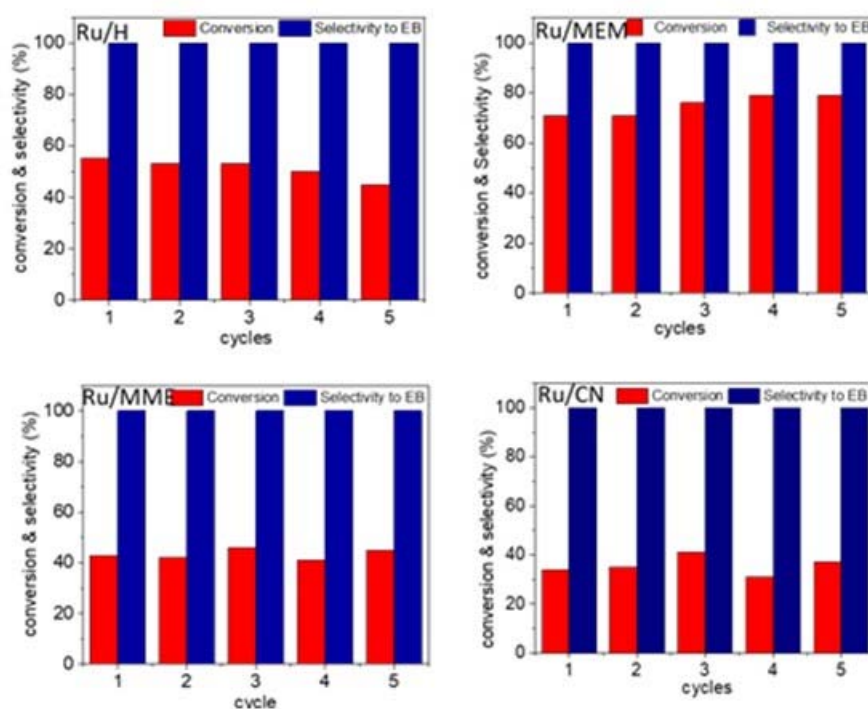


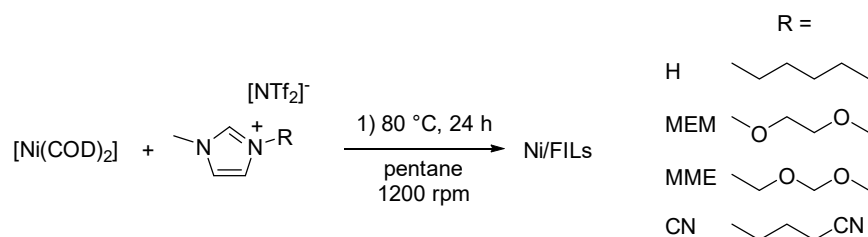
**Figure 5.** Recyclability tests of the Ru/FILs NPs catalysts in the hydrogenation of styrene performed at partial conversion: a) H (15 min), b) MEM (30 min), c) MME (30 min) and d) CN (60 min). Reaction conditions: 0.02 mmol of Ru, 4 mmol of styrene, 0.3 mmol of octane (internal standard), 5 bar H<sub>2</sub>, 30 °C, 1500 rpm.

Thus, a series of catalytic systems based on Ru NPs in a non-functionalized IL (H) and three FILs containing cyano (CN) and methoxy (MEM and MME) groups, have been synthesized, characterized, and applied for the hydrogenation of styrene. The methoxy-functionalized systems, Ru/MEM NPs and Ru/MME NPs were novel systems whereas the Ru/H and Ru/CN were reference systems previously described in literature. The collection of systems allowed to study the influence of the nature of the IL on the catalytic properties of the Ru NP catalysts. All the Ru/IL NPs were found to be efficient catalysts for the hydrogenation of styrene under mild reaction conditions (30 °C, 5 bar of H<sub>2</sub>), providing full conversion of styrene with full ethyl benzene selectivity in short reaction times (0.5-6 h). Interestingly, a clear difference in activity (TOFs) was observed as a function of the nature of the IL, following the order Ru/H (1,332 h<sup>-1</sup>) > Ru/MEM (629 h<sup>-1</sup>) > Ru/MME (212 h<sup>-1</sup>) >> Ru/CN (10 h<sup>-1</sup>). In addition, a total selectivity for ethyl benzene was also observed at longer reaction time (24 h) for the Ru/MME and

Ru/CN systems, while some successive hydrogenation to ethyl cyclohexane occurred for Ru/H (7%) and Ru/MEM (22%) after 24 h. This shows that the Ru/ILs NPs had a strong preference towards hydrogenation of the vinyl group instead of the aromatic ring under the applied reaction conditions, which is a reactivity pattern different from typically reported for Ru NPs. Accordingly, this indicates that less Ru surface was accessible in Ru/MME and Ru/CN than in Ru/H and Ru/MEM, which can be attributed partly to lower Ru NP sizes in the former catalysts, though a contributing effect may also derive from metal-IL interactions of the MME and CN FILs *via* -O-CH<sub>2</sub>-O- and -CN groups, respectively. Such interactions may, by steric and/or electronic reasons, influence the surface properties of the Ru/ILs NPs and hamper the hydrogenation of the aromatic ring. This hypothesis is supported by the XPS results which evidenced for all Ru/ILs NPs systems a bonding energy of Ru<sup>0</sup> lower than literature values for metallic Ru, indicating that the Ru NPs and the ILs closely interact. Finally, recycling of the Ru/ILs NPs systems in five catalytic runs evidenced that the FIL-stabilized catalysts were more stable than the non-functionalized Ru/H catalyst system, where Ru leaching likely occurred due to higher solubility of the Ru/H NPs in the workup solvent of the reaction mixture between catalytic runs. Nevertheless, the results show that the functionalization of IL had a positive influence on the stability of the catalysts. In perspective, the work introduces a benign and facile co-solvent free synthesis protocol to obtain well-dispersed and narrow-sized Ru NPs stabilized by FILs containing methoxy-functionalities, which present a good balance between stability and catalytic activity. This allows Ru/ILs NPs to hydrogenate styrene with activity and total selectivity towards ethylbenzene at milder reaction conditions (5 bar H<sub>2</sub>, 30 °C) than previously reported in literature [56,57].

Then novel Ni NPs and Ni-NiO NPs stabilized by two ether-FILs, 1-methoxyethoxy-methyl-3-methylimidazolium bis(trifluoromethanesulfonyl)imide, [MEMIm][NTf<sub>2</sub>] or MEM, and 1-methoxymethoxyethyl-3-methylimidazolium bis(trifluoromethanesulfonyl)imide, [MMEIm][NTf<sub>2</sub>] or MME, were synthesized by the organometallic approach using [Ni(COD)<sub>2</sub>] as Ni precursor, and characterized. The Ni/FIL NPs systems (Ni/MEM and Ni/MME) were then applied in the hydrogenation of  $\alpha,\beta$ -unsaturated carbonyl compounds with the aim to probe the surface reactivity in terms of conversion and selectivity. Ni NPs in the non-functionalized IL 1-hexyl-3-methylimidazolium bis(trifluoromethanesulfonyl)imide (Ni/H) and the cyano-FIL 1-butylcyano-3-methylimidazolium bis(trifluoromethanesulfonyl)imide [(CH<sub>3</sub>CH<sub>2</sub>CH<sub>2</sub>CH<sub>2</sub>CN)MIm][NTf<sub>2</sub>] (Ni/CN) were also prepared for the purpose of comparison. In a second stage, the as-synthesized Ni NPs were exposed to air which led to Ni-NiO NPs. Hydrogenation of several substrates using these oxidized NPs, including cinnamaldehyde and 2-cyclohexen-1-one among others, was performed to understand the effect of the NP oxidation on the catalytic performance.

The synthesis of Ni NPs was performed at 40-45 °C, using a co-solvent (pentane) to dissolve the lipophilic Ni precursor in the IL, leading to the targeted Ni NPs. Thus, based on this work, the Ni NPs were here synthesized with few modifications of the procedure. [Ni(COD)<sub>2</sub>] precursor was dissolved in pentane/IL mixture (1/3 mL) in a Fischer-Porter bottle and the reaction was allowed to proceed for 24 h at 80 °C and 1500 rpm using a magnetic stirrer (Scheme 4). Upon completion of the reaction, a black colloidal suspension was obtained for the four ILs tested, indicating the successful decomposition of the precursor under these optimized conditions. The generated cyclooctane and the solvent were removed under vacuum (~0.05 mbar) overnight. The metal content of each batch of Ni/IL was established by ICP analysis and found to be close to the expected value of 0.10 wt.% Ni (Table 4).



**Scheme 4.** Optimized synthesis of Ni/FILs.

**Table 4.** Ni content in Ni/FILs systems and Ni NP mean size.

Ni/FIL	Ionic liquid	Ni content (wt.%) <sup>a</sup>	Ni NP mean size (nm) <sup>b</sup>
Ni/H		0.11	5.6 ± 0.3
Ni/MEM		0.12	4.4 ± 0.4
Ni/MME		0.11	6.5 ± 0.3
Ni/CN		0.11	2.8 ± 0.3

<sup>a</sup> Determined by ICP analyses. <sup>b</sup> Determined from TEM analyses.

XPS, TGA, NMR and TEM analyses were performed on the catalytic systems to fully characterize them. The TEM images of the Ni/FILs systems are provided in Figure 6.

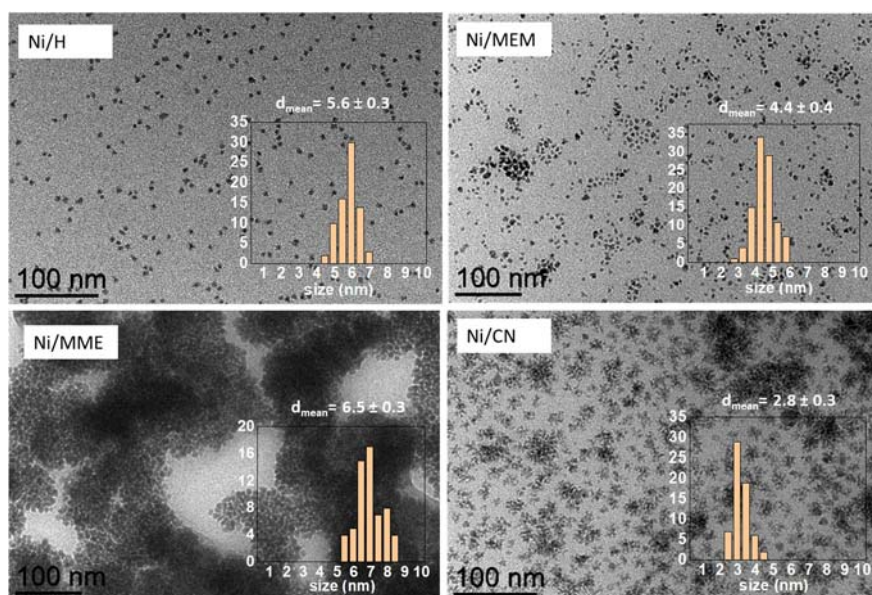
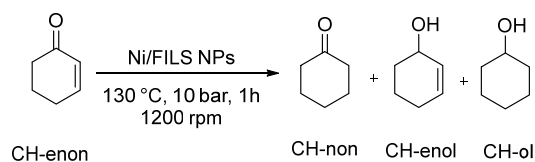


**Figure 6.** TEM images of Ni/FILs with their corresponding size distributions (scale bar = 100 nm).

### Catalysis with Ni/FILs and Ni-NiO/FILs

The catalytic performances of the Ni/FILs and Ni-NiO/FILs NPs systems were investigated for the hydrogenation of 2-cyclohexen-1-one (CH-enon) using the given reaction conditions (130 °C, 10 bar H<sub>2</sub>, 1 h, 1200 rpm, sub:Ni ratio 100:1) (Scheme 5). Table 5 summarizes the results obtained.



**Scheme 5.** Hydrogenation of 2-cyclohexen-1-one (CH-enon) to cyclohexanone (CH-non), 2-cyclohexen-1-ol (CH-enol) and cyclohexanol (CH-ol).

**Table 5.** Hydrogenation of 2-cyclohexen-1-one with Ni/FILs and Ni-NiO/FILs catalysts.<sup>a</sup>

Catalyst system	Conversion (%) <sup>b</sup>	Selectivity (%) <sup>b</sup>			TOF(h <sup>-1</sup> )
		CH-non	CH-ol	CH-enol	
Ni/H	>99	97	3	0	677
Ni-NiO/H	>99	98	2	0	
Ni/MEM	97	>99	0	0	814
Ni-NiO/MEM	78	>99	0	0	
Ni/MME	>99	>99	0	0	627
Ni-NiO/MME	89	>99	0	0	
Ni/CN	>99	>99	0	0	712
Ni-NiO/CN	>99	>99	0	0	

<sup>a</sup> Reaction conditions: 0.01 mmol of Ni, 1 mmol of 2-cyclohexen-1-one (CH-enon), 0.3 mmol of octane (internal standard), 130 °C, 10 bar H<sub>2</sub>, 1 h, 1200 rpm. <sup>b</sup> Determined by GC using internal standard technique.

As shown in Table 5, both the Ni/FILs and Ni-NiO/FILs systems were active for the catalytic hydrogenation of CH-enon in short reaction time (1 h). A complete conversion of CH-enon selectively towards CH-non was obtained for all Ni/FILs systems. The difference in conversion rate vs. the Ni/FILs systems plots have been provided in Figure 5. The initial turnover frequency (TOF) was calculated for all Ni/FILs systems at 0.25 h. The highest TOF (814 h<sup>-1</sup>) value was reached by the Ni NPs embedded in the MEM-functionalized ILs. The non-functionalized system and the nitril functionalization yielded high conversion (TOFs of 677 and 712 h<sup>-1</sup>, respectively), while the had MME methoxy functionalized, being the largest NPs in size showed the lowest (627 h<sup>-1</sup>). Nevertheless, all the systems showed high activity at the given reaction conditions with the initial order of the activity being Ni/MME < Ni/H < Ni/CN < Ni/MEM. A comprehensive study with all Ni-NiO/FILs systems was carried out under these reaction conditions. For the Ni-NiO/MEM and Ni-NiO/MME, the activity dropped to 78 and 89% respectively upon oxidation of the NPs surface. Unlike the methoxy systems, it could be noticed that the Ni-NiO/CN and Ni-NiO/H systems did not show inferior activity compared to their non-oxidized analogues. The reason could be a lower oxidation of the NPs surface during air exposure as supported by the XPS data, making these catalysts more effective in the short reaction time applied. No change in selectivity was observed upon oxidation. To assess the potential impact of temperature variation on catalyst selectivity, the hydrogenation of CH-enon was also performed at 150 and 170 °C with the systems, while keeping all other parameters constant. Notably, the hydrogenation of neither the carbonyl group nor the aromatic ring was observed at 150 and 170 °C and full conversion of CH-enon was observed.

Recyclability of all Ni/FILs NPs catalysts was tested in five successive catalytic runs (Figure 7). The recyclability tests were performed at partial conversions to provide a realistic evaluation of the catalytic performance and to easily identify the leaching of a catalyst, if any. Notably, the CH-enon conversion with the Ni/H NPs system remained constant up to three catalytic runs and started to decrease in the fourth and fifth runs, whereas the three Ni/FILs systems maintained similar CH-enon conversions upon reuse.

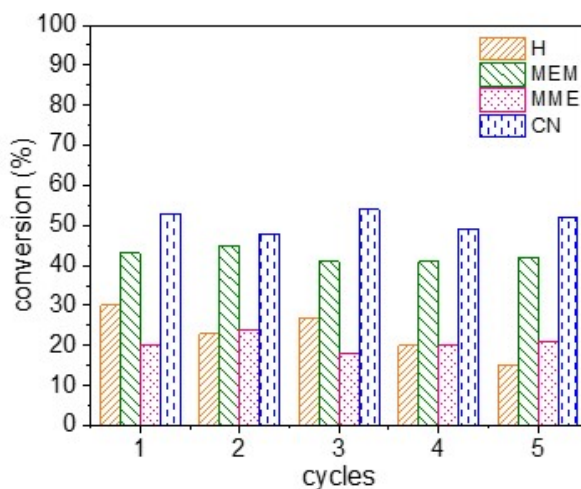


**Figure 7.** Recyclability tests of the Ni/FILs catalysts in the hydrogenation of 2-cyclohexen-1-one performed at 0.25 h. Reaction conditions: 0.01 mmol of Ni, 1 mmol of CH-enon, 0.3 mmol of octane (internal standard), 10 bar  $H_2$ , 130 °C, 1200 rpm.

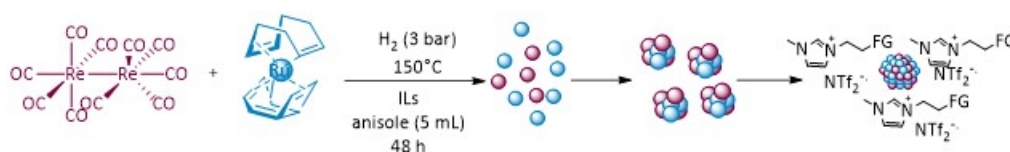
A series of catalytic systems based on Ni-containing NPs in non-functionalized IL (H) and FILs containing cyano- (CN) and methoxy-groups (MEM and MME) have been synthesized, characterized, and applied for the hydrogenation of substrates containing different functional groups. The Ni/MEM and Ni/MME catalysts were novel systems, whereas the Ni/H and Ni/CN were previously reported and here prepared for comparison purpose. Small Ni NPs were prepared using CN (2.8 nm), compared to the previous literature (7-8 nm) [58]. All the Ni/ILs systems were found to be efficient catalysts for the hydrogenation of 2-cyclohexen-1-one under the applied reaction conditions (substrate/Ni ratio of 100/1, 130°C, 10 bar  $H_2$ ), providing full conversion of 2-cyclohexen-1-one with full selectivity towards hydrogenation of the olefinic bond in short reaction time (1 h). Compared to the previous literature using Ni NPs synthesized in amine-functionalized ILs [59] (substrate/Ni of 50/1, 90°C, 10 bar  $H_2$ , 4 h, water solvent with isolated NPs redispersed in water), this work uses much less Ni metal content but slightly higher temperature to provide complete substrate conversion in much shorter time under neat conditions. Long time air exposure of the catalysts resulted in  $Ni(OH)_2$  layer formation on the Ni/FILs, which led to deactivation and a significant drop-in catalytic activity. The implementation of recyclability tests as well as the characterization of the spent catalysts will allow to complete the evaluation of the catalytic properties of the Ni/FILs. Another perspective could be to deposit the Ni/FILs NPs on a solid support like silica to obtain supported ionic liquid phase (SILP) systems, which can subsequently be used for hydrogenation reactions, including  $CO_2$  reduction. In this context, initial experiments have been performed for grafting of the catalyst system.

The synthesis of RuRe bimetallic NPs in H and MEM ILs was also studied using the organometallic approach. For this purpose, the precursors  $[Ru(COD)(COT)]$  and  $[Re_2(CO)_{10}]$  were used as they are



commercially available and possess ligands that can be eliminated under hydrogenation or heating conditions. However, it must be noted that  $[\text{Re}_2(\text{CO})_{10}]$  is very stable at room temperature and forced reaction conditions are needed to facilitate its decomposition [60]. The reduction of the Re species may be promoted by hydrogen spillover from the reduced species of the other metal present, as previously reported [61,62]. The  $[\text{Re}_2(\text{C}_3\text{H}_5)_4]$  precursor, which decomposes under milder reaction conditions [63] than  $[\text{Re}_2(\text{CO})_{10}]$ , was unfortunately unavailable.

As mentioned above, RuRe NPs were synthesized in earlier work using  $[\text{Ru}(\text{COD})(\text{COT})]$  and  $[\text{Re}_2(\text{CO})_{10}]$  as metal precursors employing the ligands PVP and HAD for the stabilization of the RuRe NPs (optimized reaction conditions: 3 bar of  $\text{H}_2$ , 120 °C, 48 h and anisole as solvent) [64]. Thus, in a first attempt the one-pot synthesis of RuRe/ILs was carried out following the same reaction conditions (Scheme 6). Monometallic Ru/IL and Re/IL were synthesized following the same procedure for comparative purposes.



**Scheme 6.** Organometallic synthesis of RuRe/IL from  $[\text{Ru}(\text{COD})(\text{COT})]$  and  $[\text{Re}_2(\text{CO})_{10}]$ .

TEM analyses were performed of both the bimetallic (Figure 8) and the monometallic samples. The TEM images of RuRe/H and RuRe/ME showed both well-dispersed NPs with average size of  $1.6 \pm 0.2$  nm and  $3.3 \pm 0.4$  nm, respectively, while an average size  $2.0 \pm 0.2$  nm and  $2.1 \pm 0.2$  nm was observed for Ru/H and Ru/MEM, respectively. Regarding the Re samples, the TEM images confirmed the lack of formation of NPs for both Re/H and Re/MEM.

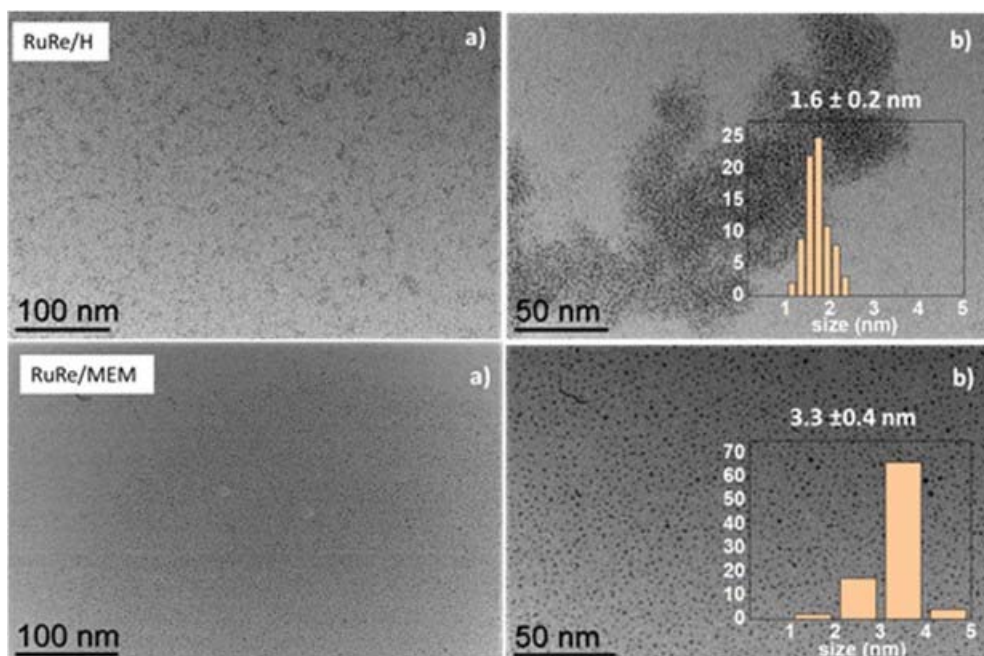


**Figure 8.** a) TEM images and b) the corresponding NPs size distributions of synthesized RuRe/ILs NPs (150 °C, 3 bar  $\text{H}_2$ , anisole) (scale bar = 100 or 50 nm).

Thus, novel RuRe-containing NPs have been synthesized, using a non-functionalized IL (H) and a methoxy-functionalized one (MEM), and characterized. TEM images show well-dispersed NPs in both H and MEM ILs. Despite the fact that the Re precursor,  $[\text{Re}_2\text{CO}_{10}]$ , requires higher decomposition temperature than  $[\text{Ru}(\text{COD}(\text{COT}))]$ , EDX analysis revealed the formation of bimetallic RuRe NPs with a Re content of ca. 18% in RuRe/H and ca. 34% in RuRe/MEM. Comparing to previous work done at LCC [64], the incorporation of Re metal in the RuRe bimetallic NPs increased in the order: RuRe/H < RuRe/PVP ~ RuRe/HDA < RuRe/MEM. Owing to an incomplete decomposition of  $[\text{Re}_2(\text{CO})_{10}]$  under the applied conditions, and the difficulty to separate soluble Re species from the formed RuRe NPs, the alternative Re precursor,  $[\text{Re}_2(\text{C}_3\text{H}_5)_4]$ , is considered for future studies. If successful, the bimetallic RuRe NPs will be supported on silica to obtain SILP systems for their investigation as catalysts for the hydrogenation of amides.

The results reported in the doctoral thesis open interesting perspectives for future research:

- 1) Ru/FILs systems were found to be highly active and selective to ethylbenzene in the hydrogenation of styrene. These catalysts may be employed in the selective hydrogenation of other substrates than vinylic substrates, such as other olefinic or alkyne compounds,  $\alpha,\beta$ -unsaturated carbonyl compounds, nitriles, or even  $\text{CO}_2$ . Initial studies on employing the Ru/MEM system in the hydrogenation of 2,3-benzofuran (substrate/Ru ratio 1000/1, 120°C, 10 bar of  $\text{H}_2$ , 1,4-dioxane solvent) showed promising results of 20% conversion and >99% selectivity towards 2,3-dihydrobenzofuran.
- 2) The substrate screening of Ni-NiO/MEM showed potential scopes for the application of all the Ni/FILs systems for various hydrogenation reactions, thus opening avenues for their implementation in catalysis.
- 3) The RuRe/IL bimetallic system would merit to be studied deeper in the hydrogenation of amides. Change in the synthesis protocol, for example by using the organometallic precursor  $[\text{Re}_2(\text{C}_3\text{H}_5)_4]$  instead of  $[\text{Re}_2\text{CO}_{10}]$  for the synthesis of the RuRe NPs could help to achieve an active catalyst. Catalytic application of the RuRe/IL system for the hydrogenation of other substrates than amides, for example as those mentioned above, is another perspective.
- 4) All the metal NP/ILs systems developed can be immobilized onto a support like silica *via* a simple impregnation process to obtain the corresponding SILP systems with a highly accessible IL film layer. This is a convenient approach to generate materials with improved surface reactivity that facilitates many molecules to simultaneously react, thus leading to enhanced reaction rates and efficiencies when applied in catalysis.

## Reference

- [1] D. R. MacFarlane, M. Kar, J. M. Pringle, *Fundamentals of Ionic Liquids: From Chemistry to Applications*, 1st ed.; Wiley-VCH: Weinheim, Germany, **2017**. DOI: [10.1002/9783527340033](https://doi.org/10.1002/9783527340033).
- [2] I. Krossing, J. M. Slattery, C. Daguinet, P. J. Dyson, A. Oleinikova, H. Weingärtner, *J. Am. Chem. Soc.* **2006**, *128*, 13427–13434. DOI: [10.1021/ja0619612](https://doi.org/10.1021/ja0619612).
- [3] E. Kianfar; S. Mafi, *Fine Chem. Eng.* **2020**, 22–31. DOI: [10.37256/fce.212021693](https://doi.org/10.37256/fce.212021693).
- [4] C. S. Consorti, P. A. Z. Suarez, R. F. De Souza, R. A. Burrow, D. H. Farrar, A. J. Lough, W. Loh, L. H. M. da Silva, J. Dupont, *J. Phys. Chem. B* **2005**, *109*, 4341–4349. DOI: [10.1021/jp0452709](https://doi.org/10.1021/jp0452709).
- [5] B. Clare, A. Sirwardana, D. R. MacFarlane, *Top. Curr. Chem.* **2009**, *290*, 1–40. DOI: [10.1007/128\\_2008\\_31](https://doi.org/10.1007/128_2008_31).
- [6] M. Pucheault, M. Vaultier, *Top. Curr. Chem.* **2009**, *290*, 83–126. DOI: [10.1007/128\\_2008\\_33](https://doi.org/10.1007/128_2008_33).
- [7] L. Han, S. J. Choi, M. S. Park, S. M. Lee, Y. J. Kim, M. Il Kim, B. Liu, D. W. Park, *React. Kinet. Mech. Catal.*

- 2012**, *106*, 25–35. DOI: [10.1007/s11144-011-0399-8](https://doi.org/10.1007/s11144-011-0399-8).
- [8] Y. Q. Cai, F. Lu, Y. Q. Peng, G. H. Song, *Chin. Chem. Lett.* **2007**, *18*, 21–23. DOI: [10.1016/j.cclet.2006.11.018](https://doi.org/10.1016/j.cclet.2006.11.018).
- [9] Z. Fei, D. Zhao, D. Pieraccini, W. H. Ang, T. J. Geldbach, R. Scopelliti, C. Chiappe, P. J. Dyson, *Organometallics* **2007**, *26*, 1588–1598. DOI: [10.1021/om060950e](https://doi.org/10.1021/om060950e).
- [10] R. Ratti, Ionic Liquids: Synthesis and Applications in Catalysis. *Adv. Chem.* **2014**, *2014*, 1–16. DOI: [10.1155/2014/729842](https://doi.org/10.1155/2014/729842).
- [11] E. D. Bates, R. D. Mayton, I. Ntai, J. H. Davis, *J. Am. Chem. Soc.* **2002**, *124*, 926–927. DOI: [10.1021/ja017593d](https://doi.org/10.1021/ja017593d).
- [12] G. R. Feng, J. J. Peng, H. Y. Qiu, J. X. Jiang, L. Tao, G. Q. Lai, *Synth. Commun.* **2007**, *37*, 2671–2675. DOI: [10.1080/00397910701465230](https://doi.org/10.1080/00397910701465230).
- [13] A. E. Visser, R. P. Swatloski, W. M. Reichert, R. Mayton, S. Sheff, A. Wierzbicki, J. Davis, R. D. Rogers, *Chem. Comm.* **2001**, 135–136. DOI: [10.1039/b008041i](https://doi.org/10.1039/b008041i).
- [14] Z. Fei, T. J. Geldbach, D. Zhao, P. J. Dyson, *Chem. Eur. J.* **2006**, *12*, 2122–2130. DOI: [10.1002/chem.200500581](https://doi.org/10.1002/chem.200500581).
- [15] S. G. Lee, *Chem. Comm.* **2006**, 1049–1063. DOI: [10.1039/b514140k](https://doi.org/10.1039/b514140k).
- [16] S. K. Singh, A. W. Savoy, *J. Mol. Liq.* **2020**, *297*, 112038. DOI: [10.1016/j.molliq.2019.112038](https://doi.org/10.1016/j.molliq.2019.112038).
- [17] G. Garg, S. Foltran, I. Favier, D. Pla, Y. Medina-González, M. Gómez, *Catal. Today* **2020**, *346*, 69–75. DOI: [10.1016/j.cattod.2019.01.052](https://doi.org/10.1016/j.cattod.2019.01.052).
- [18] H. You, S. Yang, B. Ding, H. Yang, *Chem. Soc. Rev.* **2013**, *42*, 2880–2904. DOI: [10.1039/c2cs35319a](https://doi.org/10.1039/c2cs35319a).
- [19] F. J. Heiligtag, M. Niederberger, *Mater. Today* **2013**, *16*, 262–271. DOI: [10.1016/j.mattod.2013.07.004](https://doi.org/10.1016/j.mattod.2013.07.004)
- [20] M. De, P. S. Ghosh, V. M. Rotello, *Adv. Mater.* **2008**, *20*, 4225–4241. DOI: [10.1002/adma.200703183](https://doi.org/10.1002/adma.200703183)
- [21] V.D. Willems, *Roadmap Report on Nanoparticles*, Barcelona, Spain. W&W Espana sl, Barcelona, Spain. **2005**, 157.
- [22] K. Philippot, P. Serp *Concepts in Nanocatalysis*, Wiley-VCH Verlag GmbH & Co., **2013**, 1-54, ISBN 978-3-527-33124-6.
- [23] D. Astruc *Nanoparticles and Catalysis*; Wiley-VCH, Weinheim, **2008**, ISBN: 978-3-527-31572-7.
- [24] M. Auffan, J. Rose, M. R. Wiesner, J. Y. Bottero, *Environmental Pollution* **2009**, *157*, 1127–1133. DOI: [10.1016/j.envpol.2008.10.002](https://doi.org/10.1016/j.envpol.2008.10.002).
- [25] B. Corain, G. Schmid, N. Toshima (Editors), *Metal Nanoclusters in Catalysis and Materials Science: The Issue of Size Control*. Elsevier: Amsterdam, The Netherlands, **2008**, pp. 3–20. DOI: [10.1016/B978-0-444-53057-8.X5001-6](https://doi.org/10.1016/B978-0-444-53057-8.X5001-6).
- [26] R. Narayanan, C. Tabor, M. A. El-Sayed, *Top. Catal.* **2008**, *48*, 60–74. DOI: [10.1007/s11244-008-9057-4](https://doi.org/10.1007/s11244-008-9057-4).
- [27] R. Narayanan, M. A. El-Sayed, *J. Phys. Chem. B* **2005**, *109*, 12663–12676. DOI: [10.1021/jp051066p](https://doi.org/10.1021/jp051066p).
- [28] C. Amiens, B. Chaudret, D. Ciuculescu-Pradines, V. Collière, K. Fajerweg, P. Fau, M. Kahn, A. Maisonnat, K. Soulantica, K. Philippot, *New J. Chem.* **2013**, *37*, 3374–3401. DOI: [10.1039/c3nj00650f](https://doi.org/10.1039/c3nj00650f).
- [29] K. Philippot, P. Lignier, B. Chaudret, *Top. Organomet. Chem.* **2014**, *48*, 319–370. DOI : [10.1007/3418\\_2014\\_83](https://doi.org/10.1007/3418_2014_83).
- [30] N. J. S. Costa, M. Guerrero, V. Collière, É. Teixeira-Neto, R. Landers, K. Philippot, L. M. Rossi, *ACS Catal.* **2014**, *4*, 1735–1742. DOI: [10.1021/cs500337a](https://doi.org/10.1021/cs500337a).
- [31] T. Ayvali, P. Lecante, P. F. Fazzini, A. Gillet, K. Philippot, B. Chaudret, *Chem. Comm.* **2014**, *50*, 10809–10811, DOI: [10.1039/c4cc04816d](https://doi.org/10.1039/c4cc04816d).
- [32] K. Pelzer, O. Vidoni, K. Philippot, B. Chaudret, V. Collière, *Adv. Funct. Mater.* **2003**, *13*, 118–126. DOI: [10.1002/ADFM.200390017](https://doi.org/10.1002/ADFM.200390017).
- [33] C. Pan, K. Pelzer, K. Philippot, B. Chaudret, F. Dassenoy, P. Lecante, M. J. Casanove, *J. Am. Chem. Soc.* **2001**, *123*, 7584–7593. DOI: [10.1021/JA003961M](https://doi.org/10.1021/JA003961M).
- [34] K. Pelzer, B. Laleu, F. Lefebvre, K. Philippot, B. Chaudret, J. P. Candy, J. M. Basset, *Chem. Mater.* **2004**, *16*, 4937–4941. DOI: [10.1021/CM049086B](https://doi.org/10.1021/CM049086B).
- [35] S. Jansat, D. Picurelli, K. Pelzer, K. Philippot, M. Gómez, G. Muller, P. Lecante, B. Chaudret, *New J. Chem.* **2006**, *30*, 115–122. DOI: [10.1039/B509378C](https://doi.org/10.1039/B509378C).
- [36] M. Zahmakiran, M. Tristany, K. Philippot, K. Fajerweg, S. Özkar, B. Chaudret, *Chem. Comm.* **2010**, *46*,

- 2938–2940. DOI: [10.1039/C000419G](https://doi.org/10.1039/C000419G).
- [37] J. García-Antón, M. R. Axet, S. Jansat, K. Philippot, B. Chaudret, T. Pery, G. Buntkowsky, H. H. Limbach, *Angew. Chem. Int. Ed.* **2008**, *47*, 2074–2078. DOI: [10.1002/ANIE.200704763](https://doi.org/10.1002/ANIE.200704763).
- [38] S. Wegner, C. Janiak, *Top. Curr. Chem.* **2017**, *375*, 65. DOI: [10.1007/s41061-017-0148-1](https://doi.org/10.1007/s41061-017-0148-1).
- [39] R. B. Grubbs, *Polym. Rev.* **2007**, *47*, 197–215. DOI: [10.1080/15583720701271245](https://doi.org/10.1080/15583720701271245).
- [40] F. A. Harraz, S. E. El-Hout, H. M. Killa, I. A. Ibrahim, *J. Catal.* **2012**, *286*, 184–192. DOI: [10.1016/j.jcat.2011.11.001](https://doi.org/10.1016/j.jcat.2011.11.001).
- [41] Z. Sun, Y. Wang, M. Niu, H. Yi, J. Jiang, Z. Jin, *Catal. Commun.* **2012**, *27*, 78–82. DOI: [10.1016/j.catcom.2012.07.001](https://doi.org/10.1016/j.catcom.2012.07.001).
- [42] T. Yamada, Y. Tominari, S. Tanaka, M. Mizuno, *J. Phys. Chem. B* **2017**, *121*, 3121–3129. DOI: [10.1021/acs.jpcc.7b01429](https://doi.org/10.1021/acs.jpcc.7b01429).
- [43] T. Yamada, M. Mizuno, *ACS Omega* **2021**, *6*, 1709–1717. DOI: [10.1021/acsomega.0c05769](https://doi.org/10.1021/acsomega.0c05769).
- [44] T. Moumene, E. H. Belarbi, B. Haddad, D. Villemin, O. Abbas, B. Khelifa, S. Bresson, *J. Mol. Struct.* **2014**, *1065–1066*, 86–92. DOI: [10.1016/j.molstruc.2014.02.034](https://doi.org/10.1016/j.molstruc.2014.02.034).
- [45] T. Yamada, Y. Tominari, S. Tanaka, M. Mizuno, *J. Phys. Chem. B* **2017**, *121*, 3121–3129. DOI: [10.1021/acs.jpcc.7b01429](https://doi.org/10.1021/acs.jpcc.7b01429).
- [46] T. Yamada, M. Mizuno, *ACS Omega* **2018**, *3*, 8027–8035. DOI: [10.1021/acsomega.8b00938](https://doi.org/10.1021/acsomega.8b00938).
- [47] V. H. Paschoal, L. F. O. Faria, M. C. C. Ribeiro, *Chem. Rev.* **2017**, *117*, 7053–7112. DOI: [10.1021/acs.chemrev.6b00461](https://doi.org/10.1021/acs.chemrev.6b00461).
- [48] K. Noack, P. S. Schulz, N. Paape, J. Kiefer, P. Wasserscheid, A. Leipertz, *Phys. Chem. Chem. Phys.* **2010**, *12*, 14153–14161. DOI: [10.1039/c0cp00486c](https://doi.org/10.1039/c0cp00486c).
- [49] W. Zheng, A. Mohammed, L. G. Hines, D. Xiao, O. J. Martinez, R. A. Bartsch, S. L. Simon, O. Russina, A. Triolo, E. L. Quitevis, *J. Phys. Chem. B* **2011**, *115*, 6572–6584. DOI: [10.1021/jp1115614](https://doi.org/10.1021/jp1115614).
- [50] A. Triolo, O. Russina, B. Fazio, R. Triolo, E. Di Cola, *Chem. Phys. Lett.* **2008**, *457*, 362–365. DOI: [10.1016/j.cplett.2008.04.027](https://doi.org/10.1016/j.cplett.2008.04.027).
- [51] A. Triolo, O. Russina, H. J. Bleif, E. Di Cola, *J. Phys. Chem. B* **2007**, *111*, 4641–4644. DOI: [10.1021/jp067705t](https://doi.org/10.1021/jp067705t).
- [52] T. Murphy, R. Atkin, G. G. Warr, *Curr. Opin. Colloid Interface Sci.* **2015**, *20*, 282–292. DOI: [10.1016/j.cocis.2015.10.004](https://doi.org/10.1016/j.cocis.2015.10.004).
- [53] A. Martinelli, M. Maréchal, Å. Östlund, J. Cambedouzou, *Phys. Chem. Chem. Phys.* **2013**, *15*, 5510. DOI: [10.1039/c3cp00097d](https://doi.org/10.1039/c3cp00097d).
- [54] T. Gutel, C. C. Santini, K. Philippot, A. Padua, K. Pelzer, B. Chaudret, Y. Chauvin, J. M. Basset, *J. Mater. Chem.* **2009**, *19*, 3624–3631. DOI: [10.1039/b821659b](https://doi.org/10.1039/b821659b).
- [55] K. L. Luska, A. Moores, *ChemCatChem* **2012**, *4*, 1534–1546. DOI: [10.1002/cctc.201100366](https://doi.org/10.1002/cctc.201100366).
- [56] D. Parida, C. Bakkali-Hassani, E. Lebraud, C. Schatz, S. Grelier, D. Taton, J. Vignolle, *Nanoscale* **2022**, *14*, 4635–4643. DOI: [10.1039/d1nr07628k](https://doi.org/10.1039/d1nr07628k).
- [57] H. Y. Jiang, X. X. Zheng, *Catal. Sci. Technol.* **2015**, *5*, 3728–3734. DOI: [10.1039/c5cy00293a](https://doi.org/10.1039/c5cy00293a).
- [58] H. Konnerth, M. H. G. Prechtel, *New J. Chem.* **2017**, *41*, 9594–9597. DOI: [10.1039/C7NJ02210G](https://doi.org/10.1039/C7NJ02210G).
- [59] Y. Hu, Y. Yu, Z. Hou, H. Yang, B. Feng, H. Li, Y. Qiao, X. Wang, L. Hua, Z. Pan, X. Zhao, *Chem. Asian J.* **2010**, *5*, 1178–1184. DOI: [10.1002/asia.200900628](https://doi.org/10.1002/asia.200900628).
- [60] N. V. Gelfond, N. B. Morozova, K. V. Zherikova, P. P. Semyannikov, S. V. Trubin, S. V. Sysoev, I. K. Igumenov, *J. Chem. Thermodyn.* **2011**, *43*, 1646–1651. DOI: [10.1016/J.JCT.2011.05.024](https://doi.org/10.1016/J.JCT.2011.05.024).
- [61] L. Ma, D. He, *Top. Catal.* **2009**, *52*, 834–844. DOI: [10.1007/s11244-009-9231-3](https://doi.org/10.1007/s11244-009-9231-3).
- [62] K. Baranowska, J. Okal, N. Miniajlu, *Catal. Lett.* **2014**, *144*, 447–459. DOI: [10.1007/s10562-013-1169-1](https://doi.org/10.1007/s10562-013-1169-1).
- [63] T. Ayvali, P. Lecante, P.-F. Fazzini, A. Gillet, K. Philippot, B. Chaudret, *Chem. Commun.* **2014**, *50*, 10809. DOI: [10.1039/C4CC04816D](https://doi.org/10.1039/C4CC04816D).
- [64] T. Ayvali *Rhenium Based Mono- and Bi-metallic Nanoparticles: Synthesis, Characterization and Application in Catalysis (2015)* [Doctoral Thesis, University Toulouse 3 Paul Sabatier]. <https://www.theses.fr/2015TOU30269>.



**Max MILEWSKI**

**ESR12**

**Thesis co-directors**

Dr. Anne-Marie Caminade    Laboratoire de Chimie de Coordination, Toulouse, France

Prof. Evamarie Hey-Hawkins    Universität Leipzig, Leipzig, Germany

**Thesis defense**

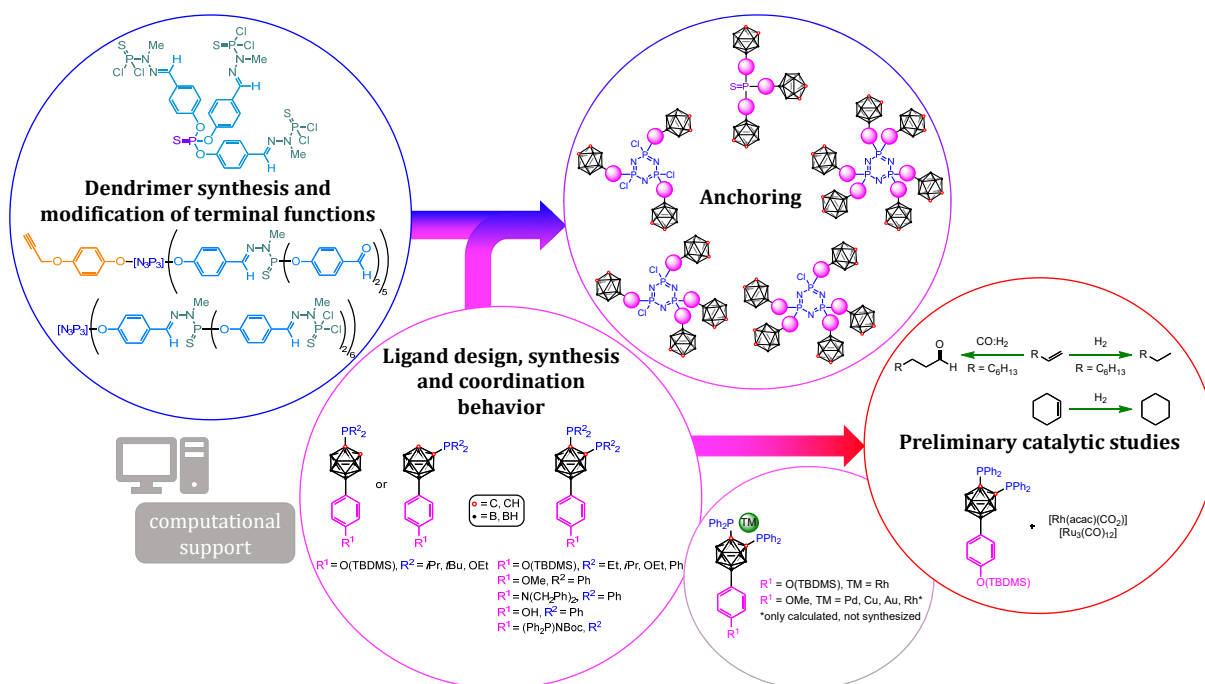
Laboratoire de Chimie de Coordination, 14 December 2023



## Carboranylphosphines Meet Dendrimers: Electron-deficient Scaffolds for Ligand Design and Application in Catalysis

### Introduction

This dissertation project aimed at preparing, characterizing, and utilizing a new ligand system for challenging catalytic transformations. The system was built on two chemical building blocks: a PPH dendritic framework, already known for its catalytic application and carboranylphosphine monomeric units, already investigated towards their interesting complexation behavior [1,2] and a few catalytic applications [3]. To combine both constructs, first a synthetic strategy for the suitable functionalization of the B9 position of the carboranylphosphines for anchoring them to supports, namely dendrimers, was developed. The second step was the investigation of different methods of linking them to the dendritic backbone. With respect to the work of CAMINADE and co-workers on PPH dendrimers [4-6], different dendritic phosphorus-containing scaffolds including symmetrical and unsymmetrical PPH dendrimers were chosen as the starting point for an anchoring. Based on previous work of HART and OWEN [7] and the HEY-HAWKINS group [8] on carboranylphosphines and their complexes, 1,2-bis(diphenylphosphino)-*ortho*-carborane was chosen as a suitable monomeric unit for further investigations (see Scheme 1).



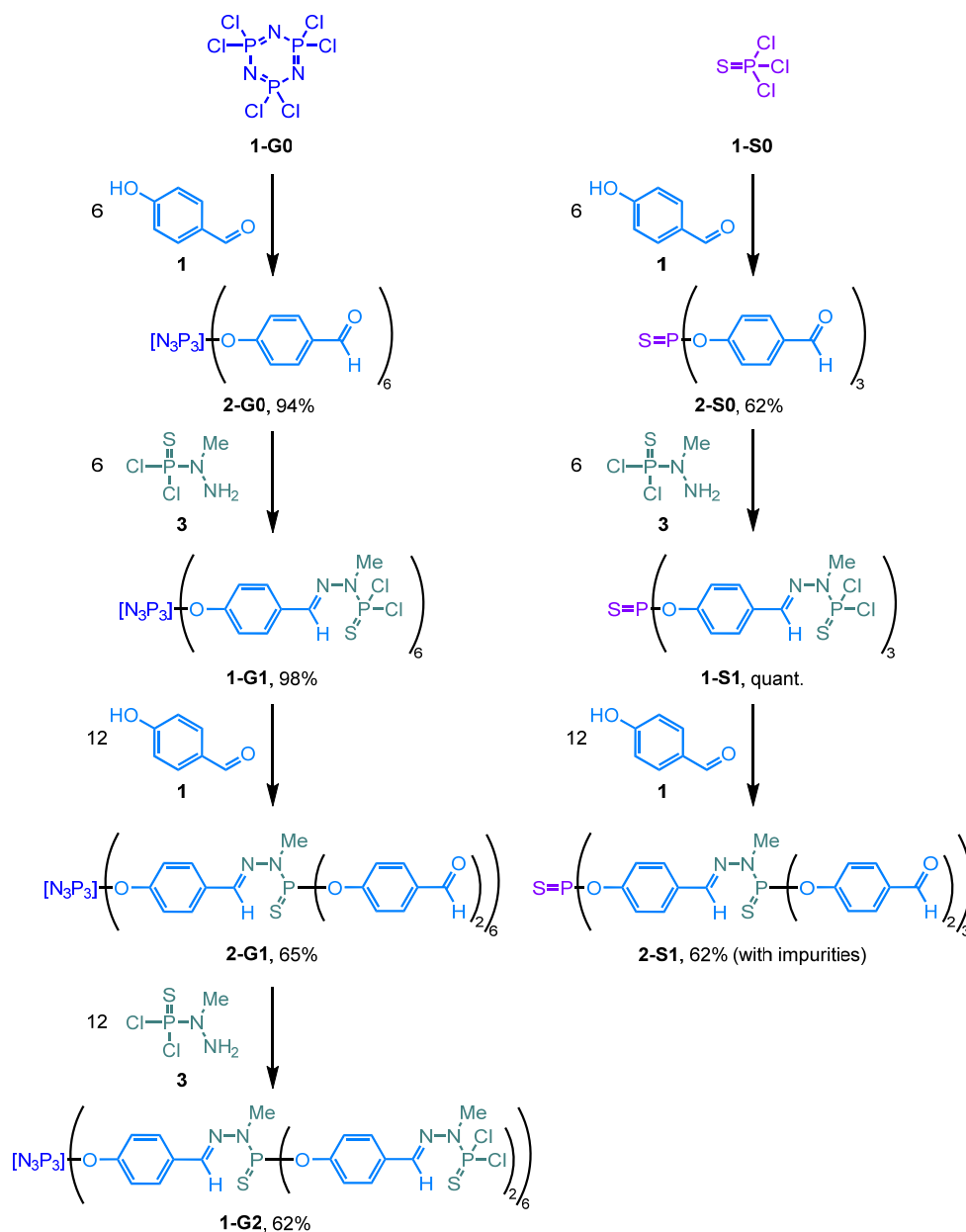
**Scheme 1.** Schematic overview of the major results obtained in the doctoral project. TM = transition metal.

### Preparation of the monomers and dendrimers

The synthesis of different dendritic compounds starting from a  $\text{P(S)Cl}_3$  (**1-S0**) or an  $\text{N}_3\text{P}_3\text{Cl}_6$  core (**1-G0**) was performed. Several classical dendrimers were obtained in good yields (62–98%) and acceptable purities up to generation **1-G2** or **2-S1**, respectively (see Scheme 2). The reiterative synthetic process, which entails a condensation reaction with the phosphorhydrazide  $\text{H}_2\text{NNMeP(S)Cl}_2$



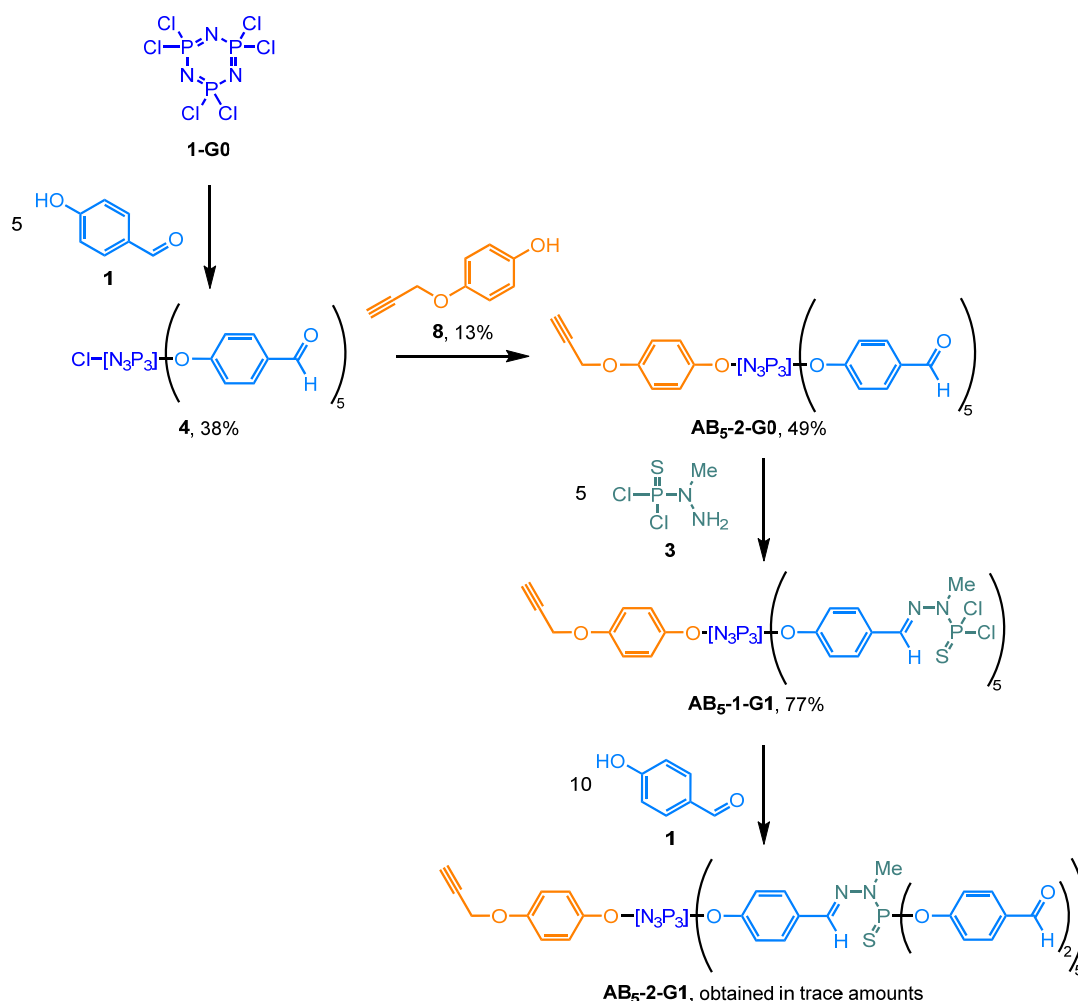
and a substitution reaction with 4-hydroxybenzaldehyde, was applied, but it could be shown that the established protocols are vulnerable.



**Scheme 2.** Overview of the synthetic steps yielding various classical dendrimers and dendritic phosphorus-containing scaffolds in the doctoral project.

Although the terminal functions of polyphosphorhydrazone (PPH) dendrimers are often similar, having two different types of terminal functions can be advantageous. For this reason, a specific functionalization of the  $N_3P_3$  core was targeted, with at least one function different from the others. Different unsymmetrical  $AB_5$  monomers and dendrimers, with one function distinct from the others up to generation  $AB_5$ -**2-G1** (A = 4-(prop-2-yn-1-yloxy)phenol, B = 4-hydroxybenzaldehyde, see Scheme 3) have been prepared. Additionally, to the synthesis of the unsymmetrical  $AB_5$  dendrimers, also a specific functionalization of only half of the terminal P-Cl groups in **1-G0** and **1-G1** was targeted to

obtain further dendritic backbones for the anchoring of different carboranes and carboranylphosphines. Problems were particularly evident during the stochastic monofunctionalization and purification of typical dendrimers.

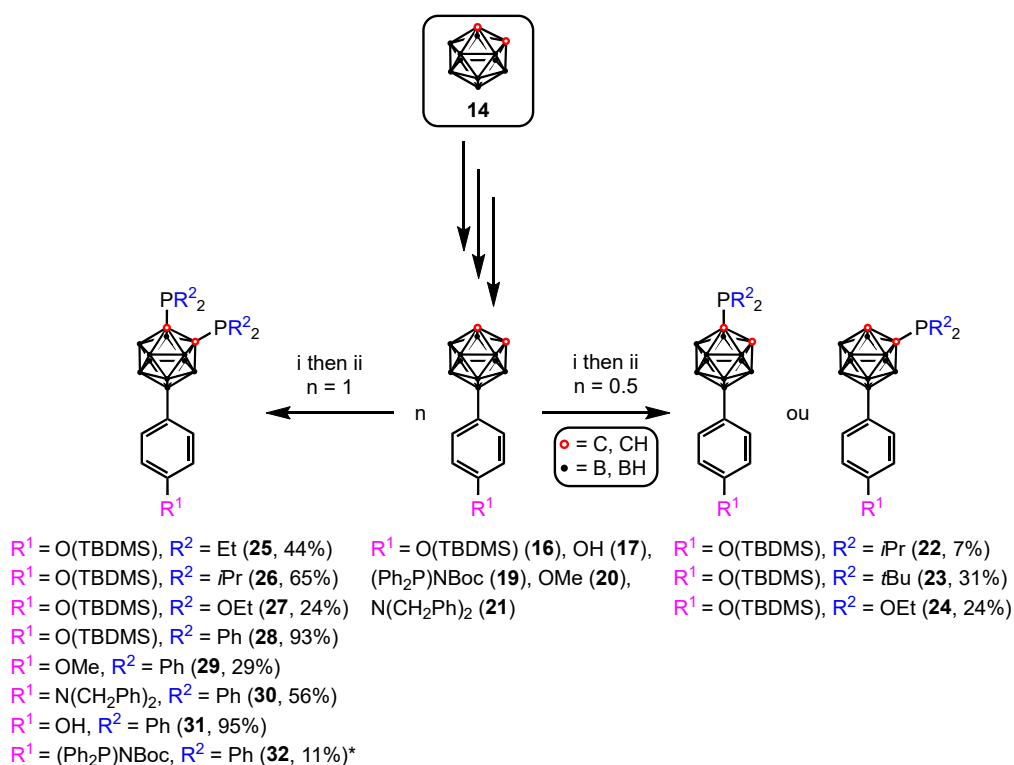


**Scheme 3.** Overview of the synthetic steps yielding various unsymmetrical AB<sub>5</sub> monomers and dendrimers in the doctoral project.

Starting from 1,2-dicarba-*closo*-dodecaboranes(12) (*ortho* isomer, **14**) a selection of different B<sub>9</sub>-substituted carboranes has been prepared. An adaption of the synthetic phosphorylation protocol of ALEXANDER and SCHROEDER [9] that had been used to prepare 1,2-phosphanyl-substituted carborane derivatives in the past was applied and modified yielding novel 1- or 1,2-phosphanyl-substituted carborane derivatives in low to excellent yields (7–95%, see Scheme 4).

While isolated side products revealed the highly stoichiometry-dependent nature of the phosphorylation step, which in the future could be used to more easily access unsymmetrically substituted phosphines, these crystalline materials frequently allowed for the elucidation of their solid-state structures (see Figure 1 and Figure 2). The synthesized carboranes and carboranylphosphines have C1–C2 (C<sub>Cage</sub>–C<sub>Cage</sub>) bond lengths that are comparable to other known compounds. The electronic and steric impact of the substituents on the P atoms causes a considerable increase in bond length in disubstituted compounds. The mean C–P bond lengths and P···P distances of the carboranylphosphines are consistent with previously described compounds. The obtained results revealed that various substituents in the B<sub>9</sub> position have only a minimal effect on the C1–C2 and C–P bond lengths, whereas

the substituents at the phosphorus atom have a significant influence. Only a few examples of the functionalized B9-position in carboranylphosphines have previously been documented [2]. This project led to new synthetic protection and deprotection strategies to modify the carborane cage further.



**Scheme 4.** Synthesis of B9-substituted carboranylphosphines. (i) *n*-butyllithium,  $\text{Et}_2\text{O}$  or THF,  $-78^\circ\text{C}$  to rt; (ii)  $\text{PR}_2\text{Cl}$ ,  $\text{Et}_2\text{O}$  or THF,  $-78^\circ\text{C}$  /  $0^\circ\text{C}$  to rt. \*The NH group in **19** was also substituted by  $\text{PPh}_2$ .

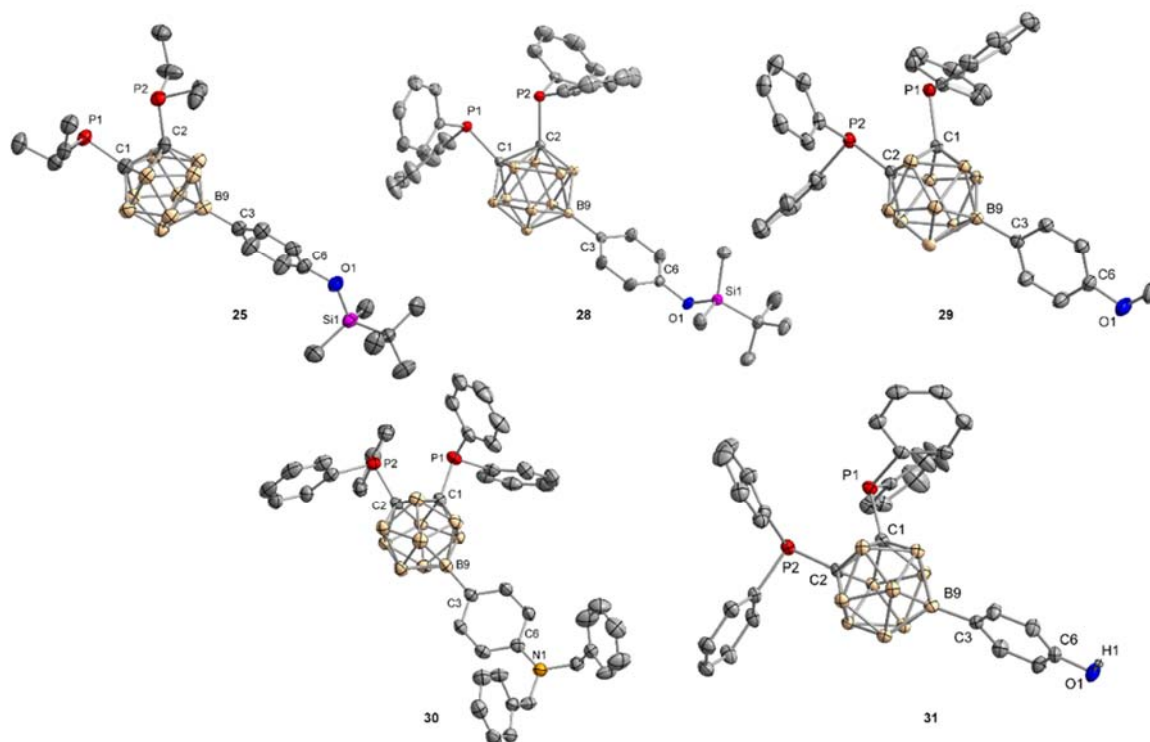


**Figure 1.** Molecular structures of carboranylphosphines **25** and **28–31** in the solid state with thermal ellipsoids drawn at the 50% probability level. Hydrogen atoms other than OH in **31** are omitted for clarity.

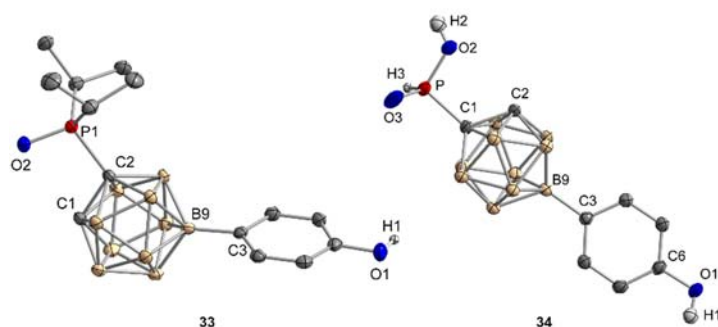


**Figure 2.** Molecular structures of carboranylphosphines **33** and **34** in the solid state with thermal ellipsoids drawn at the 50% probability level. Hydrogen atoms other than OH and PH are omitted for clarity.

### Coordination behavior

Bearing two phosphorus groups in close proximity, the new carboranylphosphines resemble already known bidentate phosphines and might be promising ligands for the complexation of different transition metals useful for homogeneous catalysis. Especially, the tunability of the steric and electronic properties of the carboranylphosphines allowed the synthesis of new ligands needed for the complexation of different transition metals (Pd, Cu, Au, Rh, Ru). Prompted by the close proximity of both phosphorus atoms when directly attached to the carborane cage (similar to an ethylene or *ortho*-phenylene moiety), the capability to accommodate different transition metals in a 1:1 coordination mode was investigated. According to DFT calculations performed with different B9-substituted carboranylphosphines (**29**, **31** and **46–49**), in most cases the formation of transition metal complexes from these ligands and different complex precursors should be thermodynamically favored (see Table 1 and Figure 3). More stable complexes can be formed after a CH<sub>2</sub> linker is inserted between the carborane cage and the phosphorus atoms. Experiments were carried out to find synthetic proof. Unfortunately, it was not possible to form any complexes with the ligands **47–49** or **53**.

**Table 1.** Computed GIBBS energies [kcal mol<sup>-1</sup>] of complexes formed with ligands **29**, **31**, **46–49** and different metal complex precursors in THF or CH<sub>2</sub>Cl<sub>2</sub> as solvents, relative to the starting materials.

Carboranylphosphine				
Metal complex precursor (solvent for calculation)				
Y = PPh <sub>2</sub> ( <b>29</b> , <b>31</b> , <b>46</b> )	[AuCl(tht)] (CH <sub>2</sub> Cl <sub>2</sub> )	-13.2	-14.3	-14.1
	[PdCl <sub>2</sub> (MeCN) <sub>2</sub> ] (THF)	-42.0	-42.1	-20.9
	[Cu(MeCN) <sub>4</sub> ](OTf) (THF)	+6.0	+4.5	+4.9
	[CuCl(PPh <sub>3</sub> ) <sub>3</sub> ] (THF)	-0.2	+0.4	+0.1
	[Rh(acac)(CO) <sub>2</sub> ] (THF)	-63.0	-62.9	-62.7
Y = CH <sub>2</sub> PPh <sub>2</sub> ( <b>47–49</b> )	[AuCl(tht)] (CH <sub>2</sub> Cl <sub>2</sub> )	-24.7	-23.5	-25.2
	[PdCl <sub>2</sub> (MeCN) <sub>2</sub> ] (THF)	-42.4	-41.9	-42.5
	[Cu(MeCN) <sub>4</sub> ](OTf) (THF)	+0.5	-0.9	not computed
	[CuCl(PPh <sub>3</sub> ) <sub>3</sub> ] (THF)	-10.3	-9.4	-9.2
	[Rh(acac)(CO) <sub>2</sub> ] (THF)	-134.2	-133.3	-133.5

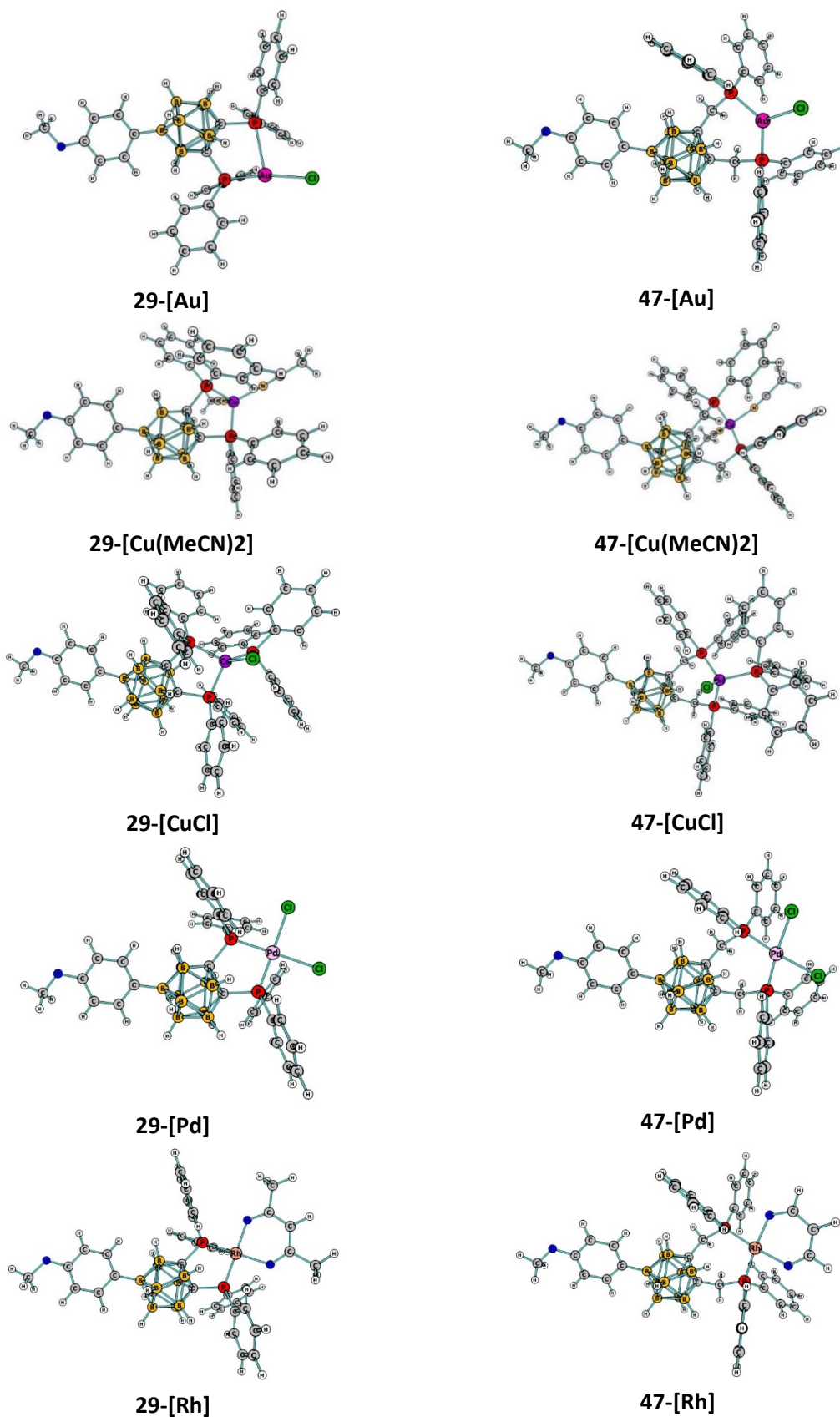
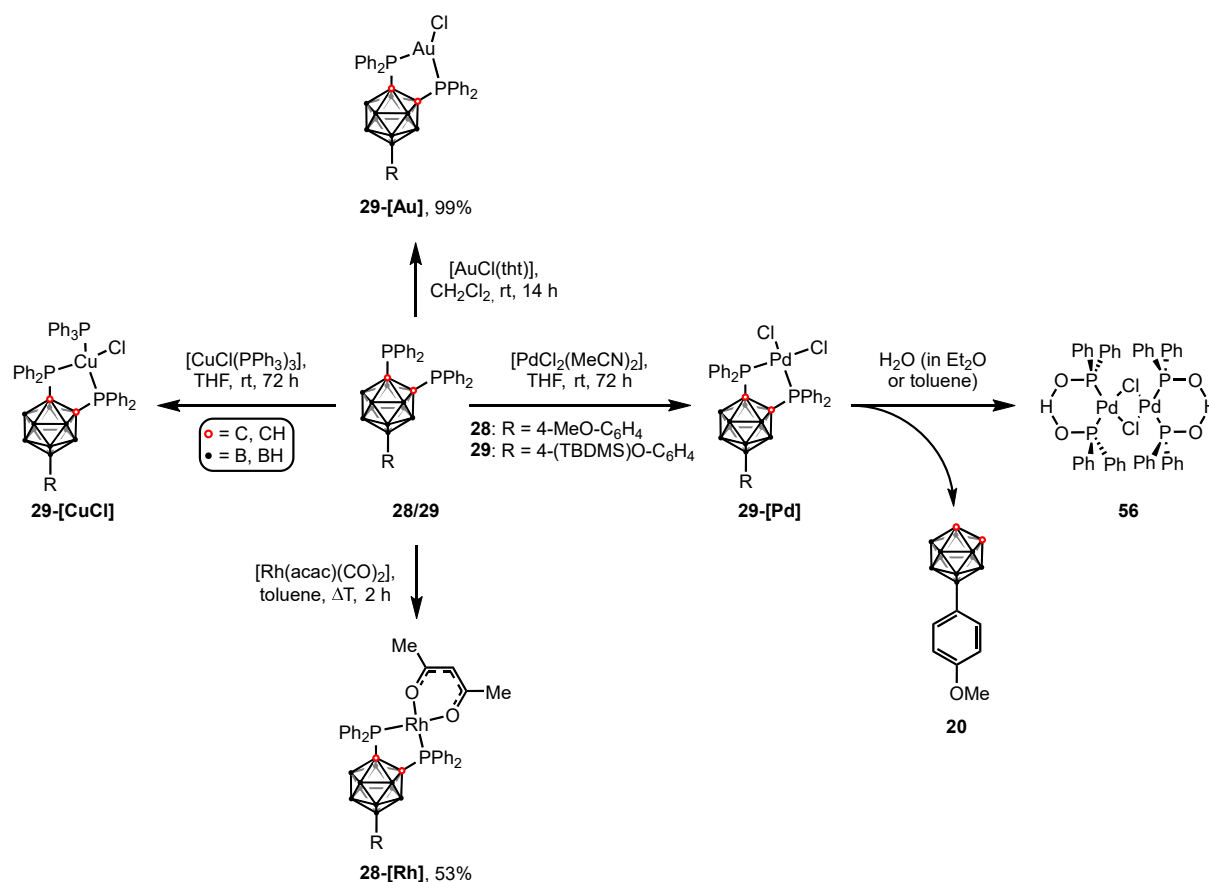


**Figure 3** Computed complexes formed from 9-(4-MeO-C<sub>6</sub>H<sub>4</sub>)-1,2-bis(diphenylphosphino)- (**29**) and 9-(4-MeO-C<sub>6</sub>H<sub>4</sub>)-1,2-bis[(diphenylphosphino)methyl]-ortho-carborane (**47**) and different metal complex precursors. All hydrogen atoms are omitted for clarity. The triflate anion in **29**- and **47**-[Cu(MeCN)<sub>2</sub>] was optimized separately. The optimized structures obtained for other B9 substituents are not displayed.

For this reason, only the monomeric carboranylphosphine derivatives 9-(TBDMS)O-C<sub>6</sub>H<sub>4</sub>-1,2-(PPh<sub>2</sub>)<sub>2</sub>-C<sub>2</sub>B<sub>10</sub>H<sub>9</sub> (**28**) and 9-(4-MeO-C<sub>6</sub>H<sub>4</sub>)-1,2-(PPh<sub>2</sub>)<sub>2</sub>-C<sub>2</sub>B<sub>10</sub>H<sub>9</sub> (**29**) have been used for the first complexation experiments with a Pd<sup>II</sup>, two Cu<sup>I</sup>, an Au<sup>I</sup>, a Rh<sup>I</sup>, and a Ru<sup>0</sup> complex precursor. The silyl ether protected carboranylphosphine **28** was the most available of all compounds produced throughout the practical work of the dissertation. The methoxyphenyl substituent in **29** mimics the phenoxy linker needed in immobilization reactions. It can be considered as the monomeric equivalent of the carboranyl-substituted dendrimers. Rhodium(I) complex **28**-[Rh], gold(I) complex **29**-[Au], and copper(I) complex **29**-[CuCl] could be synthesized and characterized by NMR spectroscopy and mass spectrometry. Additionally, it was possible to proof the formation of Pd<sup>II</sup> complex **29**-[Pd], but due to its high reactivity, an isolation was not feasible. Instead the dimeric hydrolysis product, Pd<sup>II</sup> complex **56**, was isolated (see Scheme 5).



**Scheme 5.** Overview of the synthesis of different carboranylphosphine transition metal complexes.

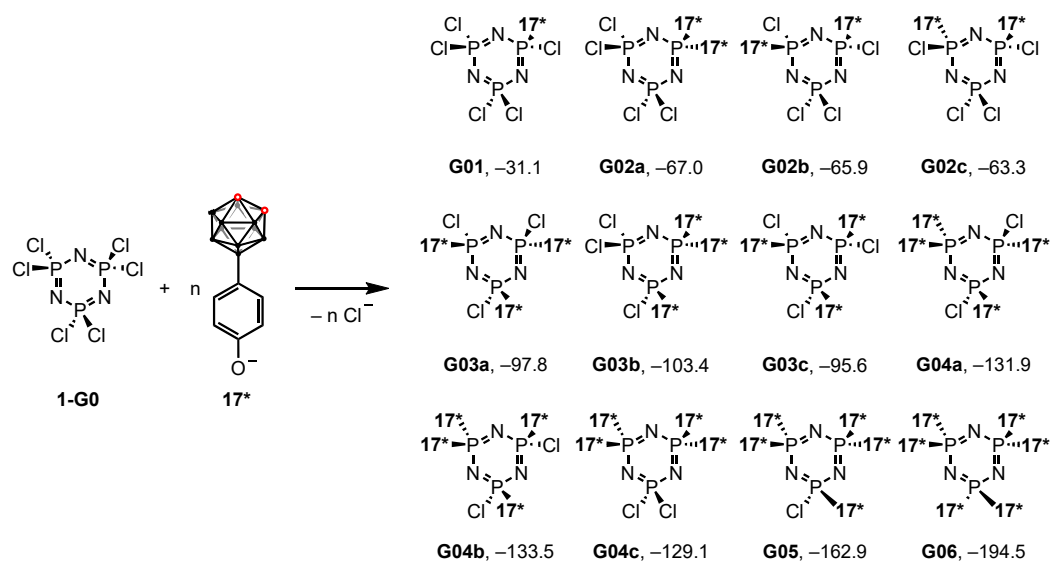
### Preliminary catalytic investigations

Using an automated parallel library screening system at BASF SE, preliminary catalytic studies for the hydrogenation and hydroformylation of oct-1-ene and cyclohexene were conducted with various rhodium and ruthenium complex precursors and 9-(4-TBDMSO-C<sub>6</sub>H<sub>4</sub>)-1,2-(PPh<sub>2</sub>)<sub>2</sub>-C<sub>2</sub>B<sub>10</sub>H<sub>9</sub> (**28**). The most promising systems were then transferred into an autoclave to test the reactions under reproducible conditions. Ligand **28** showed the best performance for the hydrogenation of oct-1-ene with [Rh(acac)(CO)<sub>2</sub>] performing better than already known systems. It further showed a better conversion in the hydrogenation of cyclohexene with [Ru<sub>3</sub>(CO)<sub>12</sub>] than the non-substituted carboranylphosphine derivative 1,2-bis(diphenylphosphino)-*ortho*-carborane (dppc, **73**), but worked

not as good as a simple bisphosphine, namely 1,2-bis(diphenylphosphino)-benzene (dppb, **67**). Despite the fact that several of the reactions demonstrated good conversion, the selectivity is not superior to other known systems; hence these systems were not subjected to additional testing in an industrial setting. However, to get more significant results, further runs would have been required. Investigation of the catalytic species produced *in situ* from the metal complexes and ligands would have been required as well. It would be essential to repeat several catalytic studies, look into the scope and limitations of the performed hydrogenation and hydroformylation, and further develop better catalytic systems in order to better comprehend the results.

### Anchoring of carboranes and polyphosphorhydrazone dendrimers

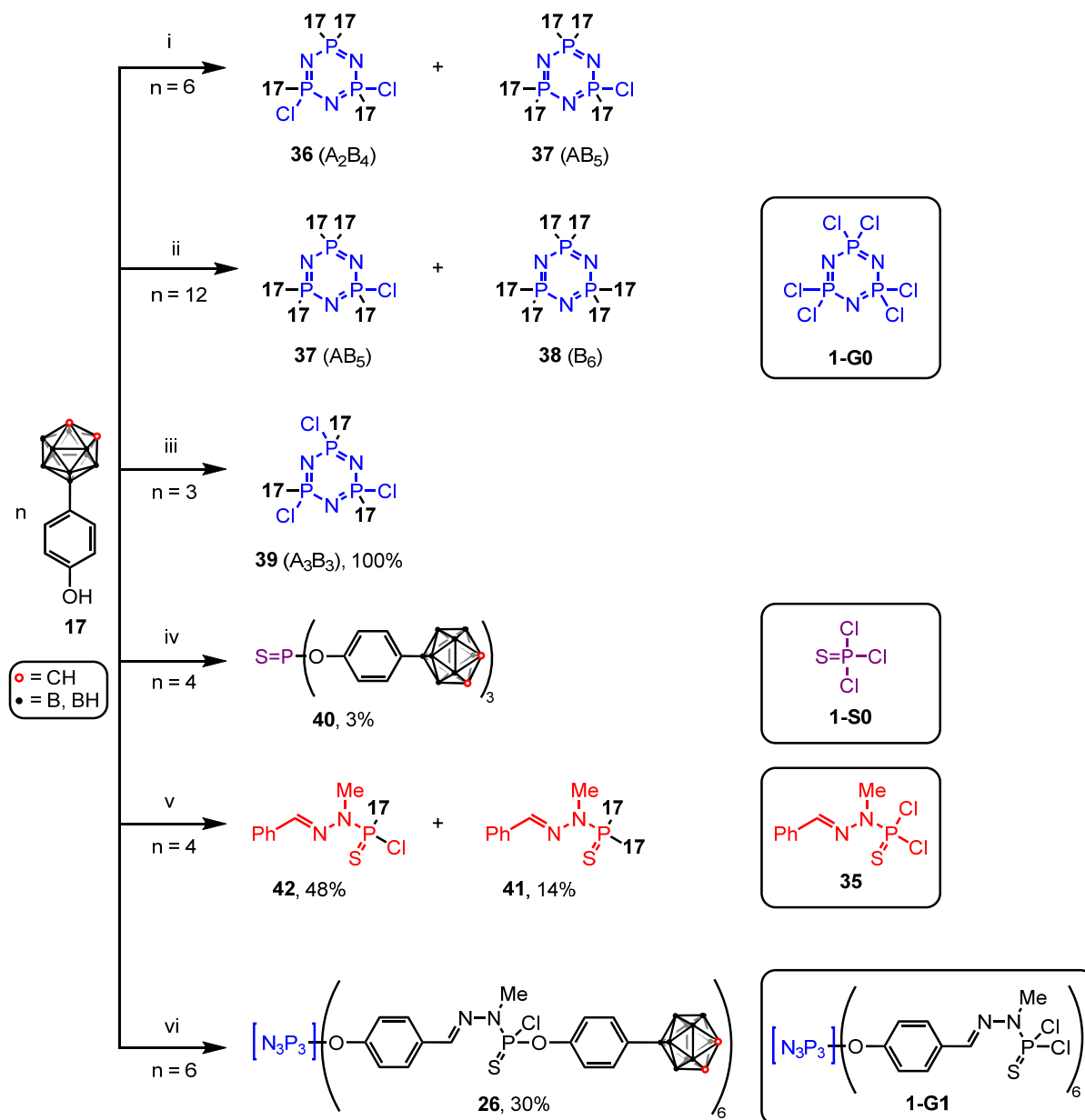
Various dendritic compounds were evaluated for their suitability of being grafted to various new phenol-linked carboranes and carboranylphosphines. DFT calculations have proven that the reaction proceeds similar to an  $S_N2$  reaction, with the nucleophilic phenoxide **17\*** approaching the electrophilic phosphorus center of the  $N_3P_3Cl_6$  core opposite to the leaving group  $Cl^-$ . Products of multiple substitution reactions with **17\*** were also optimized to computationally check the stability of such products. It could be shown that the six-fold substitution of **1-G0** forms a product with greater stability by  $194.5 \text{ kcal mol}^{-1}$  relative to the starting material (see Scheme 6).



**Scheme 6.** Computed Gibbs energy values in THF as solvent (in  $\text{kcal mol}^{-1}$ ) for the substitution of **1-G0** with  $n$  equivalents of **17\*** relative to the starting material.

As calculations support the possibility of multiple substitution of chloride centers in  $N_3P_3Cl_6$  by carboranyl groups, this hypothesis was experimentally checked (see Scheme 7). A grafting to the model molecule **35**, to different phosphorus-containing compounds **1-G0** and **1-S0** as well as to dendrimer **1-G1** was tested. Despite the lack of a full substitution with a carboranylphosphine, novel carborane-substituted dendritic compounds were synthesized. Further, the selective grafting of a single carborane per  $P(S)Cl_2$  function was investigated yielding a monofunctionalized dendrimer **43** (see Figure 4). Yet, the separation process of differently carborane-substituted dendrimers is still a focus of investigation. Also, the selective grafting of a single carborane per  $P(S)Cl_2$  function should be investigated for other generations of dendrimers because it will open the way to the grafting of

additional functionalities to replace the remaining Cl, for instance with water-solubilizing functions, in view of biological experiments [10].



**Scheme 7.** Reaction of different equivalents of **17** with the  $N_3P_3Cl_6$  core **1-G0**,  $P(S)Cl_3$  **1-S0** and model molecule **35**. Conditions: (i) **1-G0**,  $K_2CO_3$ , acetone, 40 °C for 120 h, then rt for 72 h; (ii) **1-G0**,  $C_2CO_3$ , THF, rt, 25 d; (iii) **1-G0**,  $K_2CO_3$ , acetone, rt, 72 h; (iv) **1-S0**,  $Cs_2CO_3$ , THF, 40 °C, 96 h; (v) **35**, DBU, THF, rt, 72 h; (vi) **1-G1**,  $Cs_2CO_3$ , THF, rt for 72 h, then 40 °C for 23 h. All compounds were analyzed by NMR spectroscopy and ESI-MS. Only one isomer of the incompletely substituted dendrimers ( $A_3B_3$ ,  $A_2B_4$ ) is displayed.



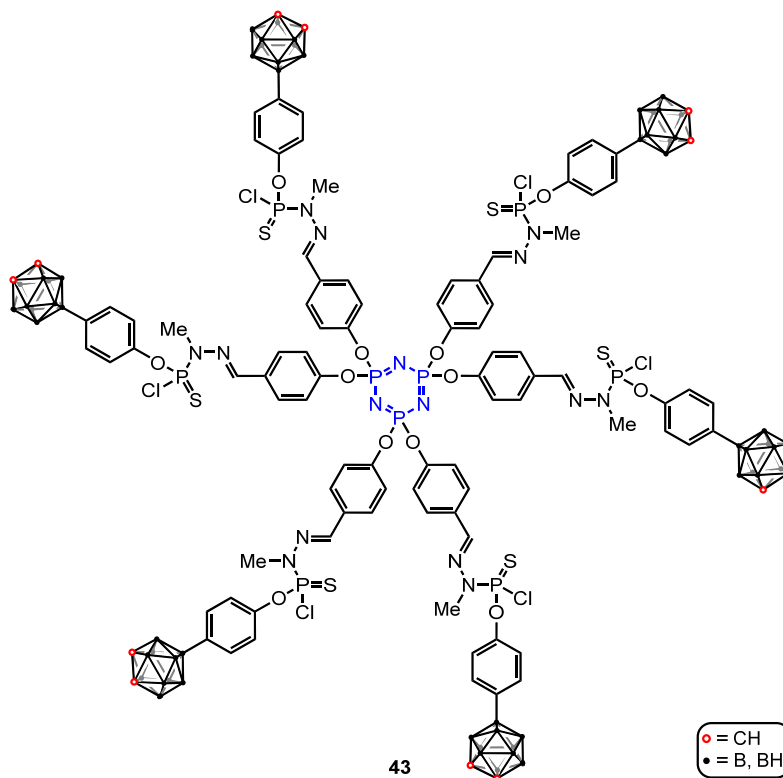


**Figure 4.** Full structure of dendrimer **43**.

### In a nutshell

Several *ortho*-carboranes bearing a phenoxy or a phenylamino group in the B9 position were prepared employing various protection and deprotection strategies. Furthermore, the synthetic access to novel 1- or 1,2-phosphanyl-substituted carborane derivatives was developed in this dissertation project. The resulting diethyl-, diisopropyl-, di-*tert*-butyl-, diphenyl- or diethoxyphosphines bearing a tunable *ortho*-carborane moiety are intriguing ligands for future applications in homogeneous catalysis or the medicinal sector. The ligand framework has shown a distinctive coordination behavior to different transition metals in a 1:1 coordination mode by the chelating carboranylbisphosphines. A catalyst generated *in situ* from a mixture of Rh or Ru complex precursors and carboranylbisphosphine derivative **28** could be used for the hydrogenation and hydroformylation of unsaturated olefins.

Following established protocols, dendritic compounds were synthesized from a hexachlorocyclotriphosphazene or thiophosphoryl chloride core, and possible anchoring options for the B9-substituted *ortho*-carboranes were investigated experimentally and theoretically (DFT). In spite of the synthetic challenges, different carborane-containing dendrimers could be obtained and the results should open the door to the synthesis of carboranylphosphine-containing dendrimers in order to improve the catalytic performance and exploring new reaction pathways. Following studies on differently substituted carboranylphosphines as well as other catalytic applications would be highly interesting. So far, only electron-deficient C–P carboranylphosphines were utilized for the anchoring. Changing the system to electron-rich B–P carboranylphosphines (similar to the work of SPOKOYNY and co-workers) [11] linking the carboranes *via* their C<sub>cage</sub> atoms to the dendrimers could be an interesting switch. It is obvious that the research in this field is not exhausted, and depending on the approach chosen, a lot of interesting results can certainly be obtained.

## References

- [1] I. B. Sivaev, M. Y. Stogniy, V. I. Bregadze, *Coord. Chem. Rev.* **2021**, *436*, 213795. DOI: [10.1016/j.ccr.2021.213795](https://doi.org/10.1016/j.ccr.2021.213795).
- [2] E. V. Oleshkevich, E. G. Rys, V. V. Bashilov, P. V. Petrovskii, V. A. Ol'shevskaya, S. K. Moiseev, A. B. Ponomaryov, V. N. Kalinin, *Russ. J. Gen. Chem.* **2017**, *87*, 2589–2595. DOI: [10.1134/S1070363217110123](https://doi.org/10.1134/S1070363217110123).
- [3] S. Bauer, E. Hey-Hawkins, *Phosphorus-Substituted Carboranes in Catalysis*, in *Boron Science* (N. S. Hosmane, Editor), CRC Press, **2011**, pp. 529–578. DOI: [10.1201/b11199-30](https://doi.org/10.1201/b11199-30).
- [4] N. Launay, A. M. Caminade, R. Lahana, J. P. Majoral, *Angew. Chem. Int. Ed. Engl.* **1994**, *33*, 1589–1592. DOI: [10.1002/anie.199415891](https://doi.org/10.1002/anie.199415891).
- [5] N. Launay, A. M. Caminade, J. P. Majoral, *J. Organomet. Chem.* **1997**, *529*, 51–58. DOI: [10.1016/S0022-328X\(96\)06293-6](https://doi.org/10.1016/S0022-328X(96)06293-6).
- [6] E. Cavero, M. Zablocka, A. M. Caminade, J. P. Majoral, *Eur. J. Org. Chem.* **2010**, 2759–2767. DOI: [10.1002/ejoc.200901291](https://doi.org/10.1002/ejoc.200901291).
- [7] F. A. Hart, D. W. Owen, *Inorg. Chim. Acta* **1985**, *103*, L1–L2. DOI: [10.1016/S0020-1693\(00\)85196-8](https://doi.org/10.1016/S0020-1693(00)85196-8).
- [8] P. Coburger, G. Kahraman, A. Straube, E. Hey-Hawkins, *Dalton Trans.* **2019**, *48*, 9625–9630. DOI: [10.1039/c9dt00628a](https://doi.org/10.1039/c9dt00628a).
- [9] R. P. Alexander, H. Schroeder, *Inorg. Chem.* **1963**, *2*, 1107–1110. DOI: [10.1021/ic50010a006](https://doi.org/10.1021/ic50010a006).
- [10] A. M. Caminade, M. Milewski, E. Hey-Hawkins, *Pharmaceutics* **2023**, *15*, 2117. DOI: [10.3390/pharmaceutics15082117](https://doi.org/10.3390/pharmaceutics15082117).
- [11] A. M. Spokoyny, C. D. Lewis, G. Teverovskiy, S. L. Buchwald, *Organometallics* **2012**, *31*, 8478–8481. DOI: [10.1021/om301116](https://doi.org/10.1021/om301116).



**Massimo PETRICCONE**

**ESR13**

**Thesis co-directors**

Prof. Rosa Maria Sebastián      Universitat Autònoma de Barcelona, Bellaterra, Spain

Dr. Anne-Marie Caminade      Laboratoire de Chimie de Coordination, Toulouse, France

**Thesis defense**

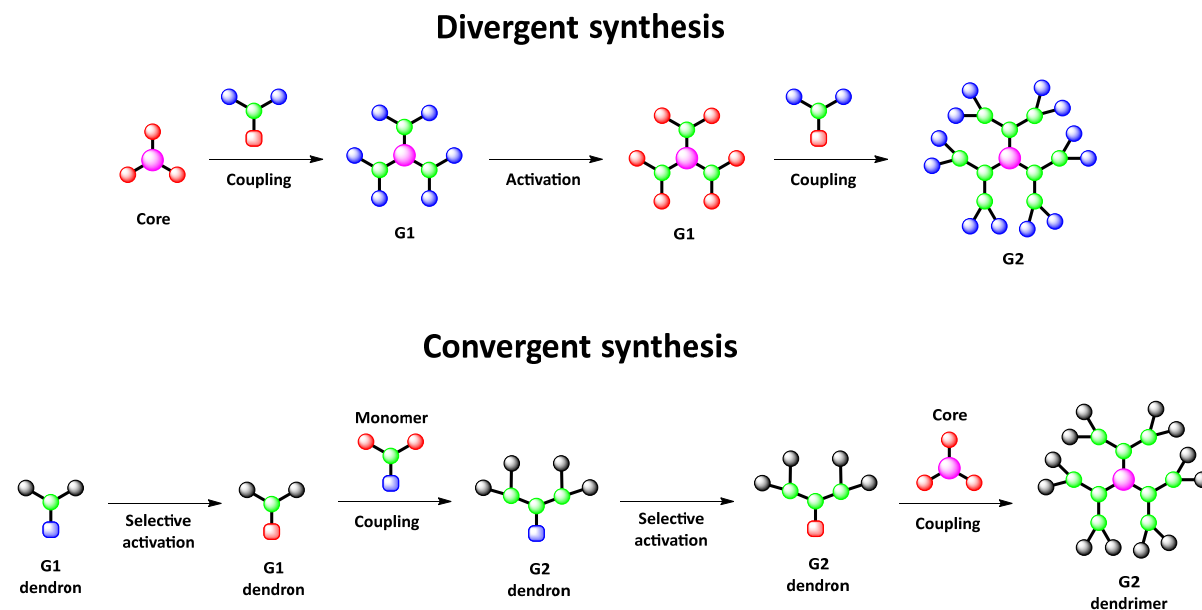
Department of Chemistry, Universitat Autònoma de Barcelona, 1 March 2024



## Specifically Functionalized Dendrimers for Catalysis in Special Media

### Introduction

Dendrimers, inspired by dendritic patterns in nature, are molecular structures widely utilized in chemistry and materials science [1,2]. With a tree-like, they offer precise control over size, shape, and surface chemistry [3]. They are synthesized through divergent [4] or convergent approaches (Scheme 1) [5].



**Scheme 1.** Synthesis of dendrimers according to divergent and convergent methods.

Dendrimers come in various structural variations and chemical compositions, including PAMAM [6], PPI [7], and more (Figure 1). Phosphorhydrazone (PPH) dendrimers, a versatile subclass, find applications in bioconjugation and metal chelation for catalysis [8-10].

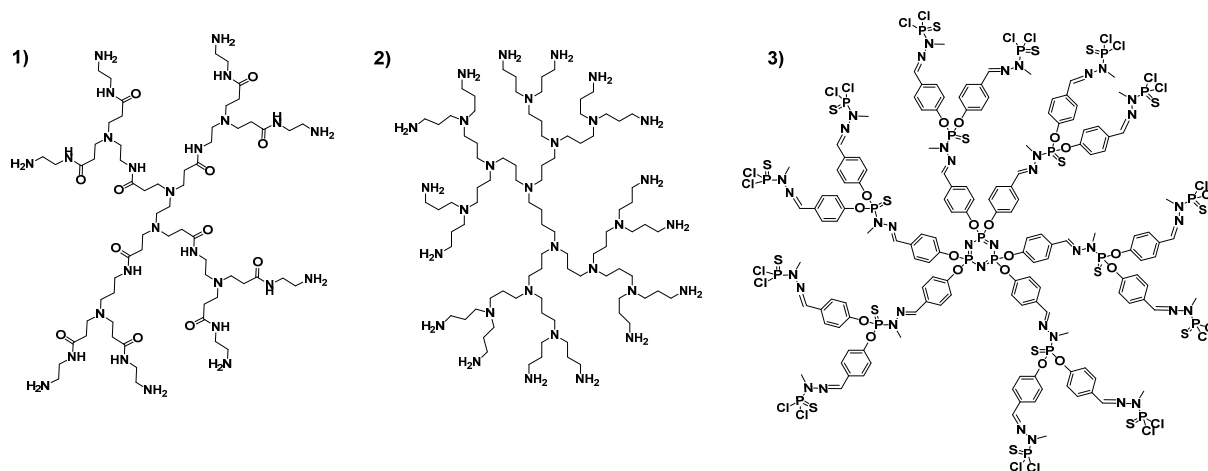


**Figure 1.** Representations of 1) PAMAM dendrimers, 2) PPI dendrimers and 3) PPH dendrimers.

Surface functionalization of dendrimers is a common and powerful strategy to tailor their properties. Examples include the addition of polyethylene glycol (PEG) chains to enhance water solubility [11], particularly valuable for biological applications. Another illustrative case involves the addition of perfluorinated polyether chains to improve solubility in environmentally friendly media (Figure 2) [12]. Phosphorhydrazone dendrimers, with specific functionalization, have demonstrated solubility in fluorinated media [13], showcasing their potential in unconventional solvents like supercritical CO<sub>2</sub> and thermo-responsive biphasic fluoruous/organic systems.

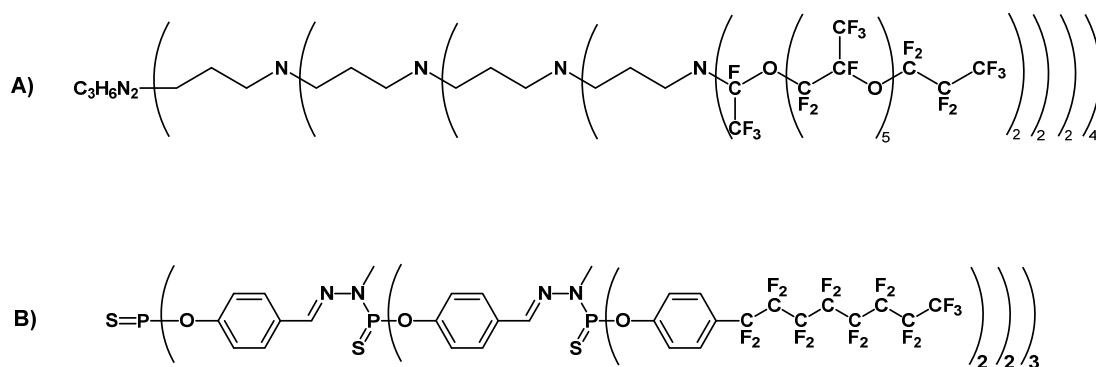


**Figure 2.** **A)** G4 PPI dendrimer functionalized with perfluorinated polyether chains; **B)** G2 phosphorhydrazone dendrimer functionalized with phenols containing alkyl perfluorinated chains.

Bifunctionalization of dendrimers represents a versatile strategy in nanotechnology, enabling the incorporation of two distinct types of terminal functions for diverse applications [14]. While terminal functions can be uniformly modified to introduce new properties, the desire for dual functionalities arises in cases where unique characteristics are required for specific applications. For instance, one terminal function might contribute to solubility, while the other imparts catalytic or biological properties. Alternatively, one function could be dedicated to grafting onto materials, while the other provides additional desirable properties (Figure 3).

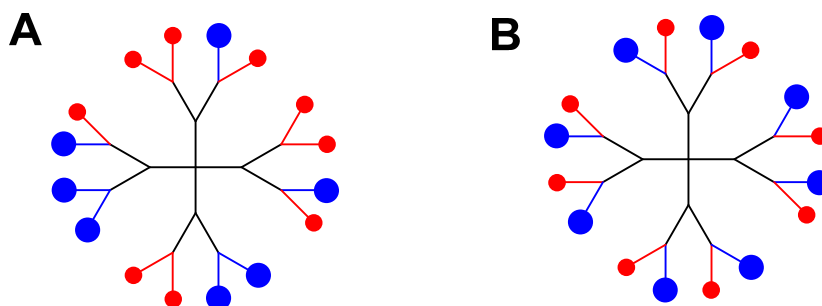
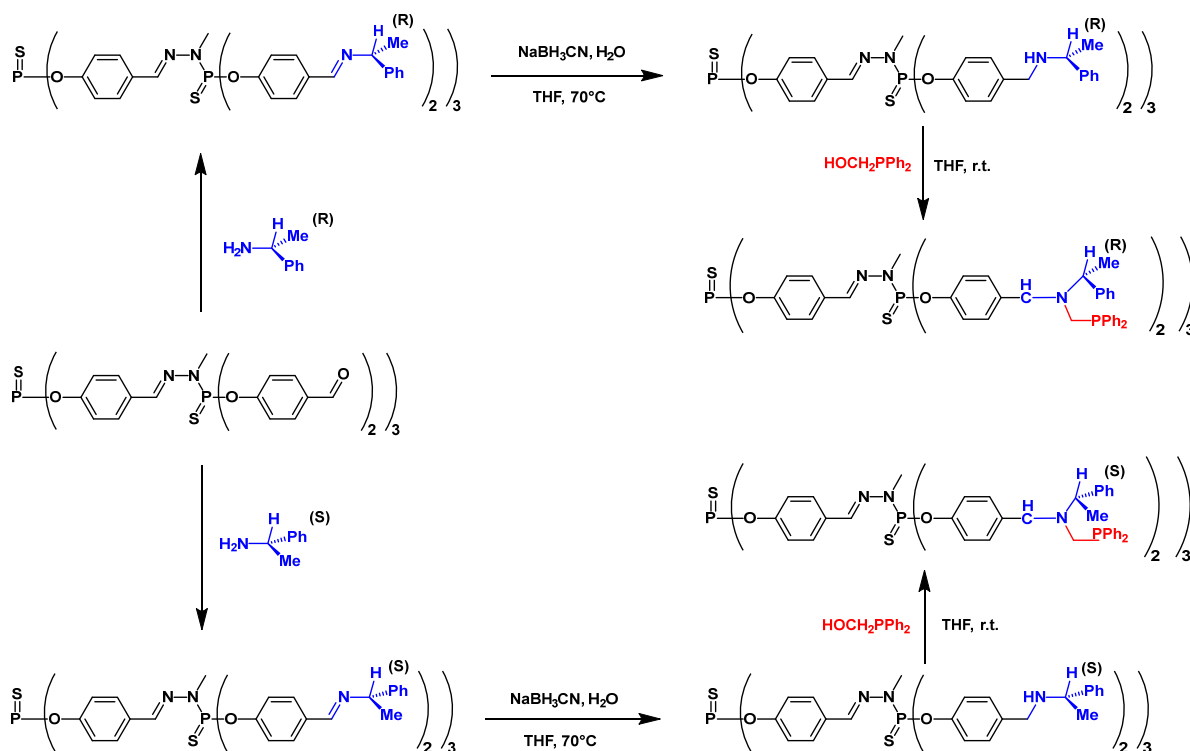


**Figure 3.** **(A)** Schematization of stochastically substituted dendrimers mixture; **(B)** schematization of precisely substituted dendrimers mixture.

However, the traditional stochastic approach to bifunctionalization, where two or more functions are introduced onto the dendrimer surface without precise control, contradicts the goal of achieving reproducibility in dendrimer synthesis. The stochastic method introduces variability in the type and location of substitutions, potentially impacting the dendrimer's activity [15]. To address this challenge, a preferable alternative involves the precise synthesis of bifunctionalized dendrimers, ensuring a consistent and controlled structure [16]. Three distinct pathways for synthesizing

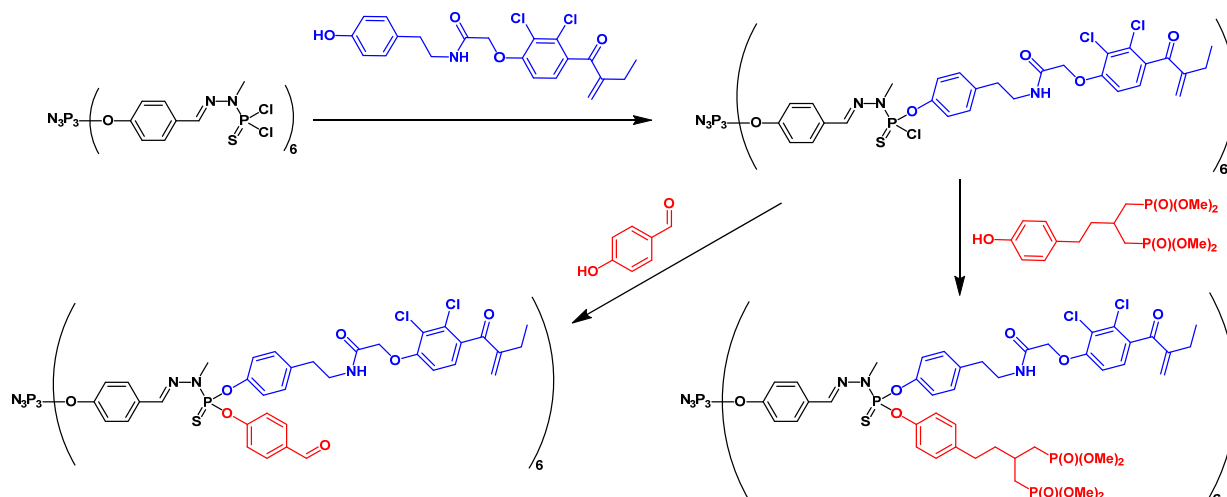






**Scheme 3.** Synthesis of PPH dendrimer functionalized with a stereogenic moiety and subsequently modified with the addition of a phosphine [18].

The sequential grafting of two different substituents on the surface of PPH dendrimers is a less common approach to bifunctionalization. It involves sequential substitution with two different functional groups, such as amines or phenols. While there are limited examples of sequential grafting with two phenols, a specific case involving the grafting of a phenol derivative of ethacrynic acid followed by the grafting of either 4-hydroxybenzaldehyde or the phenol of an azabisphosphonate demonstrates the potential in this approach (Scheme 4) [19].



**Scheme 4.** Sequential grafting of two different phenolic substituents on the P(S)Cl<sub>2</sub> terminal functions of PPH dendrimers.

In recent decades, the focus on green chemistry and atom economy has driven research towards optimizing catalytic processes, especially in organic solvents. Dendrimers, with their precisely defined structures, substantial surface area, solubility in organic solvents, and tunable chemical functionalities, have emerged as promising candidates for catalytic applications. Metallo-dendrimers, in particular, exhibit various modes of metal interaction, contributing to structural diversity and influencing reactivity [20].

The dendrimer recovery in catalysis can be accomplished through various methods, each tailored to specific properties and applications. These methods include nanofiltration, phase separation, precipitation, and magnetism [21,22].

The dendrimer effect, manifested as the multivalency dendritic effect and the generation dendritic effect, plays a significant role in influencing the properties and behaviour of functional moieties attached to dendrimers. This non-linear phenomenon can have both positive and negative effects, depending on the specific application. In the context of catalysis, the dendrimer effect can enhance reaction rates, yields, or selectivity and even play a role in improving the stability of metal complexes, reducing metal leaching, and aligning with the principles of green and sustainable chemistry [23-25].

Phosphorhydrazone dendrimers, with their solubility in various organic solvents, have gained prominence in homogeneous catalysis. The use of dendrimers with a metal core or surface-functionalized with ligands provides control over coordination chemistry, leading to enhanced catalytic efficiency and selectivity. Phosphorhydrazone dendrimers functionalized with various ligands able to complex different metals were used to perform a great variety of coupling reactions (Figure 5) [26].

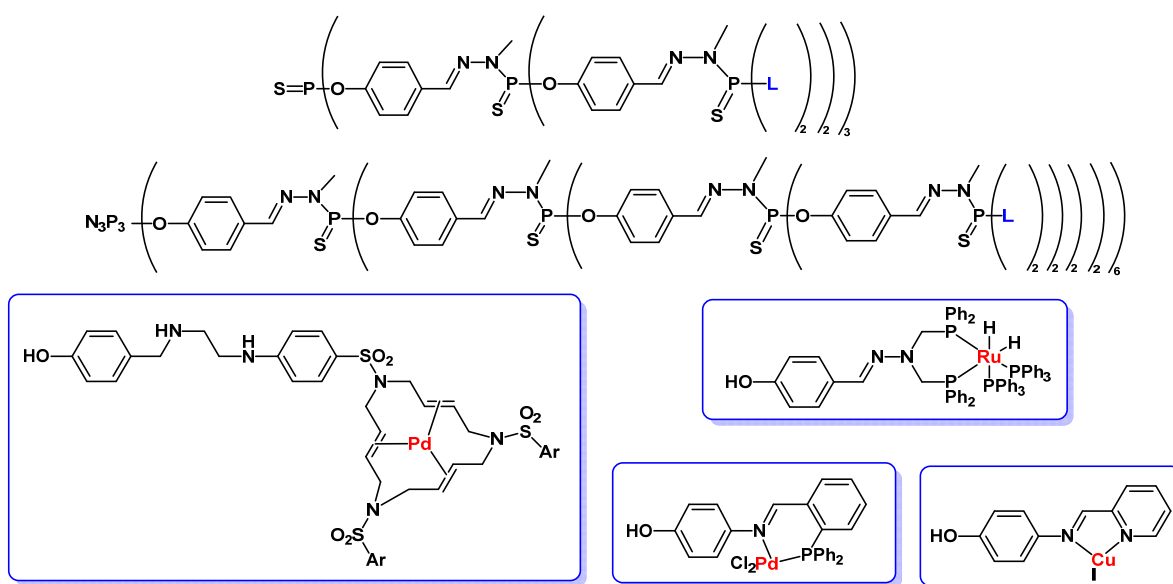
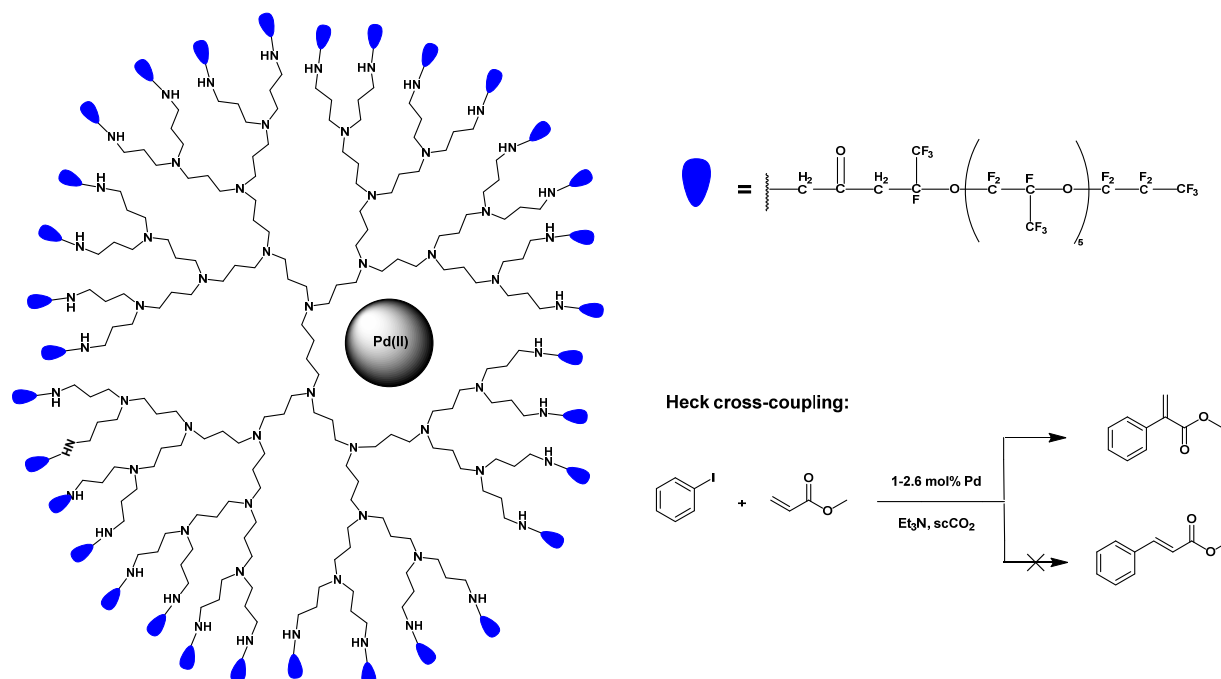


**Figure 5.** Phosphorhydrazone dendrimers with SP and  $N_3P_3$  cores, functionalized on the surface with different metal complexes.

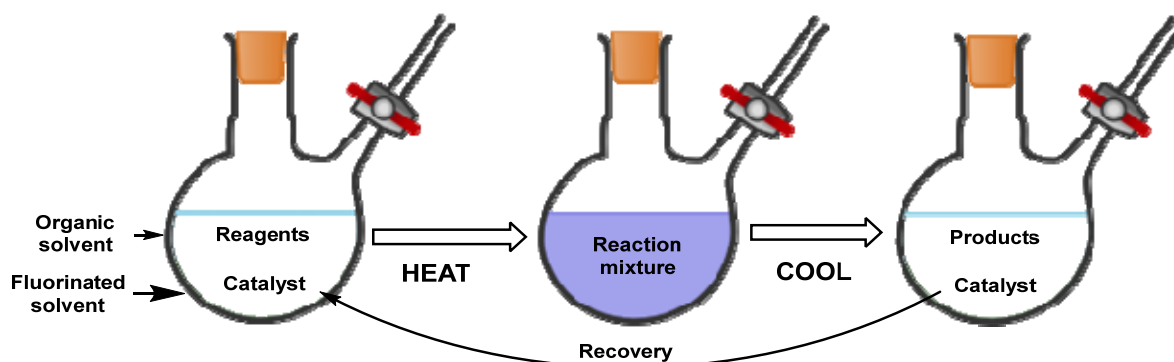
Exploring unconventional solvents in homogeneous catalysis, such as supercritical carbon dioxide ( $scCO_2$ ), represents a significant stride towards sustainable practices. Dendrimers have been employed in catalysis in  $scCO_2$ , albeit limited examples. For instance, carbosilane dendrimers with  $PdCl_2$  complexed with phosphorus at the core exhibited activity in the Heck cross-coupling reaction in  $scCO_2$ . Additionally, the control of a PPI dendrimer's solubility in  $scCO_2$  through surface

functionalization with perfluorinated polyethers facilitated the Heck cross-coupling reaction with high selectivity (Scheme 5) [28,29].

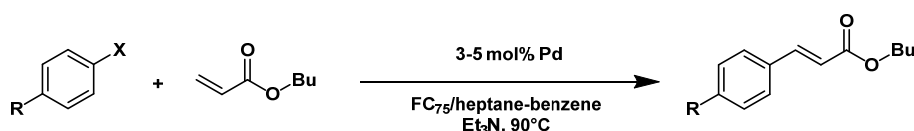


**Scheme 5.** PPI dendrimer functionalize on the surface with perfluorinated polyethers chains, encapsulating Pd nanoparticles to perform Heck cross-coupling in  $scCO_2$ .

Homogeneous catalysis in fluoruous/organic biphasic systems, particularly those with thermoreversible characteristics, offers a unique approach to catalytic methodologies (Figure 6) [30]. The integration of dendrimers into such biphasic systems is a relatively unexplored area. However, a notable example involves PPI dendrimers surface-functionalized with perfluorinated polyethers and encapsulated with Pd nanoparticles, demonstrating potential in the Heck cross-coupling reaction (Scheme 6) [31].



**Figure 6.** Representation of the principle of fluoruous/organic biphasic systems in homogenous catalysis, in thermomorphic behaviour.

**Heck cross-coupling:**

**Scheme 6.** Heck cross-coupling performed in a fluorous biphasic system using as catalyst a PPI dendrimer encapsulating Pd nanoparticles.

In conclusion, the multifaceted applications of dendrimers in bifunctionalization, homogeneous catalysis, and unconventional solvent systems underscore their versatility in nanotechnology and green chemistry. The controlled synthesis of bifunctionalized dendrimers provides reproducibility, while the dendrimer effect enhances catalytic efficiency. The exploration of unconventional solvents and biphasic systems further expands the potential applications of dendrimers in sustainable and efficient catalytic processes.

**Synthesis of dendrimeric catalysts**

The research embarked on a nuanced exploration into the intricate realm of phosphorhydrazone (PPH) dendrimers, shedding light on their meticulous synthesis and detailed functionalization through para-substituted phenols [19]. This journey is marked by a meticulous sequence of reactions initiated from the dendrimer core, ultimately leading to the incorporation of carefully chosen functional groups, with a specific focus on creating precisely asymmetrically disubstituted dendrimeric catalysts. The multifaceted nature of this study unfolds in various stages, each contributing to a comprehensive understanding of the synthesized dendrimers and their potential catalytic applications.

In the early sections of the research, the stage is set by elucidating the meticulous preparation of para-substituted phenols. These phenols serve as crucial precursors for the subsequent functionalization of PPH dendrimers. Two distinct sets of para-substituted phenols are synthesized, with one set designed to act as ligands for future metal introduction [32], and the other set endowed with moieties tailored to impart the desired solubility in non-conventional media. This strategic approach underscores the intent to create versatile dendrimeric catalysts with specific attributes for enhanced functionality.

The study introduces two metal ligands, compounds **2** and **3**, subjected to detailed exploration for their catalytic potential. The catalysts are evaluated in Stille cross-coupling reactions in organic solvents, highlighting their utility and paving the way for broader catalytic applications [32,33]. The careful selection and subsequent synthesis of these ligands underscore the nuanced considerations involved in developing effective dendrimeric catalysts (Figure 7).

An essential facet of the research involves addressing challenges associated with the solubility of dendrimers in non-conventional media. This is achieved through the incorporation of perfluorinated ligands, with a particular emphasis on creating phenols with alkylpolyfluorinated chains. The synthesis journey explores different routes, optimizing reaction conditions to achieve the desired products (Figure 7). This pursuit not only underscores the meticulous nature of the research but also emphasizes the importance of solubility in non-conventional solvents for the envisioned catalytic applications.

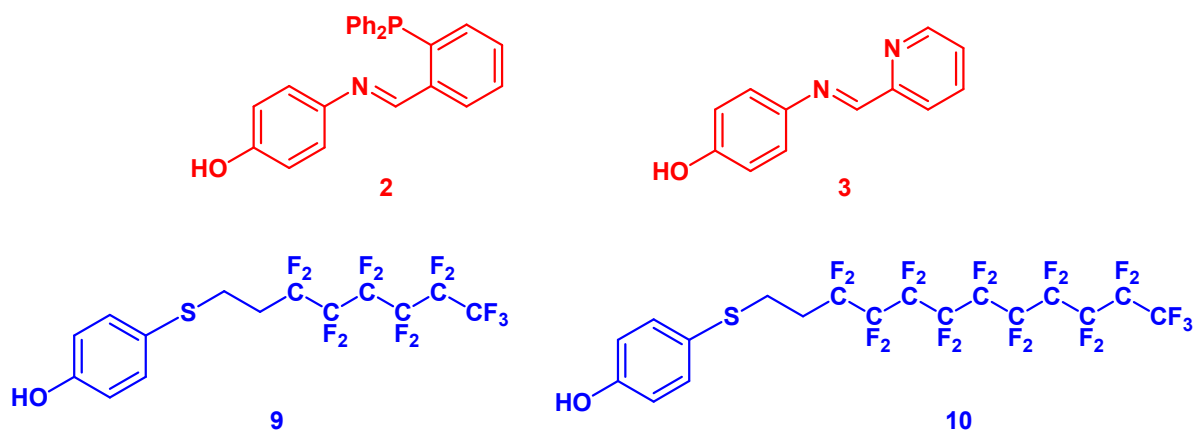


**Figure 7.** Representation of phenolic moieties with bidentate ligand (red), phenolic moieties tailored to tune the solubility (blue).

Moving forward, the study delves into the synthesis of PPH dendrimers, meticulously progressing from the first generation to subsequent generations. Each generation is synthesized through a two-step process, with nucleophilic substitutions and condensation reactions carefully orchestrated to yield dendrimers with distinct structures. The synthesis is tracked through  $^{31}\text{P}$ -NMR spectra, providing a visual representation of dendrimer growth and surface modifications (Figure 8) [19].

The crux of the research lies in the precise functionalization of PPH dendrimers. The endeavour to achieve asymmetric substitution while minimizing di-symmetric substitution is a key challenge addressed in the synthesis. A detailed exploration of reaction conditions, base selection, and sequential substitution strategies results in the triumphant synthesis of precisely asymmetrically disubstituted dendrimers, such as **prc-G1** and **prc-M**. The meticulous efforts to control substitution patterns underscore the fine-tuned nature of dendrimer synthesis (Figure 9) [34].

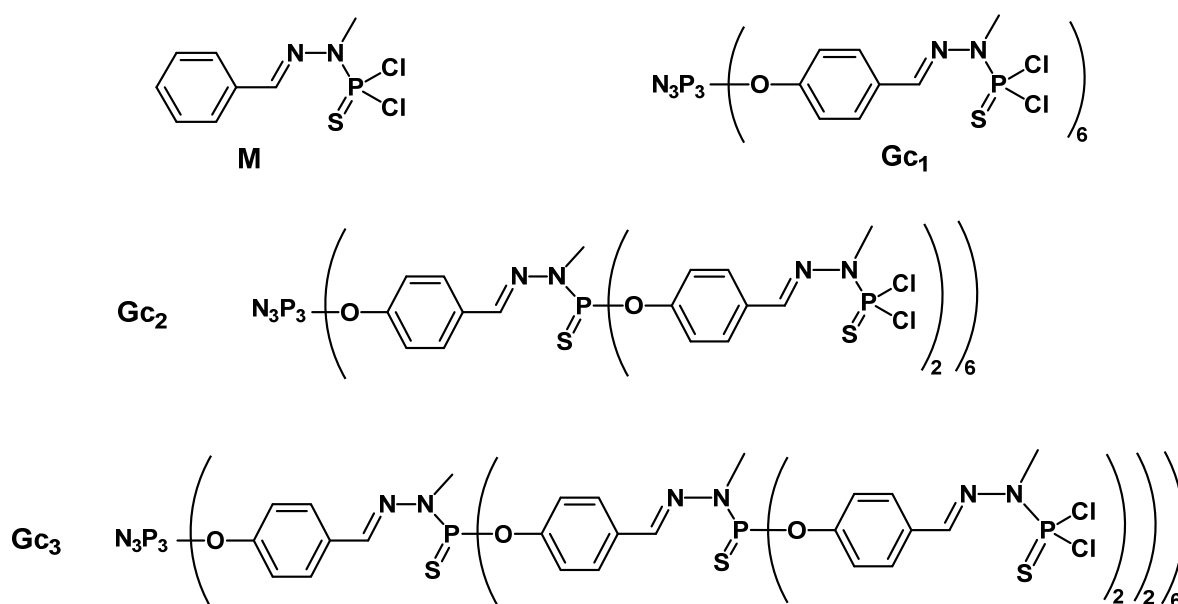


**Figure 8.** Representation of model molecule (*M*) and PPH dendrimers (*Gc<sub>1</sub>*, *Gc<sub>2</sub>* and *Gc<sub>3</sub>*) synthesized.

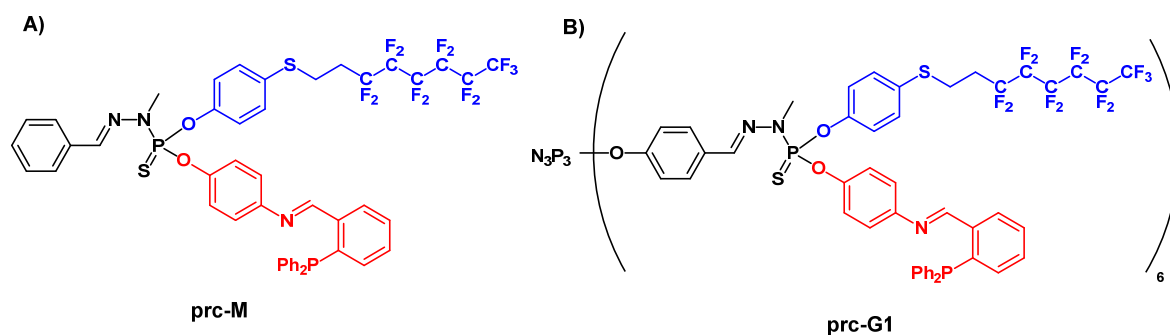


**Figure 9.** Representation of precise substituted products **A) prc-M** and **B) prc-G1**.

Metal complexation, particularly with palladium, emerges as a critical step to enhance stability and reactivity of the synthesized dendrimers. The successful complexation is a testament to the careful design and execution of synthetic methodologies. The resulting metal-complexed dendrimers undergo thorough characterization, encompassing various spectroscopic techniques, ensuring a comprehensive understanding of their structural attributes. Using this methodology where synthesized different precisely substituted PPH dendrimers up to the third generation (Figure 10).

A comparative turn in the research introduces stochastically substituted dendrimers, characterized by a more random distribution of substituents. The stochastic substitution process is detailed, and resultant mixtures undergo metal complexation, mirroring the methodology applied to precisely substituted counterparts. This comparative analysis sets the stage for exploring potential differences in activities between precisely substituted and stochastically substituted dendrimers (Figure 11).

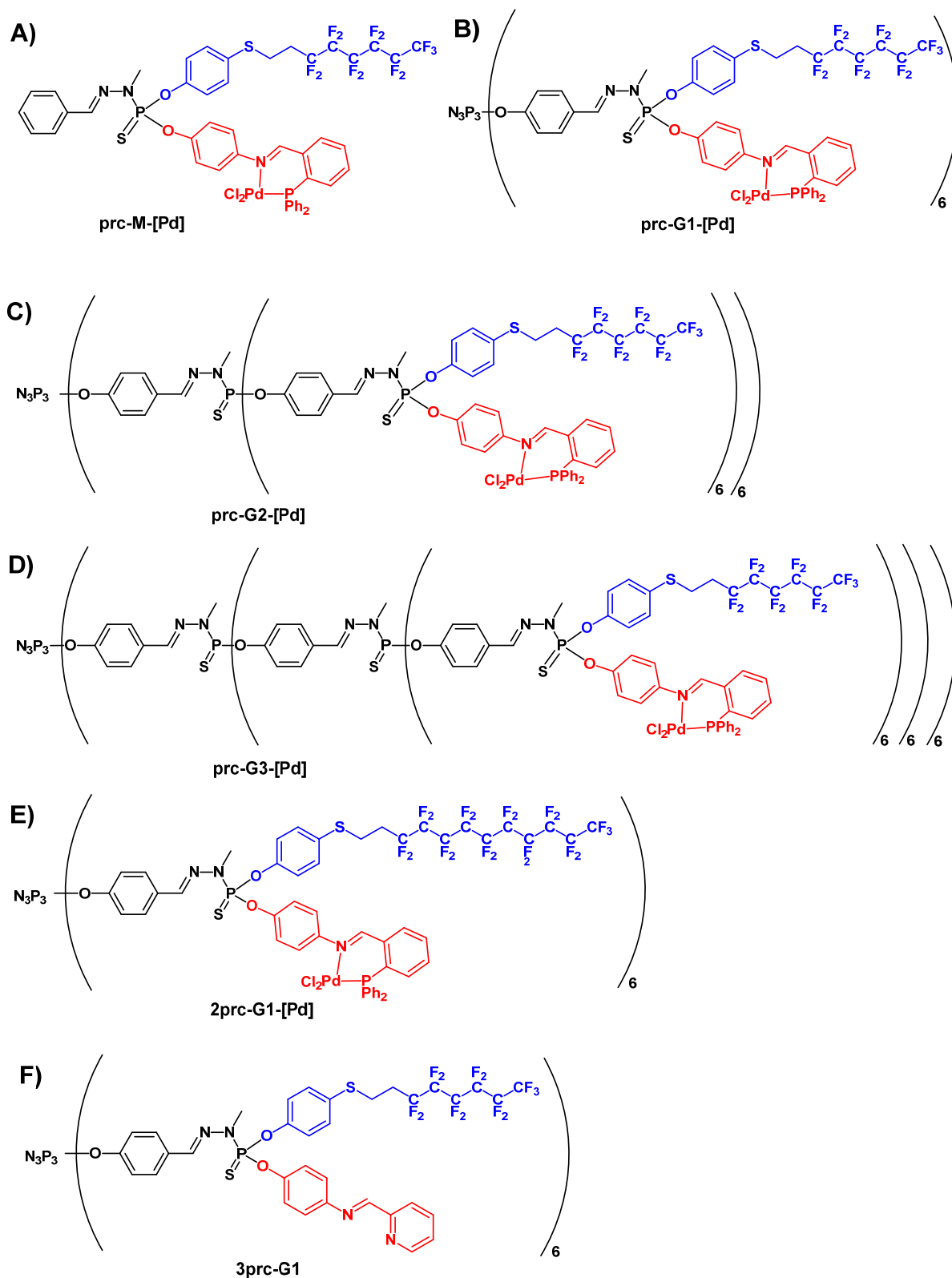


**Figure 10.** Representation of precise substituted products **A) prc-M-[Pd]**, **B) prc-G1-[Pd]**, **C) prc-G2-[Pd]**, **D) prc-G3-[Pd]**, **E) 2prc-G1-[Pd]** and **F) 3prc-G1**.

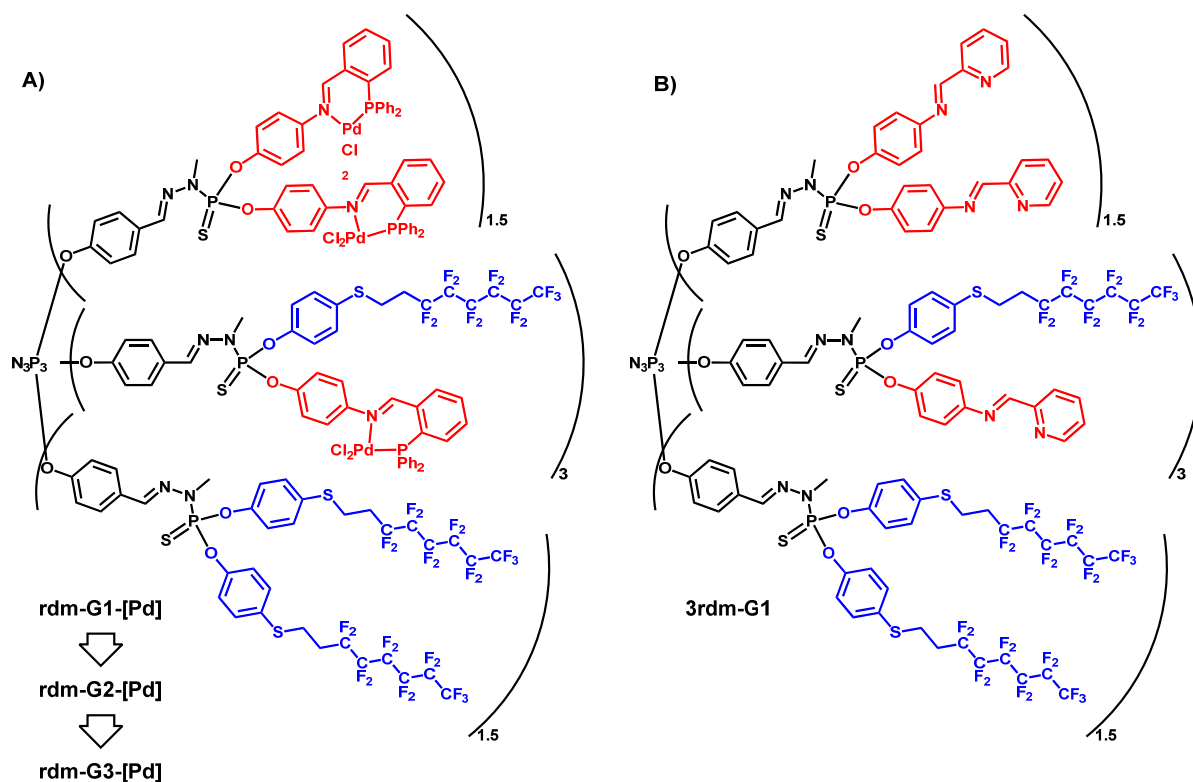


**Figure 11.** Representation of precise substituted products **A) rdm-G1-[Pd]** and **B) 3rdm-G1**.

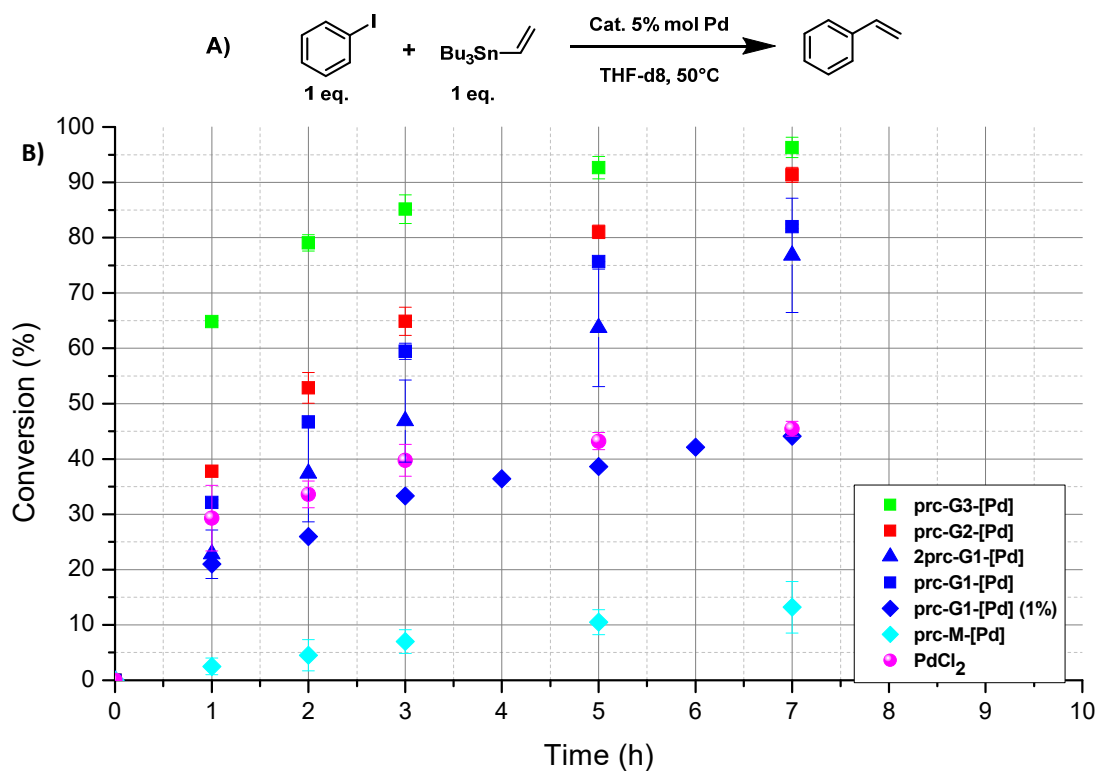
As the research narrative unfolds, the emphasis extends to the successful scaling up of synthesis protocols to gram-scale production. This not only speaks to the reproducibility of the methods but also positions the dendrimers for practical applications in larger quantities. The comprehensive characterization of the synthesized compounds encompasses a range of analytical techniques, including  $^1\text{H-NMR}$ ,  $^{13}\text{C-NMR}$ ,  $^{19}\text{F-NMR}$ ,  $^{31}\text{P-NMR}$ , IR, and melting point determination, ensuring a robust understanding of their chemical attributes.

### Study of catalytic activity

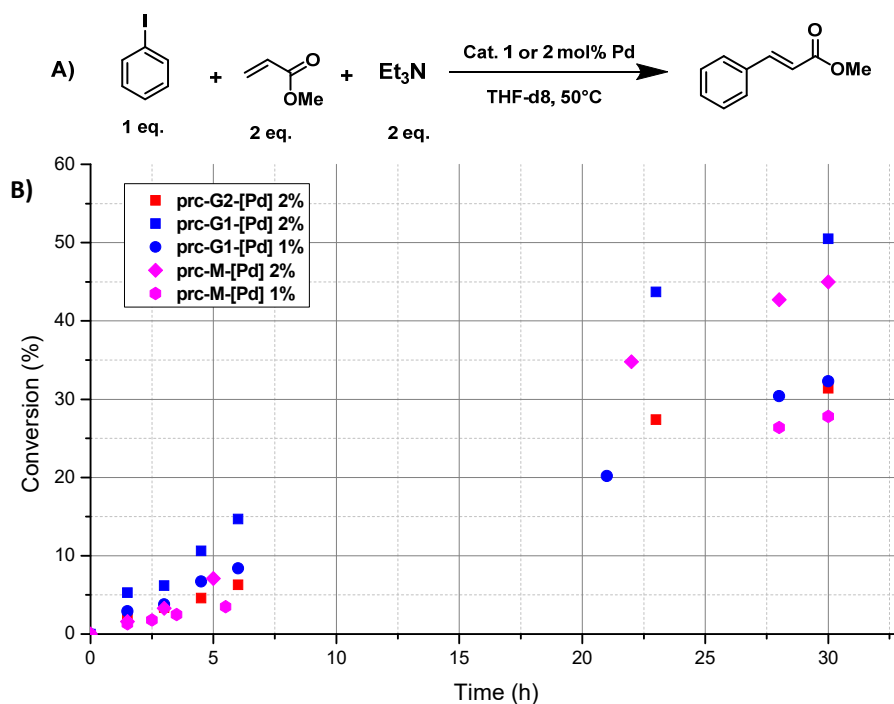
We have used **prc-Gn-[Pd]** for different C-C coupling reactions in organic solvents to demonstrate the activity of the catalyst [32].

- Catalysts **prc-Gn-[Pd]** demonstrated a good activity for the Stille cross-coupling in THF, showing a positive multivalence and generation dendritic effect. We also tried the recycling of the catalyst **prc-G1-[Pd]**, obtaining a 50% drop of the conversion from the second entry, we can attribute this loss of activity to the leaching of palladium and the formation of palladium nanoparticles that probably are less active than the complexed palladium.
- The catalyst **prc-G1-[Pd]** was showing activity for the Heck cross-coupling giving specific stereoselectivity for the trans isomer [31]. The catalyst **prc-G1-[Pd]** was showing a positive multivalence dendritic effect, while the catalyst **prc-G2-[Pd]** showed a negative generation dendritic effect (Scheme 8).





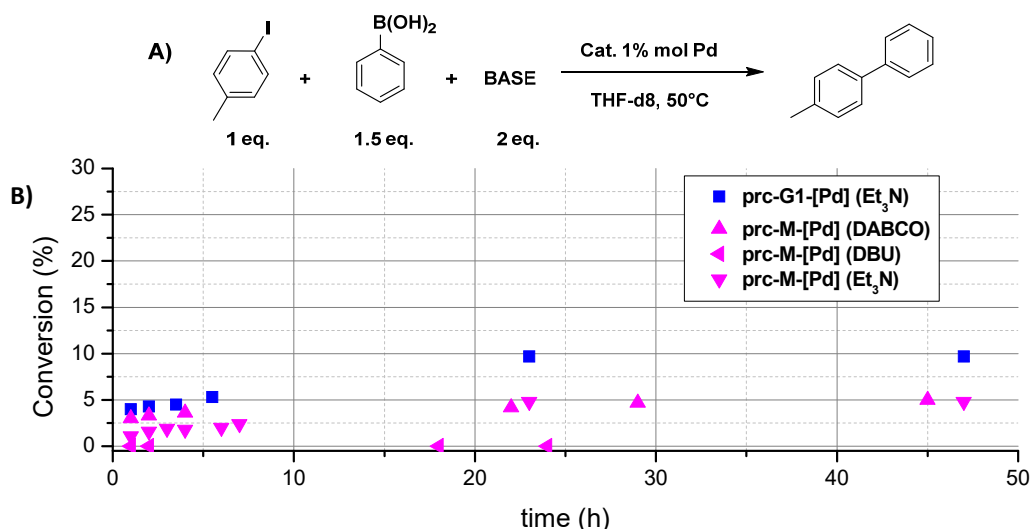
**Scheme 7. A)** Scheme of the Stille cross-coupling reaction; **B)** Graph of the conversion in the Stille cross-coupling under stirring with different catalysts.



**Scheme 8. A)** Scheme of the Heck cross-coupling reaction; **B)** Graph of the conversion in the Heck cross-coupling with different catalysts.

- The model molecule **prc-M-[Pd]** was used to perform the Suzuki coupling showing activity for this reaction using an inorganic base ( $\text{Cs}_2\text{CO}_3$ ) [35]. In order to translate the reaction in non-conventional solvents we needed to perform the reaction using organic bases, in these

conditions **prc-M-[Pd]** and **prc-G1-[Pd]** showed a very low activity for this reaction (Scheme 9).



**Scheme 9.** **A)** Scheme of the Suzuki coupling reaction tested in this chapter section; **B)** graph of the conversion for the Suzuki coupling using different catalysts.

After verifying the activity of the catalyst in organic solvents we have moved to verify the solubility and the activity of our catalysts in non-conventional solvents starting from  $scCO_2$ .

- Surprisingly despite the presence of alkylpolyfluorinated chains on the surface of our dendrimeric catalysts, they were not showing solubility in  $scCO_2$ .
- We have decided to perform catalysis in heterogeneous conditions, optimizing reaction conditions for the Stille cross-coupling reaction in  $scCO_2$  in a little reactor (6 mL) without the stirring. We obtained that the optimal amount of catalyst was 5%, and that the optimal pressure was 100 bars (Table 1).

**Table 1.** Table showing the conversion of the Stille cross-coupling reaction in 6 ml  $scCO_2$  reactor following conditions in Scheme 4.6.

<b>Cat.</b>	<b>Pd mol%</b>	<b>Time (h)</b>	<b>Conv. (%)<sup>(a)</sup></b>
<b>prc-M-[Pd]</b>	5	4	0
	5	22	0
<b>prc-G1-[Pd]</b>	5	4	43
	5	22	43
	10	4	39
	10	22	39

<sup>(a)</sup> Determined by <sup>1</sup>H-NMR (CDCl<sub>3</sub>, 400 MHz).

- We moved to perform the reaction in a big reactor (29 mL) with the mechanical stirring, where we performed the Stille cross-coupling reaction using optimal conditions previously found. We have observed a good activity of catalysts **prc-Gn-[Pd]** in this reaction, showing a positive multivalence and generation dendritic effect from the first to the third generation (Table 2).
- We have tried to recover the catalyst **prc-G1-[Pd]**, but for the geometry of the reactor used it was not possible to perform the purification of the catalyst *in situ*, while after the washing and purification we have experienced a partial recovery of the catalyst.
- We have also performed the Heck cross-coupling in *scCO*<sub>2</sub> using as catalyst **prc-G1-[Pd]** obtaining a low conversion.

**Table 2.** Table showing conversion of the Stille cross-coupling reaction in 29 ml *scCO*<sub>2</sub> reactor following conditions in Scheme 4.6.

<i>Cat.</i>	<i>Pd mol%</i>	<i>Time (h)</i>	<i>Conv. (%)<sup>(a)</sup></i>
<b><i>prc-G1-[Pd]</i></b>	5	4	39
	5	22	82
	1	4	15
	1	22	36
<b><i>prc-G1-[Pd]<sup>(b)</sup></i></b>	5	22	51
<b><i>2prc-G1-[Pd]</i></b>	5	4	18
	5	22	25
<b><i>prc-G2-[Pd]</i></b>	5	4	66
<b><i>prc-G3-[Pd]</i></b>	5	4	68

<sup>(a)</sup> Determined by <sup>1</sup>H-NMR (CDCl<sub>3</sub>, 400 MHz). <sup>(b)</sup> Reaction performed using 1/10 of concentrations of all reagents.

We have also verified the solubility of our catalyst **prc-G1-[Pd]** in perfluorinated solvents in order to perform catalysis in biphasic fluoruous/organic systems.

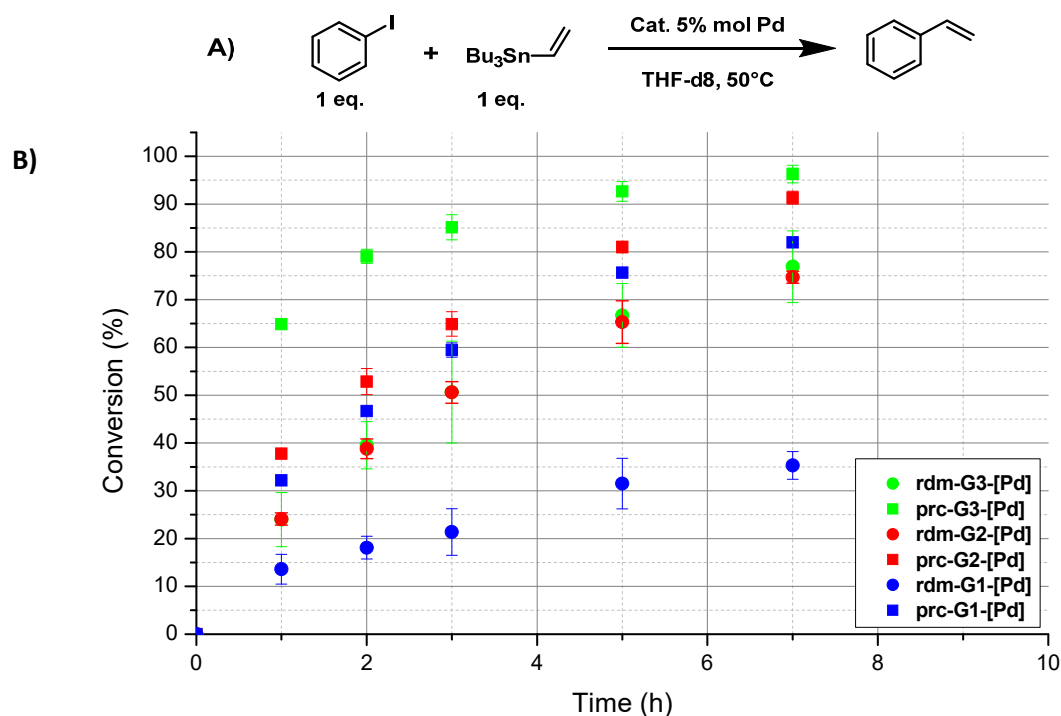
- We have tried to solubilize **prc-G1-[Pd]** in two perfluorinated solvents (perfluorodecalin and perfluoromethylcyclohexane), our catalyst resulted to be slightly soluble in perfluorodecaline and partially soluble in perfluoromethylcyclohexane.
- Despite the partial solubility of **prc-G1-[Pd]** in perfluoromethylcyclohexane we have decided to perform the Heck cross-coupling in heterogeneous conditions, obtaining a similar result obtained in organic solvents, but it was not possible to recycle and to proceed with the reuse of the catalyst.

### Precise versus stochastically functionalized PPH dendrimers in catalysis

In the last part of this work we have focused our attention on the comparison of the activity between precisely (**prc-Gn-[Pd]**) and stochastically substituted (**rdm-Gn-[Pd]**) phosphorus dendrimeric catalysts.

- Catalysts **prc-Gn-[Pd]** and **rdm-Gn-[Pd]** were used for the Sille cross-coupling reaction in organic solvent. In stochastically substituted catalysts (**rdm-Gn-[Pd]**) we observed a positive

generation dendrimeric effect, going from the first to the third generation, as we observed for precisely substituted catalysts (**prc-Gn-[Pd]**). While we observed for all generations a higher activity of **prc-Gn-[Pd]** compared to the activity of **rdm-Gn-[Pd]** (Scheme 10).



**Scheme 10.** **A)** Scheme of the Stille cross-coupling reaction; **B)** Graph representing results of the Stille cross-coupling using different catalysts.

- Catalysts **3prc-G1** and **3rdm-G1** were complexed *in situ* with CuI and used for the C-N coupling [33]. Both showed a higher activity compared to the CuI alone. For this reaction the stochastically substituted catalyst (**3rdm-G1**) showed a higher activity compared to the precisely substituted catalyst (**3prc-G1**) (Scheme 11). We speculate that this behaviour may be explained by two catalytical sites in the vicinity working in a cooperative way, but more research is required to confirm this.

**Scheme 11.**

Cat./Ligand	Time (h)	Conv. (%) <sup>(a)</sup>
CuI	20	33
<b>3prc-G1</b>	20	46
<b>3rdm-G1</b>	20	59

**Scheme 11.** Scheme of the C-N coupling reaction and table of results of the C-N coupling in biphasic fluoruous/organic system. <sup>(a)</sup> Determined by <sup>1</sup>H-NMR (CDCl<sub>3</sub>, 400 MHz).



- [23] A. M. Caminade, A. Ouali, R. Laurent, C. O. Turrin, J. P. Majoral, *Chem. Soc. Rev.*, **2015**, *44*, 3890–3899. DOI: [10.1039/C4CS00261J](https://doi.org/10.1039/C4CS00261J).
- [24] P. Heegaard, U. Boas, D. Otzen, *Macromol. Biosci.*, **2007**, *7*, 1047–1059. DOI: [10.1002/mabi.200700051](https://doi.org/10.1002/mabi.200700051).
- [25] M. Zloh, T. Barata, *Exp. Op. Drug*, **2020**, *15*, 1015–1024. DOI: [10.1080/17460441.2020.1769597](https://doi.org/10.1080/17460441.2020.1769597).
- [26] A. M. Caminade, R. Laurent, A. Ouali, J. P. Majoral, *Inorg. Chim. Acta*, **2014**, *409*, 68–88. DOI: [10.1016/j.ica.2013.06.022](https://doi.org/10.1016/j.ica.2013.06.022).
- [27] A. M. Caminade, R. Laurent, *Coord. Chem. Rev.*, **2019**, *389*, 59–72. DOI: [10.1016/j.ccr.2019.03.007](https://doi.org/10.1016/j.ccr.2019.03.007).
- [28] R. W. J. Scott, O. M. Wilson, R. M. Crooks, *J. Phys. Chem.*, **2005**, *109*, 692–704. DOI: [10.1021/jp0469665](https://doi.org/10.1021/jp0469665).
- [29] L. K. Yeung, C. T. Lee, K. P. Johnston, R. M. Crooks, *Chem. Comm.*, **2001**, 2290–2291. DOI: [10.1039/B106594G](https://doi.org/10.1039/B106594G).
- [30] I. T. Horvath, J. Rabai, *Science*, **1994**, *266*, 72–75. DOI: [10.1126/science.266.5182.72](https://doi.org/10.1126/science.266.5182.72).
- [31] L. K. Yeung, R. M. Crooks, *Nano Letters*, **2001**, *1*, 14–17. DOI: [10.1021/nl0001860](https://doi.org/10.1021/nl0001860).
- [32] M. Koprowski, R. M. Sebastián, V. Maraval, M. Zablocka, V. Cadierno, B. Donnadieu, A. Igau, A. M. Caminade, J. P. Majoral, *Organometallics*, **2002**, *21*, 4680–4687. DOI: [10.1021/om011076m](https://doi.org/10.1021/om011076m).
- [33] A. Ouali, R. Laurent, A. M. Caminade, J. P. Majoral, M. Taillefer, *J. Am. Chem. Soc.*, **2006**, *128*, 15990–15991. DOI: [10.1021/ja066505s](https://doi.org/10.1021/ja066505s).
- [34] N. El Brahmi, S. El Kazzouli, S. Mignani, R. Laurent, S. Ladeira, A. M. Caminade, M. Bousmina, J. P. Majoral, *Tetrahedron*, **2017**, *73*, 1331–1341. DOI: [10.1016/j.tet.2017.01.044](https://doi.org/10.1016/j.tet.2017.01.044).
- [35] H. Chiririwa, N. Freeman, E. Muzenda, A. J. Muller, *Trans. Met. Chem.*, **2013**, *38*, 393–399. DOI: [10.1007/s11243-013-9703-y](https://doi.org/10.1007/s11243-013-9703-y).



**Aswin CHANDRAN**

**ESR14**

**Thesis co-directors**

Dr. Mary Grellier

Laboratoire de Chimie de Coordination, Toulouse, France

Prof. Jason Lynam

Dr. John Slattery

University of York, York, United Kingdom

**Thesis defense**

Laboratoire de Chimie de Coordination, 13 December 2023





## Coordination of Si–H and Ge–H Bonds to Ruthenium Metal Centres: Structure, Reactivity and Catalytic Applications

### Introduction

This thesis discusses the coordination chemistry and reactivity of ruthenium complexes with silicon and germanium hydrides. Gaining fundamental insights into new reactivities of E–H bonds (E = Si, Ge) to transition metals and coordination modes of these hydrides with transition metals is crucial for developing new selective catalytic systems. This thesis focuses on elucidating the mechanism governing the activation of Si–H and Ge–H bonds at the ruthenium metal centre.

The first part provides a brief introduction to the importance of investigating the coordination of silicon and germanium with transition metals. It focuses on the different coordination modes of silicon and germanium at transition metal centres, including  $\sigma$ -complexes and oxidative addition adducts.

Among all the elements in the periodic table, transition metals play the most significant role in homogenous catalysis due to their unique characteristics. The ability to change their formal oxidation state and coordinate a wide range of substrates leading to various transition metal coordination complexes, providing an alternate reaction pathway with lower activation energy makes them the best candidates for very efficient and selective catalysts for numerous chemical reactions [1]. These catalytic processes enabled the synthesis of many chemical compounds, materials, and polymers.

Silicon and germanium compounds are an important class of organic compounds with a wide range of applications in synthesis leading to products ranging from things we handle in a day-to-day life at household to spacecrafts in the lower earth orbitals [2-6].

Organosilicon compounds have found widespread applications in materials science, synthetic chemistry, and pharmaceutical synthesis and some of the important applications include the following. Organosilanes and siloxanes are commonly used to modulate the hydrophobicity and surface properties of materials [7,8]. Side-chain liquid-crystalline siloxanes are utilized in the manufacturing of electronic device displays [9]. Organofunctionalized silicates can be used to immobilize peptides and as supports for metal complex catalysts [10,11]. Organosilanes serve as coupling agents between organic polymers and silicate materials, leading to applications in dental composites [12] and adhesives [13]. They are also used as precursors for silicon carbide ceramics [14]. In synthetic chemistry, organosilicon reagents enable mild, selective, and functional group-tolerant transformations. They are widely used as protective groups in organic synthesis [15]. Additionally, they are also used in stereospecific oxidations and carbon-carbon bond formations like cross-couplings, olefinations, and allylations [16-18].

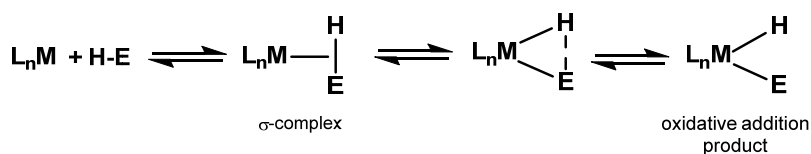
While organogermanium chemistry and applications have been less explored compared to silicon [5,19,20], germanium compounds have found utility in medicinal and catalytic roles. Certain germanium compounds exhibit promising bioactivities or medicinal properties. [21] Germylated steroids have displayed potential as antitumor and antiviral agents [22]. The organogermanium compounds, Asaigermanium and propagermanium have been reported as pharmaceutical drugs for use in Japan [21]. Beyond medicine, organogermanes also hold promise as catalysts in the emerging trend of main group based catalysts. Germanium compounds have been studied as catalysts for the polymerization of lactide monomers [23]. Additionally, heavier Ge(II) species can serve as catalysts [24] for cyanosilylation [25] and hydroboration of carbonyl compounds [26], hydroboration of CO<sub>2</sub> [27],

oxidative coupling catalysts for silane functionalization using aldehydes [28]. They are also good ligands to various transition metals [29].

An efficient transition metal-based catalyst for synthesising useful silicon and germanium compounds at ambient reaction conditions is highly desirable. A transition metal based catalyst can selectively activate targeted bonds of the substrates and form new bonds between them leading to desired products with very high efficiency. Hydrometallation reaction in which a hydrogen-silicon/germanium bond is added to C–X multiple bonds such as alkynes, alkenes, and nitriles is one of the best methods to synthesise these organosilicon/germanium compounds using simpler hydrosilanes and germanes [30]. The selective monohydrometallation reaction of hydrosilanes or hydrogermanes with more than one hydrogen can lead to the synthesis of organosilicon/germanium compounds of a higher value that still have at least one Si–H or Ge–H bond, which can be further used as building blocks in synthetic chemistry. Understanding the bonding between the E–H bond of  $R_2EH_2$  (E = Si, Ge, R = alkyl, aryl) and the transition metal centre is essential for developing a better homogenous catalyst for hydrometallation reactions.

The second part details an in-depth spectroscopic and structural analysis of the coordination and activation of Si–H bonds of diphenylsilane at a ruthenium *bis*-dihydrogen dihydride complex,  $[RuH_2(H_2)_2(PCy_3)_2]$  (**1**). A new reactivity leads to the formation of new ruthenium  $\sigma$ -silane complexes such as  $[Ru(H)_2(\eta^2-H_2)(\eta^2-HSiHPh_2)(PCy_3)_2]$  (**2**), followed by  $[Ru(H)_2(\eta^3-H_2SiPh_2)(PCy_3)_2]$  (**3**) by the sequential displacement of the  $H_2$  ligands of the precursor complex is discussed. This reveals unique bonding interactions and provides greater clarity on secondary silane coordination to the ruthenium metal centre.

Hydrosilanes, compounds having a silicon-hydrogen bond, can react with transition metals leading to the formation of different transition metal-silicon products [31]. The interaction of the Si–H bond with a coordinately unsaturated transition metal can vary from weak interaction to complete oxidative addition. The weak interaction or  $\sigma$ -Si–H coordination can be represented as a three-centred two-electron bond between the transition metal, silicon, and hydrogen atoms. The complete oxidative addition of the Si–H bond to the metal centre can lead the transition metal to classical bonding interactions with the hydrogen and the silicon. The type of coordination can be based on the degree of activation of the Si–H bond at the transition metal centre. The Si–H bond activation can be represented as a continuum between the  $\sigma$ -Si–H complex and the oxidative addition product [32]. Hence the formation of  $\sigma$ -Si–H complex is considered as a result of incomplete Si–H bond activation by an electrophilic metal centre [33]. They are usually represented as shown in Scheme 68.



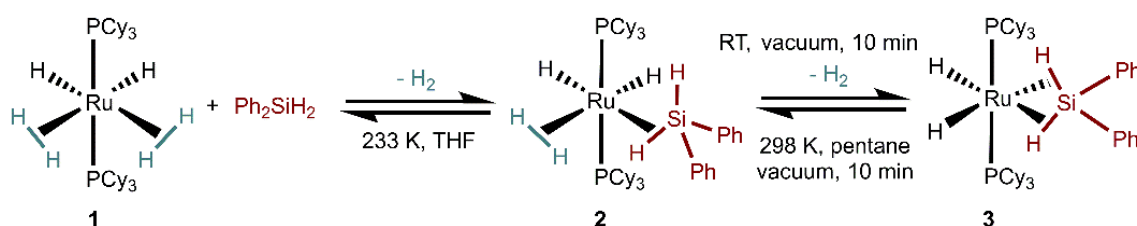
**Scheme 68.** E–H bond activation at transition metal centre; a continuum between the  $\sigma$ -complex and the oxidative addition product.

Compared to the most widely explored  $\sigma$ -dihydrogen ligand,  $\sigma$ -silane complexes exhibit an asymmetry in electronegativity, size, and coordination mode, which makes the Si–H bond more basic than the H–H bond. The silane  $\sigma$ -coordination can be explained by the  $\sigma$ -donor property of the Si–H bond and, at the same time, its better ability to accept  $\pi$  electrons to the  $\sigma^*(Si-H)$  orbital. Hence the

silane  $\sigma$ -coordination is more favoured when compared to the  $\sigma$ -dihydrogen analogue [33]. This has enabled the synthesis of various  $\sigma$ -silane complexes from dihydrogen complexes [34,35].

The coordination of silicon-hydrogen bonds to ruthenium metal centre is interesting because of the silicon coordinated complexes has already proved its potential to steer various catalytic hydrosilylation reactions. The ruthenium poly hydride complex  $[\text{RuH}_2(\text{H}_2)_2(\text{PCy}_3)_2]$  (**1**) being a good candidate complex that has marked its remarkable ability to activate various S-H bonds at ambient conditions, was chosen as a candidate to study the coordination of secondary silanes to ruthenium metal centre. Previous studies on the coordination of secondary and tertiary silanes led to the redistribution reaction of silane and the in-depth knowledge on the coordination of silicon compounds with more than one hydride to ruthenium complex **1** have been lacking up to now. In this study, an investigation of the reaction between diphenylsilane and the ruthenium complex  $[\text{RuH}_2(\text{H}_2)_2(\text{PCy}_3)_2]$  under controlled, low temperature conditions has been carried out. The reaction of the ruthenium *bis*-dihydrogen complex **1** with diphenylsilane was investigated using NMR spectroscopic monitoring, X-ray crystallography and DFT calculations. The step-by-step pathway for silane coordination and activation has been studied using variable temperature NMR. The reaction was found to coordinate silane Si-H bonds to the ruthenium metal centre via  $\sigma$ -bonds. It led to the formation of new ruthenium  $\sigma$ -silane complexes such as  $[\text{Ru}(\text{H})_2(\eta^2\text{-H}_2)(\eta^2\text{-HSiHPh}_2)(\text{PCy}_3)_2]$  (**2**), followed by  $[\text{Ru}(\text{H})_2(\eta^3\text{-H}_2\text{SiPh}_2)(\text{PCy}_3)_2]$  (**3**) by the sequential displacement of the  $\text{H}_2$  ligands of the precursor complex.

The addition of diphenylsilane to a THF solution of **1** at 233 K, followed by slow warming to room temperature, resulted in the formation of  $\sigma$ -Si-H complexes  $[\text{Ru}(\text{H})_2(\eta^2\text{-H}_2)(\eta^2\text{-HSiHPh}_2)(\text{PCy}_3)_2]$ , **2**, and  $[\text{Ru}(\text{H})_2(\eta^3\text{-H}_2\text{SiPh}_2)(\text{PCy}_3)_2]$ , **3** (Scheme 69).



**Scheme 69.** Reversible coordination of  $\text{Ph}_2\text{SiH}_2$  to complex **1** to form complexes **2** and **3**.

The molecular structures of **2** and **3** were established by detailed NMR spectroscopy experiments. Complex **3** was subsequently isolated and its structure was also confirmed by single crystal X-ray diffraction. Crystals of **3** suitable for study by single crystal X-ray diffraction were obtained by the slow cooling of a pentane-THF solution of **3** to 233 K. The ORTEP view of the molecular structure obtained by X-ray diffraction analysis of **3** is shown in Figure 1.

DFT calculations assisted to confirm the spectroscopic and X-ray elucidated molecular structures. The new reactivities and description of binding modes observed have expanded current knowledge of secondary silane interactions with ruthenium. It is important to note that the stepwise dehydrogenation of the dihydrogen ligands with the coordination of each of the Si-H bond can be utilized for selective catalytic reactions. The fundamental insights gained from this reactivity and coordination study can guide future development of silane coordinated transition metal systems for the development of selective catalysts.

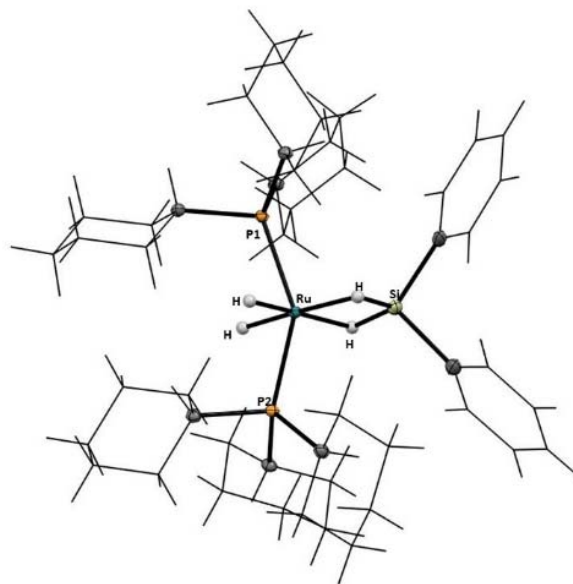


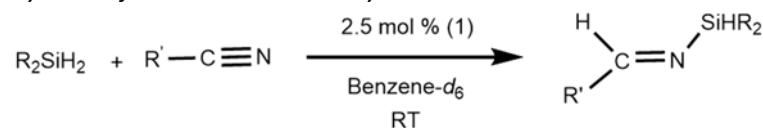
**Figure 30.** X-ray molecular structure of complex **3**,  $[\text{RuH}_2(\eta^2\text{-H}_2\text{SiPh}_2)(\text{PCy}_3)_2]$  drawn at 50% probability as ellipsoids ( $\text{PCy}_3$  and phenyl groups are shown in wireframe for clarity).

The third part demonstrates the efficacy of the ruthenium *bis*-dihydrogen dihydride complex for selective monohydrosilylation of nitriles to *N*-silylimines. A range of nitriles and silanes are used in the catalytic scope study, and a close look at reactivities between silane, nitrile, and ruthenium centres is discussed. The identification and structural characterisation of a new ruthenium  $\sigma$ -*N*-silylimine complex (**4**), along with a possible new mechanism involving this complex, is described. Mechanistic investigations provide critical insights into the activation of the Si–H and  $\text{C}\equiv\text{N}$  bonds.

The mechanism and role of ruthenium  $\sigma$ -complexes in catalytic hydrosilylation of nitriles were evaluated, leading to the identification of complex **1** as a highly efficient catalyst for monohydrosilylation of nitriles using secondary silanes. This reaction exhibited exclusive selectivity for the formation of *N*-silylimines. A comprehensive understanding of the interactions between the nitrile group and the silicon and hydrogen atoms of the silane was developed.

Catalytic hydrosilylation of nitriles with a series of secondary silanes and nitriles was observed with 2.5 mol% of **1** (Table 9). The results showed that the catalyst was found to be highly active and efficient, achieving near-complete conversion and excellent yield for the desired reaction at room temperature. The complete conversion was typically observed in 15 minutes with a maximum turnover frequency (TOF) of 400 and an impressive 99% yield (Table 9, entry 3), highlighting the extraordinary effectiveness of **1** in catalytic hydrosilylation reaction.

The detailed mechanistic and spectroscopic data show how the initial addition of the nitrile to the complex occurs at silicon rather than ruthenium and provide pathways for C–H and N–Si bond formation, leading to the selective formation of *N*-silylimines. The direct detection of *N*-silylimine bound to the ruthenium also demonstrates the synergy between the transition metal and main centres in the formation of the new Si–N and C–H bonds. To gain a deeper understanding of the reaction mechanism, selected stoichiometric reactions were conducted under controlled temperature conditions, and key ruthenium  $\sigma$ -complex involved in the catalytic reaction was identified.

**Table 9.** Catalytic hydrosilylation of nitriles with secondary silanes.<sup>a</sup>

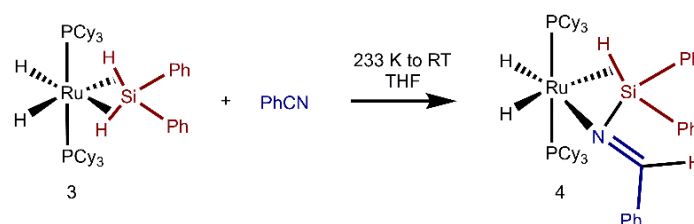
Entry	Nitrile	Silane	TON	TOF [h <sup>-1</sup> ] <sup>[b]</sup>	Conversion <sup>[c]</sup> (min)	Yield <sup>[d]</sup> (%)	Product
1	PhCN	Ph <sub>2</sub> SiH <sub>2</sub>	40	185 (100%)	>99% (13)	96%	
2	PhCN	Et <sub>2</sub> SiH <sub>2</sub>	40	171 (100%)	>99% (14)	97%	
3	PhCN	PhMeSiH <sub>2</sub>	40	400 (100%)	>99% (6)	87%	
4		Ph <sub>2</sub> SiH <sub>2</sub>	40	240 (100%)	>99% (10)	89%	
5		Ph <sub>2</sub> SiH <sub>2</sub>	40	240 (100%)	>99% (10)	96%	
6		Ph <sub>2</sub> SiH <sub>2</sub>	38	53 (44.5 %)	>99% (150)	85%	
7		Ph <sub>2</sub> SiH <sub>2</sub>	40	200 (100%)	>99% (12)	86%	
8		Ph <sub>2</sub> SiH <sub>2</sub>	40	160 (100%)	>99% (15)	99%	
9		Ph <sub>2</sub> SiH <sub>2</sub>	40	160 (100%)	>99% (15)	89%	
10	PhCN	2 Ph <sub>2</sub> SiH <sub>2</sub>	40	160 (100%)	>99% (15)	100%	No further reaction after heating 60 °C for 1 day.
11	CH <sub>3</sub> CN	Ph <sub>2</sub> SiH <sub>2</sub>	0	0	0	0	No catalytic reaction

[a] General procedure – 2.5 mol % of [RuH<sub>2</sub>(η<sup>2</sup>-H<sub>2</sub>)<sub>2</sub>(PCy<sub>3</sub>)<sub>2</sub>] was added to a solution of nitrile and silane in C<sub>6</sub>D<sub>6</sub>.

[b] Calculated at the conversion shown in parentheses. [c] Calculated from <sup>1</sup>H NMR data. [d] Yield is determined by <sup>1</sup>H NMR.

The reaction of the ruthenium *bis*- $\sigma$ -Si-H complex **3** with benzonitrile gives a quantitative formation of a ruthenium  $\sigma$ -*N*-silylimine complex **4**. Complex **4** stands as the first example for the direct evidence of *N*-silylimine coordinating to ruthenium metal centre. The molecular structure of **4** were established by detailed NMR spectroscopy experiments, and the compound was isolated and characterised by X-ray diffraction.

The stoichiometric reaction of ruthenium *bis*  $\sigma$ -Si-H complex **3** with an equivalent of benzonitrile was thoroughly examined, with a specific emphasis on the potential for the addition of the activated Si-H bond to the benzonitrile. This reaction was of great interest due to the prospect of new Si-N and C-H bond formation. It was found that the reaction led to the formation of a new ruthenium complex, designated as **4**, which contains an *N*-silylimine ligand resulting from the selective addition of only one Si-H bond of diphenylsilane to the nitrile group (Scheme 70).



**Scheme 70.** Reactivity of complex **3** with benzonitrile.

The molecular structure of **4** in solid state was determined by single crystal X-ray diffraction analysis (Figure 31), which demonstrated the unique coordination mode of *N*-silylimine to the ruthenium metal centre. Specifically, the *N*-silylimine moiety coordinates to the ruthenium atom via an  $\eta^2$ -Si-H bond and the nitrogen atom, resulting in a pseudo-octahedral environment and is located in a plane along with Si, N, and hydrogen atoms.

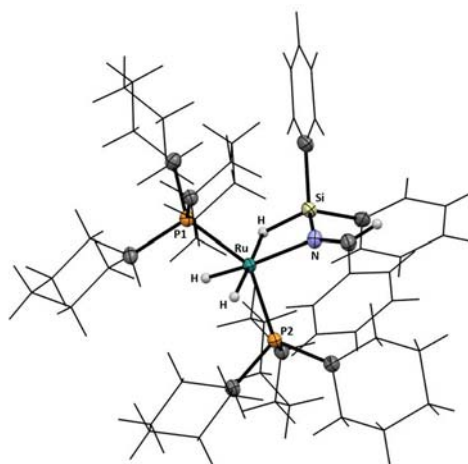
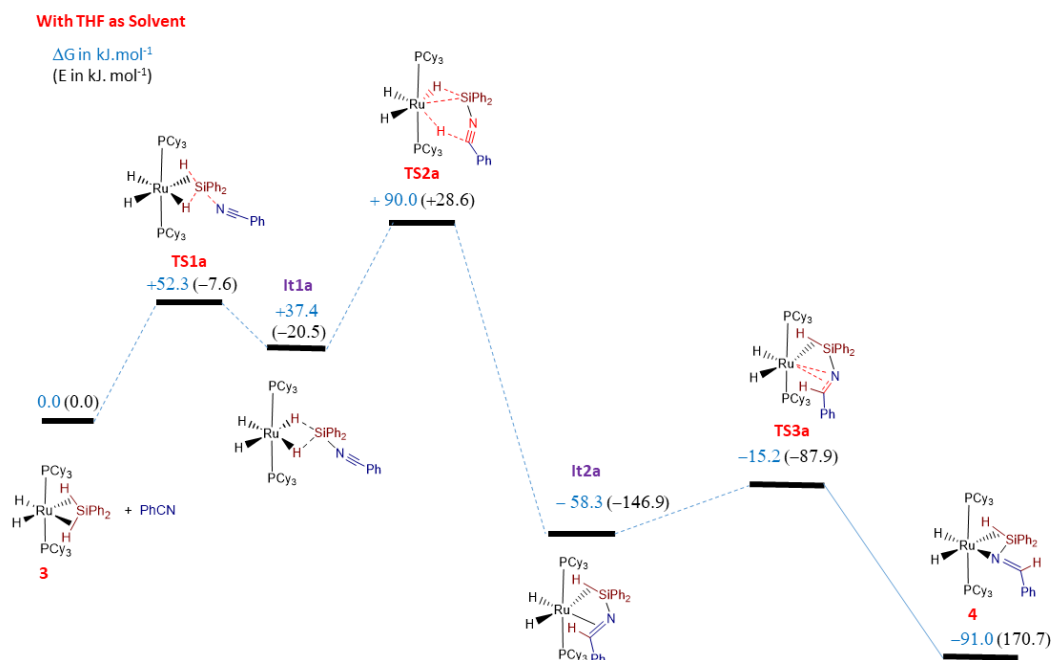


**Figure 31.** X-ray molecular structure of complex **4** [ $\text{RuH}_2(\eta^2\text{-HSiPh}_2\text{NCHPh}(\text{PCy}_3)_2)$ ] drawn at 50% probability as ellipsoids ( $\text{PCy}_3$  and phenyl groups are shown in wireframe for clarity).

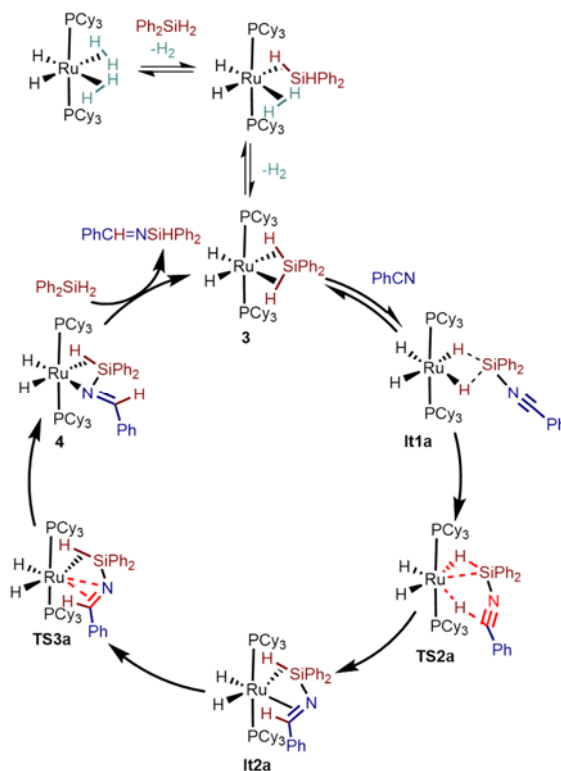
Complex **4** features a unique  $\sigma$ -Si-H interaction alongside the nitrogen atom of the imine coordination to the ruthenium centre. The successful isolation of complexes **3** and **4** and the demonstration of their active participation in catalysis helped to understand the mechanism of the catalytic reaction better. Two possible mechanisms were studied using DFT calculations, and along with the experimental pieces of evidence, a favourable mechanism developed using DFT is proposed. The ruthenium-based system of  $\sigma$ -Si-H complexes has proved its competence for the challenging

transformation of nitriles to an imine level selectively but also enables low-energy pathways for Si–H bond cleavage and C–H bond formation.



**Scheme 71.** DFT calculated the steps of the catalytic hydrosilylation process at 298K, involving the nitrile coordination to the silicon centre.

Based on the experimental and DFT observations, we propose an overall representation of the pathway of the catalytic reaction, which involves the coordination of the diphenylsilane before the coordination of the nitrile and, thus, the catalytic cycle (Scheme 72).

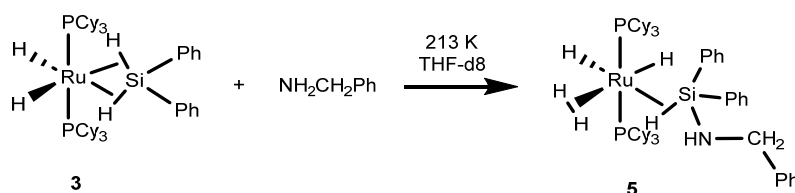


**Scheme 72.** Representation of the overall steps of the catalytic hydrosilylation process.

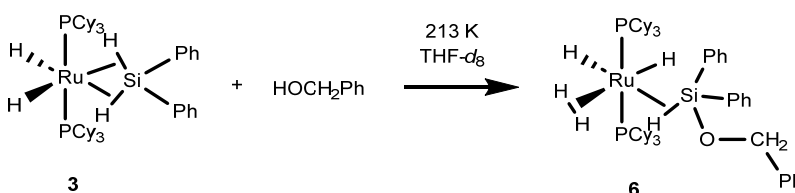


The fourth part examines the reactivity of the ruthenium *bis*- $\sigma$ -silane complex (**3**) with amines and alcohols. The new reactivity study of complex **3** with benzylamine and benzylalcohol disclosed new ruthenium amino (**5**) and alkoxy (**6**) functionalised silane complexes. The role of these reactivity studies that led to a highly efficient ruthenium-catalysed dehydrogenative coupling reaction of silanes with amine and alcohol is explained.

In summary, this work has conducted an in-depth investigation into the reactivity of the silane coordinated complex **3** with benzylamine and benzylalcohol under controlled reaction conditions. Through extensive NMR spectroscopic analysis at low temperature conditions and structural elucidation, the coordination of these substrates to the silicon centre has been explained. This has provided a better mechanistic insight into the dehydrogenative coupling reaction of silane with amine or alcohol. The molecular structures of new ruthenium complexes **5** and **6** formed after the reaction with amine and alcohol have been characterized using multinuclear 1D and 2D NMR spectroscopic techniques.

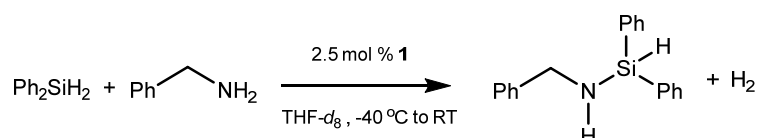


**Scheme 73.** Reactivity of benzylamine with  $[Ru(H)_2(\eta^3\text{-}H_2SiPh_2)(PCy_3)_2]$  to form new aminosilane coordinated ruthenium complex.

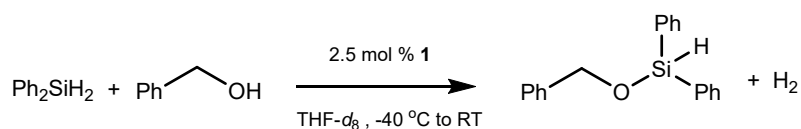


**Scheme 74.** Reactivity of benzylalcohol with  $[Ru(H)_2(\eta^3\text{-}H_2SiPh_2)(PCy_3)_2]$  to form new alkoxy silane coordinated ruthenium complex.

Leveraging the understanding of this new fundamental reactivity, the  $[Ru(H)_2(H_2)_2(PCy_3)_2]$  complex has been proved to be an efficient pre-catalyst for the dehydrogenative coupling of silanes with amines and alcohols. The catalytic products have been thoroughly characterized by NMR spectroscopy, confirming the formation of new Si–N and Si–O bonds. By systematically investigating the stepwise reactivity of silanes, amines, and alcohols at the ruthenium centre, more insights into the mechanism of the catalytic dehydrogenative coupling reaction was developed which helped to propose a mechanism for this catalytic reaction. Overall, this study has opened a new strategy and methodology to synthesise new organosilicon compounds with Si–N and Si–O bonds efficiently at room temperature conditions.

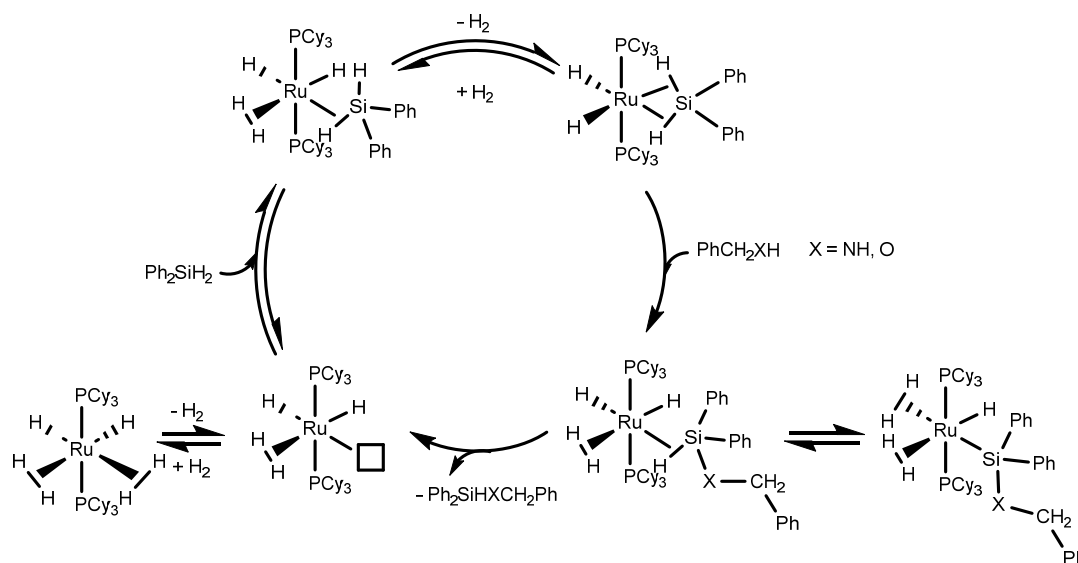


**Scheme 75.** Catalytic dehydrogenative coupling reaction of benzylamine and  $Ph_2SiH_2$ .



**Scheme 76.** Catalytic dehydrogenative coupling reaction of benzylalcohol and  $\text{Ph}_2\text{SiH}_2$ .

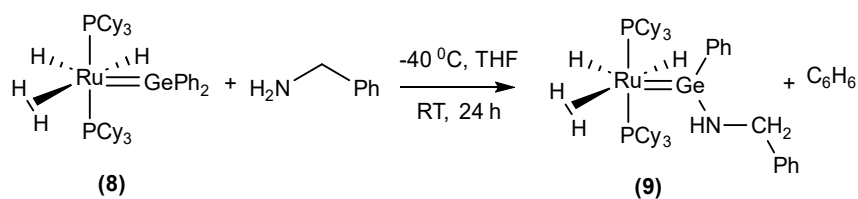
These stoichiometric reactions with benzylamine and alcohol demonstrated the electrophilic nature of silicon in the ruthenium *bis*- $\sigma$ -Si-H complex **3**. The similar results and spectroscopic signals across the series of these new ruthenium complexes **5** and **6** implies they have analogous molecular structure and probably similar mechanism for catalysis. Based on the above discussed reactivity studies between the ruthenium precursor, silane, amine/alcohol substrates, a mechanistic pathway for the dehydrogenative coupling catalysis is proposed as shown below in Scheme 77.



**Scheme 77.** Proposed mechanism for catalytic dehydrogenative coupling of silanes with amines and alcohols using  $[\text{Ru}(\text{H})_2(\text{H})_2(\text{PCy}_3)_2]$  complex.

The fifth part details the isolation and reactivity studies of a ruthenium germylene complex  $[\text{Ru}(\text{=GePh}_2)(\text{H})_2(\text{H}_2)(\text{PCy}_3)_2]$  (**8**). The germylene complex **8** is shown to undergo a substitution reaction with amines and alcohols, elucidating new amino and alkoxy germylene complexes (**9-13**). The structure of new functionalised germylene complexes is elucidated with the help of NMR spectroscopy, X-ray diffraction and DFT calculation. This study expands the coordination chemistry of ruthenium-germylene species.

This work has undertaken an extensive investigation into the reactivity study of the ruthenium germylene complex  $[\text{Ru}(\text{=GePh}_2)(\text{H})_2(\text{H}_2)(\text{PCy}_3)_2]$  (**8**) formed from  $[\text{RuH}_2(\text{H}_2)_2(\text{PCy}_3)_2]$  and diphenylgermane. Through a scaled-up synthesis and isolation of this key intermediate complex, new reactivity studies of this complex with benzylamine and benzylalcohol have been conducted. The reaction was closely monitored using low-temperature NMR spectroscopic techniques. The new ruthenium germylene complexes (**9-13**) have been characterized by NMR spectroscopy. The molecular structure of aminogermylene complex **9** has been obtained by X-ray analysis.



**Scheme 78.** Synthesis of ruthenium aminogermylene complex.

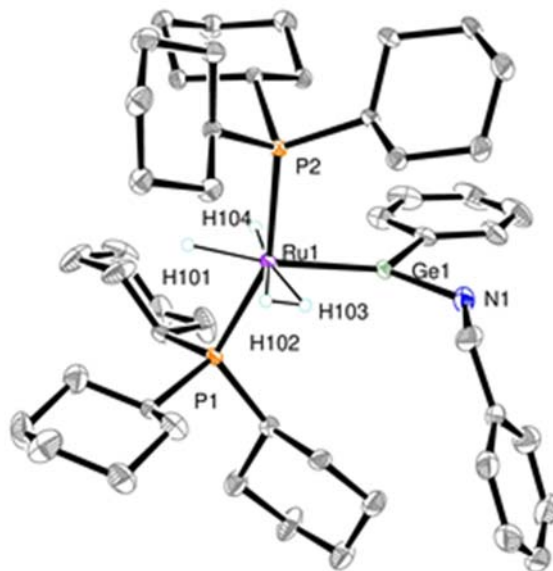
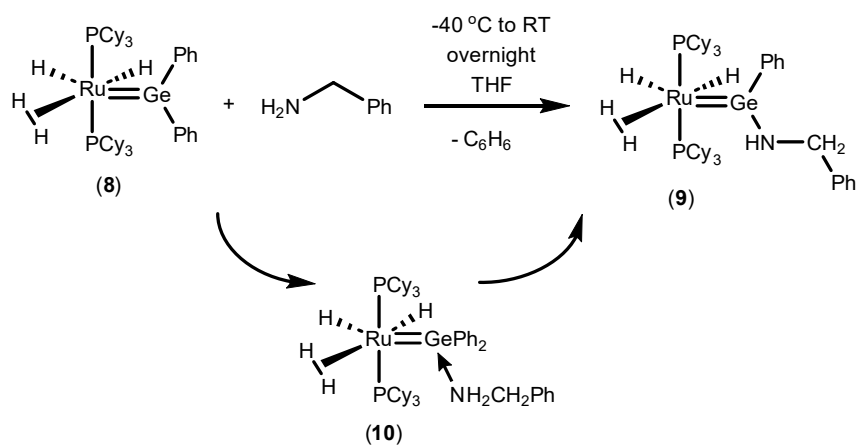
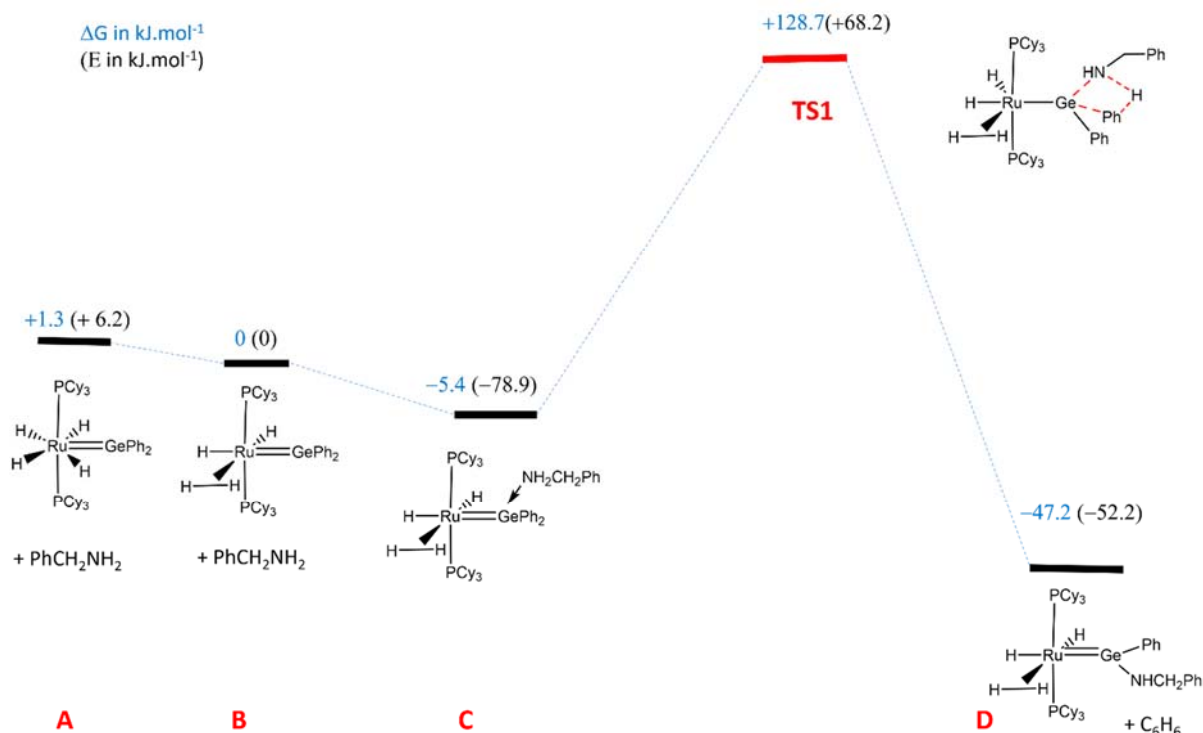


**Figure.32.** X-ray structure of aminogermylene complex **9**.

The Ru–Ge bond length of 2.347 Å along with DFT calculations confirmed the Ru–Ge double bond character, a ruthenium germylene type of coordination. Low  $T_1$  relaxation time values confirmed the presence of dihydrogen ligand in this complex. DFT calculations were performed to figure out the possible intermediates and transition states formed during the reaction between benzylamine and the ruthenium germylene complex. A possible mechanism was proposed based on the calculations and the NMR spectroscopic evidence. The reaction was found to proceed through a complex **10** in which benzylamine nitrogen atom is coordinated to the germanium centre.

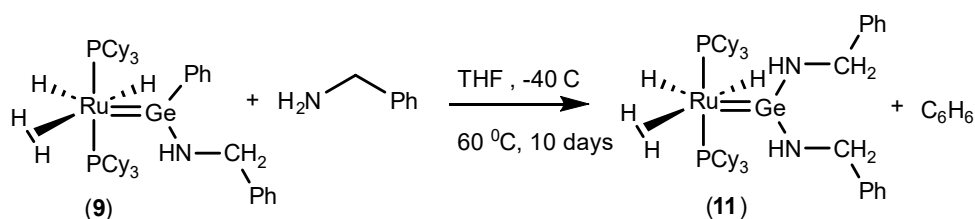


**Scheme 79.** Proposed structure for intermediate complex **10** formed in reaction before aminogermylene **9**.



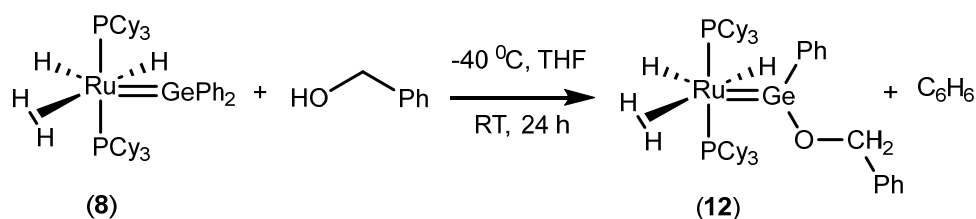
**Scheme 80.** Proposed energy profile for the reaction of benzylamine with ruthenium germylene complex. B3PW91 functional, 6-31G\*\* basis set. Pseudo potential SDDALL for Ru and Ge.

It was found that the aminogermylene complex **9** further reacted with an additional equivalent of benzylamine to form the diaminogermylene complex **11**. It was unfortunate that decomposition of the reaction occurred in parallel due to heating reaction conditions, due to an existing competition between the diaminogermylene formation and decomposition reaction. Even though isolation of the product from the reaction mixture containing the liberated byproduct phosphine was not achieved, the diaminogermylene complex **11** was fully characterized using various NMR spectroscopic techniques. This study has successfully demonstrated the stepwise reactivity of the electrophilic germanium centre in **8** with benzylamine to synthesise new amino functionalised ruthenium germylene complexes.

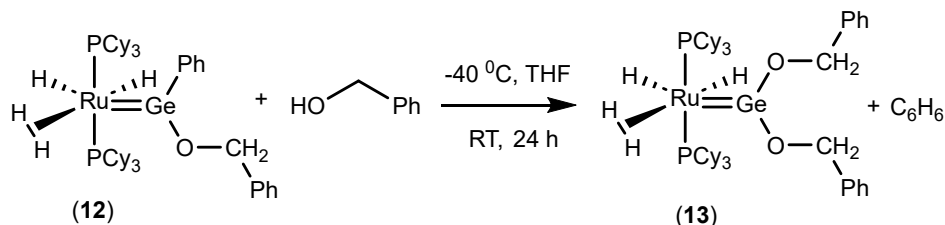


**Scheme 81.** Reaction with the second equivalent of benzylamine

The reaction of benzylalcohol with diphenylgermylene was also investigated and resulted in the formation of the new alkoxygermylene complex **12**. Similarly to the amine reactivity, the addition of the second equivalent of benzylalcohol resulted in the complete transformation to the dialkoxygermylene complex **13**. These new ruthenium alkoxy germylene complexes were also characterised by multinuclear NMR spectroscopy. This reactivity further supported the electrophilic nature of the germanium centre in the ruthenium germylene complex.



**Scheme 82.** The reaction of diphenylgermylene with benzylalcohol

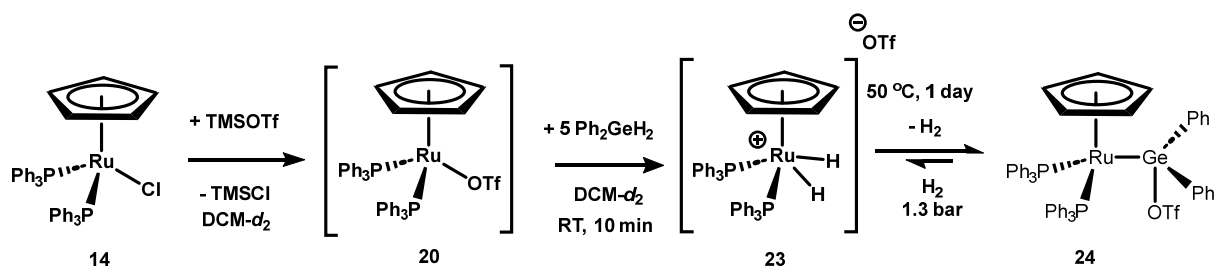


**Scheme 83.** The reaction of alkoxy-germylene with the second equivalent of benzylalcohol

Overall, this work has significantly expanded the chemistry of ruthenium germanium coordinated complexes which paves new paths for applications of these new germylene complexes in future.

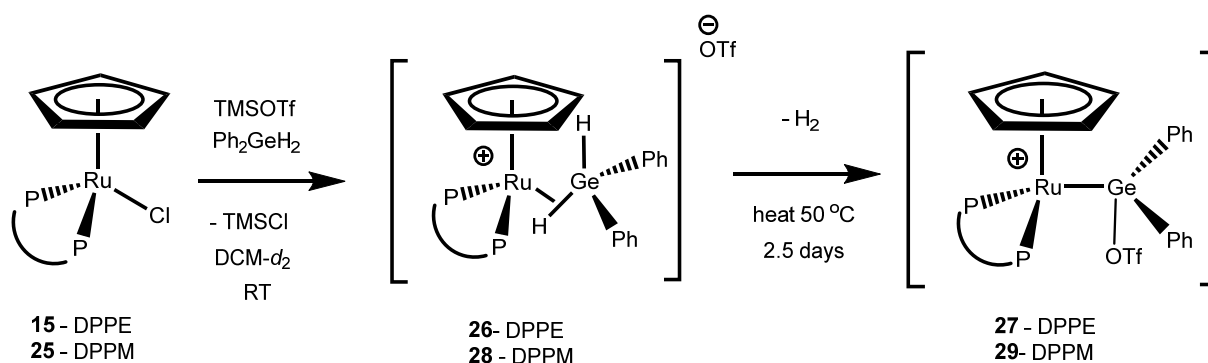
Finally, the sixth part explores the reactivity of cationic ruthenium half-sandwich diphosphine complexes with diphenylgermane. This reveals initial Ge–H bond activation at various coordinatively unsaturated ruthenium complexes, leading to new ruthenium germanium complexes (**24**, **26–29**). A stoichiometric Markonikov hydrogermylation of phenylacetylene was achieved, and the involvement of the new ruthenium germanium complexes and ruthenium vinylidene complexes in the course of the hydrogermylation reaction is described.

This study has successfully investigated the reactivity of  $\text{GePh}_2\text{H}_2$  with a number of half-sandwich ruthenium diphosphine complexes. To examine the interaction of Ge–H bonds to the activated alkyne, ruthenium vinylidene complexes were synthesised and characterized. Extensive investigation into the reactivity of these complexes with diphenylgermane has revealed new insights into the interaction between Ge–H bonds and the metal centre. Further detailed spectroscopic and structural analysis enabled the pathways between diphenyl germane and cationic complexes  $[\text{CpRuP}_2\text{OTf}]$ ,  $\text{P}_2 = (\text{PPh}_3)_2$ , dppe leading to the instantaneous formation of a ruthenium dihydride complex **23** or Ge–H sigma complex **26** to be established. This complex was later found to transform to a germanium-coordinated complex **24**.



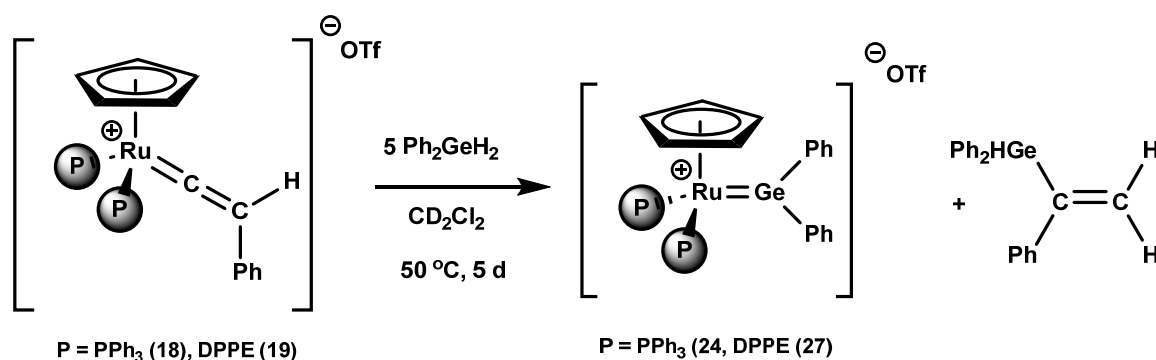
**Scheme 84.** Overall reaction of bis-triphenylphosphine ruthenium complex with TMSOTf and diphenyl germane.

This work has shed light on the mechanism by which the germanium-hydrogen bond is activated at the ruthenium centre. Importantly, bidentate phosphine ligands such as dppe and dppm have shown different reactivity profile compared to *bis*-PPh<sub>3</sub> ligands.



**Scheme 85.** Reactivity of ruthenium bidentate diphosphine complexes with diphenyl germane.

Finally, a detailed spectroscopic analysis of the reaction between the vinylidene complex with excess of diphenylgermane enabled the identification of a hydrogermylated product. Thus, a stoichiometric Markonikov hydrogermylation of phenylacetylene was achieved using the ruthenium vinylidene complexes **18** and **19**.



**Scheme 86.** Reactivity of ruthenium vinylidene complex with diphenyl germane.

This stepwise investigation represents a significant advancement in understanding the mechanism of metal vinylidene complex-mediated, transition metal-catalysed hydrogermylation of alkynes. While catalytic hydrogermylation was not directly accomplished under the reaction conditions examined, the fundamental coordination chemistry principles established here provide a critical foundation for future efforts.

Even though the bonding of the ruthenium  $\sigma$ -germane complexes (**26**, **28**) and germanium-triflate bound complexes (**27**, **29**) were identified and characterised by NMR as discussed, further evidence were required to establish the bonding between ruthenium, germanium and triflate moieties in these complexes. Hence, DFT calculations were carried out to optimize the molecular structures of ruthenium dppe germanium complexes **26** and **27** (Figure 33). The major bond lengths provided insight into the bonding interactions.

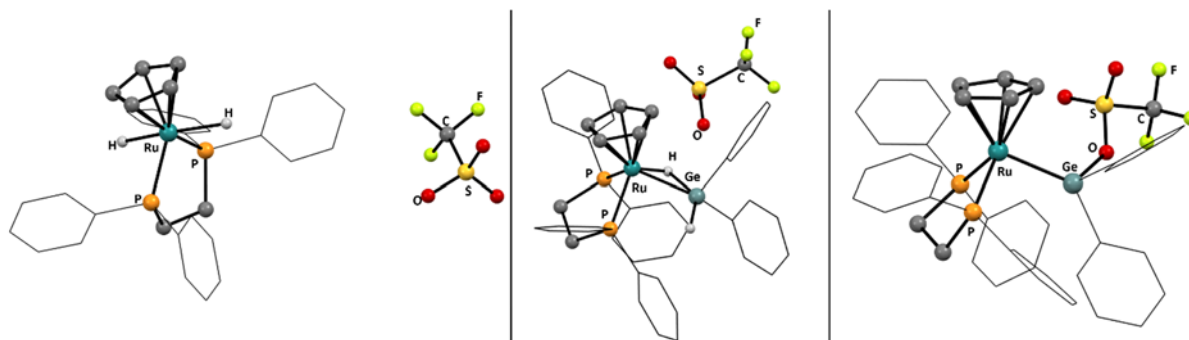


**Figure 33.** DFT calculated molecular structures of complexes  $[CpRu(dppe)H_2][OTf]$  (left),  $[Ru(Cp)(dppe)(\eta\text{-}H_2GePh_2)][(OTf)]$  (**26**) (centre) and  $[Ru(Cp)(dppe)(GePh_2OTf)]$  (**27**) (right). Phenyl groups drawn in wireframe and CH hydrogens omitted for clarity.

In summary, this thesis has significantly expanded the fundamental coordination chemistry of ruthenium complexes with silicon and germanium hydrides through extensive spectroscopic, structural and computational analysis. The insights gained on the activation of Si–H and Ge–H bonds using the reactive ruthenium systems provide a basis for expanding the scope of new catalytic transformations. For instance, the extension of the scope of ruthenium-catalysed hydrosilylation of nitriles and the dehydrogenative coupling is an interesting target for the synthesis of diverse organosilicon compounds at room temperature conditions.

Changing the ligands on the ruthenium centre with different steric and electronic properties can definitely lead to complexes with different properties and reactivities and such influence can be studied on the ability of the metal centre to activate Si–H and Ge–H bonds. Furthermore, new reactivity studies of this electrophilic silicon and germanium centres with other nucleophiles like ketones and ammonia would be interesting. It is important to note that both Si–H and Ge–H bonds were activated using these ruthenium complexes under ambient conditions, still their bonding interactions with similar metal centres was found different, especially in the case of  $[RuH_2(H_2)_2(PCy_3)_2]$  complex, diphenylsilane led to *bis*- $\sigma$ -Si–H complex, meanwhile diphenylgermane led to germylene complex. This difference arises curiosity in bonding of heavier analogues, Sn and Pb coordination to ruthenium centre in these complexes. Also, similar reactivity studies with other Group 14 hydrides such as Sn–H could be interesting to synthesise inaccessible organotin compounds. In the case of ruthenium half-sandwich diphosphine complexes, the Si–H bond activation of hydrosilanes and the addition of the activated alkynes through ruthenium vinylidene complexes is an interesting future study.

## References

- [1] R. H. Crabtree, *The Organometallic Chemistry of the Transition Metals*, John Wiley & Sons, Ltd: Weinheim, **2014**, 224–258. DOI: [10.1002/9781118788301](https://doi.org/10.1002/9781118788301).
- [2] C. Qin, L. Gao, and E. Wang, *Germanium: Inorganic Chemistry*, in *Encyclopedia of Inorganic and Bioinorganic Chemistry*, R.A. Scott (Ed.), **2011**. DOI: [10.1002/9781119951438.eibc0074](https://doi.org/10.1002/9781119951438.eibc0074).
- [3] M. M. Banaszak Holl, D. R. Peck, *Germanium: Organometallic Chemistry*, in *Encyclopedia of Inorganic Chemistry* (R. B. King, R. H. Crabtree, C. M. Lukehart, D. A. Atwood and R. A. Scott, Editors), Wiley, **2009**. DOI: [10.1002/0470862106.ia080.pub2](https://doi.org/10.1002/0470862106.ia080.pub2).
- [4] N. Auner, J. Weis, *Introduction: Organosilicon Chemistry—Recent Highlights in a Fascinating Research Area*, In *Organosilicon Chemistry VI* (N. Auner and J. Weis, Editors); John Wiley & Sons, Ltd: Weinheim, **2008**. DOI: [10.1002/9783527618224.ch](https://doi.org/10.1002/9783527618224.ch).
- [5] T. Hiyama, M. Minami, A. Mori, *Transition-Metal-Catalyzed Cross-coupling of Organosilicon Compounds*, in

- Organosilicon Chemistry: Novel Approaches and Reactions* (T. Hiyama, M. Oestreich, Editors), John Wiley & Sons, Ltd: Weinheim, **2020**; pp 271–332. DOI: [10.1002/9783527814787.ch9](https://doi.org/10.1002/9783527814787.ch9).
- [6] G. A. Harvey, T. J. Lash, J. R. Rawls, *Outgassing products from orbiter TPS materials*, in *LDEF: 69 Months in Space. Third Post-Retrieval Symposium* (A.L. Levine, Editor), **1995**, pp 13-20. Document ID: [19950017376](https://doi.org/19950017376).
- [7] Z. Li, X. Wang, H. Bai, M. Cao, *Polymers* **2023**, *15*, 543. DOI: [10.3390/polym15030543](https://doi.org/10.3390/polym15030543).
- [8] L. Li, B. Li, J. Dong, J. Zhang, *J. Mater. Chem. A Mater.* **2016**, *4*, 13677–13725. DOI: [10.1039/C6TA05441B](https://doi.org/10.1039/C6TA05441B).
- [9] G. C. Chien, J. F. Kuo, C. Y. Chen, *J. Polym. Sci. A Polym. Chem.* **1993**, *31*, 2423–2436. DOI: [10.1002/pola.1993.080311002](https://doi.org/10.1002/pola.1993.080311002).
- [10] G. A. Martin, M. C. Durupty, C. Mirodatos, N. Mouaddib, V. Perrichon, *Stud. Surf. Sci. Catal.* **1991**, *63*, 269–278. DOI: [10.1016/S0167-2991\(08\)64591-7](https://doi.org/10.1016/S0167-2991(08)64591-7).
- [11] E. L. Margelefsky, R. K. Zeidan, M. E. Davis, *Chem. Soc. Rev.* **2008**, *37*, 1118–1126. DOI: [10.1039/B710334B](https://doi.org/10.1039/B710334B).
- [12] J. M. Antonucci, S. H. Dickens, B. O. Fowler, H. H. K. Xu, W. G. McDonough, *J. Res. Natl. Inst. Stand. Technol.* **2005**, *110*, 541. DOI: [10.6028/jres.110.081](https://doi.org/10.6028/jres.110.081).
- [13] V. V. Verkholtantsev, *European Coatings Journal* **2011**, 503–517.
- [14] Z. F. Zhang, F. Babonneau, R. M. Laine, Y. Mu, J. F. Harrod, J. A. Rahn, *J. Am. Ceram. Soc.* **1991**, *74*, 670–673. DOI: [10.1111/j.1151-2916.1991.tb04080.x](https://doi.org/10.1111/j.1151-2916.1991.tb04080.x).
- [15] M. Lalonde, T. H. Chan, *Synthesis (Germany)* **1985**, *1985*, 817–845. DOI: [10.1055/s-1985-31361](https://doi.org/10.1055/s-1985-31361).
- [16] T. Komiyama, Y. Minami, T. Hiyama, *ACS Catal.* **2017**, *7*, 631–651. DOI: [10.1021/acscatal.6b02374](https://doi.org/10.1021/acscatal.6b02374).
- [17] Y. Yamakado, M. Ishiguro, N. Ikeda, H. Yamamoto, *J. Am. Chem. Soc.* **1981**, *103*, 5568–5570. DOI: [10.1021/ja00408a049](https://doi.org/10.1021/ja00408a049).
- [18] Y. Nakao, T. Hiyama, *Chem. Soc. Rev.* **2011**, *40*, 4893–4901. DOI: [10.1039/C1CS15122C](https://doi.org/10.1039/C1CS15122C).
- [19] E. Rosenberg, *Germanium-Containing Compounds, Current Knowledge and Applications*, in *Encyclopedia of Metalloproteins* (R.H. Kretsinger, V.N. Uversky, E.A. Permyakov, Editors) **2013**, 847–855. Springer: New York, NY. DOI: [10.1007/978-1-4614-1533-6\\_582](https://doi.org/10.1007/978-1-4614-1533-6_582).
- [20] K. Kojima, S. Uchida, H. Kinoshita, K. Miura, *Org. Lett.* **2021**, *23*, 4598–4602. DOI: [10.1021/acs.orglett.1c01314](https://doi.org/10.1021/acs.orglett.1c01314).
- [21] T. Nakamura, Y. Shimada, K. Sato, *Bioorganic and Medicinal Organogermanium Chemistry*, in *Organogermanium Compounds: Theory, Experiment, and Applications*, John Wiley & Sons, Ltd: Weinheim, Germany, **2023**, Vol. 2, pp. 839–865. DOI: [10.1002/9781119613466.ch19](https://doi.org/10.1002/9781119613466.ch19).
- [22] V. M. Dembitsky, *Biomedicines* **2023**, *11*, 2698. DOI: [10.3390/biomedicines11102698](https://doi.org/10.3390/biomedicines11102698).
- [23] R. D. Rittinghaus, J. Tremmel, A. Růžička, C. Conrads, P. Albrecht, A. Hoffmann, A. N. Ksiazkiewicz, A. Pich, R. Jambor, S. Herres-Pawlis, *Chem. Eur. J.* **2020**, *26*, 212–221. DOI: [10.1002/chem.201903949](https://doi.org/10.1002/chem.201903949).
- [24] N. Sen, S. Khan, *Chem. Asian. J.* **2021**, *16*, 705–719. DOI: [10.1002/asia.202100038](https://doi.org/10.1002/asia.202100038).
- [25] R. Dasgupta, S. Das, S. Hiwase, S. K. Pati, S. Khan, *Organometallics* **2019**, *38*, 1429–1435. DOI: [10.1021/acs.organomet.8b00673](https://doi.org/10.1021/acs.organomet.8b00673).
- [26] S. Sinhababu, D. Singh, M. K. Sharma, R. K. Siwatch, P. Mahawar, S. Nagendran, *Dalton Trans.* **2019**, *48*, 4094–4100. DOI: [10.1039/C8DT05121F](https://doi.org/10.1039/C8DT05121F).
- [27] T. J. Hadlington, C. E. Kefalidis, L. Maron, C. Jones, *ACS Catal.* **2017**, *7*, 1853–1859. DOI: [10.1021/acscatal.6b03306](https://doi.org/10.1021/acscatal.6b03306).
- [28] E. Fritz-Langhals, *Reactions* **2021**, *2*, 442–456. DOI: [10.3390/reactions2040028](https://doi.org/10.3390/reactions2040028).
- [29] J. Baumgartner, C. Marschner, *Rev. Inorg. Chem.* **2014**, *34*, 119–152. DOI: [10.1515/revic-2013-0014](https://doi.org/10.1515/revic-2013-0014).
- [30] L. D. Almeida, H. Wang, K. Junge, X. Cui, M. Beller, *Angew. Chem. Int. Ed.* **2021**, *60*, 550–565. DOI: [10.1002/anie.202008729](https://doi.org/10.1002/anie.202008729).
- [31] J. Y. Corey, *Chem. Rev.* **2011**, *111*, 863–1071. DOI: [10.1021/cr900359c](https://doi.org/10.1021/cr900359c).
- [32] S. Lachaize, S. Sabo-Etienne, *Eur. J. Inorg. Chem.* **2006**, 2115–2127. DOI: [10.1002/ejic.200600151](https://doi.org/10.1002/ejic.200600151).
- [33] G. I. Nikonov, *Adv. Organomet. Chem.*, **2005**, *53*, 217–309. DOI: [10.1016/S0065-3055\(05\)53006-5](https://doi.org/10.1016/S0065-3055(05)53006-5).
- [34] S. Lachaize, S. Sabo-Etienne, *Eur. J. Inorg. Chem.* **2006**, *2006*, 4697–4699. DOI: [10.1002/ejic.200600151](https://doi.org/10.1002/ejic.200600151).
- [35] G. Alcaraz, S. Sabo-Etienne, *Coord. Chem. Rev.* **2008**, *252*, 2395–2409. DOI: [10.1016/j.ccr.2008.02.006](https://doi.org/10.1016/j.ccr.2008.02.006).





**Agustin MORALES**

**ESR15**

**Thesis co-directors**

Dr. Sébastien Bontemps  
Dr. Olivier Baslé

Laboratoire de Chimie de Coordination, Toulouse, France

Prof. Agustí Lledós

Universitat Autònoma de Barcelona, Bellaterra, Spain

**Thesis defense**

Laboratoire de Chimie de Coordination, 15 December 2023



## Single Electron Reduction of NHC-CO<sub>2</sub> and NHC-CO<sub>2</sub>-BR<sub>3</sub> Adducts

### Introduction

The carbon dioxide radical anion [CO<sub>2</sub>]<sup>•-</sup> is a highly reactive species of fundamental and synthetic interest. However, the direct one-electron reduction of CO<sub>2</sub> to generate [CO<sub>2</sub>]<sup>•-</sup> occurs at very negative reduction potentials, which is often a limiting factor for applications. My doctoral work concerns the synthesis of NHC-CO<sub>2</sub> and NHC-CO<sub>2</sub>-BR<sub>3</sub> adducts (BR<sub>3</sub>: borane) and the evaluation of their one-electron reduction chemistry through a combined experimental and theoretical study. Firstly, a brief literature review is given followed by a theoretical study on the one-electron reduction of NHC-CO<sub>2</sub> and NHC-CO<sub>2</sub>-BR<sub>3</sub> adducts with the aim of understanding how these species behave after the addition of one electron. This study would guide us towards the choice of adduct/s that may exhibit most accessible reduction potential for its further synthesis. We show that NHC-CO<sub>2</sub>-BR<sub>3</sub> species undergo single electron reduction at a less negative potential than free CO<sub>2</sub>. A net gain of more than one volt was notably measured with a <sup>Cy</sup>CAAC-CO<sub>2</sub>-B(C<sub>6</sub>F<sub>5</sub>)<sub>3</sub> adduct, which was chemically reduced to afford [CAAC-CO<sub>2</sub>-B(C<sub>6</sub>F<sub>5</sub>)<sub>3</sub>]<sup>•-</sup>. This room temperature stable radical anion was characterized by EPR spectroscopy and by single-crystal X-ray diffraction analysis. A theoretical analysis is presented, where the computational method is initially validated based on previous experimental results, and then various properties related to the one-electron reduction of these adducts are rationalized using quantum chemistry-based tools. Of particular interest, DFT calculations showed that, thanks to the electron withdrawing properties of the Lewis acid, significant unpaired spin density is localised on the carbon atom of the CO<sub>2</sub> moiety. Finally, these species were shown to exhibit analogous reactivity to the carbon dioxide radical anion [CO<sub>2</sub>]<sup>•-</sup> toward DMPO. This work demonstrates the advantage provided by FLP systems in the generation and stabilization of [CO<sub>2</sub>]<sup>•-</sup> like species. For more information about this work, see [1].

### Bibliographic section

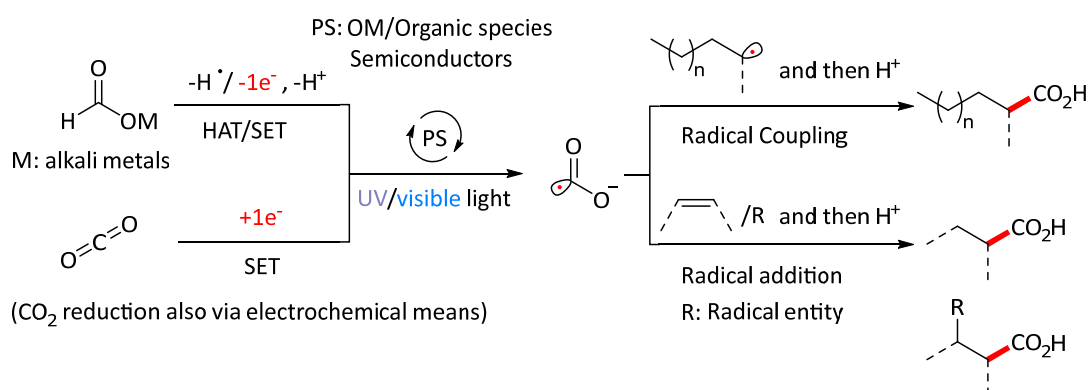
In this first section, the subject of this work will be contextualised with relevant examples reported in the literature. The two pathways for generating the radical anion of CO<sub>2</sub>, [CO<sub>2</sub>]<sup>•-</sup>, will be briefly described. Then, we will provide two key examples of its reactivity towards open-shell and unsaturated species as alkenes. The second part will focus on the one-electron reduction of NHC-CO<sub>2</sub> adducts through electrochemical and chemical means. Finally, the synthesis of NHC-CO<sub>2</sub>-BR<sub>3</sub> adducts reported in the literature will be also summarised.

#### *Generation of CO<sub>2</sub> radical anion and formation of C-C bonds*

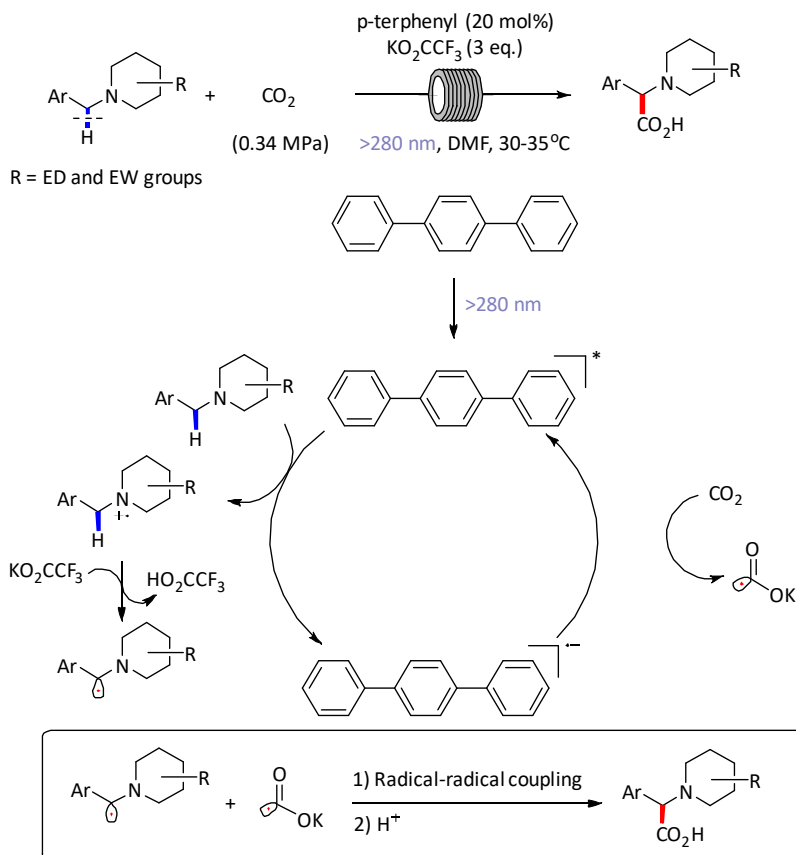
As shown in the diagram below, the generation of the CO<sub>2</sub> radical anion can originate from two main sources: either from CO<sub>2</sub> gas or from a formate salt through electrochemical and photochemical means (on the left, Scheme 1). It has been demonstrated that it can then react either with an open-shell species via radical-radical coupling or with alkenes via radical addition (on the right, Scheme 1).

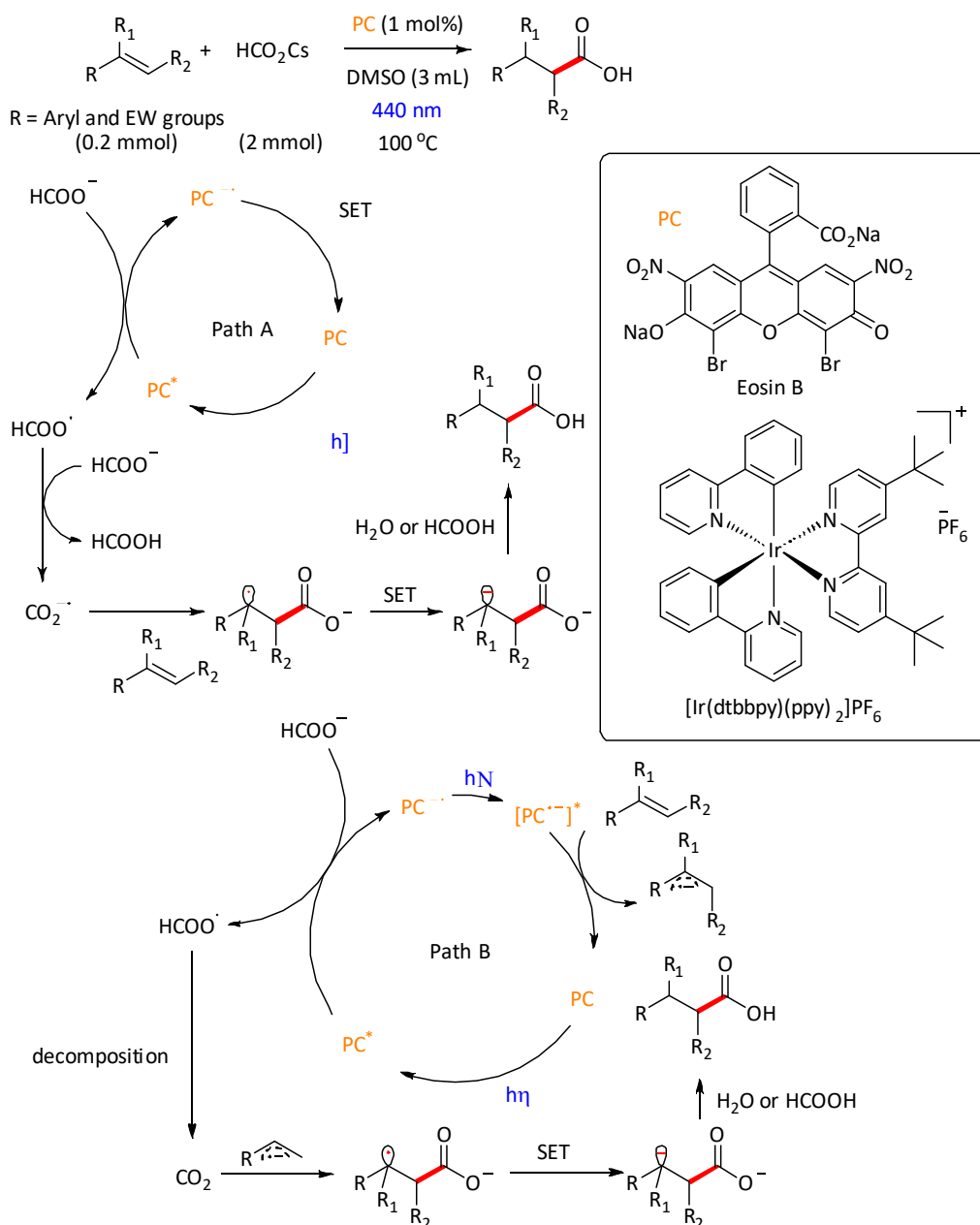
The direct one-electron reduction of carbon dioxide is the most straightforward process to generate the CO<sub>2</sub> radical anion, [CO<sub>2</sub>]<sup>•-</sup>. However, this approach is challenging as it requires particularly high negative potentials,  $E_{\text{red}} = -2.2$  V in DMF and -3 V in CH<sub>3</sub>CN in respect to Fc<sup>+0</sup> redox couple [2-5]. In the literature, the use of organic dye species such as *p*-terphenyl as a photocatalyst to achieve this

transformation using ultraviolet (UV) light has been reported. As a key example, Jamison and collaborators [6] disclosed a photoredox strategy for the synthesis of  $\alpha$ -amino acids in continuous flow under UV light through the carboxylation of the C(sp<sup>3</sup>)-H bond of tertiary benzylamine derivatives (*N*-benzylpiperidine derivatives) in the presence of a base, KCO<sub>2</sub>CF<sub>3</sub>. Open-shell species are generated as follows: upon irradiation of the photocatalyst, its singlet excited state undergoes a reducing quenching with the amine, resulting in the oxidised form of the amine and the reduced photocatalyst. Then, the oxidised amine is deprotonated by a base, producing a carbon-centred radical. After the formation of the carbon dioxide radical anion via one-electron transfer with the reduced form of the photocatalyst, a new C-C bond is formed through radical-radical coupling, ultimately resulting in  $\alpha$ -amino acids with yields of up to 99% and a regioselectivity of 52:1 in just 10 minutes (Scheme 2).



**Scheme 1.** Generation of CO<sub>2</sub> radical anion [CO<sub>2</sub>]<sup>•-</sup> and its use in C-C bond formation.



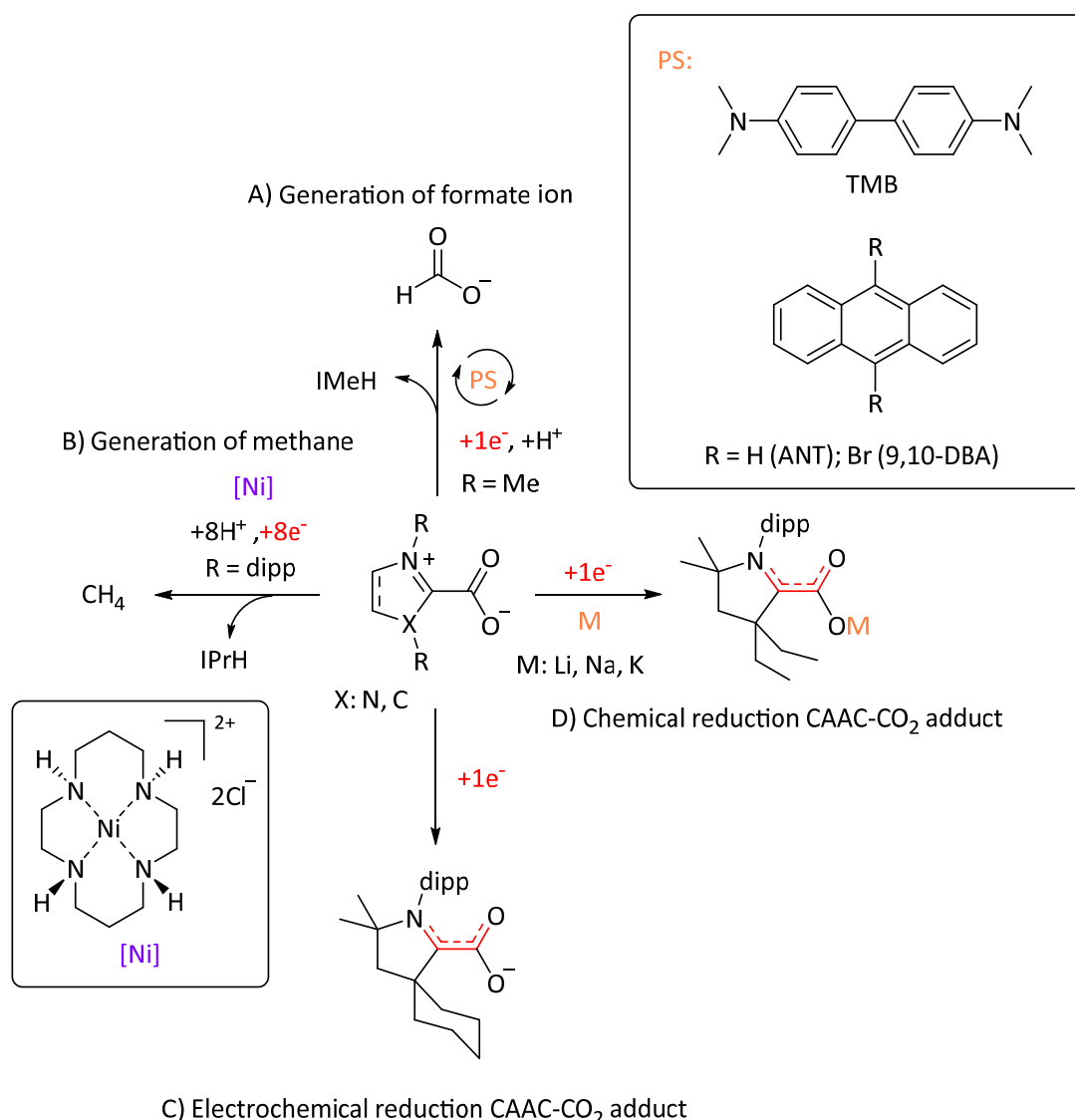
**Scheme 2.** Photoredox activation of carbon dioxide for amino acid synthesis in continuous flow by Jamison's group.**Scheme 3.** Hydrocarboxylation of alkenes derivatives with formate salts catalysed by either an organic or an Ir-based photocatalyst.

Furthermore, formate salts have been used instead of  $CO_2$  in order to avoid highly reducing potentials required for the generation of the  $CO_2$  radical anion. The radical anion of carbon dioxide can be generated through hydrogen atom transfer (HAT) from formate using a suitable HAT agent or by single-electron oxidation. As a key example, Li and colleagues [7] described the  $\beta$ -selective hydrocarboxylation of substituted alkenes using either Eosin B or an iridium-based photocatalyst (Scheme 3). The authors suggested two plausible mechanisms. In strategy A, the excited state of the photocatalyst oxidises the formate salt to form a formyloxyl radical capable of trapping one hydrogen atom from the formate salt and producing  $[CO_2]^{\bullet-}$  and formic acid. Subsequently,  $[CO_2]^{\bullet-}$  undergoes a radical addition to the alkene, resulting in a Giese-type species that it is subsequently reduced. This

latter species is protonated to yield the desired product. In strategy B, the reduced form of the catalyst can be excited again and reduce the alkenes to form an alkene radical anion, which could react with the  $\text{CO}_2$  generated *in situ* from the formate salt. Finally, the resulting functionalized alkene radical anion is reduced and protonated as in strategy A to yield the desired carboxylate product (Scheme 3).

#### Reduction of NHC- $\text{CO}_2$ adducts

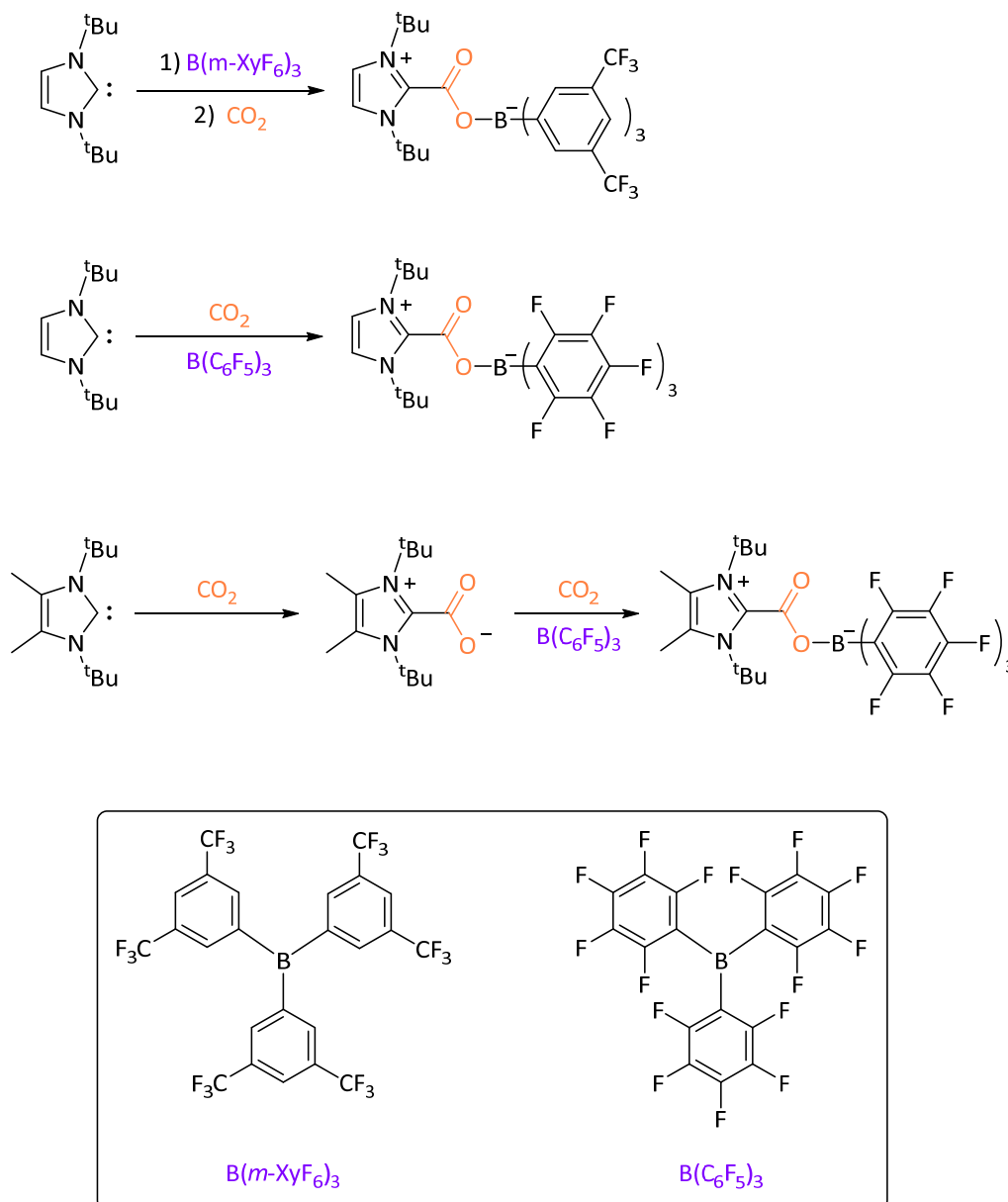
Examples of one-electron reduction in NHC- $\text{CO}_2$  adducts is rather limited in the literature (Scheme 4). During the reduction of these adducts, it can lead to the formation of formate (Scheme 4A) and methane (Scheme 4B) in the presence of a proton source. In the absence of any proton source, its radical anion (product of one-electron reduction) is generated either through electrochemical (Scheme 4C) or chemical means (Scheme 4D).



**Scheme 4.** Reduction of NHC- $\text{CO}_2$ -based adducts. A) Generation of the formate ion. B) Generation of methane. C) Electrochemical reduction of CAAC- $\text{CO}_2$  adduct. D) Chemical reduction of CAAC- $\text{CO}_2$  adduct.

#### Synthesis of NHC- $\text{CO}_2$ - $\text{BR}_3$ adducts.

Over the past decade, Tamm and colleagues [8,9] have described three examples of NHC-CO<sub>2</sub>-BR<sub>3</sub> adducts in the context of Frustrated Lewis Pair (FLP) chemistry. These systems consist of two components: a classic bulky diamino-carbene with *tert*-butyl groups as *N*-substituents and a bulky boron-based Lewis acid, tris[3,5-bis(trifluoromethyl)phenyl]borane (abbreviated as B(*m*-XyF<sub>6</sub>)<sub>3</sub>) and tris(pentafluorophenyl)borane, B(C<sub>6</sub>F<sub>5</sub>)<sub>3</sub>).



**Scheme 5.** Synthesis of NHC-CO<sub>2</sub>-BR<sub>3</sub> adducts.

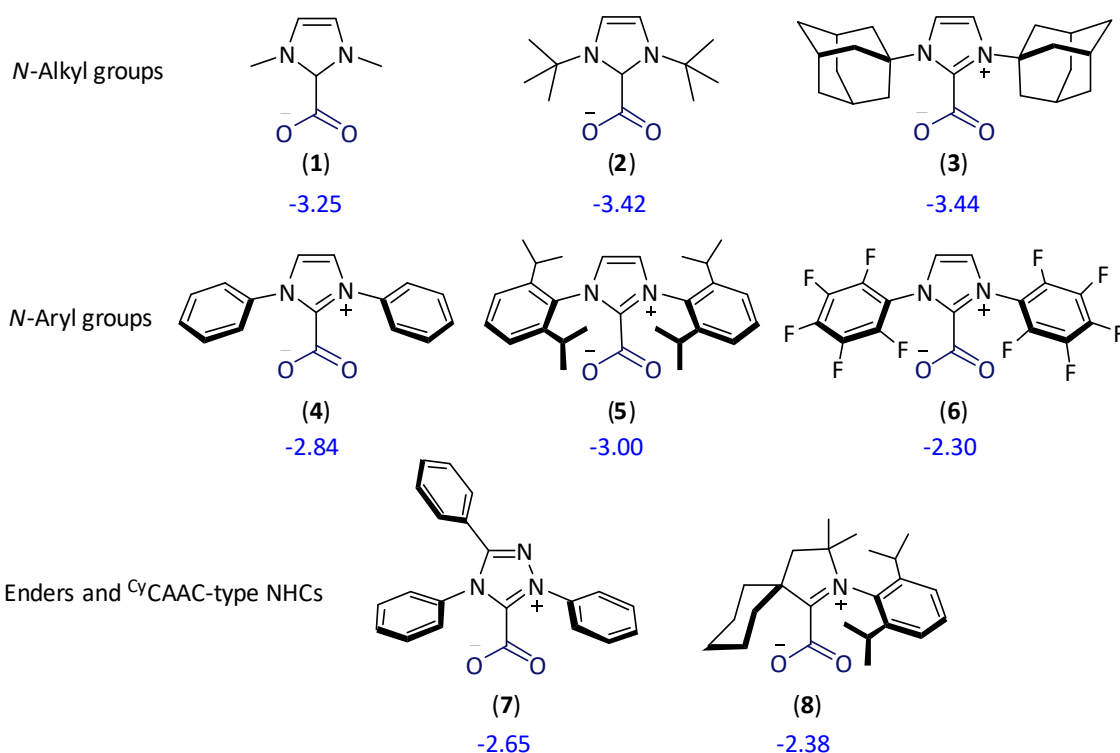
### Computational study on reduction potentials of NHC-CO<sub>2</sub> and NHC-CO<sub>2</sub>-BR<sub>3</sub> adducts.

Firstly, we investigated the influence of the *N*-Heterocyclic Carbenes (NHC) in the one-electron reduction of NHC-CO<sub>2</sub> adducts. In this work, we aimed to estimate the reduction potential of a collection of NHC-CO<sub>2</sub> adducts bearing different *N*-substituents, as well as other types of NHC-based compounds (**1-8**) (Scheme 6).



Using the "direct approach," the Gibbs energy associated with the one-electron reduction of NHC-CO<sub>2</sub> adducts allowed us to estimate an absolute reduction potential for each adduct. The next step is to refer it to a reference electrode or redox couple. The most commonly used reference electrodes are the Standard Hydrogen Electrode (SHE) and the Saturated Calomel Electrode (SCE). In the literature, the absolute reduction potential of SHE,  $E_{\text{red}}^{\text{SHE}}$ , has been theoretically determined in various ways. However, it can vary from 4.05 V to 4.44 V depending on parameters used, such as the Gibbs energy of H<sup>+</sup> and the surface potential, among others [10-13]. The theoretical reduction potential of SCE depends on SHE, which can complicate the assessment of precise reduction potentials. Therefore, we used the ferrocenium/ferrocene (Fc<sup>+0</sup>) redox couple as a reference as it does not depend on the SHE. The absolute reduction potential used for this redox couple was 4.780 V [14].

In NHC-CO<sub>2</sub> systems where *N*-substituents are alkyl groups such as methyl (**1**), *tert*-butyl (**2**), and adamantyl (**3**), their reduction potential is more negative than the reduction of a free CO<sub>2</sub> molecule (approximately -3 V vs. Fc<sup>+0</sup>). In the case of adducts based on diaminocarbene with aryl derivatives as *N*-substituents (**4-6**, Scheme 6), the reduction potential of these species is more favourable than the reduction potential of the previous NHC-CO<sub>2</sub> adducts (**1-3**, Scheme 6). Only adduct **6** has a reduction potential less negative than in the case of free CO<sub>2</sub>. The use of NHCs with *N*-substituents as aryl groups allowed for more accessible reduction potentials than in the case of adducts with alkyl groups. In other specific cases such as Enders' and <sup>Cy</sup>CAAC carbene adducts, their reduction is more accessible than in the case of free carbon dioxide (Scheme 6).



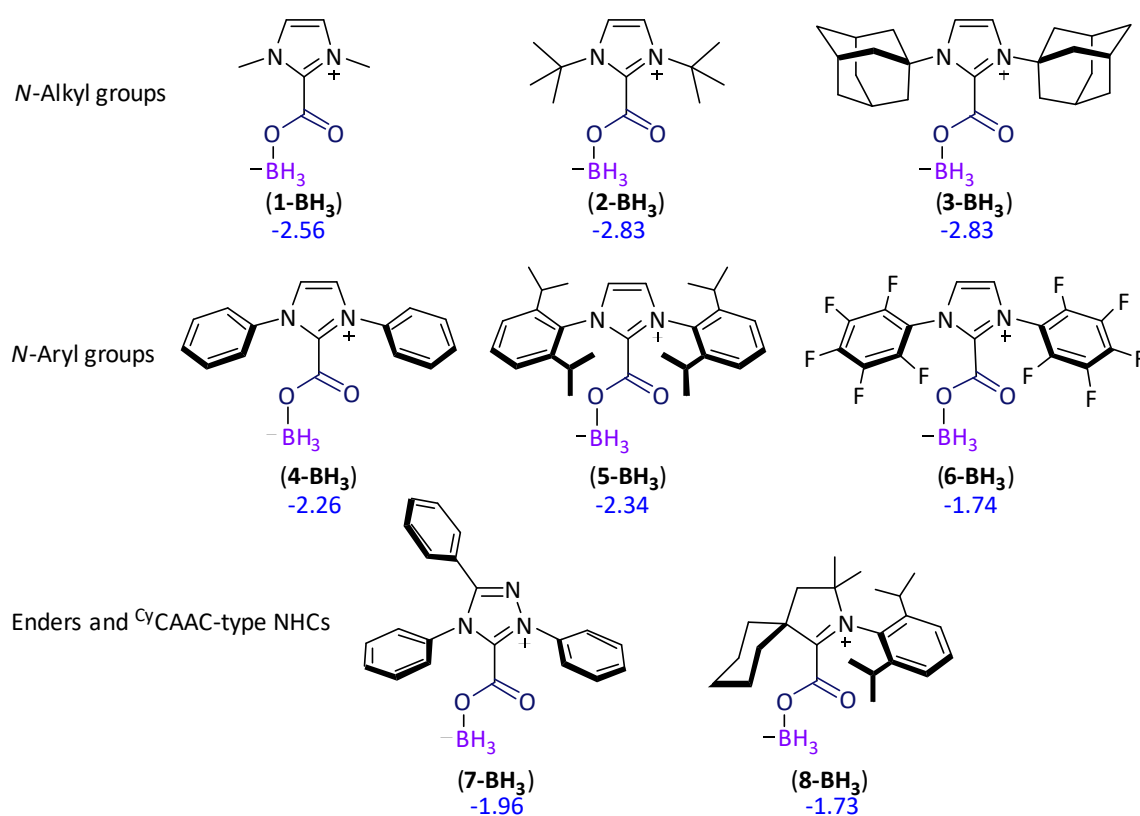
**Scheme 6.** The studied NHC-CO<sub>2</sub> adducts with their calculated theoretical reduction potential in dichloromethane using the M06-2X-D3 functional (in blue). Potentials are expressed in volts (V) in respect to Fc<sup>+0</sup>.

Next, the influence of adding a borane was studied. We wondered if a borane (BR<sub>3</sub>) would facilitate the reduction of NHC-CO<sub>2</sub> adducts to less negative reduction potentials. We considered the use of three different boranes with different Lewis acidities: the simplest borane BH<sub>3</sub> and two more acidic boranes, BCl<sub>3</sub> and B(C<sub>6</sub>F<sub>5</sub>)<sub>3</sub>.

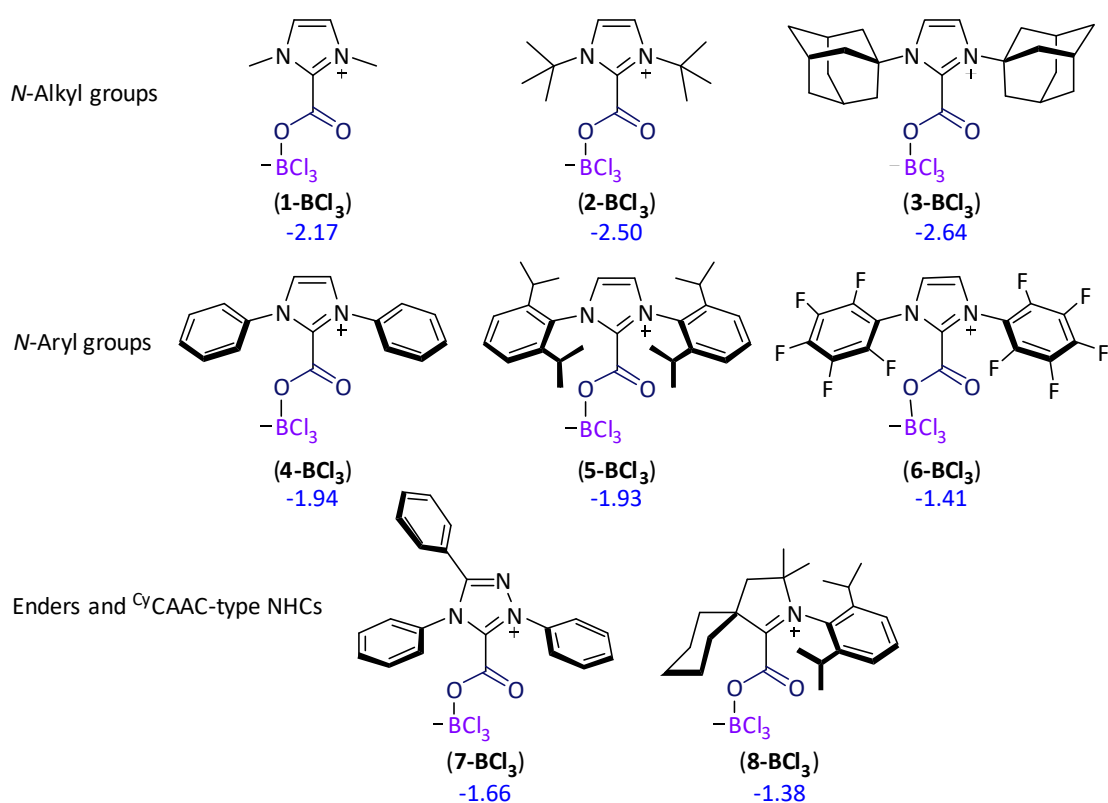
As shown in Scheme 7, the trend of the reduction potential remains unchanged compared to the adducts without borane (**1-8**, Scheme 6). The addition of a borane has a beneficial impact on facilitating the one-electron reduction of NHC-CO<sub>2</sub> adducts (**1-8**, Scheme 6). With the addition of a borane, these adducts ((**1-8**)-BH<sub>3</sub>, Scheme 7) exhibit less negative reduction potentials than NHC-CO<sub>2</sub> adducts (**1-8**, Scheme 6). At this stage, the reduction potential of the adducts (**1-8**)-BH<sub>3</sub> is less negative than in the case of the free CO<sub>2</sub> molecule.

After observing that there is an impact on the reduction potentials of NHC-CO<sub>2</sub>-BR<sub>3</sub> adducts, we also wondered about the impact of the Lewis acidity of the borane on the reduction potentials. The results are shown in Scheme 8. By increasing the Lewis acidity of the borane, we can access even less negative reduction potentials (Scheme 8) than in the case of free CO<sub>2</sub>, NHC-CO<sub>2</sub> adducts, and NHC-CO<sub>2</sub>-BH<sub>3</sub> adducts (Scheme 8).

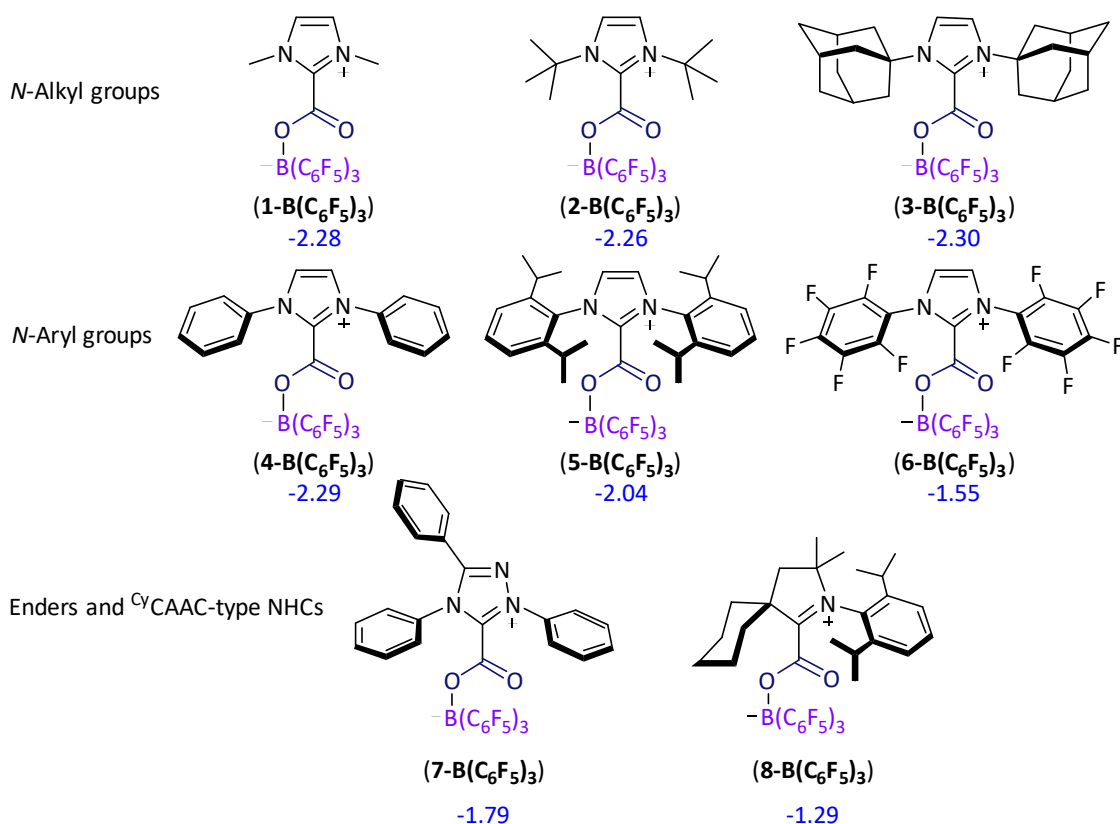
After evaluating NHC-CO<sub>2</sub>-BR<sub>3</sub> adducts by increasing the Lewis acidity of the borane ((**1-8**)-BCl<sub>3</sub>), we were interested in using highly acidic boranes to experimentally synthesise adducts with these properties. According to the literature, there is experimental evidence that NHC-CO<sub>2</sub>-B(C<sub>6</sub>F<sub>5</sub>)<sub>3</sub> adducts can be synthesised with moderate yields. We questioned if these adducts (**1-8**)-B(C<sub>6</sub>F<sub>5</sub>)<sub>3</sub> exhibited similar behaviour to their analogues, (**1-8**)-BCl<sub>3</sub>. The reduction potential of NHC-CO<sub>2</sub>-B(C<sub>6</sub>F<sub>5</sub>)<sub>3</sub> adducts (**1-8**)-B(C<sub>6</sub>F<sub>5</sub>)<sub>3</sub> is slightly lower than the reduction potential of NHC-CO<sub>2</sub>-BCl<sub>3</sub> adducts. Despite this fact, the reduction potential of (**1-8**)-B(C<sub>6</sub>F<sub>5</sub>)<sub>3</sub> is more accessible than in the case of NHC-CO<sub>2</sub> adducts (**1-8**) and the free CO<sub>2</sub> molecule (Scheme 9).



**Scheme 7.** The studied NHC-CO<sub>2</sub>-BH<sub>3</sub> adducts with their calculated theoretical reduction potential in dichloromethane using the M06-2X-D3 functional (in blue). Potentials are expressed in volts (V) in respect to Fc<sup>+0</sup>.



**Scheme 8.** The studied NHC-CO<sub>2</sub>-BCl<sub>3</sub> adducts with their calculated theoretical reduction potential in dichloromethane using the M06-2X-D3 functional (in blue). Potentials are expressed in volts (V) in respect to Fc<sup>+0</sup>.



**Scheme 9.** The studied NHC-CO<sub>2</sub>-B(C<sub>6</sub>F<sub>5</sub>)<sub>3</sub> adducts with their calculated theoretical reduction potential in dichloromethane using the M06-2X-D3 functional (in blue). Potentials are expressed in volts (V) in respect to Fc<sup>+0</sup>.

**Experimental approach to one-electron reduction in NHC-CO<sub>2</sub>-BR<sub>3</sub> adducts.**

We conducted an exploratory study with the ultimate goal of understanding the behaviour of NHC-CO<sub>2</sub>-based species upon the addition of a single electron to avoid the synthesis of a large collection of NHC-CO<sub>2</sub> and NHC-CO<sub>2</sub>-BR<sub>3</sub> adducts. Nevertheless, to validate whether the computational methodology accurately describes reduction in NHC-CO<sub>2</sub> and NHC-CO<sub>2</sub>-BR<sub>3</sub> adducts, a significantly smaller collection of NHC-based adducts was experimentally tested. According to theoretical results, DFT analysis suggests that NHC-CO<sub>2</sub>-BR<sub>3</sub> adducts would result in less negative reduction potentials compared to NHC-CO<sub>2</sub> adducts. According to DFT analysis, the addition of boranes with higher Lewis acidity (such as BCl<sub>3</sub> and B(C<sub>6</sub>F<sub>5</sub>)<sub>3</sub>) should more easily promote one-electron reduction compared to cases where the borane is less acidic (like BH<sub>3</sub>) or absent (NHC-CO<sub>2</sub> adducts).

In the literature, reports have confirmed the experimental isolation of NHC-CO<sub>2</sub>-BR<sub>3</sub> adducts where the NHC and highly acidic borane are sterically hindered, inspired by a Frustrated Lewis Pair (FLP) approach in the presence of CO<sub>2</sub>. Following the work of Tamm [8,9], we considered the synthesis of NHC-CO<sub>2</sub>-B(C<sub>6</sub>F<sub>5</sub>)<sub>3</sub> adducts. To confirm if our theoretical methodology is suitable for predicting reduction potentials in NHC-CO<sub>2</sub> and NHC-CO<sub>2</sub>-BR<sub>3</sub> adducts, regardless of the electronic properties of the NHC, we tested several types of NHC. We synthesised <sup>t</sup>Bu-CO<sub>2</sub>-B(C<sub>6</sub>F<sub>5</sub>)<sub>3</sub> (**2-B(C<sub>6</sub>F<sub>5</sub>)<sub>3</sub>**, previously reported by Tamm [9]) and IAd-CO<sub>2</sub>-B(C<sub>6</sub>F<sub>5</sub>)<sub>3</sub> (**3-B(C<sub>6</sub>F<sub>5</sub>)<sub>3</sub>**), with adamantyl groups as *N*-substituents, IPr-CO<sub>2</sub>-B(C<sub>6</sub>F<sub>5</sub>)<sub>3</sub> (**5-B(C<sub>6</sub>F<sub>5</sub>)<sub>3</sub>**) with substituted aromatic groups as *N*-substituents, and finally, <sup>Cy</sup>CAAC-CO<sub>2</sub>-B(C<sub>6</sub>F<sub>5</sub>)<sub>3</sub> (**8-B(C<sub>6</sub>F<sub>5</sub>)<sub>3</sub>**) inspired by the previous works of Machan and Gilliard (<sup>Cy</sup>CAAC-CO<sub>2</sub>, **8**) [15,16]. This allowed us to test our theoretical methodology in a diverse group of systems.

After the synthesis and characterisation of NHC-CO<sub>2</sub>-B(C<sub>6</sub>F<sub>5</sub>)<sub>3</sub> adducts (**2-**, **3-**, **5-**, **8-B(C<sub>6</sub>F<sub>5</sub>)<sub>3</sub>**), we measured their reduction potential. Measurements were performed by cyclic voltammetry. Due to the stability of the compounds in dichloromethane (NMR spectra were recorded in CH<sub>2</sub>Cl<sub>2</sub>), this solvent was used for measuring the reduction potential of the synthesised adducts.

After defining the experimental conditions, we tested the reproducibility of our system for determining the reduction potential of NHC-CO<sub>2</sub> and NHC-CO<sub>2</sub>-BR<sub>3</sub> adducts. To our knowledge, there is only one example where the reduction potential of NHC-CO<sub>2</sub> adducts has been successfully determined experimentally. Machan, Gilliard, and their colleagues jointly reported the reduction potential of <sup>Cy</sup>CAAC-CO<sub>2</sub> adduct (**8**) as -2.08 V (in CH<sub>3</sub>CN) and -2.15 V (in THF) vs. Fc<sup>+0</sup> [15]. We measured a reduction potential of <sup>Cy</sup>CAAC-CO<sub>2</sub> at -2.13 V vs. Fc<sup>+0</sup> in CH<sub>2</sub>Cl<sub>2</sub>. Next, we measured the reduction potentials of all studied adducts (**2-**, **3-**, **5-**, **8-B(C<sub>6</sub>F<sub>5</sub>)<sub>3</sub>**) (Figure 1).

In the case of adducts with alkyl *N*-substituents, *tert*-butyl (**2-B(C<sub>6</sub>F<sub>5</sub>)<sub>3</sub>**) and adamantyl (**3-B(C<sub>6</sub>F<sub>5</sub>)<sub>3</sub>**), an irreversible behaviour with a reduction potential at -2.30 V (**2-B(C<sub>6</sub>F<sub>5</sub>)<sub>3</sub>**) and -2.44 V (**3-B(C<sub>6</sub>F<sub>5</sub>)<sub>3</sub>**) vs. Fc<sup>+0</sup>, respectively, was observed. This may indicate a potential instability of the monoreduced NHC-CO<sub>2</sub>-B(C<sub>6</sub>F<sub>5</sub>)<sub>3</sub> generated. For the compound **5-B(C<sub>6</sub>F<sub>5</sub>)<sub>3</sub>**, which has aryl derivatives as *N*-substituents, its reduction potential is -2.08 V vs. Fc<sup>+0</sup> (Figure 1, brown curve). It is slightly less negative than in the previous cases (**2-** and **3-B(C<sub>6</sub>F<sub>5</sub>)<sub>3</sub>**). Finally, the compound **8-B(C<sub>6</sub>F<sub>5</sub>)<sub>3</sub>**, with the NHC moiety based on CAAC exhibits a "duck-shaped" curve associated with a perfectly reversible process. The reduction potential of this adduct was determined to be -1.34 V vs. Fc<sup>+0</sup>. Among all synthesised adducts, **8-B(C<sub>6</sub>F<sub>5</sub>)<sub>3</sub>** presented the most accessible reduction potential. In this example, one-electron reduction is more favourable than in other synthesised adducts (**8**, **2-**, **3-**, **5-B(C<sub>6</sub>F<sub>5</sub>)<sub>3</sub>**). As predicted by our preliminary theoretical studies, the presence of B(C<sub>6</sub>F<sub>5</sub>)<sub>3</sub> in a NHC-CO<sub>2</sub>-B(C<sub>6</sub>F<sub>5</sub>)<sub>3</sub> adduct enable the

assessment of less negative reduction potentials. For example, the addition of  $B(C_6F_5)_3$  to the  $^{Cy}CAAC-CO_2$  adduct (**8**) results in a difference of 0.79 V compared to adduct **8**.

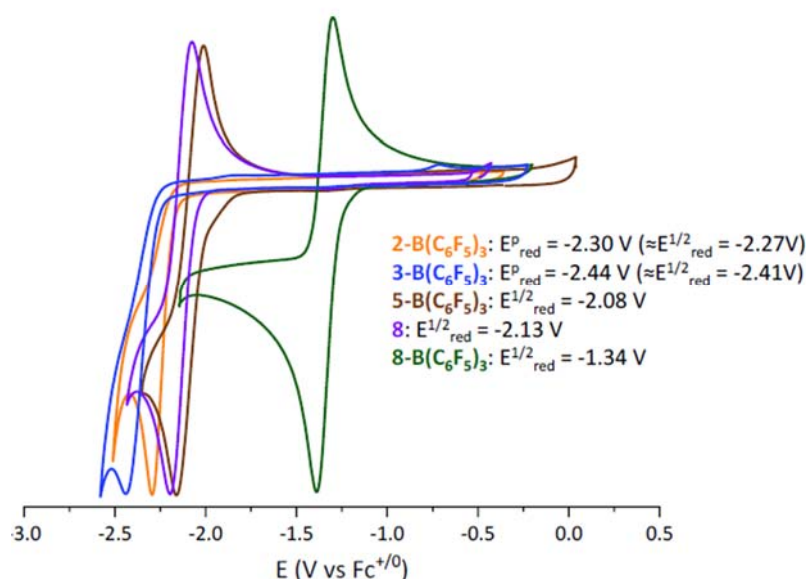


**Figure 1.** Determination by voltammetry of the reduction potentials of the adducts **2-**, **3-**, **5-**, **8-B(C<sub>6</sub>F<sub>5</sub>)<sub>3</sub>** in  $CH_2Cl_2$  in respect to  $Fc^{+/0}$ .

We also considered the formation of the corresponding monoreduced species by chemical means. To our knowledge, only the groups of Machan and Gilliard have jointly reported the one-electron reduction of NHC- $CO_2$  adducts by chemical means.

Until now, chemical reduction of NHC- $CO_2$ - $B(C_6F_5)_3$  adducts has not been reported in the literature. In our study, chemical reactions were conducted at room temperature in THF using a stoichiometric amount of  $KC_8$ , the reducing agent to avoid the possibility of forming dianionic species. Potassium graphite ( $KC_8$ ) is a powerful reducing agent capable of reducing systems with low reduction potentials to -2.73 V vs. SCE in THF (-3.29 V vs.  $Fc^{+/0}$ ) [17,18]. Therefore, the reduction of the studied adducts (**2-**, **3-**, **5-**, **8-B(C<sub>6</sub>F<sub>5</sub>)<sub>3</sub>**) is thermodynamically favourable using  $KC_8$ .

In the case of **2-** and **3-B(C<sub>6</sub>F<sub>5</sub>)<sub>3</sub>**, no colour change was observed 10 minutes after the addition of  $KC_8$ . The transparent solution turned into a black heterogeneous mixture after 12 hours. In contrast, marked colour changes were observed for initially colourless solutions of **5-** or **8-B(C<sub>6</sub>F<sub>5</sub>)<sub>3</sub>** after the addition of the reducing agent. The adduct [**8-B(C<sub>6</sub>F<sub>5</sub>)<sub>3</sub>(K)**]<sup>•</sup> was isolated by recrystallisation from a saturated solution of THF-pentane at -37 °C, yielding orange crystals suitable for X-ray diffraction analysis.

In the case of [**8-B(C<sub>6</sub>F<sub>5</sub>)<sub>3</sub>(K)**]<sup>•</sup>, the  $^{Cy}CAAC$  part is completely planar (0.1°) with respect to the  $CO_2$  moiety, unlike its neutral form (**8-B(C<sub>6</sub>F<sub>5</sub>)<sub>3</sub>**) (79.2°). After reduction, the carbon atom of  $CO_2$  exhibits a closer  $sp^2$  hybridisation than in its neutral form. Additionally, the C-O bonds are elongated, while the C-C bond between the NHC part and the  $CO_2$  moiety is shortened. The potassium cation coordinates to the terminal oxygen of the  $CO_2$  moiety and interacts with the aromatic  $\pi$  system and two THF molecules. However, despite several attempts, the isolation of the adduct [**5-B(C<sub>6</sub>F<sub>5</sub>)<sub>3</sub>(K)**]<sup>•</sup> in its crystalline form was unsuccessful.

To prove the formation and electronic structure of the resulting monoreduced NHC-based systems, Continuous-Wave X-band Electron Paramagnetic Resonance (CW-EPR) spectroscopy was

performed in diluted THF solutions at room temperature. As expected, no signal was observed following the reduction of **2-B(C<sub>6</sub>F<sub>5</sub>)<sub>3</sub>** adducts (Figure 2), as previously indicated; no signal was observed. The irreversibility in the CV curves is related to the instability of monoreduced forms during reduction. Despite several attempts, this might explain the difficulty in measuring an EPR signal for the monoreduced adducts, **[2-B(C<sub>6</sub>F<sub>5</sub>)<sub>3</sub>(K)]<sup>•</sup>** and **[3-B(C<sub>6</sub>F<sub>5</sub>)<sub>3</sub>(K)]<sup>•</sup>**, respectively. Regarding the other adducts (**[5-B(C<sub>6</sub>F<sub>5</sub>)<sub>3</sub>(K)]<sup>•</sup>** and **[8-B(C<sub>6</sub>F<sub>5</sub>)<sub>3</sub>(K)]<sup>•</sup>**), an EPR signal was obtained. In the case of monoreduced adducts based on CAAC, **[8(K)]<sup>•</sup>** (Figure 2, violet curve) and **[8-B(C<sub>6</sub>F<sub>5</sub>)<sub>3</sub>(K)]<sup>•</sup>** (Figure 2, green curve), the EPR signal consists of a triplet corresponding to the coupling interaction between the unpaired electron and the nitrogen atom of the CAAC part. Regarding the EPR coupling constant ( $a_N$ ), the addition of B(C<sub>6</sub>F<sub>5</sub>)<sub>3</sub> has a minor effect on this constant.

We also considered the use of a less powerful reducing agent, decamethylcobaltocene (CoCp<sup>\*</sup><sub>2</sub>), which has a less negative reduction potential (-1.94 V vs. Fc<sup>+0</sup> in CH<sub>2</sub>Cl<sub>2</sub>) [18]. Nevertheless, it is still thermodynamically capable of transferring an electron to the adduct **8-B(C<sub>6</sub>F<sub>5</sub>)<sub>3</sub>** (-1.34 V vs. Fc<sup>+0</sup> in CH<sub>2</sub>Cl<sub>2</sub>) and generating the corresponding monoanionic radical, **[8-B(C<sub>6</sub>F<sub>5</sub>)<sub>3</sub>(Co)]<sup>•</sup>**. The EPR experiment showed a very similar signal to the previous measurement using KC<sub>8</sub> as a reducing agent (Figure 2, red curve). The addition of B(C<sub>6</sub>F<sub>5</sub>)<sub>3</sub> allows the use of less strong reducing agents to obtain monoanionic radicals.

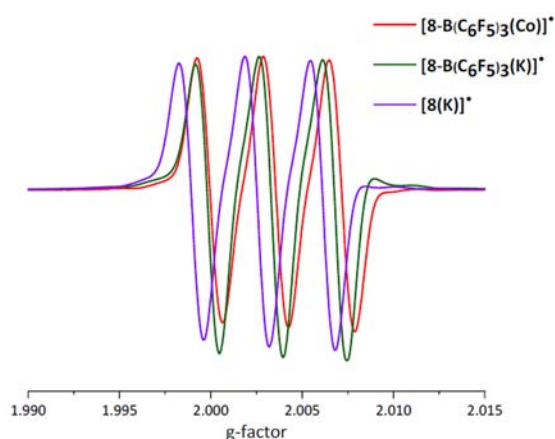


**Figure 2.** Continuous-wave X-band EPR spectra of **[8(K)]<sup>•</sup>** and **[8-B(C<sub>6</sub>F<sub>5</sub>)<sub>3</sub>(K)]<sup>•</sup>** taken in a THF solution, as well as **[8-B(C<sub>6</sub>F<sub>5</sub>)<sub>3</sub>(Co)]<sup>•</sup>** in a CH<sub>2</sub>Cl<sub>2</sub> solution at room temperature.

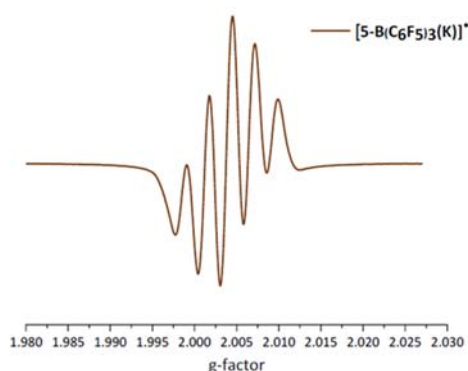


**Figure 3.** Continuous-wave X-band EPR spectrum of **[5-B(C<sub>6</sub>F<sub>5</sub>)<sub>3</sub>(K)]<sup>•</sup>** taken in a THF solution at room temperature.

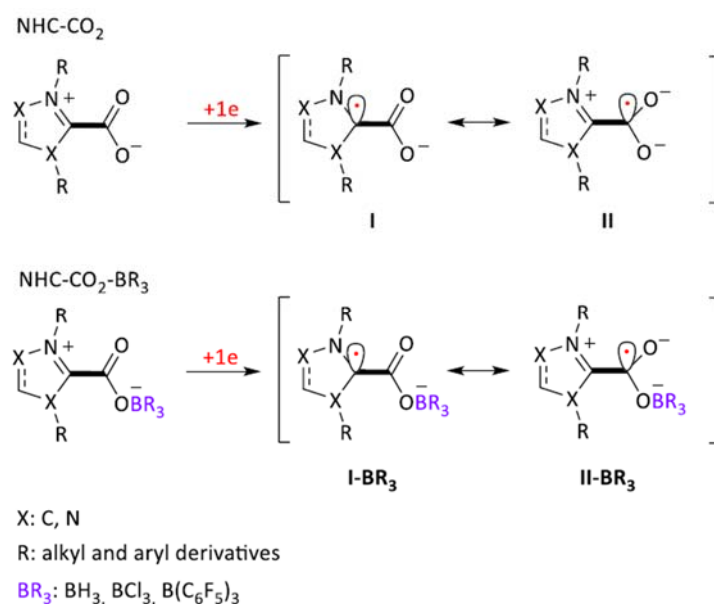
In the case of the adduct based on NHC IPr, **[5-B(C<sub>6</sub>F<sub>5</sub>)<sub>3</sub>(K)]<sup>•</sup>**, the EPR signal exhibited a quintuplet corresponding to the interaction between the unpaired electron and the two equivalent nitrogen

atoms of the NHC part (Figure 3). Regarding the coupling constant, it has the lowest value among all the studied adducts (4.45 G). Following the previous explanation for adducts **[8(K)]<sup>•</sup>** and **[8-B(C<sub>6</sub>F<sub>5</sub>)<sub>3</sub>(K)]<sup>•</sup>**, one can extrapolate that the spin density at the carbene carbon decreases with the addition of borane and the change in the NHC part. This fact could allow the localisation of spin density at the carbon of the CO<sub>2</sub> moiety.

### Theoretical analysis of the one-electron reduction of NHC-CO<sub>2</sub> and NHC-CO<sub>2</sub>-BR<sub>3</sub> adducts.

Finally, we evaluated other parameters of interest using DFT-based tools that would ultimately allow us to rationalise the behaviour of these adducts after their one-electron reduction after the validation of the computational methodology. Among these parameters, we can highlight the distribution of spin density in the one-electron-reduced NHC-CO<sub>2</sub> and NHC-CO<sub>2</sub>-BR<sub>3</sub> adducts, particularly at the carbon of the CO<sub>2</sub> moiety and the orbital description of these adducts in their neutral and one-electron-reduced forms, among others. In this summary, we will only address the spin density distribution.

In addition to determining the reduction potentials of NHC-CO<sub>2</sub> and NHC-CO<sub>2</sub>-BR<sub>3</sub> adducts, we investigated whether their one-electron-reduced species mimic the behaviour of the CO<sub>2</sub> radical anion. For this reason, we studied how the spin density (additional electron) is localised in their one-electron-reduced species. During the reduction of NHC-CO<sub>2</sub> adducts, the additional electron will likely be localised in the vacant *p*-orbital of the carbene carbon atom (I, Scheme 10). Through resonance, some of the spin density could also reside at the carbon of the CO<sub>2</sub> group (II). We wondered if the addition of a Lewis acid enhances the spin density at the carbon of the CO<sub>2</sub> group (II-BR<sub>3</sub>, Scheme 10).



**Scheme 10.** Resonance structures in the monoreduced form of NHC-CO<sub>2</sub> and NHC-CO<sub>2</sub>-BR<sub>3</sub>.

According to the computational analysis, their reduced forms in the absence of a highly acidic borane exhibit more than half of the total spin density localized in the carbene carbon, between 0.56 and 0.66. The common feature for all NHC-CO<sub>2</sub> adducts is that none of them displays spin density at the carbon of the CO<sub>2</sub> group. In comparison with the free CO<sub>2</sub> radical anion, the one-electron-reduced

NHC-CO<sub>2</sub> adducts seem to be far from reproducing the spin density distribution of the free CO<sub>2</sub> radical anion.

In the case of one-electron-reduced NHC-CO<sub>2</sub>-BH<sub>3</sub> adducts, the addition of BH<sub>3</sub> does not significantly alter the spin density at the carbon of the CO<sub>2</sub> moiety. Using more acidic Lewis acids such as BCl<sub>3</sub> or B(C<sub>6</sub>F<sub>5</sub>)<sub>3</sub>, we observed that spin density can also reside at the carbon of the CO<sub>2</sub> group but with a greater effect. The use of more acidic boranes, such as BCl<sub>3</sub> and B(C<sub>6</sub>F<sub>5</sub>)<sub>3</sub>, has a beneficial effect on the spin density at the CO<sub>2</sub> group. Among all the studied one-electron-reduced NHC-CO<sub>2</sub>-BR<sub>3</sub> compounds, [5-B(C<sub>6</sub>F<sub>5</sub>)<sub>3</sub>]<sup>•-</sup> has the highest spin density at the carbon of the CO<sub>2</sub> moiety (0.42).

The accessible reduction potentials found for NHC-CO<sub>2</sub>-BR<sub>3</sub> adducts allow the use of milder conditions to generate their reduced form than in the case of CO<sub>2</sub>. Furthermore, the presence of spin density on the carbon atom of the CO<sub>2</sub> moiety in their reduced form is also one of the beneficial properties of these molecules that could make them good candidates as C1 synthons to construct new C-C chemical bonds.

## References

- [1] A. Morales, C. Gonçalves, A. Sournia-Saquet, L. Vendier, A. Lledós, O. Baslé, S. Bontemps, *Chem. Sci.* **2024**. DOI: [10.1039.D3SC06325A](https://doi.org/10.1039/D3SC06325A).
- [2] W. H. Koppenol, J. D. Rush, *J. Phys. Chem.* **1987**, 4429–4430. DOI: [10.1021/j100300a045](https://doi.org/10.1021/j100300a045).
- [3] E. Lamy, L. Nadjo, J. M. Saveant, *Electroanal. Chem. Interfacial Electrochem.* **1977**, 78, 403–407. DOI: [10.1016/S0022-0728\(77\)80143-5](https://doi.org/10.1016/S0022-0728(77)80143-5).
- [4] D. C. Grills, Y. Matsubara, Y. Kuwahara, S. R. Golisz, D. A. Kurtz, B. A. Mello, *J. Phys. Chem. Lett.* **2014**, 5, 2033–2038. DOI: [10.1021/jz500759x](https://doi.org/10.1021/jz500759x).
- [5] J. Wu, Y. Huang, W. Ye, Y. Li, *Adv. Sci.* **2017**, 4, 1700194. DOI: [10.1002/advs.201700194](https://doi.org/10.1002/advs.201700194).
- [6] H. Seo, M. H. Katcher, T. F. Jamison, *Nat. Chem.* **2017**, 9, 453–456. DOI: [10.1038/nchem.2690](https://doi.org/10.1038/nchem.2690).
- [7] Y. Huang, J. Hou, L. W. Zhan, Q. Zhang, W. Y. Tang, B. D. Li, *ACS Catal.* **2021**, 11, 15004–15012. DOI: [10.1021/acscatal.1c04684](https://doi.org/10.1021/acscatal.1c04684).
- [8] E. L. Kolychev, T. Bannenberg, M. Freytag, C. G. Daniliuc, P. G. Jones, M. Tamm, *Chem. Eur. J.* **2012**, 18, 16938–16946. DOI: [10.1002/chem.201202840](https://doi.org/10.1002/chem.201202840).
- [9] E. Theuergarten, T. Bannenberg, M. D. Walter, D. Holschumacher, M. Freytag, C. G. Daniliuc, P. G. Jones, M. Tamm, *J. Chem. Soc. Dalton Trans.* **2014**, 43, 1651–1662. DOI: [10.1039/c3dt52742e](https://doi.org/10.1039/c3dt52742e).
- [10] W. R. Fawcett, *Langmuir* **2008**, 24, 9868–9875. DOI: [10.1021/la7038976](https://doi.org/10.1021/la7038976).
- [11] C. P. Kelly, C. J. Cramer, D. G. Truhlar, *J. Phys. Chem. B* **2006**, 110, 16066–16081. DOI: [10.1021/jp063552y](https://doi.org/10.1021/jp063552y).
- [12] C. P. Kelly, C. J. Cramer, D. G. Truhlar, *J. Phys. Chem. B* **2007**, 111, 408–422. DOI: [10.1021/jp065403l](https://doi.org/10.1021/jp065403l).
- [13] A. A. Isse, A. Gennaro, *J. Phys. Chem. B* **2010**, 114, 7894–7899. DOI: [10.1021/jp100402x](https://doi.org/10.1021/jp100402x).
- [14] N. Ree, C. L. Andersen, M. D. Kilde, O. Hammerich, M. B. Nielsen, K. V. Mikkelsen, *Phys. Chem. Chem. Phys.* **2018**, 20, 7438–7446. DOI: [10.1039/C7CP08687C](https://doi.org/10.1039/C7CP08687C).
- [15] L. E. Lieske, L. A. Freeman, G. Wang, D. A. Dickie, R. J. Gilliard, C. W. Machan, *Chem. Eur. J.* **2019**, 25, 6098–6101. DOI: [10.1002/chem.201900316](https://doi.org/10.1002/chem.201900316).
- [16] L. A. Freeman, A. D. Obi, H. R. Machost, A. Molino, A. W. Nichols, D. A. Dickie, D. J. D. Wilson, C. W. Machan, R. J. Gilliard, *Chem. Sci.* **2021**, 12, 3544–3550. DOI: [10.1039/D0SC06851A](https://doi.org/10.1039/D0SC06851A).
- [17] L. B. Ebert, D. R. Mills, J. C. Scanlon, *Mater. Res. Bull.* **1982**, 17, 1319–1328. DOI: [10.1016/0025-5408\(82\)90168-4](https://doi.org/10.1016/0025-5408(82)90168-4).
- [18] N. G. Connelly, W. E. Geiger, *Chem. Rev.* **1996**, 96, 877–910. DOI: [10.1021/cr940053x](https://doi.org/10.1021/cr940053x).









UNIVERSITY  
*of York*



UNIVERSITATEA DIN  
**BUCUREȘTI**  
VERITATE ET SAPIENTIA



UNIVERSITÄT  
LEIPZIG



Danmarks  
Tekniske  
Universitet



UNIVERSITAT  
ROVIRA I VIRGILI



UNIVERSITÉ  
TOULOUSE III  
PAUL SABATIER



TOULOUSE  
**INP**



A Bluestar Company

**tecnal:a**

MEMBER OF BASQUE RESEARCH  
& TECHNOLOGY ALLIANCE



**BASF**

We create chemistry



**Henkel**



**Italmatch Chemicals**



Johnson Matthey



**SOLVAY**

PROGRESS BEYOND

The CCIMC beneficiaries and partners